



Grant Agreement No.: 226479

SafeLand

Living with landslide risk in Europe: Assessment, effects of global change, and risk management strategies

7th Framework Programme
Cooperation Theme 6 Environment (including climate change)
Sub-Activity 6.1.3 Natural Hazards

Deliverable 1.2

Geomechanical modelling of slope deformation and failure processes driven by climatic factors: shallow landslides, deep landslides and debris flows

Work Package 1.2 – Geomechanical analysis of weather-induced triggering processes

Deliverable/Work Package Leader: AMRA

December, 2010

Deliverable Responsible	Controlled by	Date
AMRA	ETHZ	2010-12-22



SUMMARY

This Deliverable is aimed to provide a general framework of the relations between weather and slope behaviour, taking into account the very different situations existing in Europe, regarding both the nature of soils and the climatic features of the territory, and focusing on the main mechanisms which can lead to slope instability. In particular, the role of both precipitations and snow-melting on the stability of either coarse-grained or fine-grained soils will be considered. Based on such a knowledge, methods and criteria for prediction of weather-induced landslides are reported.

CONTRIBUTORS

Lead partner responsible for the deliverable:

[AMRA]

Deliverable prepared by:

L. Picarelli

L. Olivares

L. Comegna

E. Damiano

G. Rianna

Partner responsible for quality control:

[ETHZ]

Deliverable reviewed by:

S. Springman

L. Seward

Other contributors:

[CNRS]

[EPFL]

[FUNAB]

[GIR]

[UNISA]

[UPC]

[ICG]

CONTENTS

1. Foreword.....	5
2. Mechanisms and classification of weather-induced landslides.	6
2.1 Examples of weather-induced landslides in Europe	11
3. Weather impact on the stability of slopes (rainfall, snowmelting, and potential role of climate changes).....	27
3.1 Experience gathered through well-monitored natural and engineered slopes	27
3.1.1 Failure mechanisms of landslides in granular soils	28
3.1.1.1 Cases of landslides in pyroclastic soils.....	31
3.1.1.1.1 The case of Pizzo d'Alvano landslides	37
3.1.1.2 A landslide in weathered gneissic soils.....	43
3.1.2 Failure mechanisms of landslides in fine-grained soils	48
3.1.2.1 Cases of slides.....	52
3.1.2.2 Cases of earthflows	57
3.2 Experience obtained through physical modelling.....	62
3.2.1 Experience on granular soils gathered through small scale physical modelling	62
3.2.1.1 Experiments performed on pyroclastic soils.....	13
3.2.2 Experience gathered through full-scale physical modelling	87
3.3 General considerations about the mechanical effects of weather on the behaviour of slopes	97
4. Geomechanical modelling of weather effects	99
4.1 Modelling of rainfall effects	99
4.1.1 Material modelling.....	99
4.1.1.1 Soil properties	99
4.1.1.1.1 Pyroclastic soils.....	99
4.1.1.1.2 Clays.....	106
4.1.1.1.2.1 Fissured clays	106
4.1.1.1.2.2 Structurally complex formations.....	107
4.1.1.2 Material Models	114
4.1.1.2.1 Constitutive models in Geomechanics	114
4.1.1.2.1.1 Introduction	114
4.1.1.2.1.2 Generalized plasticity theory: fundamentals and the basic model for sands.....	116
4.1.1.2.1.3 Extension to collapsible soils	119
4.1.1.2.1.4 A state parameter based generalized plasticity model	122
4.1.1.2.1.5 An extension for unsaturated soils	124

4.1.1.2.2	Modelling soil instability and landslide triggering processes.....	129
4.1.1.2.2.1	Introduction	129
4.1.1.2.2.2	Constitutive model	130
4.1.1.2.2.3	A framework for soil instability	134
4.1.1.2.2.4	Application to landslides	137
4.1.2	Numerical modelling of the boundary value problems.....	141
4.1.2.1	Description of the main commercial codes (slope scale)	141
4.1.2.2	Description of the main commercial codes (regional scale)	161
4.1.2.3	Description of the available home-made codes	173
4.1.2.4	Parametric studies	198
4.1.2.4.1	Introduction	198
4.1.2.4.2	Sensitivity analyses on the impact of rainfall on slope behaviour in pyroclastic soils	198
4.1.2.4.3	Stability analyses of partially saturated slopes in alpine regions	214
4.1.2.4.4	Conclusions	228
4.1.3	Scenarios of slope behaviour	230
4.1.3.1	La Frasse – Large landslide in tertiary flysch (Swiss Alps)	230
4.1.3.2	Analysis of progressive failure in brittle materials using the MPM. A case study: the Aznalcóllar slide.....	234
4.2	Numerical modelling of snow-melting effects	257
4.3	Potential scenarios related to climate changes.....	266
4.3.1	Analysis of a test-case in fine-grained soils.....	267
5.	References	279

1. FOREWORD

(AMRA)

Weather is the factor having the highest impact on the stability of slopes. This depends on both the geomorphological and geotechnical characteristics of the slope and the climatic features of the zone where this is located.

The main goal of this report is to draw a general framework of the relations between weather and slope stability, accounting for the very different situations existing in Europe, concerning both the nature of soils and the climatic features of the territory (chapter 2), and focusing on the main mechanisms which can lead to slope failure. In particular, the role of both precipitations and snow-melting on the stability of either coarse-grained or fine-grained soils will be considered (chapter 3). In fact, a good knowledge about the mechanics of landslide triggering due to adverse weather conditions is a fundamental tool for a quantitative prediction of landslide occurrence over both a spatial and a temporal scale.

Based on such a knowledge, methods and criteria for landslide prediction due to precipitations or snow-melting are reported (chapter 4). For this reason, material models (section 4.1.1) and both commercial and home-made numerical codes are shortly described (sections 4.1.2 and 4.2). On this last point, a distinction is made regarding the prediction at a local scale, i.e. at the scale of the slope, and at a regional scale, i.e. at a larger scale involving a wider territory. Proposed codes are applied to parametric studies and to significant European cases (sections 4.1.2.4 and 4.1.3), and potential effects of incoming climatic changes are examined using a paradigmatic case (4.3).

2. MECHANISMS AND CLASSIFICATION OF WEATHER-INDUCED LANDSLIDES (*AMRA, with contributions from EPFL, ETHZ, GIR and UPC*)

Slope behaviour is a boundary value problem characterised by different and often complex mechanisms of deformation and rupture, which depend on slope geometry, nature, structure and properties of soil, boundary and initial conditions. Every action causing a change of one or more of these factors can induce strains and displacements. These are revealed by modifications of slope morphology (i.e. soil displacements), which can lead to local failure, first, then to a general failure of the slope, i.e. to a “landslide”.

Such actions may be subdivided into two main types: those inducing a change in the stress field and those causing a modification in the properties of soil. Natural phenomena related to weather are among the main triggers of landslides. The interaction between slope and atmosphere occurs through hydraulic exchange, consisting of liquid inflow or vapour outflow, depending on climatic conditions (rainfall, snow, temperature, relative humidity, radiation, wind), soil properties and vegetation. The governing phenomena are very complex and thus an accurate assessment of the effects of weather is not easy. In particular, hydrologic processes as precipitation (due to rainfall and snow), consequent infiltration and seepage, evapotranspiration and runoff play a fundamental role and are responsible for changes in the degree of saturation, pore pressures and porosity of soil. All these factors can strongly influence the stability conditions through an increase of the driving forces and a decrease of the shear strength. The amount of water that does not infiltrate is responsible for further negative effects as erosion produced by runoff and/or increase of the water level of basins, lakes and rivers located at the toe of the slope. Finally, the long-lasting action of climatic factors can affect the geotechnical parameters through deterioration phenomena, including “weathering”.

Slope failures lead to landslides, whose behaviour is extremely variable. This suggested different classification criteria based on the slope response to failure (mechanisms of landslides). The typical mechanisms of landslides are incorporated in the well known Cruden and Varnes landslide classification (1996). Every type of landslide considered in such a classification can be triggered by weather factors (see also D1.1). A short description of the main types of slope movement, with special reference to soil, is reported below.

Fall is an abrupt movement of material that suddenly detaches from a very steep slope or a cliff (Fig. 2.1). Looking at soils, falls typically involve very steep stiff jointed or indurated clay deposits. The movement implies, first, separation of material from the outcrop, then, fall of a single or more blocks. Separation often occurs along discontinuities such as fractures, joints, and bedding planes, and following movements occur by free-fall, bouncing and rolling. In some cases fall may be the final stage of a process of tensile or shear rupture of soil, of buckling or of other mechanical processes. Therefore, the classification of a landslide as a fall is essentially related to the post-failure mechanism of movement regardless of the mechanism of failure. However, sometimes a fall may generate a different type of landslide: for instance, impact of a block on a slope located at the foot of the cliff may generate a debris flow.

The role of weather in the triggering of falls is revealed by the action of water (clef pressures) or formation of ice within open discontinuities or by deterioration associated with climatic factors (weathering).

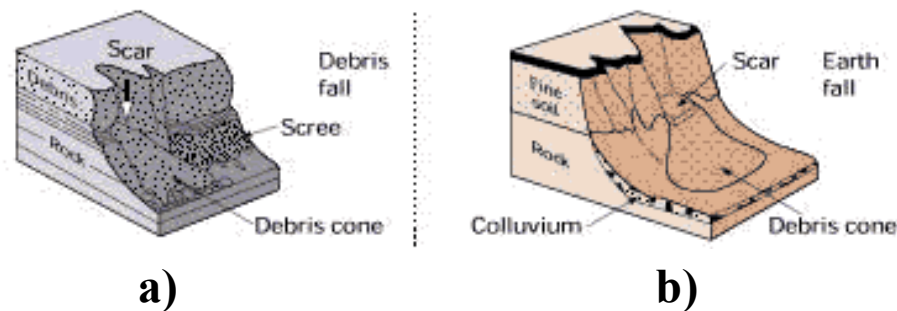


Figure 2.1 – Schematic representations of fall: a) debris fall; b) earth fall (Varnes, 1978)

Topple is a movement that implies rotation of a soil mass around a line located at its base until impact with the ground surface (Fig. 2.2). Topples are typical movements in stiff jointed clays, because their occurrence requires the pre-existence of vertical or sub-vertical discontinuities, and is essentially referred to movement following the loss of equilibrium. Toppling may represent only a stage of more complex slope movements: for instance, when involving a slab located at the crest of a steep slope, it may generate a fall.

Regarding the role of weather topples, as falls, are caused by cleft pressures caused by precipitation and the following infiltration, by ice or by weathering.

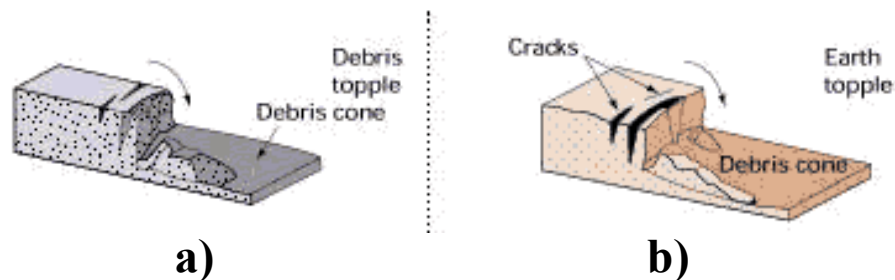


Figure 2.2 – Schematic representations of topple: a) debris topple; b) earth topple (Varnes, 1978)

Slide is caused by shear rupture along a surface (slip surface) that separates the landslide body from the underlying stable formation. According to the shape of the slip surface and to the mechanisms of following movements, different sub-categories of slides have been identified (Skempton and Hutchinson, 1969): rotational or translational slides, compound slides, block-slides, multiple or successive slips and so on. The slip surface of rotational slides (or slumps) is curved and the slide movement is roughly rotational about an axis that is parallel to the ground surface and transverse across the slide (Figs. 2.3a and 2.3b). In translational slides the landslide body moves along a roughly planar surface with little rotation or backward tilting (Figs. 2.3c and 2.3d). In stiff jointed clays sliding may occur along pre-existing discontinuities (bedding surfaces, joints). In intact soils slides are caused by formation of a fresh shear discontinuity that is preceded by small internal deformations leading to shear strain localisation within a rather thin zone, then to formation and propagation of the slip

surface. In both cases, movement following rupture is characterised by prevailing sliding along the slip surface.

Intense and/or lasting rainfall or rapid snowmelt are fundamental causes of failure due to water infiltration and consequent reduction of the shear strength because of pore water increase (or suction decrease) and increase of the shear stress due the increase of the weight or erosion. Soil deterioration and consequent loss of the shear strength caused by climatic factors (weathering and other phenomena) is another fundamental cause of sliding.

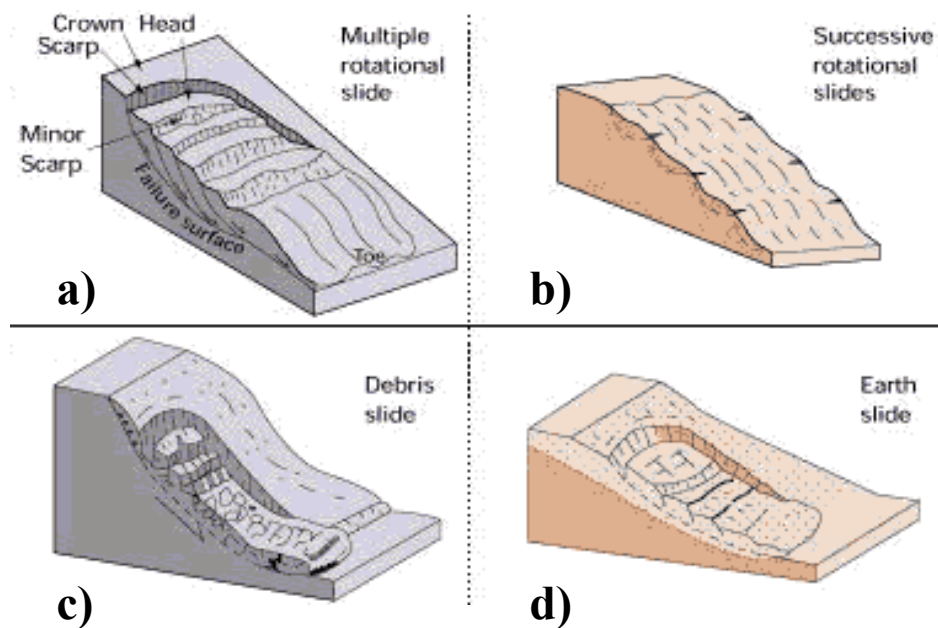


Figure 2.3 – Schematic representations of slide: a) debris slump; b) earth slump; c) debris slide; d) earth slide (Varnes, 1978)

Flow is a typical post-failure mode of deformation of soil masses which exhibit the typical movement of viscous fluids (Fig. 2.4). Movement is spatially continuous because inter-granular deformation predominates over displacements along a slip surface. In this respect, the difference between flow and slide depends on the pattern of deformation of the landslide body which in the case of slides exhibits a stiff response, the soil mass essentially moving over the slip surface. Flows occur both in granular and cohesive soils. With respect to the nature of involved materials and to the mechanical processes which are responsible for generation of flow-like movements, four main sub-categories may be recognized (Hutchinson, 2004): debris flow, debris avalanche, earthflow and mudflow.

Debris flow is characterised by very rapid to extremely rapid movement of a soil mass consisting of a mixture of loose granular soil, rock, organic matter, air and water. Typically it is channelized along existing drainage networks, and so exhibits a source, a track and a fan, but minor debris flows also occur on open hillsides. It is often triggered by intense surface-water flow, due to heavy precipitation or rapid snowmelt, or by other types of landslides that occur on steep slopes.

Debris avalanche is characterized by the extremely rapid and massive movement of rock and granular soil mixed with water which remains laterally unconfined and unchanneled almost along its total length. Generally it is widely and inversely graded and seems dry at the surface, while conditions at the base are usually unknown (Hutchinson, 2004).

Earthflow is the intermittent, relatively slow, flow-like movement of saturated fine-grained soils. The landslide body is generally elongate and advances along gentle slopes predominantly by sliding on discrete boundary shear surfaces at or near residual strength.

The term *mudflow* refers to the rapid movement of a fine-grained soil with a high mobility induced by a typical high water content that may range up to 60 percent.

The peculiar mode of deformation of flows may be independent from the mechanism of initiation. In fact, a flow style may be exhibited by landslides triggered as falls (which turn into debris flows or debris avalanches) or as topples (which turn into debris flows or debris avalanches) or as slides (which turn into earthflows or mudflows). It is often associated with the building up of excess pore pressures and the consequent drop of strength (Picarelli et al. 2008).

It's worth noting that also the term *creep*, used to classify extremely slow movements regardless of their real nature, is often associated with the category of flow-like landslides. In principle, creep should imply viscous movements of a soil mass subjected to a constant effective stress field characterised by an average shear stress smaller than the shear strength. For such a reason, creep should not imply the presence of a slip surface, which is the consequence of a shear failure; when existing, as in the case of old landslide bodies, the shear stress along the slip surface should be less than the residual shear strength.

Flows are frequently triggered by heavy precipitation and/or snowmelt occurring during the wet season. Movements involving debris and granular soils are caused by intense precipitations of relatively short duration, while those which occur in fine-grained deposits are affected by the duration rather than by the intensity of rainfall.

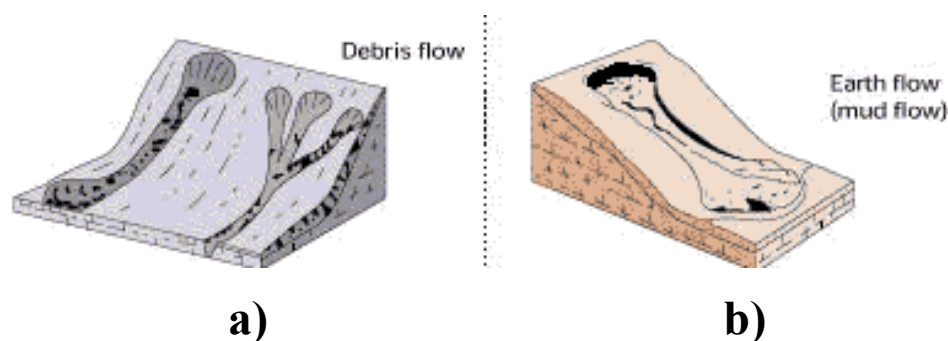


Figure 2.4 – Schematic representations of flow: a) debris flow; b) earth flow (Varnes, 1978)

Spread is a complex geological process of slope deformation often involving rock masses or rigid soils resting over a basement constituted of a softer rock or soil deposit (Fig. 2.5). The uppermost formation is subjected to lateral movements due to deformations of the lowermost formation. These may be the consequence of liquefaction (in saturated sands) or of ductile shear deformations (in clays) under high effective mean stresses.

The role of weather on spreads is less evident than in other types of movements, especially when the deforming basal formation is deep, thus is only marginally affected by climatic effects.

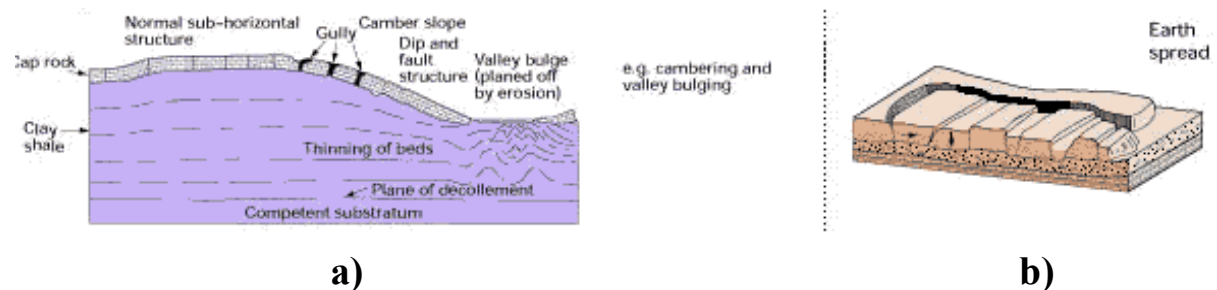


Figure 2.5 – Schematic representations of spread: a) debris spread; b) earth spread (Varnes, 1978)

A direct correlation exists between landslide type and movement rate. Based on a recent classification of the rate of slope movements reported in Table 2.1 (Cruden and Varnes, 1996), falls, topples, debris flows, debris avalanches, mudflows and spreads induced by liquefaction of granular soils are usually “extremely rapid” or “very rapid”. Earthflows are generally “rapid” or “moderate”. First-time slides involving intact brittle soils are typically “moderate” to “rapid”, while reactivations along pre-existing sliding surface are usually “slow” to “extremely slow”. Spreads in fine-grained deposits can be “extremely slow”.

Table 2.1 – Classification of the rate of slope movements (Cruden and Varnes, 1996)

Velocity class	Description	Velocity (mm/sec)	Typical velocity
7	Extremely Rapid		
	-----	5×10^3	5 m/sec
6	Very Rapid		
	-----	5×10^1	3 m/min
5	Rapid		
	-----	5×10^{-1}	1.8 m/hr
4	Moderate		
	-----	5×10^{-3}	13 m/month
3	Slow		
	-----	5×10^{-5}	1.6 m/year
2	Very Slow		
	-----	5×10^{-7}	16 mm/year
1	Extremely Slow		

2.1 EXAMPLES OF WEATHER-INDUCED LANDSLIDES IN EUROPE

In spite of the several potential causes, an increasing number of landslides in Europe are weather-induced. Data regarding some countries are reported in the following.

Italy

In Italy, the climate varies significantly from region to region. For example, yearly average temperatures range from values lower than 5°C, which are typical of some Northern Alpine Regions, to values higher than 16°C which are usual in some Southern coastal areas. Again, yearly average rainfall can vary from values smaller than 500 mm distributed within less than 60 days, characteristic of some Southern Regions, to values higher than 2500 mm distributed over more than 120 days, that are typical of the most elevated sites of some Northern and Central Regions (usually along the Alps and the Apennines chains). Moreover, rainfall peaks are concentrated in different periods going from North to South: they typically occur during summer and early autumn in Alps, during winter in Mediterranean areas and during late autumn and spring in the other regions.

The most widespread types of weather-induced landslides are slides and flows which involve both coarse and fine grained deposits in every Region (Tables 2.2, 2.3 and 2.4). They are usually triggered by rainfall, but snowmelt plays a significant role in the coldest areas of Northern and Central regions. In coarse-grained soils shallow debris flows and debris slides may be triggered by infiltration processes. These landslides are not preceded by clear warnings, and stop within a very short time interval. Well documented cases concern soils of different origin as the glacial and periglacial deposits of the Northern Alpine regions, the metamorphic deposits of the Versilia area (Toscana Region, Central Italy), the heterogeneous colluvial, residual and saprolitic soils of the Sila Grande massif (Calabria Region, Southern Italy) or the pyroclastic materials covering slopes of Campania Region (Southern Italy). Landslides in fine-grained deposits include slow translational slides and mudslides. Their displacements are essentially governed by the pore pressure regime and by its seasonal fluctuations. In particular, the highest rate of displacement is attained during the wet season, then it progressively slows down as the dry season approaches. The most of the slow landslides described in the literature cover lengths of time of many years, and some movements are known to be active even from centuries. Significant examples of earth slides concern lapideous deposits of the Langhe area (Piemonte Region, Northern Italy), along thin marly interbeds, and overconsolidated stiff clays outcropping in some Apennine slopes of Central Italy (deep-seated slides). Earthflows are widespread in structurally complex clay soils present along the Apennines chain, especially in Emilia, Molise, Campania, Basilicata and Sicilia.

Table 2.2 – Examples of weather-induced landslides in Northern Italy

<i>Region</i>	<i>Landslide types</i>	<i>Main involved formations</i>	<i>Triggering climatic factor</i>
LOMBARDIA	Debris flow; mudflow; earth slide, earth slump	Eluvial and colluvial deposit; complex heterogeneous (flysch); debris; clay	Rainfall
VENETO	Earth and debris slide; earth and debris slump; debris flow and mudflow; earth flow and soil creep; soil slide and shallow landslides	Debris deposit; marly- calcareous flysch	Rainfall
PIEMONTE	Earth and debris slide; earth and debris slump; soil slip and shallow landslides; Debris flow; earthflow, soil creep	Calcareous schist, complex heterogeneous (flysch), moraine deposits, eluvial and colluvial deposit, marl and silt	Rainfall Snowmelt
FRIULI VENEZIA GIULIA	Earth and debris slide; earth and debris slump; debris flow and mudflow	Debris deposit; conglomerate and breccia weakly cemented; flysch; evaporite and volcanic rock;	Rainfall
VALLE D'AOSTA	Complex; earth and debris slide; earth and debris slump; debris flow	Glacial and colluvial heterogeneous deposit; debris deposit	Rainfall Snowmelt
LIGURIA	Complex, earth and debris slide; earth and debris slump; earthflow and soil creep	Marl and sandstone; arenaceous flysch; argillite and siltite; calcareous-marly flysch; debris deposit	Rainfall
EMILIA ROMAGNA	Earth and debris slide; earth and debris slump; earth flow and soil creep; complex	Layered sandstone, clay and marly clay (Flysch ligure); clayey deposits	Rainfall Snowmelt

Table 2.3 – *Examples of weather-induced landslides in Central Italy*

Region	Landslide types	Main involved formations	Triggering climatic factor
TOSCANA	Earth and debris slide; earth and debris slump; complex; soil slip and shallow landslides; earthflow	Pelitic flysch; Calcareous-marly flysch; arenaceous flysch; debris deposit; sand and shale	Rainfall
MARCHE	Earth and debris slide; earth and debris slump; debris flow debris avalanche; earthflow and soil creep	Eluvial and colluvial deposits; pelitic and pelitic-arenaceous deposits	Rainfall
ABRUZZO	Earth and debris slide; earth and debris slump; earthflow and soil creep; complex; debris flow and mud flow	Shale deposit; arenaceous flysch; pelitic flysch; debris deposit; gravelly and sandy deposit	Rainfall
LAZIO	Earth and debris slide; earth and debris slump; complex; earthflow and soil creep; debris flow and mud flow	Flysch deposit	Rainfall
UMBRIA	Earth and debris slide; earth and debris slump; complex; earthflow; debris flow and mudflow	Terrigenous synorogenic (calcareous-marly flysch, marl, pelitic flysch, etc.) and postorogenic deposit (gravelly, sandy and clayey deposit); debris deposit; colluvial deposit	Rainfall Snowmelt

Table 2.4 – Examples of weather-induced landslides in Southern Italy

Region	Landslide types	Main involved formations	Triggering climatic factor
CALABRIA	Earth and debris slide; earth and debris slump; complex; earthflow and debris flow	Eluvial and colluvial deposit; torbitic deposit; debris deposit; metamorphic and igneous rock	Rainfall
CAMPANIA	Earth flow and soil creep; earth and debris slide; earth and debris slump; debris flow and mudflow; complex	Flysch deposit; pyroclastic deposit; volcanic rock; debris deposit	Rainfall
PUGLIA	Earthflow and soil creep; earth and debris slide; earth and debris slump; complex; mudflow and debris flow	Calcareous-marly flysch; arenaceous flysch; pelitic and clayey flysch	Rainfall
BASILICATA	Earth and debris slide; earth and debris slump; earthflow and soil creep; debris flow and mudflow	Flysch deposit (Arenaceous- marly-clayey unit; clayey- marly unit, etc) Argille varicolori	Rainfall
SARDEGNA	Earth and debris slide; earth and debris slump; complex; debris flow	Debris deposit; pyroclastic deposit; marl and arenaceous- pelitic flysch; gravelly, sandy and clayey deposit	Rainfall
SICILIA	Complex; earthflow; earth and debris slide; earth and debris slump; debris flow and mudflow	Arenaceous-clayey complex; clayey complex; pyroclastic deposit	Rainfall
MOLISE	Earthflow and soil creep; complex; earth and debris slide; earth and debris slump	Sand, sandstone and marl; calcareous-marly deposit; shale and marl of various colours	Rainfall

Spain

In a review of 20 main landslide events in Spain (Table 2.5), Ferrer and Ayala (1997) observed that failures and reactivation of slides, earthflows and debris flow occurred during abnormally intense rainfall episodes, with values ranging from 15 to 120% of mean annual rainfall. Lamas et al. (1997) found that the rainfall that caused widespread landslides in Andalusia in winter 1996-97 exceeded the historic maxima of the last 100 years in a third of the weather stations. The rainfall accumulated from November, 1996, to January, 1997, was over double the value corresponding to the same seasonal period in all the observatories in the Southeast of Andalusia. In the Cantabrian Range a relationship has been established over the last 100.000 years between periods of increased rainfall and greater frequency of landslides (González-Díez et al., 1996). At a scale of the last few decades, the relationship is well known between intense rainfall episodes (e.g., in August, 1983) and slides, in particular shallow ones (Remondo, 2001; Remondo et al., 2005).

Table 2.5 – Examples of weather-induced landslides in Spain

<i>Region</i>	<i>Landslide types</i>	<i>Main involved formations</i>	<i>Triggering climatic factor</i>
Pyrenees	Shallow slides, debris flows, rock fall	Colluvium, till, weathered claystones	Short-lasting high-intensity rainfall events (autumn)
Pyrenees, Cantabrian and Baetic ranges	Mudslides-large earthflows, rotational slides	Clayey formations, shales, flysch	Long-lasting low-intensity rainfall season (winter)

The duration and intensity of rainfall episodes, the materials comprising the slope and the morphology thereof are the main factors controlling the type of landslide. In the Pyrenees, three situations have been distinguished that cause slope failure or the reactivation of slides (Corominas et al. 2002): (a) short duration high-intensity rainfall cause widespread shallow slides, debris flow and rockfalls; (b) rainfall episodes of moderate to low intensity that last for several days or weeks reactivate rotational and translational slides and mudslides; (c) abnormally rainy seasonal and interannual episodes cause the reactivation of large-scale slides. In particular geological contexts, short duration rainfall can also cause reactivation.

Rockfalls

Rockfalls are frequent during rainy periods. However, rockfalls are also caused by the effect of freeze-thaw cycles, root penetration or in a spontaneous manner, due to the action of weathering mechanisms. For this reason, the relationship with rainfall is weak.

Shallow slides

On slopes covered with surficial deposits (colluvium) and weathered rocks, intense rainfalls of short duration are capable of triggering slides, debris flows and rockfalls. In the Eastern Pyrenees, analysis of the isohyets and their relationship with the distribution of landslides in different recent episodes has allowed the establishment of a rainfall intensity threshold of about 190 mm in 24-36 h (Gallart and Clotet 1988; Corominas and Moya 1999). Recent episodes analysed with rainfall gages providing hourly data show that shallow slides may also

occur during intense rainfall episodes lasting for a few hours. In these cases, antecedent rainfall was not necessary. To the contrary, persistent low-intensity or moderate rainfall hardly causes shallow slides at all. This is due to the presence of large interparticular voids in the colluvium and of macropores (root casts, piping, animal burrowing) in weathered claystone formations, which facilitates rapid drainage of infiltrated water from low-intensity and moderate rainfall. Only high-intensity rainfall can generate significant increases in pore water pressure leading to the failure.

Particular local contexts can modify these relationships. In the Cantabria range the occurrence of shallow slides has been noted on steep slopes, sculpted in Keuper materials, with rainfall intensities of between 50 and 65 mm/h, well below what was expected. The current hypothesis is that during months with greater accumulated rainfall, a strong groundwater flow is generated through existing piping in Keuper clays, rich in gypsum. When rainfall intensity increases, water rapidly concentrates in the pipes and is capable of triggering “argayos” (shallow slides) at the groundwater outlet point (Domínguez, 2003).

Slides and earthflows

Earthflow and rotational and translational slides, with volumes from a few tens to hundreds of thousands of cubic metres, are usually reactivated during moderately intense episodes, between 40 and 100 mm of rainfall in 24 h, provided that 90 mm or more of rainfall has accumulated in the preceding days (Corominas and Moya, 1999). This type of slide occurs in low-permeability clay and silty-clayey formations. In these formations, the infiltration of rainwater is controlled by the size of the particles and, to a lesser degree, by fissures and by recharge through the more permeable layers, such as interbedded sandstone. The authors quoted have established the following threshold for the Pyrenees:

$$I = 66.1 D^{-0.59}$$

Where I, is average rainfall intensity in millimetres per day and D is the duration of the storm in days. The expression is valid for rainfall episodes of a duration of more than one week, and which have accumulated at least 90 mm of rain.

Large landslides

Historical records show that most first-time failures in large landslides were caused by non-climatic factors (Corominas, 2000). To the contrary, rainfall is the most frequent cause of reactivation of dormant slides and of the acceleration of those that are already active. It is not easy to establish the relationship between rainfall and slide activity; this is because sufficient knowledge of the hydrological behaviour of large slides has not yet been gathered. Advances in this field require complex mechanical-hydrological modelling, which needs a great deal of data on the terrain and instrumental ones, which are rarely available. In general, long rainy periods (at seasonal, annual or ten-year scale) appear to have a certain influence in the reactivation of large landslides although the relationship can often only be established in a qualitative manner.

However, in very particular geomorphological contexts that favour instability, either through extraordinary amounts of groundwater (e.g. contact with karstic massifs) or due to brusque topographic changes (e.g. toe erosion), landslides can be reactivated by very intense, short-lived rainfall episodes. Some cases were observed during the intense rainfall on November

6th-7th, 1982 in the Eastern Pyrenees (Corominas and Alonso, 1990). Some slides are also in permanent movement, like in Vallcebre (Eastern Pyrenees), with a volume estimated at over $20 \times 10^6 \text{ m}^3$ (Corominas et al., 1999). The presence of cracks, which facilitate rainfall infiltration into the slide, together with toe erosion by a torrent can facilitate the acceleration of the movement in a question of a few hours.

Romania

In Romania, weather-induced landslides play a major role in shaping the evolution of landforms in the intra- and extra-Carpathian hills, plateaus and in the flysch-built mountainous regions. At national level, some Authors (Topor, 1964) consider high magnitude landslide occurrence to be related to heavy rainfall with a return period of approximately 30 years (1313 – 1317; 1342; 1370; 1404; 1456 – 1457; 1490; 1526 – 1533; 1593; 1618; 1668; 1716; 1783; 1805; 1831 – 1837; 1859 – 1860; 1893 – 1897). In particular, the period 1893-1897 has been probably the one with the maximum extent of landslides in Europe. Dikau and Schrott (1997) stress that only 15% of the landslides occurred in that period were triggered by earthquakes, while 30% were weather-induced, especially by rainfall.

In the 1912 – 1915 period the amount of precipitations exceeded the multi-annual average. Surdeanu (1998) highlights the alternation of extreme deficit/excess periods (1890 – 1894; 1902 – 1905; 1923 – 1935; 1942 – 1946; 1960 – 1967; respectively, 1895 – 1899; 1909 – 1913; 1936 – 1942; 1969 – 1974) in the flysch mountainous areas; here, the daily regime affects only the shallow landslides dynamics, while deep-seated landslides are regulated by monthly and annual regime. Most landslides occur as a result of a combination of causal factors - preparatory or triggering - seldom attributed to a single causal factor (Popescu, 2001).

Weather-induced landslides distribution in Romania generally reflects the interaction between weather characteristics and the general configuration of the relief conditioned by its geological evolution, especially in Quaternary. Moreover, the evolution of different land use surfaces, deforestation, mineral resources exploitation etc., represent major potential premises of mass movement development triggered by rainfall or snowmelting.

Weather-induced landslides occur especially in areas where permeable deposits overburden clays and clayey-marls formations. The most affected areas (Tab. 2.6 and Fig. 2.6) are briefly presented below.

The Subcarpathians are formed predominantly of folded and faulted molasse deposits, therefore slopes may be highly unstable. Landslides are most frequently represented by shallow (sheet) slides, landslides of medium depth and mudflows typically 300-700 meters in length. The most affected areas lie within the Curvature Subcarpathians.

The Eastern Carpathians, formed predominantly of Cretaceous and Paleocene flysch deposits, periglacial or immediate postglacial colluvial materials are major sources of mass movements. These deposits generally range from 10 to 30 meters in depth, and landslides are commonly activated or reactivated by heavy rainfall, regional deepening of the valley network or deforestation practices. Because of their association with stream valleys, these landslides often affect towns, communication lines, and roads, and may partially or totally block valleys.

In **The Moldavian Plateau** landslides occur on slopes built up of alternations of marls and clays, with intercalations of conglomerates and sandstones. In The Moldavian Plateau, shallow recent earth slides are dominant whilst the Sucevei Plateau is characterized mainly by reactivated Pleistocene earth slides. In the Central-Moldavian Plateau oolitic limestones and thick layers of sandstones with underlain clays prevail. In The Moldavian Plain marls, sands and clays are predominant; here, recent shallow landslides are very frequent. To the South, although clay deposits increase in extension, the relative altitude decreases, thus the landslides magnitude declines.

In **The Transylvanian Plateau** climatic variations (pluvial periods) critically changed the slopes morphology starting with the Upper Pleistocene period. Deep earth slides are commonly reactivated by heavy rainfall. Earth slides and flows are mostly developed in clay and marl complexes with intercalations of Sarmatian sandstones and sands in contact with sandstones, conglomerates and tuff. Mass movements in Secaselor Plateau, Somesan Plateau and Transilvanian Subcarpathians are mainly shallow earth flows and debris flows affecting deluvial deposits or debris deposits.

In **The Getic Plateau** landslides develop in alternating argillaceous marls covered by gravels and heterogeneous sands; irregularly distributed (especially in the northern part of the piemond), shallow landslides are triggered by rainfall and rarely snowmelt.

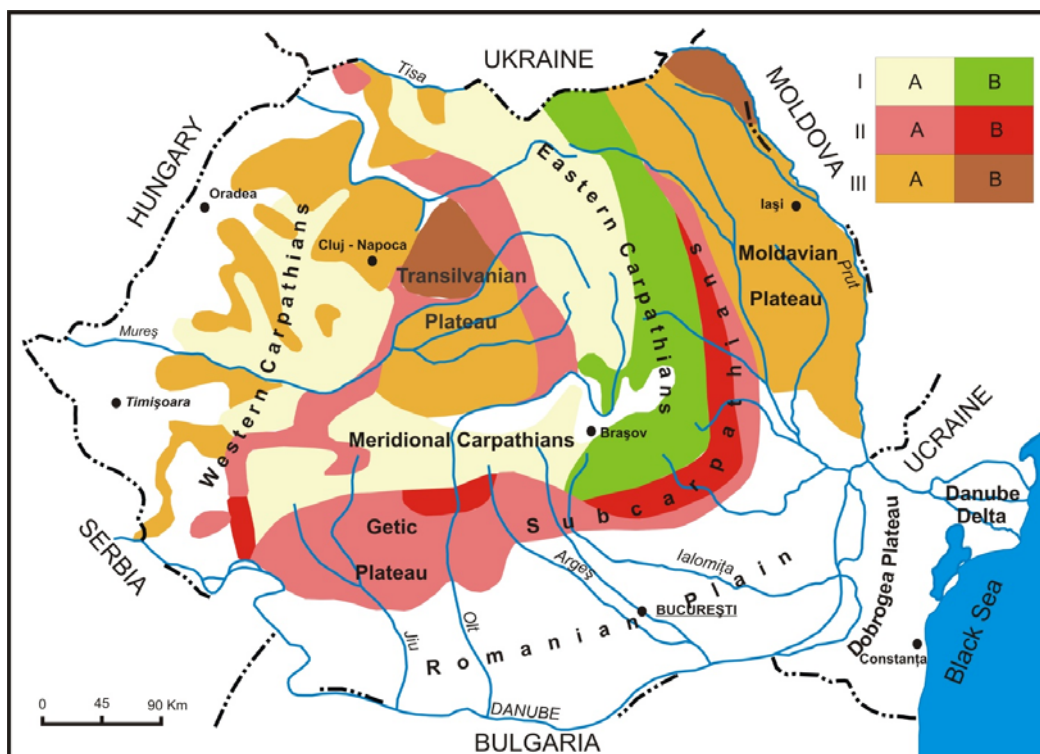


Figure 2.6 - Landslides frequency in Romania with special consideration to weather-induced landslides (Bălteanu, 1997, with modifications) I - mountainous regions: A-low; B-high; II – hilly regions: A-high; B-very high; III – plateau and basin regions: A-medium; B-high

Table 2.6 – Examples of weather-induced landslides in Romania

<i>Region</i>	<i>Landslide types</i>	<i>Main involved formations</i>	<i>Triggering climatic factor</i>
THE SUBCARPATHIANS	Shallow landslides, earth and debris flow, earth slide; complex; mudflow; slump	Molasse deposits; colluvial and eluvial deposits	Rainfall Snowmelt
THE EASTERN CARPATHIANS	Debris flow; deep-seated and shallow landslides;	Cretaceous and Paleocene flysch deposits; deluvial deposits	Rainfall Snowmelt
THE MOLDAVIAN PLATEAU (Sucevei Plateau, Moldavian Plain, Central-Moldavian Plateau)	Earth slides; complex; earth and mudflow; shallow landslides	Intercalations of sandstones and conglomerates, layered marls and clays, colluvial deposits; oolitic limestones	Rainfall
THE TRANSYLVANIAN PLATEAU (Transylvanian Plain, central and eastern Târnavelor Plateau, Someşan Plateau)	Earth and debris flow; earth slide; shallow landslides; complex	Clay and marl complexes; intercalation of Sarmatian sandstones and sands in contact with sandstones, conglomerates and tuff	Rainfall
THE GETIC PLATEAU	Shallow landslides	Alternations of argillaceous marls covered by gravels and heterogeneous sands	Rainfall

Recent studies (Dragotă et al., 2008) in the Buzău Subcarpathians (Muscel Basin – Fig. 2.7) demonstrate the relationship between the amount of precipitation (susceptibility classes liable to triggering/reactivating landslides based on Angot Pluvial Index attributes) and the slope response.

The input series of data used for the Angot Pluvial Index ($k_{\text{month/year}}$) was registered at Pătârlagele station - 284 m (monthly precipitation) over the 1961 – 2007 period.

The index calculation formula and value grid (Table 2.7) is:

$$K - p/P \quad [2.1]$$

where:

$$p = q/n \quad [2.2]$$

q = monthly amount of precipitation; n = number of days/months;

$$P = Q/365 \quad [2.3]$$

Q = multi-annual amount of precipitation.

Index values can be used to detect dry or rainy intervals by listing them under precipitation susceptibility classes corresponding to the precipitation attributes assigned.

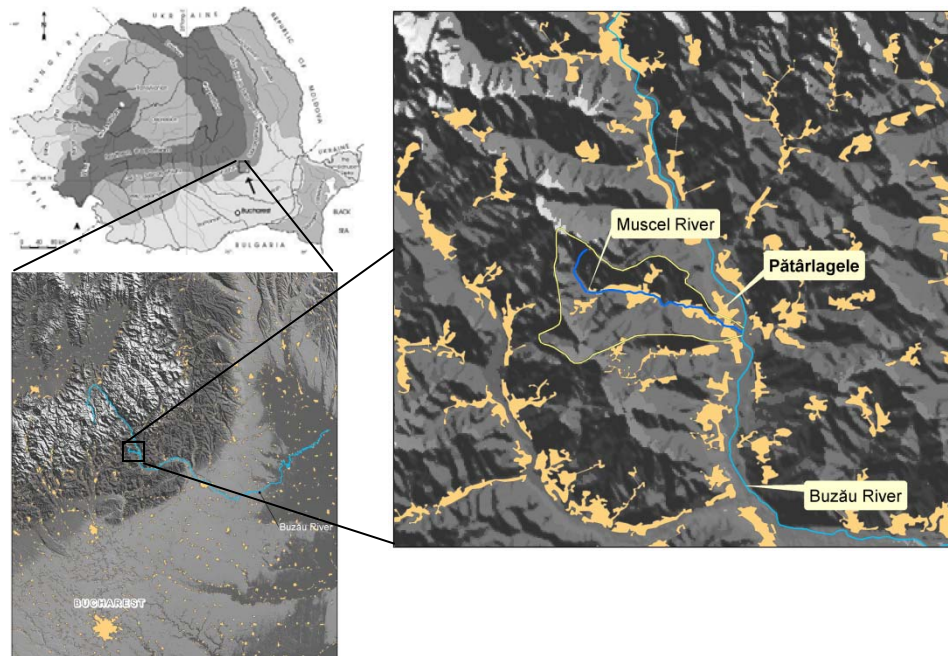


Figure 2.7 - Location of the Muscel Basin and Pătărlagele weather station

Table 2.7 - Susceptibility classes of precipitation liable to triggering/reactivating landslides based on Angot Pluvial Index attributes (Dragotă et al., 2008)

Pluviometric attributes	Very dry	Dry	Normal	Rainy	Very rainy
Susceptibility classes	Very low	Low	Moderate	High	Very high
Angot Index values (K)	<0.99	1.00 – 1.49	1.50 – 1.99	2.00 – 2.49	>2.50

The results reveal:

- **The multi-annual monthly regime:** rainiest months (July 1975 (k_{month} 9.11) and 2002 (6.95); May 1988 (6.72) and 1971 (6.43); June (6.27); driest months (August 1962 (0.00); November 1990 and December 1975 (0.02); October 2000 and November 1986 (0.03)
- **Seasonal differences of precipitation quantity distribution:** winter is the most stable season with 78% average landslide frequency of all cases in the *low* and *very low* susceptibility classes; summer indicates the highest average frequency of the *very high* susceptibility class (54%) while the probability to have the *very low* class is weaker (August 24%)
- **Semestrial differences:** the warm semester (April 1 – November 30) registers the highest frequency of precipitation induced landslides (40%) and only up to 20%, stability-related conditions; in the cold semester (October 1 – March 31) land stability is very high, with only 10% probability for pluvial events to trigger landslides

- **Annual regime:** the driest five years of low pluvial impact (unlikely to trigger landslides) were 1973, 2000, 1985, 1982 and 1987 with 50% rain deficit, but rain moths also (25%)
- **Decennially** distribution of precipitation susceptibility shows that extreme events were absent and the moderate class prevailed; the rainiest decade was 1971 – 1980 and the driest one, 1981 – 1990.

Pluvial excesses were however registered in **1975** (cumulated monthly quantities and within short-time intervals – July - Fig. 2.8) and **2005** (cumulated annual quantities – Fig. 2.9).

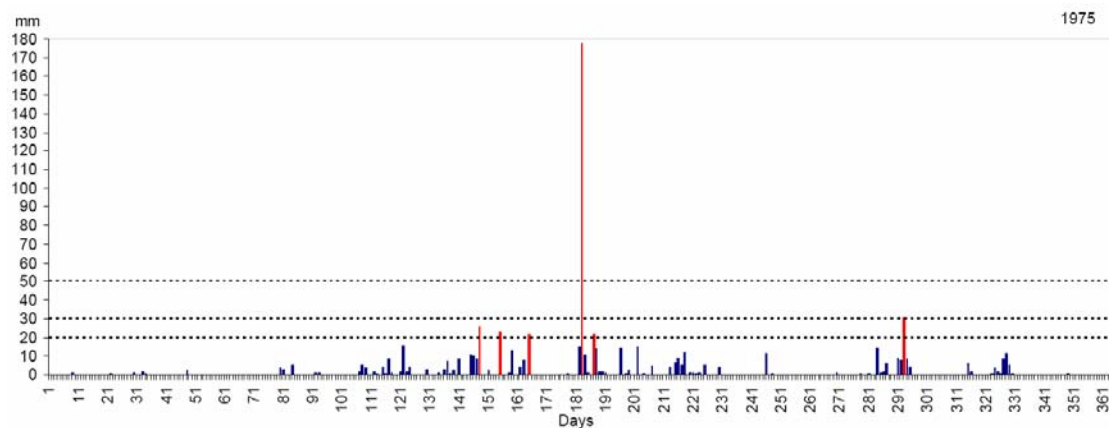


Figure 2.8 - Daily variations of precipitation quantities in 1975 – Pătârlagele station (Dragotă et al., 2008)

July 1975 reached the maximum value of 9.11 individual Angot Index from the five rainiest months of the studied period. In contrast with 2005 year, 1975 registered only a major peak (177.8 mm on 2 July), exceeding the presumed pluvial threshold of >30.0 mm/24 hrs under dry soil conditions. As a result, several areas were subjected to catastrophic floods by the Buzău and Bâsca Rozilei rivers, rock-falls in the Lupului and Sibiciul valleyside slopes, landslides in Muscel, Via, Croitorul, Porcăreața and Bâsca Chiojdului Basins, and landslides turning into mudflows in the Via Hill (Bălțeanu, 1983 cited by Dragotă, 2008).

The year 2005 was a particularly rainy period in Romania. At Pătârlagele station, four of the 2005 months (May, July, August, September) were characterized by an over 130 mm record, and 100 mm in February due to snowmelt. In terms of the multi-annual mean (635.1 mm), 2005 may be considered a historical record year at Pătârlagele weather station (993.5 mm). Moreover, only in 13% of the cases annual amounts over 800 mm were recorded throughout the 1961 – 2007 period.

The 2005 maximum amounts of precipitation fallen over short-time intervals (24,48 and 72 hours) were more evenly distributed over the year (Fig. 2.9).

Individual Angot values in years of significant excess rain reached over 9.00 on July 1975 and more than 2.80 in February and May – September 2005 (5.34 in August). In the Muscel basin, these values correspond to landslides episodes described by the relationship between the amounts expressed by Angot values and the moment these processes occurred (Fig. 2.10).

Biagioni and Rapetti (2005) calculated the soil moisture budget based on a series of data registered in 1961 – 2003 period, at Pătârlagele weather station. During an average year the field capacity (150 mm, in the Muscel valley) is never reached while during the study period

this value is reached and even exceeded in almost all months. Therefore, the soil saturation increased the landslide susceptibility prior to 2005 pluvial excess event.

The interval in which weather-induced landslides are likely to occur in Muscel basin is May – September. The most slide-affected areas, after 2005 excess event, are formed of clay-marls and schists formations of the Mio-Pliocene molasse, corresponding to the median sector of the basin. The most frequent types of mass movement are mudflows and shallow landslides.

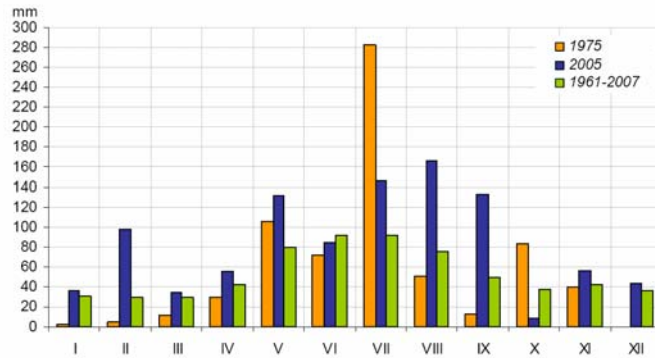


Figure 2.9 - Monthly quantities of precipitation in 1975 and 2005 referred to the multi-annual mean, 1961 – 2007 - Pătârlagele weather station (Dragotă et al., 2008)

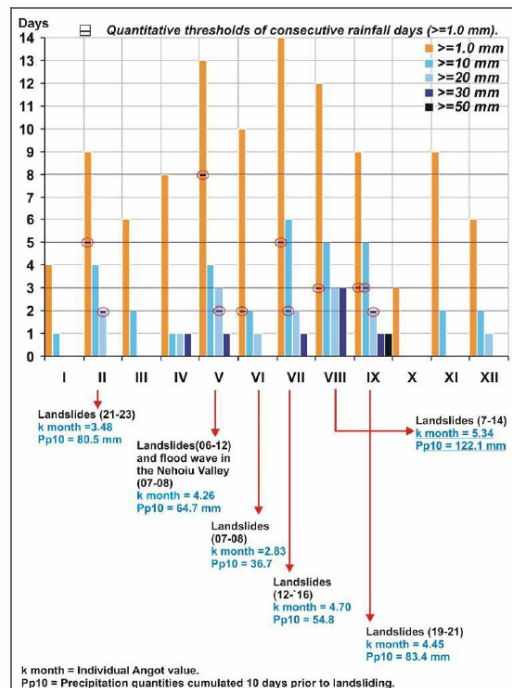


Figure 2.10 - Quantitative thresholds of consecutive rainfall days and their landsliding impact in the Muscel Basin– Pătârlagele station (Dragotă et al., 2008)

Switzerland

Due to the mountainous terrain and associated weather conditions found in Switzerland, landslides provide a hazard across almost the entire country. Figure 2.11 shows the occurrence of landslides which caused financial losses during the time period 1972-2002. The map shows the highest concentrations in the cantons of Ticino and Schwyz, along with a band of higher density across the centre of Switzerland where the population density is greatest. Landslides are commonly triggered by rainfall, snowmelt, permafrost degradation, glacier retreat and undercutting of slopes: such information are summarized by Tables 2.8 that take into account a regional scale (Table 2.8a) and a provincial scale (Table 2.8b and 2.8c)

Landslide hazards do not have a characteristic type due to the varied geology and topography of the country, moreover, most types of landslide identified by Cruden and Varnes (1996) pose a threat. Degrading permafrost and erratic climatic conditions are providing an environment where a greater landslide risk is predicted in future years.

In the past 2 decades, 1999 and 2005 both saw a greater than average occurrence of landslides within Switzerland (PLANAT, 2000; BAFU, 2005; Mueller & Loew, 2009). In 1999 these landslides tended to occur in February and May, and were caused by above average rainfall between October 1998 and April 1999, and a late and strong snowmelt in April/May 1999 both contributing to high pore pressures and a loss of strength in mountainous areas. In August 2005, excessive rainfall caused flooding throughout Central Switzerland and triggered landslides in this area.

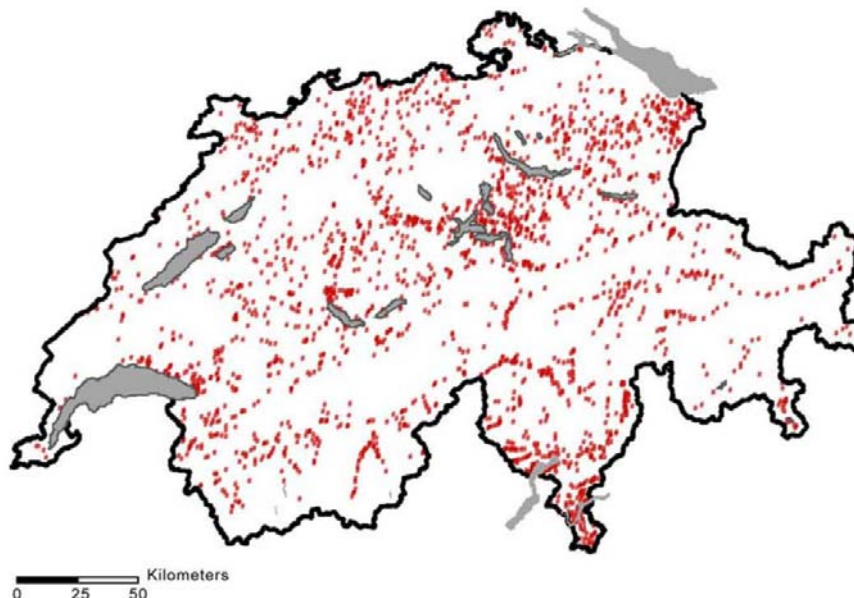


Figure 2.11 - Distribution of landslides causing financial damage between 1972-2002 in Switzerland (Schmid et al., 2004)

Table 2.8a – Examples of weather-induced landslides in Switzerland

<i>Region</i>	<i>Landslide types</i>	<i>Main involved formations</i>	<i>Triggering climatic factor</i>
ALPS Nappes pénniques Lepontin Aarmassif / Gotthardmassif Bündnerschiefer	Rock fall, rock topple, rock slide, rock flow (deep creep), debris fall, debris topple, debris flow, complex	Crystalline rock, often heavily folded, overlapped, jointed and of schistous nature. Moraine deposits	Rainfall Snowmelt Melting permafrost
PREALPS Romandes Nappes helvétiques	Debris fall, debris topple, debris slide, debris spread, debris flow, earth slide, earth flow (soil creep), complex	Mesozoic and tertiary sediments, heavily folded with strong overlapping. Flysch (schistous marl with limestone inclusions and sandstone intercalations)	Rainfall
MITTELLAND Molasse of the Swiss Plane Subalpine molasse	Debris slide, debris flow, debris spread, earth slide, earth flow	Molasse: Tertiary sediments (upper & lower sea water and upper & lower freshwater molasse) with high porosity, low consolidation and horizontal bedding	Rainfall
JURA Faltenjura & Tafeljura	Rock fall, rock topple, debris fall, debris topple, debris flow, earth slide, earth flow, complex	Limestones, often with marl intercalations. Silty sands with clay component, often with boulders (ground moraine) or mixed with pebbles or boulders (surface moraine) Gravel and sand, pure or with a silty component, locally clay components (opalinus stone) in the Tafeljura, locally cemented Angular rock debris of different size	Rainfall

Table 2.8b – Examples of weather-induced landslides in Switzerland

Region	Landslide types*	Main involved formations	Triggering climatic factor
AARGAU	Small scale slides; Debris flow; Slide; Rock fall	Siltstone; Sandstone; Evaporites; Colluvial clays; Alluvial sediments; Marl	Rainfall
APPENZELL	Earth Slide	Marls; Sandstones; Conglomerates	Rainfall
BASEL		Limestone; Marl	
BERN	Rock avalanche; Transitional Slide; Slide; Debris slide; Rock slide	Limestone; Schist; Conglomerate; Sandstone; Marl	Glacier retreat; Rainfall; Snowmelt
FRIBOURG	Deep-seated creeping mass; Slide; Rotational slide 1. Prealpes (PA) 1.1 Flysch: “creeping mass”, earth flow, rotational and big scale transitional slides, 1.2 Préalpes medianes: Rock slides, spontaneous, small scale rotational slides (water pressure) 2. Lowlands 2.1 Sandstone (molasse): mud flow/ debris flow 2.2. Moraine: rotational slides	Flysch (PA); Klippendecke (PA); Dolomite; Limestone; Marl	Rainfall; Snowmelt
GENEVA		Limestone; Marl	
GLARUS	Rock avalanche; Soil creep; Debris flow; Slide	Slate; Limestone	Rainfall
GRAUBÜNDEN	Rock avalanche; Soil creep	Schist; Glacial moraine; Granite, Gneiss; Flysch; Amphibolite; Limestone	Rainfall; Snowmelt; Groundwater flow
JURA		Evaporites; Marl; Schist; Gneiss; Limestone	
LUZERN	Earth Slump; Soil Creep; Rotational Slides; Transitional slides; Debris flow; Slide	Gneiss; Granite; Sandstone; Limestone; Clay; Marl	Rainfall; Groundwater exfiltration
NEUCHATEL		Evaporites; Marl; Schist; Gneiss; Limestone	Rainfall
NIDWALDEN	Earth flows; Debris flow; Debris slide; Slide	Molasse; Sandstone; Conglomerate; Limestone	Rainfall
OBWALDEN	Slide; debris flow	Flysch; Limestone; Marl; Sandstone	Rainfall
ST. GALLEN	Debris flow; Slide	Marls; Sandstone; Limestone	Rainfall
SCHAFFHAUSEN	Soil creep; Transitional slides	Flysch; Limestone	Rainfall; Snowmelt
SCHWYZ	Rockfall	Molasse (conglomerates); Limestone; Sandstone; Marl	Rainfall; Undercutting by fluvial erosion
SOLOTHURN		Evaporites; Marl; Schist; Gneiss; Limestone	Rainfall

Table 2.8c – *Examples of weather-induced landslides in Switzerland*

Region	Landslide types*	Main involved formations	Triggering climatic factor
THURGAU		Sandstone; Conglomerate	
TICINO	Sags; deep-seated creep and rotational slides	Fluvio-glacial deposits; metamorphic (esp. schist and gneiss); molasses; Amphibolite; Limestone	Rainfall
URI	Rockfall; Slide; Debris slide	Limestone; Sandstone; Marl	Rainfall
VALAIS	Rockfall; Transitional slide; Debris Flows; Rockslide; Rock avalanche; Slide; Rotational slide	Gneiss; quartzite; schist; glacial deposits; limestone; fluvial deposits; marl	Rainfall; Snowmelt
VAUD	Soil creep; Slide; Transitional slide	Flysch; limestone; marls; schist	Rainfall
ZUG			
ZÜRICH	Slide; Debris slide	Flysch; Limestone; Glacial moraine; Sandstone; Conglomerate	Rainfall

3. WEATHER IMPACT ON THE STABILITY OF SLOPES (RAINFALL, SNOWMELTING, AND POTENTIAL ROLE OF CLIMATE CHANGES)

3.1 EXPERIENCE GATHERED THROUGH WELL-MONITORED NATURAL AND ENGINEERED SLOPES *(AMRA, UNISA, EPFL)*

The ways how weather could affect the slope behaviour are strictly related to a number of factors as slope angle, thickness of the deposit, stratigraphy, mechanical and hydraulic properties of the soil, initial conditions, boundary conditions etc. Therefore, the same event can produce totally different consequences for different combinations of these factors. For example, some landslides are usually activated by short intense rainfalls, while others are induced by long lasting precipitations. Again, the landslide can involve the entire deposit or only a superficial part of it. All these aspects are very important, because they affect the features of the post-failure stage and so the magnitude of the potential induced damage.

Landsliding in response to weather changes involves physical and, sometimes, chemical modifications of the soil properties. In the case of precipitation-induced landslides occurrence and features depend on the rainfall characteristics (frequency, magnitude and recurrence intervals) in combination with other initiatory natural (slope morphology, stratigraphy and lithology, soil moisture etc) or anthropogenic (built up and forested surfaces evolution, modification of slope geometry etc) factors. The number of landslides, triggered in a recurrence cycle, is in direct ratio with the recorded amount of rainfall (Govi et al., 1980; Crozier, 1986). A similar relation has been observed between the number of triggered landslides in a given area and the rainfall duration (Glade, 1997). In some cases it has been demonstrated that landslides are more likely to occur (i) after droughty periods followed by heavy rainfall; (ii) after snowmelting or long periods of rain followed by low amount of precipitations (Surdeanu, 1998).

In landslide analysis, the modelling of pore pressure variations induced by rainfall often contributes significantly to the understanding or predicting of natural phenomena, as illustrated by parametric studies about typical situations (Rulon and Freeze 1985; Reid 1997; Tsaparas et al. 2002) as well as interpretation of case histories (Leach and Herbert 1982; Lim et al. 1996; Fourie et al. 1999; Gasmo et al. 2000; Rahardjo et al. 2001). Studies of case histories are usually based on: systematic investigations to define the characteristics of the geo-environmental context; detailed monitoring of the groundwater regime, often over long periods of time; accurate analyses with advanced mathematical models of physical processes induced by rainfall and controlling the stability of slopes.

Some indications about the response of slopes to weather will be provided in the following, thanks to data from the literature. In particular, due to their intrinsic differences, cases regarding coarse-grained deposits will be examined separately from those involving fine-grained soils. After such a general overview, detailed information about well documented cases, regarding different geo-environmental contexts will be provided.

3.1.1 Failure mechanisms of landslides in granular soils

(AMRA)

Before being subjected to unfavourable weather conditions, the most of slopes in granular soils are featured by negative and positive pore-water pressures that develop respectively above and below a more or less deep groundwater table (Fig. 3.1). In particular, immediately above the groundwater table the soil is saturated within the capillary fringe, whose thickness grows with the air-entry value. As a matter of fact, negative pore-water pressures significantly contribute to the shear strength of the soils and consequently to the stability of the deposits.

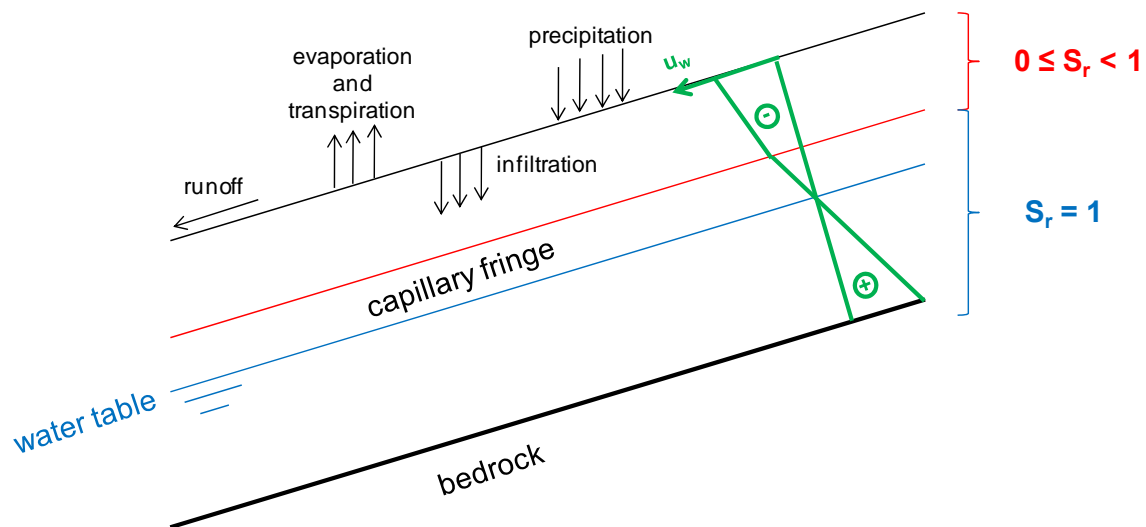


Figure 3.1 - Scheme of typical initial conditions of a slope in coarse-grained soils before being subjected to weather

An expression of the shear strength τ_{lim} which can be associated to the portion of deposit located **above the capillary fringe** is furnished by the following well known formulation (Fredlund, 1979)

$$\tau_{lim} = [c' + (u_a - u_w) \cdot \chi \cdot tg \varphi'] + (\sigma - u_a) \cdot tg \varphi' \quad [3.1]$$

where c' and φ' are the saturated effective shear strength parameters (cohesion and friction angle); u_a is the relative air pressure; $u_a - u_w$ is the matric suction, χ is a coefficient function of various factors (as confining total stress, suction, degree of saturation, void ratio, etc.); σ is the total normal stress. The coefficient χ , whose value is less than one, can be in turn expressed through the equation proposed by Vanapalli et al. (1996)

$$\chi = \Theta^k \quad [3.2]$$

where $\Theta = \frac{\theta - \theta_r}{\theta_s - \theta_r}$ is the relative volumetric water content; θ is the volumetric water content; θ_s is the saturated volumetric water content; θ_r is the residual volumetric water content; k is a

fitting parameter. Combining the equations [3.1] and [3.2] and assuming nihil the effective cohesion c' as typical for granular deposits, the shear strength takes the following expression

$$\tau_{\text{lim}} = (u_a - u_w) \cdot \Theta^k \cdot \text{tg} \varphi' + (\sigma - u_a) \cdot \text{tg} \varphi' \quad [3.3]$$

where the factor $(u_a - u_w) \cdot \Theta^k \cdot \text{tg} \varphi'$ is also known as “apparent cohesion” c . Such formulation points out that the wetting-drying cycles, which seasonally affect the slope, can influence the soil strength (Nuth and Laloui, 2008; Melinda et al., 2004).

At the same time, in the saturated portion of the deposit set **within and below the capillary fringe**, featured by a relative volumetric water content Θ equal to one, the shear strength takes the expression

$$\tau_{\text{lim}} = (\sigma - u_w) \cdot \text{tg} \varphi' \quad [3.4]$$

known as the classical Mohr-Coulomb failure criterion.

Both the expressions [3.3] and [3.4] highlight that during rainfall events, the hydrological response is strictly related to the geotechnical response of the deposit. In particular, the rates of rain water infiltration, runoff and pore-water pressure increase affect the rates of shear strength reduction and so the stability conditions of the slope. The soil response to is affected by several factors as geometrical aspects, rainfall characteristics, soil properties, initial conditions, boundary conditions: different combinations of these factors lead to completely different consequences in terms of time and depth of collapse. For example, experience shows that if an impervious boundary not so far from the ground surface exists, the failure occurs under saturated or unsaturated conditions depending on the rainfall intensity, respectively high or moderate. Otherwise, if the impervious bottom is very far from the ground surface or the deposit includes intermediate strata of low permeability, the failure is typically shallow.

Anyway, other hydro-mechanical processes can trigger slope movements during meteoric events. Upon that, the mobilized fluid flow can exert a destabilizing downhill frictional drag within the soil. Moreover, if the rainfall intensity is higher than the capacity of the soil to absorb water, this runs over the ground surface giving rise to concentrated erosion phenomena. Again, under strong cyclic variations of the environmental conditions, the shallowest soil layer is subjected to continuous strains and is exposed to weathering and destructuration: this leads to a decay of the shear strength (Leroueil, 2001).

The most widespread types of landslides triggered by infiltration in granular soils are slides and flows. Slides are caused by the formation of a continuous shear surface over which the landslide body slips displaying relatively small internal deformation. Flows display high displacements and very large internal strains, not clearly revealing a shear surface. Several worldwide examples show that in the same area, landslides with different styles can occur. Silvis and de Groot (1995) show, for example, that the coastlines of the Dutch province of Zeeland are affected by either slides or flowslides: slopes subjected to slides remain relatively steep after failure; those experiencing flow-like movements take a gentler morphology but the failed mass reaches a much larger distance than in previous case.

Experience suggests that even small details in the geomorphological features of the slope, in soil properties or in the internal effective stress field can be responsible for slide or flow movement pattern. Picarelli et al. (1993) describe the post-failure behaviour of landslides

occurred under saturated conditions through energetic considerations for the simple case of infinite slope consisting of a non-viscous soil subjected to a constant driving force due to its own weight, and to constant pore pressure. If the post-peak soil behaviour is stable (Fig. 3.2a), the resisting force along the slip surface is constant and its work is equal to the one made by the driving force for any post-failure displacement. When the resisting force is equal to the driving force, the slope is at limit equilibrium and the displacement rate is nil or constant. In this case, the equality between the two works doesn't let the soil mass to experience plastic strains during movement, thus it slides without internal strain like a rigid block. If the soil behaviour is brittle (Fig. 3.2b), the work made by the driving force after failure is larger than the one due to the resisting force that decreases during movement. The consequent kinetic energy may be calculated accounting for the energy dissipated by friction and internal plastic deformation. If pore pressure changes at the onset of failure or even after failure, it can affect the shear strength and so the velocity and behaviour of the landslide. In particular, generation of positive excess pore pressures is a fundamental triggering mechanism of flow-like landslides (Bishop, 1973; Dawson et al., 1998; Blight et al., 2000; Sassa, 2000). In particular, granular soils can liquefy and fluidize over their entire thickness, giving rise to extremely fast catastrophic events.

Typical landslides in granular soils are reported in the following sub-sections.

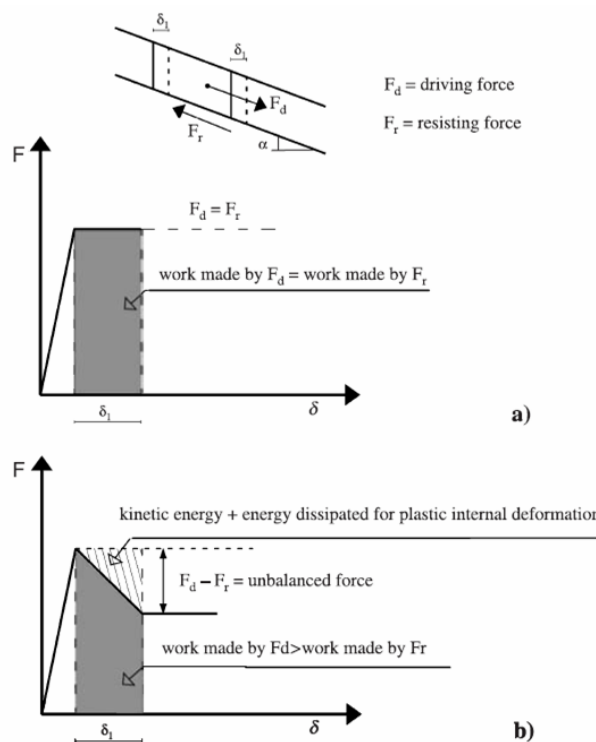


Figure 3.2 - Energetic considerations regarding the movement of a translational slide: a) stable behaviour; b) unstable behaviour (modified after Picarelli et al., 2003).

3.1.1.1 Cases of landslides in pyroclastic soils

(AMRA)

During the last decades, several flow-like rainfall-induced landslides involved the shallow pyroclastic deposits of Campania Region (Southern Italy), mainly originated by the explosive activity of the Somma-Vesuvius volcano. They caused hundreds victims and huge economical damages, inducing the scientific community to study in depth their characteristics. Olivares and Picarelli (2001) and Olivares and Damiano (2004) show that some of them stop at the base of the slope covering relatively short distances, while others turn into catastrophic flowslides, able to run kilometres even along very gentle slopes. As an example, Figure 3.3 reports some landslides occurred on 16th December, 1999, in Cervinara: landslide A was a fast flowslide that ran a couple of kilometres along the bed of a creek located at the foot of the slope, before impacting some houses; in contrast, landslides B and C stopped before reaching another parallel creek, although involved materials were similar.

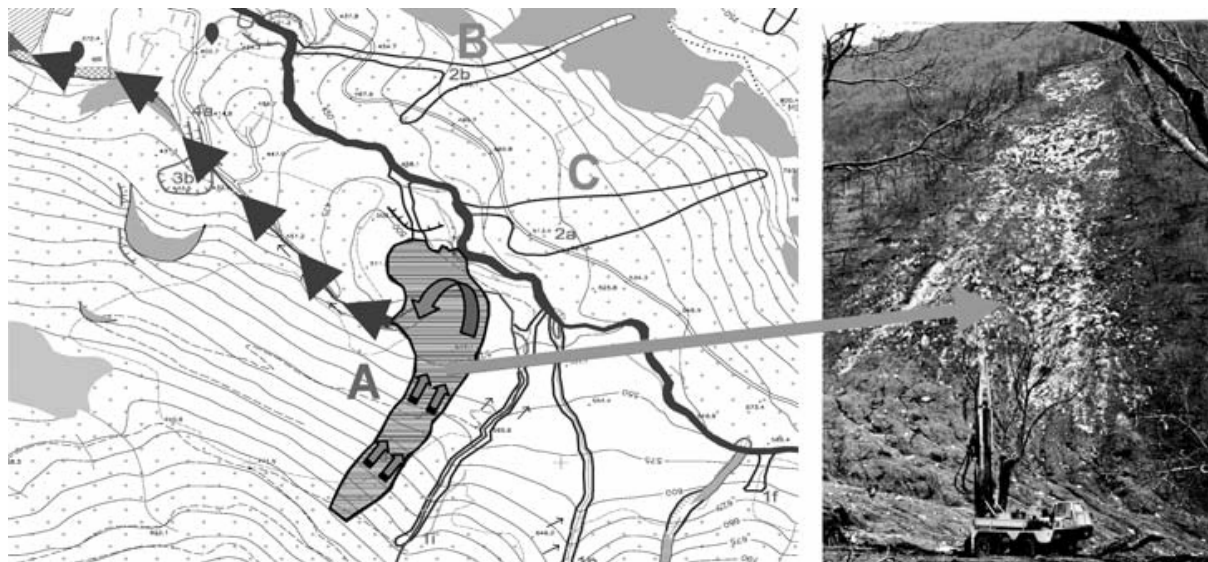


Figure 3.3 - Landslides triggered by rainfall in December, 1999, in the Cervinara area (from Olivares and Picarelli, 2001).

Several other examples could be mentioned for the same geomorphological context. In September, 2001, December, 2004, and May, 2005, intense storms triggered many landslides in Naples and in a wide area around the town: slides occurred along slopes generally steeper than 45°, travelling only tens metres; in contrast, flows were triggered along gentler slopes (35–40°) covering much larger distances. Olivares et al. (2002) remark that the degree of saturation of deposits at the onset of landslide is determinant to control the post-failure behaviour: in particular, adopting the infinite slope model and assuming nil the effective cohesion, failure occurs in unsaturated or saturated conditions if the inclination of the slope is higher or lower than the critical friction angle of the soil (Fig. 3.4). On May 1998, tens of debris flows killed 159 people in Sarno, Siano, Bracigliano and Quindici, North-East to Naples (Cascini et al., 2000): the peculiar aspects of this event are broadened in the next section. Next to this area, on March, 2005, a flowslide occurred along a 36° slope close to

Nocera Inferiore (Fig. 3.5), the last and more significant event among a large number of phenomena that had involved the Lattari Mountains (Table 3.1). The mobilised area was 24.600 m² and the soil mass 33.000 m³ with depth ranging between 1 and 3 m: the landslide was likely triggered in the uppermost zone, featured by a slope angle of about 39° (de Riso et al. 2007), and propagated downward. The pyroclastic cover is made up of loose non-plastic silty sands (volcanic ashes) that lie on a bedrock consisting of a highly fractured limestone. The rate of displacement was so high (about 12 m/s) to destroy a house and kill three people. The landslide was triggered by a cumulated rain $h_{24h} = 149$ mm, that fell down during the last 24 hours, and after an unfavourable preparatory condition set up by a precipitation $h_{2months} = 540$ mm during the last 2 months: both the h_{24h} and $h_{2months}$ resulted the highest values measured since 1950 by a rain-gauge far just some hundreds of meters from the site. Based on available information about the main hydrological, geomorphological and geotechnical factors, the Nocera Inferiore case has been analyzed by Pagano et al. (2010) to calibrate a simple numerical procedure for assessing the evolution with time of water content and degree of saturation, as well as of the piezometric regime, due to water infiltration.

In order to have a procedure fast enough to timely predict the critical event, the analysis contains some simplified hypotheses: i) the soil skeleton is rigid; ii) the slope is infinite and homogeneous; iii) the seepage is vertical (1D). The behaviour of the investigated slope has been simulated adopting as hydraulic boundary conditions at the ground surface the hourly rainfall data measured from January, 1998 to June, 2009. Figures 3.6 and 3.7 show the calculated suctions at depths of 0.5, 1, 1.5 and 2 m during the reference period. These are clearly higher than zero in the years 2002, 2004 and 2007. Since the slope angle is equal to the friction angle of soil, the effective cohesion being nil, failure should occur when suction vanishes; in fact, such analyses justify the good slope stability in that period, as confirmed by the fact that no landslides involved neither that slope nor other nearby similar slopes during those years. On the contrary, suction values close to zero at small depths and very small values at deeper points have been calculated for the other years. In particular, on 5th May 1998, i.e. at the time of the killer Sarno event, only 8 km far from Nocera Inferiore, the calculated suction is close to zero until a depth of 0.5 m. Similar considerations hold for the situation on 16th December 1999, i.e. at the time of the Cervinara flowslide, when simulated suction is very little until 1 m from the ground surface. The worst situation has been recognized for 9th January 2003 and for 2nd January 2006, when the analysis yields the lowest suction values, only slightly higher than those calculated for the landslide of March 2005, suggesting that during those two rainfall events the slope had a very small safety factor. According to the Authors, the proposed procedure is potentially extendable to the short-term prediction of landslides in unsaturated slopes that experience essentially 1D infiltration during wet seasons.

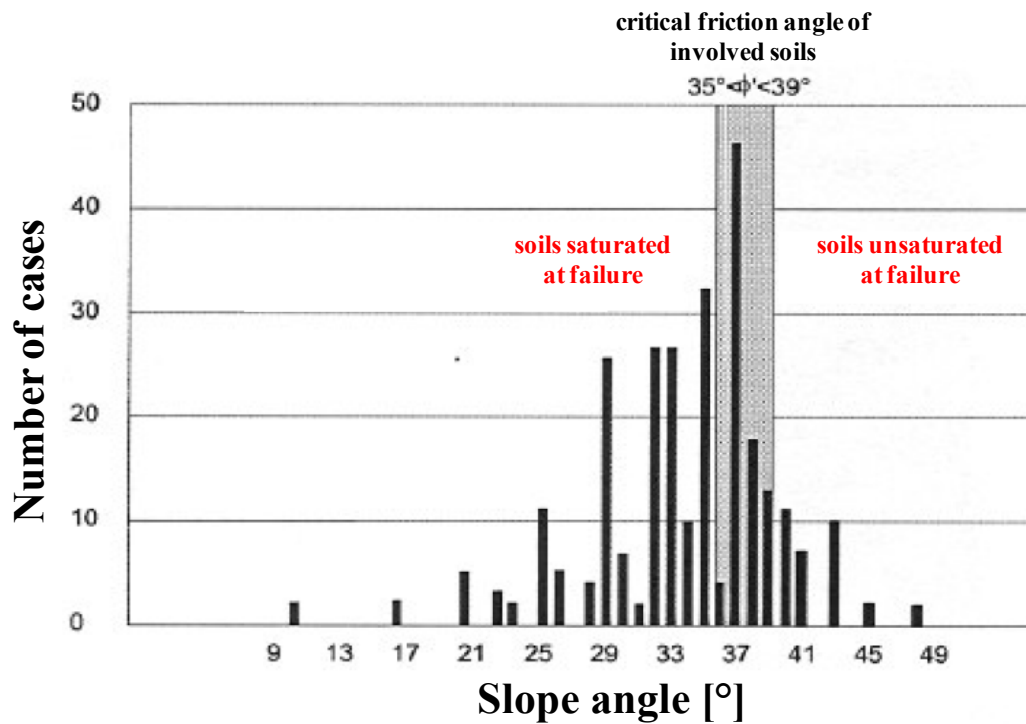


Figure 3.4 - Landslides occurred in *Quindici*: inclination of involved natural slopes (modified from De Riso et al., 1999).

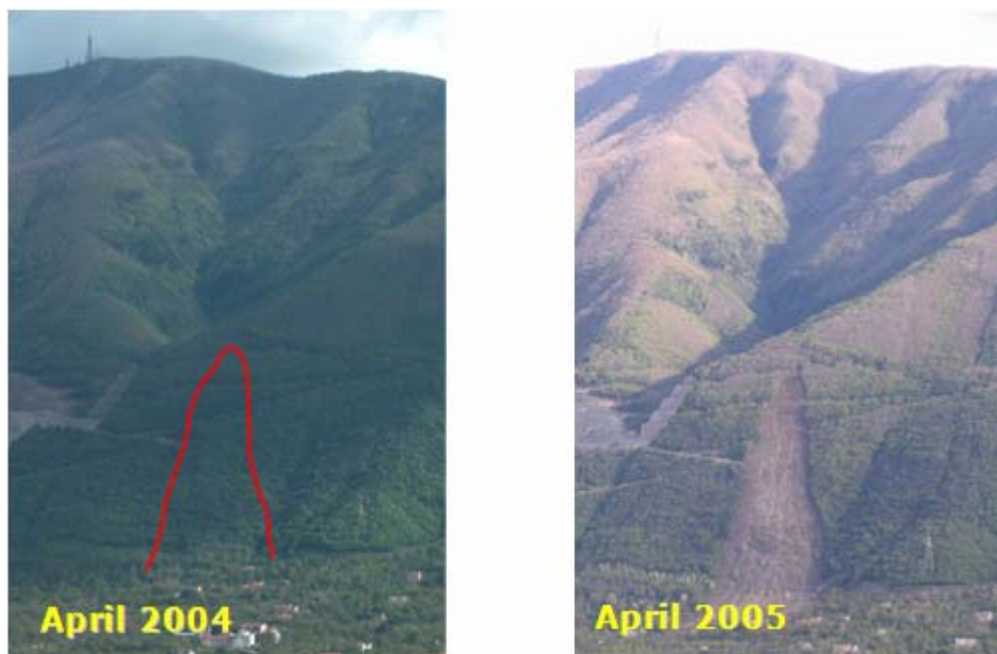


Figure 3.5 - The *Nocera Inferiore* landslide, one year before and one month after the event.

Table 3.1 - Most significant flowslides triggered in the Lattari mountains during the last decades (de Riso et al., 2005).

N.	Flowslide	Date	Height (m)	Runout (m)	Volume (m³)	Angle of reach (°)
1	Scrajo	23/11/66	220	300	10.000	36
2	M. Pendolo	02/01/71	205	375	7.500	28
3	S. Pantaleone	06/03/72	90	180	5.000	26
4	Mitigliano	16/02/73	200	272	9.000	36
5	Palma C.	22/02/86	185	400	8.000	25
6	S. Pantaleone	10/01/97	135	240	4.500	29
7	M. Pendolo	10/01/97	125	210	4.500	31
8	Rimonte	10/01/97	130	135	750	43
9	S. Egidio	10/01/97	215	500	10.000	23
10	Bracigliano	12/04	220	468	-	25
11	Nocera	04/03/05	295	530	33.000	29
12	M. Faliesi	04/03/05	200	400	15.000	27

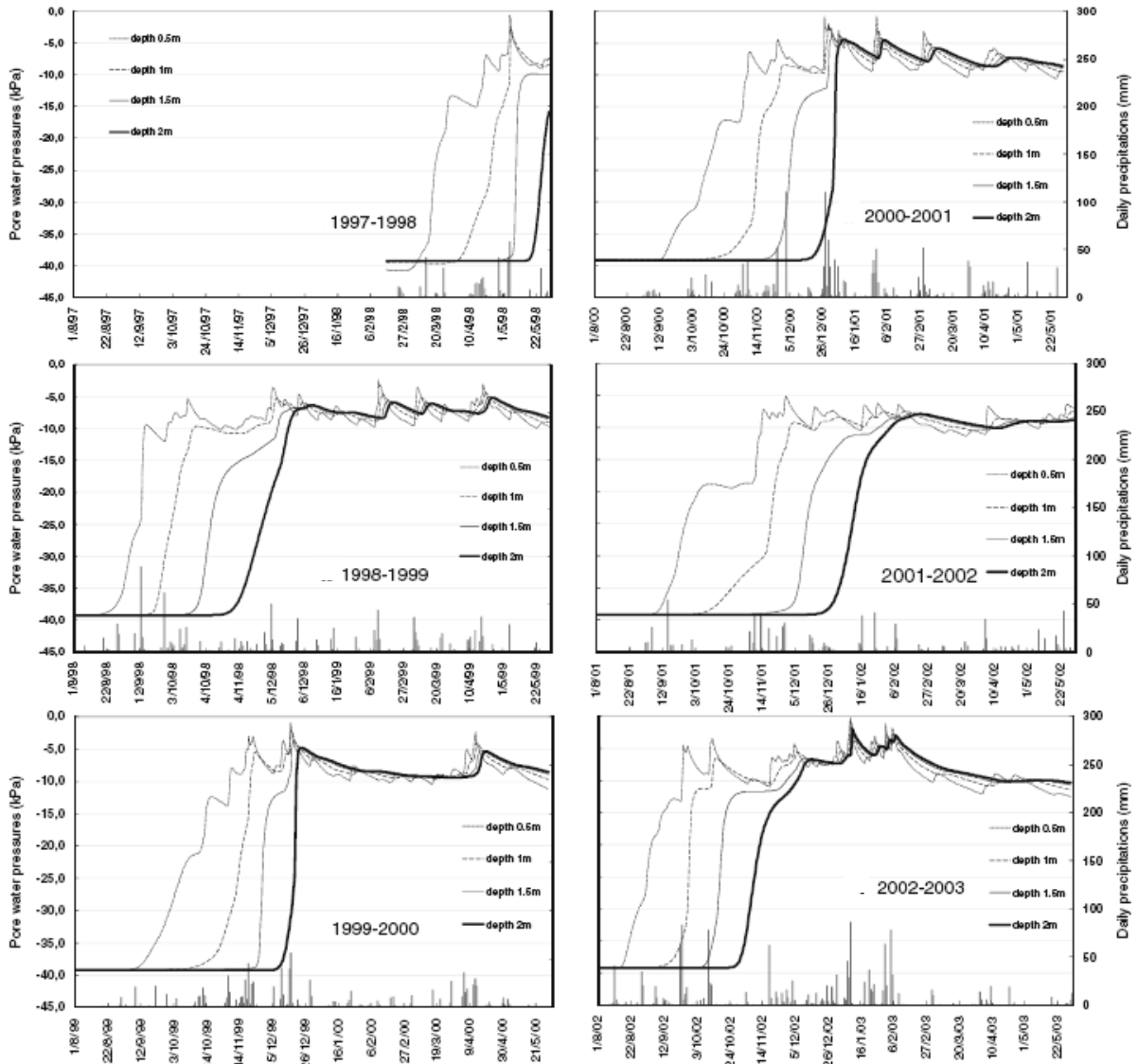


Figure 3.6 – Response of the Nocera Inferiore slope to rainfall events: suction simulated at different depths during the period 1998-2003 (after Pagano et al., 2010)

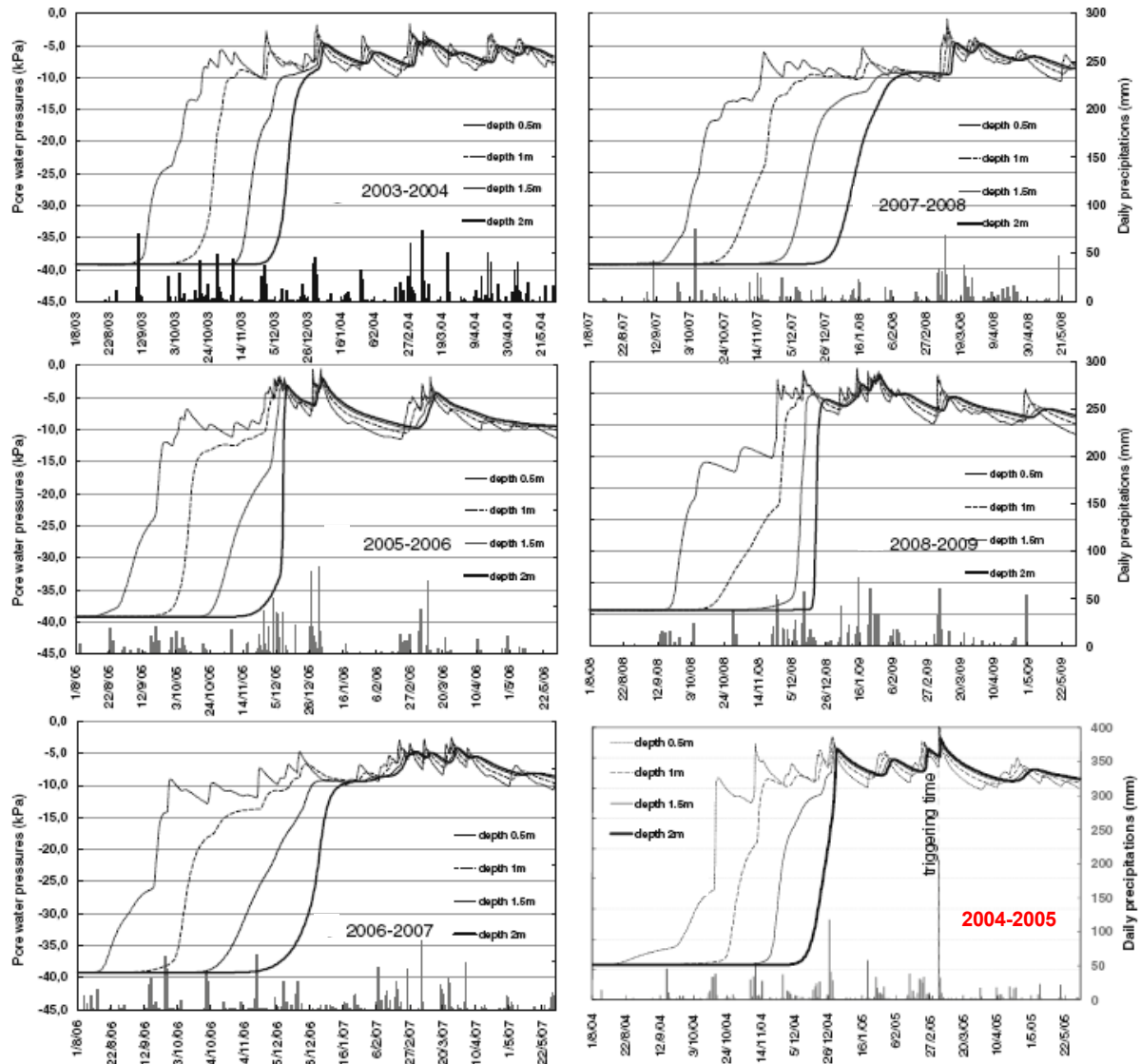


Figure 3.7 – Response of the Nocera Inferiore slope to rainfall events: suction simulated at different depths during the period 2004-2009 (after Pagano et al., 2010)

3.1.1.1.1 The case of Pizzo d'Alvano landslides

(UNISA)

An important case history is the event of 4-5 May 1998 which involved the slopes of the Pizzo d'Alvano Mt (60 km² area) (Fig. 3.8). During this event, tens of landslides of the flow-type caused 159 victims and relevant damage to buildings. Descriptions of the landslides and of their consequences are available in the scientific literature (Cascini 2004) as well as contributions dealing with triggering (Cascini et al. 2008a) and propagation (Pastor et al. 2008).

With the goal to understand the mechanisms and deepen on the failure stage of these landslides, Cascini et al. (2008a) adopt a multidisciplinary approach based on geology, geomorphology and geotechnics. In particular, the main geological and geomorphological features of both the bedrock and pyroclastic deposits are included in three hillslopes models capable of providing a general framework for the analysis of landforms and landslide processes. Furthermore, hydrogeological and anthropogenic factors are taken into account, which allow to identify six typical triggering mechanisms, illustrated in Figure 3.9 (Cascini et al., 2008a; Cuomo, 2006), which have been recognised in different geomorphological units (i.e. zobs, open slopes, flanks of valley, etc.) originating different landslide source areas (elongated, triangular, etc.).

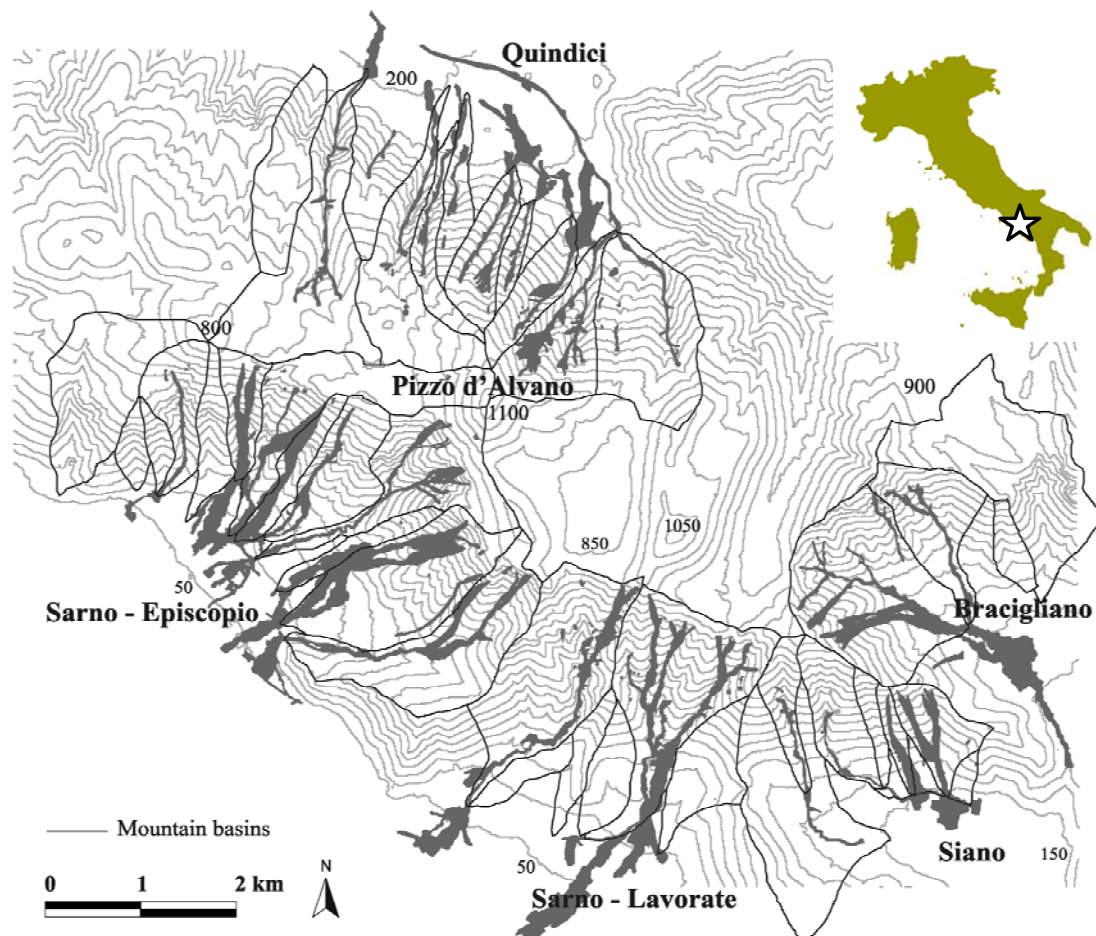


Figure 3.8 - Pizzo d'Alvano massif: overview of the main landslides of the flow-type occurred in May 1998 (from Cascini et al., 2008a).

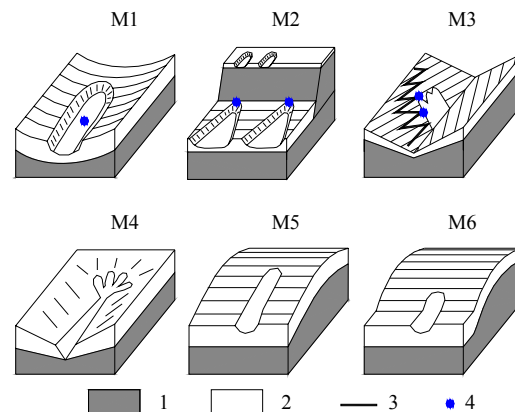


Figure 3.9 - Triggering mechanisms (M1-M6) for the May 1998 landslides of the flow-type: 1) bedrock, 2) pyroclastic deposit, 3) track, 4) spring from bedrock (modified from Cascini et al. 2008a).

In order to provide a geomechanical validation of such mechanisms, these have been analysed with the aid of advanced engineering models both at local (site) and general (massif) scale. The role played by the geological and geotechnical features on the different triggering mechanisms is evidenced by either classical or advanced geotechnical analyses. In order to show the potentialities of these advanced models, hereafter the geomechanical modelling of the triggering mechanisms M1, M2 and M3 is discussed (Cascini et al., 2008b; 2008c; 2010). Referring to the triggering mechanism M1 which was the most widespread during the May 1998 event, Cascini et al. (2010) propose some reference schemes. This triggering mechanism occurs inside Zero Order Basin (Cascini et al., 2008a) and is induced by either infiltration from the ground surface either spring from bedrock. However, major differences have been recognized among slides, slides turning into flows and flowslides. These landslide typologies are, in fact, characterised by different effective stress paths. However, the eventual sudden acceleration of the failed mass (post-failures stage) arises as a consequence rather than a cause of the slope instability process, as experimentally demonstrated by Eckersley (1990) and Chu et al. (2003). From that, it is concluded that the failure and post-failure stages can be separately analysed.

Starting from this point, Cascini et al. (2010) describe the mathematical framework, mainly derived from the fundamental contributions of Zienkiewicz et al. (1980, 1999), which can be profitably used to simulate the landslide failure and post-failure stages. From this framework, three different approaches (limit equilibrium analyses, FEM uncoupled stress-strain analyses and FEM coupled stress-strain analyses) are derived. Among these, the selected method derives from the addressed issue (failure stage or failure and post-failure stages) and other relevant aspects such as, for instance, the scale of the analysis and the available data-set. Anyway, the integrated use of different models is strongly recommended in order to capture the essential aspects of complex real boundary value problems, so obtaining significant answers from an engineering point of view.

Following this framework, Cascini et al. (2010) use limit equilibrium analyses to point out, at site scale, the role played by local stratigraphy, initial and hydraulic boundary conditions as predisposing and triggering factors of multiple slides characterised by a complex failure time sequence. Particularly, they examine a detailed slope section by using numerical commercial

codes. The analyses primarily concern the modelling of pore water pressure changes during the time period from January 1, 1998 to May 5, 1998. Using the computed pore pressures values, slope stability conditions are evaluated through classical limit equilibrium methods and a full parametric analysis is performed changing initial suction and hydraulic boundary conditions in order to obtain a satisfactory fitting among the failure time sequence and the available eyewitnesses. Slope stability analyses allow well reproducing the observed slope instability phenomena (Fig. 3.10). Particularly, multiple slides are simulated along the slope according to a complex time sequence, which is strictly dependent on suction initial conditions, as well as to the presence and starting time of the spring from the bedrock (Cascini et al., 2005, 2008). Taking into account the change of slope geometry, retrogressive multiple slides are simulated in drained conditions, in agreement with the results provided by Take et al. (2004) and Ng (2008) with centrifuge tests.

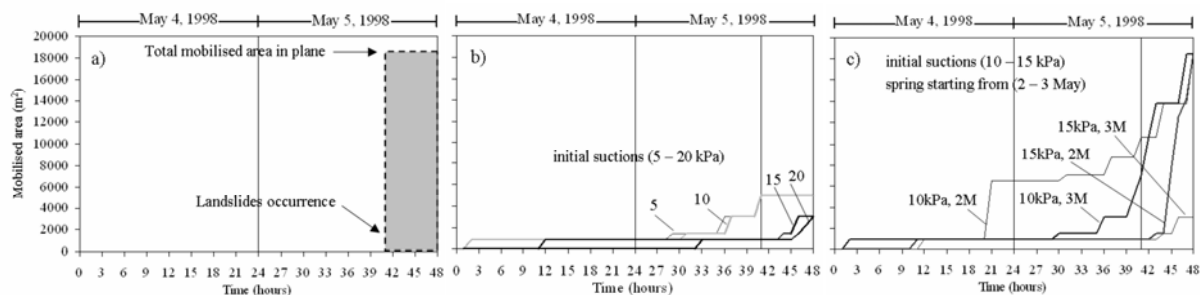


Figure 3.10 - Slope failure time sequence simulated for a detailed slope section.

At massif scale, limit equilibrium analyses (Fig. 3.11) are performed referring to more general site conditions. To this aim, infinite slope schemes are referred and parametric analyses are performed with typical slope angles, depths and stratigraphical settings provided by the in-situ evidences. A parametric analysis is performed whose details can be found in Cascini et al. (2010). Here the main results are briefly summarised. Rainfall infiltration from ground surface and spring from the bedrock increase the pore water pressures up to the slide occurrence, independently from the assumed stratigraphical setting and for any shear strength among those considered in the analysis. This is clearly pointed out by the correlation between the maximum pore water pressures along the critical slip surfaces and their factors of safety (points P1-P3 along slip surfaces S1-S3 in figure 3.11). Different stratigraphical settings and mechanical properties of pyroclastic deposits, in turn, determine different depths of the slip surfaces.

More detailed information and further insights on the failure stage are obtained through 2D uncoupled stress-strain analyses performed by numerical commercial codes. The obtained results highlight that, disregarding the spring from the bedrock, rainfall infiltration from the ground surface induces low deformation rates in the slope and the observed failure onset cannot be simulated. On the contrary, by considering the spring from bedrock, higher pore water pressures, stress ratios and deformation rates are simulated in the portion of the slope corresponding to the spring zone, in agreement with the limit equilibrium analyses (Fig. 3.12). The modelling of both failure and post-failure stages is finally addressed through more sophisticated coupled 2D and 3D stress-strain analyses using the GeHoMadrid code (Mira, 2002; Pastor et al., 2004). For the analyses, an infinite slope scheme and the stratigraphy of

the scheme 3 of figure 3.14 is used, considering the same initial and hydraulic boundary conditions as well as the same simple constitutive model. Moreover, these analyses are also extended to 3D conditions, to check the validity of previous results. Particularly, a 3D slope characterised by a concave transversal bedrock profile and a variable depth for the overlying pyroclastic deposit is considered. The results obtained through 2D and 3D analyses confirm that significant plastic strains are simulated only if both rainfall and spring from the bedrock are considered. It is worth noting that the results of 3D coupled analyses (Fig. 3.13) agree with the slope instability scenarios obtained through 2D coupled analyses and they well match the results obtained with simplified models and the time failure well agree those obtained with the previous simplified analyses (Figs. 3.11, 3.12), thus highlighting their capability to capture the global behaviour of the slope.

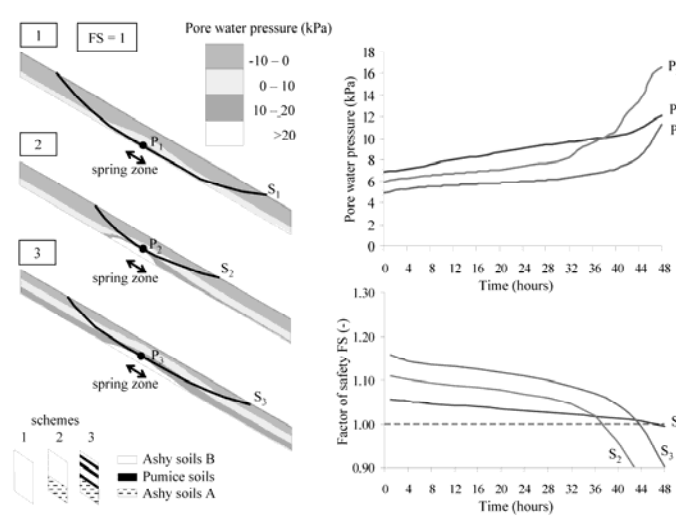


Figure 3.11 - Limit equilibrium analyses at massif scale: pore water pressures and slope factor of safety (FS) during the 4-5 May 1998 event (from Cascini et al. 2010).

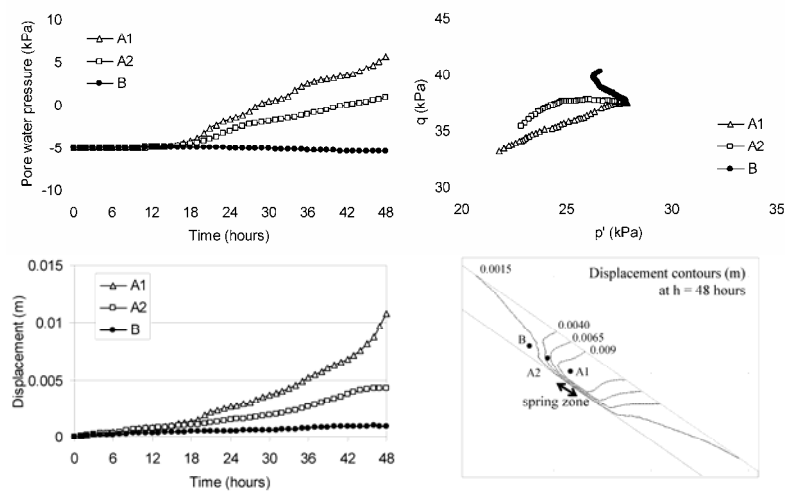


Figure 3.12 - Uncoupled stress-strain analyses at massif scale: pore water pressures, displacements and stress paths for the scheme 1 of figure 3.12 (from Cascini et al. 2010).

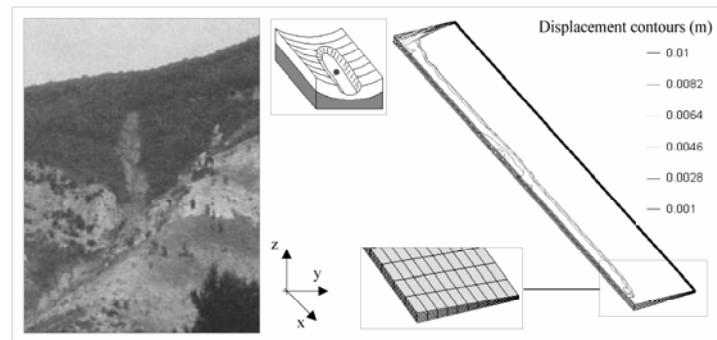


Figure 3.13 - 3D coupled stress-strain analyses: displacement contours.

In conclusion, these analyses demonstrate the occurrence of a slide due to both rainfall infiltration and spring from bedrock and they highlight the potential for this slide in turning into flow because of the deformation mechanism. This last aspect, however, will be properly addressed only when a suitable constitutive model will be available. To this regard, a constitutive model is proposed within the UNISA contribution in the section 4.1.1.2.

Concerning the mechanism M2 (Fig. 3.14), the previous advanced engineering models have been also used by Cuomo (2006) and Cascini et al. (2008c). Particularly, the failure stage is studied through both hydro-mechanical uncoupled and coupled approaches based on groundwater modelling, limit equilibrium and stress-strain analyses. The geomechanical analyses show that, for the mechanism M2a (Fig. 3.14a), karst springs at the base of bedrock scarps are as a severe hydraulic boundary condition. In fact, the induced transient pore water pressures cause the failure onset mostly depending on the stratigraphy, even for short durations of the springs. Referring to the impact phenomena (M2b in Fig. 3.14b), the failure onset is not simulated assuming drained conditions. Conversely, in undrained conditions, the increase of pore water pressures determines the failure onset that is satisfactorily justified by limit equilibrium analyses. Analogous scenarios are obtained through stress-strain analyses that also point out the high decrease of mean effective stresses and the possibility of liquefaction phenomena.

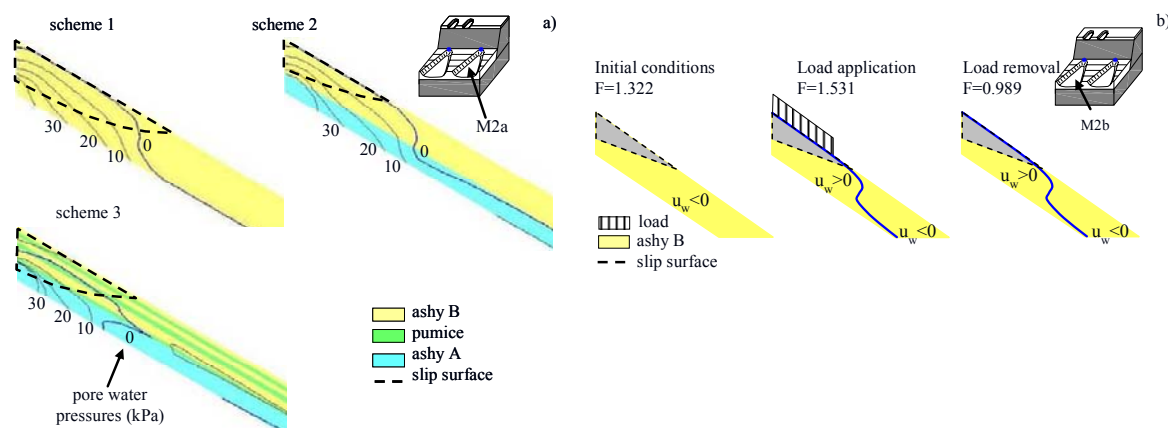


Figure 3.14 - Failure stage induced by a) karst springs from bedrock, b) impact phenomena in undrained conditions (modified from Cascini et al. 2008c).

For the triggering mechanism M3, Cuomo (2006) and Cascini et al. (2008b) stress the fundamental role played by some anthropogenic factors such as mountain tracks and cut slopes (Fig. 3.15) which often correspond to geometrical discontinuities in the slope morphology. Mountain tracks are responsible for conveying large amount of superficial rainwater in singular points along the slopes, so inducing severe hydraulic ponding conditions at the ground surface. To this regard, groundwater modelling highlights that ponding conditions strongly affect the transient pore water pressures, mostly depending on the local stratigraphical setting. Limit equilibrium and stress-strain analyses, in turn, outline that geometrical discontinuities act as aggravating factors for slope stability conditions while stratigraphy is demonstrated as the key factor for the failure onset (Fig. 3.15).

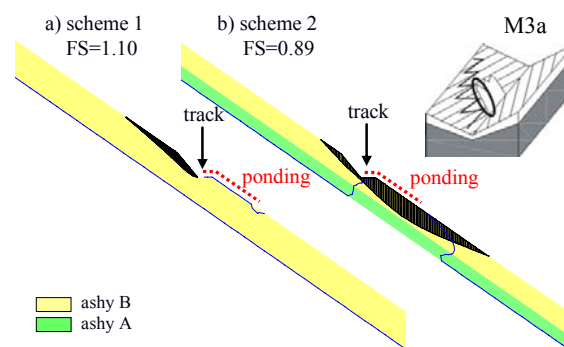


Figure 3.15 - Limit equilibrium analyses for zones close to bends of tracks (from Cascini et al. 2008b).

At massif scale, Sorbino et al. (2007, 2009) deal with the modelling by using three different physically based models developed in a GIS framework: SHALSTAB (Montgomery & Dietrich 1994), TRIGRS (Baum et al. 2002) and TRIGRS-unsaturated (Savage et al. 2004). The evaluation of the results provided by the three models is carried out through the definition of two percentage indexes able to quantify the “Success” and the “Error” of each model in interpreting the observed source areas. The obtained results highlight that the transient TRIGRS models provide, for the same Success Index values, Error Index values lower than those obtained by the steady-state SHALSTAB model (Fig. 3.16). This latter provides a systematic overestimation of the observed source areas, due to the transient characteristic of the pore pressure regime and unsaturated conditions which characterise the landslides source areas. As for the simulation of the six triggering mechanisms of figure 3.9, both TRIGRS models provide the best results for the M4 mechanism because they properly take into account the main characteristics of the triggering mechanism. Similar good results are not obtained for the other mechanisms, as these last are related to local boundary conditions that are not considered in the selected models e.g. water inflows in M1, bedrock scarps in M2, influence of anthropogenic elements in M3, and convex/concave longitudinal slope profiles in M5 and M6.

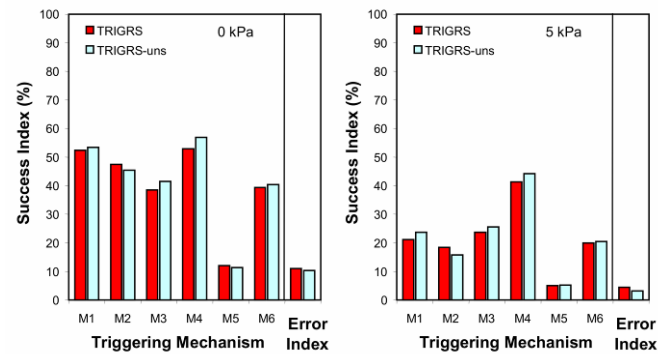


Figure 3.16 - Results obtained for the entire area of Pizzo d'Alvano massif with the TRIGRS and TRIGRS-unsaturated codes for the triggering mechanisms of figure 3.7 (from Sorbino et al. 2007).

3.1.1.2 A landslide in weathered gneissic soils

(UNISA)

Figure 3.17 shows the study area of about 7.5 km² in the Sila Grande massif where the most of landslides involve a heterogeneous gneissic cover composed of colluvial, residual and saprolitic soils along slopes with angles between 21°-23°. These landslides are characterised by sudden reactivations, not preceded by clear warnings, and paroxysmal phases which end within a very short lapse of time. Generally, long time intervals separate reactivations, with the consequent obliteration of the morphological signs of landslides.

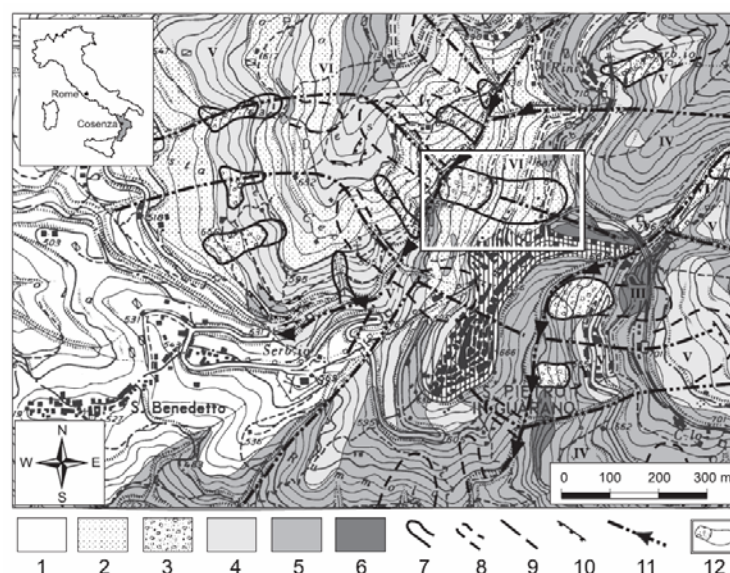


Figure 3.17 - Part of the weathering grade and landslides map of the Western Sila study area (Calabria-southern Italy): 1) sedimentary soils; 2) colluvial and residual soils (class VI); 3) landslide debris; 4) completely weathered gneiss (class V); 5) highly weathered gneiss (class IV); 6) moderately weathered gneiss (class III); 7) recent landslide scarp; 8) old landslide scarp; 9) fault; 10) rock landslide scarp; 11) deepening ditch; 12) studied landslide (from Cascini et al. 2006).

Due to both the difficulty in recognizing landslides and the heterogeneity of the involved materials, the analysis of instability phenomena inside the study area called, first of all, for a classification of the weathering grade of the gneiss (Cascini et al. 1992b, 1994a, 1994b, Gullà and Matano 1997) that was drawn up referring essentially to the procedures developed in Hong Kong (G.C.O. 1984, 1988) on similar rocks. This classification was then used as a standard for surface geological surveys that, together with detailed geomorphological analyses, allowed to set up a landslides inventory map where landslides distribution is compared with morphology, tectonics and weathering grade of the outcropping gneiss in the area (Fig. 3.17) (Cascini et al. 1992b). With reference to the most representative phenomena, a slope evolution model was successively implemented, essentially based on geological analyses. In order to validate such a model and to deepen the triggering mechanism of the landslides, geotechnical investigations at a very detailed scale were carried out.

One of the most investigated landslides (Fig. 3.17), having an area of about 20000 m² lies within a small town; its first reactivation during the last century was recorded in 1931. After a long period of quiescence (Cascini 1986), another reactivation occurred on January 1981 causing severe damage to many public and private buildings. During this event, movements ceased within about 48 hours, as indicated by topographic measurements acquired soon after the paroxysmal phase. Both reactivations (1931 and 1981) occurred after heavy rainfall, as highlighted by a hydrologic analysis of rainfall data available from 1923 onward (Cascini and Versace 1988).

Some months after the last reactivation, piezometers and inclinometers were installed in the landslide area. Inclinometers readings, carried out from the beginning of 1981, confirmed the absence of movements. Consequently, it was not possible to establish pore pressure values responsible for landslide reactivations, notwithstanding the accurate data set collected during monitoring. For this reason, it was necessary to model the groundwater regime on the basis of the stratigraphic conditions of the slope and the geotechnical properties of soil.

In particular, in-situ investigations (Fig. 3.18) consisted of: drilling of 28 boreholes with a maximum depth of 70 m and installation of 46 piezometers (35 Casagrande and 11 open-pipe); collection of samples for laboratory testing; in situ permeability tests.

The in-situ investigation, together with geological surveys, showed that the subsoil is formed by a gneissic cover filling up a paleo-gully, whose axis is aligned with a structural discontinuity (Fig. 3.17). Along the cross sections of the slope, the gneissic cover has a thickness ranging between 20 and 25 m (Fig. 3.18).

Based on geological surveys, the cover results essentially composed of residual and saprolitic soils (classes VI and V), systematically including zones of colluvium and landslide debris, whose size ranges from few decimetres to several meters. Following the geomorphological evidences, the landslide slip surfaces develop inside the cover (Fig. 3.18) at the contact between the cover and the bedrock. The bedrock is composed of highly to moderately weathered gneiss (Classes IV and III) and slightly weathered or fresh gneiss (Classes II and I) with fault gauge.

Concerning the rainfall pattern, the area is characterised by dry summer and wet winter seasons. The theoretical cumulated rainfall distributions for different return periods, obtained with the method of statistical hydrology (Cascini and Versace 1988), highlight that the most critical rainfall events coincide with a cumulated daily rainfall attaining 900-1000 mm over a period of 100-110 days, having a return periods of about 40-50 years.

Piezometer measurements (Fig. 3.18) taken from 1981 to 2001 in the slide area (Fig. 3.19)

have revealed the presence of two distinct, locally interconnected aquifers: one is located in the cover and is characterised by a perched water table; the other is in the bedrock (Cascini and Gullà 1988; Cascini et al. 1995). The perched water table is strongly influenced by winter rainfall events, when significant excursions of piezometer levels are recorded. However, for the most of the landslide area, the highest piezometer levels were systematically recorded at depths well below the ground surface, indicating permanent conditions of partial saturation within the gneissic cover (Cascini et al. 2006).

The role played by partially saturated zones in the formation of perched water tables within the study area was ascertained by several tensiometers installed in a small slide area located near the one shown in Fig. 3.18 (Sorbino 1994; Gullà and Sorbino 1996). In this area, suction measurements indicate that the formation of the perched water table is a consequence of progressive upward saturation of the soil; they also reveal rainfall infiltration processes occurring under partially saturated soil conditions (Gullà and Sorbino 1996; Leroueil 2001; Calvello et al. 2008).

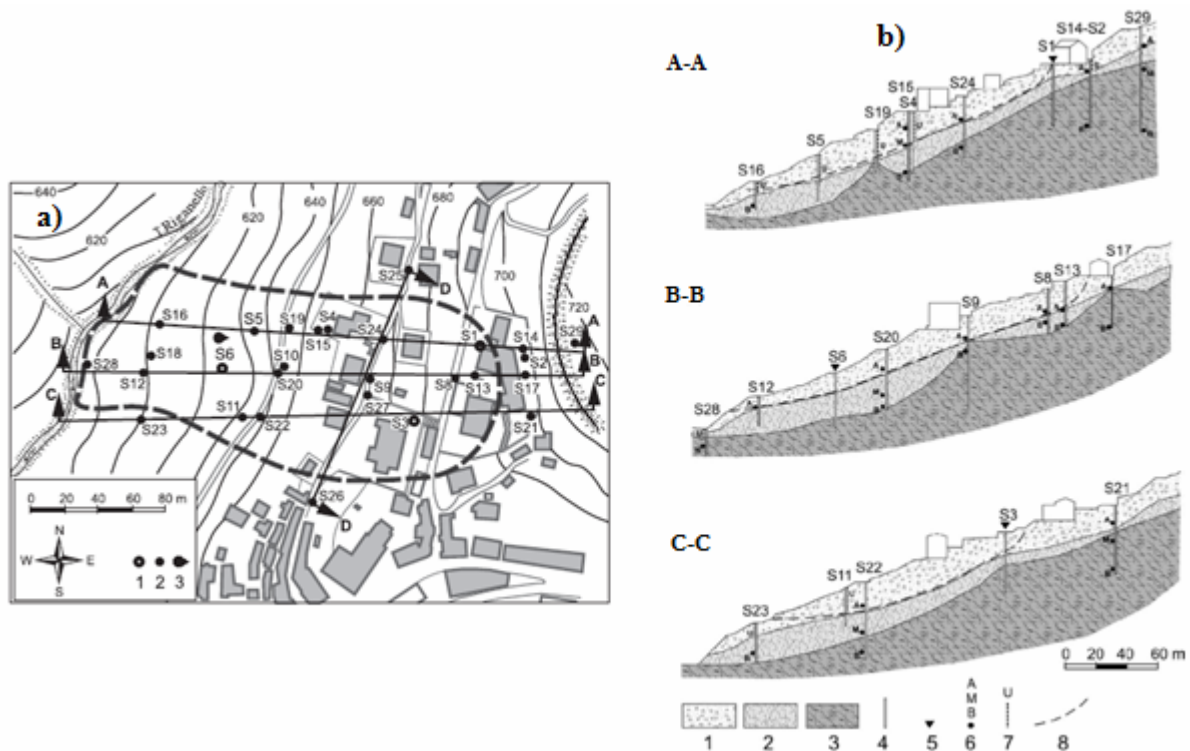


Figure 3.18 - a) Landslide area, boreholes and spring location: 1) inclinometer; 2) piezometer; 3) spring; b) Cross sections of the landslide area: 1) Gneissic cover (colluvial, residual and saprolitic soils – Classes VI and V); 2) Weathered gneissic bedrock (highly-completely, highly and moderately weathered gneiss - Classes IV-V, IV and III); 3) Gneissic bedrock (slightly weathered and fresh gneiss with fault gauge - Classes II and I); 4) borehole; 5) inclinometer; 6) Casagrande piezometer; 7) open-pipe piezometer; 8) slip surface (from Cascini et al. 2006).

Physical and mechanical characterisation of the weathered soils of class VI and V was determined by a number of in-situ and laboratory tests. Referring to Cascini and Gullà (1993),

Gullà and Sorbino (1994) and Sorbino (1994; 1995) for a detailed description of the experimental procedures, the obtained results allowed to carefully define the saturated and unsaturated hydraulic properties, as well as the shear strength characteristics of both weathering classes.

All data were adopted to model the significant pore pressure variations in the superficial aquifer induced by rainfall. To this aim, the modelling followed two distinct phases, namely: a calibration/validation phase and a prediction phase (Cascini et al. 2006). The calibration/validation phase had the objective to identify the relevant soil hydraulic properties able to furnish the better simulation of the recorded piezometer levels; the prediction phase dealt with the evaluation of the unknown piezometer levels during the last landslide reactivation through the use of the calibrated/validated model.

In order to take into account of partially saturated conditions over large portions of the cover, the analysis of the groundwater regime for the two phases was performed considering the water flow both in saturated and partially saturated zones. In particular, Richards equation was considered and its numerical integration was carried out by using the finite element code SEEP/W (Lam et al. 1987; Geo-Slope 2004).

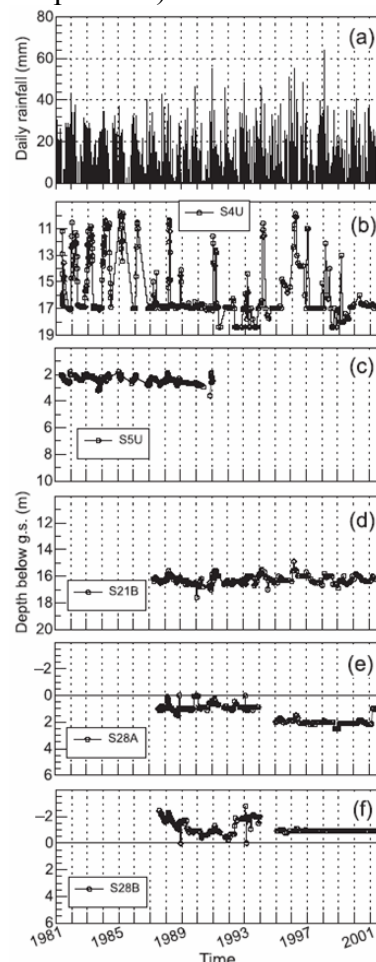


Figure 3.19 - (a) Daily rainfall record for the study area. (b–f) Typical time trend of piezometer levels in the gneissic cover (b), at piezometer S5U (c), in the gneissic bedrock (d), and at the landslide toe (e, f). (from Cascini et al. 2006).

Figure 3.20 shows the results obtained in the simulation of the recorded levels at five piezometers by adopting different assumptions on the hydraulic heterogeneity of the soil and the boundary conditions (Cascini et al., 2006). The assumption of a homogeneous cover sharing the same characteristics as more permeable soils, is able to model the measured excursions of the piezometer levels only for the part of the slope where the local observed heterogeneity does not play a relevant role. The improvement of the modelling for the whole slope was thus pursued by taking into account the macro-heterogeneity and the interactions between the superficial aquifer and the deep one in some portions of the slope (Fig. 3.20).

Figure 3.21 shows the results obtained for the period December 1980 – March 1981 by using the calibrated/validated geotechnical model of the slope. As it can be seen, the adopted scheme systematically provides, at the end of January 1981 and all over the slope, critical piezometer levels higher than those measured during the observation period. At this regard, it must be noted that the estimated critical levels, under the assumption of homogeneous cover (Cascini et al. 1995), turned out to be lower than those measured during the observation period, when the landslide was totally quiescent, so highlighting the need for a complex stratigraphical slope model.

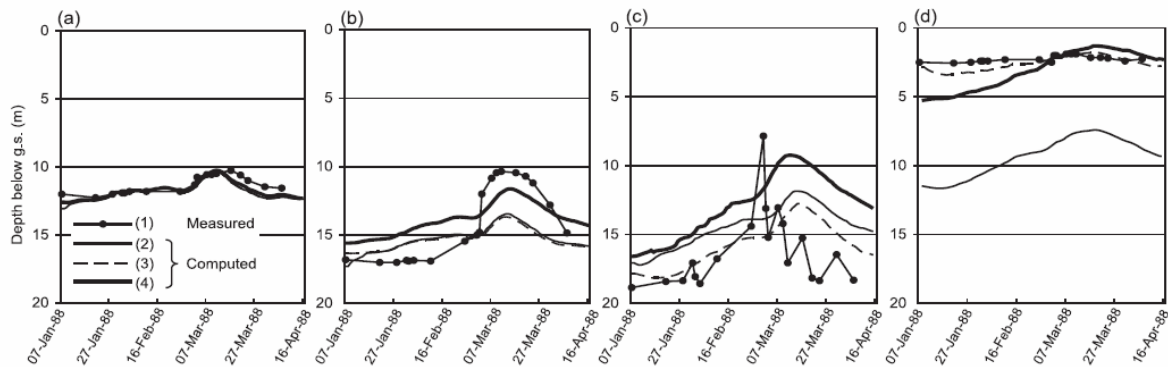


Figure 3.20 - Comparison between measured and computed piezometric levels for the 1987–1988 hydrologic year at piezometers S24A (a), S4U (b), S19U (c), and S5U (d). 1, measured levels; 2, computed levels assuming a homogeneous cover; 3, computed levels assuming a homogeneous cover and local boundary flows; 4, computed levels assuming a heterogeneous cover and local boundary flows, (from Cascini et al. 2006).

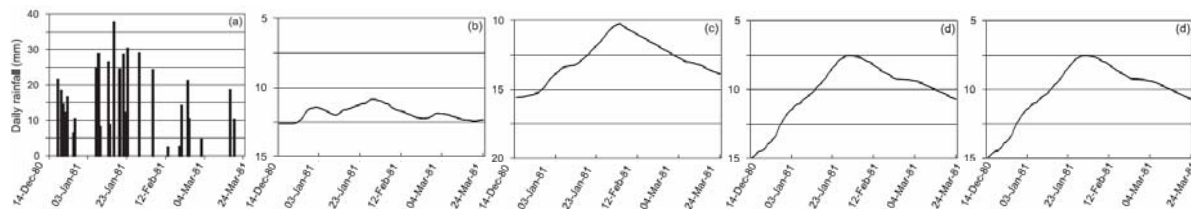


Figure 3.21 - (a) Daily rainfall record for the study area. (b–e) Computed piezometer levels for the period 14 December 1980 – 24 March 1981 at piezometers S24A (b), S4U (c), S19U (d), and S5U (e) assuming a heterogeneous cover and local boundary flows, (from Cascini et al. 2006).

Due to the lack of data on critical piezometer levels, the reliability of the results of Figure 3.21 was firstly checked by comparing these last with those furnished by a statistical model

(Cascini et al. 1992a) that provides the critical levels attained for a representative piezometer (S4U) on the basis of statistical correlations between rainfall and measured piezometer levels. The agreement between the two models is shown by Figure 3.22.

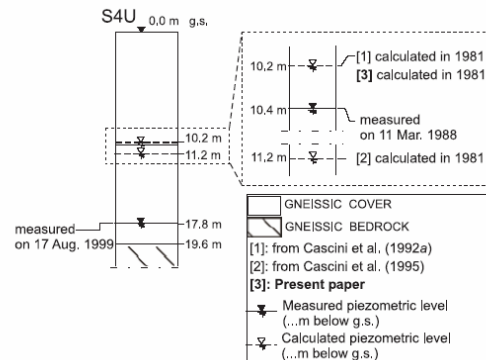


Figure 3.22 - Comparison between measured and computed piezometric levels at piezometer S4U using different models, (from Cascini et al. 2006).

3.1.2 Failure mechanisms of landslides in fine-grained soils

(AMRA)

Landslides involving the most of fine-grained deposits outcropping in wide European regions are typically translational slides and earthflows. Due to translational motion the driving force remains more or less constant with time and the post-failure displacements are essentially governed by the pore pressure regime and by its fluctuations, in turn regulated by the seasonal environmental conditions. In particular, the rate of displacement attains its peak value during the wet season, then it progressively slows down as the dry season approaches.

Natural slopes consisting of fine grained soils are characterized by a typical low permeability (less than 10^{-6} m/s) with consequences on the relation between environmental conditions and piezometric regime. In fact, due to the low hydraulic conductivity of soil, the precipitations have general delayed effects on pore pressures, that are consistent with seasonal rainfalls cumulated over long-lasting time periods (usually some months) and generally decrease with depth (Kenney and Lau, 1977). For such a reason, short intense rainfalls scarcely influence the piezometric regime.

The continuous change of the hydraulic boundary conditions plays an important role during the entire life of a slope. In order to better understand the consequent mechanical implications, it's useful to take into account the scheme proposed by Leroueil et al. (1996), who subdivide the behaviour of slopes into four different stages: *pre-failure*, *failure*, *post-failure*, and *reactivation*.

Pre-failure stage

Figure 3.23 shows the effects of precipitations at an assigned point of a natural slope. Pore pressures cyclically fluctuate within an interval, whose minimum and maximum values are not necessarily reached during each cycle (Fig. 3.23a). Of course, these oscillations provoke only changes in mean effective stresses, but the shear stress along any potential failure surface doesn't attain the strength envelope (Fig. 3.23b). Clayey deposits are generally

“overconsolidated”, i.e. in the past they have been subjected to effective stresses higher than the current values. As far as the stress path remains within the yield surface, changes in mean effective stresses induce only small strains. With the passing of time, effects related to mechanisms as creep, softening, weathering, fatigue determine the weakening of soil, which consists in the reduction of both elastic domain and strength envelope: as a consequence, the same cyclic groundwater fluctuations are able to induce plastic deformations. Mitchell and Eden (1972) and Tavenas and Leroueil (1981) state that creep develops at rates increasing with the stress level. Therefore, when the effective stress approaches the peak envelope, its effects become relevant and a local failure occurs if the peak shear strength is attained (Figs. 3.23c and 3.23d). According to these considerations, rainfall can represent the factor capable to trigger slope failure even though this has been reached thanks to other factors (Vaunat et al., 1994). Deformations following local failure cause a consequent reduction of the shear strength due to progressive failure (Bjerrum, 1967) that causes with increasing velocity the onward propagation of a failure surface until a general failure (landslide) takes place (Fig. 3.24). A likely evolution of slope displacement is reported in Figure 3.24d: movements are characterised by increasing velocity and acceleration, due to reduction of soil stiffness and strength. If the displacement induced along the shear surface is very large (more than 1 m), clayey particles becomes oriented along the direction of movement and the shear strength attains its minimum value, i.e. the residual strength, which is characterized by nihil cohesion and a friction angle φ'_{res} much smaller than φ'_{cr} in soils made up of platy particles (Lupini et al., 1981). All the processes are relevant in highly overconsolidated and plastic clays, because of their high brittleness and stiffness.

Failure stage

A first-time general failure occurs when the progressive formation of the shear surface involves the entire soil mass. As a result of the induced mechanism, the operational strength parameters are generally different along the failure surface (they can vary from peak to residual). Therefore, defining the representative overall mobilized strength parameters is a hard matter; most importantly, they can strongly differ from the peak values measured through standard laboratory tests.

Post-failure stage

Immediately after failure, the soil mass accelerates due to shear strength reduction (Fig. 3.25). As displacements develop, the landslide velocity slows down because of the induced morphological changes that cause a reduction of the driving shear stress along the slip surface. Experience shows that movements may occur for very long times (especially in the case of translational slides), so that periods of inactivity alternate to activity phases.

According to the energetic considerations (Picarelli et al., 2003), already reminded in section 3.1.1, the rate of movement and the run out distance covered by the landslide body are directly related to the part of potential energy initially available at failure that turns into kinetic energy (Fig. 3.2): such a part results high or low depending on the brittle or ductile behaviour of the clays. At the same time, if the soil is saturated and subjected to rapid deformations, excess pore-pressures can be generated and consequently the landslide body shows smaller strength and stiffness: such mechanisms should justify the transformation of typical slides in earthflows (Picarelli, 2001).

Reactivation stage

Once a landslide has occurred, during the long-lasting post-failure stage, piezometric fluctuations are able to periodically reactivate the landslide along the already formed continuous failure surface (Fig. 3.25b). Usually, if the landslide body has experienced displacements so large to provoke a re-orientation of plate-shaped clay particles along the entire surface, the mobilized strength parameter to take into account is the residual friction angle: on an intact clay, such a value can be measured through direct shear tests performed on reconstituted samples. The style of movements consists in sliding of a soil mass over an essentially rigid base and the related rate is variable according to the seasonal changes of the groundwater level and resulting generally small (0.01-1 m/year).

The most of the landslides which are described in the literature cover lengths of time of many years, and some movements are known to be active even from centuries. Some significant examples are reported in the follow.

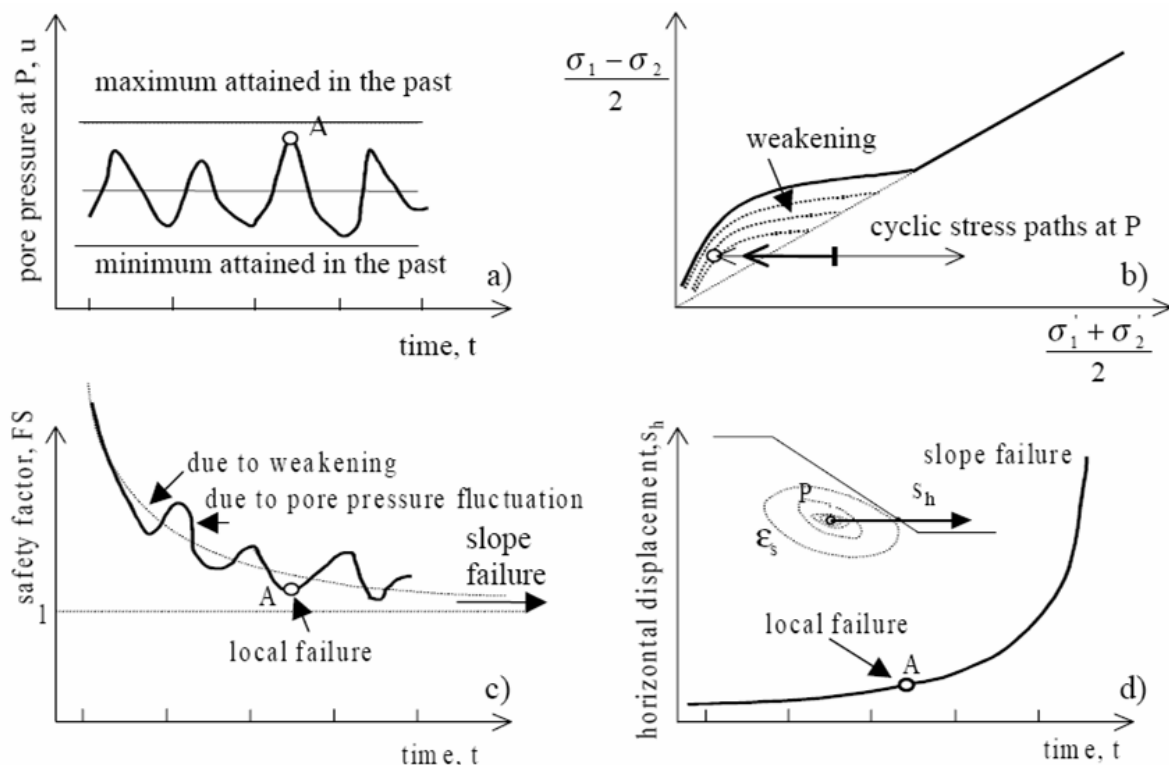


Figure 3.23 – Influence of pore pressure oscillation on the pre-failure behaviour of a slope in fine-grained soils: a) pore pressure fluctuation at an assigned point P; b) cyclic stress-path at the point P; c) safety factor trend during time; d) horizontal displacement at the point P (Picarelli et al., 2000)

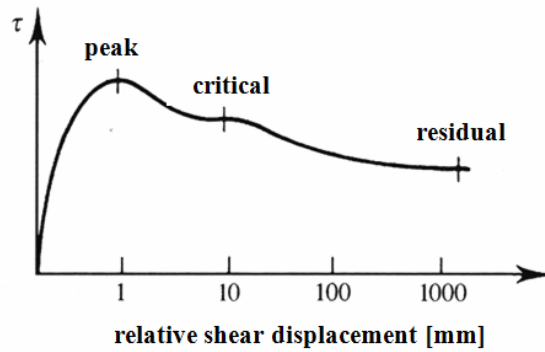


Figure 3.24 – Shear strength τ as a function of the relative shear displacement (modified after Atkinson, 1993)

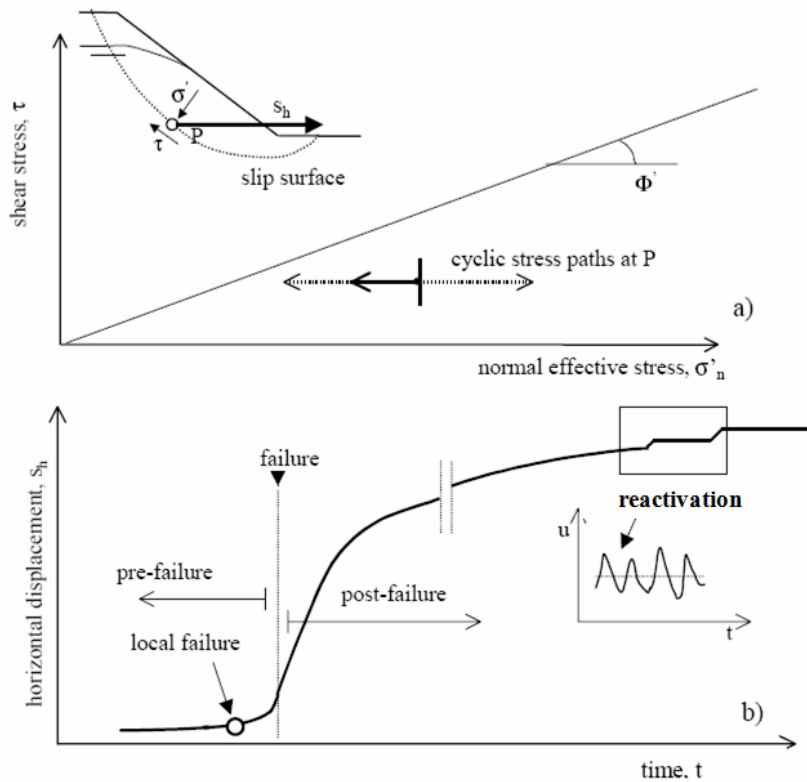


Figure 3.25 – Influence of pore pressure oscillation on the post-failure behaviour of a slope in fine-grained soils: a) cyclic stress-path at an assigned point P belonging to the failure surface; b) horizontal displacement at the point P (Picarelli et al., 2000)

3.1.2.1 Cases of slides

(AMRA)

A well-documented example of long-lasting active landslide is the Fosso St. Martino slide (Fig. 3.26), Abruzzo Region, Central Italy (Bertini et al., 1986). Monitoring, covering a six-years period, shows that movements are regulated by the pore pressure regime (Fig. 3.27). In particular, the rate of movement is around 0.35 mm/day when the depth of the groundwater surface is less than about 3 m, while the landslide practically stops if the groundwater level drops below such a critical value. Moreover, the yearly cumulated displacements seem to be affected by the total precipitation cumulated during the rainy seasons (Fig. 3.26b). Similar considerations are reported by Tommasi et al. (2006), who describe the relationship between rainfall, pore pressures and landslide behaviour in an area occupied by stiff OC clays, very close to Orvieto, Umbria Region, Central Italy (Fig. 3.28). The landslide evolution is again characterized by very small rates (millimetres per year) and by a complete stop when the pore pressure regime drops below a threshold.

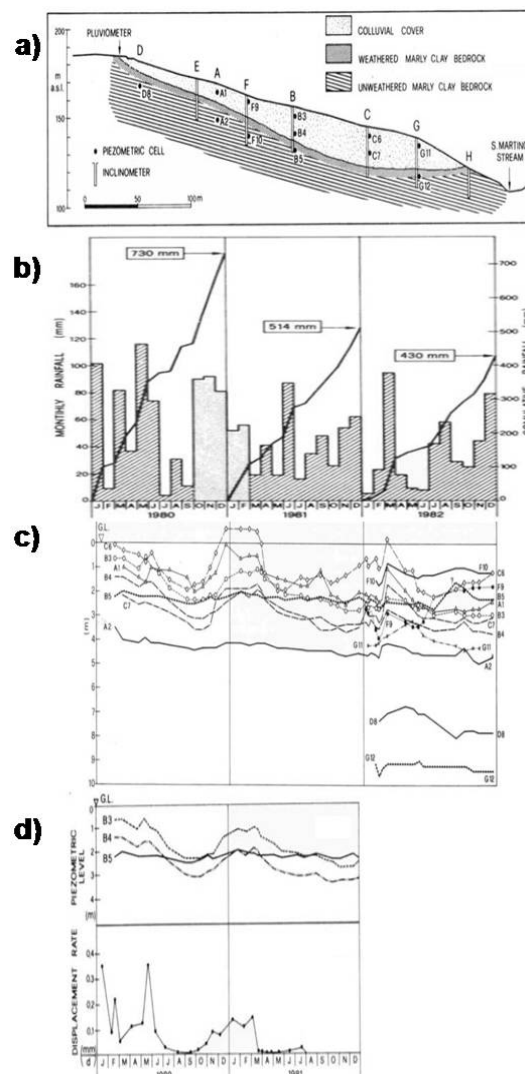


Figure 3.26 - The Fosso St. Martino slide: a) geological cross section of valley left side and field instrumentation; b) monthly rainfall and cumulative curves in 1980-1982 (spotted area is the longest period of continuous rainfall); c) piezometric levels; d) piezometric levels vs. time and displacement rate vs. time (Bertini et al., 1984)

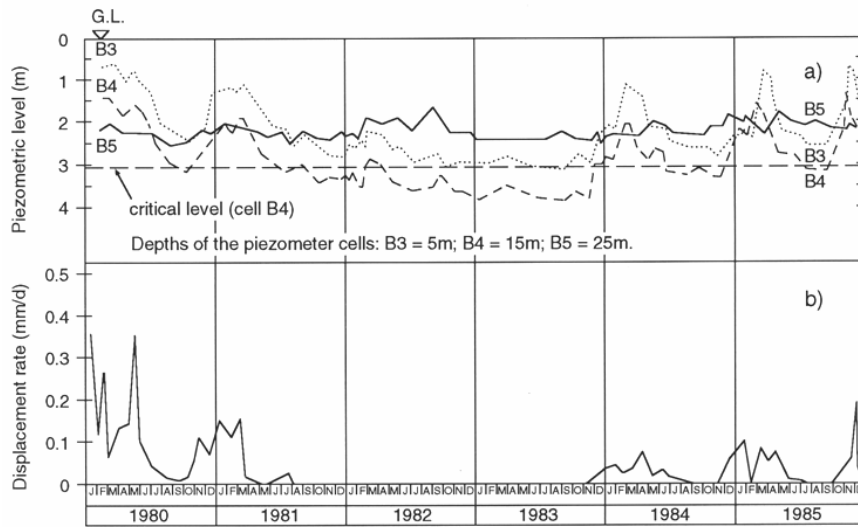


Figure 3.27 - Pore pressures and displacement rate of the Fosso St Martino slide (Bertini et al., 1986).

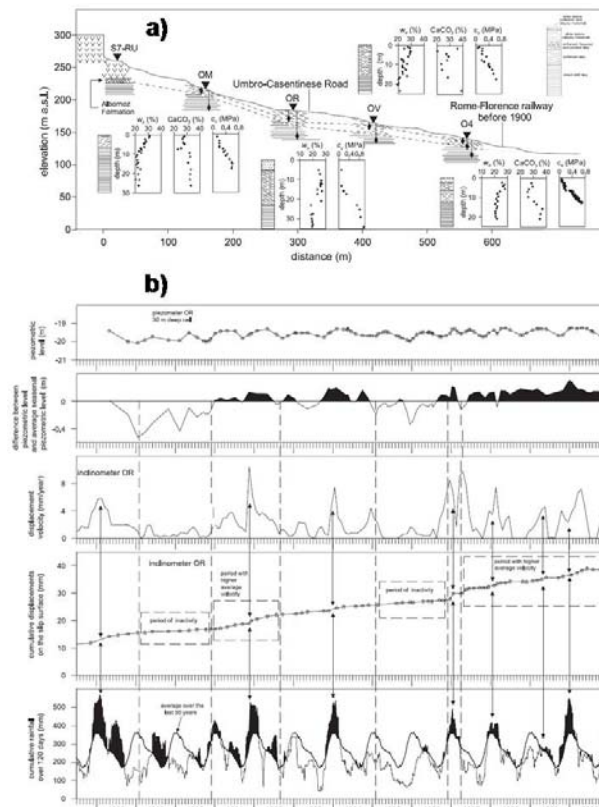


Figure 3.28 - The Orvieto hill slide: a) geotechnical section parallel to the slope; b) rainfall regime, piezometer levels and displacements of the deep-seated slide measured by borehole OR. (Tommasi et al., 2006).

Corominas et al., (2005) describe the Vallcebre landslide, Eastern Pyrenees, Spain (Figure 3.29), that is active from several centuries. The landslide, which involves shale, gypsum and claystone layers moving over a thick limestone bed, is 1200 m long and 600m wide and covers an area of 0.8 km² where superficial shear surfaces and tension cracks can be recognised. The landslide consists of three distinct units: an upper, an intermediate and a lower one. In particular, the lower unit has been monitored since 1996 using conventional surveying and photogrammetry, differential GPS, boreholes equipped with inclinometers, wire extensometers and piezometers. The landslide activity is very sensitive to rainfall (Figure 3.30). The displacements never stop and are characterized by velocities that tend to zero only during dry periods. Infiltration takes place along cracks, which represent preferential drainage pathways too. Piezometers set in tension zones (as S5) measure rather small changes in groundwater levels (ranging between 0.5 and 2 m) and a fast drainage if compared to the piezometers located elsewhere (for example S2, S4 and S11), which experience changes of groundwater level up to 5 m and a slower rate of pore water decrease.

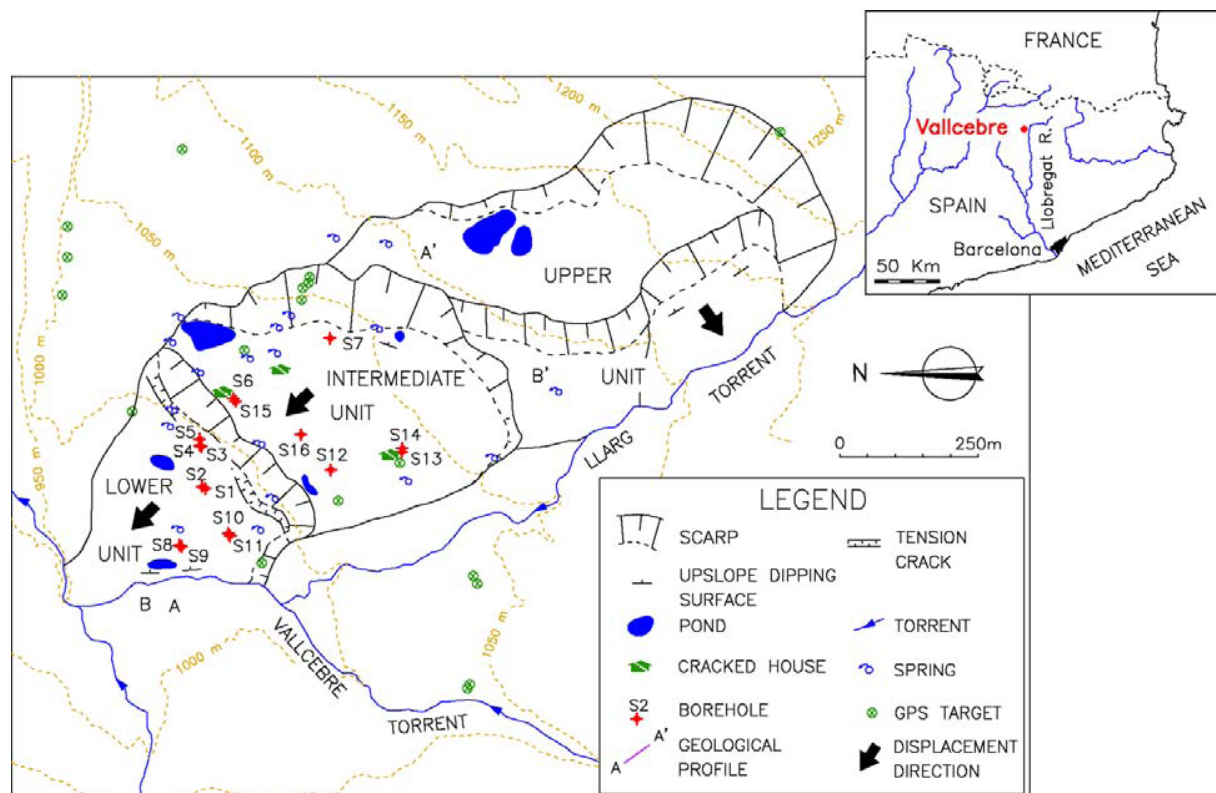


Figure 3.29 – Plan view of the Vallcebre landslide, Spain (Corominas et al., 2005).

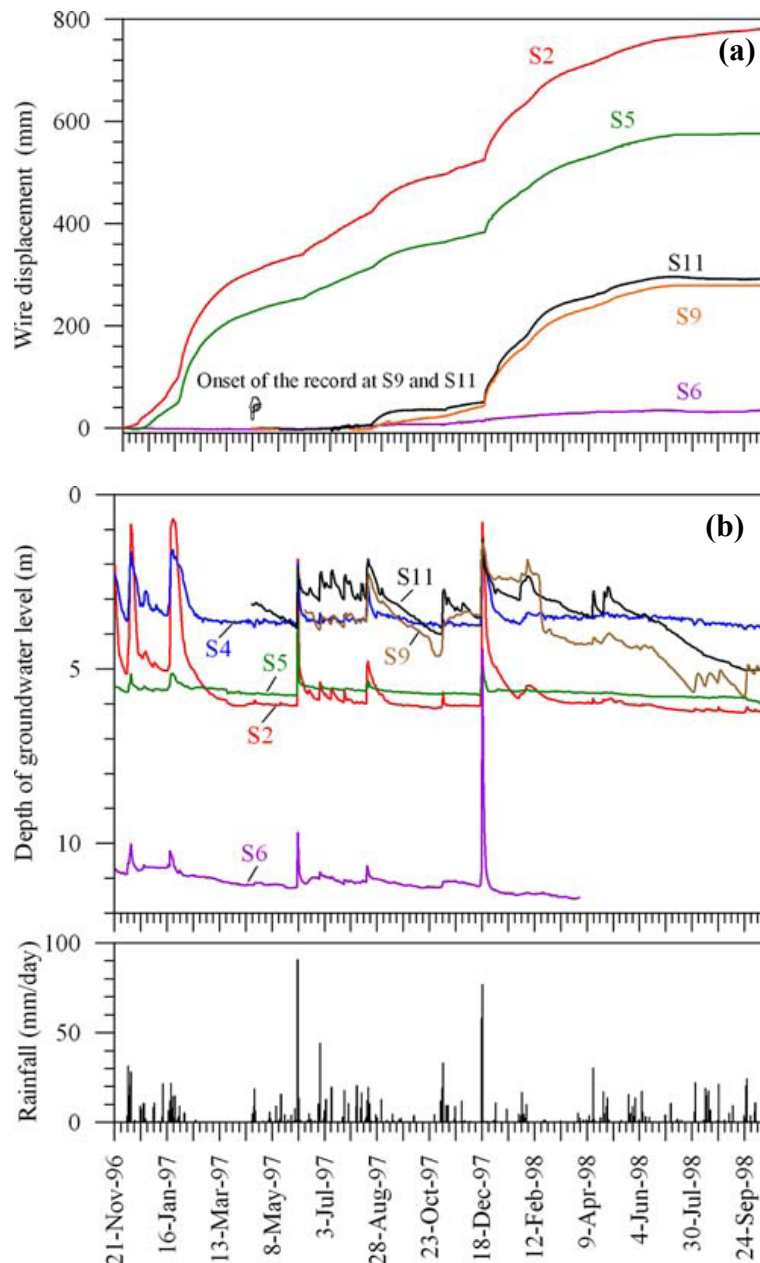


Figure 3.30 – Vallcebre landslide: a) wire displacements measured at boreholes S-2, S-5, S6, S9 and S-11; b) piezometric levels measured at boreholes S2, S4, S5, S6, S9 and S11 (Corominas et al., 2005)

Concerning cases of not actually active landslides, Govi and Sorzana (1982), Govi et al. (1985), Simeoni (1998) and Chiappone (1999) describe well documented planar slides occurred in the Langhe region (Piemonte Region, Northern Italy). These involved more than 2000 flysch deposits and were characterized by very different size (thickness changing in the range 5÷40 m, volume varying in the interval $10^3 \div 10^5 \text{ m}^3$). They moved over $8^\circ \div 15^\circ$ inclined failure surfaces, developed within very thin (about 10÷40 mm thick) marly layers (Fig. 3.31), with rates changing from 0.5 to 100 m/h. All landslides were triggered by infiltration of rain water favoured by quasi-vertical open discontinuities. Figure 3.32 shows the correlation between landslides events and rainfall and the thresholds found by Govi et al. (1985) based on 27 landslides occurred from 1917 to 1976. Such data suggest that the failure should be correlated not only to the rainfall event (i.e. precipitations cumulated during 1÷3 days before the event), but also to previous cumulated precipitation, P_{60} , over the 60 days preceding the landslide, that is always higher than 100 mm. Moreover:

- the maximum P_{60} values (about 300 mm) occurs after the dry season, that is responsible for the deepest depth of the groundwater table;
- the minimum P_{60} values (about 140 mm) occur at the end of the wet season, when the groundwater table is rather shallow.

The importance of antecedent rainfall events for slopes with low permeability has been pointed out by several Authors, based on experimental data and numerical studies (Johnson and Sitar 1990; Ng and Shi 1998; Tsaparas et al. 2002; Cai and Ugai 2004).

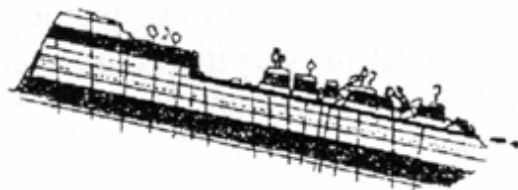


Figure 3.31 - Scheme of the planar slide occurring in the Langhe region, Piemonte Region, Northern Italy (from Chiappone, 1999).

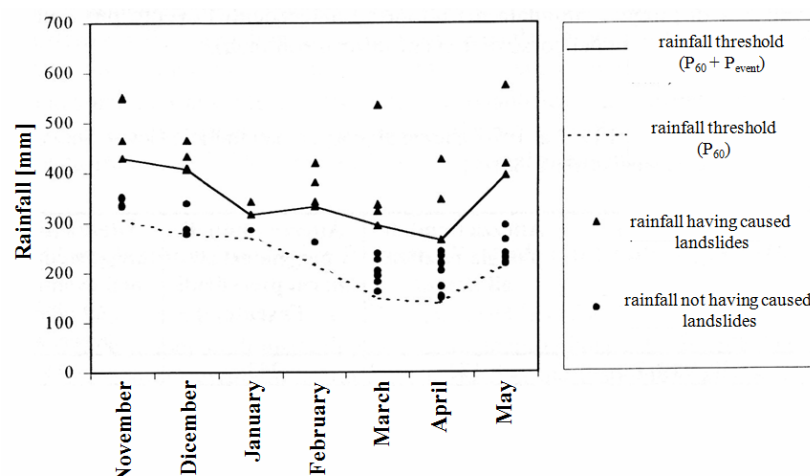


Figure 3.32 - Rainfall thresholds of the planar slide occurring in the Langhe region (Piemonte Region, Northern Italy). P_{60} is the rainfall cumulated during the 60 days antecedent the landslide event (modified after Govi et al., 1985).

3.1.2.2 Cases of earthflows

(AMRA)

Earthflows are featured by the movement of clayey deposits which experience internal deformation and contemporary slide along the boundary slip surfaces. They usually occur on cliffs and slopes of overconsolidated, fissured clays and clay-shales and are often triggered by falls and slides occurring in a steeper upslope source area. The deposits proceed along a main track and tend to discharge on a gently inclined downslope accumulation zone. Their size may be extremely variable: the volume of the smallest ones is some hundreds of cubic metres, but there are cases attaining millions of cubic metres.

In the first stage of movement following triggering, the velocity is quite rapid and can reach tens of metres per hour, as in the case of Covatta, Southern Italy (Picarelli and Napoli, 2003), or even metres per minute, as reported for the case of Minnis North, Antrim, UK (Hutchinson et al., 1974). During such starting phase, internal strain prevails over displacement concentrated along the slip surface, thus the landslide displays a marked flow-style.

On the contrary, in the long-term, the displacement rate slows down to extremely low values (order of millimetres per year) and the movements turn from a flow to a slide style (Iaccarino et al., 1995). Being the strength mobilized along the shear surface at or near the residual value, the landslide may be cyclically reactivated by pore pressure fluctuations for tens of years, and the movements tend to be strongly seasonal. As a result of both fairly high velocity and duration of movements, the travel distance may reach hundreds of metres (Pellegrino et al., 2004). In particular, such distance is strongly controlled by the inclination β of the slope on which the moving deposit discharges. According to Hutchinson (2004), if β is lower than the limiting slope β_3 calculated for a three-dimensional earthflow (Bhandari, 1970), the travel is restricted and a lobate earthflow results, as typical of coastal landslides. On the contrary, if β is higher than β_3 , an elongate form results, which can reach an up to 5 Km long extent.

Figure 3.33 shows the displacement rate of three active earthflows in highly fissured tectonized clay shales located in the Basento valley (Southern Italy), measured or evaluated through field measurements or aerial photographs. The behaviour of the three landslides is characterized by sudden accelerations leading to peak velocities higher than 10 cm/day and subsequent decreases of the displacement rate. According to some Authors (Hutchinson and Bhandari, 1971; Picarelli, 1988; Pellegrino et al., 2004), acceleration is justified by the building up of excess pore pressures induced at the onset of rupture or just after it by alimentation (undrained loading) and/or by other causes. As reported in Figure 3.34, measurements of excess pore pressures in an earthflow body occurred at the coast of the Isle of Sheppey, England, and due to an undrained loading occurred by the over-riding of material coming from the steeper source area, are reported by Hutchinson and Bhandari (1971). In the following stage, excess pore pressures decrease as a consequence of consolidation, thus their dissipation favours the decline of the displacement rate. However, Figure 3.33 shows that the movement never stops, in fact the velocity may suddenly increase due to a new alimentation stage which in turn is generally a consequence of bad weather conditions. The alimentation definitely stops when the slope reaches a mature and gentle morphological configuration, but the landslide can still move due to pore pressure fluctuations.

In the phase of deceleration the landslide style is predominantly featured by movements along a well defined slip surface located at the base of the landslide. For instance, similar characteristics have been found in earthflows occurred at Sochi, Russia (Ter-Stepanian et al., 1968) or at Beltinge, England (Hutchinson, 1970), where shearing on basal shears accounted for values higher than 92% of the displacement monitored at the ground surface, thus

revealing virtually complete sliding block. In this mature stage, the displacement field is strongly governed by the piezometric evolution, in turn regulated by the rainfall cumulated over a time period ranging from 2 to 4 months. The investigations carried out on another earthflow in the Basento Valley (Fig. 3.35) show a good matching between the groundwater levels in the earthflow body and the precipitations P_{90} , cumulated over 90 days (Vassallo and Di Maio, 2006; Di Rosario, 2008). Again, Figure 3.36 displays an evident relationship between the mobility of the Valle al Pero earthflow (Tuscany Region, Central Italy) and climate conditions occurred between 1964 and 1966 as reported by D’Elia and Tancredi (1979).

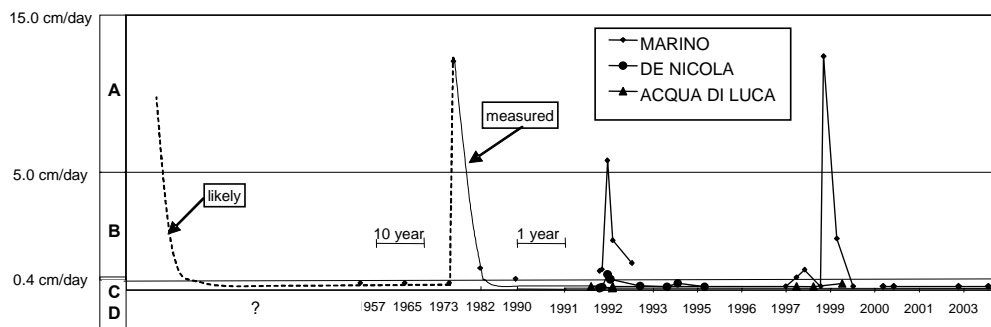


Figure 3.33 - The displacement rate of three earthflows in the Basento valley, Southern Italy (Picarelli et al., 2005)

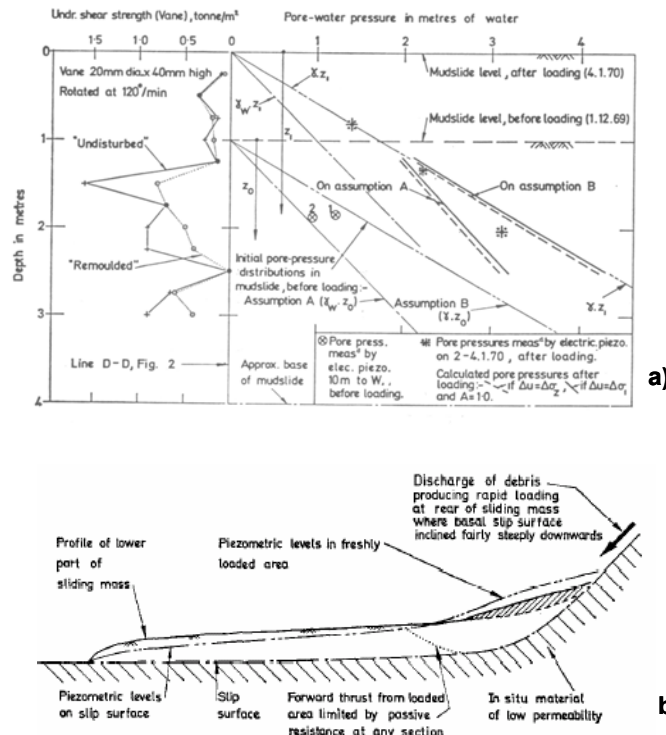


Figure 3.34 – Sheppey earthflow, England: a) pore-water pressures measured before and after failure; b) mechanism of undrained loading (after Hutchinson and Bhandari, 1971)

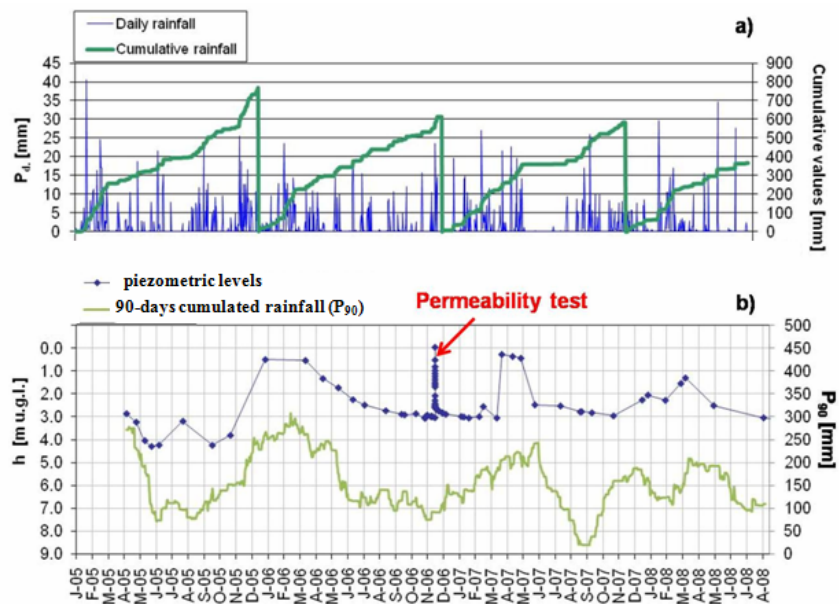


Figure 3.35 - Piezometric and rainfall data about an earthflow in the Basento valley, Southern Italy (modified after Di Rosario, 2008)

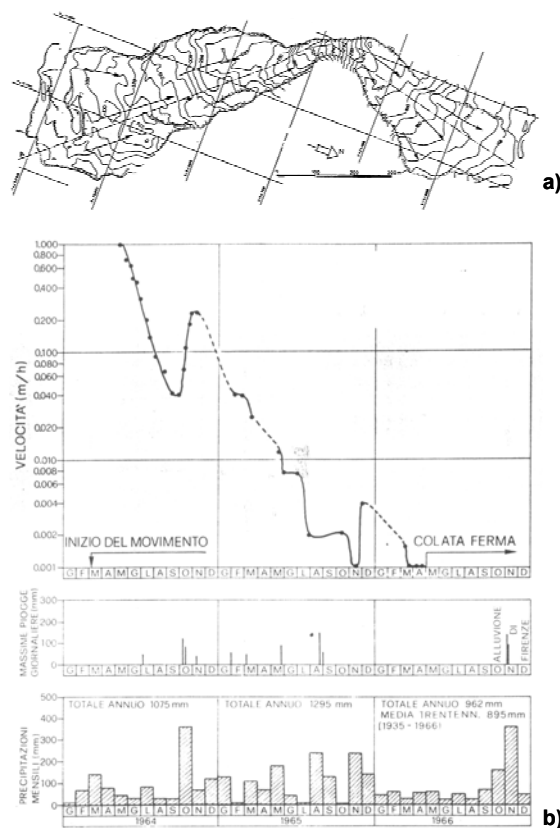


Figure 3.36 – Valle al Pero earthflow, Central Italy: a) plain view; b) rate of movements related to meteoric events (modified after D’Elia and Tancredi, 1979)

Figure 3.37 shows the main results of monitoring between 1993 and 1999 of the very long-lasting Torrente Miscano earthflow, Campania Region, Southern Italy (Picarelli et al., 1999). In that period, the area was subjected to moderate rainfalls, mainly concentrated in the time interval November ÷ April, with a maximum monthly height of about 250 mm and a maximum cumulated annual height of 788 mm (Fig. 3.37c). Figure 3.37d reports the groundwater level depth measured between March, 1993 and April, 1999 by four Casagrande piezometers installed within the landslide body. The pore pressure fluctuations follow a seasonal trend with peak values measured between January and March, and minimum values measured between October and January. During wet seasons, the time lag between rainfalls and groundwater recharge is very short, while in dry seasons the groundwater level declines very slowly and does not show any appreciable response to isolated rainfalls, even if very intense. Both the maximum groundwater level (very close to the ground surface) and the minimum level (that reaches a depth between 2.0 and 2.5 m) measured in the landslide body seem to be strongly affected by the rain amount: for instance, the peak value is higher at the beginning of 1994 and 1996 than in 1995, which follows a dryer period. Figure 3.37e shows the yearly cumulated displacements measured by the inclinometers next to the ground surface. These are quite different along the slope and with time, ranging between about 0.5 and 8 cm/year, so that the landslide may be classified as slow to extremely slow. The variability of displacements with space suggests that the landslide body experiences internal deformation, thus its behaviour depends on the local induced strain field. The variability with time essentially depends on the pore pressure regime, in turn affected by rain amount. The influence of rainfall is clearly evidenced by Figure 3.37e that shows a significant increase of the landslide activity systematically following a rainy period: the high displacement rate in the first months of 1994 and 1996, for instance, is clearly related to the preceding cumulated rainfalls. In particular, the inclinometer I3, which is the only working since 1993, shows that every year slope mobility practically stops between May and September, as an immediate response to the pore pressure decline (Fig. 3.37d, f), while it restarts during the wet season. Such evidence agrees with what already shown by Bertini et al. (1986), who observe that slowly moving landslides are characterised by a threshold pore pressure above which movements are cyclically triggered. With regard to T. Miscano earthflow, such average threshold groundwater level ranges between 1 and 1.5 m (Fig. 3.37d).

Figure 3.38 shows the relationship between the depth of the groundwater table and the displacement rate of the T. Miscano earthflow compared with the Fosso St. Martino slide (Bertini et al., 1986), that has been described in the previous section. The behaviour of the two landslides appears very similar, even though different types of slope movements (an earthflow and a slide) are concerned. The figure suggests a highly non linear pore pressure – displacement rate relationship. Therefore, a correct prediction of the slope movement based on the forecast of the water levels as a function of weather conditions may be a useful tool for land management (Mandolini and Urciuoli, 1999; Picarelli and Russo, 2004).

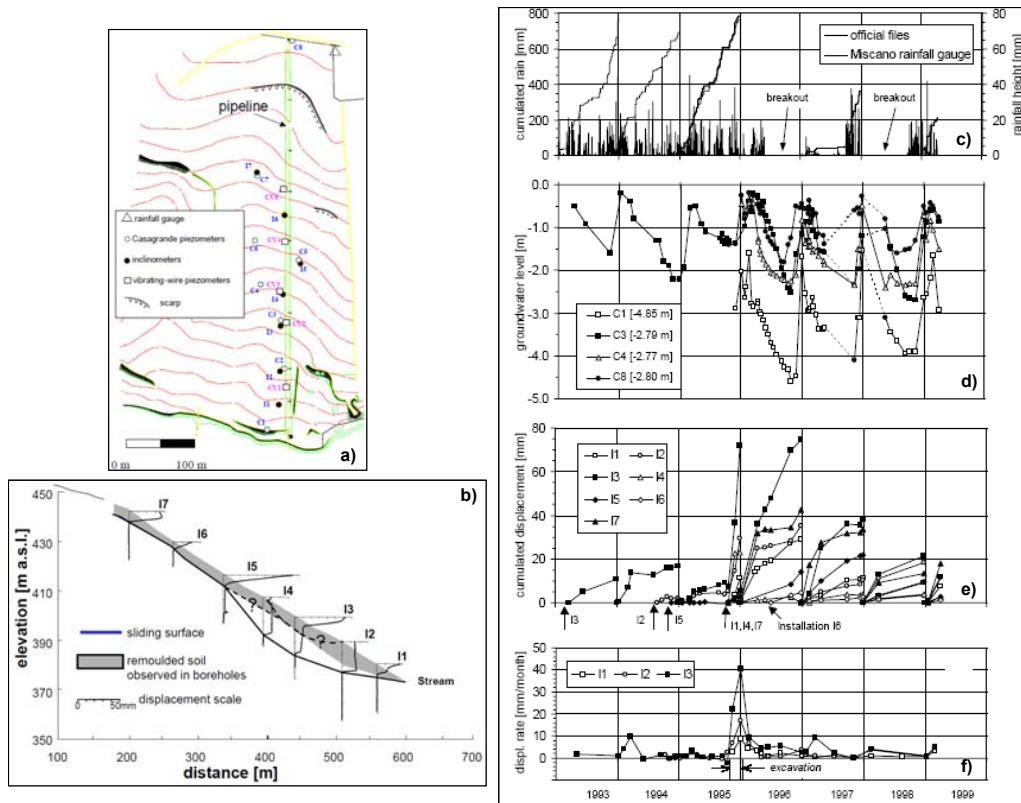


Figure 3.37 – Torrente Miscano earthflow, Southern Italy: a) instrumentation location; b) landslide body detected by inclinometers; d, e, f) cumulated rainfall, water levels and cumulated displacements (after Picarelli et al., 1999)

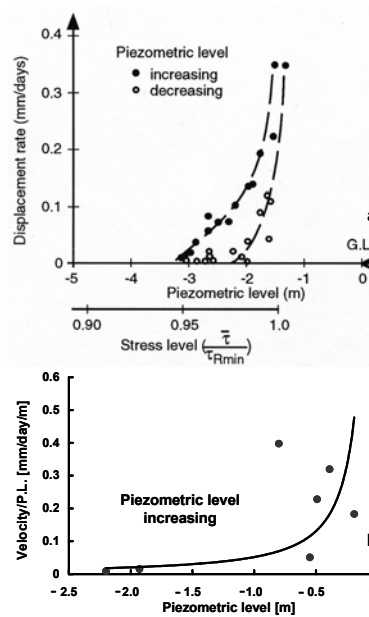


Figure 3.38 - Groundwater level – displacement rate relationship for Fosso St Martino slide (a) and T. Miscano earthflow (b), Central Italy (Picarelli and Russo, 2004)

3.2 EXPERIENCE OBTAINED THROUGH PHYSICAL MODELLING

3.2.1 Experience on granular soils gathered through small scale physical modelling (ETHZ)

Physical modeling may be adopted to make predictions about specific modes of soil behavior. A key aspect of physical modeling is the idealization process for representing soil behavior, such as geometrical, loading, environmental and construction effects. These must be incorporated within any similitude requirements and will lead to model design. Contributing behavior sets should be identified individually and then in concert (Mayne et al. 2009). However, the reproduction of the process at a greatly reduced scale is widely acknowledged to be not fully representative of full-scale behaviour due to the difference in stress levels between model and prototype (Schofield 1980, Take et al. 2004). If the N-times-downscaled model is subjected to an acceleration field N times greater than Earth's gravity the gradient of body stresses within the model will be similar to the prototype, ensuring similarity of effective stresses at equivalent depths.

During raining over model slopes in centrifuge tests, seepage dominates in the movement of water through the fills, implying that Darcy's law holds for this case (Kimura et al. 1991). It is generally accepted that the seepage velocity in the centrifugal field of Ng is N times that in the gravitational field, as long as the identical material is used for the model and prototype soil (Goodings 1984, Garnier et al. 2007). Since the intensity of rain has the same dimension as the seepage velocity, the intensity of rain in the Ng field is N times that in the gravitational field.

In recent decades, many small-scale landslides have been triggered under laboratory conditions in sandy soils. For example, Sassa (1972, 1974) performed a series of flume tests on Toyoura sand and concluded that the changes in rigidity of sand and upper yield strain within a slope are essential to the analysis of slope stability. Eckersley (1990) triggered flowslides in coking-coal stockpiles by raising the water table, and inferred that excess pore pressures were generated during, rather than before, the movement. Another laboratory flowslide study was conducted on loose saturated fine quartz sands, in which the motion of liquefied sands and pore pressures during motion were analyzed (Spence and Guymer, 1997). Kubota (1997) performed a series of tests on silica sand and loess to study the mechanisms of flowslides under rainfall conditions. He concluded that the generation of pore pressure was a result of sudden initiation of subsidence. Iverson and his colleagues triggered landslides and debris flows in a large flume with emphasis on examination of landslide movement and intergranular pore pressures (Iverson and LaHusen, 1989; Iverson, 1997; Iverson et al., 1997, 2000; Major and Iverson, 1999). Those studies showed that landslide rates are significantly dependent on the initial soil porosity, and rapid fluidized landsliding involves partial or complete liquefaction of the mass by high pore fluid pressure. Several failure mechanisms have been investigated by different researchers in centrifuges modelling of sandy slope failures due to rainfall. Kimura et al. (1991) performed 21 tests on sandy slopes varying the initial conditions of the soil in terms of water content and void ratio, the inclination of the slopes and the rain intensities. Their tests indicate the occurrence of mainly two types of failures, complete failure along a well-defined deep slip surface where the wetting front has passed and local instabilities at the toe after appearance of ground water flow. Take et al. (2004) and Lee & Bolton (2006) performed a series of tests to evaluate different triggering

mechanisms of slips and flowslides due to heavy rainfalls. The hypotheses that were explored during these tests were static liquefaction and localised build up of transient pore water pressures due to layering and significant changes in the inclination of the underlying lower permeability layers.

The factors affecting the mechanisms of initiation and spreading of landslides in sandy soils due to precipitations, based on flume and centrifuge tests will be discussed in this section.

a) Effect of initial void ratio on the failure mechanism (based on Iverson and LaHusen, 1989; Iverson, 1997; Iverson et al., 1997, 2000; Wang & Sassa 2001, 2003)

a.1) Flume tests

As soils approach specific critical-state porosities during shear deformation, it has been suggested that landslide behaviour may depend on initial soil porosity (Casagrande and Boston, 1936; Schofield and Wroth, 1968). Due to dilation of the soil the pore pressures can decrease and by increasing effective stresses and shear strength may affect continued deformation, whereas contraction can increase pore pressures and hence reduce shear strength (Reynolds, 1886). To isolate the effect of initial soil porosity on landslide style and rate, Iverson et al. (1997 & 2000) conducted large-scale flume experiments under closely controlled conditions using a 95 m long, 2 m wide concrete chute with a 31° slope, roughened bed, and smooth side walls (Iverson et al. 1992). In each experiment a tabular prism of 6.1 to 6.4 m³ of moist, granular soil was formed by dumping behind a rigid, 0.65-m-high retaining wall installed near the head of the flume (Iverson et al. 1997). The landslide experiments included individual tests with initial porosities ranging from 0.39 ± 0.03 to 0.55 ± 0.01 (± 1 SD sampling error for an individual experiment). Ring shear and triaxial tests of the soil under various initial densities produced dilative shear failure when initial porosity was ≤ 0.41 and contractive shear failure when initial porosity was ≥ 0.46 .

Landslides developing in soils with differing porosities displayed sharply contrasting dynamics (compare Figs. 3.39 and 3.40). Landslides with initial porosities > 0.5 failed abruptly and accelerated within 1 s to speeds > 1 m/s. The surfaces of these landslides appeared fluid and smooth, and data from dynamic piezometers confirmed that pore water pressures rose rapidly during failure and reached levels nearly sufficient to balance total normal stresses and liquefy the soil (Figure 3.39).

Three landslides with initial porosities indistinguishable from the critical porosity (0.44 ± 0.03 , 0.44 ± 0.03 , and 0.42 ± 0.03) displayed inconsistent behaviour, including slow slumping of a single soil block, episodic slumping of multiple blocks, and moderately rapid (~ 0.1 m/s) slumping that ceased after < 0.5 m displacement. Dynamic piezometer data from these experiments revealed a complex mix of dilative and contractive soil behaviour during failure.

In experiments with landslides in initially dense soil, the observed failure geometry was similar to that of the loose soil but the data revealed markedly different landslide dynamics (Figure 3.40). Precursor pore water pressures necessary to trigger failure of the dense soil were roughly twice as large as the pore pressures necessary to trigger failure of the loose soil (owing to high peak strength of the dense soil). On average, motion of the landslide with dense soil proceeded about 300 times more slowly than motion of the landslide with loose soil (compare Figs. 3.39 and 3.40). The landslide with the lowest and least variable initial porosity (0.41 ± 0.01) displayed the clearest dilative soil behaviour as it underwent slow episodic motion (Figure 3.40).

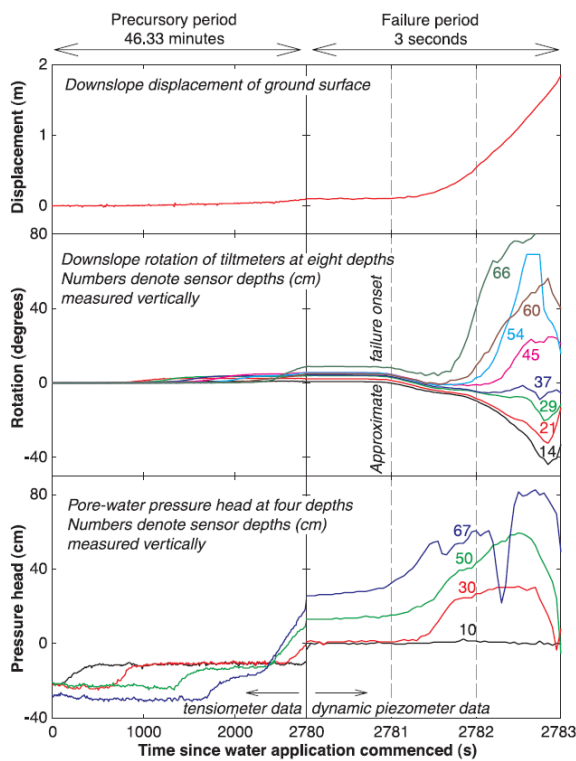


Figure 3.39 - Data recorded in a landslide experiment with loose soil (initial porosity 0.52 ± 0.02). To reveal details of behaviour during the 3-s failure period, the time axis is expanded 927 times (after Iverson et al. 2000).

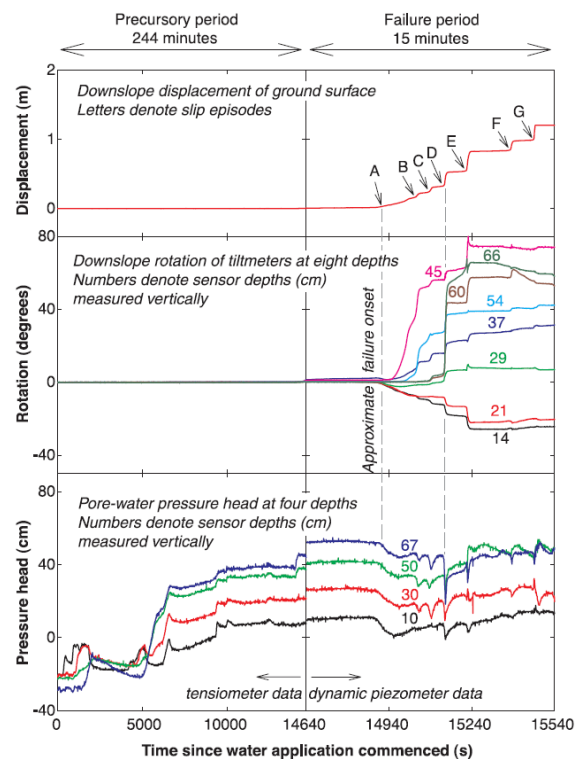


Figure 3.40 - Data recorded in a landslide experiment with dense soil (initial porosity 0.41 ± 0.01). To reveal details of behaviour during the 15-min failure period, the time axis is expanded 16 times (after Iverson et al. 2000).

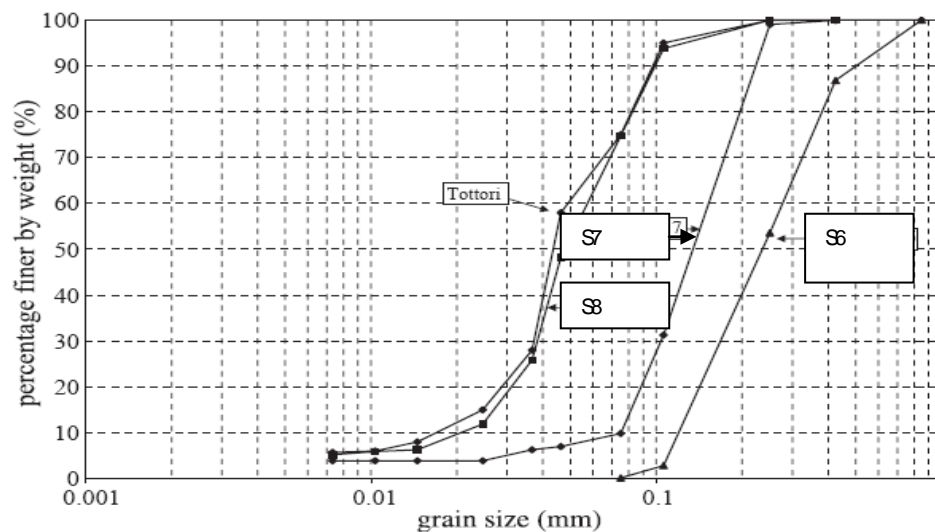


Figure 3.41 - Grain-size distribution curves for silica sand no. 6 to 8 (after Lourenco et al. 2006)

Wang & Sassa (2001, 2003) conducted a series of tests on silica sand no. 7 ($D_{50} = 0.13$ mm) and no. 8 ($D_{50} = 0.05$ mm) (Figure 3.41) to investigate the effect of initial dry densities on pore-pressure generation and failure behaviour of a landslide mass.

They observed different types of failure modes and divided each failure type into four periods:

- (1) **Wetting**: after sprinkling, the water gradually flowed toward the base, and the wetting front was approximately parallel to the base. During this period, there appeared obvious normal displacement in the tests on extremely loose samples;
- (2) **Precursory slides**: after the wetting front reached the base, with the rising of saturation degree, retrogressive compound shallow sliding appeared at the toe part of the slope;
- (3) **Major failure**: following the retrogressive compound shallow sliding, major failure occurred. The displaced soil slid a certain of distance (ΔS , as shown in Figure 3.42), and then stopped;
- (4) **Successive movement**: after the major failure, with continuing of sprinkling, failed landslide soil began to move again and flowed downward slowly.

Each failure mode was greatly affected by the initial density in these series of tests. Usually, in the series of tests on S7, the sand with density index ($I_d \leq 0.01$ ($I_d = (e_{\max} - e) / (e_{\max} - e_{\min})$)) was likely to suffer from the failure of Type A (Figure 3.42), but when the initial density indexes ranged from 0.17 to 0.49, the samples were more likely to suffer from failure of Type B. In the series tests on S8, failure of Type C occurred when $0.14 \leq I_d \leq 0.30$, and failure of type D when $0.30 \leq I_d \leq 0.46$.

Effect of initial density on pore-pressure build-up

Presenting a time series for pore pressure and sliding distance, Wang and Sassa (2001) found that high pore pressure was built-up after, not prior to, the initiation of failure. They plotted the pore-pressure build-up after onset of failure (Δu), against the initial density index (I_d) for

each test, and found that there was an optimal density index (I_{dm}) at which Δu reaches a maximum value (Figure 3.43). They interpreted the existence of I_{dm} as a combined effect of different factors. For tests in which $I_d < I_{dm}$, the permeability is greater, thus the dissipation must be quicker. Accordingly, the effect of greater pore pressure dissipation rate is likely to exceed the effect of greater pore pressure generation. For tests in which $I_d > I_{dm}$, the volume reduction during shear is small, thus less pore water pressure generation is likely to accompany the failure.

Moreover, the optimal density index (I_{dm}) for S7 differs from that of S8 (Figure 3.43). This shift can be interpreted by the volume-reduction potential, which is directly related to the generation of pore-water pressure for a saturated sample under undrained conditions during shearing, which can be attributed to the difference in grain size distributions.

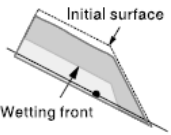
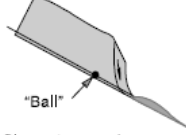
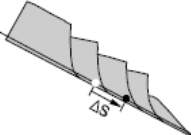
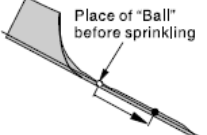
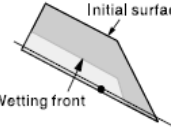
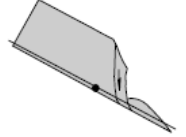
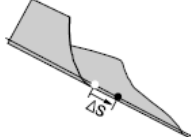
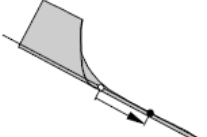
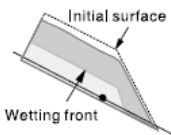
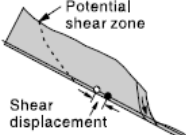
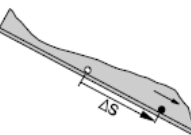
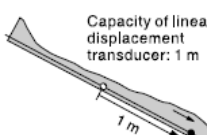
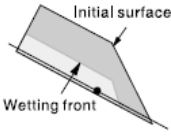
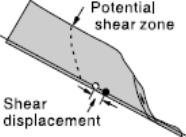
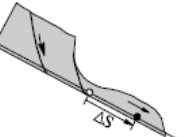
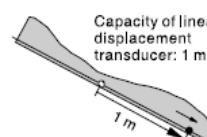
Failure mode	Wetting	Precursory slides	Major failure	Successive motion
Type A $I_d \leq 0.01$ Retrogressive sliding	 Initial surface Wetting front Visible normal displacement	 "Ball" Slow retrogressive toe sliding	 Sudden multiple sliding ΔS	 Place of "Ball" before sprinkling Very shallow flowslide
Type B $0.01 < I_d \leq 0.49$ Retrogressive sliding	 Initial surface Wetting front No visible normal displacement	 Slow retrogressive toe sliding	 Slow retrogressive sliding ΔS	 Very shallow flowslide
Type C $-0.14 \leq I_d \leq 0.30$ Flowsliding	 Initial surface Wetting front With ($I_d < 0$)/without ($I_d \geq 0$) visible normal displacement	 Potential shear zone Shear displacement Slow retrogressive toe sliding with visible deformation as a whole	 Flowsliding with relative motion between soil layers ΔS	 Capacity of linear displacement transducer: 1 m Slow sliding
Type D $0.30 < I_d \leq 0.46$ Flowsliding	 Initial surface Wetting front Without visible normal displacement	 Potential shear zone Shear displacement Slow retrogressive toe sliding without visible deformation as a whole	 Retrogressive sliding followed by movements with relative motion between soil layers ΔS	 Capacity of linear displacement transducer: 1 m Slow sliding

Figure 3.42 - Summarized failure modes, types A and B observed in samples with S7, and types C and D observed in samples with S8 (after Wang & Sassa 2003).

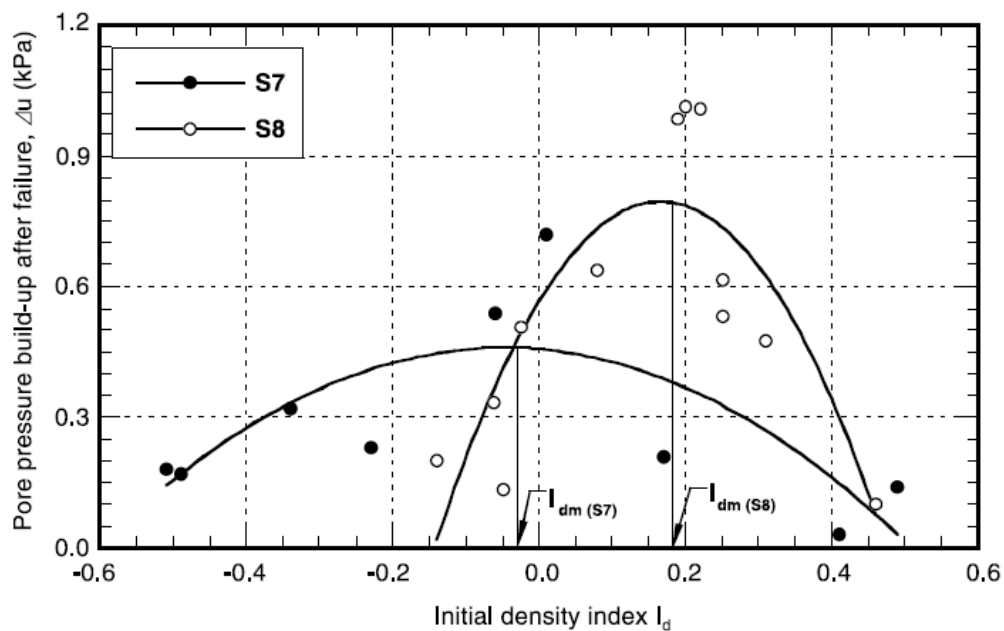


Figure 3.43 - Pore-pressure build-up after failure versus initial density index (after Wang & Sassa, 2003).

a.2) Centrifuge tests

Performing a series of centrifuge tests under a nominal centrifugal acceleration of 50g, Kimura et al. (1991) investigated the stability of slopes subjected to heavy rains. Their focus was mainly on the effect of initial void ratio and water content of the soil in some tests (case I, Figure 3.44) and the influence of rain intensity and slope inclination in other tests (case II, Figure 3.45). They used an artificial mixture of 50% of Kanto loam with 33% Toyoura sand and 17% crushed Toyoura sand being classified as SM. In case I, 11 tests (Tab. 3.2) were done on slopes of 45° inclination and the rain was applied by 10 nozzles arranged in 2 lines with an intensity of 600 mm/hr, which is identical to 12.0 mm/hr in the prototype. While 10 tests (Tab. 3.3) were performed for case II, with rain intensities of 2250, 1400 and 700 mm/hr (45, 28 and 14 mm/hr at prototype scale, respectively) and the angle of slope of 60°, 45° and 30° for tests conducted.

Pore pressure transducers and conductivity sensors were installed at locations shown in Figure 3.45. Deformations of the fills and the movement of wetting front were recorded by photographing the models for both test cases I and II.

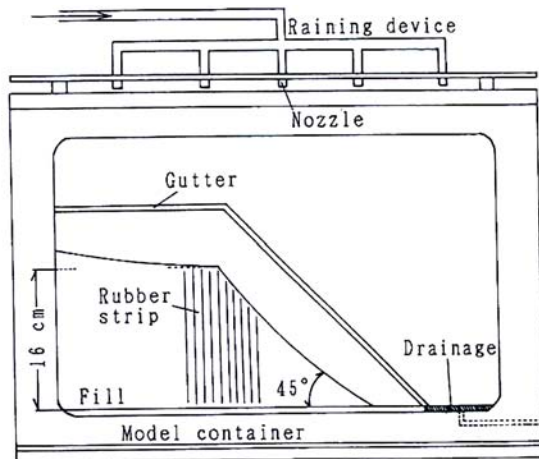


Figure 3.44. Setup test for test case I (after Kimura et al. 1991).

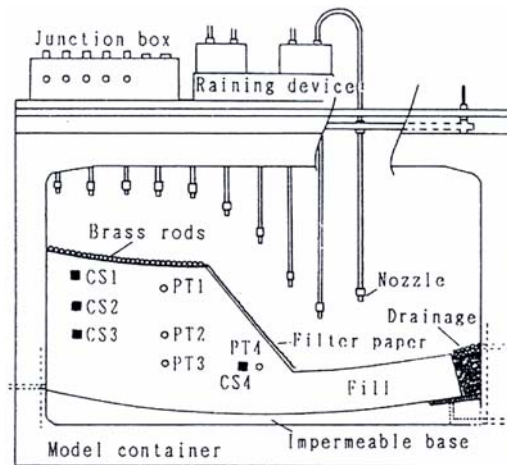


Figure 3.45 - Setup test for test case II (after Kimura et al. 1991).

Table 3.2 - Test conditions and results for test case I (after Kimura et al. 1991).

Test No.	Initial condition		Time to failure (s)	Pattern of failure
	e_{ini}	w_{ini}		
A-1	1.75	27.9	--	No failure
A-2	1.81	27.3	--	No failure
A-3	1.86	25.5	--	Local
A-4	1.86	24	--	Local
B-1	1.66	36.2	--	No failure
B-2	1.72	36.6	44	Complete
B-3	1.81	38.3	48	Complete
C-1	2	25.5	50	Complete
C-2	2.02	27.6	42	Complete
D-1	1.94	37.1	30	Complete
D-2	2	33.2	13	Complete

Table 3.3 - Test conditions and results for test case II (after Kimura et al. 1991).

Test No.	Angle of slope (°)	Rain intensity (mm/hr)	Time to failure (s)	Pattern of failure
E-60 (1)	60	2250 (45)*	35	Complete failure
.(2)	60		36.8	
E-45 (1)	45		66	
.(2)	45		50.5	
E-30 (1)	30		97	Local failure
.(2)	30		90	
F-45	45	1400 (28)*	58	Complete failure
G-60	60	700 (14)*	61.5	Complete failure
G-45	45		250	Local failure
G-30	30		400	Local failure

* Bracketed figures are in prototype scale
(The average initial void ratio $e=1.87$ and water content $w=28.5\%$)

The fills described as *complete failure* in Tables 3.2 and 3.3, failed along a well-defined deep slip surface while the description as *local failure* indicates local instabilities at the toe of the slopes.

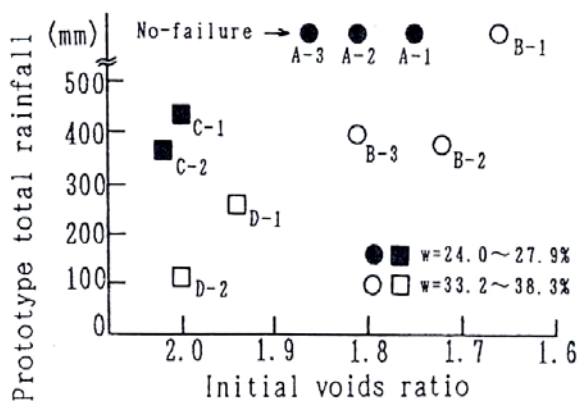


Figure 3.46 - Relationship between prototype total rain and initial void ratio (after Kimura et al. 1991).

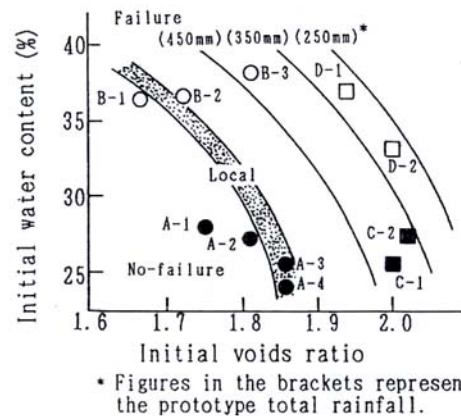


Figure 3.47 - Effect of the initial conditions of fills on the stability (after Kimura et al. 1991).

As indicated in Figures 3.46 and 3.47, the fills with higher initial void ratios fail at lower rain intensities and when the initial void ratios are similar, more rainfall is necessary to cause failure in the fills with lower initial water content.

b) Soil thickness overlaying the sliding surface (based on Wang & Sassa 2001, 2003; Eckersly 1990)

Eckersly (1990) found that the build up of pore pressures might be affected by shear deformation, dissipation, thickness of mass overlying the sliding surface, and other not completely understood factors. Also it has been shown by triaxial laboratory tests that the initial shear stress under drained conditions strongly affects static liquefaction resistance (Kramer & Seed, 1988; Hird & Hassona, 1990; Ishihara, 1993).

Wang and Sassa (2001) performed two series of flume tests to investigate the effect of initial soil thickness on the landslide behaviour. They plotted the pore pressure build up after the initiation of major failure against initial density index. In both series of tests they observed an optimum value for density index (I_d) that builds up the highest value of pore pressure. However, the maximum value of pore pressure for the tests with higher thickness is greater than that for the thinner sample, while the optimum density index is lower. They interpreted this data by attributing lower values of dissipation rates of pore pressure and existence of higher initial stress state to the thicker slopes (Figure 3.48). They also measured higher peak velocities of the sliding mass for the thicker sample, which can be due to the greater build up of pore pressure because of the lower dissipation rate in the initially thicker sample.

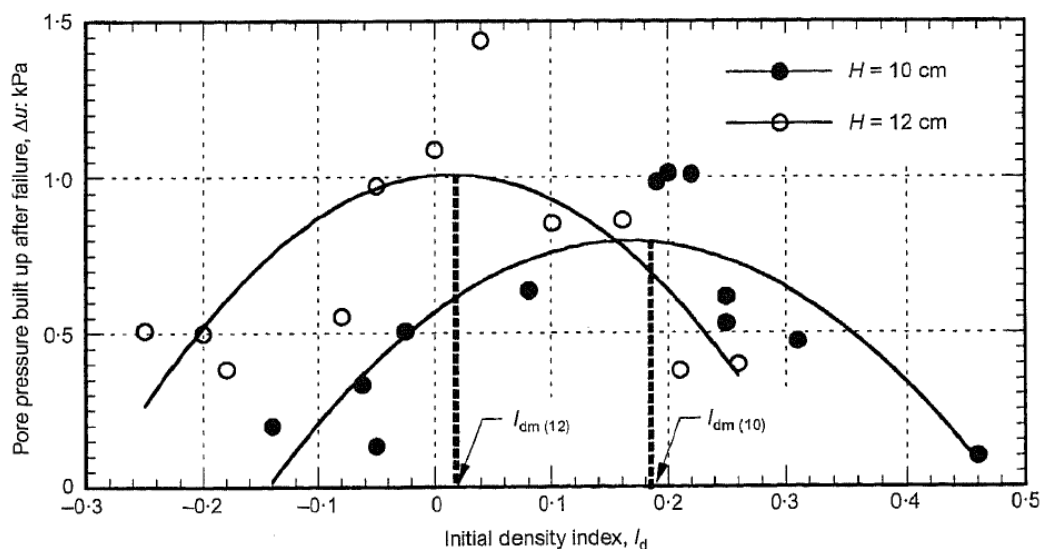


Figure 3.48 - Relationship between pore pressure build up after failure and initial density index for samples with different thicknesses (after Wang & Sassa 2003).

c) Fine-particle content (based on Wang & Sassa 2001, 2003, Iverson and LaHusen 1989 and Iverson et al. 1997)

Iverson and LaHusen (1989) and Iverson et al. (1997) pointed out that the pore-pressure build-up mainly depends on the rate of landslide motion and soil deformation as well as the permeability of soils. If the moving velocity of a failed landslide mass is the same, the soil with greater permeability will have quicker dissipation, and thus smaller pore-pressure build-up. As indicated in Figure 3.43, the pore-pressure build-up after the initiation of failure for S8

is generally greater than that for S7. This observation indicates that higher pore pressure was easier to be built-up in finer sand S8.

As introduced in Figure 3.42 Wang & Sassa (2001 & 2003) reported that the grain size of the soil influences significantly the type of the movement of the mass. In the tests on S7, retrogressive slides were initiated, whereas rapid flowslides were observed in the tests on S8. This observation can be explained by: (1) smaller pore-pressure build-up after failure for tests on S7 (Figure 3.43); (2) quicker dissipation of the generated pore-water pressure for S7 during movement due to higher permeability (Figure 3.40).

d) Effect of soil layering on triggering mechanisms of landslides (based on Lourenco et al. (2006))

d.1) Flume tests

Permeability variations in natural slopes can be due to lateral and vertical variations of porosity and grain size distribution, existence of a shallow hard impermeable bedrock, and impermeable geological structures (e.g. faults filled by clayey material) where water could accumulate and perched water tables can be formed. Using a flume, Lourenco et al. (2006) studied pore water pressure generation in models typically 1 m in length and 40 cm in height with different permeabilities, and the corresponding failure mode. Experiments were conducted for different arrangements of soil layers (by changing the soil layer position), and infiltration direction (downward infiltration by sprinkling water on the soil, and upward infiltration from the bottom of the lower soil layer). All experiments used two industrial sands: a course grained sand, silica sand no. 6; and a very fine sand, silica sand no. 8 (Figure 3.41). Sand was deposited in the loosest possible conditions for both layers in every test. The permeability for sand no. 8 in a loose condition was approximately $5.0 \cdot 10^{-5}$ m/s, as obtained by laboratory experiments (Wang and Sassa, 2001); for no. 6 sand Terzaghi's (1955) formula for uniform sands gave $3.87 \cdot 10^{-4}$ m/s.

They observed great influences on the failure onset introduced by variations in permeability. Seepage erosion was found to dominate failure if the lower layer was coarser, while retrogressive failure of the upper layer was the most relevant failure mechanism if the lower layer was finer.

Regarding the effect of infiltration direction, upward infiltration resulted in a rise in the pore water pressure from the bottom to the top whereas by downward infiltration perched conditions were formed within the upper finer layer.

d.2) Centrifuge tests

Take et al. (2004) performed a series of tests on highly instrumented centrifuge models to evaluate *static liquefaction* and *transition from slide to flow due to localised transient pore water pressures* as two failure mechanisms.

The soil used in the model fill experiments was decomposed granite. Index tests performed in Hong Kong by the Public Works Central Laboratory on this material indicate that the soil is a

slightly clayey, silty, very gravely sand (GEO, 1999) with a mean grain size of 1.1 to 1.4 mm and approximately 16% of relatively low-plasticity fines (plasticity index of 11–14%). Proctor compaction tests indicate that the maximum dry density of the soil is 1.920 kg/m^3 and is achieved at an optimum water content of approximately 11–12%.

d.2.1) Evaluation of the static liquefaction mechanism

Terzaghi (1956) referred to the phenomenon of sudden change of loose deposits of sand into flows, due to a slight disturbance, as spontaneous liquefaction accompanied by substantial shear strength reduction of the soil when subjected to undrained shearing. Static liquefaction is widely described as the loss of strength of the loose contractive material and the consequent conversion of the fill into a fast moving slide (or flow) (Knill et al. 1976, Olson et al. 2000, Chu et al. 2003, Casini et al. 2010).

For specimens that compress and have degrees of saturation higher than critical, undrained conditions lead to effective stress paths with decreasing shear stresses, and run-away instability is observed provided the yield surface opens up in the outward direction of the hydrostatic axis. Thus, instability occurs inside the failure surface. Instability is not synonymous with failure, although both may lead to catastrophic events (Lade 1989). For undrained conditions and compressive material, the instability is self-sustaining and unconditional, i.e., it is not dependent on conditions outside the soil element. Loose, fine sands and silts have relatively low permeabilities and small disturbances in load or even small amounts of volumetric creep may produce undrained conditions in such soils, and instability of the soil mass follows. As long as the soil remains drained, it will remain stable in the region of potential instability. When the condition of instability is reached, the soil may not be able to sustain the current stress state. This stress state corresponds to the top of the current yield surface as shown schematically on the diagram of effective mean normal stress (p') versus deviatoric stress (q) in Figure 3.49. Following this top point the soil can deform plastically under decreasing stresses. Figure 3.45 shows a schematic p' versus q diagram in which the line connecting the tops of a series of effective stress paths from undrained tests on loose soil provides the lower limit of the region of potential instability. In the region above this instability line the soil can deform plastically under decreasing stresses. Experiments show that this line is straight. Since it goes through the top points of the yield surfaces, which evolve from the origin, the instability line also intersects the stress origin (Lade, 1993).

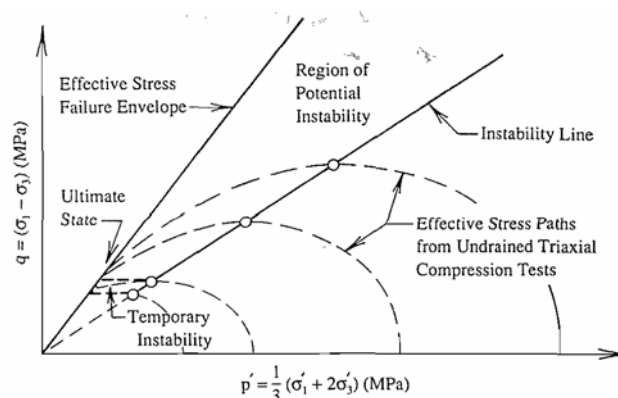


Figure 3.49 - Schematic diagram of the location of instability line (after Lade, 1993).

Figure 3.49 also shows a region of temporary instability, which is located in the upper part of the dilating zone. It is a region where instability may initially occur, but conditions allow the soil to dilate after the initial instability, thus causing the soil to become stable again (Lade, 1993).

For the fill material used by Take et al. (2004) a critical state angle of friction of 34° was determined in drained triaxial compression tests. Based on the saturated triaxial tests in very loose conditions, similar fill materials have a well documented susceptibility to static liquefaction in saturated (e.g. Ng et al. 2004). Undrained triaxial tests performed on very loose samples of the Beacon Hill decomposed granite (relative compaction about 70% of Proctor optimum compacted density, circa 0% relative density) indicate that the model fill material is similarly collapsible with an instability line inclined of 22° . Accordingly, when the samples maintain large void ratio of about unity while it becomes saturated, and if collapse is so fast that excess pore pressures can not dissipate, static liquefaction could occur at a stress ratio much lower than the critical state (Take et al. 2004).

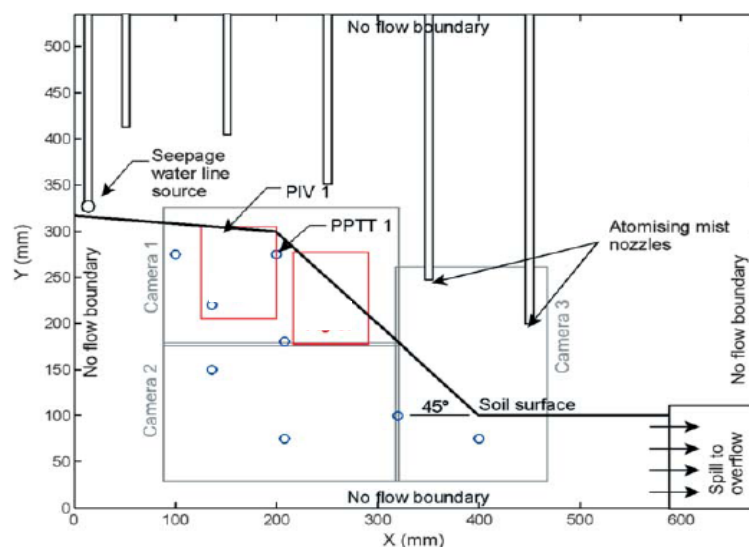


Figure 3.50 - Static liquefaction model test geometry (after Take et al. 2004).

Using a network of miniature (7 mm in diameter) pore pressure and tension transducers (PPTT), Take et al. (2004) measured positive and negative pore water pressures. The PPTTs were buried within the model fill at each of the locations indicated by open circles in Figure 3.50. The deformations of the model fill slopes have been measured by a new image-based system of deformation measurement, which combines the technologies of digital imaging, the image processing technique of particle image velocimetry (PIV), and close range photogrammetry (White et al. 2003). Rainfall was induced by uniformly applying atomised mist in two rows of five nozzles placed just above the soil surface of the model to investigate the mechanism of static liquefaction (Figure 3.50). The nozzles provide small droplets and applied rain represented a severe weekly rainfall in Hong Kong (4.2 mm/hr). As shown in Figure 3.50, a no-flow boundary condition is provided on all boundaries of the model fill slope, with the exception of the bottom right-hand corner, in which seepage water is allowed to spill to overflow once the water level has reached the elevation of the toe of the slope. The

experiments were conducted in a sealed atmospheric chamber to avoid unintentional drying of the model during centrifuge testing (Take & Bolton, 2002).

The model fill was slowly brought to the testing acceleration of 60 g in 10 g increments. With increase of “gravity” bigger pores shed their pore water vertically downwards into the fill, creating an initial suction distribution, which increases with elevation from a value of approximately zero at the toe to -25 kPa at the crest (PPTT1 in Figure 3.51b). Moreover, as the loose fill material becomes incrementally heavier, a cumulatively larger percentage of the loose fill can no longer support this increase in total stress and rapidly decreases its void ratio. Large settlements at the crest of the fill (Figure 3.51c) correspond to a settlement of over 2 m at prototype scale. The high compressibility observed in these loading increments indicates that the entire fill slope is on its normal compression line. Therefore, it is impossible to have a looser slope at the current effective stress levels (Take et al. 2004).

The fill slope was subjected to the equivalent of six weekly periods of rainfall infiltration (Figure 3.51a). As shown in Figure 3.51b, the arrival of rainfall on the slope surface at time A destroys a significant portion of the soil suction very rapidly at the shallow location of PPTT1. The loose model fill responds immediately to this loss of surface tension, by collapsing the macro-voids, which had survived self-weight consolidation. The resulting settlement of the bench above the fill slope is purely vertical. Similarly, the loss of suction in the region of static shear stress (i.e. beneath the sloping portion of the embankment) also causes macro-voids to collapse, with a significant down-slope displacement. Despite being subjected to an additional five infiltration events of identical severity, the model slope was observed neither to achieve positive pore water pressures nor to experience any significant additional deformation (Take et al. 2004).

Although the fill has experienced instability, a flow failure has not been triggered by the mechanism of static liquefaction. In triaxial tests on loose, saturated, samples of the same fill material, static liquefaction was observed to occur when the model fill was unable to drain when its volume attempted to reduce. The fill material in the model test remained very loose near the surface, despite being subjected to an increased self-weight. It is likely, therefore, that the difference in observed behaviour relates to the model fill slope’s ability to accommodate the wetting collapse through the compressibility and ease of migration of the pore air. Thus, the unsaturated nature of the fill material, and the lack of groundwater pounding, has eliminated the possibility of creating static liquefaction in this model (Take et al. 2004).

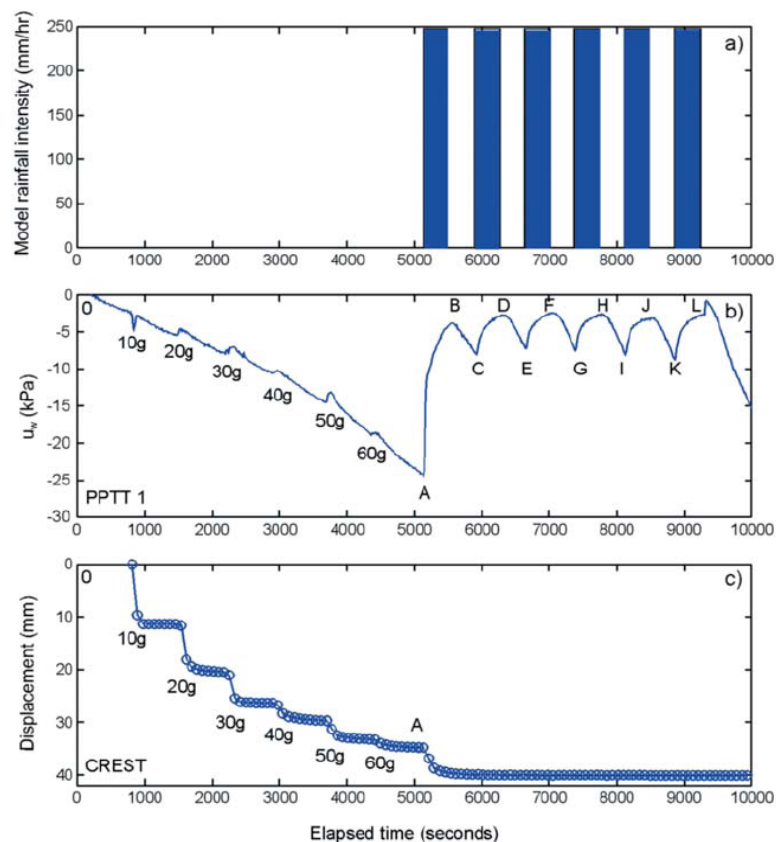


Figure 3.51 - Observed behaviour of static liquefaction model (after Take et al. 2004).

The infinite slope analysis predicts that a 45° slope (such as the above mentioned model fill slope) is potentially in danger of failure. However, due to the high compressibility of the fill material, the model fill slope achieved an average angle of inclination of 33.5° prior to rainfall infiltration. Here, as was observed in the model fill experiment, the unsaturated infinite slope may experience instability but, if the voids can collapse, undrained failure will be averted and the stress path remains inside the failure line (Take et al. 2004).

Accordingly, the mechanism of static liquefaction, although easy to reproduce in saturated triaxial specimens, is much more elusive in physical models. Particularly, the unsaturated nature of the fill material, and the lack of groundwater ponding, has eliminated the possibility of creating static liquefaction in this model. The results indicate that CDG is too permeable to develop sufficient depth of wetting front (Yeung, 2002) and turn into a flow as water can quickly drain out from the soil pores. In addition, static liquefaction is unlikely to occur if the model fill is unsaturated and the bedrock is deep enough. Since the air in the unsaturated void is highly compressible, the model fill slope may exhibit wetting collapse instead of undrained failure (Take et al. 2004).

However, Take et al. (2004) concluded that the non-appearance of an event in certain circumstances can not be taken to mean that the event will never occur under any circumstance. Therefore, the conventional understanding of static liquefaction in loose CDG fill slopes can not be dismissed on the evidence of one centrifuge test. Furthermore, there is a

factor arising out of centrifuge testing that may indeed have militated against liquefaction. Inertial events such as the duration of a pressure pulse due to soil collapse will take the form $t_{\text{pulse}} \propto \sqrt{h/g}$. In centrifuge tests, fall distances h are reduced by factor N whereas accelerations are increased by factor N . Accordingly, $t_{\text{pulse, model}} = t_{\text{pulse, field}} / N$. Diffusion processes, such as the release of air or water from a collapsing void, have durations of the form $t_{\text{dissipation}} \propto h/v$ where the flowrate v may be deduced from Darcy's Law. As explained before, v is increased by factor N and h reduced by factor N in a centrifuge test, so $t_{\text{dissipation, model}} = t_{\text{dissipation, field}} / N^2$. This means that the release of trapped pressure in a centrifuge model, during a collapse event, will be greater in proportion than that found at full scale. This problem is well-known in centrifuge earthquake liquefaction studies, Taylor (1995). Two corrective strategies to slow down rate of dissipation by factor N are: to increase fluid viscosities by factor N , or to reduce pore sizes (i.e. grain sizes) by factor \sqrt{N} . These further studies will be valuable in the clarification and classification of fast landslides (Take et al. 2004).

d.2.2) Evaluation of the slide to flow mechanism due to localised build up of transient pore pressures

Take et al. (2004) and Lee & Bolton (2006) investigated the transformation of initially slow moving slopes to flowslides as an alternative hypothesis of the triggering mechanism of fill slope failures. Take et al. (2004) performed two centrifuge model tests at centrifugal acceleration of 30 g to investigate this mechanism in both loose and dense fill slopes. The geometry adopted for both fill slopes is presented in Figure 3.52.

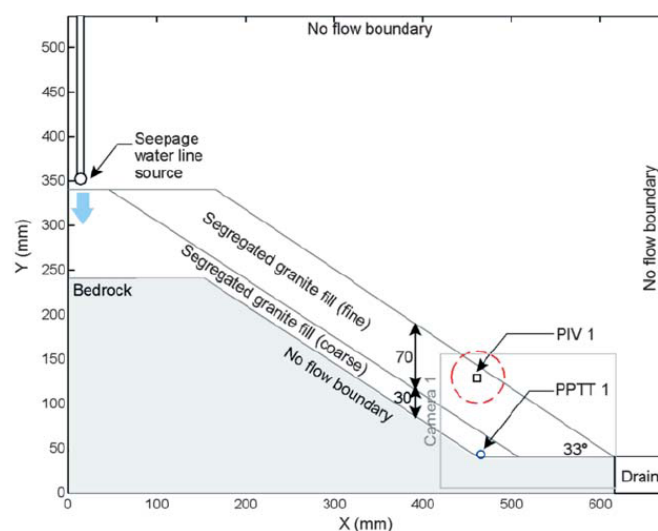


Figure 3.52 - Slide-to-flow landslide triggering mechanism model (after Take et al. 2004).

The chosen soil profile for the model fill also represents an idealised case of layering, in which the decomposed granite fill material has been sieved and separated into its coarse and fine fractions and placed one on top of the other to form a layered backfill. In this scenario, the layer ends blindly at the toe of the slope, which is also notably the location of the flow constriction. The intended triggering mechanism combines the two closely related pore pressure generation scenarios of flow constriction and heterogeneity, thereby compounding

the landslide risk. Firstly, elevated transient pore water pressures will be generated at the toe as the inclination change of the impermeable bedrock will constrict seepage flow. Water must be stored at this location, and will be forced to seep through the fill material at the toe of the slope. The presence of the layering in this model will reduce the intensity and duration of rainfall infiltration required for failure (Take et al. 2004).

Loose Layered Fill Slope

The layered slope is very loose, with an approximate relative compaction of 77% and it was intended to be representative of tipped fill and was placed with only a minimal compaction effort. As expected, the loose model fill material experienced significant settlement due to increased acceleration (Take et al. 2004).

As intended, the rate of water transfer into the toe region has exceeded the seepage velocity through the model fill, causing a transient increase in pore water pressure at the toe. The measured pore pressure versus time after the first arrival of the seepage water is plotted in Figure 3.53. The local pore water pressure was observed to increase at a nearly constant rate reaching a maximum value of 16 kPa at point B in Figure 3.53a. As this seepage front has been progressing towards the toe, the slope has been slowly creeping. Image analysis performed on the images prior to final acceleration of the failure (times B and C in Figure 3.53a), indicates that the toe is accelerating horizontally with an average velocity of approximately 6 mm/s (Figure 3.54). The observed displacement field over this time interval indicates that the surface of the model fill is moving down-slope at a slower velocity.

As the toe continues to accelerate horizontally, the surface of the model fill accelerates towards the toe, with the velocity increasing (Figure 3.53b). When the fill material has finally come to rest, it has formed a low-angle run-out (Take et al. 2004).

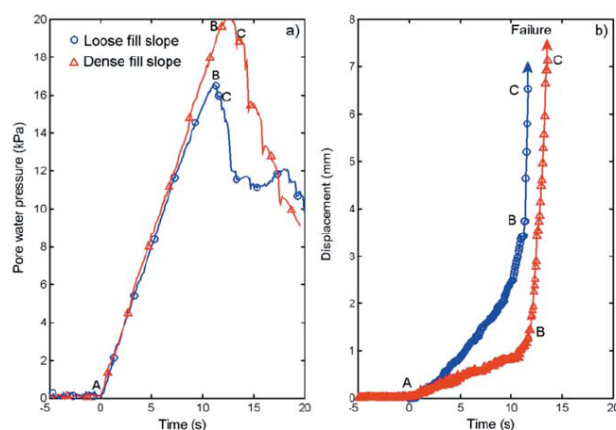


Figure 3.53 - Observed behaviour of slide-to-flow models (after Take et al. 2004).



Figure 3.54 - Displacement field prior to final acceleration of loose fill model (after Take et al. 2004).

Dense layered fill slope

The experiment was repeated with a fill compacted to 95% maximum Proctor density whilst keeping all other factors constant. After introducing the seepage water to the crest of the fill it

was quickly transmitted to the toe of the slope, building up localised transient pore water pressures at an identical rate to the loose fill model (Figure 3.53a). The dense slope exhibits a much stiffer response to the build up of pore water pressures, with less than one half of the pre-failure displacements warning of the onset of failure. Just before reaching the failure pore water pressure, the brittle fill material cracked and water rapidly entered the fill. As high pressure water entered this crack, the acceleration of the slide increased. After time B, the slope mass is observed to accelerate, albeit at a slower slide velocity than observed in the loose fill slope (points B-C on Figure 3.53b). Higher density of the fill slope compared to the loose model has slightly increased the pore water pressure required to trigger the failure, but on the hand has made the failure more brittle (Take et al. 2004).

Lee & Bolton (2006) also conducted two centrifuge tests at 40g on Completely Decomposed Granite (CDG) to investigate the potential importance of layering effect in a fill slope. The geometry of both fill slopes is presented in Figure 3.55. The slope angle for the model slope is 35°, which is slightly higher than the critical state angle of friction. Infiltration was introduced to the crest of the model slope from a water source located at the end of the model. Presumably, water seeps through and builds up in the gravel layer. Pore water pressure is expected to develop at the interface between layers and this will force the water to seep through the fill material at the mid-slope and trigger a failure. The build up of transient pore water pressure measured by PPT1 at the interface is shown in Figure 3.56.

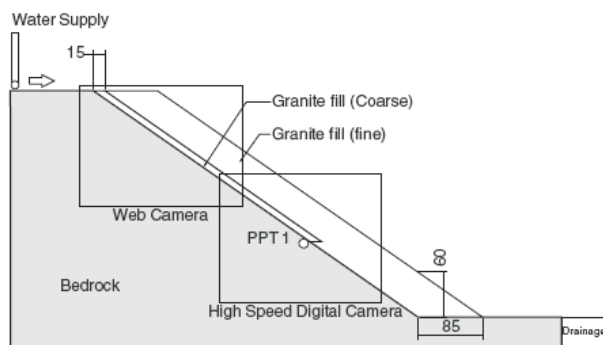


Figure 3.55 - Model geometry of the slope model (after Lee & Bolton 2006).

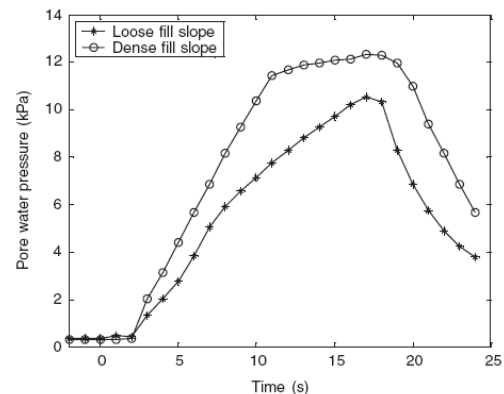


Figure 3.56 - Development of pore water pressure in model slopes (after Lee & Bolton 2006).

Failure was induced when layered fill slopes were subjected to seepage flow from a more permeable layer (Figure 3.57). The results indicate that shear failure can be developed when transient pore water pressure is allowed to build up in a more permeable layer underneath a fill slope, even though the top fill layer is compacted to a high degree (Lee & Bolton 2006).

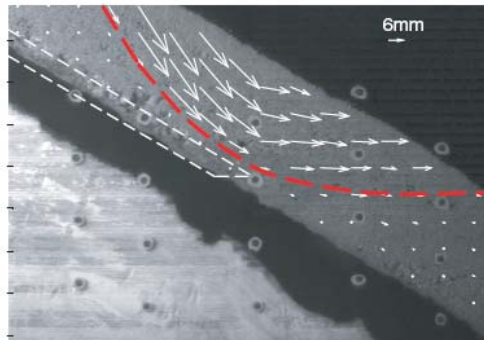


Figure 3.57 - Displacement vector field of the mid-slope (after Lee & Bolton 2006).

e) Failure processes (based on Moriwaki et al. 2004)

To clarify the failure process of a landslide triggered by rainfall, Moriwaki et al, (2004) conducted a full-scale model landslide experiment. A 23-m long and about 8-m high flume was used and the slope was instrumented by surface displacement meters, pore-water pressure gauges, and piezometers (Figure 3.58). The flume was filled with loose coarse sand ($D_{50} = 0.4\text{mm}$) and sprinkled at a constant intensity of 100 mm/h. The landslide occurred first in the upper slope about 154 min after the sprinkling started, following a creep movement within 41 min. The sliding mass slid with maximum speed of 1.2 m/s to a stop in about 5 s, compressing soils in the lower gentle slope and horizontal sections.

They observed that the velocity curve of surface displacement until the rapid landslide can be approximately classified into three stages: (A) an asymptotic increase, (B) an exponential increase, and (C) a linear increase (Figure 3.59).

Figure 3.60 shows changes in piezometric levels (P.L.) during the rapid slide. For reference, surface displacement at the middle part of the 30° slope (D-3) is also shown. Values throughout the slope and horizontal section increased rapidly. In the 30° slope, the peak value at each sensor was low because the original piezometric levels were low just prior to the rapid slide. On the other hand, piezometric levels in the lower part of the 10° slope and in the horizontal layer were higher than in the upper part of the slope and the peak occurred at the connecting point at the downslope end of the 10° slope. Small oscillations (1–2.5 Hz) in waveform were observed at sensors G-1, G-3, and G-5 in the 30° slope, where the soil layer slid down parallel to the slope. The other sensors showed no remarkable cyclic fluctuations. Iverson and LaHusen (1989) reported a generation of a 1-Hz fluctuation in a 10-m-long slope failure experiment. The small pressure increase in the upper slope was likely caused by the soil shearing, whereas the higher pressures in the horizontal layer and the lower part of the slope were likely caused by a mix of soil compression and shearing by the sliding mass. High pore-water pressures also developed outside of the landslide mass due to the compression induced by the landslide mass, as shown by G-11.

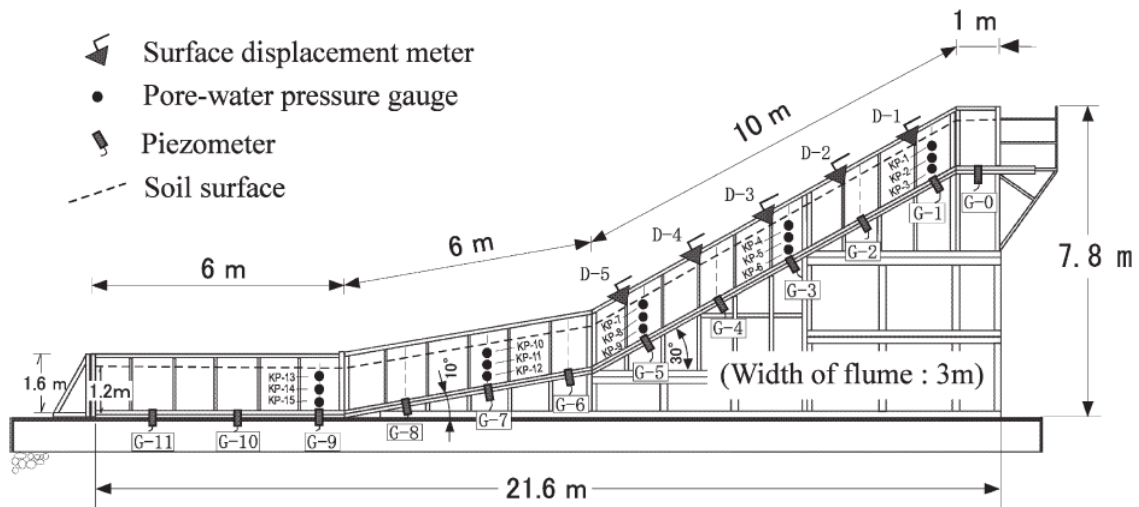


Figure 3.58 - Model slope and location of sensors after Moriwaki et al, (2004).

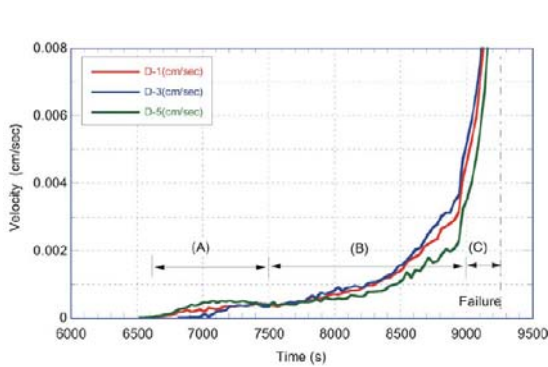


Figure 3.59 - Change in velocity of surface displacement before the slide (computed using each 30 s of data) after Moriwaki et al, (2004)

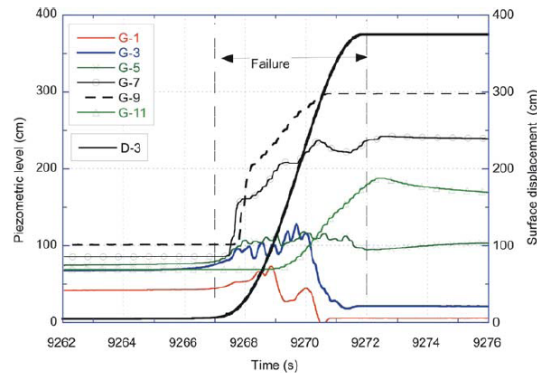


Figure 3.60 - Fluctuation of piezometric levels during the slide (D-3; surface displacement) after Moriwaki et al, (2004)

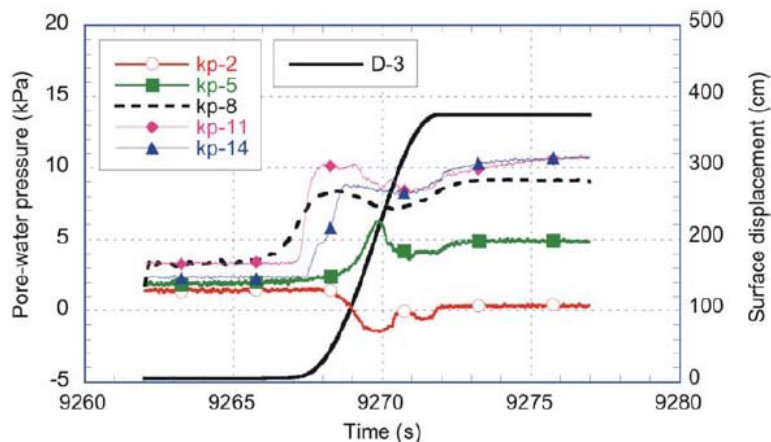


Figure 3.61 - Fluctuation of pore-water pressures at 60 cm depth throughout the soil during rapid failure, after Moriwaki et al, (2004)

Also the pore-water pressures inside the soil mass rapidly increased throughout the slope as soon as rapid failure occurred. Figure 3.61 shows all pore-water pressure changes at a depth of 60 cm. Pore-water pressures in the 10° slope (kp-8, Kp-11) and the horizontal section (kp-14) responded sequentially starting from upslope. On the other hand, those in the 30° slope (kp-2, kp-5) reacted late and pressure at the top of the slope decreased after the soil moved downslope. From the time sequence of pore-water pressure increase and the observed deformations, it is inferred that shear deformation appeared at first near kp-8, and then extended gradually downwards and upwards. The smaller tendency of pore-water pressure in kp-2 might be the result of the extensive deformation and the unsaturated state. Most pressures peaked at 1–2 s after the slide started and then receded slowly.

f) Comments

To isolate the effect of initial soil porosity on landslide style and rate, Iverson et al. (2000) conducted large-scale experiments under closely controlled conditions. They found landslides with differing porosities displayed sharply contrasting dynamics. Landslides with *initial porosities* > *critical porosity*, failed abruptly and accelerated within 1 s to speeds > 1 m/s. The landslides with initial porosities indistinguishable from the critical porosity displayed inconsistent behaviour, including slow slumping of a single soil block, episodic slumping of multiple blocks, and moderately rapid (~0.1 m/s) slumping. Data from the experiment with dense soil imply failure geometry similar to that of the loose soil but reveal markedly different landslide dynamics. On average, motion of the landslide with dense soil proceeded about 300 times more slowly than motion of the landslide with loose soil.

Wang & Sassa (2001, 2003) conducted a series of tests on silica sand to investigate the effect of initial dry densities on pore-pressure generation and failure behaviour of a landslide mass. They observed different types of failure modes and divided each failure type into four periods: Wetting, Precursory slides, Major failure, and Successive movement. Each failure mode was greatly affected by the initial density in these series of tests. In presenting a time series for pore pressure and sliding distance, they found that high pore pressure was built-up after, not prior to, the initiation of failure. In the analysis of the relationship between pore-water pressure build-up after initiation the major failure and the motion of failed landslide mass, they plotted the pore-pressure build-up after onset of failure (Δu), against the initial density index (I_d) for each test, and found that there was an optimal density index (I_{dm}) at which Δu reaches maximum.

Kimura et al. 1991 found that two types of failure appear when a fill is subjected to a heavy rain. One is the failure along a well-defined deep slip surface taking place in the areas where the wetting front has passed. The other is the failure in toe areas taking place after the appearance of the ground-water flow on top of an impermeable base layer. They observed that the downward movement of the wetting front takes place with a constant rate which is related to the rain intensity and has a shape similar to the geometry of the slope. The fills with higher initial void ratios failed at lower rain intensities and in case of similar void ratios more rainfall was necessary to cause failure in the fills with lower initial water contents.

Eckersly (1990) also found that the build up of pore pressures might be affected by shear deformation, dissipation, thickness of mass overlying the sliding surface, and other not completely understood factors.

Lourenco et al. (2006) found out variations in permeability can greatly influence the failure onset. Seepage erosion was found to dominate failure if the lower layer was coarser, while retrogressive failure of the upper layer was the most relevant failure mechanism if the lower layer was finer.

Take et al. (2004) concluded that in contrast to the static liquefaction mechanism it has been easy to create the slide-to-flow mechanism of landslide triggering by creating local groundwater mounds and hence increases in pore water pressure and local reduction in effective stress where seepage was restricted. The initial slide has been observed to create rapid flow events with low run-out angles apparently very similar to those occasionally observed in Hong Kong fill slopes. These model flowslides were just as striking in dry, dense fill as in wet, loose fill. If these model events are realistic, the priority in hazard reduction should be in preventing triggering of a slip. Interception of groundwater percolation would be more useful than densification as a remedial measure, although the removal, mixing, and compaction of loose fill would have the coincidental benefit of eliminating permeable layers. Attention should particularly be focussed on regions of slopes where springs of seepage are observed after rainstorms. Shallow horizontal drains should be particularly effective in suppressing slip triggering in such locations.

Similarly, Lee & Bolton (2006) concluded that shear failure can be developed when transient pore water pressure is allowed to build up in a blind layer underneath a fill slope, even though the top fill layer is compacted to a high degree of compaction.

During failure in a full-scale landslide experiment, Mirowaki et al. 2004 observed rapid increase of subsurface water pressure in the slope and horizontal soil layers. It was inferred that the increased water pressures in the upper slope resulted from collapse of loose soil structure during shearing in the translational slide, whereas those in the lower portion of the slope resulted from a mix of soil compression and shearing by the sliding mass.

3.2.1.1 Experiments performed on pyroclastic soils*(AMRA)*

During the recent decades, several fast flowslides involved many slopes in the distal area of Vesuvio's volcano (Campania Region Southern Italy), mobilizing the so-called pyroclastic deposits, whose origin is associated with Late Quaternary (Holocene) volcanic activities. Due to their nature and depositional mode, these pyroclastic soils mainly consist in alternating layers of volcanic ashes and pumices. The ashes are essentially sandy soils with a significant non-plastic silty component, while the pumices fall in the sandy gravel or gravelly sand grain-size domain and are characterized by the presence of intra-particle voids. The overall behaviour can be assimilated to that of granular soils.

In order to focus on the hydrological response up to failure of unsaturated pyroclastic covers, some experiments on heavily instrumented small-scale physical models have been performed using a 2.2 m long and 0.50 m wide flume, which has been built at the Geotechnical Laboratory of the Department of Civil Engineering, Seconda Università di Napoli (Olivares et al. 2009). As the thickness/length ratio is below 1/10, the slope can be considered infinite, thus reproducing the most frequent case in the investigated areas. The slope is reconstituted by a moist-tamping technique (Olivares and Damiano, 2007). In the experiments conducted so far, slope inclination has been 38°-40°, slightly larger than saturated friction angle of soil, and an impervious bottom has been reproduced allowing investigation of a typical scenario in Campania, characterized by the presence of a less pervious layer at the top of the bedrock. A geotextile drain was placed at the toe of the slope, in order to let free water outflow when soil approaches saturation. The experiments have been conducted on pyroclastic soils taken at Cervinara (Olivares and Picarelli, 2003), Monteforte Irpino (Papa et al., 2008) and Bracigliano, all sites located north-eastern of Naples.

Table 3.4 - Test conditions

Test	Soil	Geometry			Initial conditions				i [mm/h]	t [min]
		α [°]	L [m]	h [m]	w	n [%]	S_r [%]	$(u_a - u_w)$ [kPa]		
FL1	Cervinara	40	1.00	0.08	0.18	62.6	27.9	70.0	20	110.0
FL2		40	1.00	0.08	0.30	70.8	32.0	53.0	20	180.0
FL3		40	1.20	0.12	0.25	67.7	31.1	57.0	40	71.0
FL4		40	1.20	0.10	0.30	70.0	33.4	32.0	40	25.0
FL5		40	1.20	0.10	0.32	63.2	48.4	29.0	40	49.0 ⁺
FL6		40	1.00	0.09	0.35	69.0	40.9	20.0	40	81.0
FL7		40	1.00	0.16	0.31	71.1	33.2	67.0	80	-
FL8		40	1.10	0.10	0.30	70.4	32.8	70.0	60	31.0
FL9		40	1.10	0.10	0.37	73.1	35.3	59.2	60	30.0
FL10		40	1.10	0.10	0.43	65.0	59.6	51.7	60	-
FL11		40	1.30	0.12	0.31	72.7	30.3	-	60	-
FL12		40	1.00	0.10	0.40	69.8	45.0	55.3	60	-
FL13	Bracigliano	35	1.25	0.14	0.64	79.0	43.6	34.3	60	37.0
FL14	Cervinara	40	1.30	0.16	0.43	74.0	39.3	75.0	60	86.0
FL15		40	1.00	0.10	0.50	75.4	42.4	17.5	55	36.0
FL16	Bracigliano	40	1.00	0.10	0.40	75.7	33.3	41.0	56	30.0
FL17		38	1.20	0.10	0.52	77.4	39.6	62.8	40	62.0
FL18	Monteforte Irpino	40	1.40	0.14	0.42	75.8	35.4	54.0	50	121.0
FL19		40	1.10	0.10	0.39	68.8	46.7	68.5	54	88.0
FL20		40	1.10	0.11	0.50	71.6	52.4	31.0	55	76.0
FL21_1		40	1.10	0.10	0.47	76.1	39.0	38.0	50	21.0 ⁺
FL21_2		40	1.10	-	-	-	-	15.5	55	58.0
FL22_1		40	1.10	0.10	0.43	75.9	36.0	28.0	50	27.0 ⁺
FL22_2	40	1.10	-	-	-	-	15.0	45	58.0	

⁺ rainfall end

A summary of tests performed is reported in Table 3.4. With the exception of some experiments (FL5, FL21_1 and FL22_2), all tests were carried out under uniform and constant rainfall until slope failure. In most cases, although the rainfall intensity was much higher than the saturated hydraulic conductivity of soil, no significant surface runoff was observed. This demonstrates that the potential infiltration was not exceeded.

Figure 3.62 shows the typical response of a slope reconstituted at a porosity close to the natural value ($n=73\%$). A marked suction decrease occurs starting from the ground surface towards the base of the layer as revealed by a comparison of readings at shallow and deep tensiometers. This suggests that a wet front progressively moves downwards. In all cases suction growth is characterized by a steep front, followed by a further long-lasting slow increase until slope failure. It is worth noting that this phenomenon continues even after stopping of rainfall. In fact, in the tests FL21_1 and FL22_2 consisting in two wetting stages, after rain stopping, the tensiometers located in the middle of the slope recorded a small increase in suction, while the deepest ones displayed a decrease. A uniform distribution of both suction and water content was reached only 20 minutes after the stop. This suggests that a critical slope stability condition could be attained even after the end of rainfall.

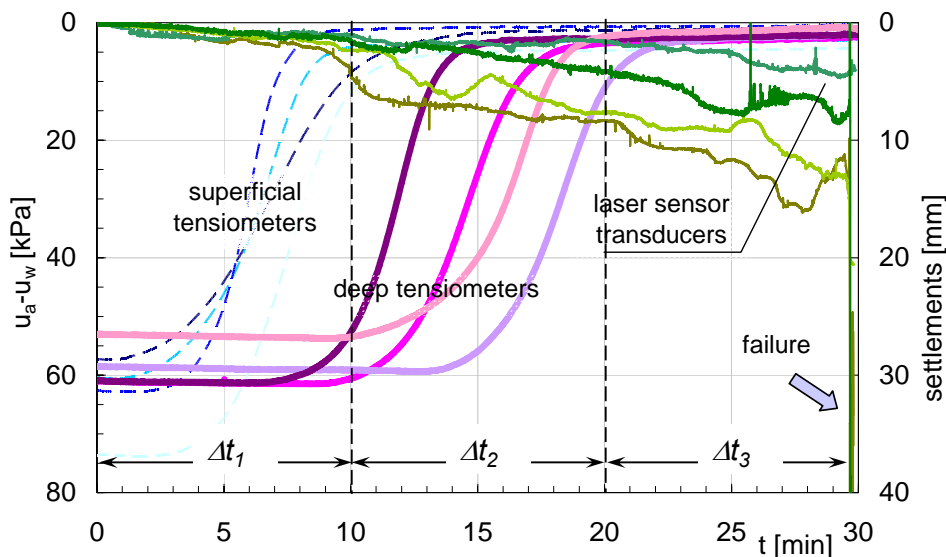


Figure 3.62 – From wetting to failure: typical response of loose deposits

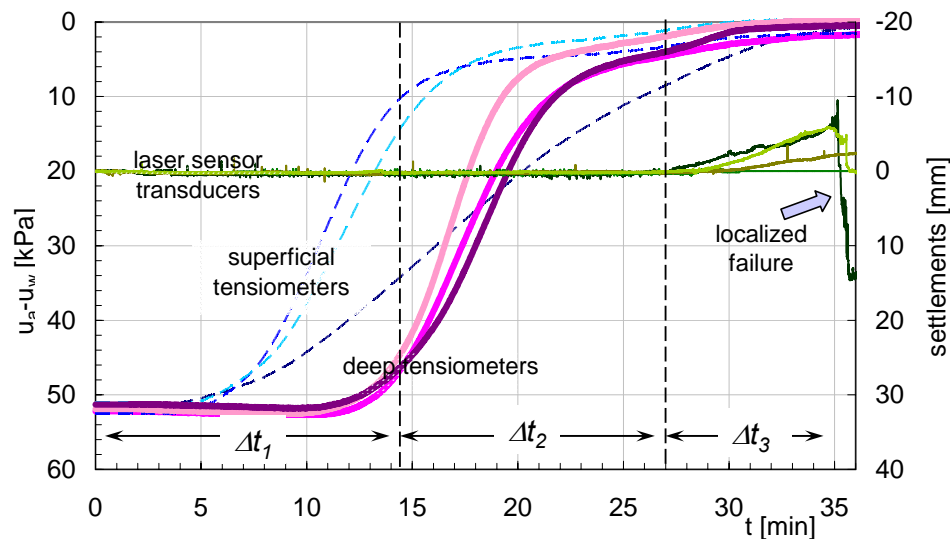


Figure 3.63 – From wetting to failure: typical response of dense deposits

Such tests also show that rainfall intensity plays a fundamental role. For example, a comparison of the results of experiments FL16 and FL22_2 demonstrates that, despite the greater initial water content of soil, in test FL22_2, a lower rainfall intensity (45mm/h) requires double the time (58min in test FL22_2, 30min in test FL16) to trigger failure. Also soil porosity seems to significantly affect infiltration: the results of tests FL19, FL20 and FL21_2 show that, under the same rainfall intensity, a lower initial porosity requires a longer rainfall for slope failure.

Porosity also influences other aspects of slope behaviour, including the failure and post-failure stages. In fact, in all tests performed on loose soil (porosity higher than 73%), saturation is accompanied by a significant volumetric strain which can attain values in the order of 7% (Fig. 3.62) and failure involves the whole layer which displays a clear flow-like evolution. In contrast, volumetric deformation is practically negligible for a lower initial porosity, as shown in Figure 3.63 which illustrates the response of a relatively dense slope: furthermore, in this case failure involves only the uppermost part of the layer and the post-failure movement does not display an evident evolution in flowslide.

All experiments on loose deposits show that slope stability is ensured by the effects of suction on the shear strength. When suction vanishes, the slope fails and a rapid acceleration occurs. The flow-like post-failure evolution is a consequence of a sudden increase in pore pressure (static liquefaction) as shown in Figure 3.64. Both the high shear strain rate and the maximum pore pressure recorded at the base indicate that the process evolves towards complete fluidization, i.e. a complete loss of strength (Olivares and Damiano, 2007). Conversely, tests performed on relatively dense soil show that the reduction in suction is not accompanied by a complete slope collapse since the pore pressure maintains more or less the same values as before failure (Fig. 3.65): as a consequence, the soil mass does not take the features of a flowslide.

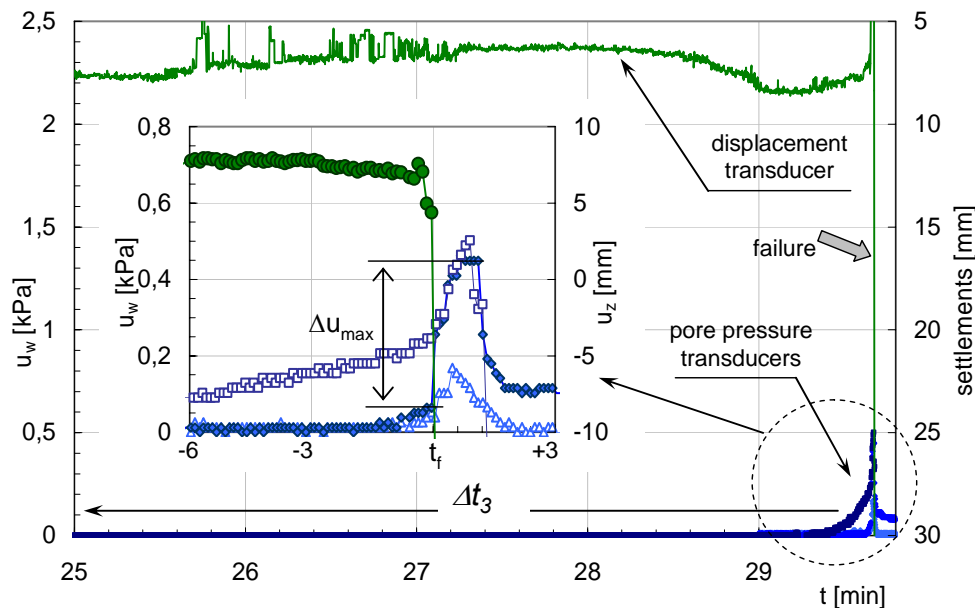


Figure 3.64 - Typical response at failure and early post-failure of loose deposits

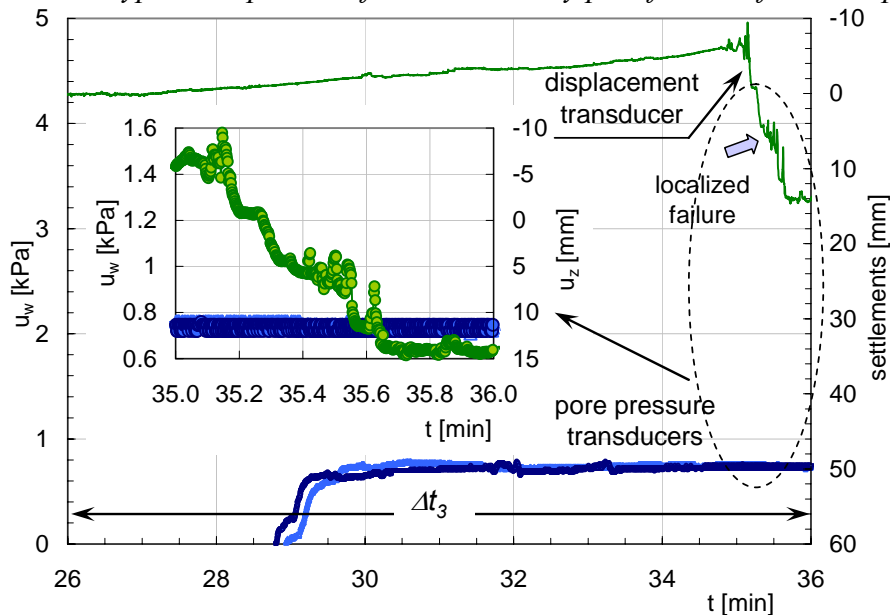


Figure 3.65 - Typical response at failure of dense deposits

Such data, in conjunction with the results of conventional and not conventional laboratory triaxial tests on natural specimens (Olivares and Damiano, 2007), demonstrate that the field void ratio might enable to discriminate between deposits which are prone to liquefaction and can give rise to catastrophic flowslides, and deposits whose post-failure behaviour should rather be of slide style, thus less catastrophic. For typical thickness of pyroclastic covers (1-4m) thus accounting for the average state of stress, the critical void ratio could be established around 1.8, which is generally less than the natural void ratio of the most air-fall deposits. However, in boundary value problems further aspects, such as the probability of progressive failure, should be accounted for (Picarelli et al., 2008).

Experiments on physical models provide further useful information. In fact, coupling the changes of suction with the values of the volumetric water content at the same depth, which are measured with a TDR probe, allow the water retention curve experienced by the soil during infiltration to be obtained. These curves are compared with those obtained through conventional long-term laboratory techniques (Damiano and Olivares, 2010). Figure 3.66 shows the experimental results which have been fitted by the van Genuchten (1980) expression. In spite of some data scattering, the characteristic curve extrapolated by flume tests (curve 2 in Fig. 3.66) clearly shows that for θ_w higher than 0.38, suction is lower than that obtained by conventional laboratory tests (curve 1 in Fig. 3.66). This effect is probably related to the different rate of suction decrease imposed in the two procedures accounting for the nature of the particles which present an internal porosity. Similar results have been carried out for the Monteforte Irpino ash. This suggests that great attention should be paid in determining the characteristic curve around the air-entry region.

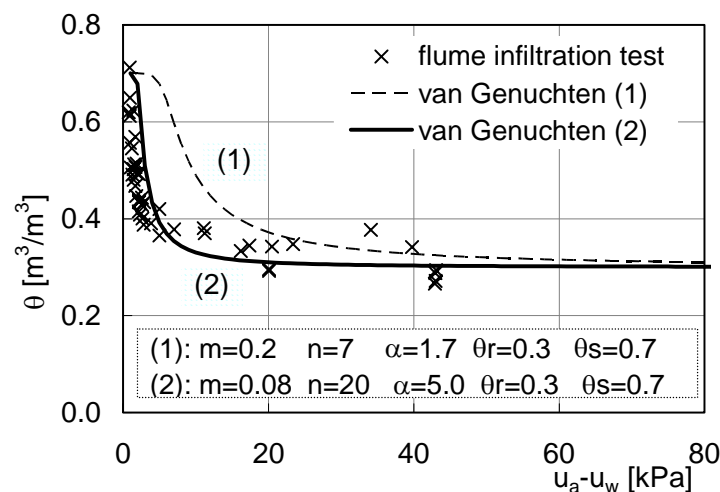


Figure 3.66 – SWRC of Cervinara volcanic ash derived from flume infiltration tests compared with SWRC obtained from laboratory tests (from Damiano and Olivares, 2010).

3.2.2 Experience gathered through full-scale physical modelling

(ETHZ)

a) Artificially induced rainfall instabilities on moraine slopes - Gröben

A combination of field and laboratory tests was carried out on shallow slips in alpine moraine slopes to investigate slope stability in moraine as a function of degree of saturation and relative density of the soil. Three field tests were conducted on a 100 m² surface area in 1999 and 2000 (31° slope, field test 1) and on a smaller plan area of 55 m² in 2000 (42° slope, field test 2). The problem is complicated by the strong heterogeneity of moraine soils, with particle sizes varying from silts to boulders. The test fields were located ca. 2800 mASL near to the Gröben glacier in Switzerland.

The soil characterisation tests included in situ and laboratory experiments on both saturated and partially saturated samples to determine densities (maximum, minimum, in situ and optimum from standard Proctor compaction tests) together with permeability (saturated) as a

function of normal stress, void ratio, particle size soil-water retention curves, and shear strength from consolidated drained triaxial tests carried out at constant deviator stress.

The moraine is extremely heterogeneous with a significant range of particle sizes represented in the overlying 1-2 m on the slope. Seismic refraction, D.C. resistivity and gravimetry soundings were performed during a former geophysical campaign (Vonder Mühl et al. 1996). The results indicated a maximum thickness of nearly 100 m of moraine, with looser packing in a top layer (low compression velocities $v_p = 400-600$ m/s in the top 5 m at the site), whereas the underlying moraine appears to have been well compacted with v_p increasing with depth.

The measurements of the unit weights up to 1 m depth were done with sand replacement and nuclear measurements. The soil properties are given in Table 3.5.

Table 3.5 - Soil properties of test field (in situ)

Property	Value
Dry unit weight γ_d	20.3 kN/m ³
Water content w	4.6 %
Void ratio e	0.29 [-]
Relative density D_r	77 %

The field test sites were instrumented with devices to measure suctions and volumetric water content, pore water pressures, rainfall intensity, and were provided with apparatus to create artificial rain as uniformly as possible. A layout of the instrumentation installed in field 1 and field 2 is given in Figure 3.67. More specific details of the local topography and geology, applied rainfall intensities together with the layout, installation and type of the instrumentation have been given in Springman & Teyssere (2001) and Springman et al. (2003).

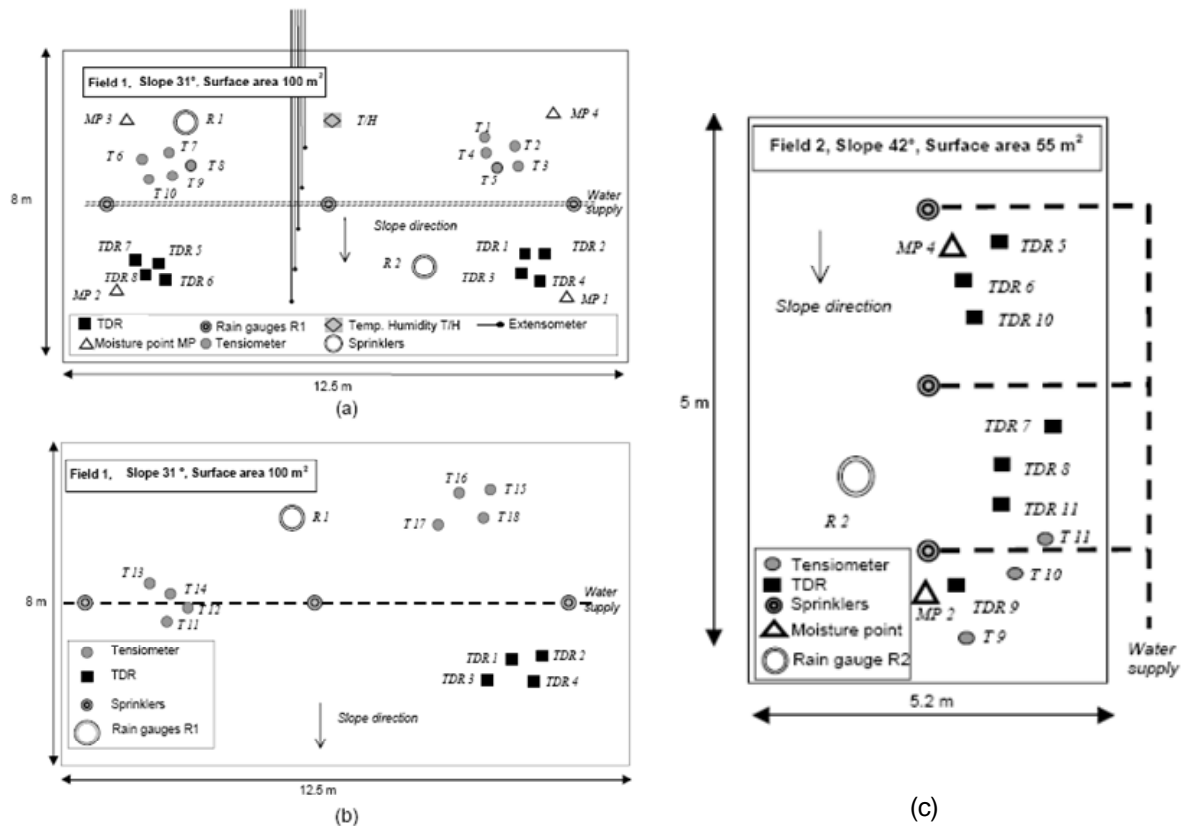


Figure 3.67 - Test field and instrumentation layout: (a) Field 1/1999; (b) Field 1/2000; (c) Field 2/2000 (after Springman et al. 2001)

A sprinkler system was constructed to supply controlled artificial rainfall, the intensity of which was also measured. The artificial rainfall events exceeded any observed storms of that duration at Simplon and have a return period greater than 500 years. It was noted (Teyssere et al., 2000) that wetting during initial infiltration followed a steep hyperbolic path, as if along the main wetting curve of the WRC from a nominally dry state, whereas pauses in rainfall caused an exponential reduction of S_r with time (along a hysteretic scanning WRC). On rewetting (also along a hysteretic scanning WRC), resaturation up to the immediate past maximum S_r occurred significantly quicker than for the drying phase, whereupon further saturation continued at the previous rate (main wetting curve). The combination of suction and water content measurement can be linked to the insitu water retention properties of the moraines (Fig. 3.68).

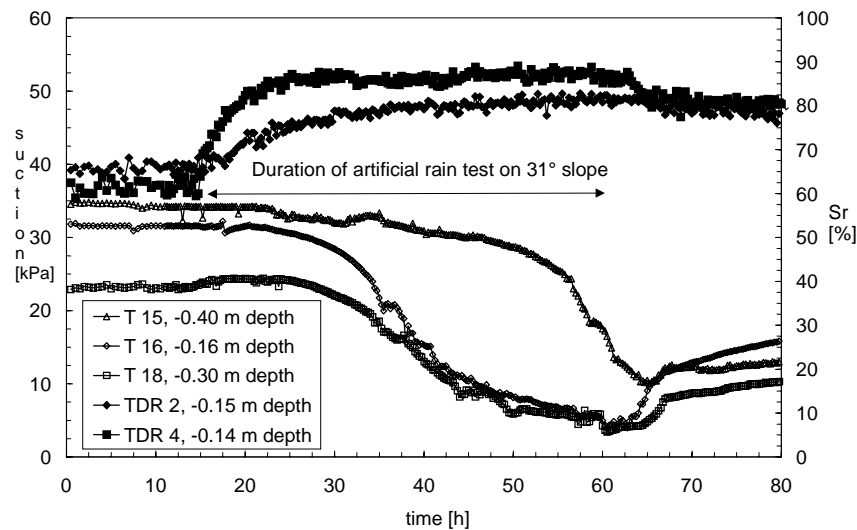


Figure 3.68 - Equivalent data for an insitu water retention curve (S_r increase following a wetting path from a TDR) combined with suctions determined from tensiometer probes (T) during artificial rainfall: Field 1/2000 (31°).

Results: Field 1/1999

A base rate of circa 10 mm/h was supplied almost continuously for one week in 1999, including peaks of between 30-40 mm/h. Figure 3.69 shows three sets of TDR measurements (TDR 1, 2, 4) compared to intensity over 7 days of intense artificial rainfall, during which time the degree of saturation in the surface layers increased from 60–75 % up to around 90 %. Pauses in the rainfall (during the 1st and 2nd days) are clearly seen on the response curves with very little delay between the cessation and the measurement of a reduction in saturation. Data of saturation degree from the Moisture point device (Fig. 3.70a) agree well with values from the TDRs (Fig. 3.69) in the upper 15 cm (curve 1; Fig. 3.70a). The degrees of saturation reduces with increasing depth (curves 2-5; Fig. 3.70a), indicating the dominant effect of infiltration. Natural rainfall following the period of artificial rainfall was also recorded in 1999 for field 1 (Fig. 3.70b) with results confirming trends developed during the extreme artificial event.

It requires large changes in the water content and a flow regime to reach unstable conditions in such soils on a slope slightly less steep than the critical state friction angle.

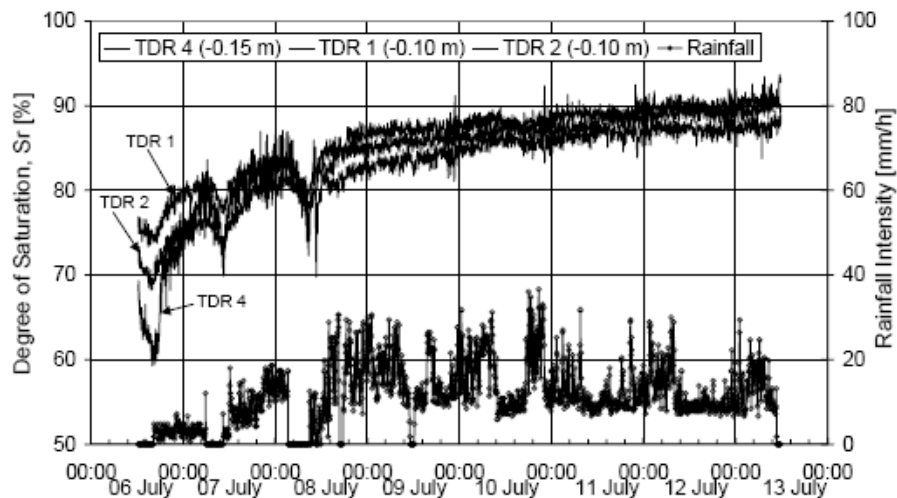
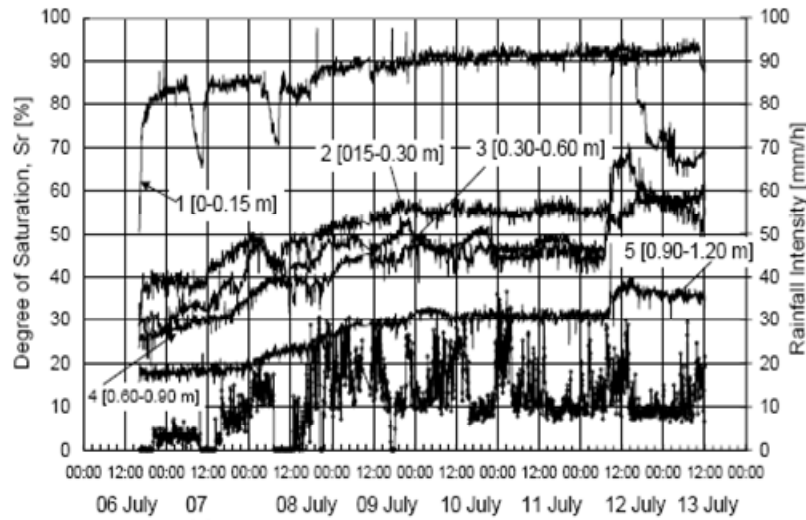


Figure 3.69 - TDR measurements (artificial rain). Field 1/1999.

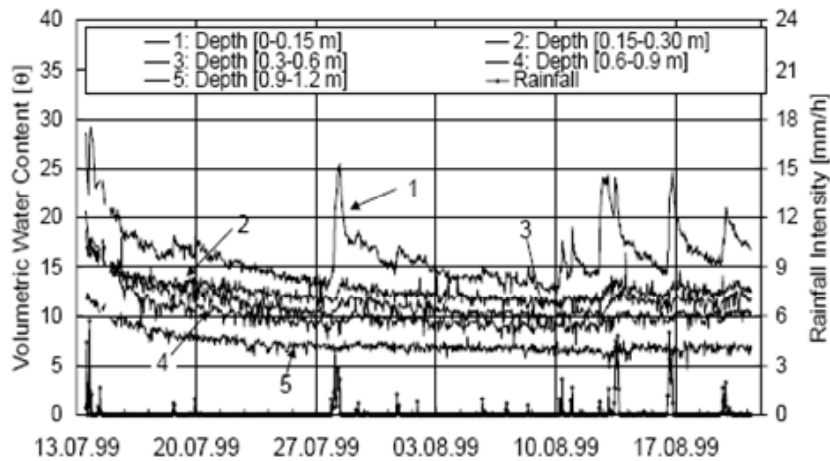
Results: Field 1/2000

Rainfall was supplied more evenly in 2000, but only for two days and two hours, with an average of 16 mm/h for the first day and 12 mm/h for the second day. TDR responses were very similar to those measured in 1999 with increases in S_r from ~60% to 75-88%. The increase was not as sharp as in 1999. The rainfall intensity was lower. S_r did not reach an asymptotic value over 2 days.

Suction was also measured at three depths between 0.16 m-0.4 m (Figure 3.70b). Since the beginning of the rainfall, suction reduced most quickly in the shallower layers, from roughly –30 kPa to a minimum value of –4 kPa. The deeper tensiometer responded more slowly.



(a)



(b)

Figure 3.70 - Moisture Point measurements Field1/1999: (a) artificial rain; (b) period following the test.

Results: Field 2/2000

A similar TDR response was noted in the steeper 42° slope (Fig. 3.71), in that the degree of saturation increased during 0.65 m of continuous steady rainfall over 2 days, in this case up to 95%, where upon a small planar slip occurred. This more or less covered the entire plan area of Field 2 and the shear surface was located at a depth of c. 0.35 m. The TDR response clearly shows the exact time of the slip. Unfortunately no data was recorded from tensiometers on this slope. Nonetheless, the summary data is given in Figure 3.72, showing the increasing saturation during artificial rainfall combined with loss of suction (Springman et al., 2003).

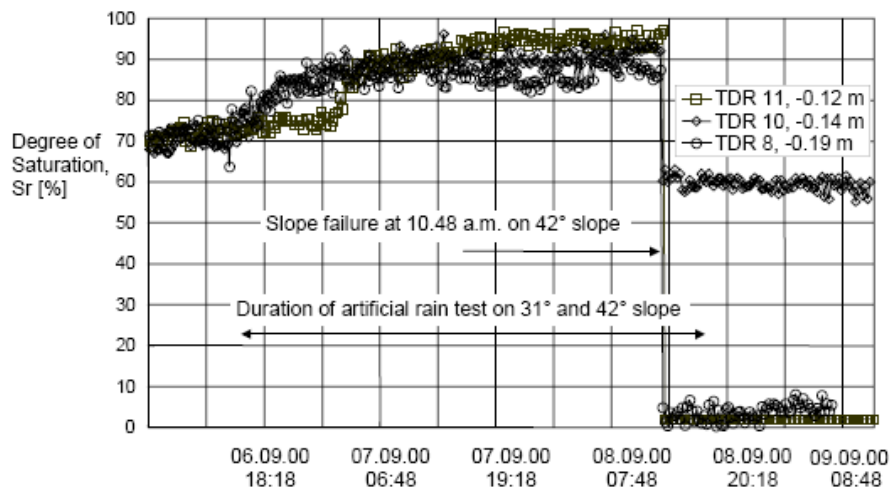


Figure 3.71 - TDR measurements (artificial rain): Field 2/2000

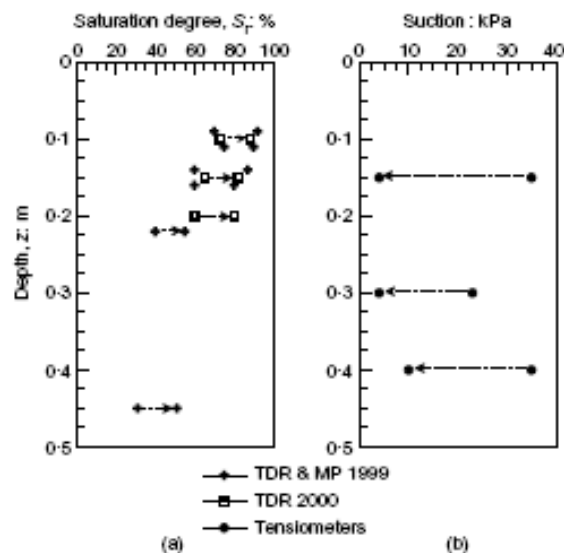


Figure 3.72 - Immediate pre- and post-rainfall event data: (a) saturation degree determined from TDR and MP probes, fields 1/1999 and 1/2000 (31°), Gruben; (b) suctions determined from tensiometers, field 1=2000 (318), Gruben (after Springman et al. 2003).

b) Landslide monitoring and triggering experiment in a silty sand slope - Rüdlingen

The selected experimental area is a steep, forested slope in Ruedlingen, North Switzerland, where 42 surficial landslides occurred in spring 2002, after an extreme rainfall event (Fischer et al. 2003).

To investigate the hydrological and mechanical behaviour of the slope, a sprinkling experiment was carried out in autumn 2008, followed by a triggering experiment in spring 2009.

The selected experimental area is located on an east facing slope on the banks of the river Rhine. The altitude is about 350 masl. The average gradient of the slope was determined using a total station theodolite to be 38° (Springman et al. 2009). During the preliminary

investigations, sandstone and marlstone were located at a depth of between 0.5 m to more than 5 m along the 30 m x 7.5 m plan section. The soil behaviour was investigated in the laboratory under saturated and unsaturated conditions (Springman et al 2009, Casini et al. 2010 a&b). The average saturated permeability of the soil is $k_{sat}=1*10^{-7}$ m/s. The soil can be classified as medium-low plasticity silty sand (ML) according to USCS.

An extensive instrumentation plan was designed to measure hydrological and geo-mechanical responses of the slope. Detailed measurements of soil suction, water level and soil volumetric water content were combined with an investigation of subsurface flow at the lowest part of the slope by means of tracer experiments. Deformations were monitored during the experiment, both on the surface via photogrammetrical methods and within the soil mass, using a flexible probe equipped with strain gauges at different points and a two axis inclinometer on the top (Askarinejad 2009). The instruments were installed mainly in three clusters over the slope. The instruments included jet-fill tensiometers, TDRs, Decagons, TDRs, piezometers, soil temperature sensor, deformation probes, earth pressure cells, acoustic sensors and rain gauges (Figure 3.73). The tensiometers were installed at depths of 15, 30, 60, 90, 120, and 150 cm below the ground surface in each cluster. Decagons were installed at shallow depths of 15 to 60 cm every 15cm, and TDRs from 60 cm to 150 cm, with a spacing of 30 cm. All the instruments were calibrated and checked in the laboratory for proper functioning before installation in the field. The hydrological responses of the soil were measured during the experiment with a logging interval of 5 minutes and the subsurface movement measurements were carried out at a frequency of 100 Hz (Askarinejad 2009).

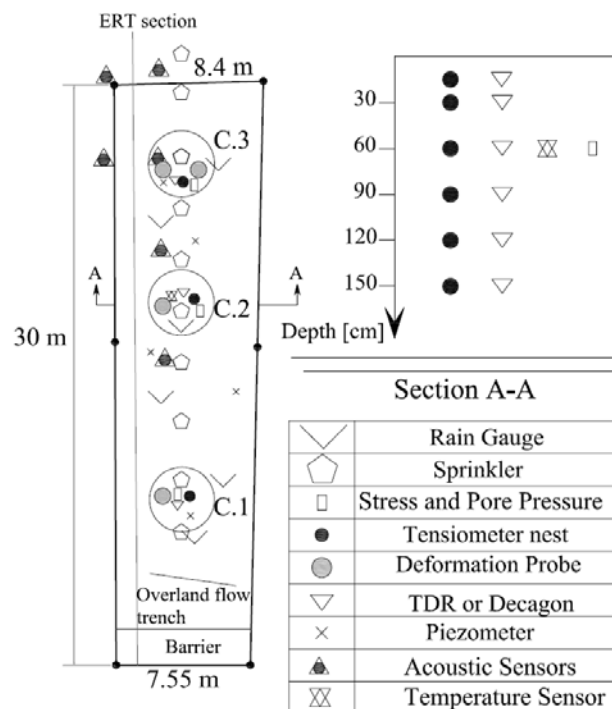


Figure 3.73 - Instrumentation plan and section (after Askarinejad et al. 2009)

The artificial rainfall was applied in the first experiment by means of 10 sprinklers located at the same spacing on the middle longitudinal line of the field. The lower sprinklers experienced higher hydraulic head as the water was supplied from the upper part of the slope.

Therefore, the rainfall was not uniformly distributed. The average applied rain intensity is shown in Figure 3.74a with an average intensity of 35 mm/hr for 3 hours as the first wetting phase (W1), followed by a 20 hour stop allowing the soil to drain (first drying phase D1). Afterwards, the slope was sprinkled for 1.5 days with an average intensity of 17 mm/hr, which increased with a short storm of 45 mm/hr to average value of 30 mm/hr for another 1.5 days (second wetting phase W2) and then the second drying phase started (D2).

Figures 3.74 b, c&d show the variations of volumetric water content (VWC) and matric suction at three different depths of 30, 60, and 120 cm in clusters 1 and 2. After changes in the intensity of the applied rainfall, the suction and volumetric water content measurements respond without significant time discrepancy at all 3 depths. This verifies the high infiltration capacity of the soil obtained from the earlier hydrological investigations. At some points during the second wetting phase of the rainfall, the changes in VWC and suction are not contemporaneous. This can be due to either the hysteretic effect of the soil–water retention curve or the difference in the location of the sensors at each depth (Askarinejad et al. 2010).

At the beginning of the second drying phase (D2), the VWC drops as the suction increases (Figures 3.74 b and c) but the suction increases up to 2.5 kPa in cluster 2 at depth of 120 cm (Figure 3.74 d) and the VWC starts to decrease only after this point. This point can be described as the air entry value of the WRC which is consistent with the value derived from the laboratory test ($s_{aev} = 2.7$ kPa).

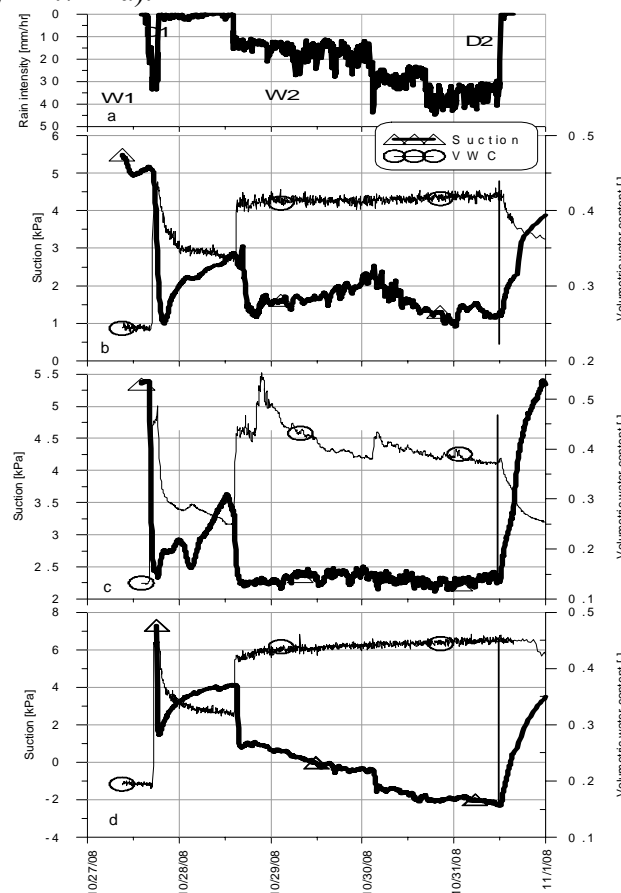


Figure 3.74 - (a) Average applied rain intensity, (b) Variations of volumetric water content and matric suction in cluster 1 at depth of 60 cm, (c) cluster 2 at depth of 30 cm, and (d) cluster 2 at depth of 120 cm (after Askarinejad et al. 2010).

A slug test was conducted close to the lowest instrument cluster above bedrock at depth of 4 m which revealed extremely high permeability. Despite applying a large amount of water in a small area no groundwater table could be developed. Furthermore, geophysical monitoring indicated the likelihood of a strata change in the underlying rocks, which would confirm the presence of fissures in the rock at the lower part of the slope. Accordingly the sprinklers were re-oriented at closer spacing, further up the slope (Fig. 3.75), where less influence was expected from the vegetation and a rising groundwater table would be possible.

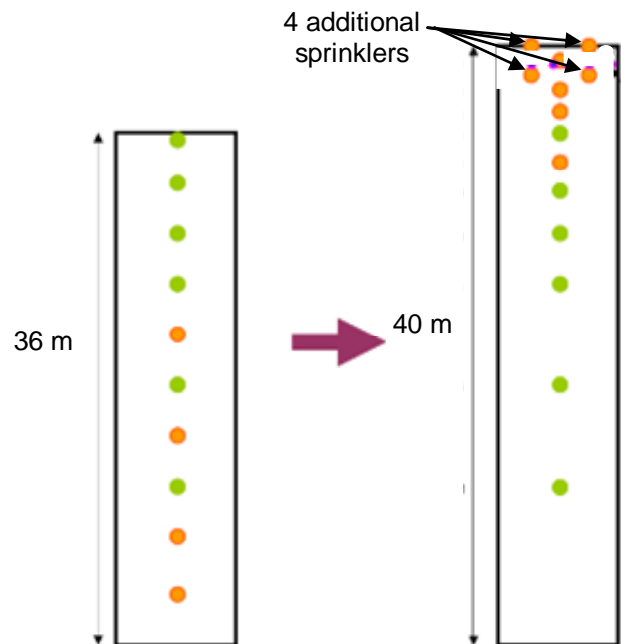


Figure 3.75 - Sprinkler locations: October 2008 (left); March 2009 (right) (after Springman et al. 2010).

With newly aligned sprinklers, the rainfall was adjusted to an average distribution mainly between 10 to 15 mm/h (Figure 3.76) and there was an instant response in the upper part of the field as the saturation degree increased, suctions dropped and then the water table rose over 5 h to about 1.5 m below ground level, where it stayed for the next 10 h. 15 h after the rainfall had begun, at 3:00 am, the upper right quadrant started to creep downslope, with the rate increasing until 3:23 am (Fig. 3.77). A tension crack opened up parallel to the top of the test field, and as the failure surface spread through the ground, the right hand side of the landslide followed the scar made through the vegetation and the left ripped away from and through the surficial vegetation (Springman et al. 2010).

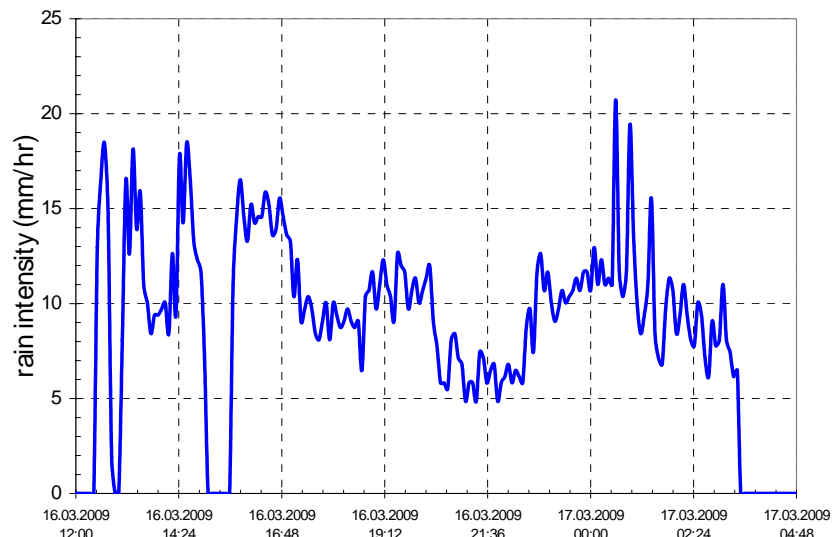


Figure 3.76 - Average applied rainfall in the 2nd experiment.



Figure 3.77 - Failure due to artificial rainfall mobilising ca. 130 m³ of debris (after Springman et al. 2010).

The failure wedge on the right hand side slipped over the bedrock at depth of ca. 80 cm while on the left hand side it is inside the soil layer with maximum depth of around 1.5 m. The length of the failure surface is 18.5 m in the middle line and has a semi elliptic general shape with maximum width of 7.5 m (Figure 3.77).

3.3 GENERAL CONSIDERATIONS ABOUT THE MECHANICAL EFFECTS OF WEATHER ON THE BEHAVIOUR OF SLOPES (AMRA)

Recent research and experiences are highlighting and clarifying the role of precipitations on slope behaviour with particular reference to the mechanics of the deformation and failure. Investigations on other weather effects, as snowmelting, deterioration of soil properties or even indirect effects (as erosion), are less active and in some cases have only a local meaning. However the research on precipitation-induced slope movements seems to go on more quickly in the case of granular soils than in the seemingly simpler case of fine-grained geomaterials.

This has certainly an explanation in the heaviest consequences of landslides in granular soils which often turn into fast catastrophic flows, and in the consequent involvement of the research community, than in the second type of materials which generally trigger slower landslides. Naturally, this is not a rule, as the large size and high velocity reached by some mudslides in fissured clay shales and planar slides in flysch (section 3.1.2) demonstrate.

The amount of data collected in the last years on precipitation-induced landslides in granular soils is impressive. These include the results of:

- A) a high number of experiments (flume as well as centrifuge tests) on well instrumented small and full-scale model slopes conducted in several laboratories located in Asia, Australia, Europe, United States, supplemented by adequate soil characterisation through laboratory tests;
- B) experiments on instrumented natural slopes led to failure through artificial rain;
- C) monitoring of instrumented natural slopes.

The main findings coming from such experiences have been presented in previous sections.

The experiments on small and full-scale model slopes (A) enabled to investigate on the role of a number of parameters which influence the mode and the mechanics of failure of ideal slopes, thus also the landslide magnitude. Similar data have been collected through experiments on natural slopes (B), these ones restricted to the cases examined which are characterised their inhomogeneities and by only inferred initial and boundary conditions. The same problem concerns the monitoring of natural slopes (C), which in addition generally cannot provide information about the mechanics of failure.

As shown in previous sections, investigations on granular soils include experiments carried out on clean sands, sands mixed with given amounts of silt, pyroclastic soils, natural decomposed granites, moraines; some experiments on model slopes have been carried out on stratified materials. These materials are generally unsaturated thus the prominent role of suction, which in the case of fine-grained soils often plays only a minor role, is accounted for. The influence on slope behaviour of boundary conditions, rain intensity and soil porosity has been deeply investigated.

In spite of the experimental difficulties, the role of all these and other parameters has been carefully examined providing important data and assuring fundamental advances in the study of slope behaviour and landslide triggering. In particular, several investigations focused on the mechanisms of generation of flow-like landslides, a critical issue since these are the most catastrophic landslides. A lot of important data and considerations have been reported, highlighting the conditions which lead to flow generation.

Data concerning fine-grained soils include only monitoring of natural slopes (C). Instrumented slopes are numerous and cover different types of materials, but investigations are often casual and not specifically addressed to the investigation of the modes of failures and to the role of selected parameters. The conclusions are then less clear than in the case of granular soils. Surprisingly, as stated above, the framework about precipitation-induced landslides in cohesive soils is less clear than the one about granular soils, being supported only by monitoring of natural slopes which is moreover connected with occasional conditions rather than with well defined research programmes. However, some information regarding the mechanisms of failure giving rise to slides or to mudslides is provided in section 3.1.

4 GEOMECHANICAL MODELLING OF WEATHER EFFECTS

4.1 MODELLING OF RAINFALL EFFECTS

4.1.1 Material modelling

Experimental data about some soil properties (water retention, permeability, shear strength etc.) of some special soils outcropping in landslide prone areas will be presented and discussed. The available material models and constraints in computational approaches will be discussed in depth.

4.1.1.1 Soil properties

4.1.1.1.1 Pyroclastic soils

(UNISA - AMRA)

Pyroclastic soil deposits are widely diffused in Campania region (Southern Italy) over an area of about 3,000 km². These soils were mainly originated by the Late Quaternary - Holocene explosive activity of Somma-Vesuvius volcano and, subordinately, by Campi Flegrei and Roccamonfina volcanic apparatus. Aimed to characterise both the physical and mechanical properties of these deposits, an extensive laboratory testing programme on undisturbed and remoulded samples was carried out in the last years at the Universities of Naples and Salerno. While referring to Cascini et al. (2000), Olivares and Picarelli (2001), Sorbino and Foresta (2002), Nicotera (2000), Lampitiello (2004), Bilotta et al. (2005) and Picarelli et al. (2006) for a detailed description of both methodologies and experimental procedures, the main obtained results concerning the hydraulic and shear strength properties of pyroclastic soils are here summarised.

Some data regarding the area around the town of Sarno recently affected by huge landslides of the flow-type are reported below.

Due to their origin (Cuomo, 2006; Picarelli et al., 2006), the pyroclastic soil deposits are characterised by a high variability in their physical and mechanical properties. However, three main soil classes were recognised by Bilotta et al. (2005) consisting in pumice soils and ashy soil layers (class A and B) (Fig. 4.1). Particularly, the shallow ashy soil (class B) is generally coarser than the deep one (class A), as confirmed by laboratory tests aimed to assess hydraulic and shear strength properties in saturated and unsaturated conditions.

The hydraulic properties of ashy soils in saturated conditions were investigated through conventional permeameter tests that provided hydraulic conductivities ranging between 5.0×10^{-6} m/s and 4.8×10^{-5} m/s; while for the pumice soils hydraulic conductivity values ranging between 1.0×10^{-5} and 1.0×10^{-2} m/s were assumed, according to the available data in literature (Pellegrino, 1967; Whitam and Sparks, 1986).

With reference to the unsaturated conditions of the ashy soils, the Suction Controlled Oedometer, the Volumetric Pressure Plate Extractor and the Richard Pressure Plate furnished water characteristic curves as in Figure 4.2; the same Figure also shows the volumetric water content and the hydraulic conductivity curves for pumice soils, obtained by using empirical relationships based on their grain size distribution (Bilotta et al., 2005).

The saturated shear strength envelopes for ashy soils provided effective friction angles ranging from 32° to 35° for class A soil, and from 36° to 41° for the class B soil (Fig. 4.3).

Referring to effective cohesion, class B soil shows values approaching to zero, while for class A soil values ranging from zero to 5 kPa are furnished by the laboratory tests up to now carried out.

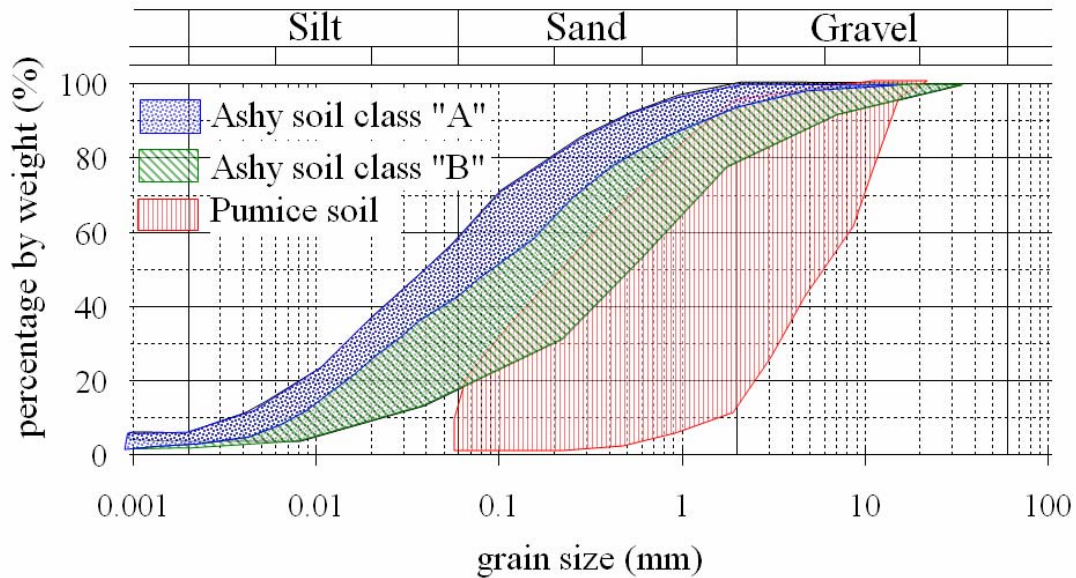


Figure 4.1 - Grain size distribution of pyroclastic soils from Pizzo d'Alvano massif in the Campania region (southern Italy) (modified from Sorbino and Foresta, 2002; Bilotta et al. 2005)

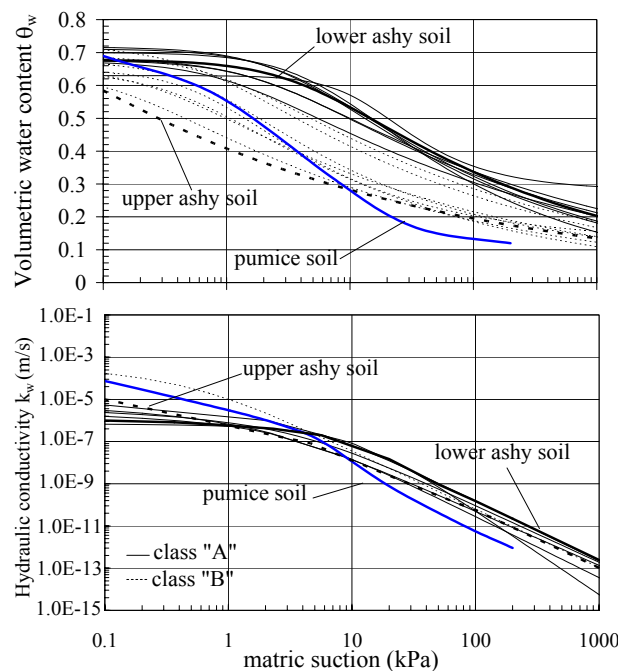


Figure 4.2 - Soil water characteristic curves (modified from Sorbino and Foresta, 2002; Bilotta et al. 2005)

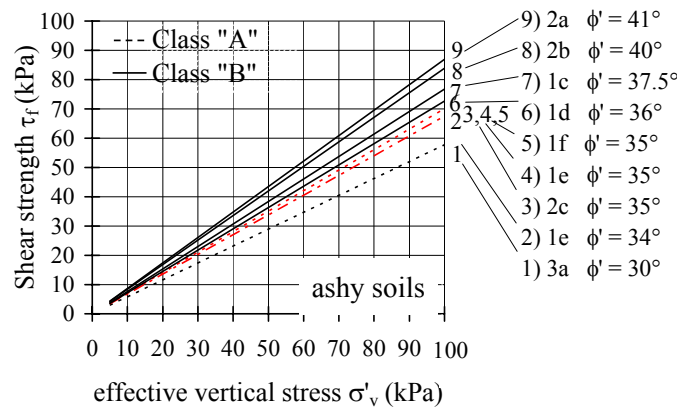


Figure 4.3 - Shear strength of the main ashy soil classes (modified from Bilotta et al. 2005).

The unsaturated shear strength was investigated on undisturbed ashy specimens by means of direct shear tests, as well as triaxial tests respectively at different water contents and at variable applied suctions, in order to reproduce the different in-situ conditions during the year. The obtained results clearly show a non-linear envelope of the shear strength in respect to suction. The increase of the shear strength with suction was found for the class A soils strongly dependent from the suction values range detected in-situ, while the class B ashy soils do not show any significant dependence for suction values exceeding 30kPa (Fig. 4.4). Finally, for both soil classes, the angle of shearing resistance in respect to suction was found to be ranging between 20° and 30° for the vertical net stresses acting in situ (Bilotta et al., 2005).

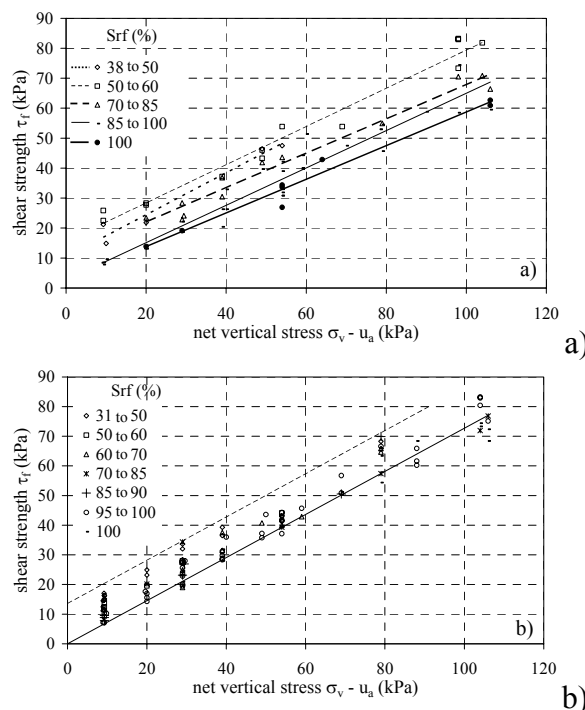


Figure 4.4 - Peak shear strength versus net vertical stress for some values range of the saturation degree (S_{rf}) for: a) soils of class "A"; b) soils of class "B" (from Bilotta et al. 2005)

A summary of the hydraulic and shear strength properties available, at the present, for the pyroclastic soil layers is furnished in Table 4.1 that also takes account of the available experimental data furnished by the scientific literature for analogous soils.

Table 4.1 - Physical and mechanical properties assumed for the pyroclastic soils. γ_d : dry unit weight, γ_{sat} : saturated unit weight, n : porosity, k_{sat} : saturated hydraulic conductivity, c' : effective cohesion, ϕ' : friction angle, ϕ^b : rate of increase in shear strength due to suction (from Cascini et al., 2010)

	γ_d (kN/m ³)	γ_{sat} (kN/m ³)	n (-)	k_{sat} (m/s)	c' (kPa)	ϕ' (°)	ϕ^b (°)	v (-)	E (kPa)	ψ (°)
Ashy soils (class A)	9.10	15.7	0.66	10 ⁻⁶	5 ÷ 15	32 ÷ 35	20	-	-	-
Pumice soils	6.20	13.1	0.69	10 ⁻⁴	0	37	20	-	-	-
Ashy soils (class B)	7.30	13.1	0.58	10 ⁻⁵	0 ÷ 5	36 ÷ 41	20	0.29	3000 ÷ 7000	0 ÷ 20

A wide experimental program aimed to investigate the mechanical and hydraulic properties of pyroclastic soils sampled in the area of Mt. Partenio and Mt. Avella, (North-Eastern of Naples) has been also conducted in the last years. Detailed information about experimental setup and technique can be found in Olivares and Picarelli (2003), Picarelli et al. (2006). Four main types of soils have been recognized: ashy soils (both top soil and layer B), weathered ashy soils (layer D) and coarse (layer A) and fine pumices (layer C). Figure 4.5 reports the grain size distributions of these soils, showing that the grain size distribution is quite uniform within each layer. In particular, volcanic ashes (B) display a high sandy component, but also a significant amount of non-plastic silt; the altered ash in layer D is finer than the ash in layer B and pumices fall in the domain of sandy gravel (A) and gravelly sand (C). Table 4.2 reports the mean values of physical properties of the different materials (Olivares and Picarelli, 2003). Porosity is very high and the soils are unsaturated with S_r depending on environmental conditions.

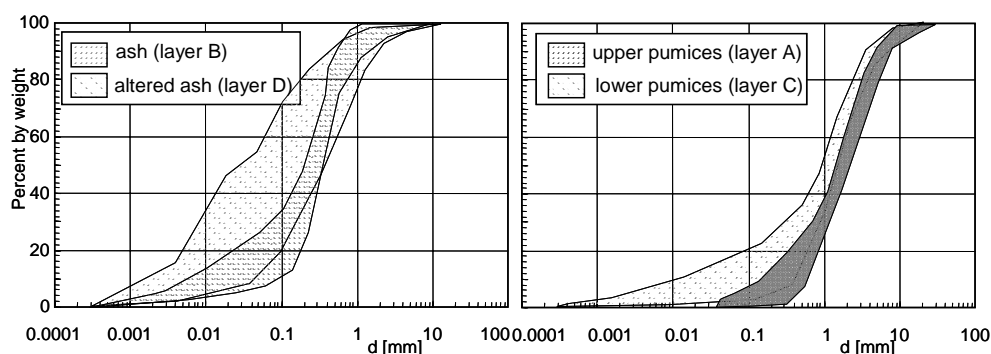


Figure 4.5 - Grain size distribution of pyroclastic soils from Mt. Partenio in Campania (from Olivares and Picarelli, 2003).

Table 4.2 - Physical properties of Cervinara pyroclastic soils. d_{max} : maximum diameter of soil particle, U : coefficient of uniformity, γ_s : specific unit weight, γ : unit weight, w : water content, n : porosity, S_r : saturation degree (from Damiano and Olivares, 2010).

Layer	Material	d_{max} (mm)	U	γ_s (kN/m ³)	γ (kN/m ³)	w^* (%)	n (%)	S_r^* (%)
A	coarse pumices	20	5	25	13	25	52	36
B	volcanic ashes	10	5	26	14	67	69	84
C	pumices	20	42	26	14	40	50	40
D	weathered ashes	10	25	26	16	54	54	75

* w and S_r obtained from samples taken at the end of the wet season

Mechanical and hydraulic characterization was carried out on undisturbed and reconstituted specimens recovered from pits. As the layers are cohesionless, undisturbed sampling was successfully carried out only in the ash (layer B) and altered ash (layer D) due to the unsaturated conditions of these materials. Data on shear strength of pumices are not available. The shear strength of saturated volcanic ashes was measured through CID and CIU triaxial tests on saturated natural samples (Olivares and Picarelli, 2001). The ash (B) is characterized by a friction angle ϕ' of 38° and a nil value of cohesion c' , while weathered ash (D) has a peak and critical state-strength characterized by ϕ' and c' equal to 31° and 11kPa and 35° and 0 respectively. As regard soil behaviour under undrained shearing, the results of CIU tests, reported in Figure 4.6, show a clear susceptibility to liquefaction. In all cases in a range of stresses comparable to the in situ one, the undrained response is always characterized by clear instability (static liquefaction).

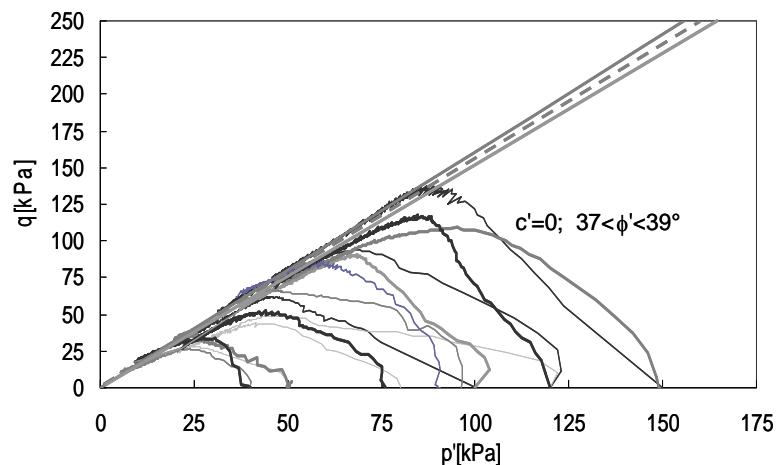


Figure 4.6 - Undrained triaxial tests on volcanic ashes taken from sites involved in flowslides (from Olivares and Picarelli, 2001)

Since suction largely governs strength and hydraulic properties of these materials, a significant part of the test programme was carried out using apparatus especially suited to

unsaturated soils. Materials were tested within the range of suction 0-80kPa that mostly occurs in situ.

The shear strength in unsaturated conditions was measured only for soil B by means of suction-controlled triaxial tests (SCTX) using a mean net stress ($p-u_a$) between 20 and 200 kPa and a suction (u_a-u_w) between 10 and 80 kPa (Olivares and Picarelli, 2003). The strength values of the unsaturated material measured at different suction values are reported (Fig. 4.7a) against the saturated shear strength envelope ($c'=0$; $\phi'=38^\circ$). All data show the significant role of suction, even at small values (Fig. 4.7b): in particular, for a suction of 4-8 kPa the correspondent intercept of cohesion is 2-6 kPa (Olivares 2001). These values are sufficient to justify the stability of shallow soil deposits on steep slopes during dry periods.

The coefficient of permeability measured through constant head tests for different effective stresses (40-70kPa) on natural saturated samples taken from layers B and D ranges between $1.0 \cdot 10^{-7}$ and $5.5 \cdot 10^{-7}$ m/s for layer B and between $8.5 \cdot 10^{-8}$ and $6.0 \cdot 10^{-7}$ m/s for layer D. The saturated permeability of reconstituted samples of pumice by constant head permeability tests ranges between $1.0 \cdot 10^{-6}$ and $6.0 \cdot 10^{-6}$ m/s (layer A) and $5.0 \cdot 10^{-6}$ and $9.0 \cdot 10^{-7}$ m/s (layer C). The unsaturated coefficient of permeability of ashes B obtained from the interpretation of the transient phase of suction equalization (Kunze et al. 1965) during SCTX tests is reported in Figure 4.8a. In the same figure the permeability values are reported against suction estimated using the expression proposed by Brooks and Corey (1964) and the permeability function obtained by Gardner's equation (1958). In both cases in the range of suction between 0 and 80 kPa, permeability decreases by about two orders of magnitude as suction increases.

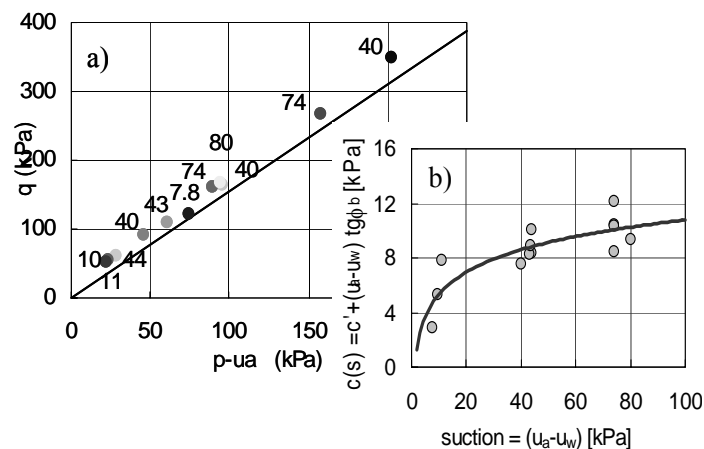


Figure 4.7 - Unsaturated shear strength of Mt. Partenio ashes: a) stress plane (numbers indicate the suction imposed); b) cohesive intercept as a function of suction

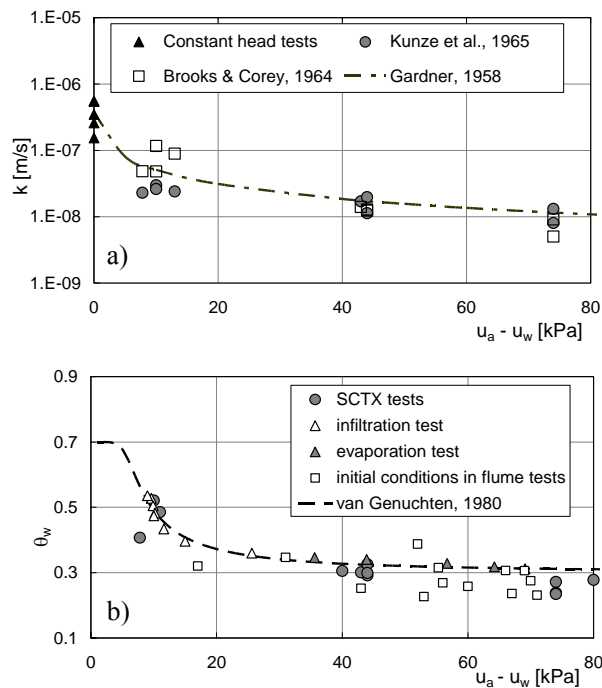


Figure 4.8 - Cervinara ashes (layer B): a) unsaturated permeability; b) retention curve (from Picarelli et al., 2006)

Figure 4.8b reports the corresponding data in terms of volumetric water content θ_w versus $(u_a - u_w)$ from SCTX tests at the end of suction equalization together with the experimental data obtained by means of conventional long-term evaporation (grey triangles) and infiltration tests (white triangles) on natural and reconstituted samples and by initial conditions of small-scale slopes reconstituted in a flume. The experimental data were fitted by the expression proposed by van Genuchten (1980) ($\theta_r=0.3$; $\theta_s=0.7$; $m=0.2$; $n=7$; $\alpha=1.7$). The obtained soil water retention curve (SWRC) is typical of coarse soils with a low air-entry value, a low value of residual water content and a steep slope within the transition zone.

4.1.1.1.2 Clays

4.1.1.1.2.1 Fissured clays

Natural stiff clays are often crossed by fissures which are the results of the stress relief and tectonic activity. Their presence can strongly influence the soil behaviour at the mesoscale ($10^{-2} \div 10^{-1}$ m), so making some problems about the choice of the correct hydro-mechanical parameters measured in laboratory tests to use in modelling.

According to Walker et al. (1987), fissured materials are influenced by the following factors: continuity, orientation, spacing, shape and superficial features of fissures (Fig. 4.9). Referring to strength, while superficial features govern the shear strength along fissures, the other factors (i.e. continuity, orientation, shape and spacing) control the global failure mechanism. Depending on such features, the shear strength measured through triaxial tests could be either close to the peak strength of the intact clayey matrix or close to the residual value: the first case could be obtained on specimens with highly spaced vertical or horizontal fissures, while the second one could be obtained on specimens having closely spaced planar, continuous and slickensided fissures with an angle about $45^\circ + \phi'/2$ to the major stress plane. Typically, the higher the influence of fissures, the smaller the influence of the overconsolidation ratio. Again, if the discontinuities are opened they can strongly govern the permeability too.

No.	Continuity	Orientation	Shape	Spacing	Surface
1	Continuous 	Actual measured angle(s) to horizontal	Planar 	<5 mm 	Striated or slick sided 
2	Not continuous; many intersections 		Undulose 	5–10 mm 	Polished 
3	Some intersections 		Conchoidal 	10–40 mm 	Smooth 
4	Very few intersections 		Irregular 	>40 mm 	Rough 

Figure 4.9 – Features of fissures in fine-grained soils (Walker et al., 1987)

As a consequence, a correct laboratory investigation program should be carried out on specimens having a size large enough to include a representative number of fissures. In particular, the lower the ratio between specimen diameter and spacing of fissures, the higher

are measured stiffness and strength, but also the scatter of data. Chandler (1984), for example, shows that both the scatter of data and the mean shear strength of the Barton clay decrease with the specimen diameter (Fig. 4.10), because of the increasing influence of fissures and of the increasing probability that at least one of these will be unfavourably oriented. Morgenstern (1977) compares the undrained cohesion measured by laboratory tests to that determined from in-situ tests: such results show that the corresponding ratio decreases with the specimen diameter (Fig. 4.11).

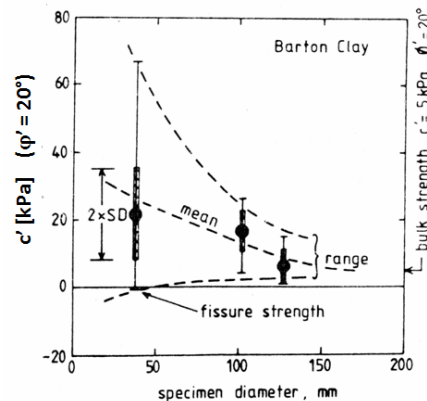


Figure 4.10 – Barton Clay: influence of the specimen diameter on the measured effective cohesion c' (Chandler, 1984)

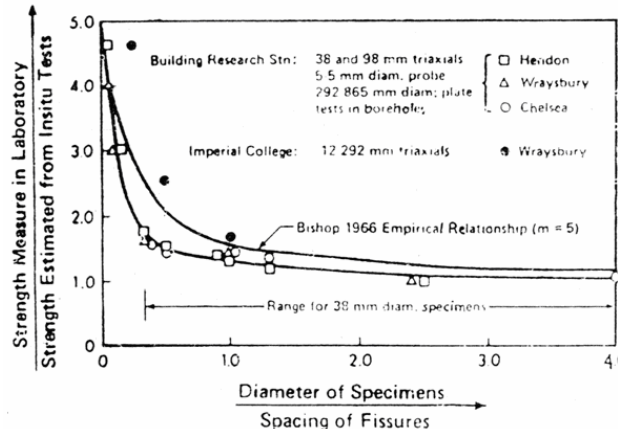


Figure 4.11 – Representativity of results coming from laboratory tests performed on specimens of fissured clays: ratio between undrained cohesion measured in laboratory and estimated from in-situ tests versus ratio between diameter of specimens and spacing of fissures (Morgenstern, 1977)

4.1.1.1.2.2 Structurally complex formations

Esu (1977) adopts the expression *structurally complex formations* for geomaterials which present special features, named *structures*, making them non homogeneous and anisotropic. Such peculiarities, which can be observed at the meso-scale ($10^{-2} \div 10^{-1}$ m), macro-scale ($1 \div 10$ m) and mega-scale ($10 \div 10^3$ m), consist of *discontinuities* and *heterogeneities*. These features are discussed by Picarelli (1986).

Discontinuities are more usual in strongly overconsolidated stiff clays than in soft clays. Main discontinuities are:

- faults and folds, which concern the mega-structure;
- bedding planes and joints, which concern the meso and the macro-structure;
- fissures, which concern the meso-structure.

Heterogeneities are due to the presence of:

- lithological or grain-size variations, which mainly affect the macro-structure;
- lapideous fragments, nodules or lithorelicts of the parent formation mixed with a softer soil (generally clay), pockets or laminae of soils of different grain size, which affect the meso-structure.

According to the classification proposed by Esu (1977), three main categories of structurally complex formations can be recognised (Fig. 4.12):

- A → homogeneous soils, consisting of stiff discontinuous clay, which in turn, can be subdivided into the following sub-categories
 - A1 → stiff layered clays and clay shales with macro-discontinuities
 - A2 → sheared clays shales
- B → heterogeneous soils, constituted by a lapideous and an argillaceous component, in turn subdivided into the following sub-categories
 - B1 → ordered sequences of both a lapideous and an argillaceous component
 - B2 → disarranged layers of both a lapideous and an argillaceous component
 - B3 → very similar to B2, but characterized by a chaotic structure
- C → more or less weathered lapideous blocks or fragments within a clay matrix.

Such a classification is essentially based on Italian experience, but in principle could be adopted also in different geological contexts.

Structures have a strong influence on slope behaviour at different scales. As a consequence, there is a problem in the choice of the best geotechnical model to adopt in the different cases, and mostly for stability analyses. Just to simplify the problem, referring to behaviours and models that are more usual to the reader, the following categories could be considered (D'Elia et al., 1998):

- jointed clays;
- sheared stiff clays and clay shales.

The first category of materials, which includes the types A1 and B1, can be investigated and modelled using the approaches of the Rock Mechanics, i.e. assuming a rigid-discontinuum model whose behaviour is governed by the arrangement and properties of persistent discontinuities.

The second category of materials includes the type A2 and the types B2 and B3, provided the overall structure of these last is disarranged enough, whose argillaceous component governs the soil behaviour.

The category C could be investigated and modelled using the continuum model, but the overall behaviour should be characterised looking at the soil behaviour at great scale.

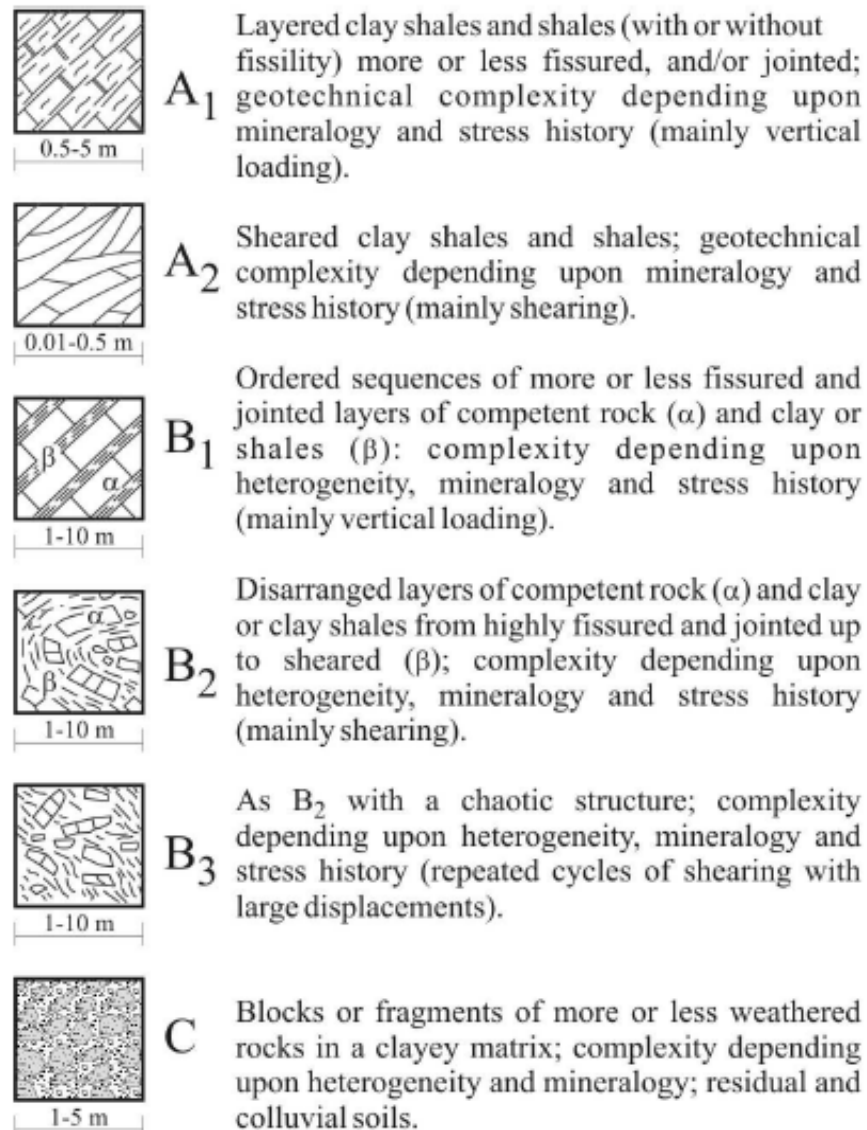


Figure 4.12 - Classification of structurally complex formations (Esu, 1977)

Jointed clays

“Jointed clays” are not so widespread. However, examples can be found along the Adriatic coast and in Tuscany (Fig. 4.13). Just as in rock masses, the strength of the clay is higher than that of the discontinuities. However, the difference is not so high as in rock, thus rupture could involve also the intact clay.

The results of some direct shear tests performed on the Valdarno clay, in Tuscany, are reported in Figure 4.14, which includes data about the clay matrix and main discontinuities (Calabresi e Manfredini, 1973). The most significant points arising from such tests are the following:

- the strength envelopes (of intact clay, joints and faults) are linear;
- intact matrix and joints present the same friction angle, but different cohesion;

- the residual strength of intact matrix and joints coincide;
- the shear strength along fault surfaces is equal to the residual one;
- residual strength along fault surfaces is lower than that of joints.



Figure 4.13 – Jointed clay in the Valdarno Basin, Central Italy (Calabresi and Manfredini, 1973)

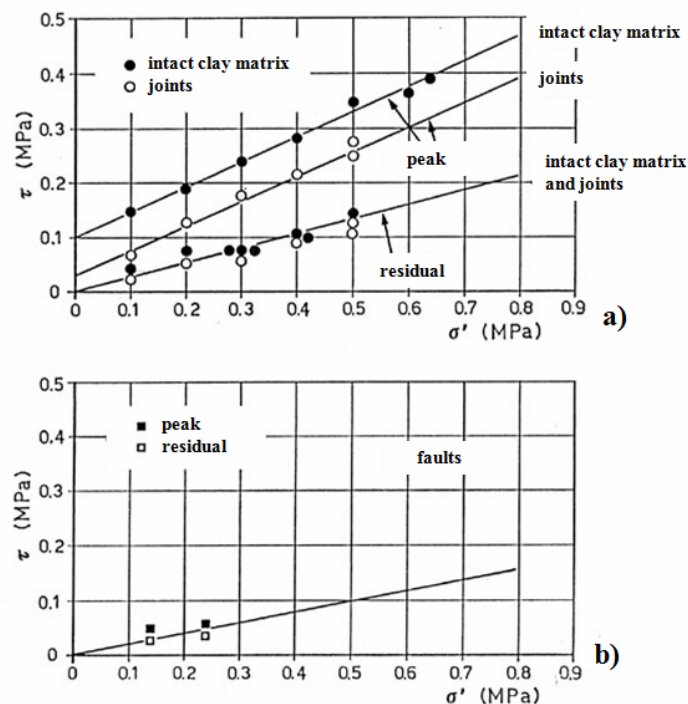


Figure 4.14 – Valdarno Basin, Central Italy: peak and residual strength measured on intact clay and along joints (a) and faults (b) (Calabresi and Manfredini, 1973)

Sheared clay shales

Sheared clay shales are the result of complex stress fields due to orogenesis and subsequent geological processes. In particular, main stress histories are related to vertical loading/unloading phases and shearing induced by the tectonic deformations, as along the Italian Apennine chain, where such formations are quite widespread. Sedimentation of soils forming the Apennines chain occurred in a marine environment about 25 - 50 millions years ago. Orogenesis and formation of the chain have been caused by tectonism which gave rise to complex sheared materials.

At the meso-scale, the soil shows small polished fissures bounding millimetric shear lenses.

It's worth noting that similar materials are also present in other parts of Europe. An example is reported in Figure 4.15. It shows the peculiar fabric of these materials which consist of small fragments of hard clay (scales, i.e. shear lenses) separated by shiny and often slickensided fissures (minor shears).

Olivares and Picarelli (1999) attempted to explain the role played by the fabric on the mechanical behaviour of sheared clay shales. Thanks to visual observations and local measurements of soil deformation in triaxial tests, the Authors argue that the mechanisms of deformation and rupture is governed by the network of shear fissures (Fig. 4.16). Referring to well known theories on the shear strength of rock joints, the strength of sheared clay shales should depend on:

- a sort of *basic friction angle*, ϕ_{μ} , along fissures depending on their superficial features;
- the "*roughness*", i_{eff} , of the sliding surface, which depends on continuity, orientation, spacing and shape of the network of fissures along which rupture takes place: it can be responsible for a sort of dilation during shear.

The shear strength of natural specimens is very close to the *basic strength* if:

- failure develops along a pre-existent planar principal (or displacement) shear (Skempton and Petley, 1967);
- fissures are planar and oriented in the same direction as the shear stress, so that the operative soil roughness and dilation are small;
- the confining stress is high, so that roughness doesn't play a key role.

The density of fissures doesn't allow to apply the "discontinuous model" in soil modelling, but requires the adoption of the classic "continuum model". Since fabric affects the hydraulic and mechanical parameters, the representativeness of specimens is a crucial problem. Another special problem regards sometimes the anisotropy which may be associated with the orientation of fissures in the field (Bilotta et al., 1985).



Figure 4.15 – A typical example of fissured clay: the Bisaccia clay shale (Picarelli et al., 2002)

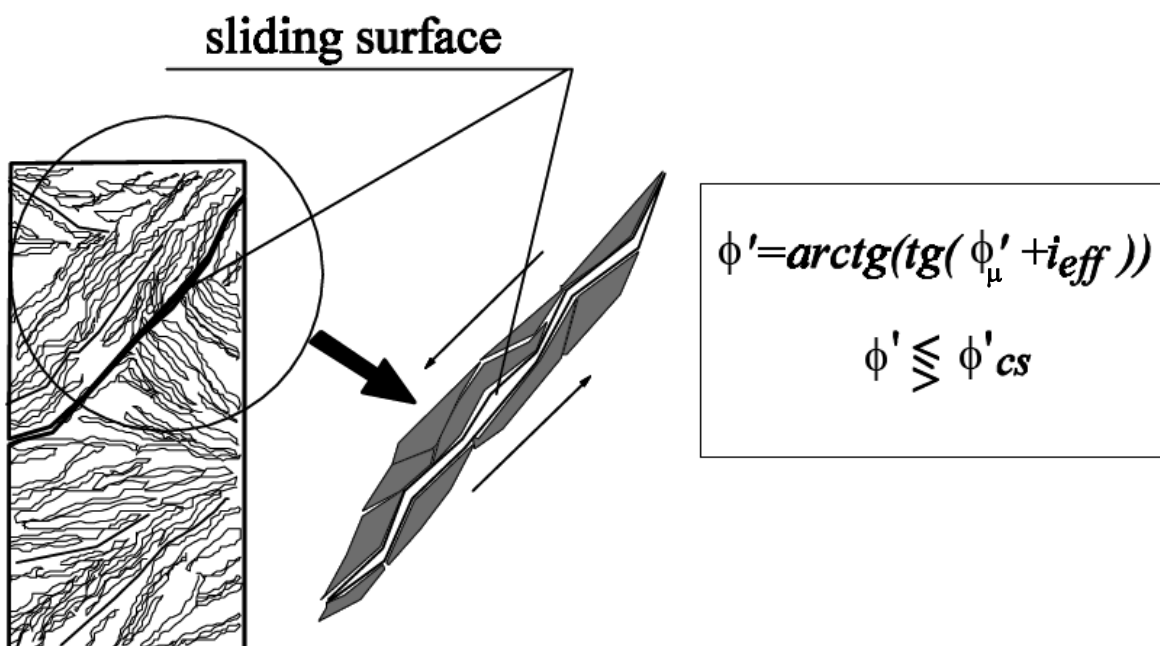


Figure 4.16 – Mechanism of shear deformation and rupture of tectonized clay shales (Olivares and Picarelli, 1999)

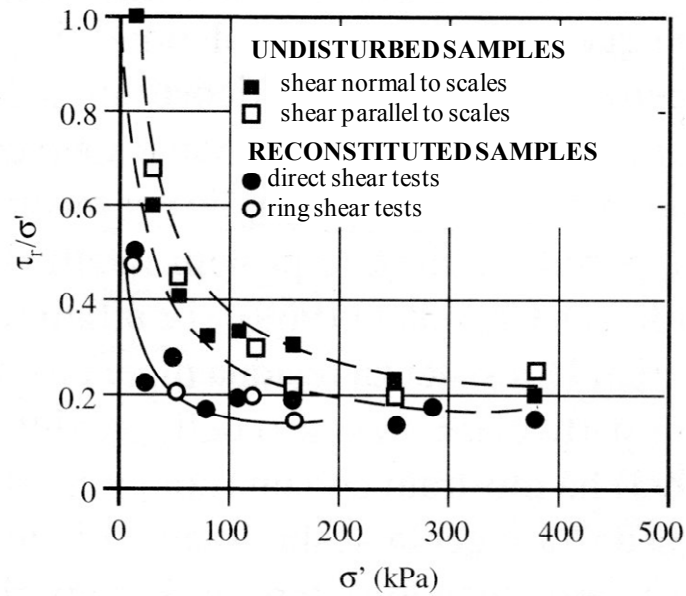


Figure 4.17 – Residual strength measured on undisturbed samples of the Laviano clay shale compared with that measured on reconstituted samples (modified after Picarelli, 1991)

4.1.1.2 Material Models

4.1.1.2.1 Constitutive models in Geomechanics

(FUNAB)

Geomaterials are mixtures of solids with voids which are filled by fluids such as air and water. Due to the strong coupling between phases, pore pressures can be generated if loading is applied fast enough. In the case of loose metastable materials, unstable behavior and catastrophic failure can happen. An important case is that of fast catastrophic landslides with large velocities caused by high pore pressures in their lower part. The purpose of this paper is to present constitutive models which describe the most relevant phenomena.

4.1.1.2.1.1 Introduction

In general, failure of geotechnical structures can be caused by (i) a decrease of strength (degradation, weathering), (ii) an increase of total stresses (external loads, earthquakes, change of geometry of the geotechnical structures), (iii) changes in pore pressures, induced by rain, external load, etc. or a combination of them.

Geotechnical engineers are concerned with the analysis of geotechnical structures under design loads and the prediction of the conditions under which failure will take place, in order to assess (i) how far are design conditions from failure (safety factor), and (ii) the failure mechanism. Knowledge of the latter allows the reinforcement of weak zones. Because of this focus, post failure phenomena are seldom studied. However, there are cases where the analysis of post failure phenomena is of paramount importance, such as fast catastrophic landslides traveling long distances at high speeds which present a high destruction power.

The study of failure conditions has attracted the attention of researchers since the early works of Coulomb (1773). Historically, three main lines of dealing with the problem and obtaining solutions were followed: (i) The slip line method, (ii) Limit theorems for plastic collapse, and (iii) limit equilibrium methods. All of them provide information on failure loads and mechanisms, but not on post failure phenomena, and because of both the type of material behavior assumed and the kinematics of failure, cannot be applied in all cases, as explained below.

Both the limit theorems of plastic collapse and the limit equilibrium methods are based on two assumptions (i) failure conditions takes place at the strength envelope, and (ii) there exists a surface where failure takes place. This corresponds to a type of failure which is referred to as “localized”. These conditions are not always satisfied, as in the case loose, collapsible materials, where instability and failure are observed at effective stresses below Mohr Coulomb strength envelope, and where failure is observed to occur in a much larger volume of soil. This type of failure has been described as “diffuse”.

Localized failure is found in overconsolidated materials presenting softening, while the diffuse mode is typical of soils having a low relative density and tending to compact when sheared. Failure takes place not in a narrow limited zone, but in a much larger mass of soil. Pore pressures developed may cause liquefaction of the soil or conditions close to it. This mechanism is believed to play an important role in landslides of the flow type.

Localized failure is characterized by a concentration of strain in very narrow and limited zones, where the phenomenon is idealized assuming there exist a discontinuity in the strain or its rate (weak discontinuity). In the case of soils, the most frequent case is that of

discontinuities in the shear strain, which are referred to as shear bands. They can evolve into discontinuities in the displacement and velocity fields (strong discontinuity). Failure mechanism is interpreted as a relative sliding of two regions where deformations are small.

Diffuse failure is related to instabilities of material behavior in loose soils. The study of these instabilities is still a young area of research. It is worth mentioning the work of Darve (1995) and Nova (1994) on constitutive instabilities and di Prisco et al. (1995) on the stability of shallow submerged slopes where liquefaction induced by sea waves can be triggered, and Darve and Laouafa (2000, 2001) and Fernández Merodo et al (2004) on diffuse mechanisms of failure in catastrophic landslides. An updated account of work done in this area can be found in Nicot and Wan (2008).

In the case of landslides, there exist several alternative classifications (Dikau et al 1996). The main types of landslides, according to them are the following: (a) Fall, (b) Topple, (c) Slides, (d) Lateral spreading, (e) Flows, and (f) complex movements. Of course, this is a simplification of the complex pattern which is often observed in reality. For instance, we could mention the case of rockfalls where the falling blocks can break into smaller ones due to fragmentation. What is interesting is that slides have a failure mechanism of localized type while flows are related to diffuse modes of failure. In the case of slides, a mass of soil moves along a surface below which material deforms much less. Depending on the shape of the sliding surface, slides are said to be translational or rotational. Localized failure is typical of overconsolidated materials presenting material softening.

Concerning modeling, it is important to note that even if simplified methods are still in use to provide a first estimation of the failure conditions, the most widespread approach is based today on mathematical, constitutive, and numerical modeling. In the case of diffuse failure, the key ingredient is constitutive modeling.

Once failure has been triggered, material can flow in a fluid like manner. Flowslides are a particular case of fast propagating mass movements, characterized by an important coupling between the solid skeleton and the pore fluids resulting on high pore pressures on the basal surface. These pore pressures generated during the initiation phase dissipate during propagation, being the consolidation and the propagation times of the same order of magnitude. It is possible therefore to have flowslides in a dry collapsible material, as it will be shown later. This is an important difference with other phenomena. In the case of dry granular avalanches, the permeability can be large enough as to dissipate the generated pore pressures in the body of the avalanche. Falling blocks disaggregate and evolve into granular fluids. The process of grain breakage provides energy to the system, increasing its mobility which results on apparent friction angles smaller than the basal friction angle. In the case of mudflows, very fluid mixtures of fine grained soils such as clays and water, the material is often studied as a monophasic cohesive-frictional fluid. Debris flows are mixtures of water and soil, originated by rain and eroded soil –or shallow landslides-. In some cases, large blocks entrained in the flow can hit structures causing their collapse. Lahars are special cases of debris flows in loose volcanic soils.

Modelling of these phenomena present important difficulties, and in the most general case, the analysis has to be based on a thermodynamically consistent formulation of mixture theory (Schneider and Hutter 2009). This is the first difficulty encountered in the analysis, and in practical cases depth integrated models (Savage and Hutter, 1991) are used as they provide a good combination of accuracy and computational cost. It is interesting to notice that while coupling of solids and pore fluids has been known in Geomechanics since the early work of

Biot (1955) and considerable progress has been done later (Zienkiewicz and Shiomi 1984, Zienkiewicz et al 1980, 1999, Coussy 1995, de Boer 2000) it has not been applied to fast landslides until recently (Hutchinson 1986, Iverson and LaHusen 1989, Iverson 1993, Iverson and Denlinger 2001, Pastor et al 2002, 2008).

The second difficulty concerns rheological modeling, which are still based on simple shear or rheometrical flows experiments carried out in laboratories. Due to the limitation imposed by their size, it has not been possible so far to perform tests with real materials found in landslides.

Concerning numerical modeling, fully coupled models are still not available. The numerical models used consider the mixture as a single phase. They can be either eulerian, and then the free surface has to be tracked using special techniques such as Volume of Fluid (VOF) or Level Set (Quecedo et al. 2004) with a high computational cost, or lagrangian, where the meshless methods such as the SPH are a very interesting alternative.

Finally, one important limitation is the lack of a constitutive model able to describe the behaviour of the material in the whole range, from solid to fluid. In traditional soil mechanics, most of today's used constitutive models are elastoplastic. There abound models able to reproduce most salient aspects of cohesive and frictional soils, including liquefaction. The transition from a soil at Critical State conditions to a fluidized mixture is an area where much research is still needed.

This paper aims to present some recent developments done by the authors which can contribute to better understand and model the behaviour of loose metastable soils and the transition from solid to fluidized soils.

First of all, we will present a generalized plasticity model incorporating a state parameter (Manzanal 2008) which is able to reproduce with a single set of parameters the behaviour of both loose and dense sands under a wide range of confining pressures. Then, we will describe an extension to loose bonded soils which can collapse with an important decrease of volume generating important pore pressures if loading is fast. Finally, we will present an extension to unsaturated soils which can explain the instabilities of loose soils under undrained loading when their degree of saturation increases.

4.1.1.2.1.2 Generalized plasticity theory: fundamentals and the basic model for sands

We will present here for completeness the Generalized Plasticity Theory introduced by Zienkiewicz and Mroz (1983) and elaborated by Zienkiewicz and Pastor (1985a, 1985b, 2000), as it provides a framework within which accurate models can be developed to describe softening and liquefaction under monotonic and cyclic loading. The basic model has been recently extended to:

- (1) Bonded geomaterials and collapsible soils by Fernández Merodo et al (2004)
- (2) Granular soils incorporating a state parameter
- (3) Non saturated soils by Tamagnini and Pastor (2004) and Manzanal (2008)

Generalized Plasticity Theory introduces the dependence of the constitutive tensor relating increments of stress and strain on the direction of the increment of stress via a unit tensor n which discriminates the states of "loading" and "unloading"

$$\begin{aligned} d\varepsilon &= C_L : d\sigma \quad \text{for } n : d\sigma^e > 0 \\ d\varepsilon &= C_U : d\sigma \quad \text{for } n : d\sigma^e < 0 \end{aligned} \quad (1)$$

where $d\sigma^e$ is the rate of stress which would be produced if the behaviour were elastic, $d\sigma^e = D^e : d\varepsilon$, and D^e is the elastic constitutive tensor.

After imposing the condition of continuity between loading and unloading states, we arrive to

$$\begin{aligned} C_L &= C^e + \frac{1}{H_L} n_{gL} \otimes n \\ C_U &= C^e + \frac{1}{H_U} n_{gU} \otimes n \end{aligned} \quad (2)$$

In above equations, subindices L and U refer to “loading” and “unloading”. The scalars $H_{L/U}$ are referred to as loading and unloading plastic moduli, and unit tensors $n_{gL/U}$ give the direction of plastic flow during loading and unloading.

The limit case, $n : d\sigma^e = 0$ is called “neutral loading”, and with the assumption done in (2), it can be seen that response is continuous as:

$$\begin{aligned} d\varepsilon_L &= C_L : d\sigma = C^e : d\sigma \\ d\varepsilon_U &= C_U : d\sigma = C^e : d\sigma \end{aligned}$$

The strain increment can be decomposed into two parts, elastic and plastic as:

$$\begin{aligned} d\varepsilon &= d\varepsilon^e + d\varepsilon^p \\ d\varepsilon^e &= C^e : d\sigma \\ d\varepsilon^p &= \frac{1}{H_{L/U}} n_{gL/U} \otimes n \end{aligned} \quad (3)$$

The main advantage of Generalized Plasticity Theory is that all ingredients can be postulated without introducing any yield or plastic potential surface. Moreover, it can be seen that both Classical Plasticity and Bounding Surface Plasticity models are special cases of the GPT.

We will describe next a simple model proposed by Pastor, Zienkiewicz, Leung and Chan (1985,1990) which is able to reproduce the basic features of sand behaviour under cyclic loading.

The main features of sand behaviour under monotonic and cyclic loading are the following:

(i) Volumetric deformations depend mainly on the stress ratio $\eta=q/p$. There is a characteristic value $\eta=M_g$ at which the behaviour changes from contractive to dilative. Ultimate state conditions at constant volume takes place also at this line, referred to as “Characteristic State Line” by Habib and Luong, and it can be interpreted as a Critical State Line for granular soils. The basic idea behind is that the soil, before failure, crosses a state at which there is no volume change, and comes back to it at residual conditions.

ii) Very loose and loose sands exhibit compaction under shearing, which results on an increase of pore pressures when the loading process is not fully drained. In the limit, liquefaction can happen.

(iii) Dense sands exhibit dilation once the Characteristic State Line has been crossed. Dilation causes softening, and the strength decreases after a peak has been reached. Here, localization of strain in shear bands shadows the experimental results as the specimen is not homogeneous.

(iv) Under cyclic loading we observe the same compaction and dilation patterns. Plastic deformation occurs and the soil compacts progressively or the pore pressure increases. Liquefaction under cyclic loading is just the result of the increase of the pore pressure and the mechanism which is observed in monotonic loading.

(v) Medium dense sands under undrained cyclic loading develop an special type of behaviour which is referred to as 'cyclic mobility'. The difference with liquefaction consists on dilation which causes the pore pressure to decrease, hardening in turn the soil. Taking into account all experimental facts described above, it is possible to develop a model within the Generalized Plasticity Theory as follows:

First of all, the direction of plastic flow in the (p,q) plane is postulated as:

$$\begin{aligned} \mathbf{n}_g^T &= (\mathbf{n}_{gv}, \mathbf{n}_{gs}) \\ \mathbf{n}_{gv} &= d_g / (1 + d_g^2)^{1/2} \quad \mathbf{n}_{gs} = 1 / (1 + d_g^2)^{1/2} \end{aligned} \quad (4)$$

where the dilatancy d_g , which is defined as the ratio between the increments of plastic volumetric and shear strain is given by:

$$d_g = (1 + \alpha)(M_g - \eta)$$

The loading-unloading discriminating relation n is obtained in a similar way:

$$\begin{aligned} \mathbf{n}^T &= (\mathbf{n}_v, \mathbf{n}_s) \\ \mathbf{n}_v &= d_f / (1 + d_f^2)^{1/2} \quad \mathbf{n}_s = 1 / (1 + d_f^2)^{1/2} \\ d_f &= (1 + \alpha)(M_f - \eta) \end{aligned} \quad (5)$$

In above equations, α , M_g and M_f are model parameters.

The third ingredient is the plastic modulus, which as to be defined both for loading and unloading. During loading, we will assume:

$$H_L = H_0 p' H_f (H_v + H_s) H_{DM} \quad (6)$$

where H_0 is a constitutive parameter. In above equations, H_f is given by

$$H_f = \left(1 - \frac{\eta}{\eta_f}\right)^4$$

and

$$\eta_f = \left(1 + \frac{1}{\alpha}\right) M_f$$

This factor varies between 1 at $q = 0$ to 0 at the straight line tangent to the yield surface at the origin.

The terms H_v , H_s and H_{DM} refer, respectively, to volumetric and deviatoric strain hardening and the discrete memory. They are given by:

$$\begin{aligned} H_v &= \left(1 - \frac{\eta}{M_g}\right) \\ H_s &= \beta_0 \beta_1 \exp(-\beta_0 \xi_{dev}) \\ H_{DM} &= \left(\frac{\xi_{max}}{\xi}\right)^\gamma \end{aligned} \quad (7)$$

where β_0 , β_1 and γ are model parameters, and ξ_{dev} the accumulated deviatoric strain.

Let us now consider each term. The volumetric term is zero at the CSL, and therefore, failure would take place there if H_s were zero. It can be observed in triaxial tests that both in drained and undrained processes, the stress paths are able to cross this line. The role of H_s is to prevent failure at this stage, but to allow it at residual conditions. This is achieved by making H_s to depend on the accumulated deviatoric strain ξ_{dev} defined from

$d\xi_{dev} = (de^p : de^p)^{1/2}$ where de^p is the increment of the plastic deviatoric strain tensor.

Finally, the variable ζ is a measure of the stress intensity, which has been taken as

$$\zeta = p' \left\{ 1 - \left(\frac{1 + \alpha}{\alpha} \right) \frac{\eta}{M} \right\}^{1/\alpha} \quad (8)$$

This basic model for sands was able to reproduce most salient aspects of sand behaviour under both drained and undrained conditions, the main limitation being the necessity of using different model parameters for different relative densities.

4.1.1.2.1.3 Extension to collapsible soils

An improvement of the Generalized Plasticity model has been recently proposed by the authors to reproduce the mechanical behaviour of bonded soils, weak rocks and other materials of a similar kind.

Following the framework introduced by Gens & Nova (1993) and Lagioia and Nova (1995), two basic concepts lie the representation of this mechanical behaviour: the fundamental role played by yield phenomena and the need for considering the observed behaviour of the bonded material in relation with the behaviour of the equivalent unstructured one.

As the amount of bonding increases the yield surface must grow up. Two parameters define the new enlarged yield locus: p_{c0} that controls the yielding of the bonded soil in isotropic compression and p_t which is related to the cohesion and tensile strength of the material. Both p_{c0} and p_t increase with the magnitude of bonding.

We can assume that the degradation of the material (decrease in bonding) is related to some kind of damage measure, that will in turn depend on plastic strains. Lagioia and Nova

proposed simple laws to describe the debonding effect on a calcarenite material. The evolution of p_t is governed by:

$$p_t = p_{t0} \exp(-\rho_t \varepsilon^d) \quad (9)$$

where p_{t0} and ρ_t are two constitutive parameters and ε^d is the accumulated plastic volumetric strain. It appears reasonable to assume that changes of the yield locus will be controlled by two different phenomena: conventional plastic hardening (or softening) for an unbonded material and bond degradation. In that case, the plastic modulus of the sand model proposed by Pastor et al. (1990), can be improved introducing H_b such as:

$$H_L = (H_0 p^* - H_b) H_f^* (H_v^* + H_s) H_{DM}^* \quad (10)$$

where we have introduced:

$$p^* = p' + p_t$$

$$H_f^* = \left(1 - \frac{\eta^*}{\eta_f}\right)^4 \quad H_v^* = \left(1 - \frac{\eta^*}{M_g}\right)$$

$$H_b = b_1 \varepsilon^d \exp(-b_2 \varepsilon^d) \quad H_{DM}^* = \left(\frac{\zeta_{max}^*}{\zeta^*}\right)^{\gamma_{DM}}$$

$$\eta^* = q / (p' + p_t) \quad \zeta^* = (p' + p_t) \left\{1 - \left(\frac{\alpha_f}{1 + \alpha_f}\right) \frac{\eta^*}{M}\right\}^{-1/\alpha} \quad (11)$$

It can be seen that value of H_b decreases when the volumetric plastic strain increases (i.e. when debonding occurs) and in the limit case, when destructuration is complete, H_b becomes zero. In this case, the new plastic modulus defined above coincides with the original plastic modulus. The assumption of softening depending on plastic volumetric strain is consistent with classical soil hardening and softening, which depends mainly on plastic volumetric strain.

It is possible to reproduce with this improvement the laboratory tests of Lagioia and Nova on the Gravina calcarenite. Figure 4.18 (Fernández Merodo et al 2004) compares experimental data and model predictions for an isotropic compression test.

This type of behaviour - destructuration with an important compaction- is a mechanism which in our opinion plays a paramount role on the generation of pore pressures and catastrophic failure of soils. This is the case of the landslide of Las Colinas (El Salvador), triggered by the first 2001 earthquake. The soil presented cementation and was unsaturated. When sheared, this material can collapse, and if the loading is fast enough, pore pressures can cause the material to liquefy. In order to show qualitatively the phenomenon, we have performed a simulation on an ideal material, a fine grained soil with cementation. The parameters we have chosen are given in Table 4.3. Figures 4.19 and 4.20 show the results of a consolidated undrained triaxial test. We have depicted in Figure 4.19 the stress path and in Figure 4.20 the deviatoric stress vs axial strain for both the bonded and the unbonded materials.

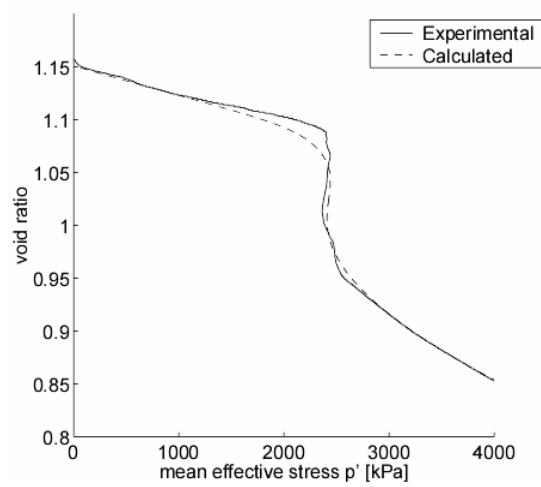


Figure 4.18 - Isotropic compression test: experimental data from Lagioa and Nova and model predictions

M_g	M_f	α	β_0	β_l	γ	p_{s0}	p_{m0}	p_{t0}	β_p	ρ_m	ρ_t	ξ
1.47	0.3	0.45	1.	0.2	9.0	120 kPa	240 kPa	24 kPa	0.06	8333	1000	-0.1

Table 4.3 - Parameters of the constitutive model for Las Colinas landslide

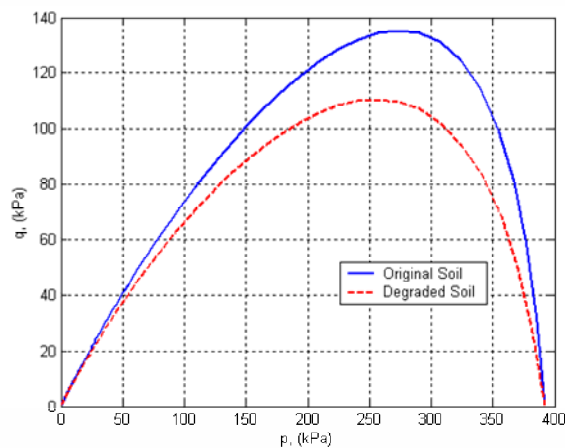


Figure 4.19 - Undrained behaviour of a bonded loose granular soil: stress path

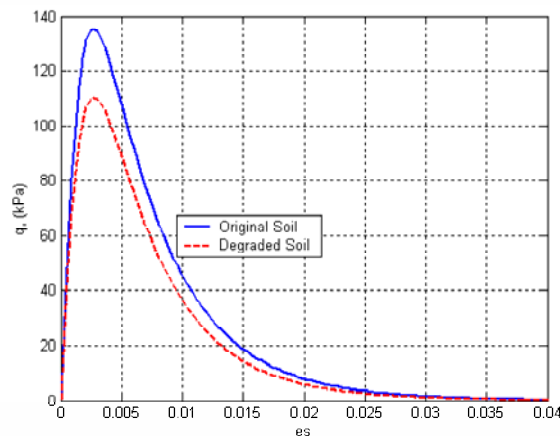


Figure 4.20 - Undrained behaviour of a bonded loose granular soil: Deviatoric stress versus axial strain.

4.1.1.2.1.4 A state parameter based generalized plasticity model

Loose or dense types of behaviour in sands depend both on density and confining pressure. This means that neither density nor confining pressure alone can fully characterize sand behaviour, but a combination of both. The idea of a joint dependency of sand behaviour on density and pressure has attracted the attention of researchers since the early works of Roscoe and Poorooshasb (1963), Wroth and Basset (1965) and Seed and Lee (1967). The latter performed two series of tests on sands of different densities at constant void ratios and constant confining pressure. By analyzing the volume change tendency at failure, they concluded that (i) for a given confining pressure, there is a critical void ratio -or a discriminant density- which separates dilative from contractive behaviour, (ii) for a given void ratio, there is a critical confining pressure separating contractive from dilative specimens, and (iii) the relationships obtained in both cases between confining pressure and void ratio coincide.

Uriel (1973, 1979) proposed a simple constitutive model able to describe with a single set of parameters the behaviour of dense and loose sands, and the effect of the confining pressure. The most widely accepted state parameter today is that proposed by Been and Jefferies (1985). It is defined as the difference of the current void ratio and the void ratio at critical state under the same confining pressure.

$$\psi = e - e_c \quad (12)$$

An alternative definition is that of Wan and Guo (1998):

$$\psi_q = e / e_c \quad (13)$$

The first ingredient of this model, is, therefore, the definition of the state parameter for which it is necessary to have an equation for the Critical State Line. We have chosen that proposed by Li (1977):

$$e = e_{atm} + \lambda \left(\frac{p'}{p'_{atm}} \right)^{\xi_c} \quad (14)$$

which depends on the two material parameters λ and ξ_c . The state parameter will enter the definitions of the three items of a Generalized Plasticity model: the directions n_g and n_f and the plastic modulus H . Concerning the dilatancy, we have used the law proposed by Li and Dafalias (2000)

$$d = \frac{d_0}{M_g} (M_g \exp(m\psi) - \eta) \quad (15)$$

where

$$d_0 = (1 + \alpha) M_g \quad (16)$$

In above equations, m is a constitutive parameter which can be obtained from experimental values of dilatancy.

The direction n_f is obtained from d_f (see eqn. 5):

$$d_f = \frac{d_{0f}}{M_f} (M_f \exp(m\psi) - \eta) \quad (17)$$

where d_{0f} is a material parameter. Manzanal (2008) has proposed the following expression for M_f

$$\frac{M_f}{M_g} = h_1 - h_2 \psi_q \quad (18)$$

which depends on the parameters h_1 and h_2 .

Finally, the plastic modulus is given by

$$H = H_0 \sqrt{p' p'_0} H_{DM} H_f (H_v + H_s) \quad (19)$$

where

$$H_0 = H'_0 \exp(-\beta'_0 \psi_q) \quad (20)$$

$$H_v = H_{v0} (\eta_p - \eta) \quad \text{with } \eta_p = M_g \exp(-\beta_v \psi)$$

where we have used the peak stress ratio η_p proposed by Li and Dafalias (2000) and introduced the new parameters H'_0 and β'_0 .

Using this state parameter based model, it is possible to reproduce the set of tests on Banded sand reported by Castro (1969) with a single set of parameters. Figure 4.21 shows the model predictions together with the experimental results.

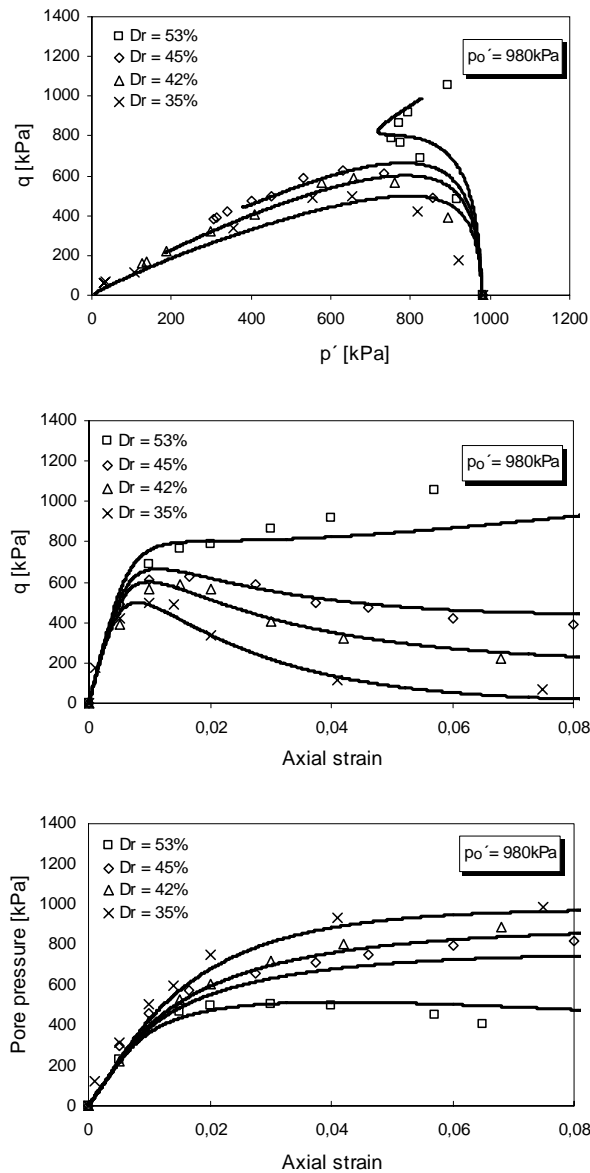


Figure 4.21 - Experimental results and model predictions for Banding sand at different relative densities (Castro, 1969)

4.1.1.2.1.5 An extension for unsaturated soils

The basic Generalized Plasticity model of Pastor, Zienkiewicz and Chan (1987) has been extended to unsaturated soils by Tamagnini and Pastor (2004), following a previous Cam Clay model of Tamagnini (2004). The model was based on the effective stress definition proposed by Lewis and Schrefler (1987)

$$\sigma' = \sigma + S_r s I - p_a I \tag{21}$$

and the definition of work in unsaturated materials provided by Houlsby (1997)

$$\delta W = (\sigma + S_r s I - p_a I) \delta \varepsilon + s \cdot (-n \delta S_r) \quad (22)$$

where S_r is the degree of saturation, s the suction, $s = p_a - p_w$, p_a and p_w the pore pressures of air and water, respectively.

Tamagnini and Pastor model was able to reproduce some salient aspects of unsaturated soils, such as the volumetric collapse when the soil is saturated, but presented some limitations which have been addressed by Manzanal (2008) and which will be described next.

The model incorporates the state parameter defined on the previous Section, which requires a suitable definition of the Critical State Line for unsaturated soils. The problem is that there is not a unique CSL because it depends on suction. Recently, Gallipoli et al. (2003) have introduced a cementation parameter defined as

$$\xi = f(s)(1 - S_r) \quad (23)$$

where the function $f(s)$ is the relationship between stabilizing pressure at a given suction s and at zero suction proposed by Haines (1925) and Fisher (1926). Instead of the expression proposed by Gallipoli et al. (2003), we will use here the alternative form between the effective pressures at a given suction and saturated at the same void ratio:

$$\frac{p'}{p'_s} = \exp(g(\xi)) \quad (24)$$

$$\text{where } g(\xi) = a \{ \exp(b\xi) - 1 \} \quad (25)$$

Figure 4.22 illustrates the normalization effect obtained. In Fig.4.22a we show the experiments performed by Sivakumar (1993) on Speswhite kaolin, which shows a set of different CSLs at different suctions. In Fig.4.22b, we have plotted the relationship between the void ratio and the effective confining pressure at saturation, obtained using (24) and (25), i.e.

$$p'_s = p' \exp(-g(\xi))$$

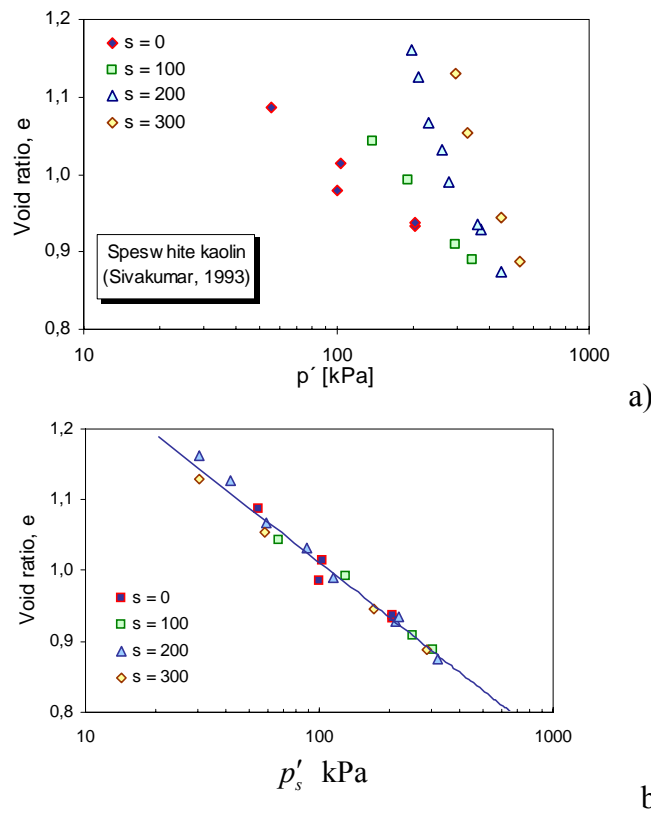


Figure 4.22 - Experiments from Sivakumar (1993): a) critical States at different suctions; b) normalization of CSL

We have found necessary to introduce a second normalization on the projection of CSL on the (p', q) plane, as the experimental data show an important dispersion. We have introduced in the definition of the effective stress a modification which takes into account the existence of a residual degree of saturation S_{r0} :

$$S_{re} = \frac{S_r - S_{r0}}{1 - S_{r0}} \quad (26)$$

This modified degree of saturation is used in the definition of effective stress, and the results can be seen in Figure 4.23, which display the CSL with and without this modification for a silty soil (Maâtouk et al., 1995)

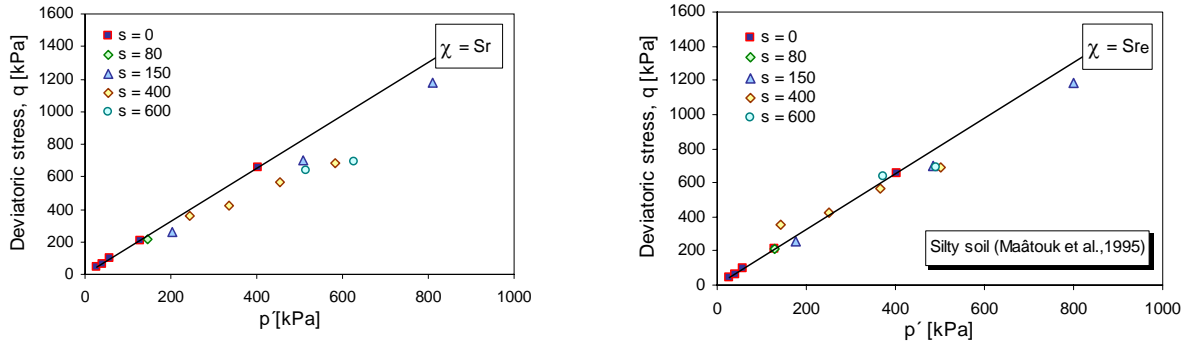


Figure 4.23 - CSL on p' - q plane: without correction (left) and using the effective degree of Saturation (right).

The increment of strain is decomposed as follows:

$$d\varepsilon_{ij} = d\varepsilon_{ij}^e + d\varepsilon_{ij}^p + d\varepsilon_{ij}^s \quad (27)$$

where the last term is given by:

$$d\varepsilon_s^p = \frac{1}{H_b} n_g ds \quad (28)$$

The plastic modulus H_b is given by

$$H_b = w(\xi) H_0 \sqrt{p' p_{atm}} H_{DM} H_v \quad (29)$$

where

$$H_{DM} = \left(\frac{\zeta_{max} J_s}{\zeta} \right)^\gamma \quad (30)$$

is a modified discrete memory function incorporating the effect of the suction,

$$J_s = \exp(c \cdot g(\xi)) \quad (31)$$

$w(\xi)$ incorporates the effect of the cementing parameter above defined.

$$w(\xi) = \begin{cases} -\left\{1 - \exp[g(\xi)]^2\right\}^2 & (wetting) \\ 1 & (drying) \end{cases} \quad (31)$$

and $H_0, H_f, H_v,$ and H_s are the same functions defined for saturated soils.

The model is completed with a suitable water retention curve, including hysteretic effects. (Manzanal, 2008).

Using this model, it is possible to reproduce a most interesting case, the effect of suction on the undrained behaviour of an unsaturated fine grained soil. We have plotted in Figure 4.24 constant volume triaxial tests run at constant suction. It can be observed that increasing saturation results on a much looser behaviour, arriving to liquefaction. If a soil at a large initial suction and different deviatoric stresses is sheared at constant volume conditions decreasing the suction, there are two options: in the case A0, the stress path will stabilize, while in the case A1 it will become unstable and fail in a catastrophic manner. It is important

to remark that this is just a qualitative example, a complete analysis based on the method proposed by Darve et al (2000, 2001) being necessary to fully understand the process.

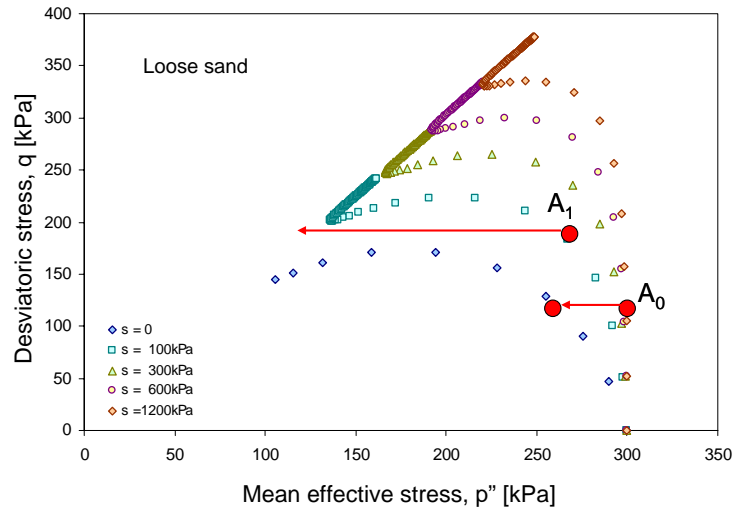


Figure 4.24 - Constant volume test for different suction

4.1.1.2.2 Modelling soil instability and landslide triggering processes

(UNISA)

The mechanical properties of natural soils involved in the onset of landslide events are the outcome of a complex interaction with the surrounding environment. The resulting behaviour of such soils is often difficult to understand using the classical soil mechanics framework, and more sophisticated approaches are necessary in order to describe the experimental evidence. The purpose of this research consists in dealing with two important factors playing a major role in the triggering of fast landslides: the potential for static liquefaction and the hydraulic degradation associated to saturation processes. These aspects are considered within the same constitutive approach, in order to set up a convenient theoretical framework for dealing with mechanical instability. Following this pattern of reasoning, unstable phenomena possibly occurring both in the saturated and unsaturated regime can be predicted. Finally, the stability of slopes under rainfall events is addressed in a simplified manner, i.e., by means of material point analyses based on the ideal scheme of infinite slope.

4.1.1.2.2.1 Introduction

An adequate modelling of soil behaviour should be an essential feature of any geomechanical approach aimed at predicting the onset of rainfall induced landslide. The importance of soil behaviour modelling becomes even more important when soil instability phenomena affect the triggering stage, as it is often the case in fast landslides of the flow type. Rainfall induced landslides, in particular, are largely affected by the hydro-mechanical phenomena taking place in unsaturated soils. Soils are indeed rarely either dry or completely saturated in nature. Despite that, until few years ago, the entire theory of the mechanical behaviour of soils was developed making reference to these limit conditions only. This was essentially due to the difficulty of taking partial saturation into account, both from an experimental and a theoretical point of view. Nevertheless, efficient constitutive models that take partial saturation into account might be of paramount importance to have a deeper insight on a variety of problems of engineering and social relevance. In the following, a strain-hardening constitutive model for unsaturated soil behaviour based on energy conjugated stress variables in the framework of superposed continua will be presented. The purpose is that of developing a model able to deal with possible mechanical instabilities by means of a consistent energy framework. Some preliminary insights concerning the topic of soil instability will be commented, trying to suggest a possible pattern of reasoning.

From a historical viewpoint, the major achievement in unsaturated soil modelling was due to Alonso, Gens and their co-workers at Barcelona (Alonso et al. 1987). These authors reckoned that the behaviour of partially saturated soils and, in particular, the volumetric changes upon soaking, could be well described, by coupling an elasto-plastic strain-hardening model such as Cam Clay (Schofield and Wroth 1968, Roscoe and Burland 1968) with the use of two independent stress variables, namely net stress and suction. This model, nowadays often referred to as Barcelona Basic Model (Alonso et al. 1990) was then extended to cope with more complex phenomena (Gens and Alonso 1992, Vaunat et al. 2000, Sanchez et al. 2005). On the same premises, other models were proposed, adding several modifications to the already developed framework (Wheeler and Sivakumar 1995, Cui and Delage 1996) or even by introducing more substantial changes to the original idea (Kogho et al. 1993, Kahlili and

Loret 2001).

Jommi and di Prisco (1994) showed, however, that unsaturated soil response, and in particular the volumetric effects upon soaking, could also be captured by using a single stress variable, provided that a good conceptual elasto-plastic strain-hardening model was used to describe soil behaviour. The stress measure responsible for the strains of the solid skeleton was in fact assumed to be defined as:

$$\sigma_{ij}^* \equiv \sigma_{ij} - [S_r \cdot u_w + (1 - S_r) \cdot u_a] \delta_{ij} \quad (1)$$

in which σ_{ij} is the total stress, u_w the pore water pressure, u_a the air pore pressure, $s = u_a - u_w$ the suction, S_r the degree of saturation and δ_{ij} the Kronecker delta.

This stress measure essentially consists in a modification of the well known Bishop's stress (Bishop 1959). A frequently used definition for it is that of *average soil skeleton stress* (Jommi 2000). The average skeleton stress has been used within an elasto-plastic constitutive framework by a number of other authors (Bolzon et al. 1996, Sheng et al. 2004). Furthermore, it has also been recently employed either with the main target of describing the effects of hydraulic hysteresis (Wheeler et al. 2003, Tamagnini 2004), or linked to other stress variables related to suction (Gallipoli et al. 2003), or to the mechanical behaviour of granular materials (Hicher and Chang 2007, Manzanal 2008).

4.1.1.2.2.2 Constitutive model

For this research the constitutive approach suggested by Jommi and di Prisco (1994) has been adopted in light of the energy framework put forward by Houlsby (1997). This modelling strategy is indeed believed to have more advantages in reproducing intense saturation processes and liquefaction instabilities arising from them. An elastoplastic strain-hardening constitutive model aimed at describing the behaviour of the solid skeleton has been then developed. The model shares the same conceptual structure of some elastoplastic laws recently proposed to deal with bonded geomaterials subject to weathering or diagenesis (Nova et al. 2003) and it is capable of modelling several kinds of instabilities induced by the loss of bonding contributions.

The skeleton stress σ_{ij}^* used for the formulation of the constitutive functions represents the intensive measure work conjugate to the strain rate. Under such a perspective, it can be considered as a sort of generalized effective stress. In the particular case of partially saturated soils, however, the energy input is not only due to the mechanical work done by the external forces. Since the soil is unsaturated the possible change in water content can alter the volume occupied by fluids without causing any strain of the soil skeleton. This water volume variation is associated to an energy exchange between water and air at the water menisci. According to Houlsby (1997) the total specific energy is then given by:

$$dW = \sigma_{ij}^* \cdot \dot{\epsilon}_{ij} - ns \cdot \dot{S}_r \quad (2)$$

where n the porosity of the soil.

Equation (2) confirms the experimental evidence that a single effective stress theory is not

able to describe the behaviour of an unsaturated soil. Three phase porous media are indeed affected by a further energy term, which can be expressed by the product of a smeared suction $s^* \equiv n \cdot s$, having the opposite of the rate of the degree of saturation $-\dot{S}_r$, as conjugate strain measure.

Starting from these premises, a coupled hydro-mechanical constitutive law for unsaturated soils has been developed. The model is conceptually similar to other models already available in the literature, but it is formulated in a way that is convenient for the analysis of the possible occurrence of instabilities, which constitutes the major goal of the research. The constitutive law is based on a coupled formulation which includes modified suction and degree of saturation as further stress and strain variables, as follows:

$$\dot{\Sigma} = \begin{Bmatrix} \dot{\sigma}_{ij}^* \\ \dot{S}^* \end{Bmatrix} = \begin{bmatrix} \mathbf{D}_{\sigma\sigma} & \mathbf{D}_{\sigma w} \\ \mathbf{D}_{w\sigma} & \mathbf{D}_{ww} \end{bmatrix} \cdot \begin{Bmatrix} \dot{\epsilon}_{ij} \\ -\dot{S}_r \end{Bmatrix} = \mathbf{D}_{\text{ext}} \cdot \dot{\mathbf{E}} \quad (3)$$

The components of the extended coupled constitutive matrix will depend on the mathematical expression adopted for the constitutive functions. At this reference, it must be noted that hydraulic hysteresis and strain dependency of the water retention curve have been neglected for the sake of simplicity and that a non associated flow rule has been used to model irreversible strains. Only some details of the mathematical features of the hardening laws will be discussed in the following, being these laws a fundamental component to describe hydro-mechanical degradation processes. A detailed description of the constitutive functions chosen to model the elastic behaviour, the yield surface and the plastic potential is available in Buscarnera and Nova (2009a).

As pointed out by Jommi (2000), in order to capture some key features of unsaturated soil response, modifications have to be introduced into the classical modelling framework for saturated soils. For this purpose, the hardening law controlling the size of the yield domain of the unbonded soil is assumed to be governed by two separate contributions, a mechanical one and a hydraulic one. The analytical expression of the hardening law used in this work is expressed as follows:

$$\dot{p}_S = \rho_S p_S (\dot{\epsilon}_V^p + \xi_S \dot{\epsilon}_S^p) - r_{sw} p_S \dot{S}_r \quad (4)$$

where ρ_S , ξ_S and r_{sw} are hardening constitutive parameters. The first term is the usual hardening relationship for granular materials, that is conveniently expressed in terms of both volumetric and deviatoric plastic strains (Nova 1977). The second hardening contribution in Equation (5) represents instead the mathematical form of a hydraulic bonding effect. In the framework herein suggested indeed the degree of saturation is seen as a global measure of the distribution of water menisci, and therefore of the capillary forces associated to surface tensions. As a consequence, the constitutive model assumes a homothetic expansion/contraction of the elastic domain as a result of drying/wetting processes. Figure 4.25 schematically shows the evolution of the yield surface in the skeleton stress space during a soaking process.

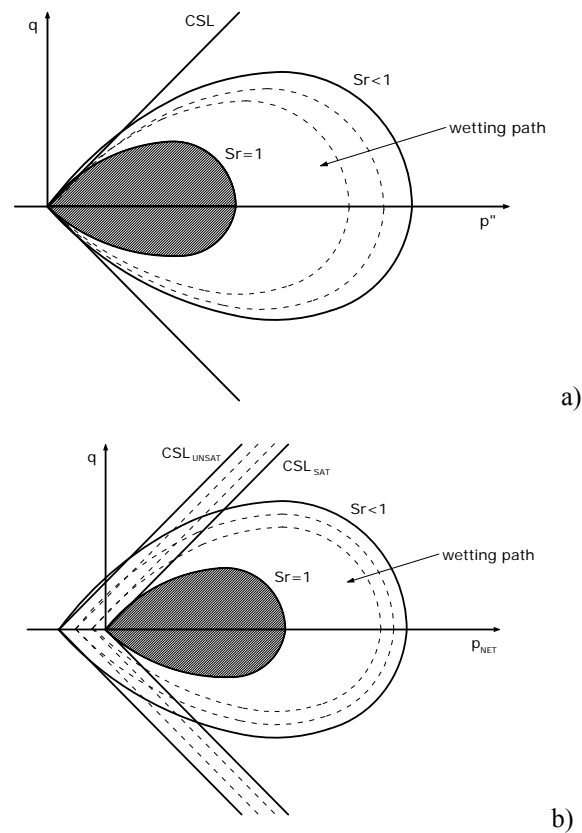


Figure 4.25 - Contraction of the yield surface due to wetting processes depicted in both the skeleton stress space and the net stress space

The structure of the model presented so far can describe the behaviour of unsaturated soils in which the only bonding contribution is provided by the apparent cohesion related to partial saturation. An extension of the model aimed at accounting also for an actual mechanical bonding between grains is straightforward, however, and it can be arranged following the approach suggested by Gens and Nova (1993), as it has been shown by Buscarnera and Nova (2009c).

The model can be proved to be capable of describing the main features of unsaturated soil behaviour (e.g., strength increase with suction and wetting collapse phenomena, as shown in Figures 4.26 - 4.27).

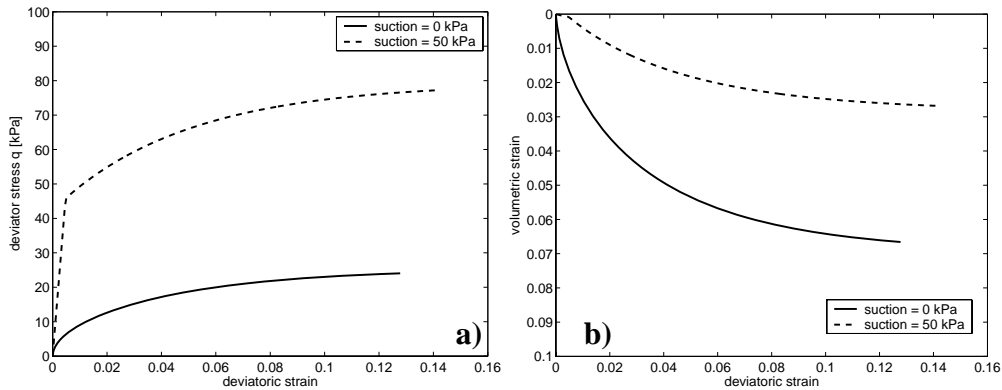


Figure 4.26 - Comparison of test results on a saturated and an unsaturated specimens in a triaxial test simulation; a) deviatoric stress vs deviatoric strain; b) volumetric strain vs deviatoric strain

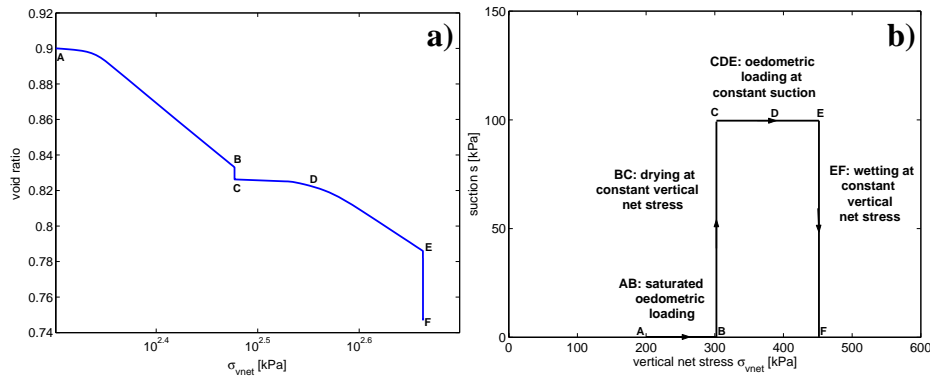


Figure 4.27 - Example of model predictions in oedometric tests: a) Void ratio versus vertical net stress in an oedometric test with final wetting stage; b) stress path imposed in the suction-vertical net stress plane

More importantly, the possibility of having instabilities upon saturation paths at constant deviatoric stresses has been pointed out in a heuristic way (Figure 4.28). The model has in fact been used as a predictive tool, in order to discuss possible unstable processes potentially occurring in situ during critical rainfall events inducing water infiltration through soil layers. The most peculiar aspect of the predicted phenomena, consists in the fact that they can occur within the unsaturated regime, i.e., when the material is not yet saturated. Another remarkable feature of the predicted collapses has been that of occurring in the form of latent instabilities, i.e., as potential unstable mechanisms whose activation depends on the fulfillment of particular boundary conditions. The model allowed also to point out the marked path dependency of hydro-mechanical instability. In other words, the definition of incipient instability conditions must be associated to the actual simulation of the perturbation event, following the specific path possibly affected by instability. In addition, test simulations like that of Figure 4.28 show that such instabilities depend on the stress level, the combination of suction and degree of saturation achieved during the saturation event and on the hydraulic control conditions (i.e., on the fact that either suction or water content could be controlled during the same event).

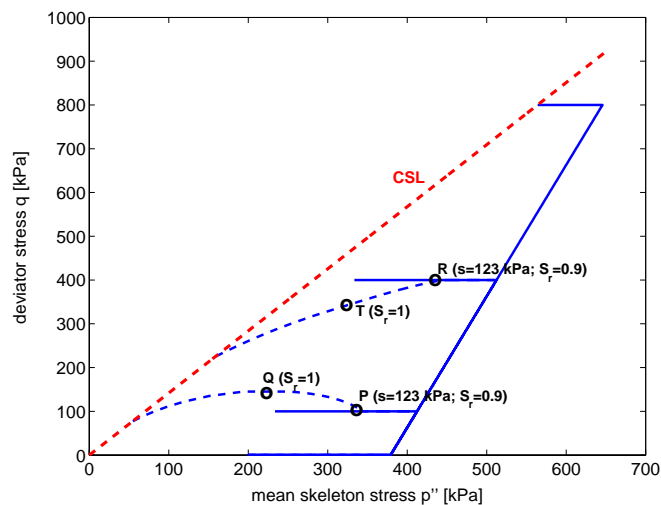


Figure 4.28 - Example of possible latent instabilities during soaking at constant deviator: according to the stress level the material exhibits either a stable or an unstable response upon water undrained loading.

4.1.1.2.2.3 A framework for soil instability

The instabilities hitherto commented can be interpreted as bifurcations of the hydro-mechanical material response. In order to have a proper theoretical tool both for the interpretation of the evidence and the prediction of future catastrophic events, it is necessary to define convenient mathematical indices able to capture the onset of a potential instability. Several approaches can be used to deal with the mechanical instability of soils (e.g., energy approaches, static approaches, bifurcation analyses etc.). In this research the theoretical framework of reference is that proposed by Nova and co-workers (Nova 1994, Imposimato and Nova 1998), often referred to as *Theory of Test Controllability*. According to this approach soil instability is tackled from the mathematical viewpoint as a bifurcation problem, focusing on the role played by test control parameters on the onset of instability.

It can be proven that several types of loss of controllability, and therefore several instability modes, are possible within the classical failure domain (Imposimato and Nova 1998). These instability modes depend on test control conditions, and can be identified by studying the vanishing of suitable mathematical operators which are associated to the particular loading programme followed during the test. The theory of test controllability can be extended to the case of unsaturated soils by making reference to the hydro-mechanical constitutive stiffness matrix of Equation (3). This idea has been firstly suggested by Vaunat et al. (2002) and subsequently used by Buscarnera and Nova (2009b). In this paper, only the most important features of this extension are presented. A more detailed description of the reference theoretical framework is indeed available in Buscarnera and Nova (2009b).

In order to define the test control conditions characterising a laboratory test on an unsaturated material, more complex loading programmes than those used for saturated soils have to be considered. Therefore, either the smeared suction or the saturation index will vary, together with appropriate combinations of stresses and strains. The definition of a loading programme implies the introduction of a control vector ϕ , grouping the hydro-mechanical variables

actually governed during a test, and a response vector ψ , which is energetically associated to the former set of control variables. A formal representation of both control variables and response variables can be expressed as follows:

$$\begin{Bmatrix} \dot{\phi} \\ \dot{\psi} \end{Bmatrix} = \begin{bmatrix} \Omega_{\phi\sigma} & \Omega_{\phi\varepsilon} \\ \Omega_{\psi\sigma} & \Omega_{\psi\varepsilon} \end{bmatrix} \begin{Bmatrix} \dot{\Sigma} \\ \dot{E} \end{Bmatrix} \quad (5)$$

The rate of the control vector $\dot{\phi}$ is always known as a function of stress and strain variables, being the loading programme fully defined. By contrast, the response vector $\dot{\psi}$ is defined only from a formal viewpoint. This vector groups the work conjugate variables associated to $\dot{\phi}$, and it has to be properly defined on the basis of energy considerations.

The two sets of variables can be linked by means of a control matrix \mathbf{X} as follows:

$$\dot{\phi} = \mathbf{X} \dot{\psi} \quad (6)$$

The mathematical expression of \mathbf{X} is derived from (3) and (5):

$$\begin{aligned} \mathbf{X} &= \left(\Omega_{\phi\sigma} D_{ext} + \Omega_{\phi\varepsilon} \right) \left(\Omega_{\psi\sigma} D_{ext} + \Omega_{\psi\varepsilon} \right)^{-1} \\ &= \left(\Omega_{\phi\sigma} + \Omega_{\phi\varepsilon} C_{ext} \right) \left(\Omega_{\psi\sigma} + \Omega_{\psi\varepsilon} C_{ext} \right)^{-1} \end{aligned} \quad (7)$$

in which C_{ext} is the extended constitutive compliance matrix.

For a general laboratory test, the rate of control variables $\dot{\phi}$ can be explicitly defined in terms of generalised stresses and strains, being matrices $\Omega_{\phi\sigma}$ and $\Omega_{\phi\varepsilon}$ always known. It is then possible to obtain the loss of controllability condition for a given mixed stress-strain hydro-mechanical loading programme.

The control of variables ϕ is indeed lost when matrix \mathbf{X} calculated for the loading programme associated to ϕ becomes singular, i.e. when:

$$\det \left(\Omega_{\phi\sigma} + \Omega_{\phi\varepsilon} C_{ext} \right) = \det \left(\Xi_1 \right) = 0 \quad (8)$$

or equivalently when:

$$\det \left(\Omega_{\phi\sigma} D_{ext} + \Omega_{\phi\varepsilon} \right) = \det \left(\Xi_2 \right) = 0 \quad (9)$$

The two mathematical quantities given in Equations (8)-(9) can be defined as instability indices, since their vanishing implies a loss of controllability for the specific control considered. Using such a mathematical approach, the inception of a potential instability can be predicted, provided that the loading programme is suitably defined. An example of this is given in Figure 4.29.

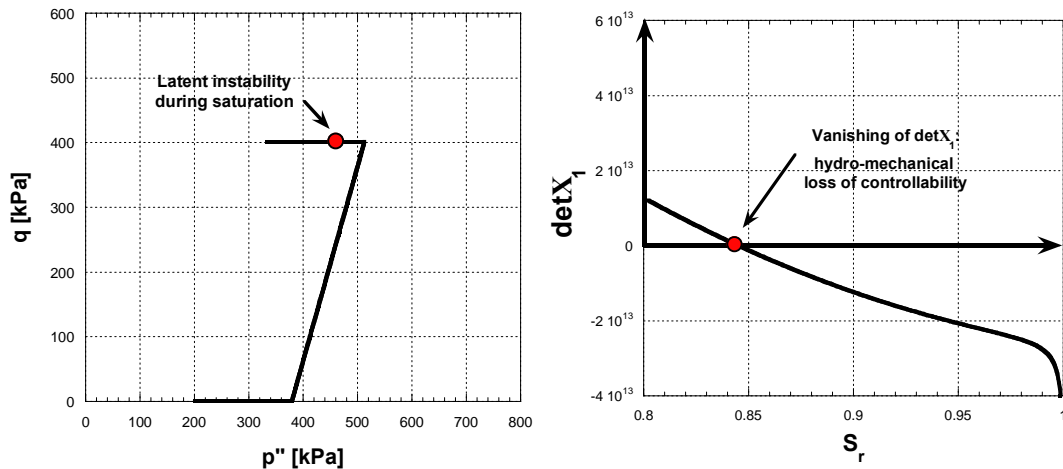


Figure 4.29 - Evidence of possible latent instabilities during soaking at constant deviator (simulation performed with suction reduction control): a vanishing point for the determinant of the extended hydro-mechanical matrix is identified for water content control (different from that used for the simulation).

The example shows that, even though the test can be carried out, and no failure is experienced upon suction reduction, potential instabilities are still possible. These instabilities can be activated upon a change of control conditions. For example Figure 4.29-b refers to the determinant $\det(X)$ evaluated for water content control.

The mechanical meaning of this result can be explained as follows: if a change of external boundary conditions is imposed (for instance switching to water undrained conditions) when the material passes beyond the limits of controllability relative to that specific loading programme, the specimen can suffer unexpected and catastrophic liquefaction instabilities (Figure 4.30).

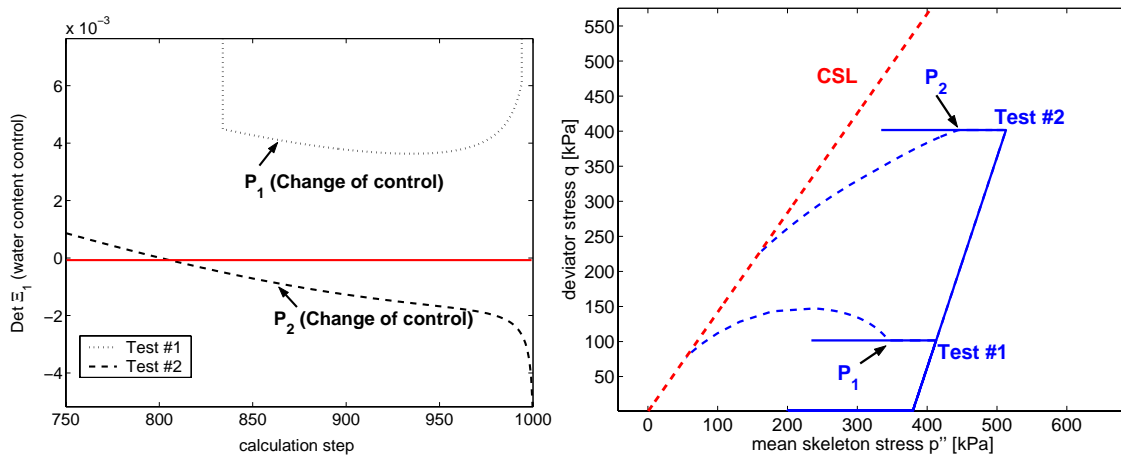


Figure 4.30 - Example of latent instability in a test in which the control is changed (axial strain rates are imposed and deviator stress is obtained as a material response): a) evolution of $\det X_1$; b) evolution of the stress state.

4.1.1.2.2.4 Application to landslides

In this last section the hydro-mechanical controllability theory previously discussed is applied to the stability analysis of infinite slopes. The theoretical framework used to evaluate stability conditions during soaking is indeed linked to a general modelling methodology aimed at describing the behaviour of an infinite slope by means of material point analyses. Such a methodology, originally suggested by di Prisco, Matiotti and Nova (1995) with reference to subaqueous flow slides, has been extended to the case of unsaturated slopes subjected to hydro-mechanical perturbations as those occurring during rainfall events. It is worth noting that the following numerical results must simply be seen as an attempt of extending the theory of material stability for unsaturated porous media to a more practical field of application. For this purpose, a series of parametric studies has been performed, with the main goal of pointing out the role played on the onset of a flow slide by some slope parameters (e.g., slope angle and deposit thickness) and some material characteristics (e.g., shear strength and soil compressibility). The results, of course, are highly associated to the adopted model parameters and to their range of variation. The results must therefore be considered only as a first attempt to explain a complex in situ evidence, and a future conclusive analysis of a real case cannot leave aside the development of a detailed quantitative characterization of the mechanical behaviour of the materials involved.

As it is well known, the effect of suction at a material point level is that of stabilising the soil structure, because of the pre-stressing action exerted by capillary forces acting on the grain contacts. The so-called apparent cohesion is the most self-evident effect of capillary phenomena on shear strength, and it is conceptually related with a sort of hydraulic bonding effect. As a result, as far as slope stability analysis is concerned, an unsaturated slope is able of maintaining steeper inclinations than those possible without such an additional strength contribution. The apparent cohesive components of the shear strength, however, can rapidly disappear as a consequence of saturation processes. This is what occurs during rainfall events, when water progressively infiltrates into the slope.

The model and the theory have been applied to the study of the response of infinite slopes by means of simple shear test simulations on both saturated and unsaturated specimens. These tests are characterised by a first deposition stage at a given slope angle and by a subsequent perturbation stage aimed at evaluating the mechanical and/or hydraulic disturbances able to induce a slope failure (Figure 4.31-4.32). The magnitude of these perturbations represents an engineering evaluation of the safety factor FS of the slope. A number of different factors of safety is evaluated, however, any of which makes reference to a different instability mode possibly affecting the system (e.g., localized shear failure, static liquefaction, wetting induced collapse etc.). In this way stability analyses are conducted in a more proper mechanical sense, accounting also for diffuse instabilities often observed in catastrophic landslides.

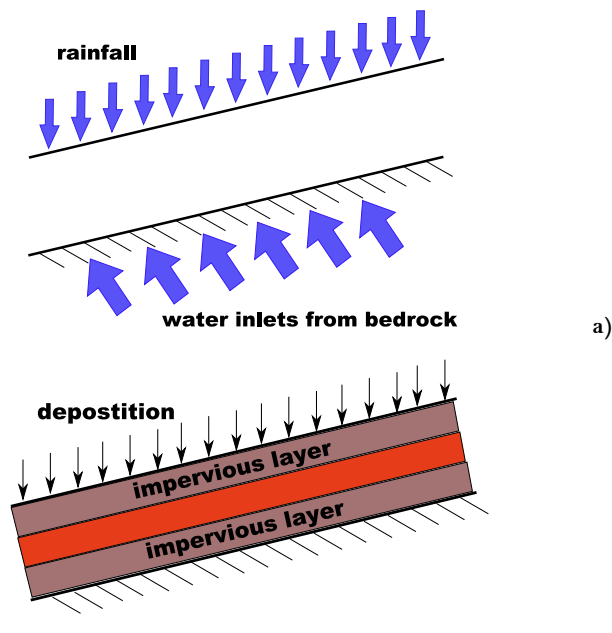


Figure 4.31 - a) Schematic description of hydraulic perturbations acting on an initially unsaturated infinite slope: effect of rain infiltration and water inlets from the bedrock; b) Example of mechanical perturbations: deposition stresses on an heterogeneous infinite slope (effect of impervious layers)

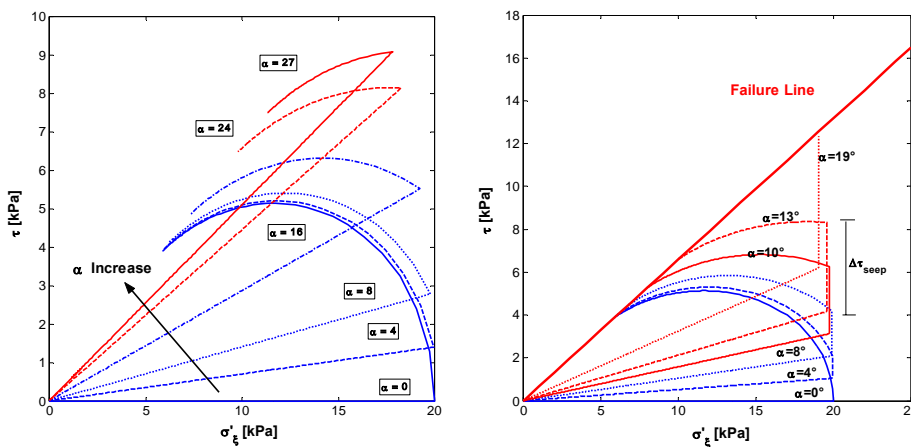


Figure 4.32 - Examples of simulation of simple shear tests on saturated infinite slopes: a) simulation of the undrained response of a saturated layer at 2m vertical depth; b) simulation of the undrained response of a saturated layer at 2m vertical depth subjected to stationary seepage

Figure 4.33 shows the results obtained on a saturated slope. It is in particular highlighted the effect of seepage on both the drained and the undrained response of the system. It is remarkable that undrained shear perturbations leading to failure are much lower than those characterising localised drained failure. As a result, even slopes with a less steep inclination than that associated to shear failure can be characterised by an incipient unstable state (i.e., the additional shear perturbation $\Delta\tau$ leading to a collapse vanishes). When a soil is highly

liquefiable the safety factor FS associated to liquefactions are then much smaller, with a predicted response that can be highly catastrophic.

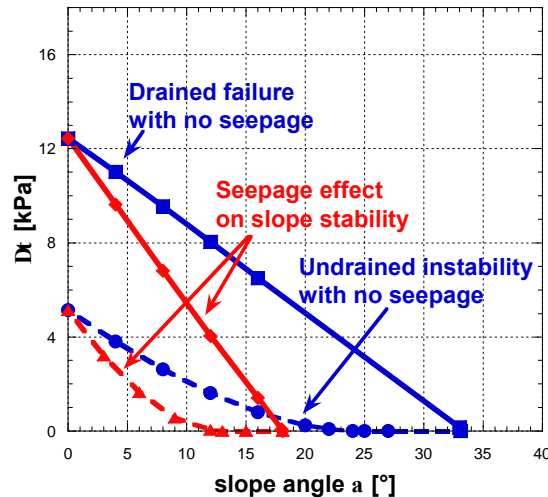


Figure 4.33 - Effect of seepage forces on the stability curves of triggering perturbations.

Similar calculations can be done with reference to unsaturated slopes, in order to investigate the influence of the initial state of saturation. Both mechanical and hydraulic triggering perturbations can be evaluated (Figures 4.34 and 4.35, respectively). Figure 4.34 shows the remarkable effect of the apparent cohesion on the predicted triggering perturbations for a 2m thick unsaturated deposit. Both suction constant and water undrained load conditions have been considered. Larger initial suctions are associated to larger perturbations leading to failure (and hence to higher values for FS). Under water undrained conditions, a marked qualitative change of the curve shape can be noticed. Under these circumstances, indeed, if model simulations are characterised by the development of large plastic volumetric strains, a different type of instability can be attained (i.e., reaching static liquefaction rather than a localised shear failure).

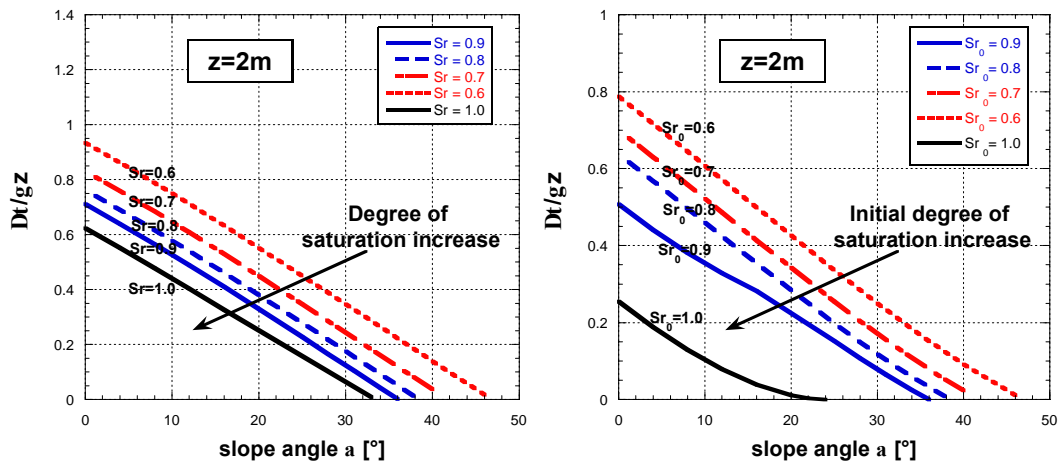


Figure 4.34 - a) Normalised stability curves at constant suction for different initial degrees of saturation: vertical depth $z=2m$; b) Normalised stability curves at constant water content for different initial degrees of saturation: vertical depth $z=2m$.

On the contrary, Figure 4.35 reports model prediction concerning hydraulic perturbations. Figure 4.35-a shows the critical pore pressure increase linked with the attainment of a localised shear failure upon saturation, while Figure 4.35-b shows the possibility of having catastrophic instabilities of the liquefaction type during saturation. These last curves have been obtained by means of parametric analysis, and it is important to remark that the predicted phenomena are remarkably linked with the deformation behaviour of the soil, and with the collapsible nature of the saturation response. As such, a complete material characterisation is necessary in order to properly predict such phenomena, and information only regarding the shear strength envelope of the unsaturated soil is not sufficient.

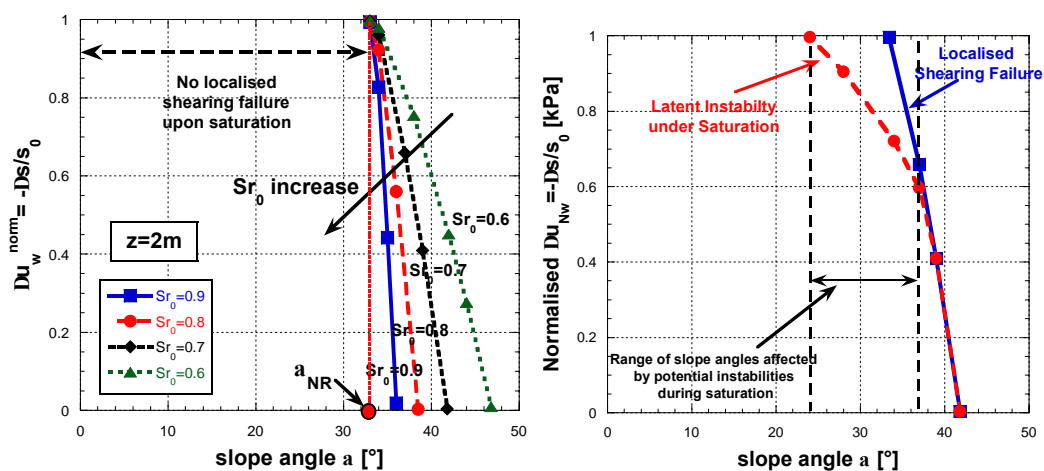


Figure 4.35 - a) Normalised stability curves of hydraulic triggering perturbations: effect of the degree of saturation on the onset of a localised failure upon saturation (vertical depth $z=2m$); b) Normalised stability curves for the case of a highly collapsible liquefiable soil

4.1.2 Numerical modelling of the boundary value problems

Numerical codes are powerful tools for practitioners and scientists working in the field of natural hazards. They complement field investigation and laboratory testing with the objective of better understanding the behaviour of landslides under variable environmental conditions. Provided that the field data is of sufficient quality, the model parameters are well calibrated and that the model itself is capable of reproducing the actual physical mechanisms of the landslide in question, such numerical codes may be a valuable tool for long term slope monitoring and early warning systems. In numerous cases, the numerical models provided valuable results for the preparation of mitigation measures for slopes in near critical conditions or causing continuous damage to infrastructure.

Numerical codes do not provide results to trust upon in blindfolded manner, but demand a sound knowledge of their features, constraints and potentialities, as well as the user's experience in interpreting their output. The objective of this section is to present the features, constraints and potentialities of some selected commercial and home-made codes with respect to landslide modelling at slope and regional scale.

4.1.2.1 Description of the main commercial codes (slope scale) (EPFL)

a) *Z_Soil*

Z_Soil (Zace, 2003) is a commercial 2D/3D Finite Element Code with integrated pre-and post-processor offering a large number of constitutive models for soils and rocks to solve user-defined boundary value problems.

List of features

- 2D/3D Finite Element Code
- Integrated pre-processor to define geometry, initial and boundary conditions of any given boundary value problem.
- Integrated postprocessor allowing the graphical display of the results
- Analysis types: plane strain, axisymmetric and 3D analysis
- Problem types: deformation, flow (steady or transient, saturated or unsaturated), deformation and flow, heat transfer and humidity transfer
- Quasi-static and time dependent calculations
- Automatic evaluation of initial stress conditions, including steady state flow
- Time dependent processes: consolidation, volumetric and deviatoric creep and swelling
- Time dependent boundary conditions: arbitrary flow with free surfaces, seepage surfaces or rain infiltration
- Non-linear small and large displacements
- Large set of constitutive models for soils and rocks
- User defined constitutive models can be implemented
- Stabilisation algorithms for incompressible and dilatant two-phase media
- Safety Factor analysis (strength reduction method)

Sign convention

Compressive stresses, in the solid matrix as well as in the fluid, are negative. Suction corresponds to positive pore water pressures.

Multiphysics

The program allows for calculations in saturated and partially saturated soils. The three-phase medium air-fluid-solid is approximated by a two-phase liquid-solid medium, where the air is assumed to be trapped in form of bubbles in the liquid phase. The air-fluid mixture forms a compressible fluid obeying Darcy's law.

Primary consolidation resulting from the coupling of load-induced Darcy flow with the motion of a quasi-saturated medium is integrated in the code.

Continuum mechanics of porous media*General equations*

The continuum mechanics of the two-phase medium are described by the following set of equations:

- 1) Conservation of linear momentum:

$$\underline{\underline{\sigma}}_{ij,j} + \underline{b}_j = 0$$

Where σ_{ij} is the 2nd rank stress tensor and b_j are internal body forces.

- 2) Mass conservation of the mixture for partially saturated and saturated media, assuming incompressible solid grains:

$$\frac{\partial n \rho^f}{\partial t} + \text{div}(n \rho^f \underline{v}^f) - Q = 0$$

Where n is the soil porosity, ρ^f is the specific mass of the fluid phase, \underline{v}^f is the average fluid velocity through the porous media and Q is a mass source term.

- 3) Constitutive stress-strain equation:

$$\dot{\underline{\underline{\sigma}}}_{ij} = C_{ijkl} \dot{\underline{\underline{\epsilon}}}_{kl}$$

Where C_{ijkl} is the 4th rank constitutive tensor and $\dot{\underline{\underline{\epsilon}}}_{kl}$ is the strain rate.

- 4) Compatibility equation (assuming small strains)

$$\underline{\underline{\epsilon}}_{ij} = \frac{1}{2} (\underline{u}_{i,j} + \underline{u}_{j,i})$$

where ε_{ij} is the small strain tensor and u_i is the solid displacement vector.

By combining the equations given above and introducing the effective stress concept given below, a set of two equations with two nodal unknowns u and p is obtained.

Effective stress concept

The effective stress concept used in the program for the two-phase medium is similar to Bishop's effective stress:

$$\underline{\underline{\sigma}}'_{ij} = \underline{\underline{\sigma}}_{ij} - Sp\underline{\underline{\delta}}_{ij}$$

Where σ'_{ij} is the effective stress tensor, σ_{ij} is the total stress tensor, S is the degree of saturation and p is the pore water pressure which is negative for partially saturated soils. Hence, in Z_{Soil} matric suction which is commonly referred to as the difference between the air pressure and pore water pressure is equal to the pore water pressure.

The stress framework allows a smooth transition between the partially saturated and fully saturated state.

Elasto-plasticity

Within classical plasticity, the Mohr-Coulomb Drucker-Prager or Hoek-Brown criterion can be used. More sophisticated models, such as the Cap model with isotropic hardening and multi-mechanism plasticity or Modified Cam-Clay model with non-linear elasticity are integrated as well. The models can account for the non-associated behaviour of soils.

Fluid flow and storage

The fluid motion in the two-phase medium is described by the groundwater flow equation which is deduced from the continuity equation for the fluid phase, considering a deformable solid matrix, a storage function $c(p)$ and integrating the generalized Darcy's law. Partial saturation is considered in the general diffusion equation via the degree of saturation S :

$$S\dot{\varepsilon}_{kk} + \underline{q}_{k,k} = c\dot{p}$$

Where $\dot{\varepsilon}_{kk}$ is the volumetric strain rate and q_k the relative fluid velocity. The storage function $c(p)$ is defined as:

$$c(p) = n \left(\frac{S}{K_F} + \frac{dS}{dp} \right)$$

Where K_F is the fluid bulk modulus.

On a constitutive level, partial saturation is considered in terms of the water relative permeability of the medium. The relationship between the water relative permeability k_r and the degree of saturation S is defined as:

$$k_r = \frac{(S - S_r)^3}{(1 - S_r)^3} = \frac{1}{\left[1 + \left(\alpha \frac{P}{\gamma_F}\right)^2\right]^{3/2}}$$

Where S_r is the residual degree of saturation, α is the saturation constant and γ_F is the specific fluid weight.

Retention behaviour

The saturation coefficient S is a function of the negative pore water pressure p . Z_Soil uses for the soil water retention curve the S-p relationship given by Van Genuchten (1980) with the fixed constants $n = 2$ and $m = 0.5$:

$$S = S(p) = \begin{cases} S_r + \frac{1 - S_r}{\left[1 + \left(\alpha \frac{P}{\gamma_F}\right)^2\right]^{1/2}} & \text{if } p < 0 \\ 1 & \text{if } p \geq 0 \end{cases}$$

Modelling natural slopes subjected to rainfall infiltration

The mechanical, hydraulic and coupled consolidation features of Z_Soil presented in the preceding sections allow a transient analysis of the stress-deformation behaviour of a natural, partially or fully saturated slope subjected to rainfall infiltration. For this purpose, initial stress and pore pressure field calculations must be run first, followed by the rain infiltration as load input. The analysis and driver input option allows running the calculation sequences automatically one after another.

The geometry of the slope, the boundary and initial conditions, as well as the finite element mesh are defined in the pre-processor (Figure 4.36). Seepage elements can be used along the slope surface in order to switch automatically between Neumann and Dirichlet boundary conditions as the soil saturates close to the surface due to rain infiltration. Load time functions allow defining variable rainfall input over time.

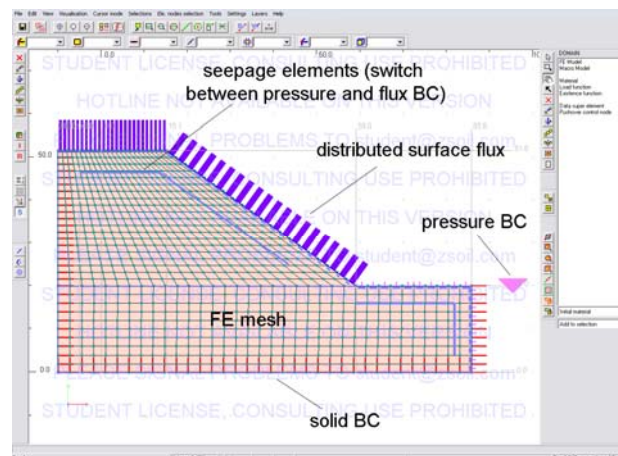


Figure 4.36 - Pre-processor in Z_Soil

The postprocessor allows to display stresses and state variables as contour maps or nodal/element time histories (Figure 4.37).

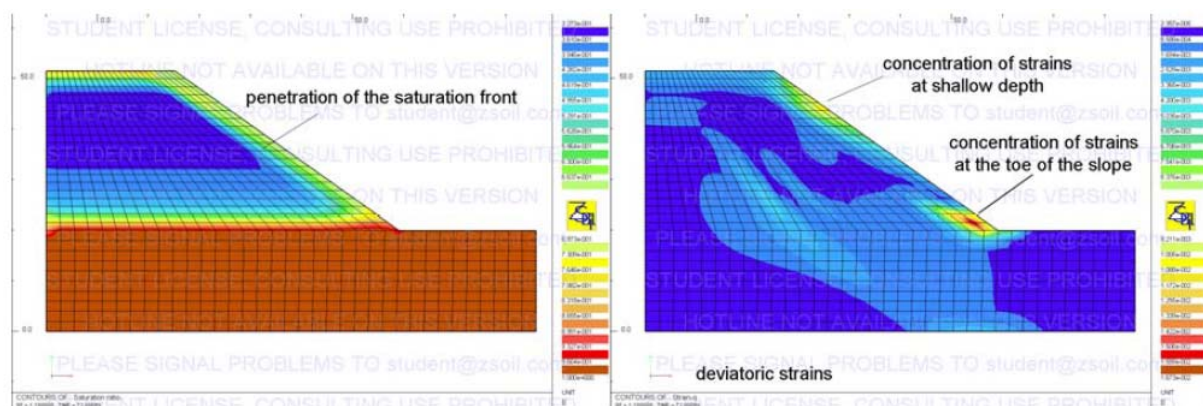


Figure 4.37 - Z_Soil: results in post-processor : saturation contours show the penetration of the saturation front from the surface into the slope (left) ; deviatoric strain contours indicate possible shallow failure mechanisms (right)

Additionally to the initial and transient analysis drivers, a safety factor analysis may be performed at any step during the transient calculation by means of the strength reduction method for two parameter (c- ϕ) yield criteria (Figure).

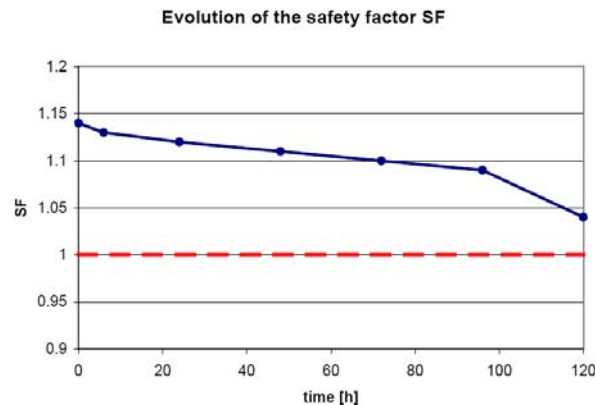


Figure 4.38 - A safety factor analysis by means of a c - ϕ strength reduction method indicates that the slope is close to possible failure and gets closer as rain infiltration lasts

In the case of a reactivated landslide with pre-existing slip surfaces it is possible to use interface elements with a large displacement formulation. The elasto-plastic friction model with a no-tension condition is used. This allows sticking, sliding and separation at the interface. Both isotropic and anisotropic flow conditions can be modelled.

b) FLAC

FLAC stands for “fast langrangian analysis of continua” and is a commercial 2D explicit finite difference program for the simulation of the behaviour of geomaterials under various loading conditions (Itasca 2008). The code offers a set of constitutive models for soils and rocks undergoing yield and plastic flow. User defined constitutive models written in C++ can also be implemented. Large 2D calculations can be run without any excessive memory requirements since no matrices are formed. The explicit, Lagrangian formulation and the mixed-discretization zoning technique allow running large strain calculations with accuracy while the material undergoes plastic flow and collapse. An automatic re-meshing tool is integrated in the program for large strain simulations.

List of features

- 2D Finite Difference Code
- Integrated pre-processor to define geometry, initial and boundary conditions of any given boundary value problem.
- Integrated postprocessor allowing the graphical display of the results
- Analysis types: plane strain, axisymmetric, plane stress (for certain models)
- Problem types: deformation, flow (steady or transient, saturated or unsaturated), deformation and flow, two-phase flow and heat transfer
- Quasi-static and time dependent calculations
- Time dependent processes: consolidation and creep calculation (creep models in a supplementary module available)
- Time dependent boundary conditions: arbitrary flow with free surfaces, seepage surfaces or rain infiltration

- Large-strain simulations possible
- Automatic re-meshing during the solution process in large strain simulations
- Large set of constitutive models for soils and rocks
- User defined constitutive models can be implemented, using C++
- Built-in language (FISH) to add user-defined features (i.e. rainfall history on a soil slope)
- Safety Factor analysis (strength reduction method)

Sign convention

Compressive stresses in the solid matrix and in the fluid are positive.

Multiphysics

In its extended version, the code is able to account for the fluid flow of two immiscible fluids through a hydraulically isotropic or anisotropic, deformable porous medium. For a fully saturated medium, hydromechanical coupling in the sense of consolidation according to Biot's theory is implemented. The fluid flow in a partially saturated medium can be simulated independently from the mechanical part using either a single-phase or two-phase flow. The single-phase flow module uses a predefined cubic law for the relation between the water relative permeability and the degree of saturation. The two-phase flow module uses the relationship of Van Genuchten (1980) for the water/air relative permeability curves.

In order to capture the capillary effects, the extended version with two-phase flow needs to be purchased, since the standard version with single-phase flow sets pore pressures to zero above the free surface. In the case of a hydromechanically coupled analysis with two-phase flow, the solid grains forming the matrix are assumed to be incompressible. The effect of matric suction on the effective stresses is accounted for through the use of Bishop's effective stress, but there is no influence of matric suction on the soil stiffness. The fluids/solid interactions works automatically in the sense that changes in effective stress induce volumetric strain and vice-versa. The influence of volumetric deformations on permeability and retention curve parameters is not captured automatically, but these functions can be implemented by the user.

Continuum mechanics of porous media

General equations

The continuum mechanics of the three-phase medium are described by the following set of equations as given in the FLAC Manual, Section 2: two-phase flow (Itasca 2008):

- 1) Conservation of linear momentum:

$$\frac{\partial \sigma_{ij}}{\partial x_j} + \rho g_i = \rho \frac{d\dot{u}_i}{dt}$$

Where σ_{ij} is the 2nd rank stress tensor, ρ is the bulk density and \dot{u}_i is velocity. For two-phase flow the bulk density is written as:

$$\rho = \rho_d + n \cdot \sum_{\alpha=1}^2 S_{\alpha} \rho_{\alpha}$$

Where n is porosity, ρ_d is the matrix dry density, ρ_{α} is the density and S_{α} the degree of saturation of fluid phase α .

- 2) Mass conservation of the fluids, assuming slightly compressible fluids:

$$\frac{\partial \zeta_{\alpha}}{\partial t} = \frac{\partial q_i^{\alpha}}{\partial x_i} + q_v^{\alpha}$$

Where ζ_{α} is the variation of fluid content and q_v^{α} is the volumetric fluid source intensity in phase α .

- 3) Constitutive stress-strain equation:

$$\Delta \sigma'_{ij} = H(\sigma'_{ij}, \Delta \varepsilon_{ij}, \kappa)$$

The change in effective stress is expressed as a functional form of the constitutive law. κ is a history parameter.

- 4) Compatibility equation

The relation between strain rate and velocity gradient is given as:

$$\dot{\varepsilon}_{ij} = \frac{1}{2} \left[\frac{\partial \dot{u}_i}{\partial x_j} + \frac{\partial \dot{u}_j}{\partial x_i} \right]$$

Effective stress concept

Bishop effective stress concept is used in the program for the three-phase medium:

$$\sigma'_{ij} = \sigma_{ij} + \sum_{\alpha=1}^2 S_{\alpha} P_{\alpha}$$

Where σ'_{ij} is the effective stress tensor, σ_{ij} is the total stress tensor, S is the degree of saturation and P is the pressure of phase α . The stress framework allows a smooth transition between the partially saturated and fully saturated state.

Elasto-plasticity

The user has the choice of a large set of constitutive models for soils and rocks to capture the elasto-plastic behaviour of those materials: Mohr-Coulomb, Drucker-Prager, Cap-yield,

double-yield, strain-softening, modified CamClay or Hoek-Brown. Models for joints are also available.

Fluid flow and storage

The motion of the fluids in the porous medium is described by the groundwater flow equation and generalized Darcy law. The general mathematical formulation of the groundwater flow equation given below couples the fluid motion to the solid skeleton deformation ε and considers the presence of two immiscible fluids via the fluid saturation S_α coefficient of each phase α .

$$n \left[\frac{S_\alpha}{K_\alpha} \frac{\partial P_\alpha}{\partial t} + \frac{\partial S_\alpha}{\partial t} \right] + \left[\frac{\partial q_i^\alpha}{\partial x_i} + S_\alpha \frac{\partial \varepsilon}{\partial t} \right] = 0$$

Where K_α is the bulk modulus of phase α , n is porosity, P_α is the pore pressure, ζ_α is the variation of fluid content and q^α is a source term in phase α .

On a constitutive level, partial water saturation of a soil is considered in terms of water and air relative permeability of the medium. The relationship between the water, respectively air relative permeability k_r^α and the saturation coefficient S in FLAC is given by Van Genuchten (1980):

$$k_r^w = S_e^b \cdot \left[1 - (1 - S_e^{1/a})^a \right]^2$$

$$k_r^g = (1 - S_e)^c \left[1 - S_e^{1/a} \right]^{2a}$$

Where a, b and c are constants and S_e is the effective saturation defined as:

$$S_e = \frac{S_w - S_r^w}{1 - S_r^w}$$

Where S_r^w is the residual wetting fluid saturation.

Retention behaviour

For the two-phase flow module, the capillary pressure or matric suction P_c is related to the degree of saturation S according to Van Genuchten (1980):

$$P_c(S_w) = P_0 \left[S_e^{-1/a} - 1 \right]^{1-a}$$

Where the scaling parameter P_0 is larger for finer material. It may be expressed either as a function of the material parameters. The “alpha-coefficient” used in other codes (i.e. Z_Soil) is related to P_0 as follows:

$$P_0 = \frac{\rho_w g}{\alpha}$$

Where ρ_w is the wetting fluid density and g is gravity.

In the standard FLAC version, matric suction is set to zero above the free surface. The retention behaviour is not reproduced.

Modelling natural slopes subjected to rainfall infiltration

In order to model the effect of rainfall infiltration on the stability of a natural soil slope by means of a transient, hydromechanically coupled calculation, FLAC needs to be used with its additional two-phase module. The single-phase module can also be used for calculations in unsaturated conditions. However, capillary effects cannot be captured and the hydraulic parameters for the flow in the unsaturated part remain constant. Hence, it is less interesting to perform a time-dependent, hydromechanically coupled analysis.

For demonstration purposes, the stability of a generic soil slope as given in Figure 4.39 with a simple Mohr-Coulomb failure criterion is considered. The idea is to investigate the influence of a rising water table after a long duration rainfall on the stability of the slope. Numerical calculations are run for long-term rainfalls of different intensities.

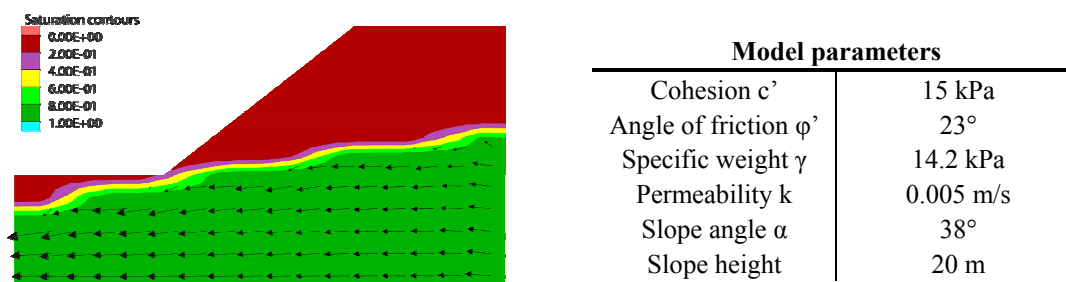


Figure 4.39 - Problem initialisation – Water table location is determined in a flow calculation (left); model parameters (right)

An uncoupled hydromechanical analysis is performed since only the steady-state solution of the pore pressure field is of interest here. Given some local piezometric measurements, a flow calculation is run first in order to establish the pore pressure distribution in the slope. A mechanical calculation is subsequently run to initialize the stresses in the slope. The fluid bulk modulus is set to a small value to prevent the generation of excess pore water pressures and consequently volumetric strains.

The same uncoupled procedure is finally applied for the rain infiltration phase. For a certain rain infiltration, the hydraulic, steady-state solution is calculated. The obtained pore pressure field serves as load input for the mechanical calculation. The factor of safety of the soil slope is calculated by means of the strength reduction method (see Figure 4.40). Assuming constant soil properties, the results of a couple of simulations with different rain infiltration rates yield a threshold value for a critical rain infiltration rate (see Figure 4.41).

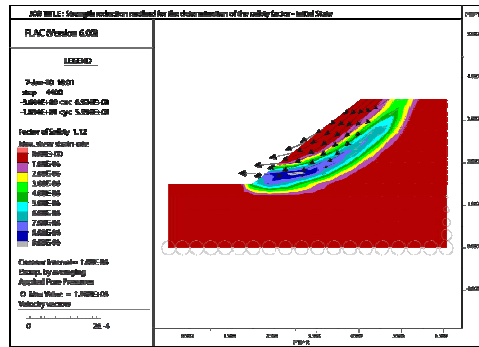


Figure 4.40 - Determination of the failure surface and factor of safety of the soil slope by means of the strength reduction method

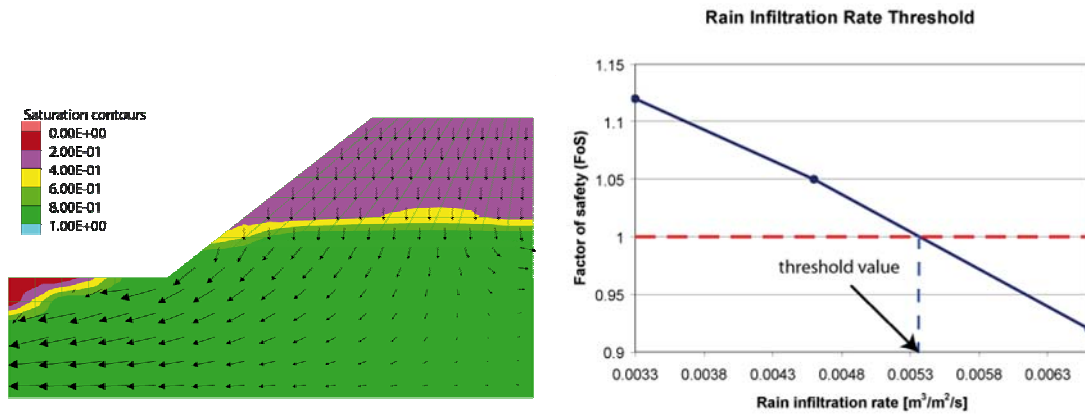


Figure 4.41 - Water table rise due to rain infiltration (left); threshold value for rain infiltration rate (right)

The explicit finite difference method and the langrangian formulation allow large strain, step-by-step calculations. Possible failure modes can hence be studied while in progress (see Figure 4.42).

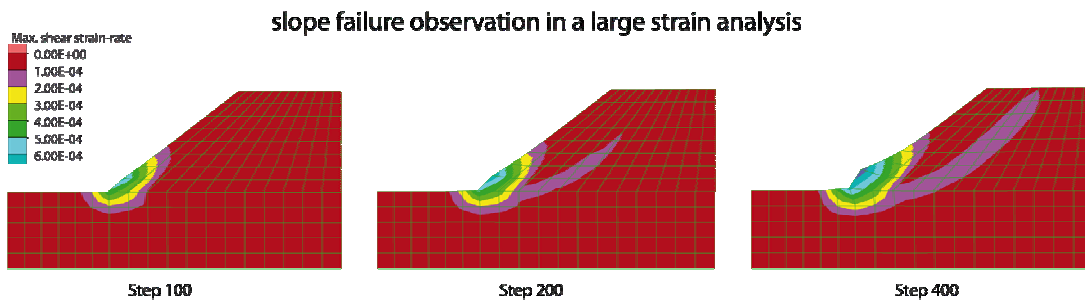


Figure 4.42 - Observation of the ongoing failure of a soil slope in a large strain simulation

c) PLAXIS

PLAXIS is a commercial 2D or 3D finite element program for the analysis of deformation and stability in geotechnical engineering. It has been originally developed at the Technical University of Delft and was later in the 90's commercialised and adapted to the Windows operating system. Simple elastic, as well as more advanced elasto-plastic constitutive models for soils and rocks can be used for simulation purposes. The program offers a user-friendly interface enabling to switch easily between pre-processor, calculation drivers and post-processor. The definition of boundary conditions as well as the initialisation of stresses and pore pressures is easily accomplished. Hydrostatic and non hydrostatic pore pressure fields are generated in the pre-processor based on user-defined water table locations. The stress field is also calculated directly in the pre-processor or in a first gravity loading simulation phase. All simulation phases (initialisation, plastic analysis, consolidation, excavation stages and strength reduction) are run automatically in a user defined sequence (Figure 4.43). Transient flow calculations can be performed with PlaxFlow, an additional finite element package. The generated time-dependent pore pressure field can be imported into the basic version of Plaxis for deformation analysis.

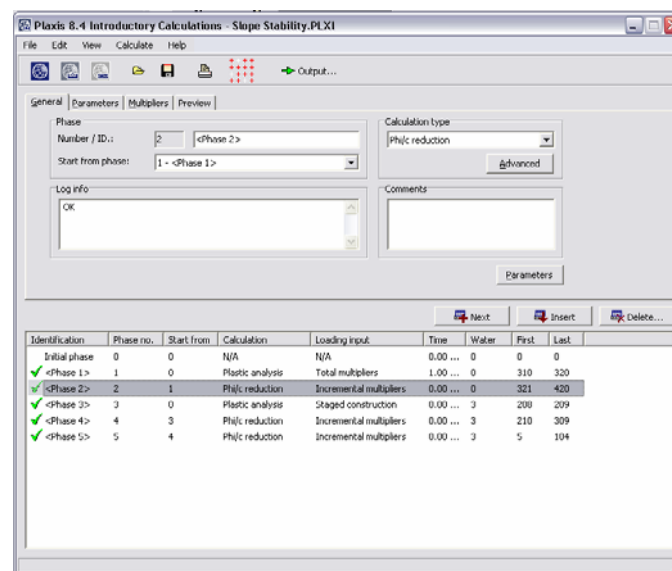


Figure 4.43 - User-defined calculation sequence in Plaxis

List of features

- 2D Finite Element Code
- Integrated pre-processor to define geometry, initial and boundary conditions of any given boundary value problem.
- Integrated postprocessor allowing the graphical display of the results: Contour maps, load-displacement curves, stress and strain paths, stress-strain diagrams and time-settlement curves
- Analysis types: plane strain, axisymmetric

- Problem types: deformation, flow/two-phase flow with the finite element package PlaxFlow (steady or transient, saturated or unsaturated), deformation and flow (uncoupled analysis)
- Quasi-static and time dependent calculations
- Time dependent processes: consolidation and creep calculation
- Time dependent boundary conditions: arbitrary flow with free surfaces, seepage surfaces or rain infiltration
- Updated mesh (Lagrange) analysis
- Use of either 6-node or 4th order 15-node triangular elements
- Large set of constitutive models for soils and rocks
- Automatic parameter analyses (with VIP extension package)
- Safety Factor analysis (c/phi strength reduction method)

Sign convention

Compressive stresses in the solid matrix and in the fluid are negative.

Multiphysics

The basic version of Plaxis offers the possibility to run hydromechanically coupled analyses in the sense of classical consolidation. The soil is considered either fully saturated or dry from a mechanical point of view. For the steady state flow, a log-linear permeability function is defined for a 0.7m thick transition soil layer above the water table in order to account for partial saturation in consolidation analyses. A time-dependent flow analysis in saturated or partially saturated, isotropic or anisotropic states with variable boundary conditions can be performed in PlaxFlow, but not in the basic version. In this case, no solid matrix deformations are considered for the two-phase porous medium. Inflow and outflow of water due to infiltration and evaporation can be modelled. The particular flow characteristics in partially saturated soils can be considered by means of the water relative permeability curve of linear or Van Genuchten type (1980). Capillary effects are not integrated in the code. Pore pressures above the water table are set equal to zero.

Continuum mechanics of porous media

General equations

The continuum mechanics of the two-phase medium are described by the following set of equations as given in the PLAXIS Manual, Section 2: deformation theory (Plaxis V8, 2006):

- 1) Conservation of linear momentum:

$$\underline{\underline{L}}^T \underline{\underline{\sigma}} + \underline{p} = 0$$

Where vector \underline{p} assembles the body forces, vector $\underline{\sigma}$ the six stress components and $\underline{\underline{L}}^T$ is the transpose of a differential operator, defined as:

$$\underline{\underline{L}}^T = \begin{bmatrix} \frac{\partial}{\partial x} & 0 & 0 & \frac{\partial}{\partial y} & 0 & \frac{\partial}{\partial z} \\ 0 & \frac{\partial}{\partial y} & 0 & \frac{\partial}{\partial x} & \frac{\partial}{\partial z} & 0 \\ 0 & 0 & \frac{\partial}{\partial z} & 0 & \frac{\partial}{\partial y} & \frac{\partial}{\partial x} \end{bmatrix}$$

2) Mass conservation of the fluid (steady flow):

$$\frac{\partial q_i}{\partial x_i} = 0$$

3) Constitutive stress-strain relation:

$$\underline{\underline{\dot{\sigma}}} = \underline{\underline{M}} \underline{\underline{\dot{\varepsilon}}}$$

Where the rate of stress is related to the rate of strain via the constitutive matrix M.

4) Compatibility equation for small strains:

The relation between strain vector ε and displacement vector u is given as:

$$\underline{\underline{\varepsilon}} = \underline{\underline{L}} \underline{\underline{u}}$$

Effective stress concept

Terzaghi's effective stress concept is used for calculations in fully saturated conditions:

$$\underline{\underline{\sigma}}' = \underline{\underline{\sigma}} - \underline{\underline{p}} \quad \text{for } p \leq 0$$

Elasto-plasticity

PLAXIS offers a set of advanced elasto-plastic models for soils: compression and shear hardening, creep behaviour, CamClay model and user-defined models

Fluid flow and storage

For the steady state flow in the basic Plaxis version, the continuity equation as given above in point 2) together with Darcy's law in saturated conditions applies. For the transient, saturated or partially saturated flow in PlaxFlow, the continuity equation is formulated as:

$$\frac{\partial q_i}{\partial x_i} + c \frac{\partial \phi}{\partial t} = Q$$

Where Φ is the pressure head, c is the effective capacity and Q is a source term. The transient part relates the change in head to a change in volumetric water content of the elementary volume via the effective capacity c . Effective capacity and effective permeability depend on the water content and the capillary pressures. The effective capacity is given as:

$$c = c_{sat} + n \frac{dS(\phi_p)}{d\phi_p}$$

Where c_{sat} is the saturated effective capacity which depends on the soil type, n is soil porosity, S is the degree of saturation and Φ_p is the pore pressure head (negative for suction). The evolution of the degree of saturation with suction is given by the retention curve (Van Genuchten type). The evolution of permeability with the degree of saturation is given by the Van Genuchten relationship (1980). The effective permeability tensor is written as:

$$K = k_{rel}(S) K_{sat}$$

$$\text{Where } k_{rel} = S_e^{g_l} \left(1 - \left(1 - S_e^{\left(\frac{g_n}{g_n - 1} \right)} \right)^{\left(\frac{g_n - 1}{g_n} \right)} \right)^2$$

$$\text{with } S_e = \frac{S - S_{residu}}{S_{sat} - S_{residu}}$$

S_e is the effective saturation, S_{sat} is the field saturation, S_{residu} is the residual degree of saturation for very high levels of suction and g_l and g_n are material parameters.

Retention behaviour

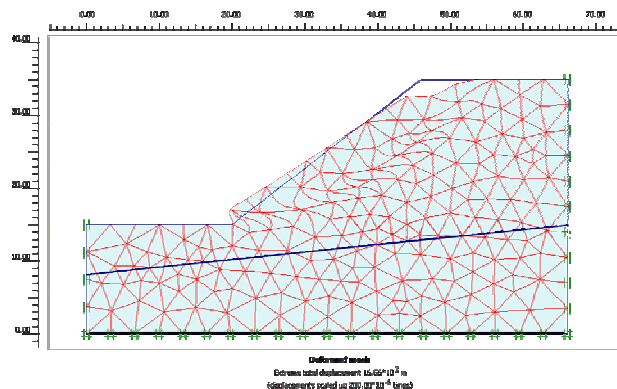
The retention behaviour is described by the Van Genuchten relationship:

$$S(\phi_p) = S_{residu} + (S_{sat} - S_{residu}) \left(1 + (g_a |\phi_p|)^{g_n} \right)^{\left(\frac{1 - g_n}{g_n} \right)}$$

Where g_a and g_n are material parameters.

Modelling natural slopes subjected to rainfall infiltration

For the analysis of natural slopes subjected to rain infiltration and seepage in partially saturated conditions, the supplementary finite element package PlaxFlow needs to be purchased. The results from the groundwater calculations performed in PlaxFlow may be integrated in the basic program for the plastic analysis. However, the code doesn't account for the effect of suction on soil strength, but only on the unsaturated flow. Hence, only uncoupled hydraulic and mechanical calculations can be run.



Model parameters	
Cohesion c'	15 kPa
Angle of friction ϕ'	23°
Specific weight γ	14.2 kPa
Permeability k	0.005 m/s
Slope angle α	38°
Slope height	20 m

Figure 4.44 - Finite element mesh, boundary and initial conditions in Plaxis

The basic code allows studying the effect of groundwater table rises and apparition of perched water tables on stresses and strains in the slope. Additionally, a c/ϕ -strength reduction analysis can be performed in order to determine the factor of safety of a slope. For illustration purposes, a simple generic slope is considered here where the initial water table is supposed to rise in the slope as a consequence of rain infiltration. The effect of the water table rise on stresses and strains is examined by means of an elasto-plastic finite element calculation. Figure 4.44 shows the boundary and initial conditions before the rainfall event, as well as the deformed finite element mesh as displayed in the post-processor after a plastic analysis and a safety factor calculation. The location of the water table is indicated by the blue line. The finite element calculation allows determining the most probable failure mechanism and the safety factor without assuming any failure surface in advance. Plastic shear strains appear at the slope toe and develop upwards to the slope crest (Figure 4.45). The initial safety factor for this slope is 1.12. After a long rainfall period, the water table is supposed to rise. The safety factor of the slope decreases and reaches a value of 1.08 for the configuration shown in Figure 4.46. The failure mechanism changes compared to the initial state. Due to the water table mounding, a more deep-seated failure would most probably occur. The failure surface passes now through the water saturated zone.

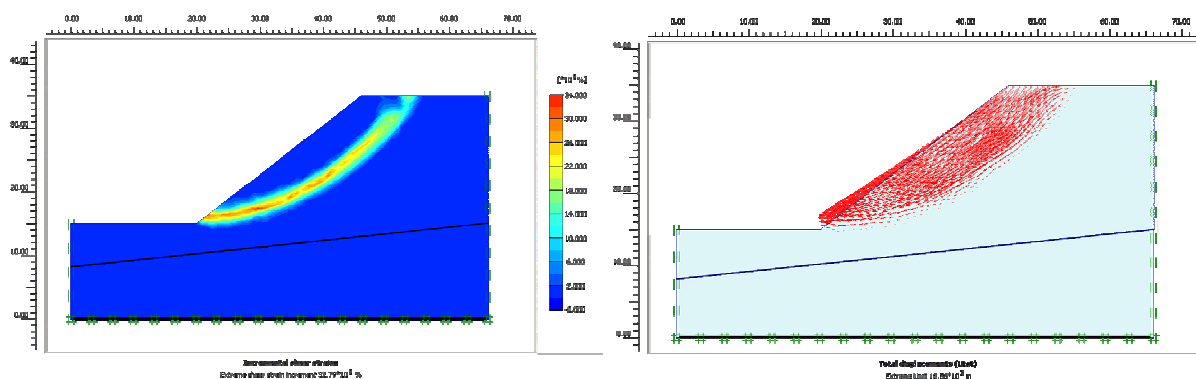


Figure 4.45 - Results of a strength reduction calculation for the initial state : incremental shear strains and total displacement vectors indicate a possible failure mechanism

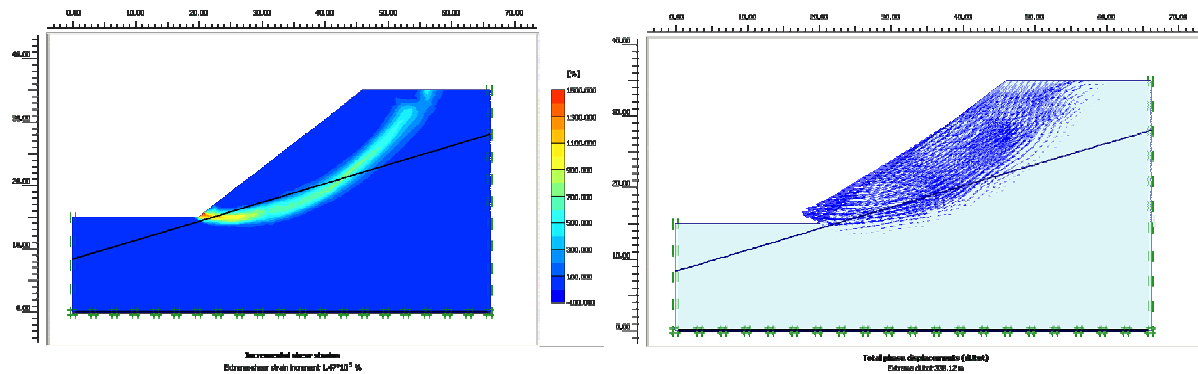


Figure 4.46 - Results of a strength reduction calculation after rainfall event: incremental shear strains and total displacement vectors indicate a possible failure mechanism

d) Geo-Slope software

Geoslope is a profitable company based in Calgary, Canada and author of the world-wide most sold slope stability software Slope/W. The software allows calculating the factor of safety of soil and rock slopes based on the limit equilibrium method. Natural as well as engineered and reinforced slopes can be analysed. The program can take into account heterogeneous soil types, complex stratigraphic and slip surface geometry, as well as variable pore water pressure conditions. The user has the choice between several types of failure criteria for soils and rocks. The slope stability analysis can be performed using deterministic or probabilistic input parameters. The Geostudio package allows coupling different software components with each other which offers solutions for complex multiphysics problems, such as slope stability under rain infiltration. It is noteworthy to mention the finite element software products Seep/W and Vadose/W, as well as Sigma/W for the numerical simulation of steady state or transient, saturated and partially saturated groundwater flow, soil surface-environment interactions and the calculation of stresses and strains in deformable porous media. Results in terms of pore water pressures obtained in Seep/W can be integrated in Sigma/W for a stress-deformation analysis. Stresses obtained in Sigma/W can then be imported in Slope/W for a limit equilibrium analysis.

List of features

The following list of features is given by the developer (Geo-Slope International, 2008):

- Limit equilibrium methods include Morgenstern-Price, GLE, Spencer, Bishop, Ordinary, Janbu, and more
- Soil strength models include Mohr-Coulomb, Spatial Mohr-Coulomb, Bilinear, Undrained ($\Phi = 0$), anisotropic strength, shear/normal function, and many types of strength functions
- Specify many types of interslice shear-normal force functions

- Pore-water pressure options include r_u coefficients, piezometric lines, pressure contours, a grid of values, spatial functions, or finite-element computed heads or pressures
- Define potential slip surfaces by a grid of centers and radius lines, blocks of slip surface points, entry and exit ranges, fully specified shapes, or automatic
- Use probabilistic soil properties, line loads, and piezometric lines
- Transient stability analyses

Graphical user interface

Slope/W offers a user-friendly and well structured interface. The user can define in the preprocessor the problem geometry, material layers and parameters, pore pressure distribution, as well as analysis settings for the slice methods. The potential slip surface is computed from a user-defined number of possibilities. Therefore, the user defines a grid of centers and tangents to the slip surfaces (Figure 4.47a). Out of all possible combinations of center points and tangents, the processor computes the most critical slip surface presenting the minimum factor of safety according to one or several slice methods. Results on safety factors and associated failure surfaces can be visualised in the postprocessor (Figure 4.47b).

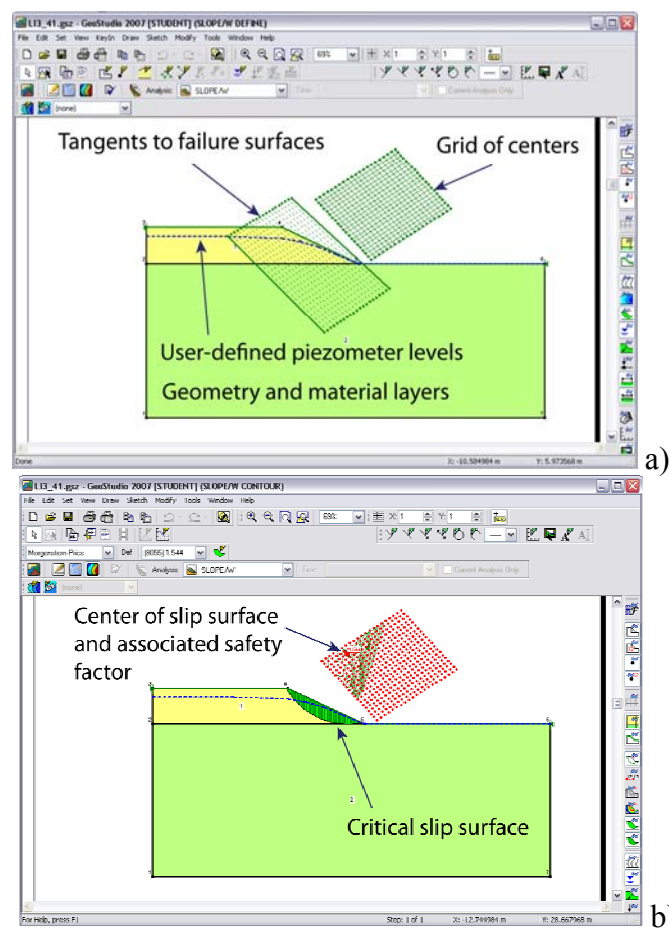


Figure 4.47 - Graphical user interface and problem definition in the pre-processor (a); Results on critical slip surface and safety factor visualised in the post-processor (b)

d.1) VADOSE/W software

(AMRA)

The software VADOSE/W is able to solve seepage problems within soils subjected to non-isothermal conditions. In fact, it takes into account the equations solving hydraulic flow (both water and vapour phases), heat flow and gas flow. So, it could be useful to assess a relationship between climate data (rainfall, temperature, relative humidity) and piezometric course.

For sake of simplicity, if we neglect the gas flow and the transpiration phenomena (that also could be taken into account by the code), the problem is governed by three differential equations:

- 1) hydraulic seepage
- 2) heat transfer
- 3) coupling of the heat and mass equations.

Equations

In 1D hypothesis, the governing differential equation for vertical hydraulic seepage can be expressed as

$$m_w \frac{\partial u_w}{\partial t} = \frac{1}{\rho_w} \frac{\partial}{\partial y} \left(D_v \frac{\partial u_v}{\partial y} \right) + \frac{\partial}{\partial y} \left[k_{wy} \frac{\partial \left(y + \frac{u_w}{\rho_w g} \right)}{\partial y} \right] + Q_w$$

where

- u_w = water pressure of soil moisture;
- u_v = vapour pressure of soil moisture;
- m_w = slope of the volumetric water content function;
- ρ_w = density of water;
- t = time;
- y = elevation head;
- D_v = vapour diffusion coefficient;
- k_{wy} = hydraulic conductivity in the vertical y-direction;
- g = gravity acceleration;
- Q_w = applied hydraulic boundary flux.

At the same time, the heat transfer is governed by:

$$\lambda_t \frac{\partial T}{\partial t} = \frac{\partial}{\partial y} \left(k_{ty} \frac{\partial T}{\partial y} \right) + \rho c V_y \frac{\partial T}{\partial y} + L_v \frac{\partial}{\partial y} \left(D_v \frac{\partial u_v}{\partial y} \right) + Q_t$$

where

- T = temperature;
- λ_t = volumetric heat capacity of soil;
- k_{ty} = thermal conductivity in the vertical y-direction;
- ρ = bulk density of soil;
- c = mass specific heat capacity of soil;

- V_y = Darcy water velocity in vertical y-direction;
- L_V = latent heat of vaporization of water;
- Q_t = applied thermal boundary flux.

Boundary conditions

The equations hydraulic and heat equations, which state that the difference during time between the flow entering and leaving an elemental volume at a point is equal to the rate of change of the volumetric water or heat contents with respect to time, contain three unknown parameters:

- 1) pore-water pressure u_w ;
- 2) pore-vapour pressure u_v
- 3) temperature T .

The solution of the problem evidently needs the use of a third equation that couples heat and mass equations. The code uses the one proposed by Edlefsen and Anderson (1943),

$$u_v = u_{vs} \cdot \exp\left(\frac{-u_w w}{\rho R T}\right) = u_{vs} \cdot h_{r,air}$$

where

- u_{vs} = saturated vapour pressure of pure free water;
- w = molecular mass of water vapour;
- R = universal gas constant;
- $h_{r,air}$ = relative humidity of air

VADOSE/W evaluates the surface boundary conditions, by coupling the moisture and heat stress states at the ground surface with climate conditions acting above the ground surface. In order to obtain the atmospheric coupling, the code calculates the soil evaporative flux based on the Penman-Wilson equation (Wilson, 1990)

$$AE = \frac{\Gamma Q + \upsilon E_a}{\upsilon A + \Gamma}$$

where

- AE = actual vertical evaporative flux from soil surface;
- Γ = slope of the $u_{vs} - T$ curve (saturated vapour pressure – temperature);
- Q = net radiant energy available at the soil surface;
- υ = psychrometric constant;
- $E_a = f(u) \cdot P_a \cdot (B - A)$
- $f(u) = 0.35 (1 + 0.15 U_a)$, function dependent on wind speed, surface roughness and eddy diffusion;
- U_a = wind speed;
- P_a = vapour pressure in the air above the evaporating surface;
- $B = 1/h_{r,air}$, inverse of the relative humidity of the air;
- $A = 1/h_r$, inverse of the relative humidity of the soil surface.

So doing, the equation that calculates the actual evaporation AE needs data about net radiation, wind speed, relative humidity of air and relative humidity of soil surface. Taking into account the assigned latitude and season as well as internally calculated ground surface albedo, the code calculates the net radiation Q available at the soil surface on the basis of the daily climate input data assigned at each time-step in terms of:

- maximum and minimum values of air temperature;
- maximum and minimum values of relative humidity of air;
- rainfall;
- average wind speed.

4.1.2.2 Description of the main commercial codes (regional scale) (UNISA)

Rainfall-induced shallow landslides represent one of the most insidious landslide phenomena (Hungri et al. 2001), because of their high potential of causing damage and human losses. This is due to: the scarcity of warning signs in the pre-failure stage when monitoring systems are not available; the collapse and the frequent high velocities in the post-failure phase; and the increase of the mobilised volumes during the downhill path, due to the erosion of further soil and/or rock masses.

These landslides can involve different soils whose mechanical characteristics vary significantly with differences in water content, sediment size and sorting. They can be triggered by different factors, either natural or related to human activities; among natural factors, rainfall is certainly one of the most frequent causes of occurrence. Significant examples are provided by multiple shallow phenomena periodically occurring in New Zealand (Crozier 2005), in the Seattle area - Washington (Baum et al. 2005), in California (Coe and Godt 2001; Coe et al. 2004), as well as in Campania - southern Italy (Fiorillo and Wilson 2004; Guadagno and Revellino 2005; Pareschi et al. 2000; Cascini 2004).

The relevance of consequence makes the assessment of the landslides susceptibility a fundamental issue towards the forecasting of these phenomena (Fell et al. 2008a). To this aim, during last decades, several and very different approaches have been proposed in the scientific literature, so that a unique and systematic classification appears a difficult task.

However, the most common approaches can be broadly divided into qualitative and quantitative ones (Fig. 4.48), in terms of the results they are able to furnish.

Qualitative approaches are essentially subjective and provide a descriptive evaluation of susceptibility while the quantitative ones furnish numerical estimates in terms of the spatial probability of occurrence of the analysed phenomena. Moreover, susceptibility methods can be also direct or indirect (Guzzetti et al. 1999; van Westen 2000; 2004). The first ones are based on the direct assessment of susceptibility through either field investigations or aerial photographs or satellite images; the second ones are stepwise and they assume the direct or indirect interrelation between the landslides distribution and some physical factors characterising the landscape.

According to Hutchinson (1995), Fell et al. (2008a), Soeters and van Westen (1996), van Westen (2000, 2004), all the available methods can be grouped in 3 categories: heuristic methods, statistical methods, physically-based methods.

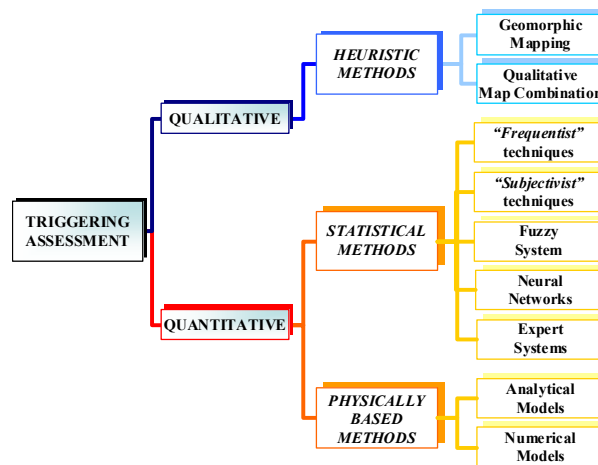


Figure 4.48 - Methods and techniques for triggering analysis

Heuristic methods are mostly qualitative while both statistical and physically-based methods are essentially quantitative indirect methods. In heuristic approach the expert opinion of the person carrying out the zoning is used to assess the susceptibility. The heuristic methods combine the mapping of the landslides and their geomorphologic setting as the main input factors for assessing the susceptibility.

The statistical (or functional) methods, which could be also referred as “black-box” methods, provide functional relationships among the principal factors that contribute to landsliding and past and present spatial distribution of slope failures (Lee et al. 2002; Chung and Fabbri 2003; Corominas et al. 2003; Santacana et al. 2003; Ayalew et al. 2004).

Finally, physically-based (process-based or deterministic) methods are essentially based on the physical laws controlling the landslide.

As pointed out by Cascini (2008) the several applicative examples presented in the scientific literature suggest the use of different approaches at different map scales and levels (Table 4.4). With reference to the map scales, qualitative methods are generally applied at scales ranging from small to medium, (1:250,000 to 1:25,000), while quantitative methods are typically used at medium-large scales, ranging from 1:25,000 to 1:2,000.

Focusing on medium-large scales, among all the approaches, a promising one is represented by the physically based models, whose application, mainly at slope-scale, are also available in the scientific literature. For instance, with reference to landslides from extremely slow to moderate (Cruden and Varnes, 1996), such models have furnished satisfactory evaluation of susceptibility, being able to interpret the mechanical behaviour of the whole phenomenon. As for shallow and flow-type landslides, the available physically based models must be distinguished in respect to the stage of the phenomenon that they are able to analyse. The general approach followed for the analysis of susceptibility concerns with the separate analysis of triggering and propagation stages. Among the models for the analysis of triggering stage, the most widespread ones are those classified as analytical (e.g. Limit Equilibrium Method) and numerical (e.g. Finite Element Method) or some combination. A comprehensive review of these approaches in slope stability analysis is beyond the scope of this work, and further details can be found in Fredlund (1984) and Espinoza et al. (1992). As for the propagation analysis numerical models are the most used ones.

Table 4.4 - Susceptibility methods, procedure and input data (Cascini 2008)

Method	Input	Topography, Landslide inventory, Geology, Geomorphology	Adding Soil classification and depth, Terrain units	Adding Hydrogeology and Geotechnics
	Procedure			
Basic	Heuristic or empirical models	*		
Intermediate	Statistical analyses	*	*	
Sophisticated	Deterministic (physically based or geotechnical) models	*	*	*

To the aim of the present Deliverable, in the following the attention is focused on the method for triggering analysis. In particular, a widely used approach concerns with the mechanical uncoupling of the analyses of the pore water pressure regime with Limit Equilibrium Methods resulting in the calculation of the factor of safety, through the adoption of a rigid-perfectly plastic behaviour of soil.

In recent times, due to the development of powerful GIS platforms, the use of such models has been extended to the analyses of larger areas. Such models, also named “distributed models”, are able to take account of the spatial variability of both in-situ conditions and mechanical properties of the involved soils. Such models are typically applied in a grid-based framework on a cell-by-cell basis.

Different types of distributed models have been proposed in literature and, among them, those that use analytical solutions for the pore-pressure response to rainfall have potential for the analysis of shallow and flow-type slope movements over large areas. On the other hand, it is worth noting that these models rely on several simplifying assumptions that limit their applicability. Proper use of distributed models requires that particular attention is to be paid to the theoretical basis each adopts and, above all, to the proper understanding of the triggering mechanisms to be modeled (Sorbinio et al. 2010).

In what follows, the main features of several physically based models for the analysis of shallow landslides over large areas are described. Particularly, among all the analytical models, the attention is focused on three particular grid-based models: SHALSTAB, TRIGRS and TRIGRS-unsaturated. Finally, some remarks on their use are provided, with specific reference to the required data as well as limitations and potential associated to their conceptual structure.

a) Distributed physically-based models

Distributed physically-based models usually couple a simplified hill-slope hydrological model with the infinite slope stability model (Ward et al. 1982, Montgomery & Dietrich 1994, Terlien et al. 1995, Wu & Sidle 1995, Pack et al. 1998, van Ash et al. 1999, Baum et al. 2002, Savage et al. 2004).

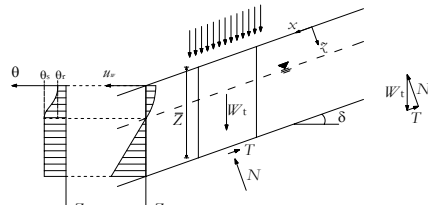


Figure 4.51 - Infinite Slope

The infinite slope model (Fig. 4.49) balances the destabilising forces of gravity and the components of the resisting forces on a failure plane parallel to the slope surface. By adopting the Mohr-Coulomb failure criterion, the factor of safety (FS) is provided by the well-known following equation:

$$FS = \frac{\tan \phi'}{\tan \delta} + \frac{c'}{\gamma_s Z \sin \delta \cos \delta} - \frac{u_w \tan \phi'}{\gamma_s Z \sin \delta \cos \delta} \quad (4.1)$$

where ϕ' is the friction angle, c' the effective cohesion, u_w the pore water pressure, δ the slope angle, γ_s the saturated unit weight of the soil and Z the vertical depth of the failure surface.

Distributed physically-based models can be conceptually classified in respect to the assumptions of the hydrological model used to compute pore water pressures (Fig. 4.50). Commonly, the hydrological model consists in the one-dimensional (vertical) infiltration form of the Richards' equation, in some circumstances combined with the kinematic wave equation for lateral flows or the Darcy's law (Sica 2008). As for the time-dependency of the pore pressure regime, such models can be divided in steady state and transient ones, used either in saturated or unsaturated conditions of soils.

Among the several distributed models developed in a GIS framework in the last two decades, the most used ones are those named SHALSTAB (Montgomery & Dietrich 1994), SINMAP (Pack et al. 1998), dSLAM (Wu & Sidle 1995), TRIGRS (Baum et al. 2002) and TRIGRS-unsaturated (Savage et al., 2004). SHALSTAB, SINMAP, and dSLAM couple a steady state vertical model with the kinematic wave equation for downhill fluxes adopting fully saturated conditions for the soils. In particular, SHALSTAB and SINMAP consider steady state conditions for the kinematic wave resulting in a steady discharge equation, while dSLAM assumes transient conditions for the lateral flows. TRIGRS and TRIGRS-unsaturated are able to analyse vertical infiltration in transient conditions of the pore pressure regime, integrating linearised solutions of Richards' equation, respectively, for saturated soils and for both saturated and unsaturated soils. As for the adopted TMU, all the above models are grid-based except dSLAM based on topographic units. Other models (Frattini et al., 2004), adopt numerical methods or a combination of analytical solutions and numerical techniques to solve the infiltration process while some models couple a tri-dimensional Limit Equilibrium Method with in-situ measurements of pore water pressures.

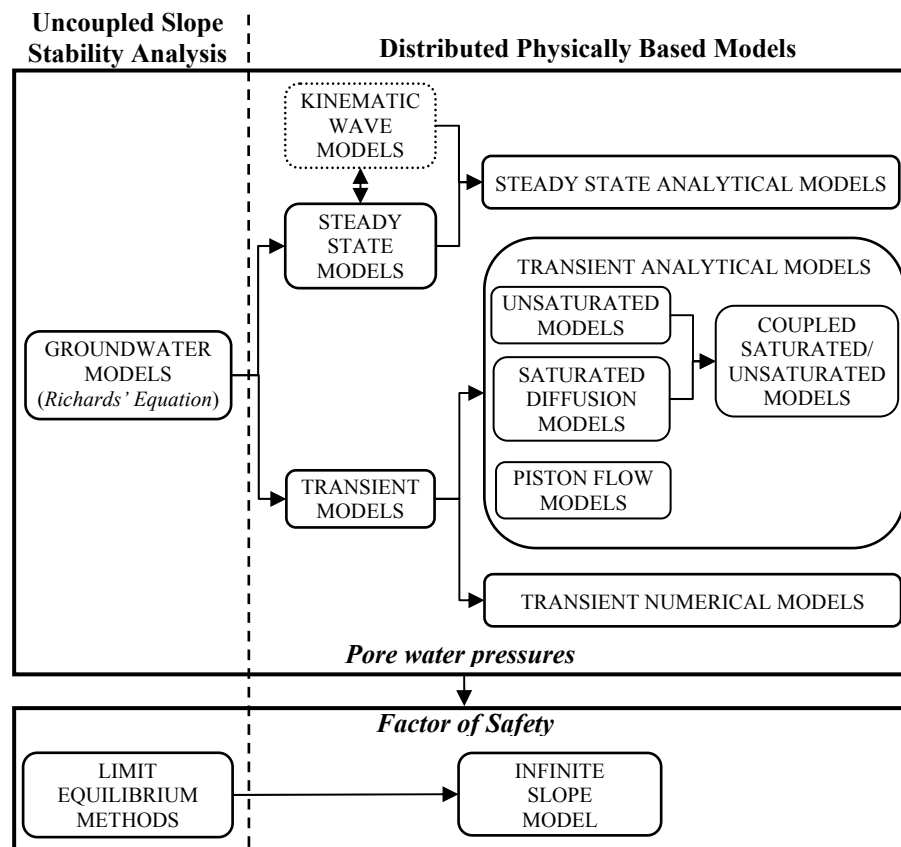


Figure 4.50 - Physically based models.

a.1) Steady State Analytical Models

Steady state analytical models generally assume saturated conditions for the soil and analyse stability conditions of slopes coupling the Infinite Slope model with a simplified hydrologic model. Among the models proposed in literature, SHALSTAB (Montgomery and Dietrich, 1994) and SINMAP (Pack et al., 1998) are the most common ones. They are both based on the same conceptual assumptions although SINMAP adds a simple probabilistic routine to take account of uncertainty of input parameters. The analysis of uncertainty of input parameters is out of the scope of the present work so that, in the following, the basic assumptions of both models are provided referring exclusively to SHALSTAB.

SHALSTAB assumes that rainfall infiltration is in equilibrium with the steady-state, saturated water flow parallel to the slope surface, above an impermeable boundary. It computes the pore pressure balancing the components of the flow in the directions normal and parallel to the slope. In particular, the slope parallel flux (Q_x) is defined by the Darcy's Law:

$$Q_x = K_x b (\bar{z} - z_w) \sin \delta \quad (4.2)$$

where K_x is the saturated conductivity, b the width of the cells, \bar{z} and z_w , respectively, the soil depth and the water table depth measured in the slope-normal direction.

The kinematic wave equation in the x -direction, parallel to the slope, is expressed by:

$$\frac{\partial Q_x}{\partial A} + \frac{\partial(\bar{z} - z_w)}{\partial t} = I \quad (4.3)$$

where t is the time, I is the infiltration rate and A the “geometric contributing area”, representing the upslope area that determines the sub-surface flux through the considered cell. In the case of steady state conditions, time dependence becomes negligible and (4.3) reduces to a steady discharge equation:

$$Q_x = I A \quad (4.4)$$

This last equation combined with (4.1) furnishes the depth of water table so that the pressure head ψ ($= u_w/\gamma_w$) at the base of the slope (z_w) can be computed adopting the following expression:

$$\psi = (\bar{z} - z_w) \cos \delta = \frac{(IA)}{(K_x b \sin \alpha)} \cos \delta \quad (4.5)$$

Finally, combining (4.5) with (4.1), SHALSTAB model allows the evaluation of critical rainfall values (I) providing a Factor of Safety equal to one at the base of the slope.

For each grid cell, SHALSTAB assumes constant thickness, hydraulic, physical and mechanical characteristics of the soil and it computes the topographic attributes, such as the slope angle and the “contributing area” from a Digital Terrain Model.

a.2) Transient Analytical Models

Transient analytical models generally couple the Infinite Slope model with a solution of one-dimensional Richards' equation in transient conditions of pore pressure regime and different conditions of saturation of the soil. Among the most common ones, the two models TRIGRS (Baum et al., 2002) and TRIGRS-unsaturated (Savage et al., 2004) have been selected. They have been considered particularly suitable for the triggering analysis of flowslide and debris flow phenomena involving saturated/tension saturated or unsaturated slopes and frequently triggered by transient rainfall events.

a.2.1) TRIGRS

The TRIGRS model performs transient seepage analysis using the linearised solution of Richards' equation proposed by Iverson (2000) and extended by Baum et al. (2002) to the case of impermeable bedrock located at a finite depth. The infiltration model applies to saturated or tension-saturated initial conditions, so that flow is in the linear range for Darcy's law and the hydraulic diffusivity is approximately constant. Following Iverson (2000) and

Savage et al., (2003), the groundwater flow field is modelled by superposition of a steady component, $\psi_0(Z,0)$, and a transient component, $\Delta\psi(Z,t)$:

$$\psi(Z,t) = \psi_0(Z,0) + \Delta\psi(Z,t) \quad (4.6)$$

The steady seepage component is given by:

$$\psi_0(Z,0) = (Z - d_{w0}) \left(\cos \delta - \frac{I_{Z0}}{K_Z} \right) \cos \delta \quad (4.7)$$

where d_{w0} is the steady-state depth of the water table measured in the Z -direction, I_{Z0} , the steady (initial) surface flux.

For the transient component of seepage, TRIGRS uses a series of Heavyside step functions to implement Iverson's (2000) suggested summation of his original solution, in the case of an impermeable basal boundary at a finite depth They are given by:

$$\begin{aligned} \Delta\psi(Z,t) = & 2 \sum_{n=1}^N \frac{I_{nZ}}{K_Z} H(t-t_n) [D_1(t-t_n)]^{\frac{1}{2}} \sum_{m=1}^{\infty} \left\{ \begin{aligned} & \left[\frac{\text{ierfc} \left[\frac{(2m-1)d_{LZ} - (d_{LZ} - Z)}{2[D_1(t-t_n)]^{\frac{1}{2}}} \right]}{2[D_1(t-t_n)]^{\frac{1}{2}}} \right] \\ & + \left[\frac{\text{ierfc} \left[\frac{(2m-1)d_{LZ} + (d_{LZ} - Z)}{2[D_1(t-t_n)]^{\frac{1}{2}}} \right]}{2[D_1(t-t_n)]^{\frac{1}{2}}} \right] \end{aligned} \right\} + \\ & - 2 \sum_{n=1}^N \frac{I_{nZ}}{K_Z} H(t-t_{n+1}) [D_1(t-t_{n+1})]^{\frac{1}{2}} \sum_{m=1}^{\infty} \left\{ \begin{aligned} & \left[\frac{\text{ierfc} \left[\frac{(2m-1)d_{LZ} - (d_{LZ} - Z)}{2[D_1(t-t_{n+1})]^{\frac{1}{2}}} \right]}{2[D_1(t-t_{n+1})]^{\frac{1}{2}}} \right] \\ & + \left[\frac{\text{ierfc} \left[\frac{(2m-1)d_{LZ} + (d_{LZ} - Z)}{2[D_1(t-t_{n+1})]^{\frac{1}{2}}} \right]}{2[D_1(t-t_{n+1})]^{\frac{1}{2}}} \right] \end{aligned} \right\} \end{aligned} \quad (4.8)$$

where d_{LT} is the depth of the impermeable basal boundary measured in the Z -direction, I_{nZ} is the surface flux of a given intensity for the n^{th} time interval, N is the total number of intervals, $H(t-t_n)$ is the Heavyside step function and ierfc is of the form:

$$\text{ierfc}(\eta) = \frac{1}{\sqrt{\pi}} \exp(-\eta^2) - \eta \text{erfc}(\eta) \quad (4.9)$$

where η is a generic function and $\text{erfc}(\eta)$ is the complementary error function.

The pressure heads at different depths and time intervals are obtained substituting (4.7) and (4.8) into (4.6). Finally, combining (4.6) and (4.1), for each cell, TRIGRS provides the vertical and temporal distribution of factors of safety. The TRIGRS model uses also a simple method for routing of surface runoff from cells that have excess surface water to adjacent down-slope cells where it can either infiltrate or flow farther down slope.

a.2.2) TRIGRS-unsaturated

TRIGRS-unsaturated is able to analyse stability conditions of large areas involving soil characterised by varying conditions of saturation. Such model considers the Infinite Slope as a two-layer system (Fig. 4.51) consisting of a saturated zone with a capillary fringe above the water table that is overlain by an unsaturated zone that extends to the ground surface.

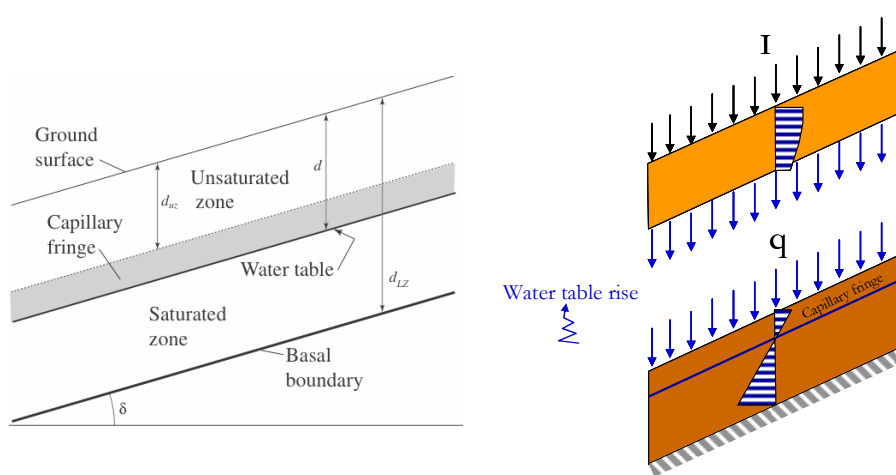


Figure 4.51 - TRIGRS-unsaturated scheme (modified from Savage et al., 2004)

According to this scheme, it couples a solution for transient unsaturated infiltration, derived from original solution proposed by Srivastava and Yeh (1991) to the original TRIGRS' equation (Savage et al. 2004).

For the unsaturated layer, the model adopts the soil water characteristic curve proposed by Gardner (1958):

$$K(\psi) = K_s \exp(\bar{\alpha}\psi) \tag{4.10}$$

$$\theta = \theta_r + (\theta_s - \theta_r) \exp(\bar{\alpha}\psi) \tag{4.11}$$

where K_s is the saturated hydraulic conductivity, $\bar{\alpha}$ is the parameter of Gardner's curve, θ_s is the water content at saturation and θ_r is the residual water content.

The solution of TRIGRS-unsaturated for time-varying flux at surface is obtained by substituting the Gardner' equations in the one-dimensional Richards' equation and solving the resulting equation in terms of K (Srivastava and Yeh 1991). The pore water pressures and volumetric water contents are derived from (4.11). Moreover, the model computes the flux at the base of the unsaturated zone adopted as upper boundary condition for the lower layer. The pore water pressures characterising the saturated layer are obtained from the original solution of TRIGRS. Finally, substituting the pore water pressure regime of both layers in (4.1), for each cell, TRIGRS-unsaturated model furnishes the safety factors at different depths and time intervals. Particularly, for the unsaturated zone, the model takes account of an average weight of soil above the water table and the increase in soil strength due to negative pore water pressures. Such last condition is considered in the model assuming the equation of effective stresses proposed by Bishop (1959).

b) Remarks on the use of Distributed Models

b.1) Required data

All the models selected for the analysis of flowslide and debris flow phenomena (SHALSTAB, TRIGRS and TRIGRS-unsaturated) adopt a discretisation of the landscape based on grid cells. To each cell are attributed a set of characteristics which can be essentially

grouped in two categories: internal, typical of the setting of the analysed area, and external, regarding the triggering factors.

As for the features of the area, the main data required are:

- Topographical features
- Geological, Geomorphological and Hydrogeological settings
- Geotechnical properties

Topographical data are typically represented as Digital Terrain Model (DTM) that is a digital (numerical) representation containing location and elevation of ground surface (Wilson and Gallant 2000). DTMs provide essentially elevations and a number of other parameters directly used in physically based models. Among such derived features, slope angle, flow direction and contributing area are the most used ones while other parameters can be derived by means of specific GIS softwares. DTMs may be prepared in a number of ways. Older methods devoted to small areas, involve interpolating digital contour maps that may have been produced by analytic photogrammetry or land surveys (for small areas). Recently, a promising method is based on remote sensing techniques which show greater accuracy and precision but some limitations. The accuracy of a DTM highly influences both elevation and DTM-derived parameters and has to be considered significant for triggering analysis. Several factors play an important role for accuracy of DTM: sampling density (elevation data collection method), grid resolution, interpolation algorithm, vertical resolution. Particularly, the influence of such factors, resulting in elevation and slope angle errors represents a typical limitation of high resolution LiDAR DTMs.

Geological, Geomorphological and Hydrogeological data are essentially gained from field survey and in-situ investigations performed by expert geoscientists. Particularly, Geology furnishes the characterisation of bedrock layers, the identification of different lithotypes present within the area as well as information about spatial distribution of cover depths and stratigraphical setting. Geomorphological data concern with past landslide distribution, cracks, discontinuities, natural and artificial cuts and all the morphological features which characterise the landscape. Finally, Hydrogeology allows the characterisation of deep and subsurface circulation of water, resulting generally in map distribution of underground flows and springs (perennial, seasonal, temporary). Among these data, bedrock setting, morphological and hydrogeological features allow the imposition of adequate boundary conditions and their accuracy has a great influence on the analysis. Distributed physically based models are, in fact, able to take into account spatially varying conditions essentially related to gradually variable settings. Particularly, all discontinuities in landscape setting such as morphological cuts, outlets and springs, pose limitations in the use of such models contradicting the basic hypothesis of infinite slope condition.

Geotechnical data can be derived from in-situ investigations and laboratory tests. Main data are related to physical, mechanical and hydraulic properties of soils. As for physical and mechanical properties, laboratory tests are devoted to the characterisation of grain size distribution, unit weights, porosity of soils and estimation of strength parameters. As for hydraulic aspects, laboratory and in-situ investigations are aimed at the characterisation of conductivity, water content and diffusivity under the condition of saturation typical of the in place soils. Physically based models are most sensitive to all these data. Particularly, hydraulic parameters assume a relevant role in the analyses influencing sensibly pore water

pressure regime.

With reference to data regarding triggering event, a fundamental role is played by records of rainfall intensities and measurements of groundwater levels. Particularly, the analysis of precipitations is necessary to estimate upper boundary conditions and intensity-duration curves to be used for the forecasting of triggering phenomena. As for the ground water level, transient models require the user to specify the initial steady groundwater flow field that can be estimated by means of in-situ investigations or, alternatively, indirect seepage analysis.

Finally, accuracy of all the above studies and investigations depends on the complexity of the analysed area and occurring phenomena so that all the process must be pursued at opportune study and map scales to be selected before a preliminary characterisation and eventually changed during the analysis. Usually, if the purpose of the triggering analysis is a map at 1:5000 scale, studies and investigations have to be conducted at scales larger than 1:5000 (detailed scale).

b.2) Conceptual limitations and potential

Distributed physically based models pose some limitations which derive from the simplified assumptions they adopt in computing pore water pressure. According to Iverson (2000) the different assumptions can be interpreted referring to opportune normalised variables.

Following Iverson (2000), the key parameters are the hydraulic conductivities in the lateral (x and y) directions and slope-normal (z) direction, K_L and K_z . so that the normalized conductivities K^* with reference to the maximum (saturated) conductivity anywhere within the flow domain, K_S , can be expressed as:

$$K^*_{L} = \frac{K_L(\psi)}{K_S}, \quad K^*_z = \frac{K_z(\psi)}{K_S} \quad (4.12)$$

Moreover, the hydraulic diffusivities (D_L , D_z , D_0) are represented by:

$$D_L = \frac{K_L(\psi)}{C(\psi)}, \quad D_z = \frac{K_z(\psi)}{C(\psi)}, \quad D_0 = \frac{K_S}{C_0} \quad (4.13)$$

where $C(\psi) = \partial\theta/\partial\psi$ is the change in volumetric water content per unit change in pressure head and C_0 is the minimum value of $C(\psi)$, typically observed when the soil becomes saturated.

Assuming as spatial scales the slope normal depth (H) and the upslope topographic area (A), (Fig. 4.52) normalised pressure head (ψ^*) and spatial coordinates (x^* , y^* , z^*) can be expressed as:

$$\psi^* = \frac{\psi}{H}, \quad x^* = \frac{x}{\sqrt{A}}, \quad y^* = \frac{y}{\sqrt{A}}, \quad z^* = \frac{z}{H} \quad (4.14).$$

On the other hand, two timescales can be assumed in conjunction with the above two length scales, referring to the saturated diffusivity (D_0):

$$t_A = \frac{A}{D_0}, \quad t_H = \frac{H^2}{D_0} \quad (4.15)$$

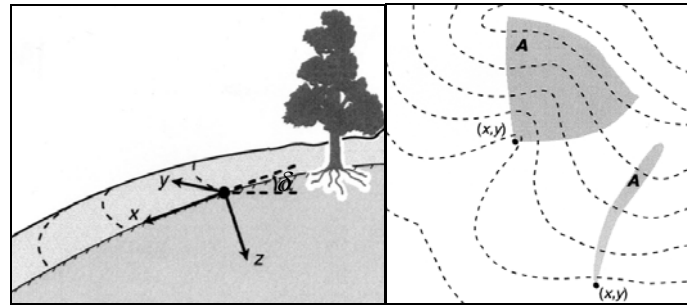


Figure 4.52 - Local coordinate system (modified from Iverson, 2000)

The timescale t_A approximates the minimum time necessary for strong lateral pore pressure transmission from the area A to the point (x, y, H) while, t_H estimates the minimum time necessary for strong slope-normal pore pressure transmission from the ground surface to depth H (Iverson, 2000; Iverson & Major, 1987).

Finally, the ratio of the timescales t_A and t_H furnishes the reference length scale ratio:

$$\varepsilon = \sqrt{\frac{t_H}{t_A}} = \frac{H}{\sqrt{A}} \quad (4.16)$$

Particularly, the infinite slope condition is related to values of the above ratio much smaller than the one ($\varepsilon \ll 1$). Under this last condition, the adoption of the above variables and the selection of an opportune normalised time variable allow the analysis of infiltration process by means of simplified forms of the Richards' equation.

Taking into account the previous considerations, the first condition to be checked for the application of the distributed physically-based models is represented by the infinite slope conditions expressed by the values of (4.16) much smaller than unity (Fig. 4.53). Such values can be computed for the whole area once estimated cover depth distribution and contributing area. Next step is devoted to the comparison between duration of critical rainfall event t and the value of the timescale t_A . The estimation of timescale poses some difficulties above all related to the estimation of a reference contributing area that is representative of the whole study area. According to Iverson (2000), an error in calculating the contributing area could induce an error in the selection of distributed models and, as a consequence, in the analysis of triggering phenomena. The best way to proceed concerns with the computation of the geometric mean of the contributing area pertaining, respectively, to the upper boundary and the closing section of the watershed (Iverson, 2000, Sica 2008). Based on the comparison between t and t_A steady state or transient models can be selected for the analysis (Fig. 4.53).

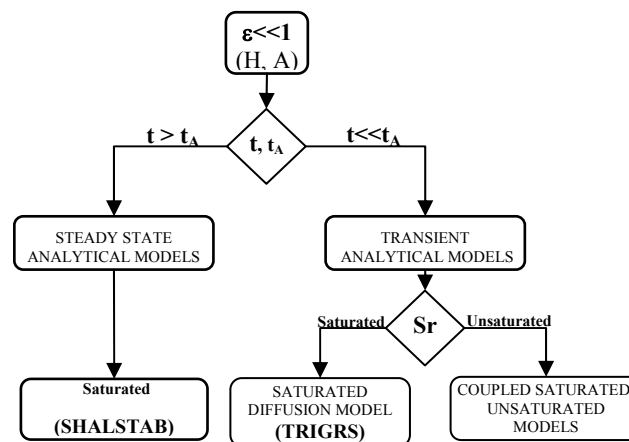


Figure 4.53 - Flow chart for the use of distributed models (from Sica 2008)

As for transient models, it must be noted that TRIGRS and TRIGRS-unsaturated are not suitable for modelling long-term effects of alternating periods of rainfall and evapotranspiration, and choosing the correct initial conditions for a given storm is critical to obtaining accurate results. Moreover, the results are very sensitive to the initial conditions so that careful investigations or analysis must be conducted. The simple method for routing surface runoff does not account for evapotranspiration and cannot be used to estimate stream flow.

In conclusion, in order to achieve significant results, the application of distributed physically based models requires a deep understanding of the conceptual assumptions, the accurate definition over broad regions of the in situ conditions of soils as well as of the pore pressure regime characteristics. Consequently, they generally need abundant and accurate spatial information. Moreover, they are sensitive to some of the required input data such as hydraulic properties of soils, initial steady-state groundwater conditions and soil depths, whose correct evaluation is often possible only using empirical models or inverse deterministic analyses (Godt et al. 2008; Salciarini et al. 2006; Sorbino et al. 2007).

On the other hand, the applicability of distributed models is strongly influenced by the adopted theoretical assumptions which make their use suitable for some particular conditions. To this aim one of the central component for their correct use is represented by a clear understanding of the triggering mechanisms of the analysed landslide phenomena, whose absence can severely lead to inappropriate results concerning the identification, size and extension of triggering areas (Sorbino et al. 2010).

4.1.2.3 Description of the available home-made codes

(EPFL)

a) LAGAMINE

LAGAMINE is a 2D/3D Finite Element Code developed at the University of Liège in Belgium since the early 80's (Charlier, 1987; Collin, 2003). The code was originally developed for non-linear large deformations problems. A PC version called CONVILAG exists, containing the LAGAMINE code, as well as a pre- and postprocessor. However, it is also possible to use an external, more user-friendly pre-processor such as GiD. The coupled finite element formulation allows for solving complex thermo-hydro-mechanically coupled multiphase problems.

List of features

- 2D/3D Finite Element Code
- Integrated pre- and postprocessor
- 3 phase physics (gas, liquid and solid) in a coupled THM finite element formulation
- Analysis types: plane strain, plane stress, axisymmetric and 3D analysis. The possible analysis types depend on the chosen constitutive laws for the solid and fluid phases.
- Problem types: deformation, hydraulic and thermal flow (steady or transient, saturated or unsaturated), coupled deformation and flow.
- Quasi-static and time dependent calculations
- Time dependent boundary conditions: arbitrary heat or fluid flow at the model boundaries.
- Non-linear small and large deformations (Updated Lagrangian formulation)
- Set of advanced constitutive models for soils and rocks
- Safety Factor analysis for the frictional constitutive model PLASOL and Mohr Coulomb (strength reduction method)
- Bifurcation analysis

Sign convention

Compressive stresses in the solid matrix are negative, but positive in the fluid phase.

Multiphysics

It is possible in LAGAMINE to treat a problem coupling fluid and heat transfer with solid deformations. Phase changes in the fluid phase can be taken into account. Water may be present as a liquid or as vapour. For the coupled finite element formulation five equilibrium equations are verified in 2D. Hence, each element has five degrees of freedom: the displacements in two directions x and y , two fluid pressures for two different fluids (i.e. one liquid and a gas mixture) and the temperature. The values of those variables are obtained in any point of the domain by applying the interpolation function to their nodal values.

Continuum mechanics of porous media

General equations

LAGAMINE has a considerable number of simple and complex constitutive models which use certain types of finite element formulations. For the fully coupled THM framework, the finite element type MWAT2 has been developed (Collin, 2003). For the hydraulics, a two-phase model (WAVAT) with phase transformations is available. Integrating a fully coupled constitutive model, such as ACMEG (François and Laloui, 2008) gives the possibility to solve complex multiphase engineering problems. For the most exhaustive case of a three-phase medium, the continuum mechanics are described by the following set of equations:

- 1) Linear momentum balance equation:

$$\underline{\underline{\sigma}}_{ij,j} + \underline{b}_j = 0$$

Where σ_{ij} is the 2nd rank total stress tensor and b_j are internal body forces.

- 2) Mass conservation is formulated for every chemical component in the porous media. Water may be present as liquid or vapour. Air may be present as dry air or dissolved in the liquid phase.

Water and vapour mass balance equation:

The mass conservation of the water components is a combination between the conservation equation for liquid water and vapour. The diffusion of dissolved air in the water is neglected. Hence, the liquid water flux doesn't contain any non-advective term. The water vapour flux is composed of an advective term for the movement of the gas phase and a non-advective term for the vapour diffusion in the gas phase:

$$\frac{\partial}{\partial t}(\rho_w n S_{r,w}) + \text{div}(\rho_w \underline{q}_l) + \frac{\partial}{\partial t}(\rho_g n S_{r,g}) + \text{div}(\underline{i}_v) + \text{div}(\rho_v \underline{q}_g) - Q_v - Q_w = 0$$

Where ρ_w and ρ_g are the water and gas mass density, n is soil porosity, $S_{r,w}$ and $S_{r,a}$ are the water and gas relative degree of saturation, q_l and q_g are the mean velocity of the liquid and gas phases, i_v is the non-advective vapour flux, ρ_v is the water vapour density and Q_v and Q_w are vapour and water source terms.

Dry air mass balance equation:

The mass conservation of the air components is written as the combination of the mass conservation of dry air and dissolved air in the water. The quantity of dissolved air is calculated using Henry's law. The flux of dissolved air is simplified to the advective term of the liquid phase. The dry air flux contains an advective term for the movement of the gas phase and a non-advective term for the diffusion of the dry air within the gas phase.

$$\frac{\partial}{\partial t}(\rho_a n S_{r,g}) + \text{div}(\rho_a \underline{q}_g) + \text{div}(\underline{i}_a) + \frac{\partial}{\partial t}(\rho_a H^s n S_{r,w}) + \text{div}(\rho_a H^s \underline{q}_l) - Q_a - Q_{a-d} = 0$$

Where ρ_a is the dry air mass density, i_a is the non-advective dry air flux, H^s is the Henry coefficient and Q_a and Q_{a-d} are a dry air, respectively dissolved air source term.

3) Heat conservation

The enthalpy conservation equation is simplified to the term for heat transfer. Additionally, a term called the latent heat of vaporisation L is introduced in order to take into account the necessary energy for the water to vapour phase transformation. For a given porous medium with the same temperature in each phase, the enthalpy conservation equation is written as follows:

$$\dot{S}_T + \dot{S}_v L + \text{div}(i_{\text{cond}}) + \text{div}\left(\sum_i H_i V_i^{\text{eff}}\right) + \text{div}(V_v)L - Q_T = 0$$

Where S_T and S_v are the quantity of stored heat, respectively vapour and L is the latent heat of vaporisation. The heat transfer has two parts: i_{cond} for the conduction flux and the summing term which stands for the heat quantity transported by the different components of the medium. V_v is the vapour mass flux and Q_T is a heat source term.

4) Constitutive behaviour

$$\dot{\sigma}'_{ij} = C_{ijkl} \dot{\epsilon}_{kl}$$

Where C_{ijkl} is the 4th rank constitutive tensor and $\dot{\epsilon}_{kl}$ is the strain rate.

5) Compatibility equation

$$\underline{\underline{\epsilon}}_{ij} = \frac{1}{2}(\underline{u}_{i,j} + \underline{u}_{j,i})$$

Where ϵ_{ij} is the small strain tensor and u_i is the solid displacement vector.

Effective stress

Depending on the problem type, different effective stress frameworks may be chosen (i.e. classical Terzaghi, Terzaghi with the negative pressure term for suction, Biot formulation, Bishop). For the fully coupled element type MWAT2, the Bishop's model is proposed:

$$\underline{\underline{\sigma}}'_{ij} = \left(\underline{\underline{\sigma}}_{ij} + p_a \underline{\underline{\delta}}_{ij}\right) - S_{r,w} (p_a - p_w) \underline{\underline{\delta}}_{ij}$$

Where p_a is the air pressure and p_w the water pressure.

Elasto-plasticity

LAGAMINE offers among others constitutive models of the type “internal friction” (i.e. PLASOL) and “CamClay” (i.e. ACMEG). PLASOL is an elasto-plastic constitutive law for solid elements at constant temperature with linear elasticity. Isotropic hardening/softening of friction angle and cohesion is possible. The strength reduction algorithm is integrated for this model. ACMEG is an elasto-plastic constitutive law for unsaturated soils under non-isothermal conditions with two plastic mechanisms. Linear or non-linear thermo-elasticity, progressive plasticity inside the yield limit, elasto-plasticity with isotropic hardening/softening and thermo-plasticity, critical state concept, cyclic behaviour through the isotropic plastic mechanism and the suction effect on the evolution of preconsolidation pressure are taken into account.

Fluid flow and storage

1) Water and vapour flow and storage

Darcy’s law for fluid flow in a partially or fully saturated medium:

$$\underline{q}_l = -\frac{k_{\text{int}}^{\text{sat}} \cdot k_{r,w}}{\mu_w} \cdot \left[\underline{\text{grad}}(p_w) + \rho_w g \cdot \underline{\text{grad}}(z) \right]$$

Where $k_{\text{int}}^{\text{sat}}$ is the intrinsic permeability tensor for a fully saturated porous medium, $k_{r,w}$ is the water relative permeability and μ_w is the fluid viscosity. LAGAMINE offers a large choice of water and air relative permeability curves.

For the mixture of the two gases, the diffusive fluxes have the following property:

$$\sum_j \underline{i}_j = 0$$

Hence, $\underline{i}_v = -\underline{i}_a$.

The non-advective flux of the water vapour is idealised by Fick’s diffusion law:

$$\underline{i}_v = -n \cdot S_{r,g} \cdot \tau \cdot D \cdot \rho_g \cdot \underline{\text{grad}}\omega_v$$

Where τ is the tortuosity of the porous medium, D is the temperature and pressure dependent diffusion coefficient and $\omega_v = \rho_v / \rho_g$ is the vapour mass content in the gas mixture.

The water and vapour storage law is obtained from the mass conservation of the components and can be written as follows:

$$\frac{\partial}{\partial t}(S_w \cdot V + S_v \cdot V) = \frac{\partial}{\partial t}(\rho_w \cdot n \cdot S_{r,w} \cdot V + \rho_v \cdot n \cdot S_{r,g} \cdot V)$$

Where S_w and S_v are the water and vapour storage quantities and V is a reference volume. The storage function depends on mass density, saturation and porosity variations. It is further possible to express the porosity variations as a function of volumetric strains.

2) Air and gas flow and storage

The flow of the gas phase is also described by Darcy's law, generalized to the case of an unsaturated medium.

Again, the diffusion of the dry air is described by Fick's law, adapted to the case of a porous medium.

The storage function of dry and dissolved air for a reference volume V is written as:

$$\frac{\partial}{\partial t}(S_a \cdot V + S_{a-d} \cdot V) = \frac{\partial}{\partial t}(\rho_a \cdot n \cdot S_{r,g} \cdot V + H^s \cdot \rho_a \cdot n \cdot S_{r,w} \cdot V)$$

Where S_a and S_{a-d} are the dry and dissolved air storage quantities.

3) Heat transfer and storage

Heat transfer is divided into three components: conduction idealised by Fourier's law considering the thermal conductivity of all components of the porous medium, convection due to the fluid fluxes and a latent flux due to vaporisation.

$$\begin{aligned} \underline{V}_T + \underline{V}_v L &= -\Gamma_m \cdot \nabla T \\ &+ \left[c_{p,w} \cdot \rho_w \cdot \underline{q}_l + c_{p,a} \left(\underline{i}_a + \rho_a \cdot \underline{q}_g \right) + c_{p,v} \left(\underline{i}_v + \rho_v \cdot \underline{q}_g \right) \right] \cdot (T - T_0) \\ &+ \left[\underline{i}_v + \rho_v \cdot \underline{q}_g \right] \cdot L \end{aligned}$$

Where $c_{p,i}$ is the thermal capacity of component i and Γ_m is the averaged thermal conductivity of the porous medium.

The storage function for the enthalpy is mainly a function of the temperature and saturation variation. Each component of the porous medium, as well as the latent term for vaporisation contributes to the system's total enthalpy:

$$\begin{aligned} \frac{\partial}{\partial t}(S_T \cdot V + S_v \cdot L \cdot V) &= \frac{\partial}{\partial t} \left[n \cdot V \cdot (\rho_w \cdot S_{r,w} \cdot c_{p,w} + \rho_a \cdot S_{r,g} \cdot c_{p,a} + \rho_v \cdot S_{r,g} \cdot c_{p,v}) \cdot (T - T_0) \right] \\ &+ \frac{\partial}{\partial t} \left[(1-n) \cdot V \cdot \rho_s \cdot c_{p,s} \cdot (T - T_0) \right] \\ &+ \frac{\partial}{\partial t} \left[n \cdot S_{r,g} \cdot \rho_v \cdot L \cdot V \right] \end{aligned}$$

Retention behaviour

There is a large choice of water and air retention models in LAGAMINE, from the classical Van Genuchten relationship (1980) to more complex, coupled relationships, such as the model proposed by Nuth and Laloui (2008). The latter accounts for the effects of mechanical deformation and temperature on the retention curve by means of a variable air entry value. An elasto-plastic approach with kinematic hardening is used to describe the hydric hysteresis for drying and wetting cycles (Figure 4.54).

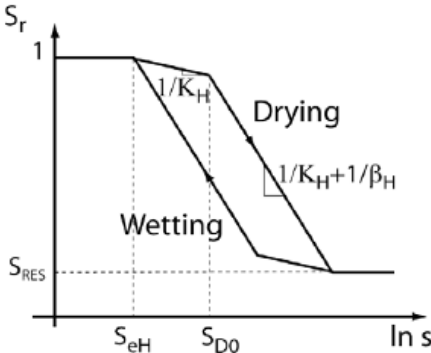


Figure 4.54 - Water retention model proposed by Nuth & Laloui (2008)

Modelling natural slopes subjected to rainfall infiltration

In LAGAMINE calculation sequences are not run automatically. The result file of the stress state initialisation needs to be copied and renamed to the input file for the 2nd calculation. When using an elasto-plastic constitutive law, gravity needs to be introduced step-wise by means of distributed surface loads in the initialisation step. It is possible to prescribe pore pressures and displacements in any point of the finite element mesh (Figure 4.55).

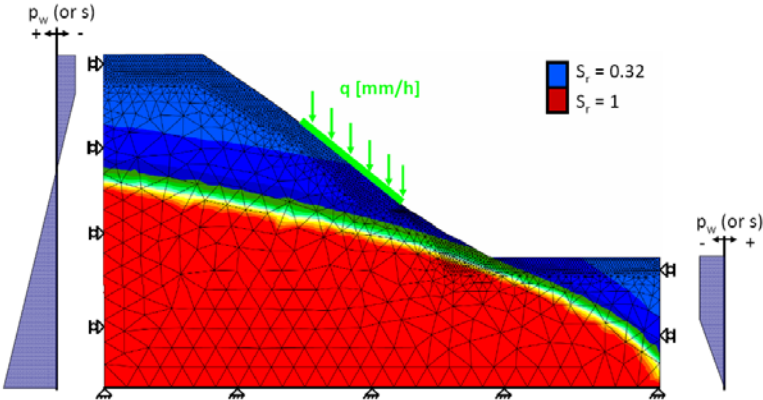


Figure 4.55 - Problem initialisation – Gravity loads and pore pressures are introduced gradually. The red colour indicates a fully saturated medium

Any given rain infiltration pattern can be simulated either as a prescribed boundary flux or a prescribed boundary pressure. Hence, it is possible to simulate drying and wetting cycles at the slope surface. The integrated postprocessor DESFIN allows displaying contour maps of

stresses and state variables (Figure 4.56a). Nodal and Gauss point variables can be recorded in data files and processed separately with any suitable software (Figure 4.56b).

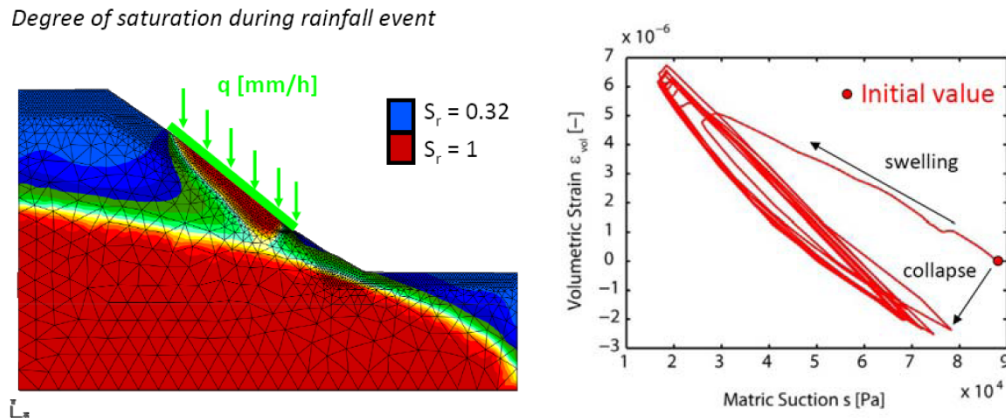


Figure 4.58 - Simulation of rainfall infiltration in a partially saturated soil (a); Gauss point data: influence of drying and wetting cycles on the volumetric behaviour of collapsible soils (b)

b) CODE-BRIGHT

(UPC)

CODE_BRIGHT is a general-purpose finite element program developed by the Department of Geotechnical Engineering and Geosciences of the Universitat Politècnica de Catalunya (DIT-UPC) for the analysis of coupled thermo-hydro-mechanical (THM) phenomena in geological media.

The development of CODE_BRIGHT started in 1990 with the purpose of modelling the response of saline materials in the context of deep nuclear waste disposal (Olivella et al. 1996). The initial capabilities were soon extended to include a wider range of geological materials and, in particular, unsaturated soils. General transport processes and their interaction with the material mechanical behaviour were added in order to develop a generalised tool for THM analysis. CODE_BRIGHT has been extensively verified and validated in international benchmark exercises (EVEGAS, CATSIUS CLAY, C2S2). It has been applied to the analysis of different geoenvironmental schemes and waste disposal designs. In the recent past many other relevant geotechnical problems involving saturated/unsaturated flow and stress strain behaviour have been analysed with the help of CODE_BRIGHT.

CODE_BRIGHT uses GiD system for preprocessing and post-processing. GiD is developed by the International Center for Numerical Methods in Engineering (CIMNE). GiD is an interactive graphical user interface that is used for the definition, preparation and visualisation of all the data related to numerical simulations. This data includes the definition of the geometry, materials, conditions, solution information and other parameters. The program can also generate the finite element mesh and write the information for a numerical simulation program in its adequate format for CODE_BRIGHT. It is also possible to run the numerical simulation directly from the system and to visualize the resulting information without transfer of files.

For geometry definition, the program works quite like a CAD (Computer Aided Design) system. The most important difference is that the geometry is developed in a hierarchical

mode. This means that an entity of higher level (dimension) is constructed over entities of lower level; two adjacent entities will then share the same lower level entity.

All materials, conditions and solution parameters can also be defined on the geometry without the user having any knowledge of the mesh. The meshing is performed once the problem has been fully defined. The advantages of doing this are that, using associative data structures, modifications can be made on the geometry and all other information will be updated automatically.

Full graphic visualisation of the geometry, mesh and conditions is available for comprehensive checking of the model before the analysis run is started. More comprehensive graphic visualisation features are provided to evaluate the solution results after the analysis has been performed. This post-processing user interface is also customisable depending on the analysis type and the results provided.

In porous media (as the natural slope), subjected to thermal, hydraulic and mechanical conditions relevant thermo-hydro-mechanical (THM) phenomena take place. In fact, there exist a number of mutual interactions that must be taken simultaneously into account in analyses. For instance, strains due to thermal loading will induce stress variations and changes in mass storage terms and hydraulic conductivity. The thermal expansion of the water in the pores itself causes changes in the degree of saturation or, if the material is saturated or quasi-saturated, increases of water pressure. Thermal induced vapor diffusion and the dependence of water viscosity on temperature also affect significantly the water transfer process.

On the other hand, changes in hydraulic conditions is induced by variation in degree of saturation induced by rainfall due to pore water pressure and pore gas pressure changes. Porosity changes due to volumetric strain (as swelling or collapse for saturation) influence pore pressure distributions because of associated variations in storage terms and hydraulic conductivity. An unavoidable consequence of all those phenomena interacting simultaneously is the need to carry out coupled THM analysis in which all the main aspects of the problem can be considered in an integrated way. Such a formulation and the numerical approach adopted to solve the governing equations are presented in the USERguide (https://www.etcg.upc.edu/recerca/code_bright).

Basic formulation features

A porous medium composed by solid grains, water and gas is considered. Thermal, hydraulic and mechanical aspects will be taken into account, including coupling between them in all possible directions. The problem is formulated in a multiphase and multispecies approach.

The three phases are:

- solid phase (s) : mineral
- liquid phase (l) : water + air dissolved
- gas phase (g) : mixture of dry air and water vapour

The three species are:

- solid (-) : the mineral is coincident with solid phase
- water (w) : as liquid or evaporated in the gas phase
- air (a) : dry air, as gas or dissolved in the liquid phase

The following assumptions and aspects are taken into account in the formulation of the problem:

- Dry air is considered a single species and it is the main component of the gaseous phase. Henry's law is used to express equilibrium of dissolved air.
- Thermal equilibrium between phases is assumed. This means that the three phases are at the same temperature
- Vapour concentration is in equilibrium with the liquid phase. Psychrometric law expresses its concentration.
- State variables (also called unknowns) are: solid displacements, \mathbf{u} (three spatial directions); liquid pressure, P_l ; gas pressure, P_g ; and temperature, T .
- Balance of momentum for the medium as a whole is reduced to the equation of stress equilibrium together with a mechanical constitutive model to relate stresses with strains. Strains are defined in terms of displacements.
- Small strains and small strain rates are assumed for solid deformation. Advective terms due to solid displacement are neglected after the formulation is transformed in terms of material derivatives (in fact, material derivatives are approximated as eulerian time derivatives). In this way, volumetric strain is properly considered.
- Balance of momentum for dissolved species and for fluid phases are reduced to constitutive equations (Fick's law and Darcy's law).
- Physical parameters in constitutive laws are function of pressure and temperature. For example: concentration of vapour under planar surface (in psychrometric law), surface tension (in retention curve), dynamic viscosity (in Darcy's law), strongly depend on temperature.

Governing equations

The governing equations for non-isothermal multiphase flow of water and gas through porous deformable saline media have been presented by Olivella et al. (1994). A detailed derivation is given there.

The equations that govern this problem can be categorised into four main groups. These are: balance equations, constitutive equations, equilibrium relationships and definition constraints. Equations for mass balance were established following the compositional approach. That is, mass balance is performed for water, air and salt species instead of using solid, liquid and gas phases. Equation for balance of energy is established for the medium as a whole. The equation of momentum balance for the porous medium is reduced to that of stress equilibrium.

Constitutive law

The following constitutive laws are available:

HYDRAULIC AND THERMAL CONSTITUTIVE MODELS (a) RETENTION CURVE INTRINSIC PERMEABILITY LIQUID PHASE RELATIVE PERMEABILITY GAS PHASE RELATIVE PERMEABILITY DIFFUSIVE FLUXES OF MASS DISPERSIVE FLUXES OF MASS AND ENERGY CONDUCTIVE FLUX OF HEAT	MECHANICAL CONSTITUTIVE MODELS ELASTICITY (b) NONLINEAR ELASTICITY (b) VISCOPLASTICITY FOR SALINE MATERIALS (b) VISCOPLASTICITY FOR GRANULAR MATERIALS (b) VISCOPLASTICITY FOR UNSATURATED SOILS BASED ON BBM (b) DAMAGE-ELASTOPLASTIC MODEL FOR ARGILLACEOUS ROCKS (c) THERMOELASTOPLASTIC MODEL FOR SOILS (d)
PHASE PROPERTIES (a) SOLID PHASE PROPERTIES LIQUID PHASE PROPERTIES GAS PHASE PROPERTIES	EXCAVATION PROCESS (e)

For the retention curve four models are available: Van Genuchten model; linear model; square law; Van Genuchten model with asymptotic branch which takes into account the influence of porosity on the retention curve. The Kozeny's model for a continuum medium is available for the intrinsic permeability. For the liquid phase relative permeability four models are available as well: Van Genuchten model; Liquid perfectly mobile; generalised power and power with initial cut off (detailed description in chapter VI USERguide).

The viscoplasticity model based on BBM is based on Desai and Perzyna theory. The yield function and the viscoplastic potential differ for the parameter b which is parameter for non-associativity. The hardening function is equivalent to BBM (Alonso et al. 1990). Also the strength can be considered as a function of suction.

c) GeHoMADRID

(FUNAB)

GeHoMadrid is a finite element program with an emphasis in geotechnical applications. The first version of GeHoMadrid was developed at the end of the nineteen nineties as a research project financed by Agencia Española de Cooperación Internacional (AECI) carried out at Centro de Estudios y Experimentación de Obras Públicas (CEDEX) in Madrid and the Hohai University in Nanking (China) under the supervision of Professor Manuel Pastor. Starting from this first version, the program has been further developed and enhanced through the collaboration with different researchers and doctoral students from other universities such as Polytechnic University of Madrid (through the Group of Mathematical Modelling in Engineering M2i – ETS de Ingenieros de Caminos), Ecole Centrale de Paris, Polytechnic University of Milan, University of Bologna, National and Technical University of Athens.

GeHoMadrid is a 2D and 3D finite element tool able to deal with linear and non linear, coupled or non coupled soil problems in static and dynamic conditions. Deformation of solid skeleton and pore fluid flow are coupled via the Biot equations in saturated and partially saturated conditions. Advanced constitutive models have been implemented in order to reproduce complex material behavior taking into account changes in degree of saturation, contaminant concentration or temperature.

GEHOMadrid is compiled within FORTRAN 90 making good use of object-oriented programming, and using a simple and flexible structure for modifications. Recently some paralleling optimizations have been made with the OPEN-MP package. The following sections include the most important features of GeHoMadrid.

Mathematical modelling features

Analysis types:

- Static (\mathbf{u})
- Steady-state analysis (\mathbf{u}, p_w)
- Quasi-static or consolidation analysis: ($\mathbf{u} \quad \dot{\mathbf{u}} \quad p_w \quad \dot{p}_w$)
- Coupled dynamic analysis: ($\mathbf{u} \quad \dot{\mathbf{u}} \quad \ddot{\mathbf{u}} \quad p_w \quad \dot{p}_w$)
- 3D and 2D (Plane strain, Plane stress, axial symmetry).

*Saturated-Partially Saturated states**Transport solver*

- Computation of convective and diffusive transport of pollutant

Initial conditions

- Equilibrium check for hydrostatic and geostatic initial conditions
- Earth pressure coefficient at rest K_0 . optional

Boundary conditions

- Simple boundary conditions using predefined “Time-Curves”.
- Special boundary conditions: Transition from Newman to Dirichlet condition.
- Control of pore-pressure minimum value to satisfy the cavitation pressure condition.
- Tied node conditions
- Simple absorbing boundary conditions, following Lysmer work.

Applied loads

- Progressive construction and excavation processes.
- Concentrated, distributed, gravity, pressure, hydrostatic loads with “Time-Curves”.
- Thermal loading.
- Seismic loading.

Constitutive models

- Elastic models: Linear and non-linear elastic isotropic model are implemented.
Elastic-Joint models
- Elastoplastic models: Von-Mises, Tresca, Drucker-Prager and Mohr-Coulomb, including softening or hardening, safety factor computations
- CamClay and other Critical State models
- Viscoplastic models: Bingham and Perzyna
- Nova’s models : Nova-Castellanza model (Nova et al. 2003), “Sinfonietta classica” model (Nova 1988).
- Pastor-Zienkiewicz models: Standard model for cyclic loading (Pastor et al. 1990), enhanced model for debonding processes (Fernandez-Merodo et al. 2004), state parameter model (Manzanal 2008), non-saturated model (Manzanal 2008).
- Using external subroutines models: externally defined constitutive model, ABAQUS UMAT format option.

- Fluid phase: Isotropic and orthotropic permeability, permeability defined as a function of void ratio or suction with “time-curve”, retention curves $S_r(s)$ (for drying and for wetting) (Fernandez-Merodo et al. 2005).

Numerical model

Space discretisation

		u formulation	u-p _w formulation
1D	Lines	L2, L3	
2D	Triangles Quadrilaterals	T3, T6 Q4, Q8, Q4SR	T6P3, T3P3STAB Q8P4, Q4P4STAB, Q4P4SR
3D	Tetrahedrons Hexahedrons	H4, H10 B8, B20, B8SR	H10P4, H4P4STAB B20P8, B8P8STAB, B8P8SR

SR = Simo-Rifai (Simo & Rifai 1990) option for standard or coupled formulations (Mira et al., 2004).

STAB = Stabilised formulation

Planar contact elements are also available in 2D and 3D.

Time discretisation

- Extended Newmark scheme.
- Automatic time stepping option.

Non linear algorithm

- Newton-Raphson algorithm.
- Prescription of maximum number of iterations for Jacobian matrix update.
- Prescription of and the maximum number of iterations before restart.
- Automatic restart using a smaller time step.

Computation of stress increment

- Explicit integration algorithm
- Implicit integration algorithm (Tamagnini et al. 2002; Tonni 2002; Mira et al. 2009)

Arclenght

Control option available for static limit load problems with softening materials

Solvers

- Profile direct solver for symmetric and non- symmetric matrices
- Preconditioned conjugate gradient
- Jacobi method for symmetric matrices.
- Pardiso solver for large 3D models.

Special emphasis in a user-friendly interface with GiD

- (PRE-PROCESS) and (POST-PROCESS) with GiD, developed by the International Center for Numerical Methods in Engineering CIMNE.
- Interfacing of GiD and GeHoMadrid through ASCII or binary files.
- Alternatively, a powerful simple Interfacing of GiD and GeHoMadrid with TCL-TK based graphical interface. This interface has been used in the computer sessions of the First Olek Zienkiewicz Course organized by ALERT Geomaterials in Madrid in June 2009.

Modelling natural slopes subjected to rainfall infiltration

In order to illustrate that GeHoMadrid is a suitable code to study weather-induced triggering processes of landslides several examples are presented.

Example 1: Delayed collapse of a cut slope in stiff clay due to an excavation construction process

This example reproduces the delayed collapse of a slope in stiff clay due to an excavation construction process. This case has been described in the literature (Potts et al. 1997). It is a 2D plane strain analysis. The London Brown clay is assumed to be elasto-plastic, with a non associated Drucker–Prager yield criterion.

The analysis is divided in 3 steps: computation of the initial conditions, computation of the excavation process including removal of 8 horizontal layers of material each 10 days, and a final step representing consolidation until failure.

During excavation a bubble of negative pore water pressure is formed just under the layer excavated. Plastic strain appears at the toe of the slope but its value remains small at 8.5% (Figure 4.57).

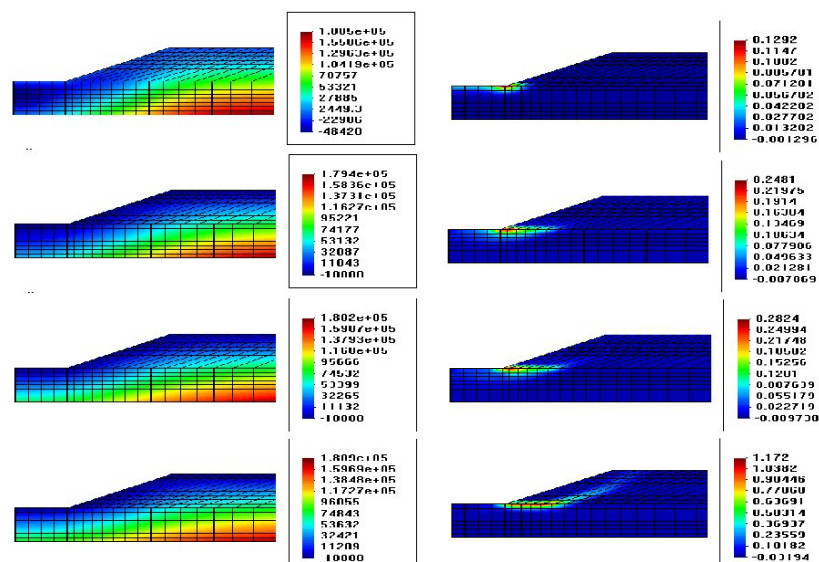


Figure 4.57 - Pore water pressure (Pa) and equivalent plastic strain during the consolidation

The influence in the final solution of some parameters such as "softening", dilatancy angle, earth pressure at rest, dilatancy angle, suction boundary and slope geometry have been studied.

Example 2: Delayed collapse of a cut slope in partially-saturated stiff clay due to rain infiltration

This example (Fernandez-Merodo 2001) is similar to the previous one but we have considered an initial suction boundary on the top equal to -20 kPa and a partially saturated material using a simple retention curve.

After checking equilibrium steady state conditions after excavation, the rain has been applied in two simplified ways:

1. Flooding, $p_w = 0$ on the top boundary
2. Rain intensity known, flow = 6 mm/day on the top boundary.

In both cases failure is reached. Figure 4.58 displays the time evolution of the horizontal displacement of the midslope point.

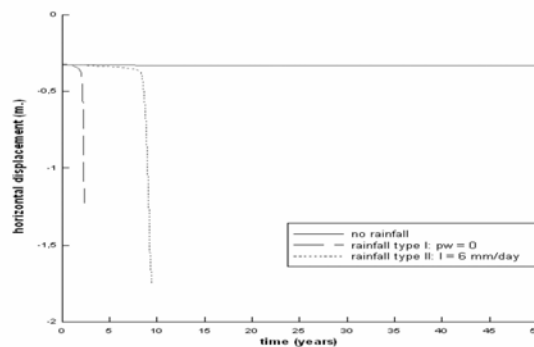
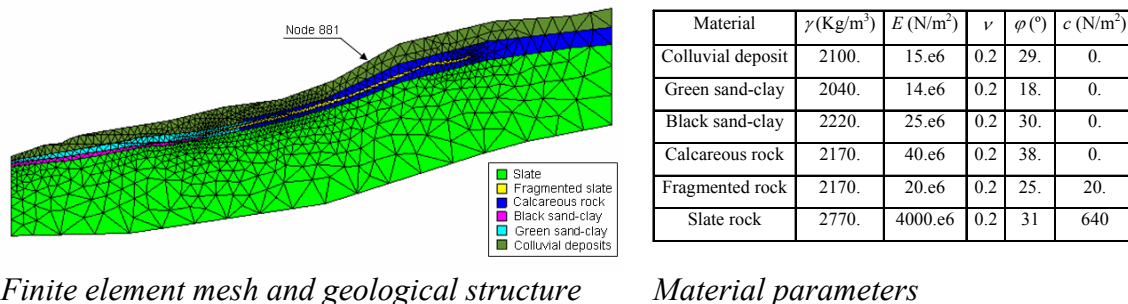


Figure 4.58 - Time evolution of horizontal displacements of a midslope point

Example 3: Modelling of the Portalet landslide mobility (Formigal, Spain) (Fernandez-Merodo et al. 2008).

The Portalet landslide is a large, active slope failure located on the upper part of the Gállego River valley, in the Central Spanish Pyrenees (Sallent de Gállego, Huesca). The landslide is located on a southwest-facing hillside of Petrasos Peak, close to the ski resort of Formigal. The dimensions of the landslide are 500 m long and up to 700 m wide at the toe extended over an area of 0.35 km² that shows superficial cracking and distinct ground displacements. Displacements are quite important (several cm in a month) since summer 2004 when the construction of a parking area was carried out by digging the foot of the slope. Field observations show a close relation between ground movement and rainfall intensity. Monitoring and predicting the landslide behaviour is necessary to guarantee the safety of this ski resort area. A fully coupled hydro-mechanical finite element analysis using GeHoMadrid in plane strain conditions using an elastoplastic constitutive model has been performed to forecast the recorded movements directly from rainfall intensity.

The geological structure of the landslide has been obtained by means of geological, geomorphological assessment and drilling data. Section AA' has been discretized using quadratic triangular elements (6 nodes for displacement degree of freedom and 3 nodes for pore pressure degree of freedom). The mesh is composed by 2151 triangles and 3975 nodes, as shown in Figure 4.59. Material behaviour has been represented with a Drucker-Prager constitutive model using material parameters defined in Figure 4.59. Saturated condition is taken in all the materials.



Finite element mesh and geological structure

Material parameters

Figure 4.59 - *Finite element model of the Portalet landslide (left); material parameters assumed for the numerical simulation (right)*

Two important factors have an influence on the slope stability: initial stress condition and ground water level position. Initial conditions have been treated in a first attempt modelling the construction process of the parking area. The excavation process induced local instability near the toe of the excavated slope. The local collapse was also observed on the field and an immediate repair solution was carried out by replacing the excavated material. Consequently the final executed profile has been chosen as the studied geometry.

No information about the position of the ground water level was available. The initial hydraulic condition has been chosen performing an initial static stability analysis. The transient response taking into account rain condition has been performed in a second analysis. Stability analysis is performed in two phases: in the first one, gravity is progressively applied using a high value of suction on the upper boundary keeping the slope in a stable state. This condition is equivalent to imposing a water table parallel to the surface at a depth of 10 metres. In the second one, suction on the upper boundary is progressively reduced performing successive static equilibrium analysis, the water table is progressively raised to the surface. Plastic deformation develops along a shear surface until failure occurs for a given boundary suction condition.

A nearly linear behaviour is observed during the first phase corresponding to the gravity activation. A more marked plastic behaviour can be observed during the second phase corresponding to the decreasing suction boundary condition. Collapse is reached when the suction is equal to 34105. Pa, it is equivalent to a water table located at 3.48 m below the surface, plastic deformation and displacement contours at this moment are presented in Figure Figure 4.60. The computed location of the rupture surface agrees very well with field observations. The observed scarps are located at the same position on the upper part of the slope. Besides, rupture surface located at 12 m given by borehole 1 fits in with the computed rupture surface.

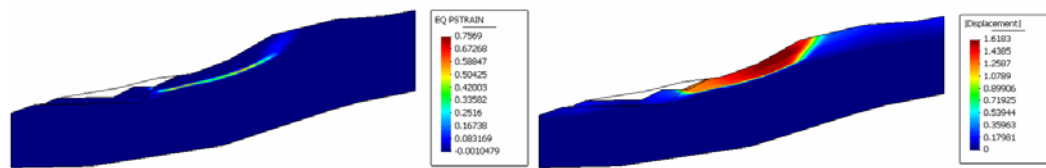


Figure 4.60 - Equivalent plastic deformation contour and displacement contour (in m) at failure

The initial condition of the transient analysis is chosen from the stability analysis. The equilibrium state corresponding to a ground water level located 6 meters below the surface has been chosen. The choice of this initial state has an influence on the transient analysis. States corresponding to the highest values of the ground water level can induce sudden collapse for small variations of pore pressure.

Rain is modelled using an input flow condition on the upper boundary. This condition supersedes the initial given hydraulic prescription. To do this an equivalent flow condition must replace the suction prescribed condition.

d) ELLIPSIS

(CNRS)

Ellipsis is a 2D code based on the Finite Element Method with Lagrangian Integration Points (FEMLIP). The FEMLIP method has been developed by a researcher group in Australia in order to model mantle convection and lithosphere deformation. In this context Ellipsis was used initially only with viscous constitutive laws. After that, it has been developed for geomechanical problems: visco-elasticity and possibility of anisotropic behaviour were introduced (Moresi et al., 2002, Mühlhaus H.-B. et al, 2002). We are now still developing Ellipsis to allow it to model plastic failure in soils.

FEMLIP principles

The objective of this method is to model within a unique framework both solids and viscous fluids. Indeed, in the lagrangian FEM, modelling fluid is impossible due to the excessive mesh deformation, which prevents a good spatial integration. Among the different alternative methods which are going through this problem, (Particle Finite Element Method –developed by Onate et al., 2008 - , Arbitrary Lagrangian Eulerian, etc...), the FEMLIP has the particularity to dissociate totally the computational points (mesh) and the material (integration) points.

The method is constructed from an Eulerian fixed mesh, in which a swarm of lagrangian particles is defined, following the material in its displacement. These particles are used as integration points instead of the usual Gauss points. The modelling of both solids and fluids is then possible due to the great versatility of Lagrangian particles, whereas the mesh remains well structured.

We have thus a separation of the distribution of the variables:

- The history variables, like stresses or hardening plastic parameters in case of plasticity, are only set on the particles, and move with them.
- The velocity variables are useful for particles to make them move from a step to another. Nevertheless, we can consider them as node variables since, before being

interpolated on particles, they were first calculated by a classical FEM solver using the mesh.

This original principle can be illustrated by the following scheme.

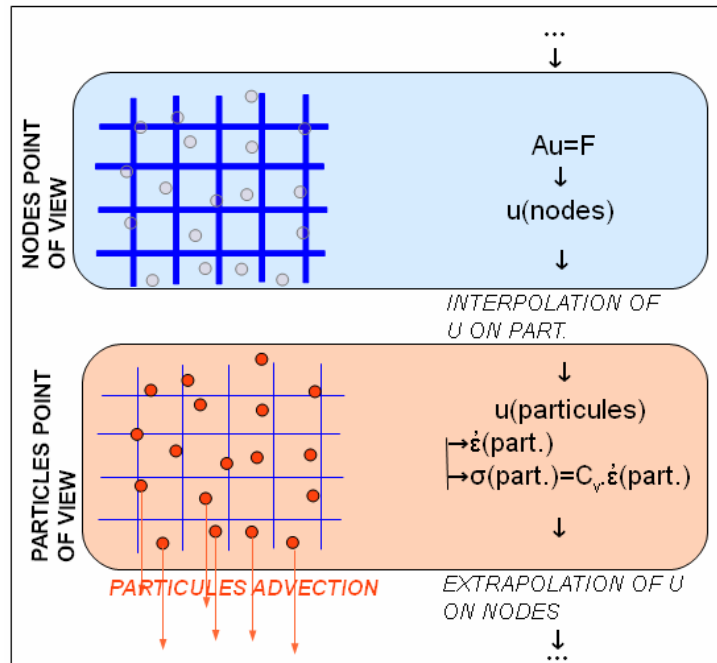


Figure 4.61 - FEMLIP including dissociation of nodes and particles variables processing, for a viscous problem at one step.

At each step of computation, we do first a FEM solving at the mesh nodes using an integration scheme over the particles. After that the particles get involved: history variables are updated on them and then they move through the mesh carrying the information up to their new position. The next step can thus begin.

From this ability to model both solid and fluid flow, it is clear that the FEMLIP is well suited to model landslides from their initiation in elasto-plastic soils until the debris transport along slopes, which is often a viscous mudflow. This is the essential reason for the choice of this numerical method to solve this solid-fluid transition in natural media, which is still a completely open question from an international viewpoint.

List of features

This code can be described by the following characteristics:

- 2D FEMLIP code.
- Coded in C language.
- Ability to take into account viscous, elasto-viscous, elasto-visco-plastic constitutive laws.
- Ability to model heat transfers.

- The solving is done with a mixed formulation, because of the possibility to have incompressible fluids to be simulated. The nodal unknowns of the problem are thus the velocity v of the material, and its pressure p . The system to be solved is:

$$\begin{bmatrix} A & G \\ G^T & M \end{bmatrix} \begin{bmatrix} v \\ q \end{bmatrix} = \begin{bmatrix} f \\ 0 \end{bmatrix} \quad (1)$$

where A is the global stiffness matrix, G the discrete gradient operator, and G^T its transpose. A is built up from particle derived material properties, as well as shape function derivatives, whereas G is purely geometrical and is associated with the mesh.

- Boundary conditions in velocity.
- Plastic law adapted to geomaterials: Plasol constitutive relation implemented.

Note: Because heat transfers are not very useful in landslide modelling we will focus in this presentation only on mechanical aspects.

Sign convention

The sign convention is the one of continuum mechanics, i.e. compressive stresses are negative; there is nevertheless an exception for the isotropic stress p , which is called pressure and in consequence is positive in compression.

Comments on viscous, visco-elastic and visco-elasto-plastic constitutive relations in the code

Basic formulation in Ellipsis: the viscosity relations

As the code was initially used for mantle convection, it has been based only on viscous constitutive laws. On one hand we have:

$$\text{Deviatoric equation:} \quad (D_{dev})_{ij} = \frac{s_{ij}}{2\eta} \quad (2)$$

$$\text{Isotropic equation:} \quad -tr(\underline{D}) = \frac{p}{\left(\xi + \frac{2}{3}\eta\right)} = \frac{p}{Kv} \quad (2bis)$$

Or equivalently:

$$\text{Deviatoric equation:} \quad s_{ij} = 2\eta(D_{dev})_{ij} \quad (3)$$

$$\text{Isotropic equation:} \quad p = -Kv.tr(\underline{D}) \quad (3bis)$$

Where \underline{D} is the strain rate tensor, \underline{D}_{dev} the deviatoric part of \underline{D} , \underline{s} the deviatoric part of Cauchy stress tensor, p the pressure, ξ and η the two viscous coefficients (η is viscosity), and $Kv = \xi + \frac{2}{3}\eta$ the volumetric compressibility modulus in viscosity.

On the other hand the momentum balance can be written as:

$$(s)_{ij,j} + (p)_{,i} + (f)_i = 0 \quad (4)$$

Where f is the external forces applied to the system.

So with equations (3), (3bis) and (4) we finally obtain:

$$2\eta(D_{dev})_{ij,j} + Kv.(tr \underline{D})_{,i} + (f)_i = 0 \quad (5)$$

Introduction of visco-elasticity

For a viscoelastic model (such as a Maxwell model), we can write in equation (2) and (2bis) the strain rate as the sum of the elastic strain rate and the viscous one:

$$\text{Deviatoric equation:} \quad (D_{dev})_{ij} = [(D_e)_{dev} + (D_v)_{dev}]_{ij} = \frac{s'_{ij}}{2\mu} + \frac{s_{ij}}{2\eta} \quad (6)$$

$$\text{Isotropic equation:} \quad -tr(\underline{D}) = -tr(\underline{D}_e) - tr(\underline{D}_v) = \frac{\dot{p}}{Ke} + \frac{p}{Kv} \quad (6bis)$$

Where \underline{D}_e is the elastic strain rate tensor, \underline{D}_v the viscous one, \dot{p} the temporal derivative of the pressure, \underline{s}' the Jaumann derivative of \underline{s} , $Ke = \lambda + \frac{2}{3}\mu$ the volumetric compressibility modulus in elasticity, and λ and μ the elastic Lamé coefficients.

If we linearize the derivatives of these two last equations on a small increment of time δte , we obtain the following expression of deviatoric and isotropic stresses:

$$(s^{t+\delta te})_{ij} = 2\eta_{eff}((D^{t+\delta te})_{dev})_{ij} + \eta_{eff} \cdot \frac{(s^t)_{ij}}{\mu \cdot \delta te} + \eta_{eff} \frac{(\omega^t(s^t)_{ij} - (s^t)_{ij} \omega^t)}{\mu} \quad (7)$$

$$p^{t+\delta te} = Kv_{eff} \cdot \left[-tr(\underline{D}^{t+\delta te}) + \frac{p^t}{Ke \cdot \delta te} \right] \quad (7bis)$$

Where $\eta_{eff} = \eta \cdot \frac{\delta te}{\delta te + T}$ and $Kv_{eff} = Kv \cdot \frac{\delta te}{\delta te + T}$ are respectively the effective viscosity and the effective compressibility modulus in viscosity, taking into account the relaxation time $T = \frac{\eta}{\mu} = \frac{Kv}{Ke}$ (supposed identical for shearing or compressibility behaviour).

If we gather all the terms depending on the previous time t , and consider this group as a new force term due to elasticity, then the balance equation can be written in the same form than in pure viscosity:

$$2\eta_{eff}((D^{t+\delta te})_{dev})_{ij,j} + Kv_{eff} \cdot tr(\underline{D}^{t+\delta te})_{,i} + (f)_i + (f_e)_{,i} = 0 \quad (8)$$

where f_e is the elastic force term.

Addition of plasticity in the visco-elastic laws

Now, we consider that in equation (2) and (2bis), the visco-elastic strain rate can be expressed as the total strain rate minus the plastic one:

$$\left((D_{ev})_{dev} \right)_{ij} = \left[(D_{tot})_{dev} - (D_{pl})_{dev} \right]_{ij} = \frac{s'_{ij}}{2\mu} + \frac{s_{ij}}{2\eta} \quad (9)$$

$$-tr(\underline{D}_{ev}) = -tr(\underline{D}_{tot}) + tr(\underline{D}_{pl}) = \frac{\dot{p}}{Ke} + \frac{p}{Kv} \quad (9bis)$$

Where \underline{D}_{ev} , \underline{D}_{pl} and \underline{D}_{tot} are the visco-elastic, the plastic and the total strain rate tensors. If we develop the derivatives on δte , we obtain these new expressions of stresses:

$$(s^{t+\delta te})_{ij} = 2\eta_{eff} \left[(D_{tot}^{t+\delta te})_{dev} - (D_{pl}^{t+\delta te})_{dev} \right]_{ij} + \eta_{eff} \cdot \frac{(s^t)_{ij}}{\mu \cdot \delta te} + \eta_{eff} \frac{(\omega^t (s^t)_{ij} - (s^t)_{ij} \omega^t)}{\mu} \quad (10)$$

$$p^{t+\delta te} = Kv_{eff} \cdot \left[-tr(\underline{D}_{tot}^{t+\delta te} - \underline{D}_{pl}^{t+\delta te}) + \frac{p^t}{Ke \cdot \delta te} \right] \quad (10bis)$$

In the same manner, if we gather all the terms depending on plastic strain rate and if we consider that they form a force term induced by plasticity, the balance equation can also be expressed as in the single viscosity case:

$$2\eta_{eff} \left((D_{tot}^{t+\delta te})_{dev} \right)_{ij,j} + Kv_{eff} \cdot (tr \underline{D}_{tot}^{t+\delta te})_i + (f)_i + (f_e)_i + (f_{pl})_i = 0 \quad (11)$$

Where f_{pl} is the plastic force term.

The way adopted in Ellipsis to take into account visco-elasto-plasticity instead of mere viscosity is thus to modify only the force term and not the rigidity matrix.

Note: To create a single elasto-plastic behaviour, we can't neglect the viscous relations on which is based all the resolution. The solution is thus to consider a very high viscosity η that will makes the relaxation time be infinite, and the visco-elastic behaviour turns quasi elastic.

A visco-elastic model of landslide

In the following simple example, we modelled a viscous slope and a visco-elastic (in fact quasi elastic) protection wall on its base. The slope is only subjected to gravity loading, and its viscosity has the particularity to be divided by 100 if a critical deviatoric stress is reached. This point has been introduced in the code to create a critical state in viscosity when the strength suddenly falls down.

In the following output pictures, we represented the wall (in green color), the slope (in blue), and the area of the slope where the strain has reached a relatively high fixed value (in red).

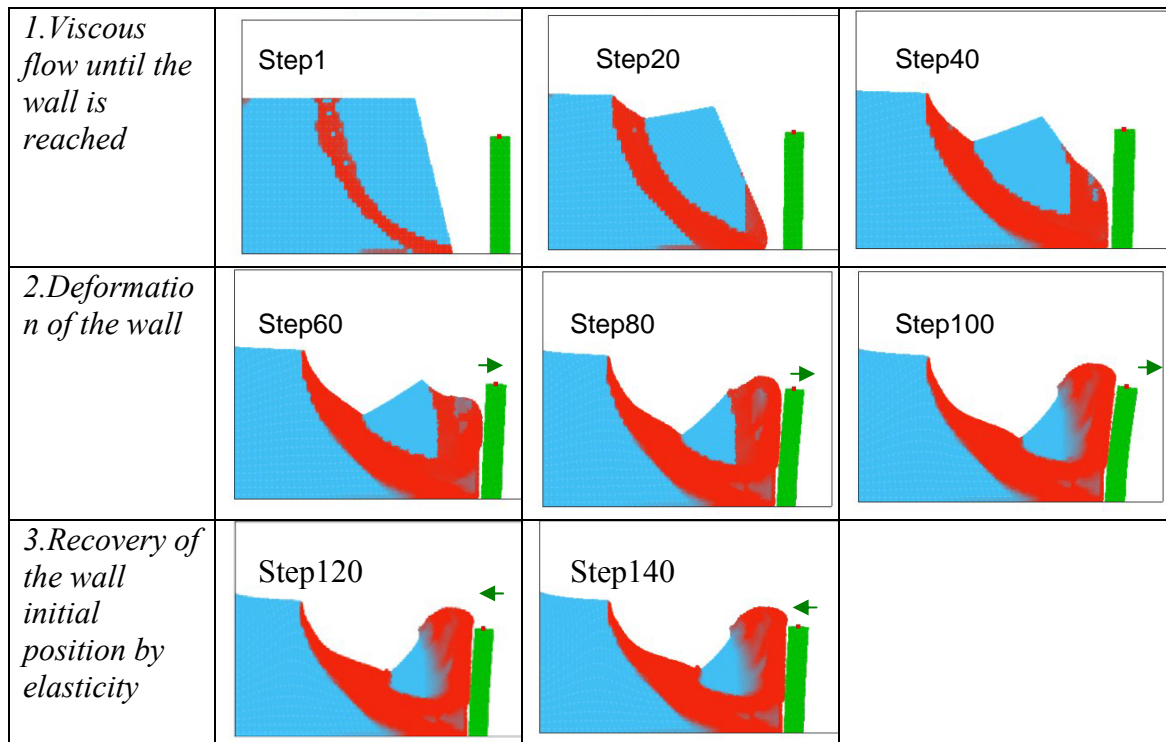


Figure 4.62 - Strain and displacement fields obtained for a viscous slope and an elastic wall, under gravity condition.

We can see the viscous flow of the slope induced by gravity. Because there is a specific criterion on strength, a localization of the strain is appearing here, like it would do in a plastic model.

Finally the elastic behaviour of the wall is put in evidence by the recovery of its initial position (step 120 and 140 in Figure 4.62) after its first flexion at the soil mass arriving (step 40, 60, 80 and 100).

e) I-MOD 3D (Infiltration Modelling in Unsaturated Granular Soil) (AMRA)

I-MOD 3D is a 3D Volume Finite Element Code developed at the Geotechnical Laboratory of Second University of Naples (Olivares & Tommasi 2008; Damiano & Olivares 2010; Olivares et al. 2010). The code was developed as a Visual Basic Application for ARC-GIS 9.2. The version called I-MOD 3D contain a pre- and postprocessor. The uncoupled volume finite formulation allows for solving complex isotherm-hydro-mechanically multiphase problems.

List of features

- 3D Volume Finite Element Code
- Integrated pre- and postprocessor
- Unsaturated soil in a uncoupled volume finite element formulation
- Analysis types: 3D analysis.
- Problem types: hydraulic isothermal flow (transient, saturated or unsaturated), uncoupled flow.
- Time dependent calculations.
- Time dependent boundary conditions: arbitrary fluid flow at the model boundaries.
- Associated stability analysis for an infinite slope

Sign convention

Compressive pressure are positive in the fluid phase.

General equations

The general governing differential equation for 3D seepage are expressed as:

- *3D seepage equation*

$$\vec{q}(x, y, z, t) = -K(\theta(x, y, z, t)) \cdot \nabla(\psi(\theta(x, y, z, t)) + z)$$

$$\frac{\partial \theta(x, y, z, t)}{\partial t} = -\nabla \cdot \vec{v}(x, y, z, t)$$

- *Conductivity and retention curves for unsaturated porous medium*

$$\psi(\theta(x, y, z, t)) = \text{retention curve}$$

$$K(\theta(x, y, z, t)) = \text{conductivity function}$$

where:

$$\theta(x, y, z, t) = \text{volumetric water content;}$$

$$\vec{v}(x, y, z, t) = \text{Darcian velocity } x, y, z;$$

$$K(\theta(x, y, z, t)) = \text{hydraulic conductivity;}$$

$$\psi(\theta) = \text{capillary pressure head}$$

- *associated stability analysis (infinite slope) (Fredlund D.G. and Rahardjo H. (1993))*

$$FS = \frac{\tau_{\text{lim}}}{\tau} = \frac{[c' + (\psi(\theta) / \gamma_w) \cdot \lambda \text{tg} \phi'] + (\sigma_\beta - u_a) \cdot \text{tg} \phi'}{\tau_\beta}$$

where:

c'	= effective cohesion;
γ_w	= water specific weight;
τ_β	= shear stresses;
$(\sigma_\beta - u_a)$	= normal net stresses;
$\psi(\theta)$	= capillary pressure head;
ϕ'	= effective frictional angle

Retention Curve and Unsaturated permeability

The retention curves are described by the Van Genuchten Relationship (1980);

$$\frac{\theta - \theta_r}{\theta_s - \theta_r} = \frac{1}{[1 + (\alpha \cdot \psi)^n]^m}$$

where

θ_r	residual volumetric water content;
θ_s	saturated residual volumetric water content;
α	$\alpha = \frac{1}{\psi_e}$ where ψ_e air entry pressure head;
m, n	Van Genuchten parameters.

The unsaturated permeability functions are described by Brooks & Corey (1964), Gardner (1958), Arbhahirama and Kridakorn (1968) or defined by the user (as function of matrix suction or volumetric water content).

Brooks & Corey (1964)

$$k_w = k_s \quad \text{for} \quad (u_a - u_w) \leq (u_a - u_w)_b$$

$$k_w = k_s \left[\frac{(u_a - u_w)_b}{(u_a - u_w)} \right]^\eta \quad \text{for} \quad (u_a - u_w) > (u_a - u_w)_b$$

where $\eta =$ empirical constant $(2+3\lambda)$; $\lambda =$ distribution index

Gardner (1958)

$$k_w = \frac{k_s}{1 + a \cdot \left(\frac{u_a - u_w}{\rho_w g} \right)^n}$$

Arbhabhrama and Kridakorn (1968)

$$k_w = \frac{k_s}{1 + \left(\frac{(u_a - u_w)}{(u_a - u_w)_b} \right)^{n'}}$$

where $a, n, n' =$ empirical constant

Modelling natural slopes subjected to rainfall infiltration

In IMOD-3D program the mesh-generation automatically starts from the Digital Terrain Model as an application a Visual Basic Application for ARC-GIS 9.2.

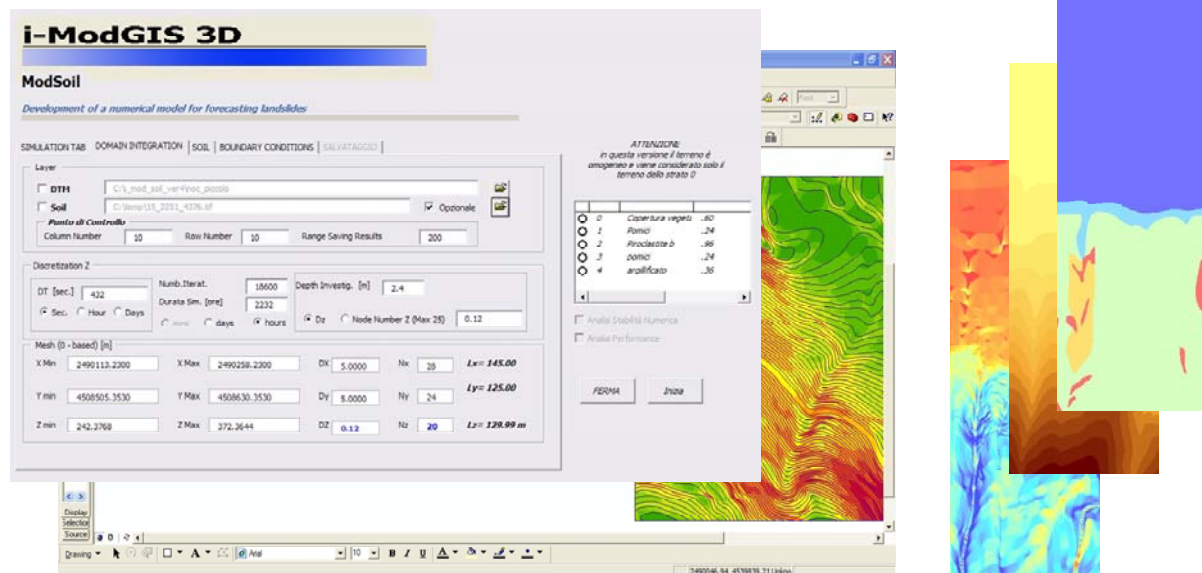


Figure 4.63 - Example of DTM used as input for pre-processor.

Any given rain infiltration pattern can be simulated as a prescribed boundary flux. The integrated postprocessor allows displaying contour maps of volumetric water content, matrix suction, safety factor FS (in the hypothesis of an infinite slope).

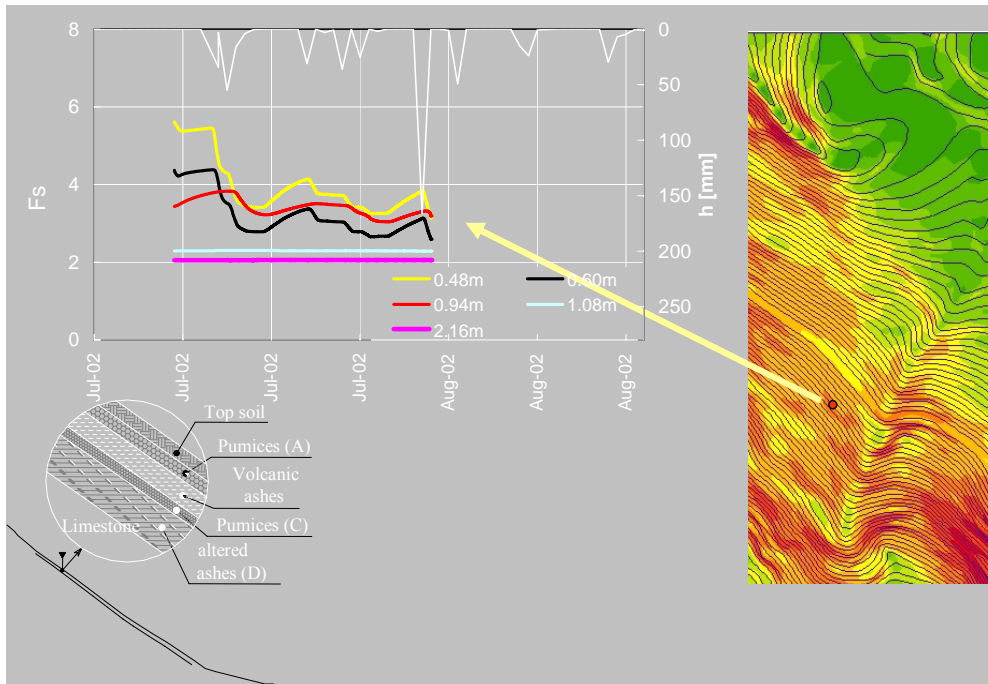


Figure 4.64 - Safety factor at different depth in a point located along the slope.

Safety Factor at 1.4 m depth

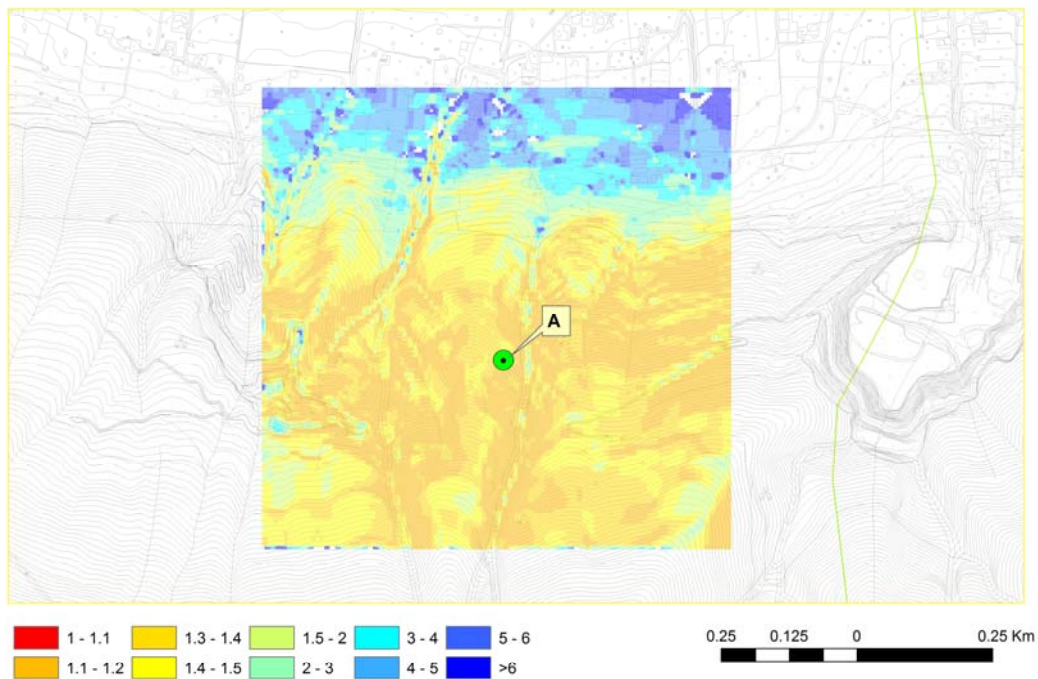


Figure 4.65 - Contour maps of safety factor FS.

4.1.2.4 Parametric studies (AMRA - EPFL)

4.1.2.4.1 Introduction (EPFL)

Rainfall-induced landslides are mostly superficial and are triggered in soil slopes where a permanent groundwater table is often absent due to slope steepness and generally dry environmental conditions. Soils in such slopes are most of the time in a state of partial water saturation. Water flow into and through the soil is primarily governed by the soil's initial hydraulic conditions expressed in terms of matric suction and the degree of saturation or alternatively its water content. Unsaturated flow from the slope surface is principally vertical and its magnitude depends on the pore pressure gradient and water relative permeability which strongly varies in the unsaturated range.

The whole sliding mass is often several meters to tens of meters wide and several tens of meters long and sums up to a couple of hundred to thousand cubic meters in volume (Moser and Hohensinn 1983; Dai et al. 1999). Shallow slides in steep (30 to 40°), loose colluvial deposits are mostly translational and mobilize completely to form debris flows. The sliding mass can develop very high velocities (up to several m/s) leading to high impact on obstacles and sadly coming in many cases as a surprise to eyewitnesses. Shallow slips occur mostly on barren and grass or bushes covered slopes where the roots extent is limited to 30-50cm in depth. The failure surface is commonly situated between 0.5 and 3 meters in soil depth and runs subparallel to the slope surface along a soil cover bedrock interface where the development of a positive pore water pressures during rainfall events is favored. Failures may also take place in the unsaturated conditions in case the underlying bedrock impedes the build up of positive pore water pressures due to its draining capacities. The two subsequent parametric studies treat each one of the aforementioned cases. The first parametric study relates to the steep slopes in southern Italy composed of pyroclastic soils which cover a permeable substratum. The second parametric study relates to the steep soil slopes of an alpine region in Austria where primary slightly colluvial and residual soil covers are encountered above a less permeable bedrock composed of crystalline schists.

The objective of the subsequent parametric studies is to analyse the relative importance of some predisposition factors related to soil hydraulic properties and initial conditions for defining quantitatively the proneness of steep soil slopes to fail under various environmental conditions. Therefore, the first study uses a one-dimensional analysis approach due to the predominant vertical flow pattern in the pyroclastic soil slopes of Southern Italy, while the second study for an alpine region in Austria uses a two-dimensional analysis approach in order to capture the important feature of subparallel flow induced by a permeability contrast at the interface between soil cover and bedrock .

4.1.2.4.2 Sensitivity analyses on the impact of rainfall on slope behaviour in pyroclastic soils (AMRA)

a) Introduction

Meteorological variables affect the stability of slopes through a modification of the hydraulic boundary conditions. Weather causes water flow through the ground surface (due to rainfall and evapotranspiration) or from cracks, or a change of the external water level (in case of

ivers, lakes and reservoirs). The impact of weather on the slope behaviour depends on one hand on rainfall duration, distribution and intensity, on temperature and external humidity, and on the other on slope-related factors, such as slope geometry, soil stratigraphy and soil properties (water retention properties and hydraulic conductivity).

In principle, the behaviour of pervious soils is affected by short and intense events (i.e. storms or floodings) and is insensitive to long lasting moderate precipitations due to their draining properties. In contrast, the behaviour of impervious soils remains insensitive to short rainfalls, but depends on long lasting precipitations, no matter of their intensity.

A special situation concerns slopes constituted by soils with intermediate hydraulic properties, which display a complex behaviour. Such is the case for unsaturated pyroclastic soils: in fact, when they are relatively dry (suction of some tens of kPa), their hydraulic conductivity is similar to that of fine grained soils (it may be as low as 10^{-9} m/s); when they are close to saturation (suction of few kPa), they are relatively pervious (hydraulic conductivity up to 10^{-6} m/s).

In order to draw conclusions on the relative importance of soil hydraulic properties and climate factors on the triggering of shallow slips in steep, unsaturated pyroclastic soils, a systematic parametric analysis has been performed. Following factors were subject of the study:

- (a) Soil properties;
- (b) Initial conditions;
- (c) Width of the meteorological window;
- (d) Rainfall intensity.

The study is carried out for an infinite slope under isothermal conditions and assuming one-dimensional, vertical flow. Some preliminary analyses are presented which aim at determining the influence of the type of hydraulic boundary conditions on the simulation results. The results are also compared with those obtained from a 2D analysis.

Two actual rainfall histories are used throughout the work, both recorded with a time resolution of 10 minutes by a pluviometer placed in the Nocera Inferiore district and corresponding to a dry season (1st August 2002- 31st May 2003) and to a wet season (1st August 2004- 31st May 2005). During this latter a landslide was triggered on March, 4th, 2005, involving a 2m thick cover having a slope of 40° and a friction angle of 39°.

b) Simulation of the boundary conditions at the base of the slope and comparison of the results obtained under 1D and 2D conditions

In case of slopes having an impervious base, seepage is characterized by a 2D flow. In case of free draining base (or of very thick layer), the possibility to reproduce the hydraulic response with a 1D approach may be investigated by checking if the results of the analysis match those yielded by a 2D analysis. To this aim, some analyses have been carried out using as reference the case of the Nocera Inferiore 2005 landslide: the rainfall history is the one preceding the event; the bedrock has been located at a depth of 2m; the slope angle is 40°; the soil has been considered homogeneous with the hydraulic properties of a material having very similar

features as the Nocera Inferiore ash (continuous lines in Figure 4.66a and 4.66b). The same data have been used also in next analyses.

The effects of water at the ground surface (infiltration/no infiltration) are reproduced by automatic switching of the hydraulic condition from an assigned flow rate (the rainfall intensity) to zero pore pressure and vice versa, depending on the value of the pore water pressure at the ground surface. Regarding the lowermost boundary, free drainage under 1D conditions has been simulated by: i) imposing a unit hydraulic gradient; ii) adopting a fictitious layer of infinite thickness. The results have been compared to those obtained with a 2D analysis only for the latter boundary condition.

A uniform initial suction of 40 kPa has been assumed along the vertical soil profile. Figure 4.67 compares the values calculated at a depth of 1 m during the considered time period. The results of the 1D analysis are practically the same for the two different boundary conditions. The figure shows that, during the most critical wet season (from December to May), the results of the 2D analysis are very similar to those obtained under 1D conditions. In particular, flow vectors are always close to vertical, confirming that the problem may be investigated as 1D. This suggests that under the hypothesis of a free draining lowermost boundary, time-saving 1D analysis may be reliably adopted instead of 2D analysis. Further, it can be concluded that either one of the two boundary conditions can be chosen for the analysis. In conclusion, for the subsequent parametric analysis, a one-dimensional approach is adopted.

c) Material properties versus rainfall history

In order to clearly identify the role of the water retention curve (WRC) on the hydrological slope response, the oversimplifying hypotheses of linear variation of suction with the degree of saturation and of constant permeability coefficient have been adopted (Figure 4.68).

A number of analyses have been carried out, combining the two water retention curves, A and B, reported in Figure 4.68. Three different values of the hydraulic conductivity (respectively $k_1=10^{-5}$, $k_2=10^{-6}$, $k_3=10^{-7}$ m/s) have been used in combination with each of the two retention curves. Both, the dry and wet rainfall histories have been adopted. In the analysis an initial suction of 40 kPa has been imposed at each depth. The corresponding steady-state condition has been defined by a hydrostatic suction distribution starting from a fictitious water table located at 20 m of depth. Therefore, a 20m thick layer has been assumed, imposing null pore water pressure at the lowermost boundary. Figures 4.69 and 4.70 show the variation of suction with time at 1m of depth, respectively for the two rainfall histories adopted. Each figure (a, b and c) compares the values calculated for the two WRCs, imposing the same hydraulic conductivity.

Figure 4.69a and 4.70a show the variation of suction obtained for a coefficient of hydraulic conductivity equal to $K_1=10^{-5}$ m/s, a value which may be considered an upper bound for pyroclastic soils. The plots show that from the starting point on, suction drops towards the steady state value, but the rapidity of such a process depends on the WRC.

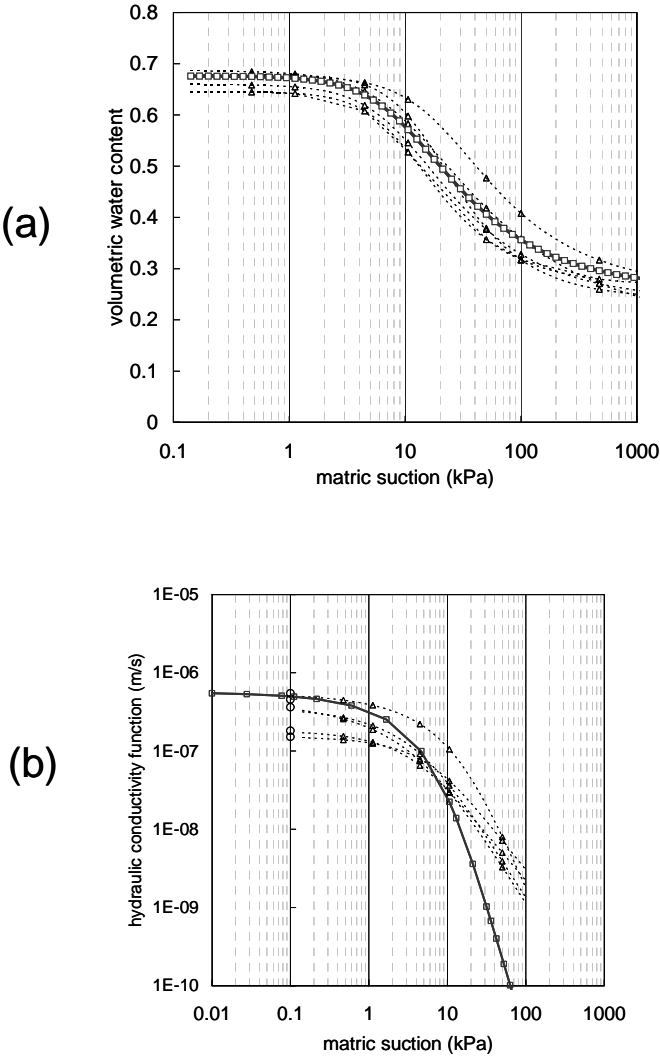


Figure 4.66 - Properties of the Monteforte Irpino air-fall volcanic ash (modified after Papa et al., 2009): a) water retention curves; b) permeability function

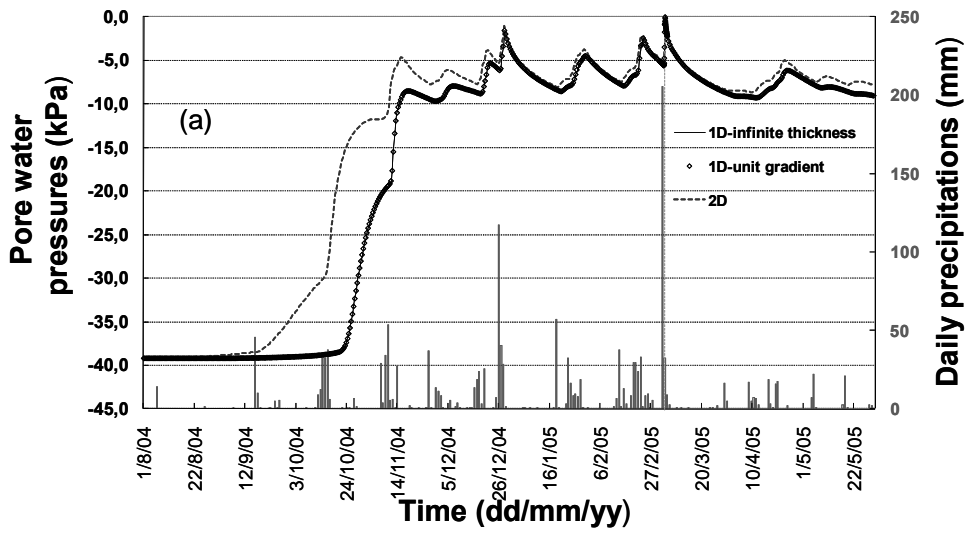


Figure 4.67 - Effect of geometry and boundary conditions on suction prediction

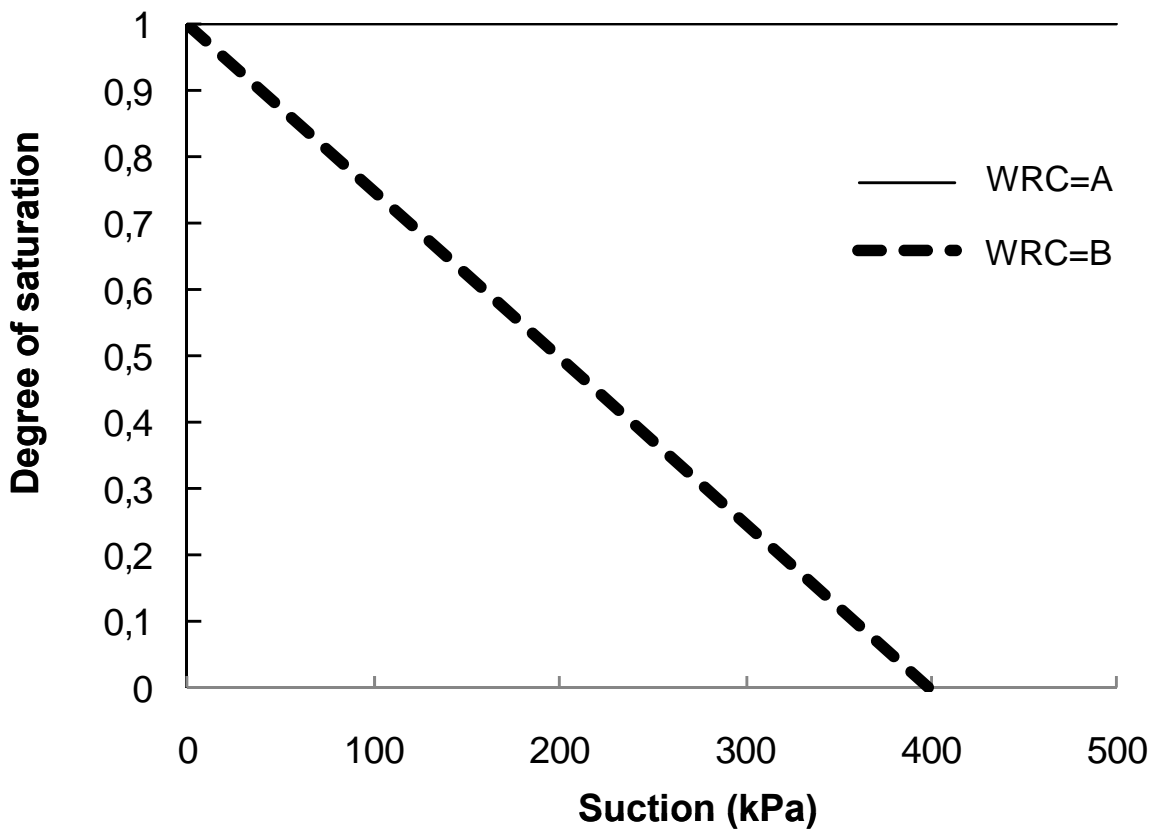


Figure 4.68 - Water retention curves adopted in the analyses

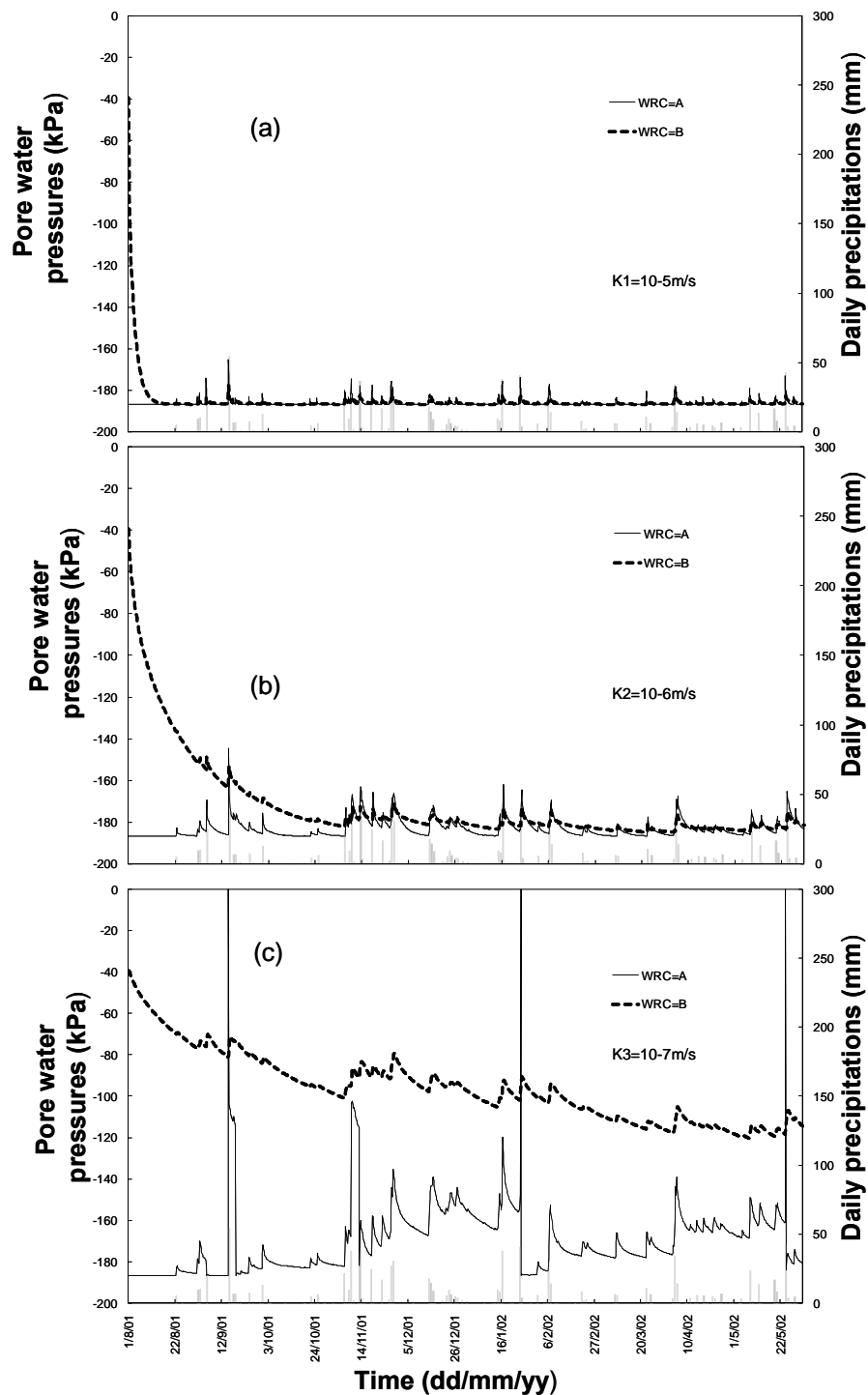


Figure 4.69 - Suction changes due to precipitations during a dry season, for different soil properties : (a) permeability coefficient $k1=10^{-5} \text{ m/s}$; (b) permeability coefficient $k2=10^{-6} \text{ m/s}$; (c) permeability coefficient $k3=10^{-7} \text{ m/s}$

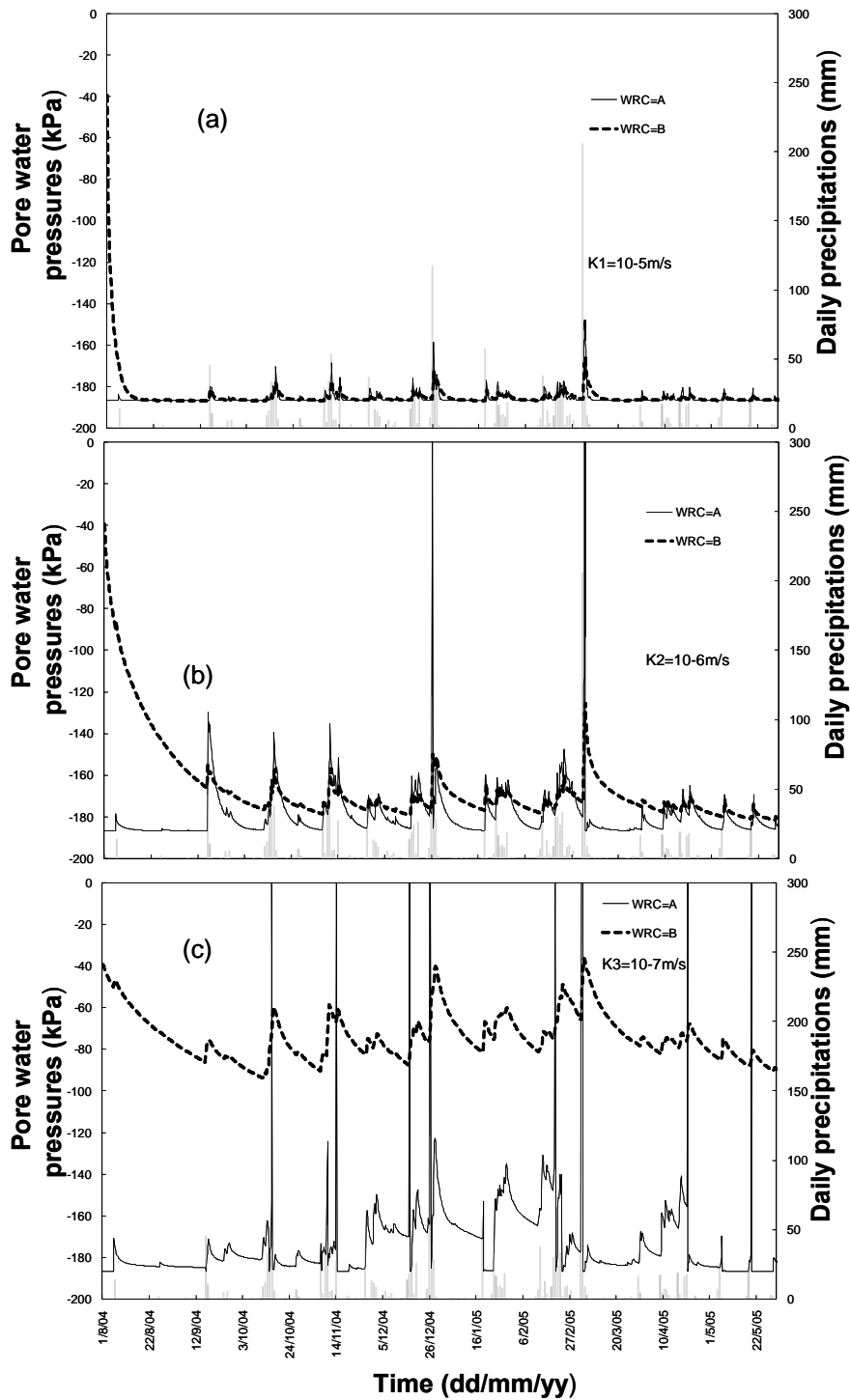


Figure 4.70 - Suction changes due to precipitations during a wet season, for different soil properties: (a) permeability coefficient $k_1=10^{-5}$ m/s; (b) permeability coefficient $k_2=10^{-6}$ m/s; (c) permeability coefficient $k_3=10^{-7}$ m/s

In particular, the water retention curve A, which is characterized by a sub-horizontal trend, is responsible for an immediate pore water pressure change. In fact, the hydraulic equalization is favoured by the very poor amount of water required. As a consequence, the time lag needed for equalization after rainfall is very low at each time, no matter of the permeability coefficient (curves WRC=A in Figs. 4.69b and c, 4.70b and c). For the highest permeability, suction fluctuates continuously around the steady-state value. However, permeability regulates the magnitude of pore water pressure increments. In fact, for less pervious soils higher pore water pressure increments are induced, due to the capability of the system to store water, increasing the water content at all depths; therefore, during rainfall, higher pore pressures than the steady state value are attained.

For the water retention curve B, which is closer to the real behaviour of pyroclastic soils, equalization requires seepage of a relatively larger amount of water, giving a more important role to permeability. The lower the permeability the longer is the transient stage, resulting in lower values of suction. Therefore, in general, for same water retention properties, a lower permeability results in higher pore pressure increments during rainfall events. This effect is due to a permeability coefficient which is closer to rainfall intensity, the soil being more effective in storing water.

Previous results suggest that more complex behaviours may be predicted when assuming more realistic soil properties. Figure 4.71 plots three different water retention functions, each one made of three straight parallel segments, associated with a different air entry value: the intermediate one is the simplified version of the average WRC reported in Fig. 4.66. The permeability function assumed in the analysis is always the same and corresponds to the one reported in Fig. 4.66b with a continuous line. Further calculations, still referred to a depth of 1 m, are reported below. A 2m thick cover has been analysed in this case, assuming a unit gradient at the lowermost boundary. These calculations give some insight about the role of the air entry value combined with the rainfall history.

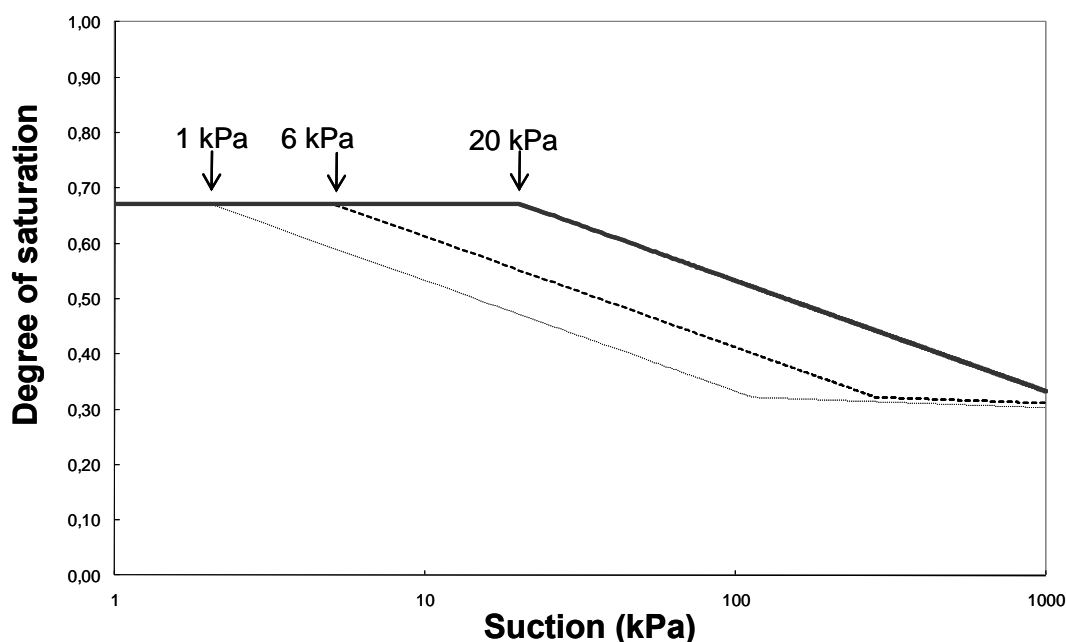


Figure 4.71 - Water retention curves assumed to investigate the effects of the air entry value

Figure 4.72a reports the results obtained for the dry season. During the first dry period, suction increases slightly (A-B line). First precipitations (B-C) cause a suction decrease. For the curve presenting the highest air entry value (20 kPa), the suction gradient is small, due to higher suction determining both lower permeability and the influence of the sloped part of the WRC with a relatively large amount of water needed for equalization. Starting from point C, the increasing permeability produces a scattered evolution of suction, with abrupt and sharp increments during rainfall events (C-D-E). Such steep and high changes in suction are often enhanced by the small water content changes required when suction goes below the air entry value. For lower air entry values (6 and 1 kPa) the fluctuations of suction is less pronounced due to the wider range of suctions for which the behaviour is controlled by the sloped part of the WRC, i.e. the system requires more water for equalization, suction being more frequently above the air entry value. The results of the analysis for the wet season are reported in Figure 4.72b. Naturally, suction is on average lower than in the dry season thus the air entry threshold is exceeded many times and the permeability is higher. Consequently, the course of pore water pressure is characterized by strong fluctuations.

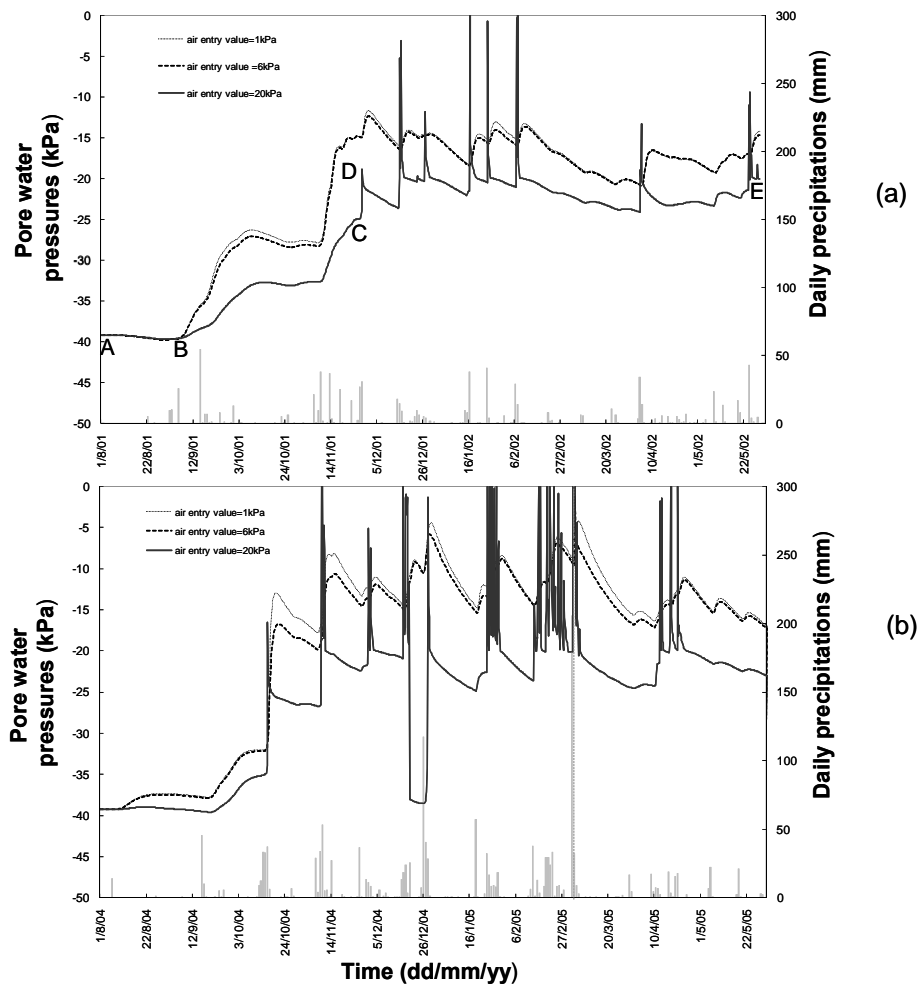


Figure 4.72 - Suction changes at a depth of 1m, for three different air entry values: a) dry season; b) wet season

For the same domain and boundary conditions as in previous analyses the role of permeability has been investigated by maintaining the same WRC. In six different analyses three different permeability functions (Figure 4.73) have been combined with the two rainfall histories adopted previously: the adopted WRC is the one of Fig. 4.71 with 6kPa air entry value. The lower permeability determines a smoother change in pore water pressure (Fig. 4.74), poorly affected by current rainfalls. In practice, its course is essentially regulated by the average value of rainfall over a wider meteorological window; this means also that pore water pressure is lower at the beginning of the season becoming progressively higher.

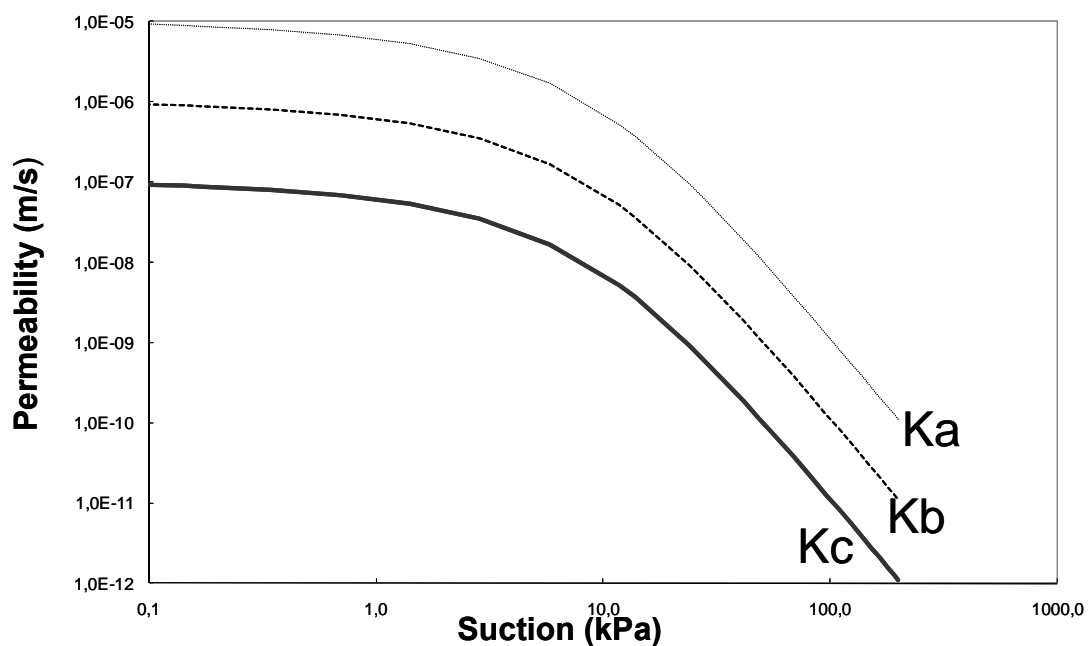


Figure 4.73 - Permeability functions assumed in the parametric study

Further analyses have been conducted to get a further insight about the influence of the hydraulic conductivity on the pore water pressures. An initial suction of 10kPa has been assumed throughout the domain, while the wet rainfall history has been adopted. However, the considered meteorological window is very short, including only the rainfalls of the 24 hours preceding the triggering time and neglecting the antecedent rainfalls. This in order to show to what extent soil permeability, represented by the functions reported in Fig. 4.73, makes the system sensitive to short and intense changes in boundary conditions.

Figure 4.75a plots the pore water pressure profiles obtained exactly at the triggering time for each permeability function. Figure 4.75b plots the same profiles computed five hours later. Results indicate that the sensitivity to a short and intense rainfall event is extremely poor for the lowest permeability, Kc, suction profiles changing only through the first 20 (Fig. 4.75a) or 40 cm (Fig. 4.75b) from the ground surface. The system is on the other hand extremely sensitive to the rainfall event for the highest permeability function, Ka, which leads to a complete change of the suction profile in the uppermost half part of the cover (Fig 4.75a) or through its entire thickness (Fig. 4.75b).

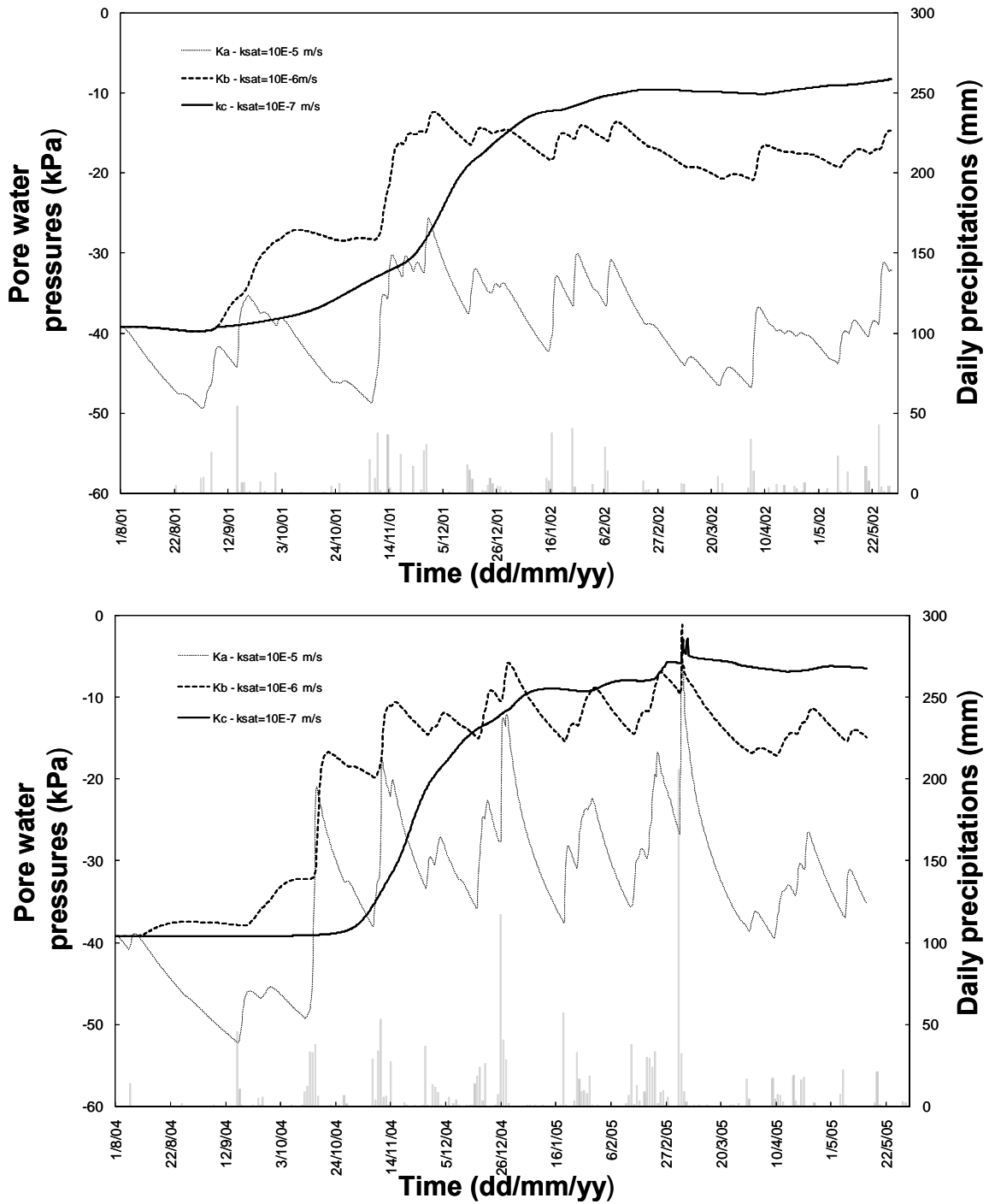


Figure 4.74 - Soil suction changes at a depth of 1m, for the three permeability functions plotted in Fig.4.73

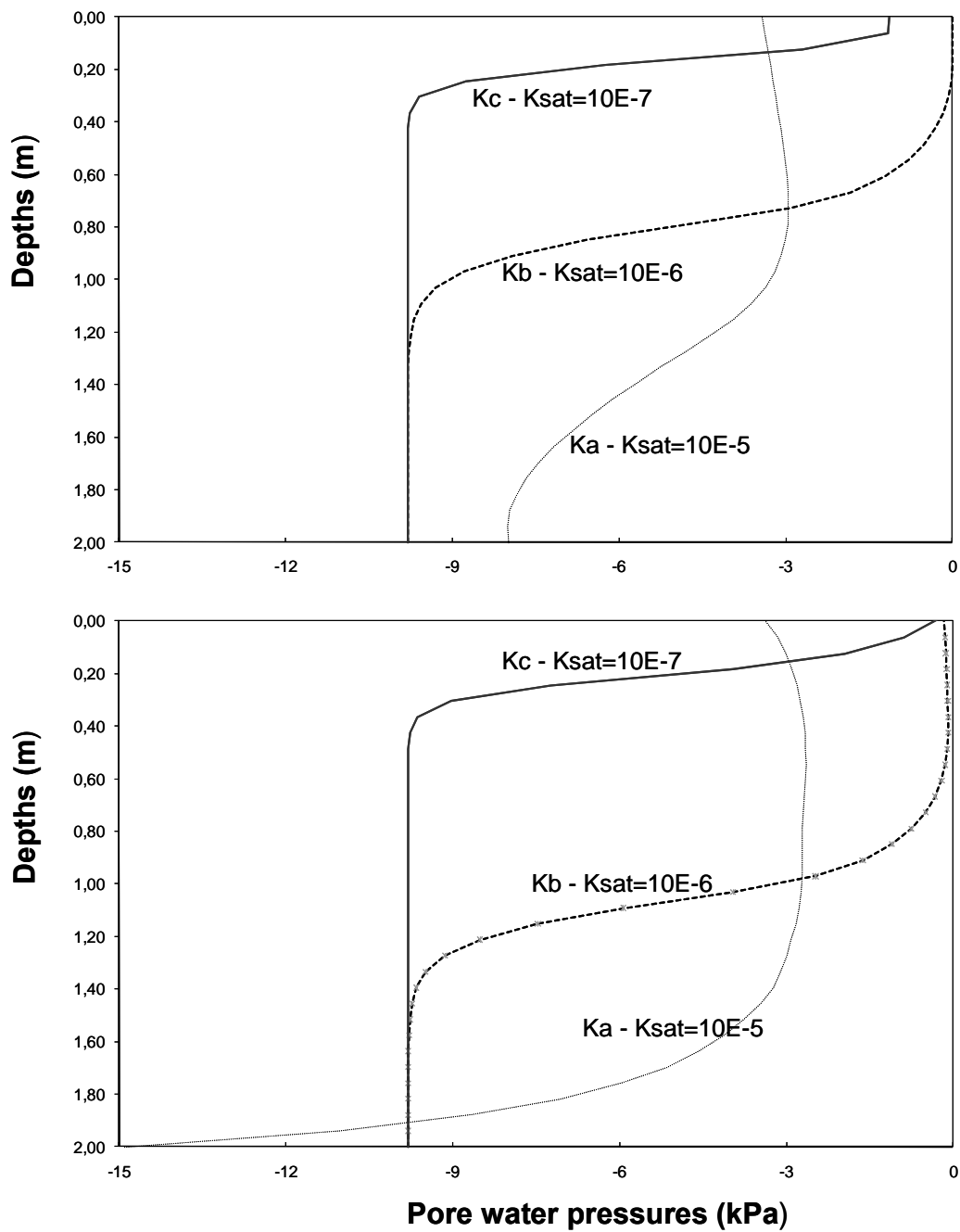


Figure 4.75 - Suction profiles obtained for the three permeability functions plotted in Fig.4.73, (a) at the triggering time and (b) 5 hours later

d) The influence of the initial conditions

Another set of analyses has been carried out to study to what extent the slope behaviour is sensitive to the initial conditions. The computation was carried out for the soil parameters, the slope geometry and the boundary conditions adopted previously, assuming for suction a uniform value along the whole soil thickness, equal to 20, 40 and 70 kPa respectively. The wet rainfall history has been adopted in the analysis.

The values calculated at a depth of 1 m (Fig. 4.76a) and 1.5 m (Fig. 4.76b) show that, after a while, suction converges, irrespective of initial conditions, to a more or less unique value; the deeper the point considered, the longer the time required for suction to converge.

From previous analyses it can be easily argued that the influence of the initial conditions is higher for a higher slope of the water retention curve and for smaller permeability.

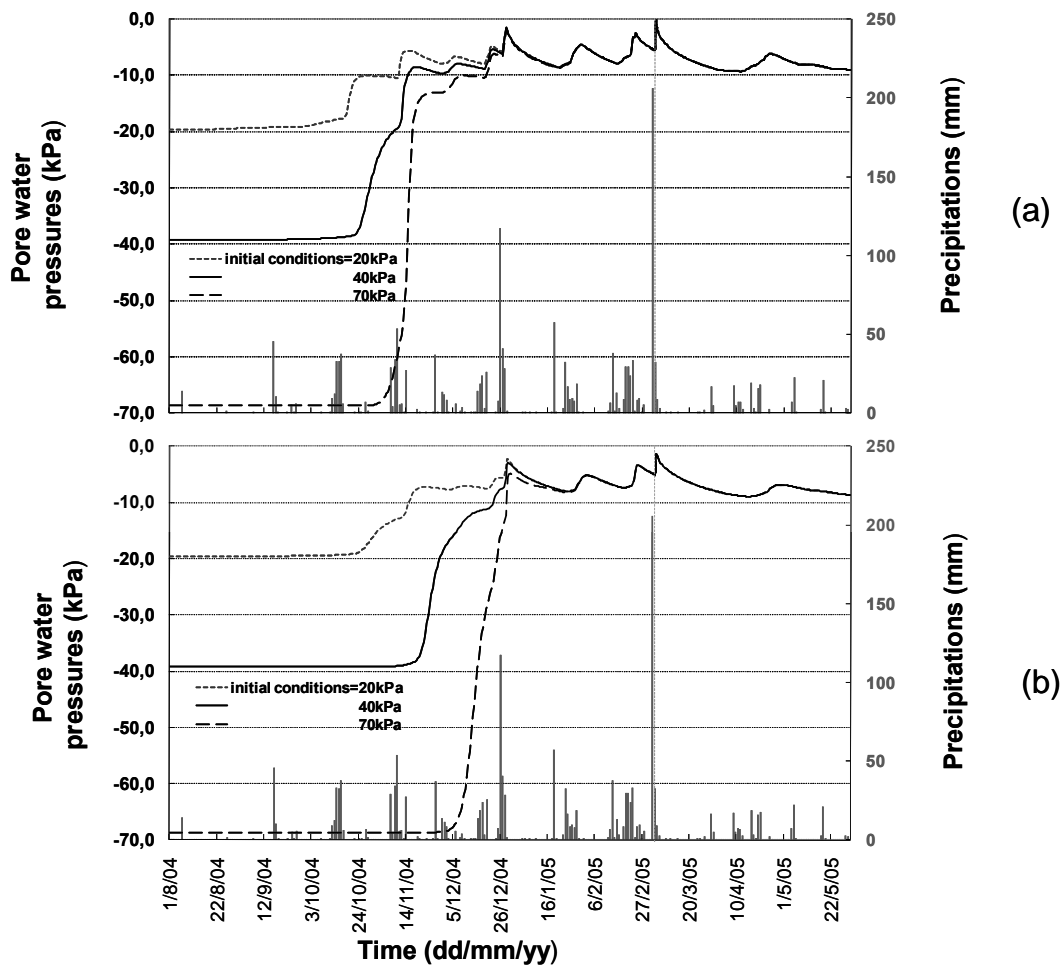


Figure 4.76 - Influence of the initial conditions on suction, assuming different initial values:
 (a) suction at a depth of 1m; (b) suction at a depth of 1.5m

e) The influence of the length of the meteorological window

To focus on the influence of the meteorological window, a number of analyses have been carried out considering, first, just the rainfall event acting alone, then the antecedent rainfalls acting over different time spans. The rainfall history is the wet one. Antecedent rainfalls have been added going progressively back in time up to find the time length for which the results become insensitive to a further extension of the meteorological window.

Figure 4.77 plots the computed suction at a depth of 1 m, for an initial uniform suction of 40 kPa and for the three different permeability functions defined in Figure 4.73a, all used in conjunction with the water retention curve of Figure 4.73b. The results show that for the maximum permeability the effect of antecedent rainfalls is negligible. On the other hand, the extension of the meteorological window affecting the results progressively increases with decreasing permeability. For the analysis conducted assuming a hydraulic conductivity $k_{sat} = 10^{-6}$ and 10^{-7} m/s, suction does not change under the mere application of the rainfall event. The progressive extension of the duration of antecedent rainfalls causes a progressive decrease in soil suction at the reference time. The length of time for which the results do not depend on the initial conditions is equal to 2 months and 4 months, respectively for the two hydraulic conductivities considered.

Obviously, if a deeper point was assumed, a longer time period would be necessary.

f) The influence of the available rainfall records

The available rainfall histories adopted above cover cumulated values over 10 minutes. However, in other cases only hourly or daily values are available, so that a question arises about the importance that this factor (time resolution of records) plays on the results of analysis. In principle, the time resolution could affect significantly the results if the analysis, as in cases here illustrated, can discriminate between the part of water which infiltrates and the run-off amount. As an example, if during a day only a storm of 20 mm occurs in 5 minutes, an analysis carried out with a time resolution of 10 minutes should quite correctly predict that most of the storm results in run off. In contrast, analyses carried out with poor time resolution, for instance a day, would predict that the whole rainfall volume is capable to infiltrate: in fact, 20 mm of water spread uniformly over a day may be well absorbed by the system.

For the case of wet rainfall history, analyses have been carried out for which the rainfall history with different time resolutions is interpreted: the highest one made available by records (10 minutes) and two resolutions typically met in practice, i.e. 1 hour and 1 day. Figure 4.78 compares the corresponding suction changes referring to specific depths (0.5m, 1m, 1.5m and 2.0m). The results indicate that suction is quite unaffected if the time resolution ranges between 10 minutes and 1 hour. If the time resolution is 1 day, the results are quite different. In particular, suction is underestimated on average, due to the higher rainfall volume which is absorbed by the ground (Fig. 4.79). Sometimes, however, suction is overestimated because a given amount of rainfall may determine lower suction if it is adsorbed in a shorter period and this effect may go lost if the analysis spreads the rainfall amount over time periods of days.

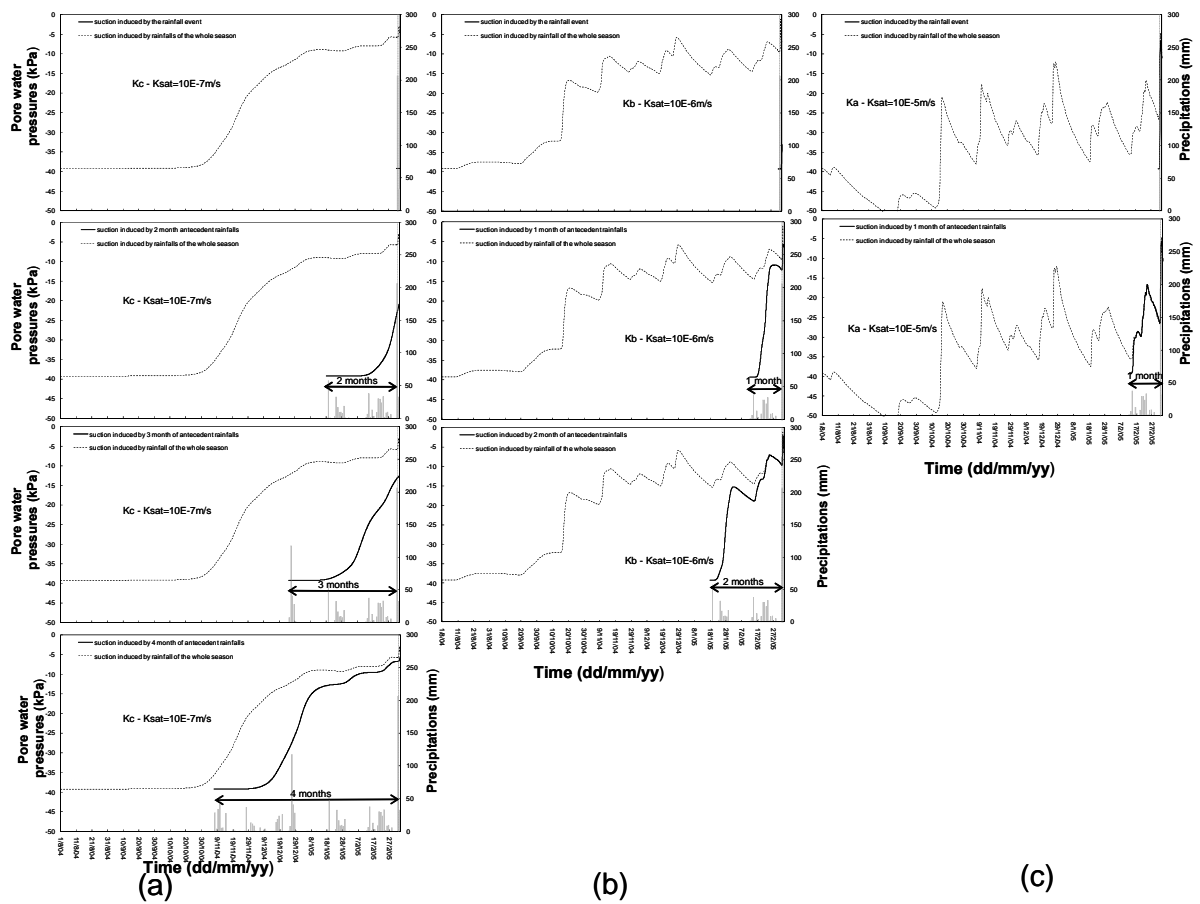


Figure 4.77 - Influence of antecedent rainfalls on value of suction at the triggering time, accounting for different rainfall histories and for the permeability functions in Figure 4.73: (a) Kc; (b) Kb; (c) Ka

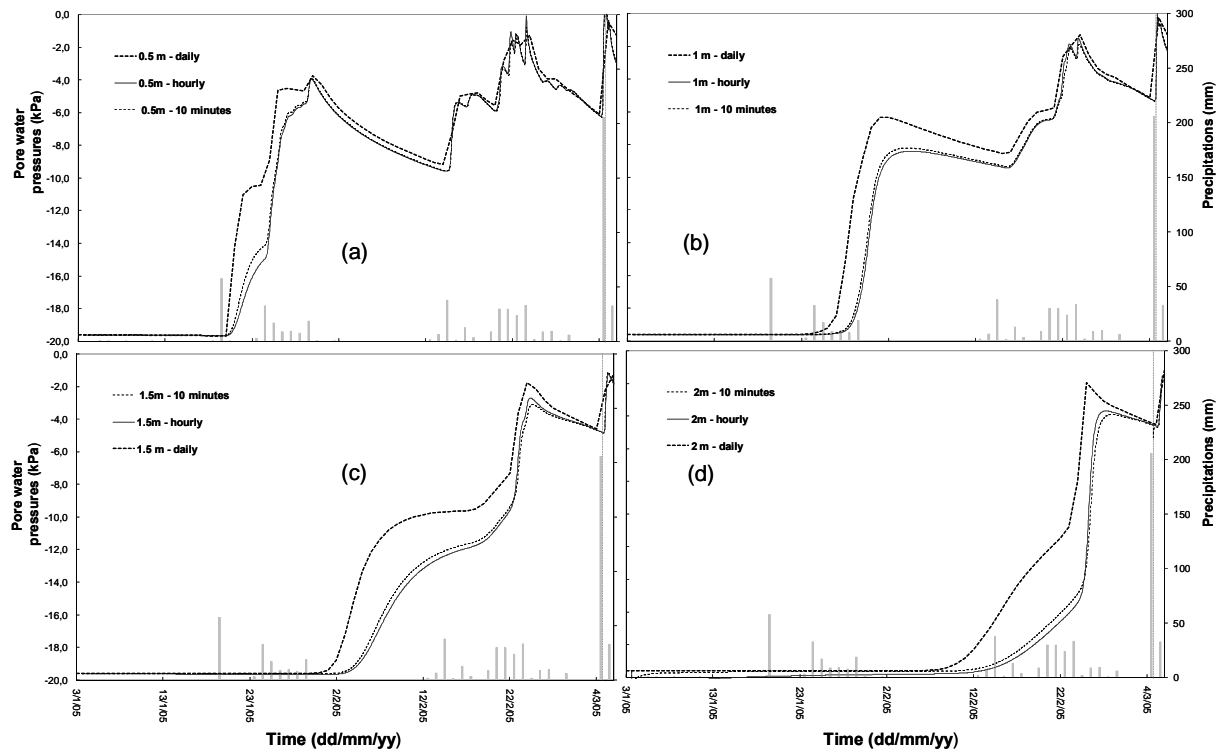


Figure 4.78 - Influence of time resolution on suction predictions, at four different depths “z”: (a) z=0.5 m; (b) z=1m; (c) z=1.5 m; (d) z=2m

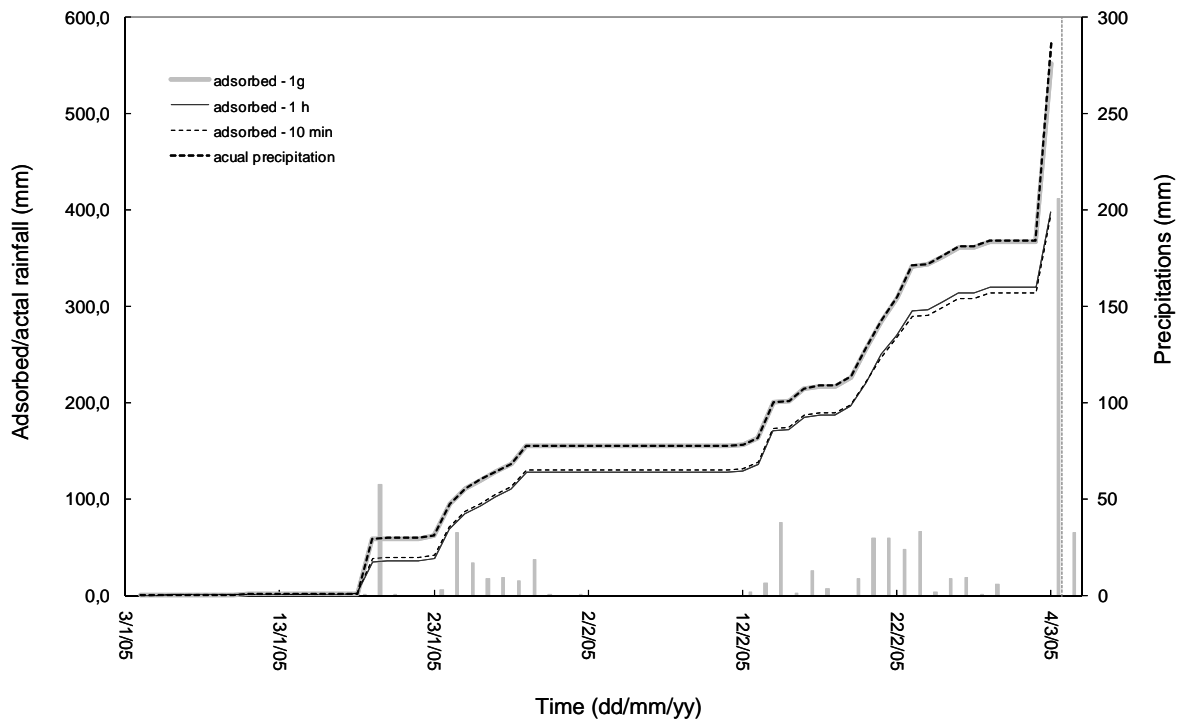


Figure 4.79 - Influence of time resolution on the amount of absorbed water

4.1.2.4.3 Stability analyses of partially saturated slopes in alpine regions (EPFL)

a) Introduction

Slope movements in Alpine regions frequently occur during heavy precipitation events or extremely fast snow melting processes. Slip surfaces mostly develop at shallow depths and the involved soil masses range between a couple of hundred to thousand cubic meters. Their occurrence depends not only on the immediate action of rain and snow melt, but also on predisposition factors related to different geological, morphological, hydrogeological, vegetational and soil mechanical conditions.

In 1966 and 1975 a series of shallow slips and debris flows occurred in the Upper Carinthia and Eastern Tyrol (Austria) as a consequence of heavy precipitation. Hohensinn (1979) and Moser and Hohensinn (1983) investigated around 140 slope movements in those regions and performed a more detailed study on 16 cases. The slope movements are reported to take principally place in slightly cohesive colluvial and residual soils of crystalline schists. The soil cover in these alpine regions rarely exceeds 2m. The reported slips occurred mostly in 1 to 2m depth.

Based on their observations, slope failures were plotted in an intensity-duration diagram shown in Figure 4.80 which allowed to distinguish between 3 different groups of mass movements: mass movements due to rainstorms of high intensity (group I), mass movements due to precipitations of several hours' duration with medium intensity (group II) and mass movements due to continuous heavy rainfall of one to two days duration frequently accompanied by heavy snow melting events (group III).

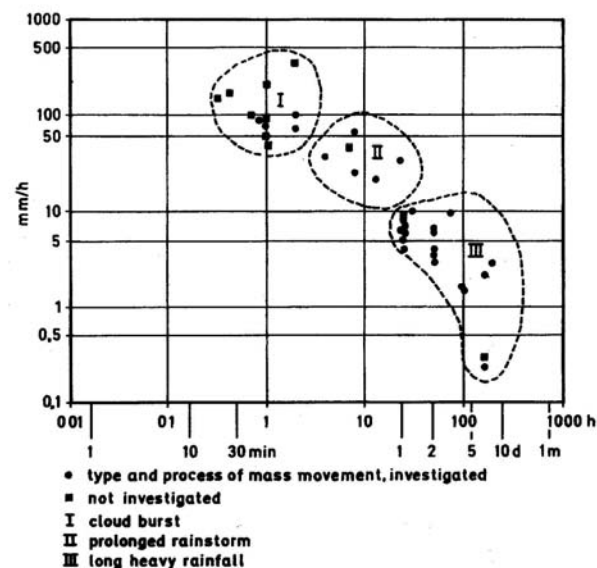


Figure 4.80 - Relation of repeated occurrence of mass movements in soils and precipitations (Moser & Hohensinn, 1983)

Based on the observations in the above-mentioned alpine regions, numerical 2D calculations are performed by means of the finite element code Z_Soil (Zace Services Ltd., 2009). The

idea is to study the influence of climate conditions and soil hydraulic parameters on the stability of partially saturated slopes in alpine regions.

b) Geomechanical model

For the following numerical 2D analyses, the soil layer of 2m thickness is assumed to be initially at a residual degree of saturation equal to 8 percent. The assumption that there is initially no groundwater flow in the slope allows isolation of the gravity-induced shear stress from the seepage-induced shear stress (Anderson and Sitar 1995). The influence of antecedent rainfall, respectively variable initial soil moisture conditions is studied in a further step. The slope has an angle of 35 degrees, a height of 56 m and a length of 80 m (Figure 4.81). Part of the bedrock is modelled as well in order to impose an initial hydraulic steady state with uniform saturation conditions in the upper soil cover. The finite element mesh contains 2600 4-noded quadratic elements and is refined in the soil layer of interest.

Seepage surfaces are defined along the slope surface in order to switch from flow boundary conditions to zero pressure boundary conditions when the soil reaches saturation. A constant head equal to 10 m is defined on the bottom boundary of the model in order to define a uniform initial state of residual degree of saturation in the soil cover. After an initial gravity loading calculation, variable rain infiltration patterns are simulated by means of imposed boundary fluxes along the slope surface.

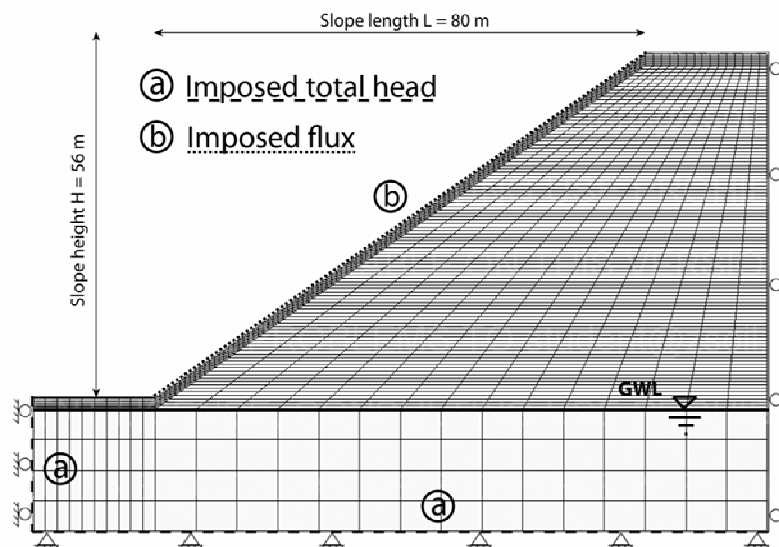


Figure 4.81 - Finite element model with initial and boundary conditions

The water retention curve of Van Genuchten type is fitted to the retention curve estimated by Tarantino and Mongiovi (2003) based on soil texture and bulk density reported by Moser and Hohensinn (1983) (Figure 4.82):

$$S_r = S_{res} + \frac{1 - S_{res}}{\left[1 + \left(\alpha \frac{s}{\gamma_F}\right)^n\right]^m} \quad \text{for } s \geq 0 \quad [1]$$

Where S_r is the degree of saturation, s is matric suction (positive), S_{res} is the residual degree of saturation equal to 8 percent, α is a scaling parameter with a value of 1.1 and γ_F is the specific fluid weight. In Z_{Soil} the exponents n and m of Van Genuchten's retention model (Van Genuchten, 1980) have fixed values of 2, respectively 0.5. The fitted curve has an air-entry value of about 2 kPa.

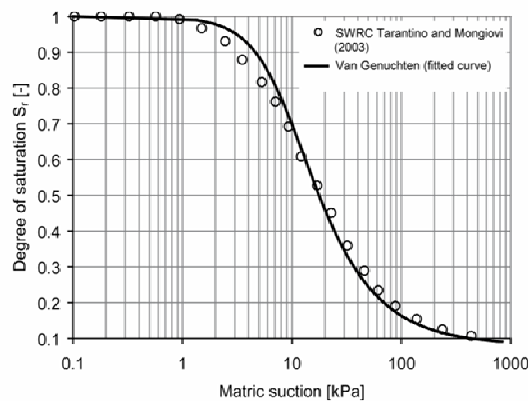


Figure 4.82 - Soil water retention curves (WRC) for the numerical simulations

Darcy's law is used to describe the fluid flow through the porous media in saturated, as well as unsaturated conditions. As reference case, the isotropic, saturated water permeability $k_{w,sat}$ of the soil cover takes a mean value of 10^{-5} m/s. For the parametric analyses, variable soil water permeabilities are assumed according to Table 2. As reported by Moser and Hohensinn (1983), the underlying bedrock is often composed of crystalline schists and thus for the numerical analysis assumed impermeable relative to the residual soil coverings. To this end, the saturated water permeability of the bedrock is given a value of 7 orders of magnitude smaller than the permeability of the soil cover. In unsaturated conditions, water relative permeability varies as a function of matric suction. The following cubic law is used in this case (Zace Services Ltd., 2009):

$$k_{r,w} = k_{w,sat} \frac{(S_r - S_{res})^3}{(1 - S_{res})^3} = \frac{k_{w,sat}}{\left[1 + \left(\alpha \frac{s}{\gamma_F}\right)^2\right]^{3/2}} \quad [2]$$

The bedrock displays an elastic behaviour while the upper soil layer is modelled as an elastic, perfectly plastic material with a simple Mohr-Coulomb yield criterion. The shear strength angle is equal to 35 degrees and the soil is assumed cohesionless in the sense that effective cohesion c' is taken equal to zero. Strength increase due to matric suction in the partially

saturated soil layer is considered by means of an increase in effective stress according to Bishop's effective stress framework (Bishop 1959; Nuth and Laloui 2008):

$$\underline{\underline{\sigma}}'_{ij} = \underline{\underline{\sigma}}_{net,ij} + S_r s \underline{\underline{\delta}}_{ij} \quad [3]$$

Where $\underline{\underline{\sigma}}'_{ij}$ and $\underline{\underline{\sigma}}_{net,ij}$ are the second order effective, respectively net stress tensors and $\underline{\underline{\delta}}_{ij}$ is the Kronecker delta.

A complete list of the hydraulic and mechanical material parameters figures in Table 4.5.

Table 4.5 - Reference material parameters for the 2D finite element simulations

<i>Mechanical parameters</i>		
Elasticity	E : Young's modulus	100 [MPa]
	ν : Poisson's coefficient	0.3 [-]
Plasticity	ϕ' : shear strength angle	35 [°]
	c' : effective cohesion	0 [kPa]
Weight and density	γ_s : specific soil weight	27 [kN/m ³]
	e_0 : initial void ratio	0.5
<i>Hydraulic parameters</i>		
Retention behaviour	n : Van Genuchten parameter	2 [-]
	m : Van Genuchten parameter	0.5 [-]
	α : Scaling parameter	1.1 [m ⁻¹]
	S_{res} : Residual degree of saturation	0.08 [-]
Permeability	$k_{r,sat}$: Saturated hydraulic conductivity	10 ⁻⁵ [m/s]

c) Simulation of rain infiltration in a partially saturated slope

The fluid motion in the two-phase medium is described by the groundwater flow equation which is deduced from the continuity equation for the fluid phase, considering a deformable solid matrix, a storage function $c(p)$ and integrating the generalized Darcy's law. Partial saturation is considered in the general diffusion equation via the degree of saturation S_r :

$$S_r \dot{\epsilon}_{kk} + q_{k,k} = c \dot{p} \quad [4]$$

Where $\dot{\epsilon}_{kk}$ is the volumetric strain rate and q_k the relative fluid velocity. The storage function $c(p)$ is defined as:

$$c(p) = n \left(\frac{S_r}{K_F} + \frac{dS_r}{dp} \right) \quad [5]$$

Where K_F is the fluid bulk modulus.

From a mechanical point of view and given the specific soil water retention behaviour, the decrease in suction during water infiltration in such a partially saturated soil leads to a

decrease of the spherical components of Bishop's effective stress tensor according to equation [3]. In Figure 4.83, the changing stress state is shown in a Mohr-Coulomb plane with the failure envelope characterised by the shear strength angle ϕ' . The apparent cohesion due to suction is considered implicitly via Bishop's effective stress. During water infiltration, the major and minor principal effective stresses $\sigma'_{1,0}$ and $\sigma'_{2,0}$ decrease until the stress state reaches the failure envelope. The available shear strength is given by the classical Mohr-Coulomb yield criterion and can be written as:

$$\tau_f = (\sigma_{net} + S_r \cdot s) \cdot \tan \phi' \quad [6]$$

Where τ_f is the shear strength and σ_{net} is the net stress corresponding to the total stress in a two-phase porous medium. In equation [6] the shear strength is not only function of the mechanical stresses, but also of the retention behaviour by means of the degree of saturation S_r . An explicit coupling between the mechanical and hydraulic behaviour is consequently established.

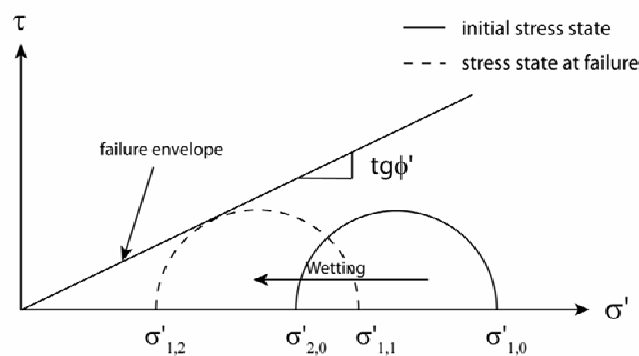


Figure 4.83 - Stress states in a Mohr-Coulomb plane. Due to a decrease in suction during wetting, Bishop's effective stress decreases too until the failure criterion is reached.

In Figure 4.84 the available shear strength is plotted against matric suction. The contribution of net stresses to the shear strength is omitted here. Due to the asymptotic nature of the analytical formulation of the water retention curve, the available shear strength increases indefinitely as suction increases. There is no continuity between the completely dry state with zero shear strength and a state with infinitely small degree of saturation. Consequently, the shear strength is clearly overestimated in the dry range at high values of suction (>300 kPa). Since matric suction reaches initially values up to 600 kPa in the numerical model, it has to be guaranteed that failure mechanisms can't occur in the suction range above 300 kPa which the model would not be able to capture because of the overestimation of the shear strength. Else, strain localisation should not occur in a zone where the degree of saturation is lower than 10%. However, analyses of suction and deviatoric strain profiles have shown that failures never occur in such dry conditions.

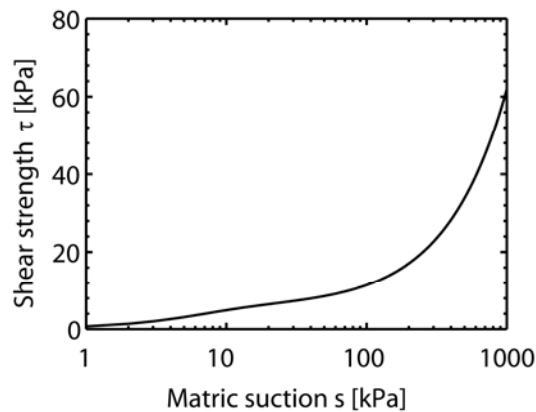


Figure 4.84 - Contribution of matric suction s to the shear strength τ of the soil

d) Safety factor analysis by means of the strength reduction method

The subsequent slope stability analyses are performed by means of the shear strength reduction technique for the finite element method (SSRFEM) (Zienkiewicz et al., 1975). The soil strength parameter ϕ'_f used in FEM procedures is defined as the actual shear strength parameter ϕ' divided by a shear strength reduction factor F_t :

$$\phi'_f = \arctan(\tan \phi' / F_t) \quad [7]$$

The shear strength reduction factor F_t increases incrementally until failure occurs. Failure can be numerically indicated by a non-convergence of the calculation which is the limit criterium chosen here. The safety factor analysis starts with a value of $F_t = 1$, performs the stress-strain calculation and in case of convergence increments F_t by a value of $\Delta F_t = +0.05$. This iteration process is run until the stress-strain calculation diverges. In that case, the final safety factor lies between the current and precedent value of F_t . Consequently, the interval of confidence is 5%.

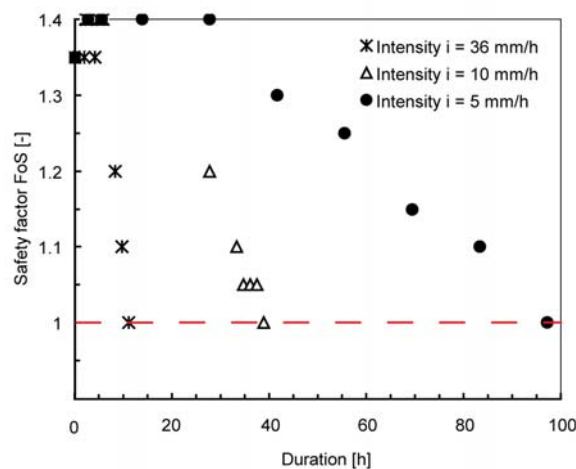


Figure 4.85 - Evolution of the safety factor of a partially saturated slope during rain infiltration

Unlike limit equilibrium methods no initial assumption is necessary for the shape of the slip surface. Safety factor and slip surface are direct results from the strength reduction method. For the transient hydromechanically coupled simulation of water infiltration and soil deformation, the safety factor analysis is run at different timesteps in order to assess critical variations and determine the time corresponding to the occurrence of the most probable failure mechanism of the slope (Figure 4.85). Initially the safety factor of the dry slope is $FoS = 1.4$.

e) Parametric analyses

The objective is to determine the influence of soil water permeability, as well as initial and boundary conditions on the stability of partially saturated soil slopes in alpine regions subjected to rain infiltration.

For the subsequent parametric analyses, intensity of a main rainfall event, intensity and duration of antecedent rainfall or snow melt and soil permeability k_{sat} are varied according to the indications in Table 4.6.

Table 4.6 - Parametric analyses

Scenario	Soil properties	Antecedent snow melting leading to water infiltration		Major rainfall event
	Sat. permeability k_s [m/s]	Intensity [mm/h]	Duration [days]	Intensity [mm/h]
A (18 combinations)	10^{-5}	{0; 2.5}	{0; 3; 6}	{0.4; 2.5; 5; 10; 50; 100}
B (2 combinations)	10^{-4}	0 2.5	0 3	10 5
C (2 combinations)	10^{-6}	0 2.5	0 3	10 5

f) Intensity and duration of rain infiltration

Critical rainfall intensity-duration curves are commonly established empirically based on recorded sliding events at a representative regional scale in order to provide a tool for landslide early warning (Caine 1980; Guzetti et al. 2007 and 2008). A representative regional scale is defined as the scale at which geomorphological, hydrogeological and geological features of slopes, as well as climatic conditions are similar. Natural slopes have been adapting themselves over thousands of years to the ambient climatic conditions. Consequently it is not astonishing that a regional scale is often detected at which slopes fail for similar climatic conditions in terms of rainfall intensity and duration (Nadim et al. 2009).

The subsequent numerical simulations for a representative, steep alpine slope can help understand some of the physical mechanisms governing the slope behaviour during rainfall events. In many cases, a substantial decrease in effective stress due to a loss in matric suction has been identified as principal mechanism leading to failure (Cho and Lee 2001; Tsai et al. 2007). This is especially the case in residual alpine soils which frequently exist in an unsaturated state. In others, mounding of the water table and development of positive pore-water pressures lead to critical conditions (Collins and Znidarcic 2004; Rahardjo 2007).

Tarantino and Bosco (2000) have shown that the shape of typically observed rainfall intensity-duration thresholds can be well reproduced if the soil is assumed to be unsaturated at the onset of precipitation. Later, Tarantino and Mongiovi (2003) performed a 1D rain infiltration and slope stability analyses for a representative case of a soil slope in the above-mentioned alpine regions. Their analyses pointed out the advantages of accounting for the partially saturated soil state in order to capture shallow failures during rain infiltration.

In the subsequent 2D analysis, time to failure and type of failure mechanism are predicted for different rain infiltration intensities. The results are compared in Figure 4.86 with the field observation data (Moser and Hohensinn, 1983) and the results from a 1D analysis performed by Tarantino and Mongiovi (2003). The general trend of the performed numerical simulations is in agreement with the data from field observations. Higher rainfall intensities lead to shorter durations up to failure. In both, numerical 1D and 2D studies, the consideration of partial saturation allows accounting for superficial failures due to loss of suction during heavy rainfall events (see also Figure 4.87a). There remain however important differences between the 1D and 2D simulations, which lie in the fact that the initial conditions in both cases are not the same, the geometry of the problem plays a role in the 2D analysis and different assumptions are made for the two safety factor calculation methods - SSRFEM in a deformation analysis and LEM in a static equilibrium analysis.

Regarding the initial conditions in the 1D infiltration analysis, antecedent rainfall was neglected and a theoretical initial suction profile resulting from a zero pressure condition at the bedrock level, a hydrostatic distribution of matric suction in the vadose zone and a superimposed 60 day evapotranspiration phase was assumed. For the present 2D analysis, a residual degree of saturation is computed in the whole soil cover. Consequently, the soil is initially drier in the present case and the volume of infiltrated water in order to reach failure is bigger.

Due to the presence of an impermeable bedrock in the 2D model, water reaching the bottom of the soil cover flows parallel to the slope, creating consequently a 2D flow. This specific hydraulic behaviour which is not captured in a 1D analysis has wider implications on the mechanical behaviour of the slope, as discussed in the next chapter.

The infinite slope stability analysis adopted by Tarantino and Mongiovi (2003) assumes that the problem is 1D with a failure surface running parallel to the slope. Indeed, for most infiltration conditions, the failure surface is located at the bedrock interface which is parallel to the slope surface. However, the 2D finite element analysis showed that shallow failures at high rainfall intensities (>10 mm/h) are rather localised in a finite zone. The finite element method in the 2D simulations actually calculates the deformations in the soil resulting from changes in effective stresses due to pore pressure variations and captures plastic strain localisations developing up to the slope surface. No failure surface is assumed a priori.

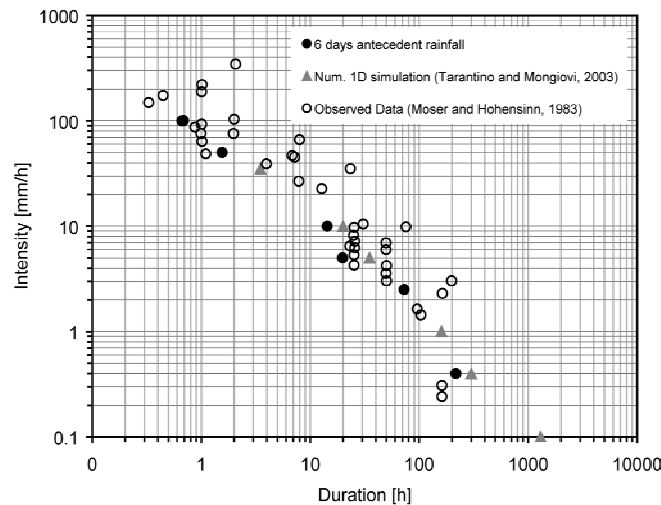


Figure 4.86 - Critical intensity-duration couples of rain infiltration according to the numerical 2D simulations, the 1D infiltration analysis by Tarantino and Mongiovi (2003) and the field observation data by Moser and Hohensinn (1983)

The field measurements of the saturated water relative permeability $k_{r,w}$ of the soils studied in Moser and Hohensinn (1983) vary between 10^{-4} and 10^{-6} m/s. Within this range the time to failure for a slope subjected to a rainfall of a given intensity may vary strongly. In the present case, for a rainfall intensity of 10 mm/h, failure occurs after 50 hours when the saturated water permeability of the soil is $k_s = 10^{-4}$ m/s, 39 hours for $k_s = 10^{-5}$ m/s and 15 hours for $k_s = 10^{-6}$ m/s. Figure 4.87 shows in fact, that the failure mechanism is not the same, depending on the water relative permeability of the soil. For a low permeability, a superficial failure (< 0.5 m) occurs because pore pressures are unable to dissipate in time (Figure 4.87a). Deviatoric strains are less important at the slope surface when the infiltrated water is able to penetrate into the soil cover (Figure 4.87b). The failure surface develops along the bedrock interface in the upper part of the slope. When the soil cover has a high permeability, the infiltrated water rapidly percolates to the impermeable bedrock interface where pore pressures begin to increase. If the volume of infiltrated water is large enough, a water table begins to form with a groundwater flow concentrated in a downwards movement. The failure mechanism is consequently located at the bedrock interface and mobilises a large volume of soil (Figure 4.87c).

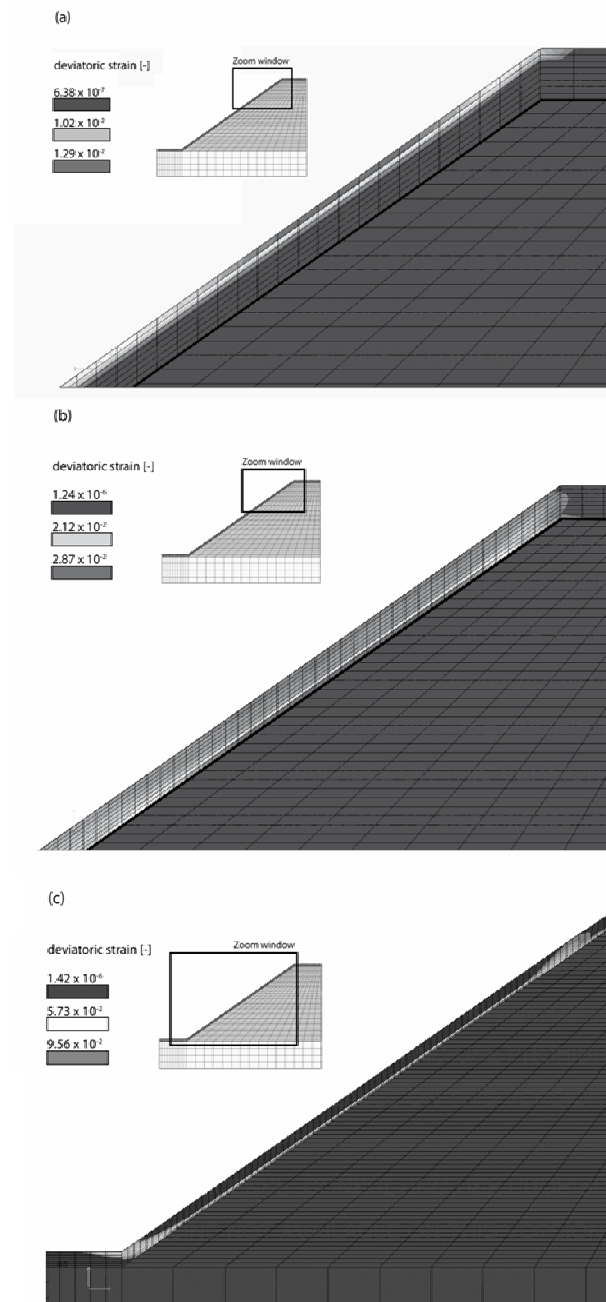


Figure 4.87 - Deviatoric strains $\varepsilon_{dev} = \sqrt{I_{2D}}$ corresponding to probable failure mechanisms.
 (a) superficial failure mechanism for $k_{w,sat} = 10^{-6}$ m/s; (b) diffuse failure for $k_{w,sat} = 10^{-5}$ m/s;
 (c) Strain localisation at the bedrock – soil layer interface for $k_{w,sat} = 10^{-4}$ m/s

g) Influence of antecedent rainfall on the susceptibility of a slope to fail

The reported cases of shallow slides in Moser and Hohensinn (1983) mostly happened in early spring due to heavy precipitation or rapid snow melting. However, the susceptibility of a slope to fail under a given extreme weather event depends on several preparatory factors of which the initial degree of saturation is in particular highlighted here. The relationship between intensity and duration of rain infiltration is not univocal. In order to evaluate the influence of antecedent rainfall on the intensity and duration thresholds, the same calculations as for the reference dry soil state are run, but considering an antecedent 3 day and 6 day snow melting phase prior to the actual extreme weather event (Figure 4.88).

In absence of rainfall, the snow melting process is mostly governed by direct sun radiation and ambient air temperature. Other factors, such as shortwave radiation and wind effects influence the melting process as well. Temperature index solutions compose one family of commonly used methods to compute snow melt when energy budget variables are not available or when a large spatial and temporal scale is considered (USACE 1998). Contrary to energy budget equations which explicitly consider the physical processes in snow melting, the simple index concept is used for a statistical description of the phenomena by means of a known variable. Air temperature is an important variable in most energy budget equations, it is easy to measure and long-term data is available. Hence it is straightforward to use it as the statistical variable in the index methods. The basic equation for the temperature index solution is

$$M_s = C_m (T_a - T_{melt}) \quad [8]$$

Where M_s is the daily snowmelt rate in mm/day, C_m is the melt-rate factor in mm/°C/day, T_a is the daily ambient temperature and T_{melt} is the threshold melt temperature. The latter is often set to 0 °C. In old melting snow, the melt-rate factor C_m typically varies between 3.5 and 6 mm/°C/day (Semadeni-Davies 1997). Considering a temperature variation of 10 °C during daytime and a melt-rate factor of 6mm/°C/day, the average snowmelt rate for a 24 h melting phase is 2.5 mm/h. For the parametric studies, a constant snow melting phase of 2.5 mm/h is adopted. This corresponds to a total infiltration volume of 180 mm in 3 days and 360 mm in 6 days. The intensity duration curves plotted in Figure 4.88 shift to the left as the duration of the antecedent rainfall increases.

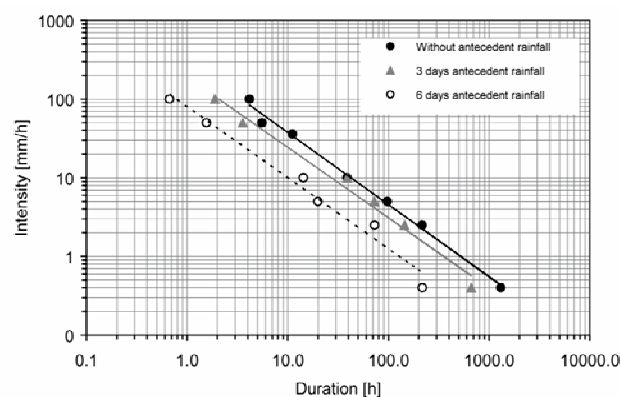


Figure 4.88 - Intensity-Duration curves for different initial conditions prior to a major rainfall event

Antecedent rainfall (or snow melting) increases the water content of the soil prior to the major rainfall event and decreases matric suction in the vadose zone. Small changes in pore water pressures might then trigger a slide. However, from a hydraulic point of view the susceptibility of a slope to fail is not alone function of the water content, but also on the water relative permeability of the porous soil. Compared to an initially dry soil, pore pressures are dissipated more rapidly within a more permeable, wetted soil. It follows as well that the time to failure of a slope subjected to rain infiltration is not per se higher when the slope experienced a period of antecedent rainfall.

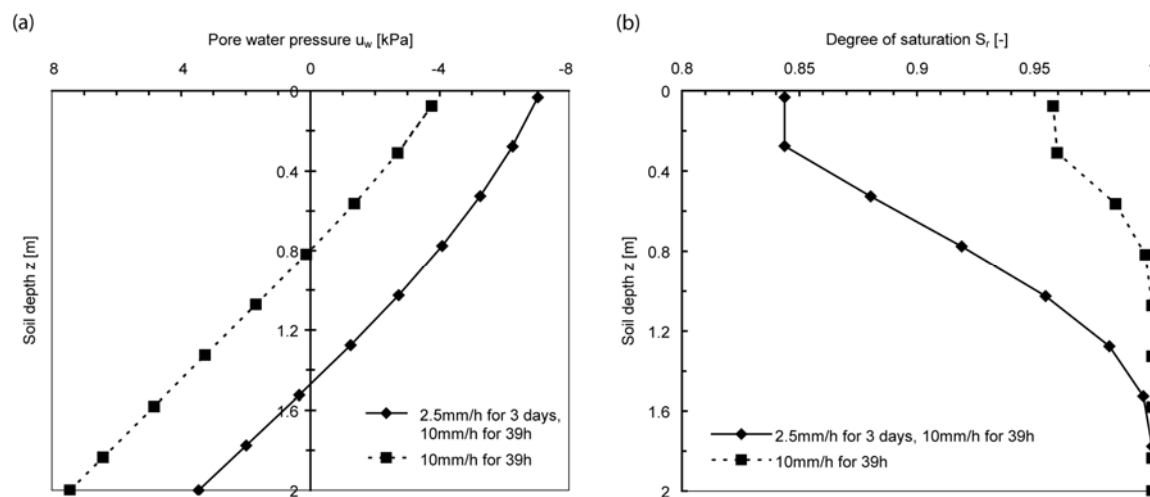


Figure 4.89 - Profiles of pore pressure u_w (a) and degree of saturation at time of failure within the failed mass for two water infiltration patterns.

Figure 4.89a and 4.89b show vertical profiles at the center of the mobilized masses of pore water pressures, respectively degree of saturation for two different rainfall patterns: The dotted line represents the case where the initially dry soil at a residual degree of saturation of $S_r = 8\%$ is directly subjected to a major rainfall event of 10 mm/h; the full line corresponds to the case where an antecedent water infiltration of 2.5 mm/h over 3 days takes place before the major rainfall event of 10 mm/h. In the latter, the degree of saturation before the major rainfall event varies between 35 and 41%. In both cases, the most probable slope failure mechanism according to a continuous safety factor analysis occurs after 39 hours of rainfall (see Figure 4.88). Hence, the critical time to failure is not lower for the soil presenting initially a higher degree of saturation. At the time of failure, the degree of saturation at the slope surface and the location of the water table are visibly lower in the case where the soil was initially wetted. In fact, the continuous wetting of the soil leads to a higher draining capacity close to the slope surface prior to the major rainfall event. Since for that case the water front penetrates more easily into the soil, a preferential flow path with high flow velocities along the impermeable bedrock interface can be established (Figure 4.90b and 4.91). Water is consequently transported from the upper to the lower part of the slope. In the case of an initially dry slope, pore pressures are unable to dissipate as fast as in a wetted soil. Since no preferential flow path between the upper and lower part of the slope is built up yet, pore pressures start to increase in the upper part of the slope (Figure 4.90a and 4.91).

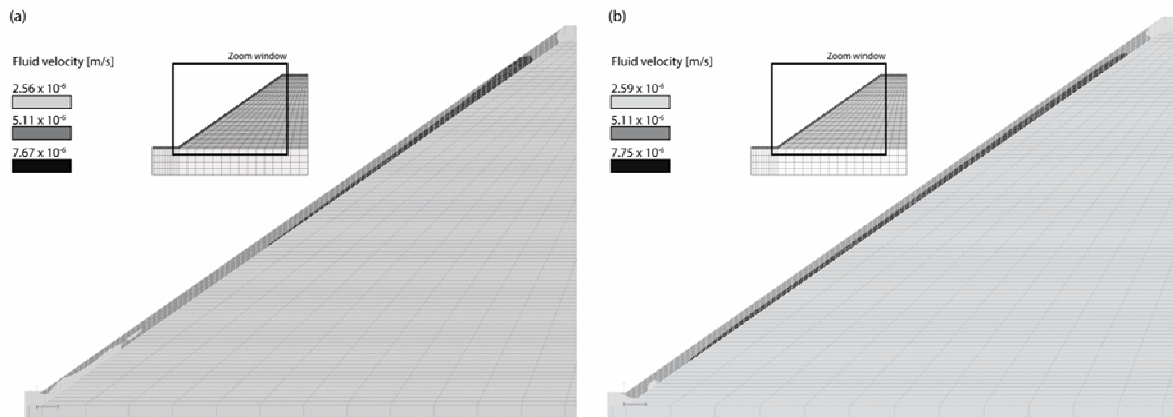


Figure 4.90 - Absolute values of fluid velocity [m/s] in the soil cover at the time of failure for the case without antecedent water infiltration (a) and with a 3 day antecedent water infiltration (b)

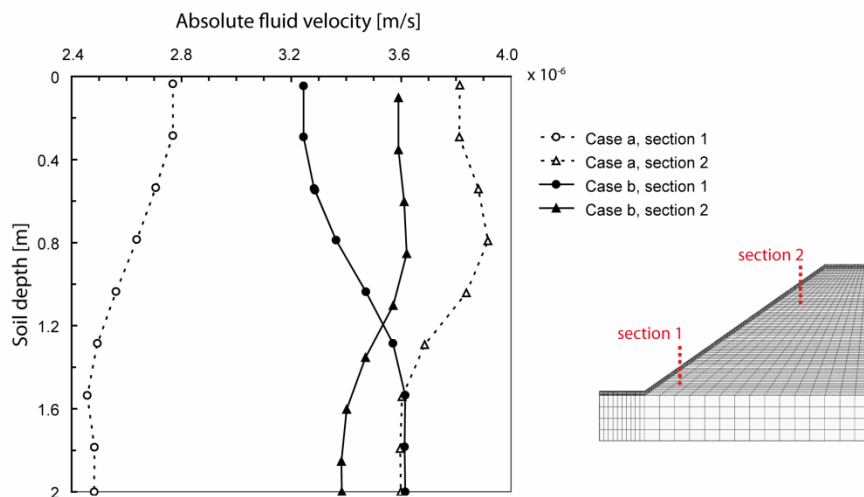


Figure 4.91 - Profiles of absolute fluid velocity [m/s] in two sections of the soil cover at the time of failure for the case without antecedent water infiltration (a) and with a 3 day antecedent water infiltration (b)

The flow behaviour described above implies that for the case of a slope subjected to antecedent water infiltration the effective stresses reduce continuously and quasi simultaneously in the upper and lower part of the slope during the major rainfall event. The numerical results for the evolution of mean effective stresses for two Gauss points at 1.8 meters soil depth in the upper and lower part of the slope confirm this (Figure 4.92): while in a dry slope subjected immediately to a major rainfall event the effective stresses reduce significantly in the upper part of the slope to the point where failure occurs (case a, section 2), they reduce simultaneously and slower in the whole slope after 3 days of light water infiltration (case b). Further it is observed that a dry soil shows a noticeable decrease in mean effective stresses during a first water infiltration phase due to the advancing water front leading to a substantial decrease in matric suction. The speed at which the water front

penetrates the soil layer depends on the infiltration rate. The higher the infiltration rate, the faster the water front advances. The initial difference in mean effective stress p' between section 1 and 2 is due to the automatic computation of initial matric suction which increases hydrostatically with the distance to the water table. Since the degree of saturation takes initially residual values in both sections, the product S_r times s is significantly higher in section 2 compared to section 1.

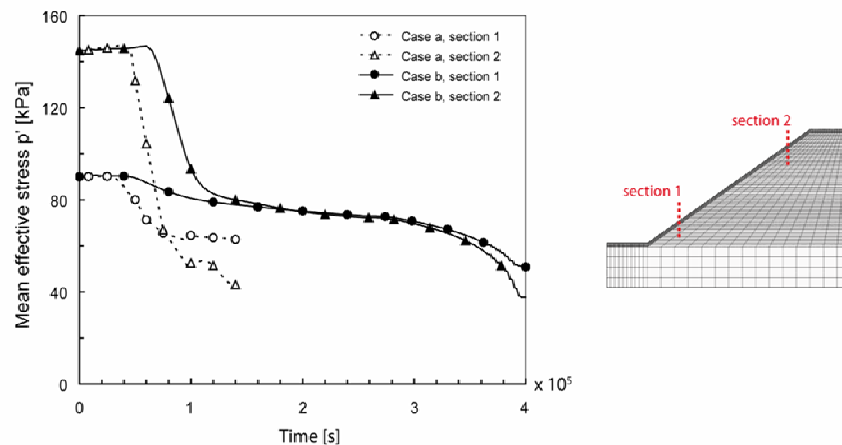


Figure 4.92 - Evolution of mean effective stresses p' [kPa] during water infiltration for two sections in the slope for the case without antecedent water infiltration (a) and with a 3 day antecedent water infiltration (b).

Without antecedent water infiltration the reduction in effective stresses is localised in the upper part of the slope and consequently the most probable failure mechanism is concentrated in a smaller area (Figure 4.93). The slip surface is in both cases localised along the bedrock due to the shallow nature of the soil cover, but the volume of soil mobilised during an event preceded by a longer period of water infiltration is more important.

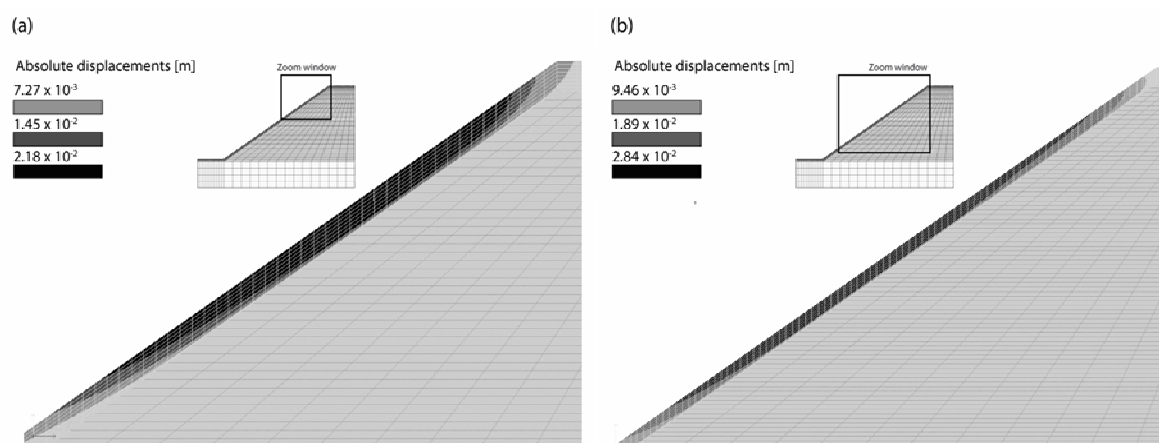


Figure 4.93 - Contours of absolute displacements indicating failure mechanisms for the case without antecedent water infiltration (a) and with a 3 day antecedent water infiltration (b)

4.1.2.4.4 Conclusions

(EPFL)

At a representative regional scale, the responses of soil slopes to a single external climatic event are observed to be similar (Moser and Hohensinn, 1983; Dai et al. 1999). Based on statistics of shallow slope failures with associated rainfall intensity and duration or cumulative rainfall amount, empirical relationships are often proposed to define critical rainfall thresholds for slope failure (e.g. I-D models, see also deliverable D1.5). These models are commonly used in practice for early-warning purposes. Within their limits and capacities to reproduce physical processes, numerical analyses performed with relatively simple models and parameters calibrated from field- and laboratory measurements allow associating basic failure mechanisms to observed field data. Critical environmental conditions leading to failure can be determined which slopes haven't experienced yet. The numerical simulations reveal also some critical points in empirical intensity-duration curves: The intensity-duration curve is sensitive to material parameters, such as soil water permeability and antecedent water infiltration prior to a major rainfall. The susceptibility of a slope to fail under a given rainfall of certain intensity and duration depends on the initial conditions prior to the major rainfall event.

Two parametric studies were performed to determine the role of soil hydraulic parameters, rainfall intensity and duration, as well as the rainfall pattern for predisposition and triggering of shallow slope failures in steep terrain. Both studies indicate that there doesn't exist one single factor controlling the landslide phenomena, but there are combinations of factors defining critical situations for slope stability. These combinations are variable, depending on soil type and the geological context of the considered slopes. The most evident example therefore is the variable importance of antecedent rainfall on the predisposition of a slope to fail. It was demonstrated that the meteorological window to consider in the hydraulic analysis is smaller for soil slopes with high water permeability. On the contrary, soil slopes with low values of permeability have a small capacity for pore pressure dissipation and therefore have a kind of "memory" for rainfall events that happened prior to any major rainfall event causing failure. Consequently, the numerical simulation of pore pressure variations within the soil slope needs to consider to a certain extent antecedent rainfall events in order to be accurate. The exact length of the meteorological window needs to be determined individually for each slope configuration since it depends on the soil type, but also on the critical soil depth to be considered for slope stability. This conclusion reduces to the generally valuable statement that for any numerical analysis of transient processes, appropriate initial hydraulic conditions need to be defined.

However, when having a closer look to the transient hydraulic response of partially saturated slopes to rain infiltration, it becomes clear that not only soil water permeability, but also the soil's retention behaviour takes a response-controlling function for a given rainfall pattern. Due to the soil's capacity to retain water, the transient hydraulic response of slopes in terms of pore pressures is dephased with respect to the considered rainfall event. In order to determine the effect of the retention curve, air-entry value and slope of the soil water retention curve ($\partial S_r / \partial s$) were chosen as parameters for the study. Results have shown that soil water retention curves presenting a relatively small slope as it is generally the case for well-graded soils, imply that changes in matric suction are important for small changes in the degree of saturation. Moreover, large variations in degree of saturation are expected in soils with a low capacity for pore pressure dissipation. The combined effect of low pore pressure dissipation

capacity and a small slope in the retention curve has shown to increase significantly the magnitude of pore pressure peak-responses.

Soil slopes may present a permeable substratum, as presented in the parametric study on pyroclastic soil slopes in Southern Italy, or a relatively impermeable substratum overlain by weathered bedrock and colluvial deposits as it is the case for many morainic alpine slopes.

The two-dimensional slope stability analysis presented in this chapter demonstrates the importance of considering saturated subparallel groundwater flow at the interface between bedrock and soil cover for determining failure susceptibility of a slope prior to any major rainfall event, failure mechanism and timing. The presence of an impermeable substratum favours the build-up of positive pore water pressures and a failure plane passing at the bottom of the soil cover. Along the interface, a preferential flow path for water is formed during a rainfall event. In that zone, groundwater is relatively rapidly transported from the top of the slope to the toe. If the slope is relatively dry prior to a major rainfall event, the preferential flow path doesn't exist initially. Infiltrated water in the upper part of a slope is stored in the soil and unable to dissipate in time if the rainfall is of high intensity. Pore pressures start to increase rapidly and a localised failure may occur. Compared to superficial failures, failures along the interface between soil cover and bedrock lead to bigger mobilised soil masses. The timing for failure does not only depend on the rainfall pattern, but also on the type of failure mechanism. Antecedent rainfall events can render a slope more susceptible to large failures since a wetted soil has an increased permeability which favors water infiltration to the bottom of the soil cover.

4.1.3 Scenarios of slope behaviour

(EPFL)

4.1.3.1 La Frasse – Large landslide in tertiary flysch (Swiss Alps)

a) General context and landslide characterisation

The La Frasse landslide is located in the Pre-Alps of the Canton of Vaud in Switzerland (Figure 4.94). It's a large landslide, mainly containing decomposed flysch (sandstone and clay schists) with an active, mobilized soil mass of around 42 million m³. Average velocities of the sliding mass are around 10-15cm/year. The slope has a mean inclination of 11° in the upper, and 20° in the lower part and moves over a length of 2km. It covers an area larger than 2km². Considering an estimated thickness of 80m in its upper section and 40m near the toe, a width between 500m in the upper and middle part and 800m in the lower part, the total volume of the sliding mass reaches 73 million m³. A limestone abutment delineates the upper, slower moving part from the lower, fast moving part of the landslide. It stabilizes around 31 million m³ of flysch above the bedrock in the upper part of the landslide. The landslide has been moving over the last 10'000 years, forming a well distinguished major slip surface. Along the main slip surface, but also within the sliding mass excess groundwater pressures (artesian levels) have been recorded (Tacher et al. 2005). The excitability of the aquifer can be related to the low values of the flysch permeability ($\sim 1 \times 10^{-6}$ m/s) and of the coefficient of specific storage ($\sim 1 \times 10^{-4}$ m/s) (Tacher et al. 2005). Measurements of rainfall and surface displacements of the landslide have revealed no simple correlation between the hydrological surface input and the reaction of the slope. Subsurface flows have been demonstrated to be of major importance for the understanding of the hydro-geological behavior of the large landslide. Measurements of pore pressures in several piezometers allowed calibrating a detailed hydro-geological finite element model for the landslide (NCG-EPFL 2004; Tacher et al. 2005). The simulated time-dependent pore pressures of the hydro-geological model were used as static boundary conditions for the geomechanical modeling which is presented hereafter. A more detailed geological description of the landslide and of the hydro-geological modelling is given in Deliverable 1.3.

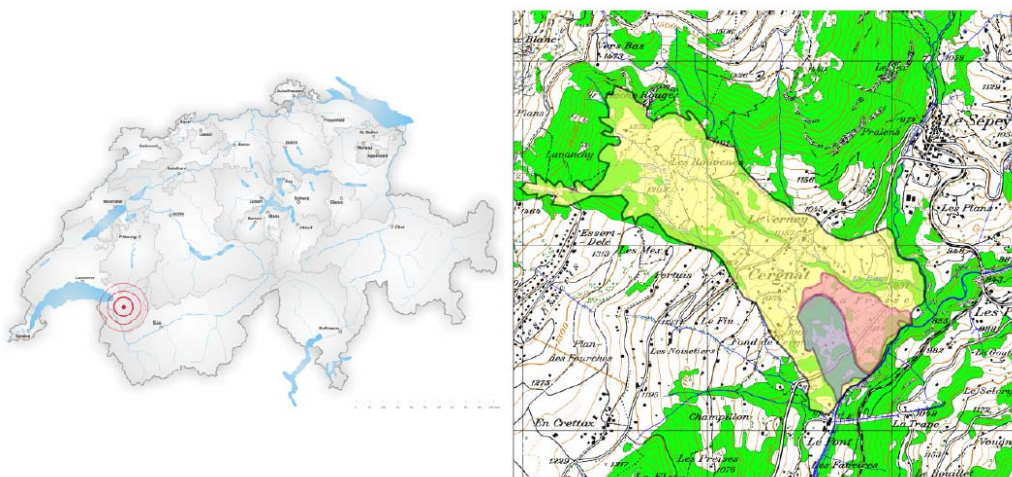


Figure 4.94 - Location of the La Frasse landslide : within Switzerland (left) ; within its topographic context (right). The most active zones (until installation of a pumping platform in 1994) of the sliding mass include Zone ++ (purple) and Zone + (pink) (Planchat 2009).

b) Hydro-mechanically coupled finite element analysis on the La Frasse landslide

In 2004, a technical association composed of the geological and geotechnical consulting groups Norbert Géologues-Conseils SA and De Cerenville Geotechnique SA, as well as the laboratories of engineering and environmental geology (GEOLEP) and soil mechanics (LMS) of the EPFL produced an extensive hydro-geological and geo-mechanical study of the landslide, on the basis of which it was decided to implement a drainage gallery (NCG-EPFL 2004). The construction of the drainage gallery was completed in March 2009. Besides computations with a 3-D model detailed in Commend et al. (2004), numerical analyses were carried out at the Laboratory of Soil Mechanics of EPFL by means of 2D finite element simulations. The calculations were run with Gefdyn[®], a finite element code developed at Ecole Centrale Paris and especially suitable for coupled thermo- and hydro-mechanical problems of continuous porous media, including both static and dynamic analyses (Aubry et al. 1986). The results presented hereafter show the important effect of pore pressure variations on the displacements of the landslide during major crisis.

Model geometry, material, boundary and initial conditions

The 2D model represents a cross section of the center of the landslide and incorporates the geometrical and geological data provided by the Laboratory of Engineering and Environmental Geology (GEOLEP) of EPFL (NCG-EPFL 2004). The main geomorphological features are captured in the model. The 1890m long and 433m high slope section is discretized in 1534 4-noded elements (Figure 4.95). Earth pressure equivalent forces are imposed on the left and right boundaries of the model. The bottom boundary of the model has kinematic constraints in both directions. For the problem initialisation, besides the lateral forces, gravity loading and initial pore pressure distribution are gradually imposed.

From a geotechnical point of view, 6 main material layers are distinguished which have their own hydro-mechanical properties. The quasi rigid body displacement above a well-defined slip surface justifies the use of an elastic-perfectly plastic Mohr-Coulomb model for the bedrock and sliding mass and a more sophisticated elasto-plastic constitutive law, namely the Hujieux model (Hujieux 1986) for the slip surface layer. Based on soil samples obtained from two boreholes in 2002, drained and undrained triaxial tests were carried out in the laboratory in order to calibrate and validate the material parameters. The heterogeneous permeability field in the landslide is determined from the detailed and calibrated hydro-geological model (NCG-EPFL 2004).

Simulation outcomes

Results are obtained from a time-dependent stress-strain analysis of the landslide subjected to pore pressure variations corresponding to those measured during the 1994 crisis over 300 days. For the analysis, pore pressures from a calibrated hydro-geological model were imposed as boundary conditions at some 95 nodes at the interface between the bedrock and the stabilized landslide mass (Tacher et al. 2005).

Figure 4.96 shows a comparison between the outcomes in terms of horizontal and vertical displacements in two selected points assuming in one case a slip surface with a Hujieux and in the second case with a Mohr-Coulomb constitutive law. The results obtained with the Hujieux model represent better the reality. The Mohr-Coulomb constitutive law is not capable of accounting for continuous plastification as it is the case for the Hujieux model.

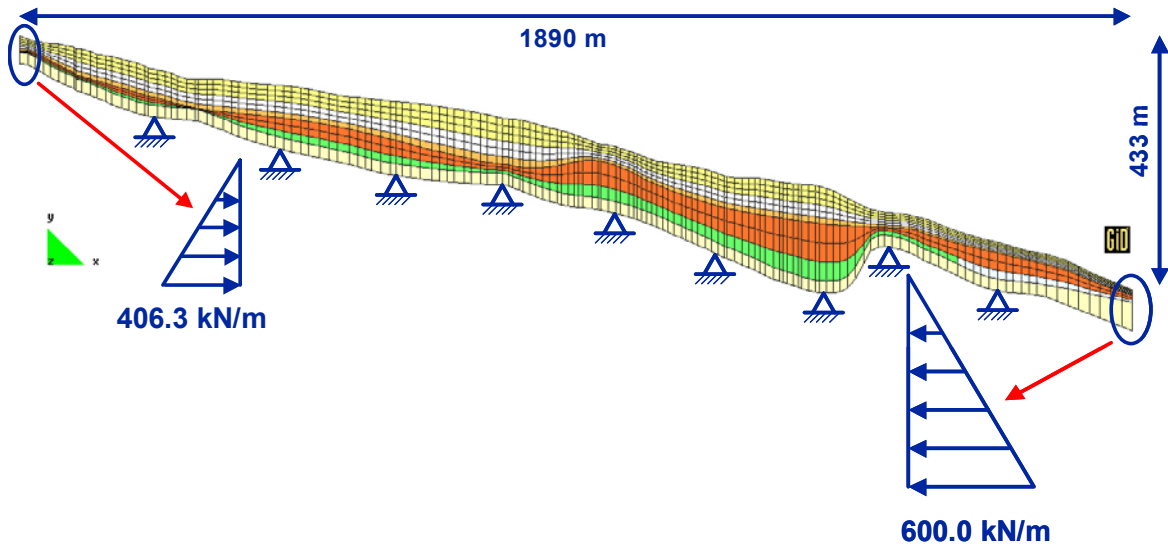


Figure 4.95 - Finite element mesh of the La Frasse landslide – Geotechnical segmentation of the landslide and mechanical boundary conditions (Laloui et al. 2004).

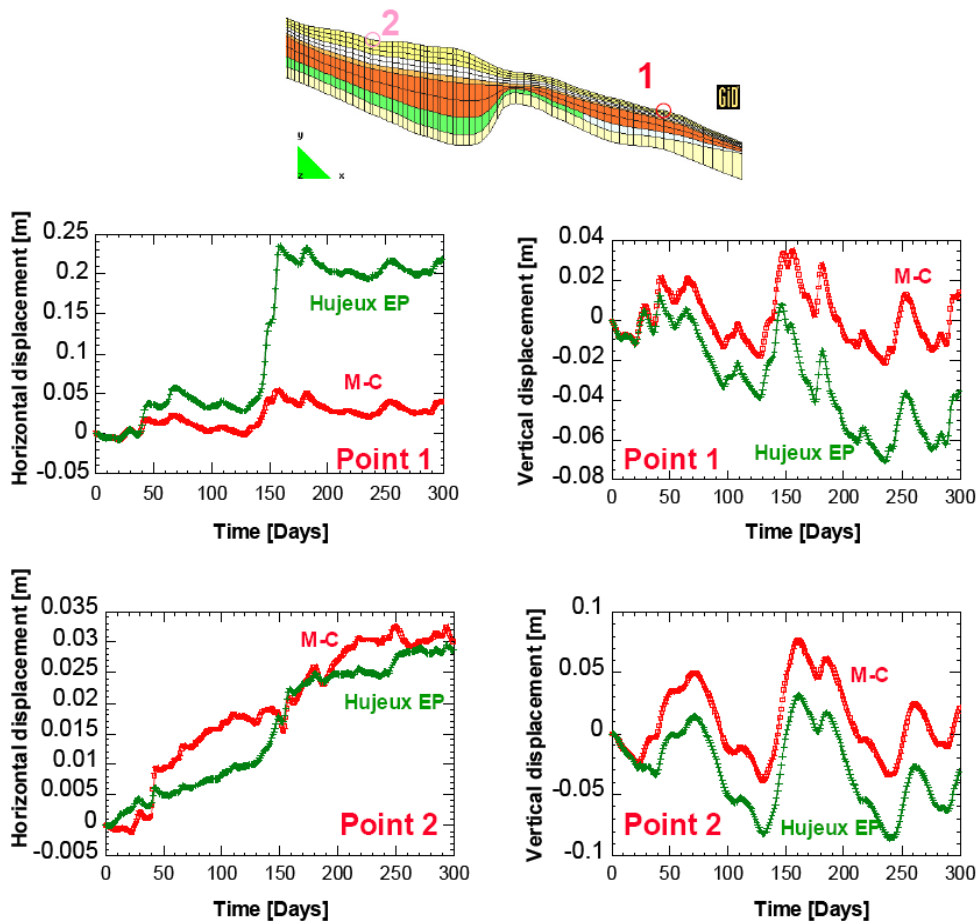


Figure 4.96 - Comparison of landslide displacements calculated with a Hujeux and Mohr-Coulomb constitutive model (Laloui et al. 2004).

Prior to the construction of a projected drainage gallery, a prediction of its future efficiency was made by means of numerical modeling. Figure 4.97 shows the effects of drainage pumping on the displacements for the 1994 crisis. Displacements in both, horizontal and vertical direction are noticeably diminished in the presence of a pumping drainage. The drainage system flattens the pore pressure response in the sliding mass and along the slip surface. Consequently the landslide reacts less.

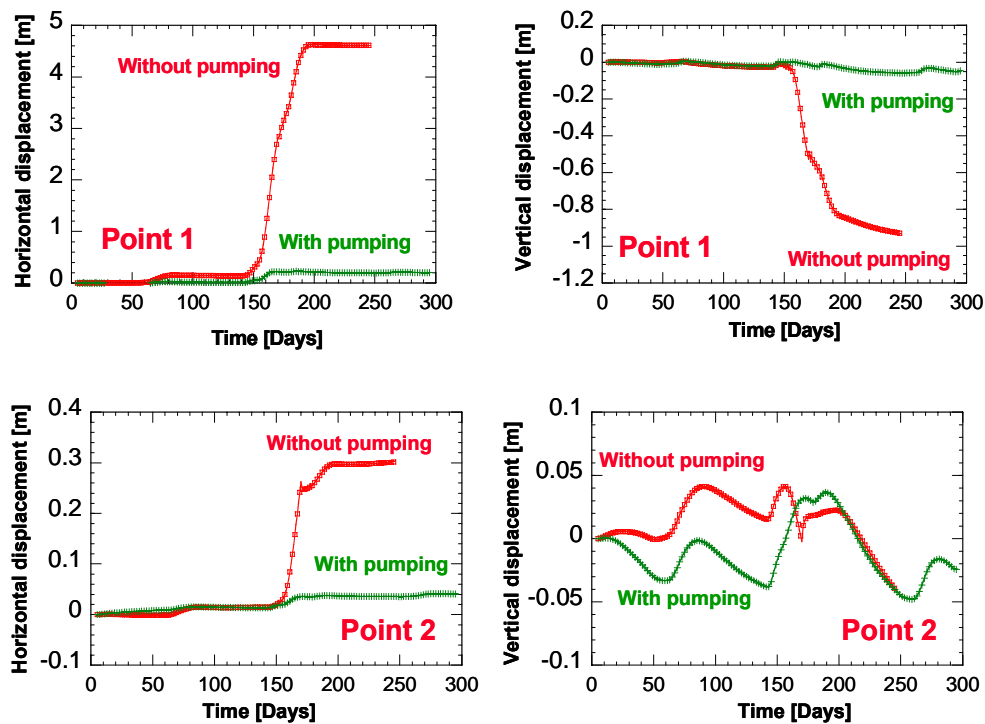


Figure 4.97 - Effect of pumping drainage on the landslide displacements (Laloui et al. 2004).

c) Conclusions

The use of a detailed hydro-geological model in combination with a sophisticated geomechanical model based on sound and long-term monitored geological data allowed understanding the general behavior of the large landslide La Frasse during major rainfall events, such as occurred in 1994. The time-dependent pore pressure input and the use of an elasto-plastic constitutive model with kinematic hardening, namely the Hujeux model, resulted in satisfying outputs in terms of displacements and allowed distinguishing different critical stress zones. The numerical simulations were a useful aid in assessing the efficiency of a pumping drainage in decreasing the surface displacements. A drainage gallery was finally constructed and is in use since March 2009.

4.1.3.2 Analysis of progressive failure in brittle materials using the MPM. A case study: the Aznalcóllar slide (UPC)

a) Introduction

This section presents a simulation of Aznalcóllar dam failure using the Material Point Method (MPM) (Sulsky *et al.* 1994, 1995, 1996). The MPM is a recent emerging numerical method that combines advantages of the finite element method and particle methods. A mesh fixed in space is used to solve the governing equations, while the continuum is represented by "material points" or lagrangian "particles" with fixed mass. The information, which is carried by the particles (momentum, stress, strains and pore pressures), is "projected" into the mesh at every step of the solution. The mesh covers the full domain of the problem and it is used to impose boundary conditions. After solving the discrete governing equations on the mesh, the particles positions are updated. At the end of every step of the solution, the background mesh can be discarded because the particles transport all the necessary information. This avoids mesh distortion for large displacements and convection errors. The method is well suited for dynamic problems with large displacements and incorporates in a natural way a contact algorithm. MPM is equivalent to the finite element method in the case of small displacements, because the weighting functions which are used in the mesh are of the same type as those used in the FEM, and the "particles" can be seen as Gauss integration points.

The MPM is now being used in geotechnical engineering and some interesting applications have been developed. It was applied to the modelling of anchors placed in soil (Coetzee *et al.* 2005), to excavator bucket filling (Coetzee *et al.* 2007), to problems of granular flow in a silo (Wieckowski 2003), to the simulation of experiments related to fault induced ground deformations (Johansson *et al.* 2007), to run-out analysis of earthquake-induced soil flows (Konagai *et al.*, 2004) and to geomembrane response to settlement in landfills (Zhou *et al.* 1999). Also, a quasi static version of MPM has been developed for large deformations in geomechanics (Vermeer, 2008).

Aznalcóllar dam failed suddenly and catastrophically in April 1998 (Alonso and Gens, 2006a). It was built on a continuous basis from 1978 until its collapse. Figure 4.98 shows a cross section of the slide interpreted from borehole data and surface topography. The dam failed through an almost horizontal sliding surface in the foundation and moved forward approximately 50 m. The collapse resulted in the release of pyritic acid tailings contained in the southern lagoon to the Agrio River and caused serious environmental damage. The foundation materials are described in Table 4.7.

Based on field studies and analysis (Alonso and Gens, 2006a and Gens and Alonso, 2006, which are taken as a reference background information for the remaining of the analysis presented here) it was concluded that the dam failed due to the combined effect of the following circumstances:

a- Very low clay permeability and therefore a persistence of high pore pressures in the foundation during dam construction and pond filling.

b- Quasi-brittle clay behaviour. The foundation clay shows two different softening mechanisms. First, a sharp strength reduction associated with loss of cementation and possibly some micro-structural breakdown, which was observed in direct shear box tests for relative displacement of about 1mm. At increasing shearing, strength reduction is more

gradual. This behaviour has been interpreted as a loss of effective cohesion of the fracture surface which occurs at virtually no relative movement, considering the scale of the problem, and a progressive reduction of effective friction angle that ends in a residual friction angle.

c- The downstream construction method which generated high shear stresses at the slope toe as the dam was being built, without increasing the foundation strength in the same amount by the associated consolidation process.

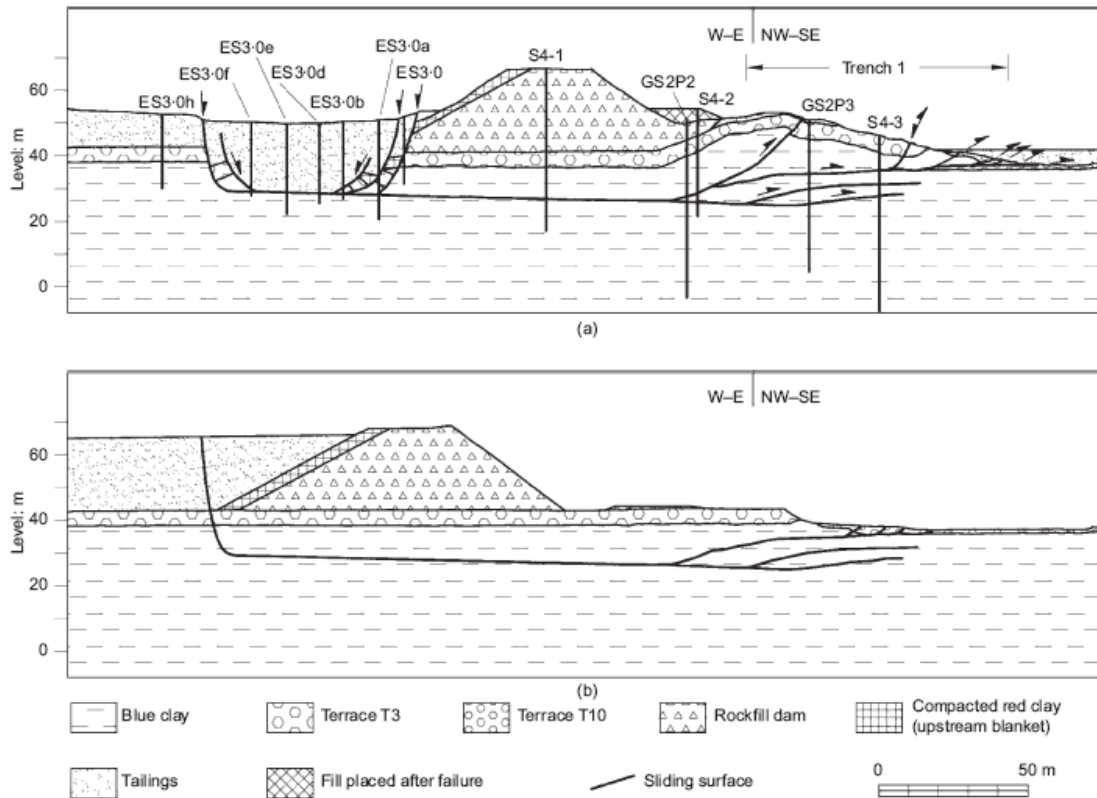


Figure 4.98 - Cross-section of slide. (a) Geometry after the slide, as interpreted from borehole data and surface topography ;(b)reconstruction of position of sliding surface before failure. (Alonso & Gens, 2006)

An appropriate numerical model to simulate these features should reproduce the coupled hydro-mechanical behaviour during dam construction and the quasi-brittle behaviour of the clay foundation. Moreover, the solution should not depend on the discretization mesh and the development of failure surface (s) should be appropriately captured.

The foundation marine clay was very homogeneous and sedimentation layers, dipping 2° - 4° in the direction of the failure motion, could hardly be distinguished. It was concluded that most of the failure surface followed a sedimentation plane. It was reckoned, on the basis of the conventional FE analysis performed, that some strength loss along sedimentation planes (if compared with the intact matrix peak strength) was necessary to initiate yielding. Then, the development of the failure surface was attributed to a progressive failure mechanism which started at an early stage of dam construction and ended in a sudden rupture, which was not preceded by observable warning signals. This interpretation was essentially based on a consolidation/elastic analysis of stress conditions under the advancing dam and by some indirect evidence derived from limit equilibrium results. The FE analysis reported in Gens and Alonso (2006) was not able to simulate the location of the failure surface in its actual position, which was well identified by field observations. It was also unable to follow the development of progressive failure. In fact, in order to reproduce the failure, a weak layer had to be artificially introduced in the position of the failure surface. Otherwise, the FE analysis performed predicts a deep circular-like failure surface.

At the time of the analysis reported in the reference papers it was felt that the presence of a sedimentation surface having a reduced or damaged strength could be a reason for the actual location of the failure surface and for the initiation of the progressive failure mechanism. However, the simple elastic-consolidation analysis performed provided some support to an alternative explanation, namely that the location of the failure surface was a consequence of the evolving geometry of the problem, the consolidation process and the constitutive behaviour of the clay foundation.

Therefore, two important aspects of Aznalcóllar failure: the reason behind the location and shape of the failure surface and the process of progressive failure did not receive a proper answer. This analysis addresses these two issues. Since the MPM handles large displacements in a natural way it may also provide information on the finite motion of the slide once the instability has started. This aspect, which was covered in Alonso and Gens (2006b), will not be covered in detail in this analysis.

The MPM is described briefly in the Appendix. If compared with previous developments, a novel formulation for coupled flow-deformation problems was developed.

b) Model of Aznalcóllar dam and its foundation

Figure 4.99 shows the domain considered for the simulation of the dam failure. A background mesh having 1m x 1m square elements covers the entire domain of the problem. The mesh, with a size of 300 x 102 cells, spreads in the two dimensional space even to areas without material points. The foundation, dam and tailings materials are discretized with particles. Two models were used to obtain the results shown below, one that considers one initial particle per cell, totalling an amount of 26,915 particles and a second one having 4 particles per cell in the zone of significant displacements, which reaches 50,540 particles. There are no differences in

accuracy of the results between both models because the mesh used for both is the same. The greater number of particles per cell avoids the generation of "holes" in the discretization or the loss of connections among particles during the solution.

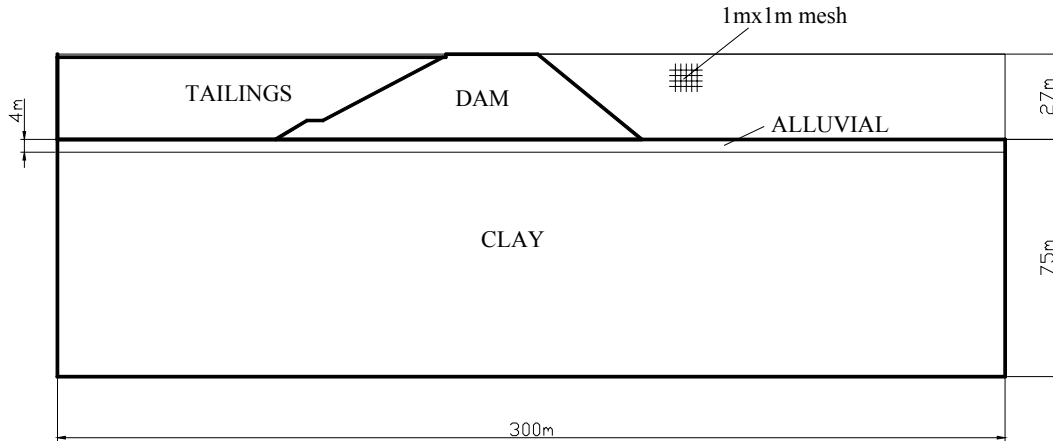


Figure 4.99 - Aznalcóllar dam. Domain considered in the model.

To simulate the construction process 15 stages have been defined. The geometry of these stages is shown in Figure 3. Table 4.8 describes the evolution of this geometry in time.

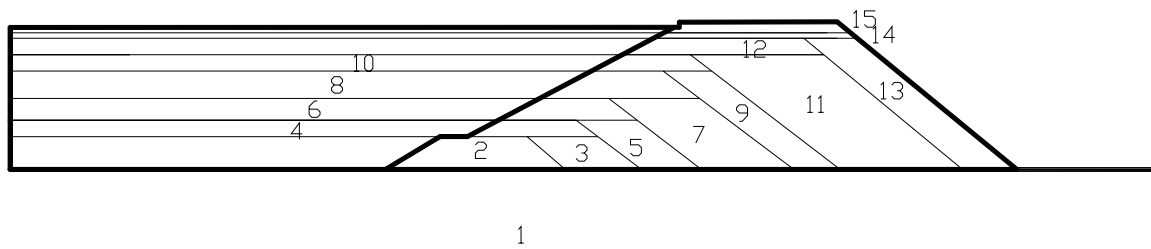


Figure 4.100 - Construction stages.

The numerical stability of the solution in the explicit version of MPM developed requires that the integration interval Δt meets the Courant-Friedrichs-Levy condition (CFL): $\Delta t < \Delta t_{crit}$.

The critical time interval is:

$$\Delta t_{crit} = \frac{l}{c_p} \tag{1}$$

where l is the mesh size and c_p the pressure wave velocity of the soil-fluid mixture

$$c_p = \sqrt{\frac{Q + \frac{4}{3}G}{\rho}} \tag{2}$$

where

Q : combined compressibility modulus of the fluid and solid phase (see Appendix)

G : shear modulus of the solid phase

ρ : density of the soil-fluid mixture

The CFL condition imposes a very small time step for saturated materials. In this case the critical interval is totally incompatible with the time scale of construction and consolidation. Since the problem is quasi-static during construction and therefore the inertia forces are not relevant because the accelerations are very small, the material's density can be scaled if the saturated specific weights are preserved by reducing proportionally the gravity acceleration. This technique is completed with the addition of artificial damping to the discrete equations system in order to suppress dynamic response. (See Appendix: Dynamic relaxation). A time interval $\Delta t = 1 / 4 \text{ day}$ was used in the model for the construction process.

c) Constitutive relationships

Tailings stored in the lagoon and alluvial materials of the foundation were modelled using a non-associated Mohr-Coulomb constitutive equation. The rockfill dam was considered elastic because the failure occurred without observable dam plastic strains. The dam travelled downstream essentially as a rigid body.

A modification of a non-associated Mohr-Coulomb constitutive equation was used for the clay foundation material. The sharp strength decrease, that follows the peak strength observed in direct shear box tests (Figure 4.101) (Alonso and Gens, 2006a), was simulated by reducing cohesion to zero when the stress state reaches the Mohr-Coulomb plastic surface.

The progressive decrease in friction angle, from the peak value (24°) to the residual value (11°) is represented by a negative exponential function of the equivalent shear plastic strain, ε_{eq}^p .

$$\phi' = \phi'_{res} + (\phi'_{peak} - \phi'_{res}) e^{-\eta \cdot \varepsilon_{eq}^p} \quad (3)$$

where ϕ'_{peak} and ϕ'_{res} are the peak and residual effective friction angles and η is a constant parameter. The equivalent plastic shear strain is defined as:

$$\varepsilon_{eq}^p = \left(\frac{2}{3} \mathbf{e}^p : \mathbf{e}^p \right)^{1/2} \quad (4)$$

where \mathbf{e}^p is the deviatoric plastic strain tensor.

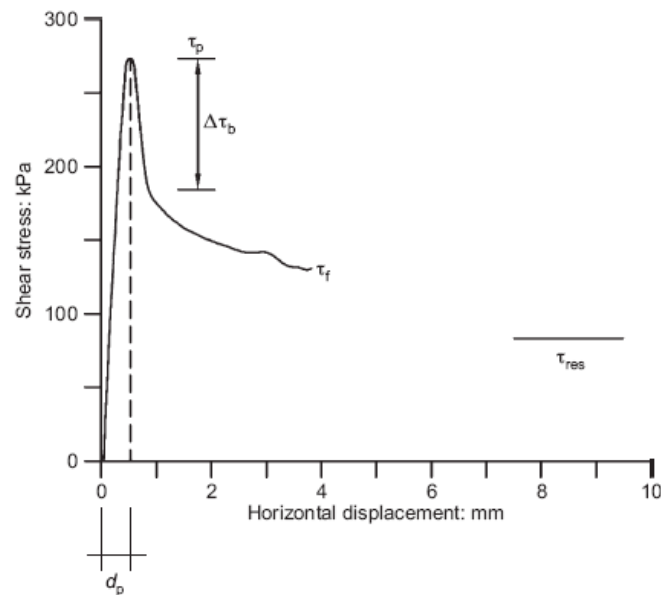


Figure 4.101 - Direct shear test on a specimen of foundation clay. Normal effective stress 400 kPa. (Alonso & Gens, 2006)

The coefficient of consolidation of the clay foundation and the derived permeability were given in the reference papers ($c_v = 0.001 \text{ cm}^2/\text{s}$; $k = 2 \cdot 10^{-11} \text{ m/s}$). The alluvial upper layer provides a free draining boundary for the clay. The lower aquifer in direct contact with the Guadalquivir blue clay is also a free draining boundary.

The modelling parameters are collected in Table III. Note the high saturated unit weight of the tailings, due to the presence of pyrite as the main mineral constituent. A zero dilatancy angle was adopted in calculations.

Table 4.8 - Aznalcóllar dam foundation materials.

Description	Depth: (m)
Alluvial gravels and sands. Terraces of Agrio river	0-4
Carbonate marine high-plasticity clay (Guadalquivir blue marl)	4-75
Gravels, sands and sandstones	75-82
Shales	>82

In order to regularize the solution the concept of smeared crack in a mesh element has been used. The plastic work dissipated by a mesh element must be equal to the fracture energy dissipated at the crack or sliding surface. Therefore the plastic softening modulus is dependent on the mesh size. The strength of this smeared or sliding surface is assumed to be a function of the relative displacement at the discontinuity. The exponential function parameter, η , is calibrated ($\eta=100$) to obtain a shear stress-relative displacement relation for the fixed size of the mesh element (1mx1m), which corresponds to the shear stress-displacement results of the shear box tests. This is shown in Figure 4.102, which indicates the actual shear stress-

displacement relationship for the foundation clay effectively taken in the analysis. This relationship can be compared with one of the tests reported in Alonso and Gens (2006a) reproduced in Figure 4.101.

Table II. Dam construction stages.

Stage	Dam height (m)	Tailings height (m)	Crest width (m)	Time (days)
1	0	0	0	0
2	6	6	16	100
3	6	6	29	600
4	9	9	14	1125
5	9	9	25.5	1525
6	13	13	14	2005
7	13	13	29.4	2280
8	18	18	14	2430
9	18	18	22.1	3025
10	21	21	14	3525
11	21	21	37	3835
12	24	24	27.7	3985
13	24	24	37.5	4135
14	25	25	34.2	6600
15	27	26	29	7300

Table III: Model parameters

Material	γ_{sat} [kN/m ³]	c' [kPa]	ϕ'_{peak}	ϕ'_{res}	η	k [m/seg]	c_v [cm ² /seg]
Clay	20	65	24	11	100	2. e-11	0.001
Alluvium	20	0	35	35	-	2. e-06	-
Dam	20	Elastic	-	-	-	-	-
Tailings	31	0	37	37	-	-	-

d) Simulation of the construction and failure process

Two different cases were analyzed maintaining the same strength parameters but varying the coefficient of pressure at rest, K_0 , of the clay foundation. It was found that K_0 had a significant influence on the results. Horizontal stresses were not measured in the foundation clay. The Miocene origin of the clay foundation and the known tectonic activity, summarized in Alonso and Gens (2006a) favours K_0 coefficients in the vicinity of 1. The two cases analyzed correspond to $K_0 = 0.5$ and $K_0 = 1.0$.

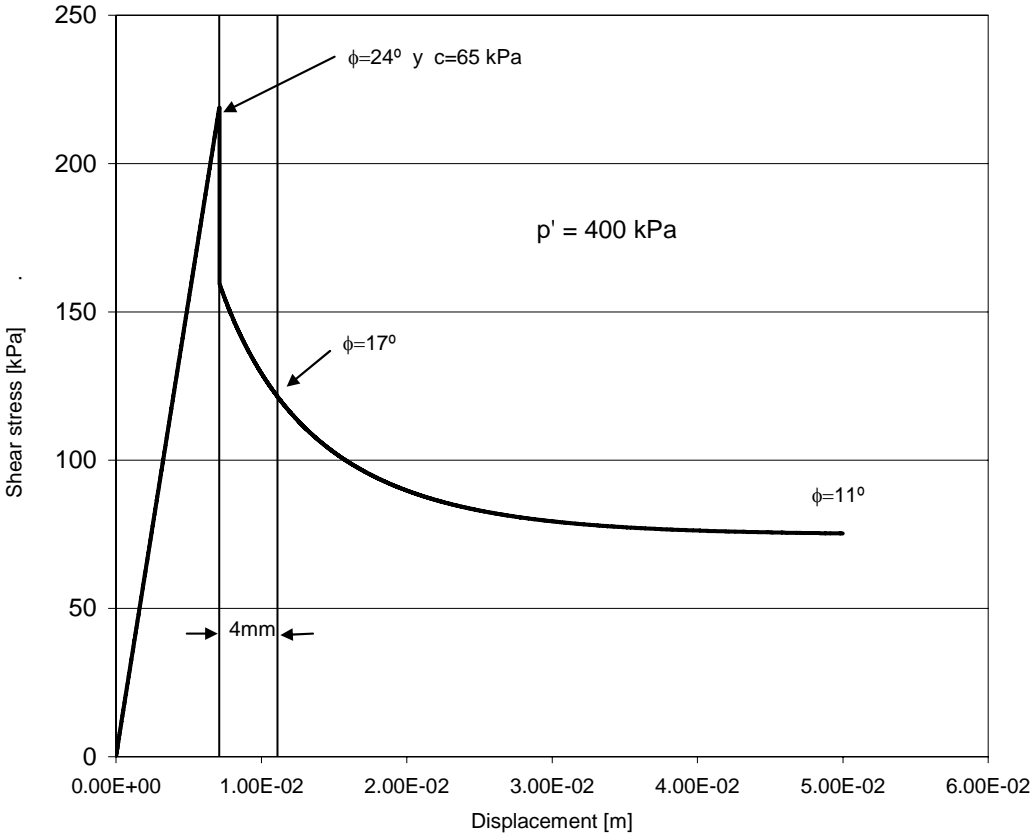
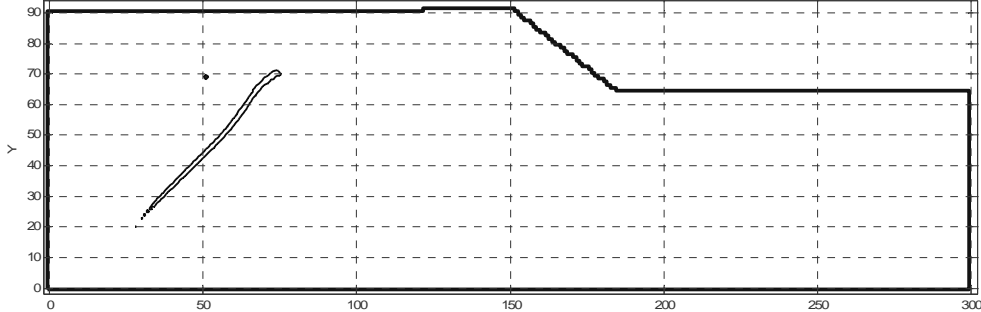
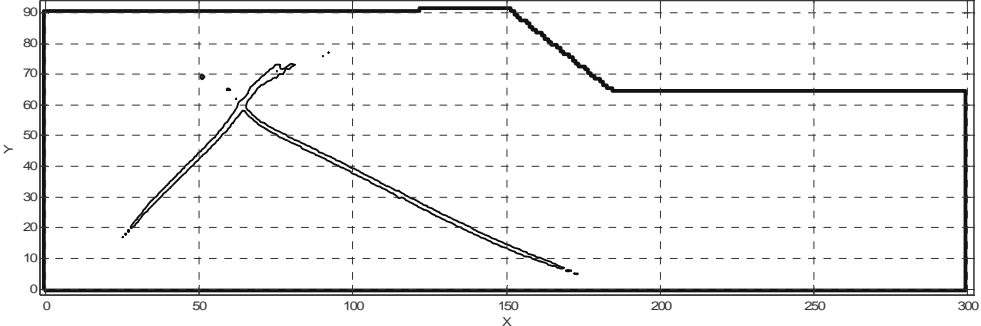


Figure 4.102 - Shear stress-relative displacements function for a clay particle in 1mx1m cell.

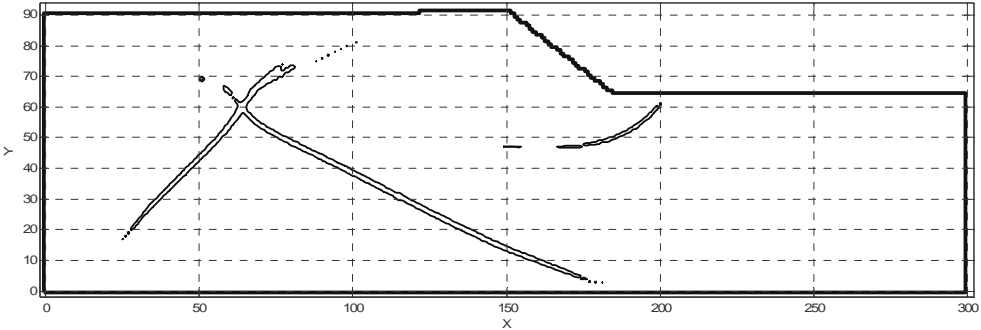
Consider first the results for $K_0 = 0.5$. The sequence of Figures 4.103-a to 4.103-g show contours of equivalent plastic shear strain. Two levels of equivalent plastic strain are plotted: 1% and 5% in order to distinguish the localized areas of highest strain intensity. The 1% contour is first established. As strain accumulates, a thinner 5% contour develops inside the areas bounded by the 1% contour. Figure 4.103-a shows the plastic strains (1% contour) at the end of stage 12 when the dam had reached a height of 24 m and the crest width was 27.7 m. The localization band shown is a diagonal surface or "crack", and it is associated with the tailings load on the foundation. This is already a high uniform total stress applied by the pond (750 kPa). It is a long shear band which ends in the proximity of the underlying stiff boundary of the clay. Immediately afterwards a second diagonal and long shear band develops, in a direction approximately perpendicular to the initial one. It extends under the dam and reaches also a position close to the lower boundary (Fig. 4.103-b)



a)



b)



c)

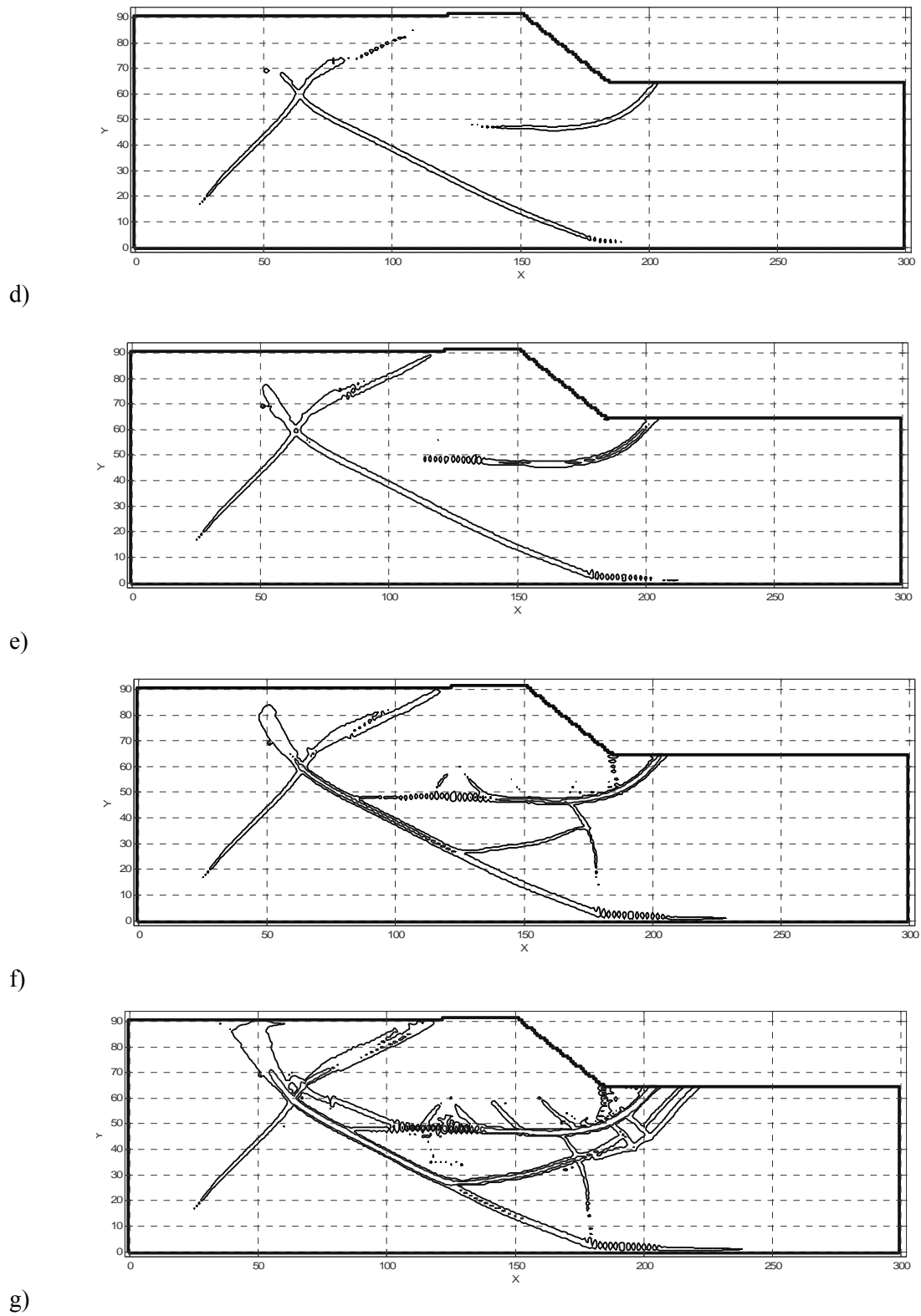


Figure 4.103 - Sequence of contours of equal equivalent plastic strain 1% and 5%.

$$c_v = 0.001 \text{ cm}^2/\text{seg} \text{ and } K_0 = 0.5$$

When the stage 14 is finished (dam height is already 25 m; see Fig. 4.103c) a "surface" shear band appears for the first time at the slope toe. This band propagates from downstream to upstream as time increases towards the end of stage 15. This is indicated in the series of plots c, d, e of Figure 4.103. This shear band becomes a horizontal failure surface at a depth of 18 m from the original ground surface (Fig. 4.103-e).

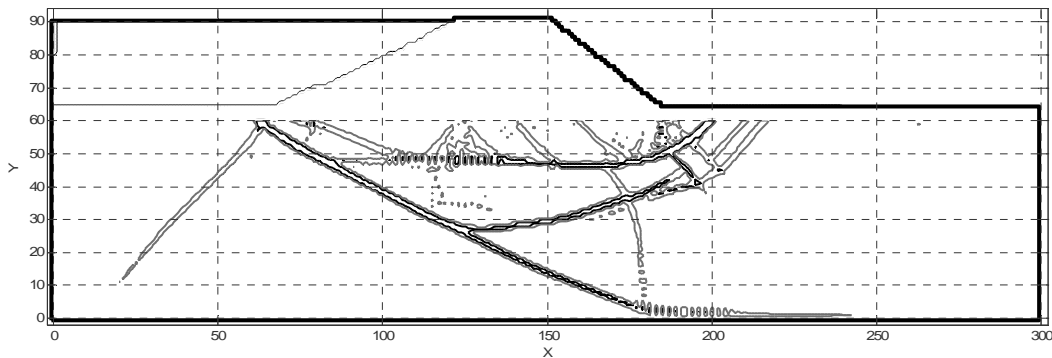


Figure 4.104 - Contours of equal angle of friction.

The two initial “diagonal” bands have now evolved upwards and are now defining an “active wedge” upstream of the dam. It is interesting to note the development of a shearing zone at the contact between dam and tailings. This sheared contact was responsible for the upstream failure of the tailings, directly over the upstream slope of the dam when the dam slid forward (see Alonso and Gens, 2006b). The upstream evolution of the shear zone under the dam eventually connects the horizontal failure surface with the previously developed diagonal cracks at the end of stage 14 (Fig.4.103-e, 4.103-f). This connection takes 1300 days to develop. At this time a kinematically admissible mechanism is fully developed. At the end of stage 15 additional strain localization zones develop and a more complex rupture pattern evolves. The model predicts also deeper circular failure mechanism connected also to the initial diagonal shearing surfaces developed initially. The “passive” exit zone is highly sheared and several sub-parallel localization bands develop.

Note also that in this model the lower boundary has some effect on the overall behaviour. The long diagonal shear band, dipping under the dam towards the underlying rigid boundary, eventually reaches it and bends to follow this contact. Secondary shear bands originated at the main ones have also developed.

Effective stress paths of some representative points under the dam are shown later, but it is interesting at this point to examine the attained friction angle in points of the foundation.

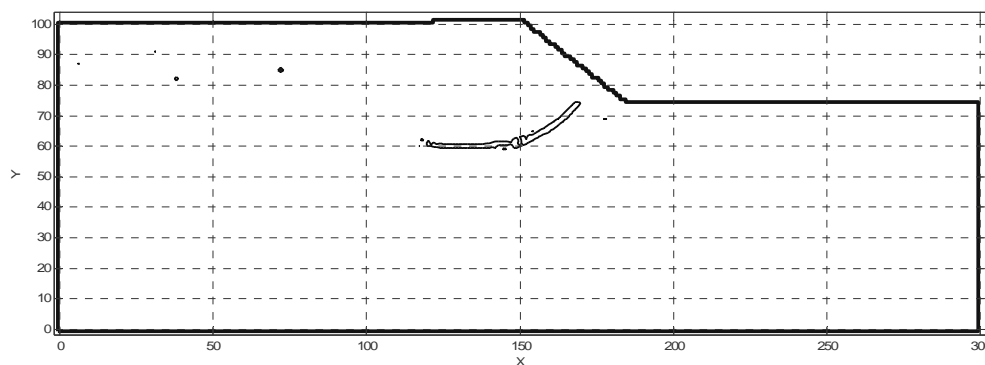
Figure 4.104 shows the contours of friction angle at the end of the analysis. The plotted curves correspond to an intermediate value of 17° and to a residual value of 11° . As a reference, an equivalent effective friction angle close to 17° was identified in Gens and Alonso (2006) as the average friction angle which results in a Safety Factor = 1 in a conventional limit equilibrium analysis (Morgenstern-Price method of slices) when the actual failure surface derived from field observations is imposed. It can be seen in Figure 4.104 that the contours of $\phi' = 17^\circ$ (or less) follow, as expected, the pattern indicated by the contours of equivalent plastic strain of Figures 4.103-a to 4.103-g. The curves corresponding to $\phi' = 11^\circ$

have a similar distribution but are less extended in the strain localization zones. This result confirms that a full sliding mechanism could be developed with an average friction angle greater than $\phi' = 11^\circ$. The horizontal failure surface predicted by the analysis for $K_0 = 0.5$ is 18 m below the original ground surface, against field observations which located it at a depth of 14 m under the axis of the dam.

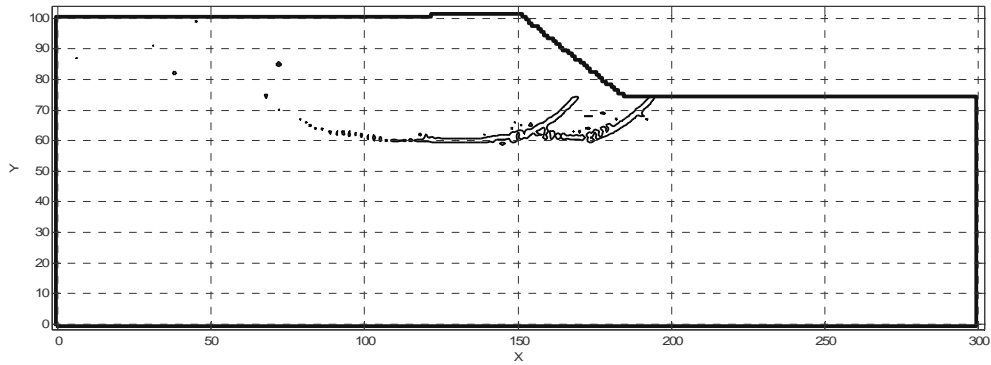
Consider, however, the analysis for $K_0 = 1$ a value which may be acceptable in view of the geological history of the marine clay. Under this hypothesis the clay foundation is initially free of deviatoric stresses.

Figures 4.105-a to 4.105-e show calculated contours of equal equivalent plastic shear strain. Figure 4.105-a corresponds to the end of stage 12. Figures 4.105-b and 4.105-c correspond to intermediate states during stages 13 and 14. In this case the localization bands crossing in a diagonal pattern the clay foundation did not develop. This is a direct consequence of the initial state of stress. The initial shear band develops at the end of stage 12 (Figure 4.105a). It starts in the vicinity of the downstream slope and progresses upstream, describing a circular shape. However, it soon becomes horizontal. Their progression upstream may be seen in Figures 4.105a, 4.105b and 4.105c. At some intermediate time during stage 13 (Figure 4.105b) a new circular band connects the initial one to a surface point downstream from the dam toe. The most striking result, however, is that the position of the horizontal shear band is now almost exactly located in the position of the actual sliding surface observed “in situ”.

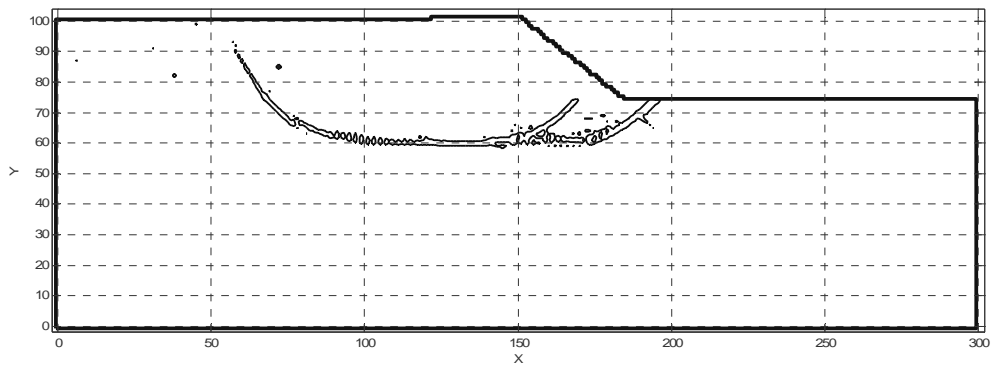
The horizontal shear band bends upwards some time during stage 14 at the position of the dam upstream toe. It then crosses the tailings deposit at an angle of approximately 60° with the horizontal. The remaining construction period, covered by stage 15, only results in an accumulation of plastic shearing strains in the already developed band (Figures 4.105d and 4.105e). An active wedge within the tailings deposit is hinted at the end of the simulation period. The failure mechanism develops in a clear and straightforward manner in this case. No indication of boundary effects is now found. The mechanism is remarkably similar to the actual one. Even the passive zone at the toe of the dam is composed by a number of subparallel rupture surfaces, a feature also observed in trenches excavated after the failure (Figure 4.98).



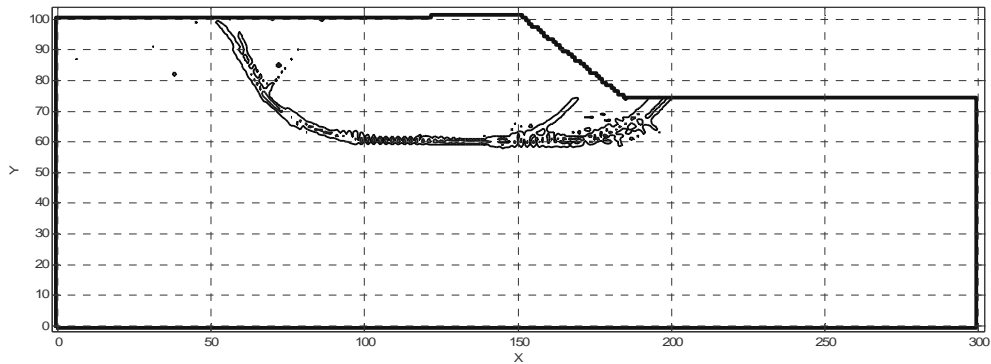
a)



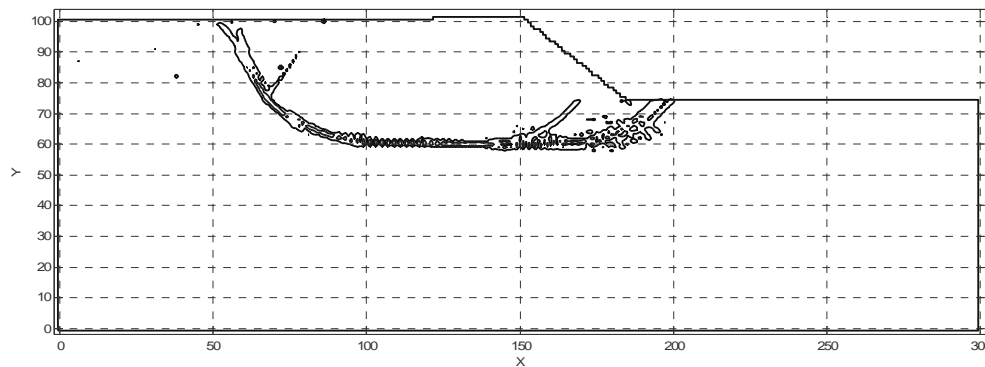
b)



c)



d)



e)

Figure 4.105 - Sequence of contours of equal equivalent plastic strain, 1% and 5%. $c_v = 0.001 \text{ cm}^2/\text{seg}$ $K_0 = 1$

e) Pore pressure distribution

Pore pressures were not recorded during the life span of the dam. However, vibrating wire piezometers were installed soon after the failure in cross sections of the dam which remained stable and also under the failed and displaced dam. The measurements could be reproduced fairly accurately by estimating the excess pore pressures associated with dam and pond construction and dissipating them through a vertical one dimensional theory (Terzaghi). It was also found that a more detailed two-dimensional FE coupled analysis provided essentially the same results (Gens and Alonso, 2006). Matching the pore pressures measured after failure was therefore a good validation for any modelling of the conditions leading to failure.

A hydrostatic pressure, fixed during construction, was imposed at the bottom boundary of the foundation model. This water pressure assumption is based on field data on the lower aquifer. A deep piezometer installed in the lower sands measured a pore pressure equivalent to the height of the clay layer. At the upper boundary of the clay layer the pressure condition was considered variable. Upstream of cut-off wall water pressure was given by the height of stored tailings (tailings remained always covered by a shallow water depth). Downstream from the cut-off, a free water surface was present on the thin granular alluvium.

Figure 4.106 shows the vertical distribution of pore pressures in the foundation clay, under the tailings away from the dam, at the end of stages 9, 13 and 15. The pressures calculated through the one-dimensional consolidation theory of Terzaghi are plotted for comparison. Also, a point is plotted for the stage 15, which represents the measured pressure in a piezometer located in the approximate position of the sliding surface in an unfailed section, north of the slide.

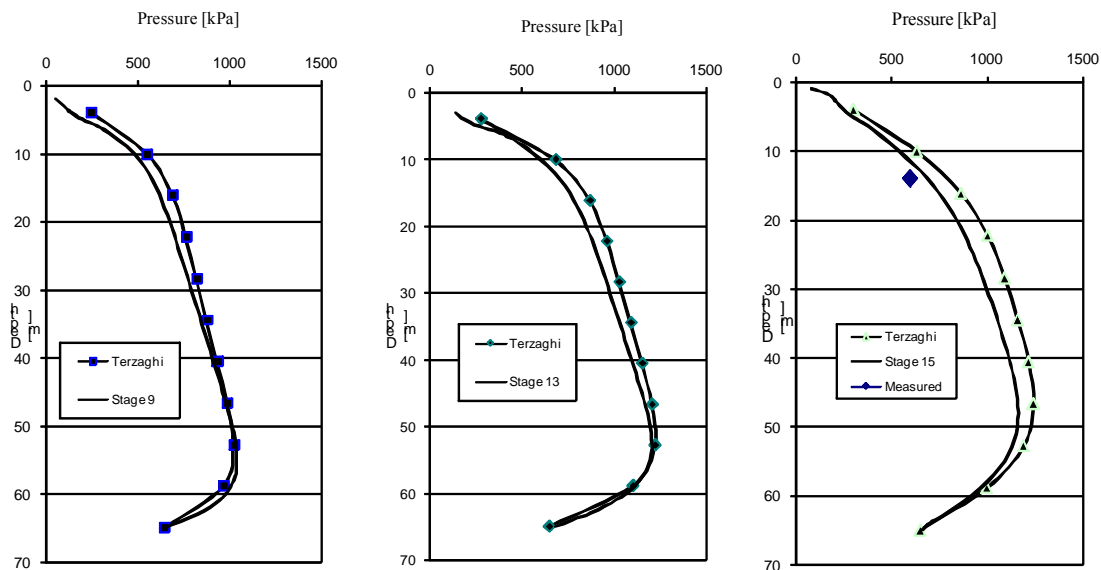


Figure 4.106 - Vertical distribution of pressure in the clay layer at the end of stages 13, 14 and 15.

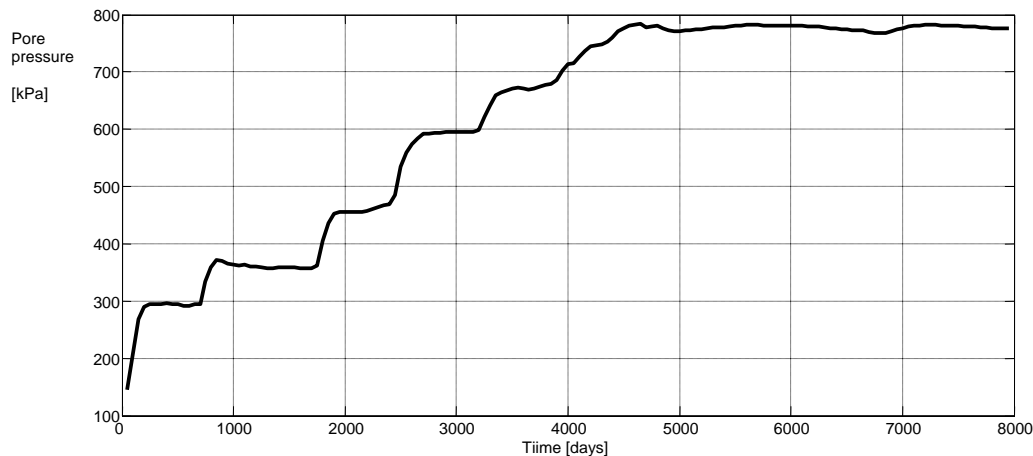


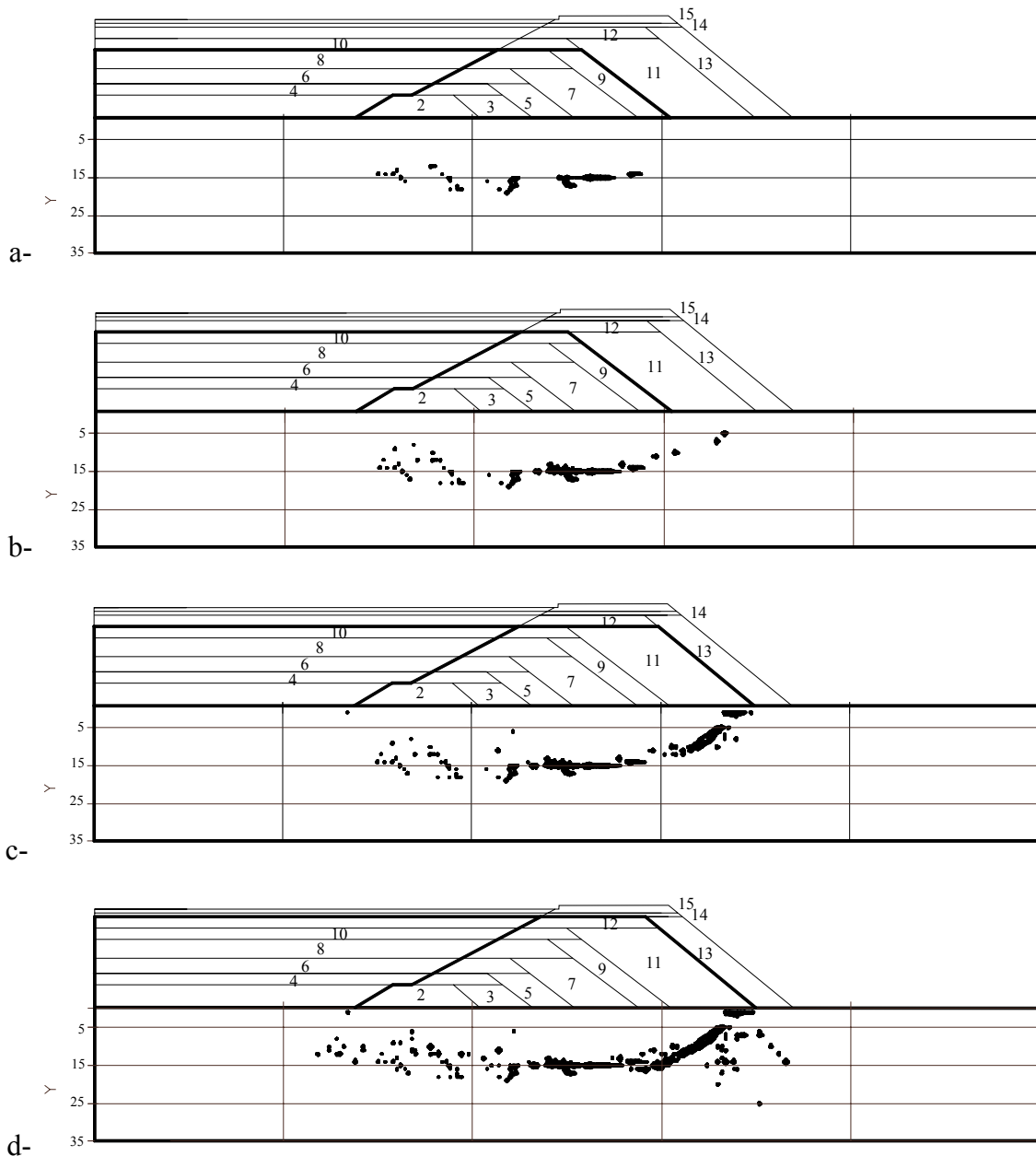
Figure 4.107 - Pore pressure evolution for a particle under the tailings at a depth of 14 m from ground level.

The agreement is good. The one dimensional dissipation should overestimate somewhat the actual pore pressures because it does not include two-dimensional effects. This is reflected in the plots. The calculated pore pressures increase in depth due to the combined effect of the hydrostatic initial distributions and the tailings and dam loading. The plot shows also the

effect of the under-drainage of the lower aquifer, although it did not affect the pore pressures developed on the critical failure surface.

Figure 4.107 shows the pore pressure response as a function of time for a particle located under the waste pond, away from the dam, at the depth of the actual sliding surface (14 m from the original ground surface). The pore pressure dissipation over the years is very limited because of the low clay permeability. The calculated pressure increments have almost no dynamic oscillations.

f) Progressive failure



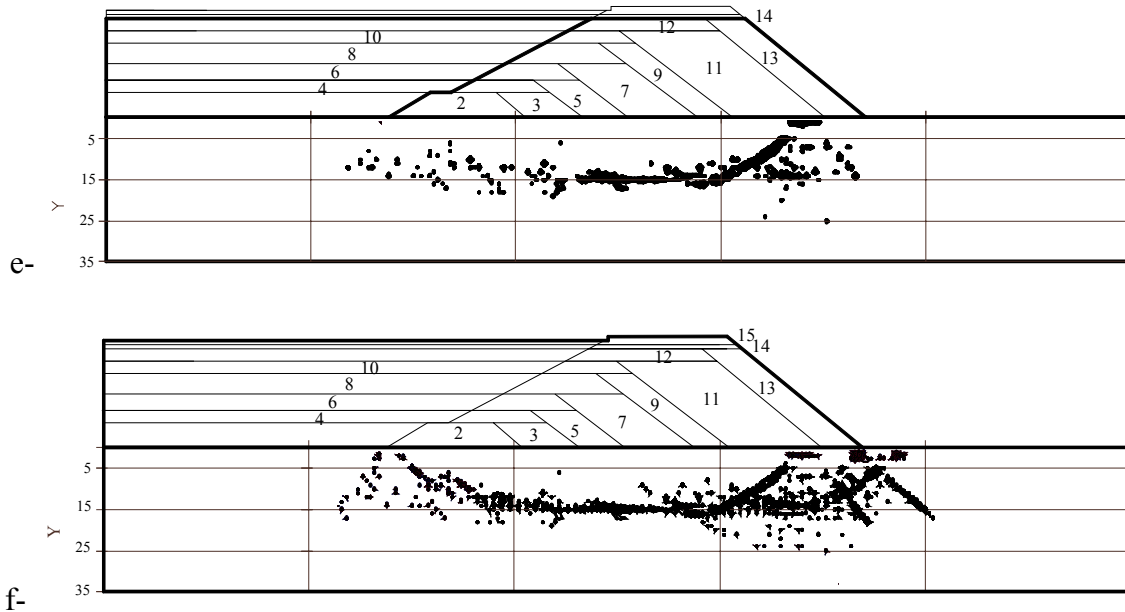


Figure 4.108 - Zones where the clay strength is reached at different stages of construction.

At the end of stage 12 (Figure 4.108d) the failed zone extends essentially from the dam toe to approximately half distance of the dam base, in an upstream direction. At this time the band developed in terms of accumulated plastic shear strain is shown in Figure 4.105a. The two shapes are similar as could be expected. The plot in Figure 4.108d shows, however, the existence of a planar stressed zone in the upstream direction which will be enhanced in the remaining stages (Figures 4.108e and 4.108f). In parallel the shear band will progress in the upstream direction and eventually it bends upward.

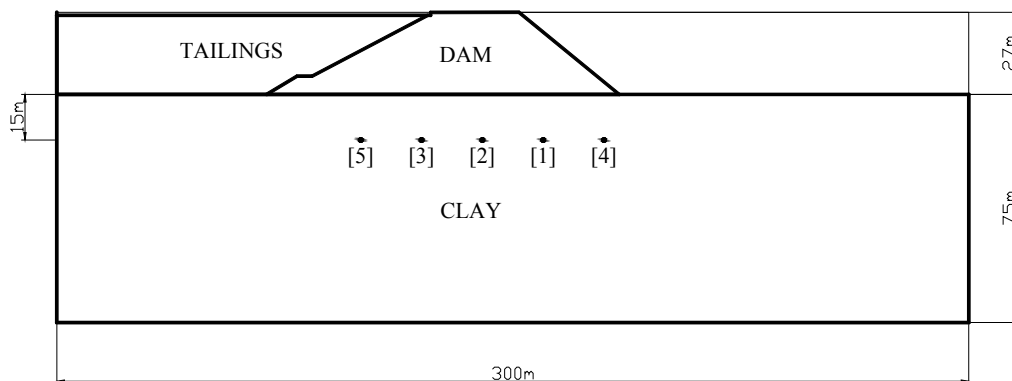


Figure 4.109 - Failure sequence for points at a depth of 15 m from the original surface of the ground.

The sequence of clay failure in representative points of the sliding surface is shown in Figure 4.109. Only five points are shown to simplify the representation of stress paths in the

foundation. The clay failed in the sequence [1] - [2] - [3] - [4] - [5]. Total horizontal shear strains as a function of time are shown in Figure 4.110 for these five points at a depth of 15 m. The figure also shows the time when a given point reaches its shear strength. Figure 4.109 shows the location of points [1] to [5] on the horizontal failure surface. Before reaching peak conditions shear deformations are very low. The calculated shear strains are high afterwards (6% - 16%) as the dam increased its height.

The stress-strain history of the selected five points under the dam is given in Figure 4.110. The left column shows the stress deviator q vs. horizontal strain γ_{xy} and the right column the stress path plotted in a $p' = (\sigma'_1 + 2\sigma'_3)/3; q = \sigma_1 - \sigma_3$ space. Also indicated in the stress space are the failure envelopes for triaxial compression and extension, for peak ($c' = 65$ kPa; $\phi'_{peak} = 26.4^\circ$) and residual conditions ($c' = 0$ kPa; $\phi'_{res} = 11^\circ$).

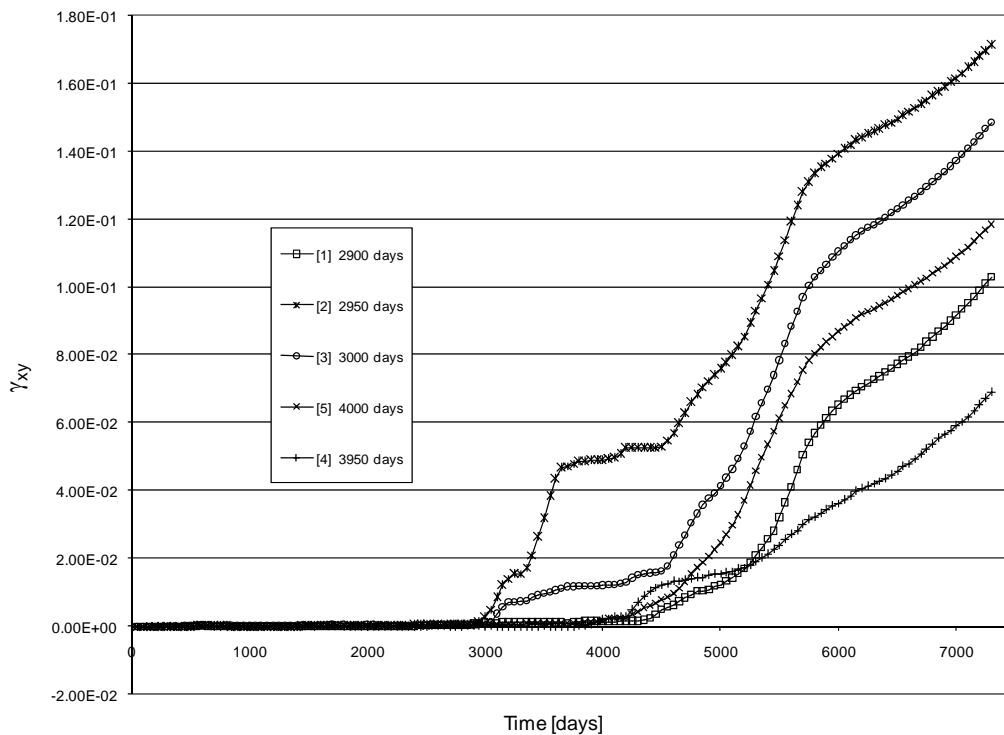
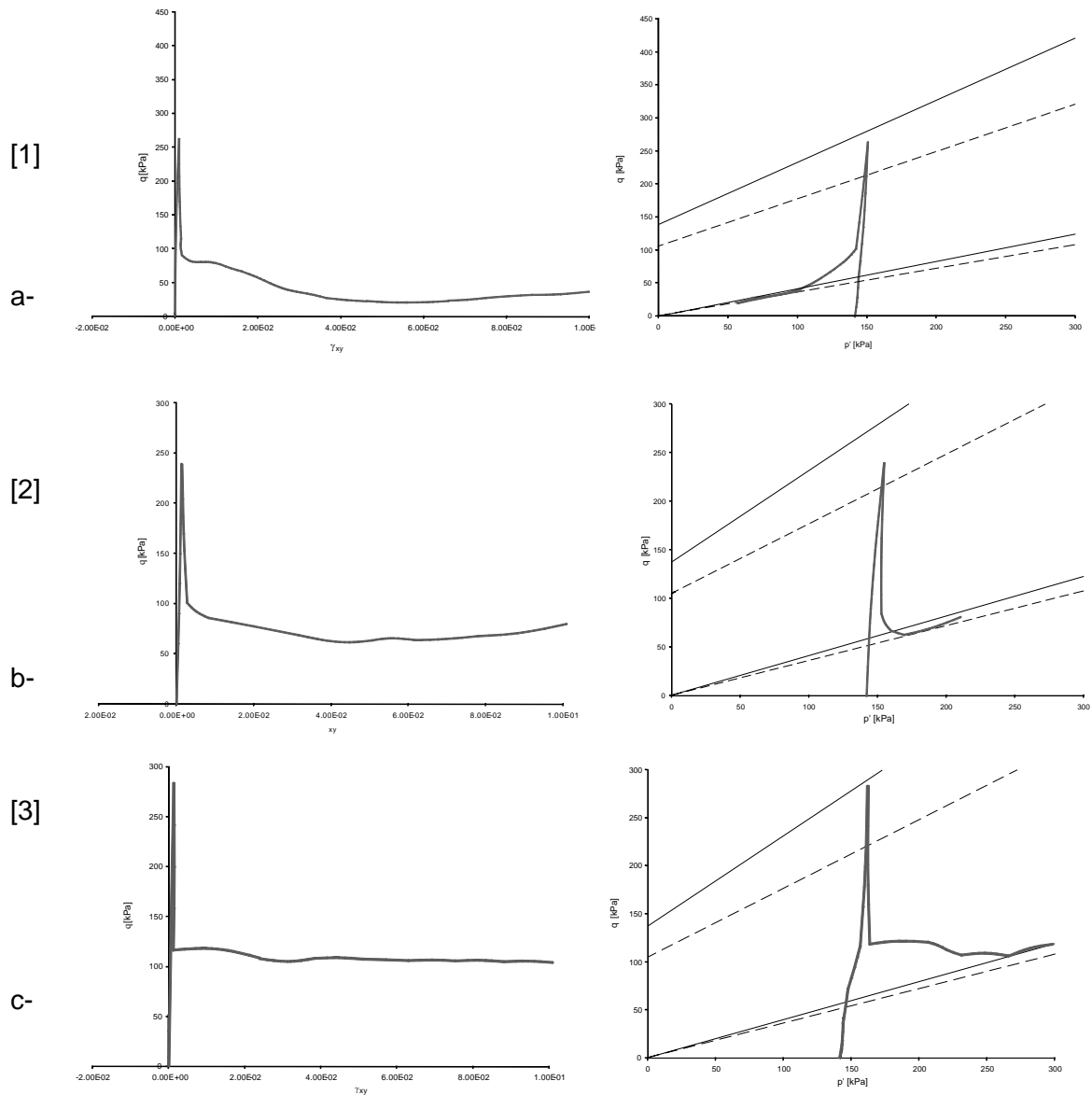


Figure 4.110 - Horizontal shear strain as a function of construction time.

The deviatoric stress q reaches a sharp peak value for very small strains (aprox. 0.15 %). The rapid loss of effective cohesion implies also a rapid reduction of q . The points evolve towards residual conditions in a rather complex way. At point 2 the peak strength is reached at an early stage and the subsequent stress points follow the degradation of strength as the dam is being built in a relatively straightforward manner. Consider, however, point 5, closer to the tailings pond. The point experiences a succession of deviatoric stress peaks, as a consequence

of the stress redistributions associated to the yielding and stress softening of neighbouring areas. The peak strength is reached under extension conditions when the progression of the shear band reaches position [5]. Then the rapid strength degradation moves down the stress path. The actual details of each one of the represented stress paths are a consequence of the strength degradation, the details of the dam geometrical evolution, the consolidation process and the stress transfer associated with progressive failure and strain localization in the shear band.



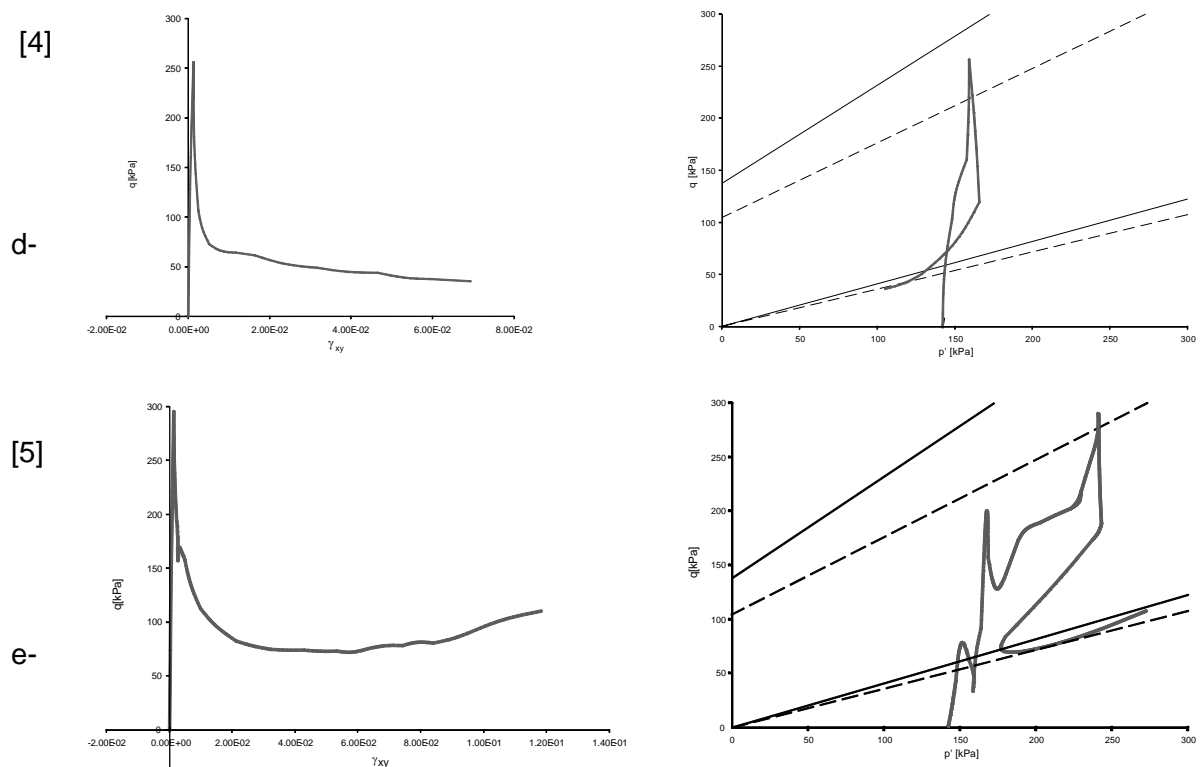


Figure 4.111 - Horizontal shear strain γ_{xy} vs. deviatoric stress q and effective pressure p' vs. q at points of the horizontal failure surface.

g) Simulation of large displacements

The MPM offers the possibility of analyzing large displacements in a natural manner due to its conception as a “particle” method. The dynamics of the motion of the dam were analyzed by means of a “block” model type of analysis in Alonso and Gens, 2006b.

Aznalcóllar dam moved forward a distance of approximately 50 m after the initial failure. This motion will not be analyzed in this analysis, which concentrates in the conditions leading to the initiation of the failure, but it is interesting to show the modelling capabilities by examining the changes that take place at the initiation of the motion, when the dam displaces a few meters. The transition from a stable state to an accelerated motion was attributed to a combination of two effects: the final stage in the process of progressive failure, when the friction is reduced to its final residual value and the increase in tailings thrust against the dam due to the liquefaction of tailings. The liquefaction of tailings, instants after the beginning of the dam forward motion, is supported by direct observations and by the calculation given in Alonso and Gens (2006b). The former include the presence of small volcanoes, scattered on the surface of the tailings deposit, immediately upstream of the displaced dam.

The liquefaction process of tailings is not modelled here. It will assumed that, at the end of construction, the tailings liquefied and behaved as a heavy liquid. At this time the scaling of the mass and gravity acceleration is turned to one, and the added damping is reduced to a small value of 2 %. From this moment onwards the model becomes dynamic with virtually no dissipation of pore pressures and simulates failure using many small time steps.

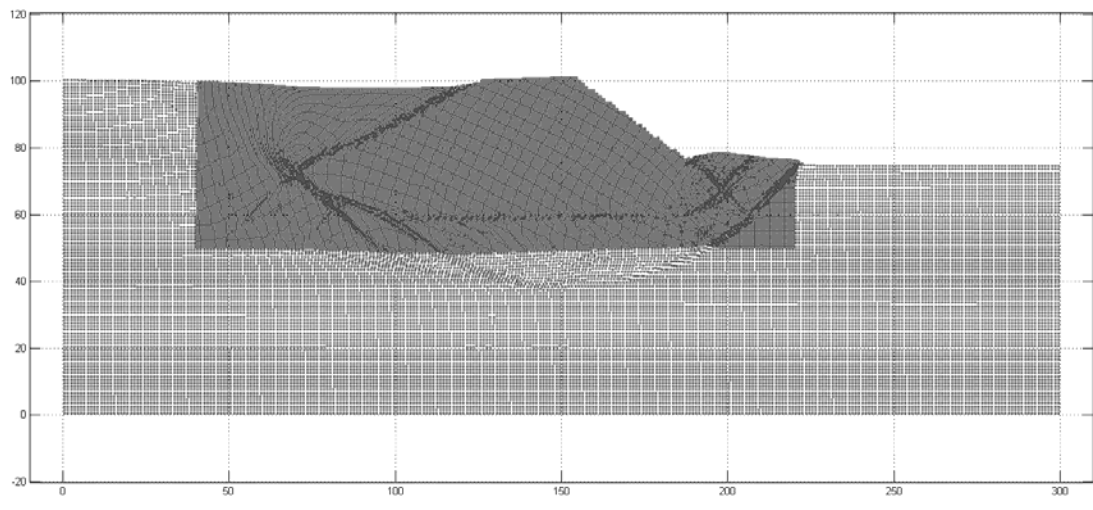


Figure 4.112 - Particle model a few seconds after tailings liquefaction.

Figure 4.112 shows the particle model a few seconds after the tailing's liquefaction without any amplification of the particle displacements. The dam moved horizontally approximately 4 meters. The darker zone has initially four particles per cell and the rest of the figure only one. In this figure it is possible to see the "failure surface" as an optical effect. Interestingly, in addition to the well developed horizontal failure surface, a deeper circular failure pattern begins to develop at this stage of the solution. It contributes to the development of passive wedges on the downstream of the dam. The accumulation of these wedges was observed in the field and it is represented in Figure 4.98. Figure 4.113 provides a detail of the passive wedge which is pushed upwards as the movement progresses. The formation of localized shearing bands is well apparent. Figure 4.114 shows a detail of the tailings movement during the initial few seconds. A shearing zone develops at the tailings – upstream dam slope. A wedge of tailings is mobilized and initiates a subsidence type of motion as the dam accelerates forward. The upstream limit of this wedge is still diffuse at this time of the motion and a few shearing bands begin to form. However, particles tend to separate in these zones, showing the initial stage of a tensile fracture. The dam upstream toe is a critical point: All shearing bands converge towards this point in a natural way.

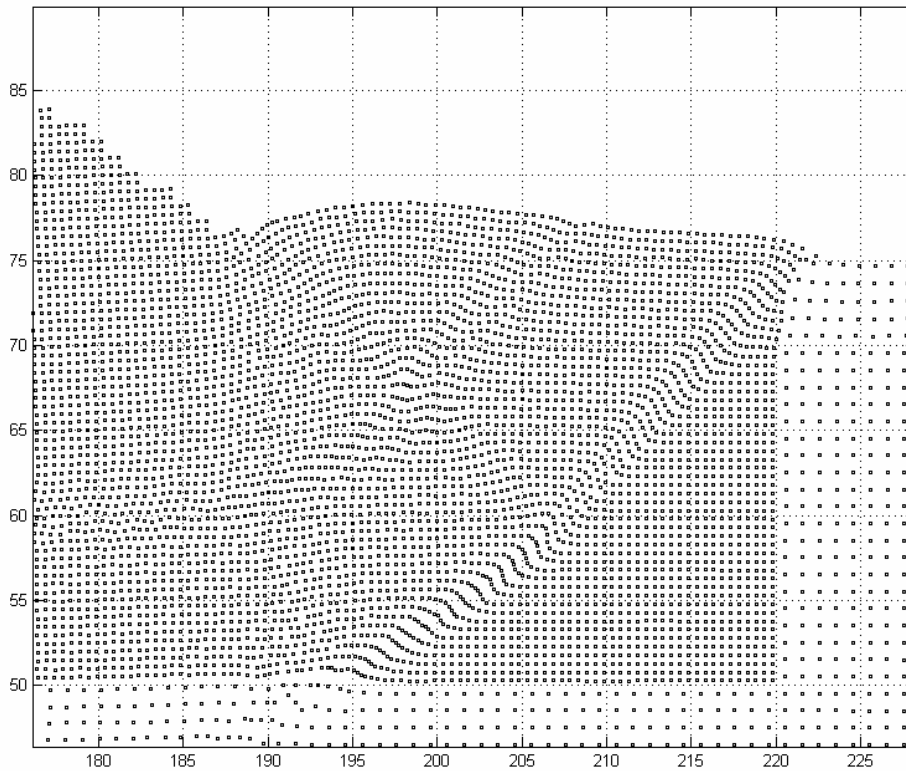


Figure 4.113 - Particle displacements. Passive wedge

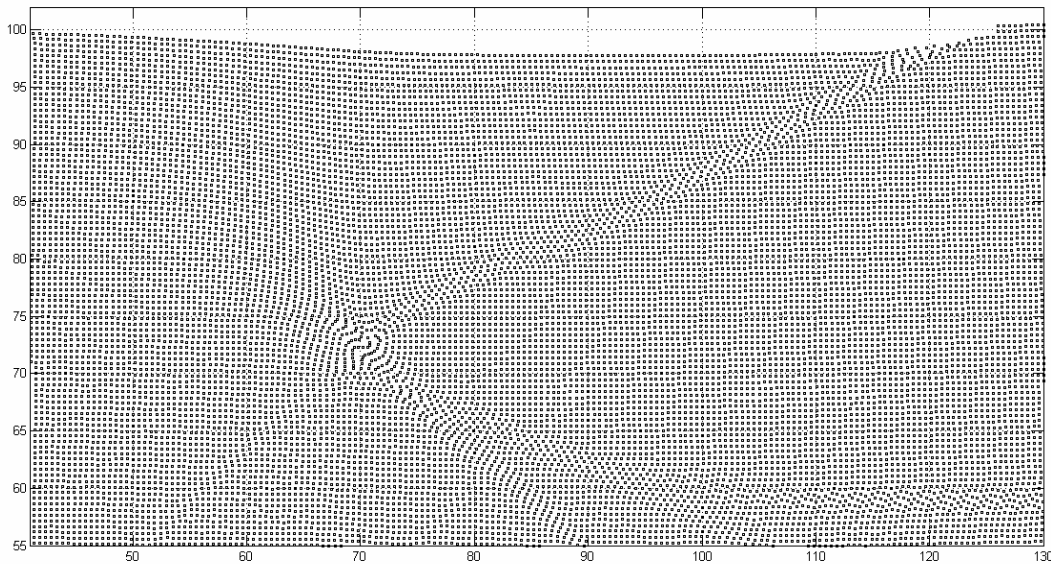


Figure 4.114 - Pattern of particle displacements. Tailings movement.

h) Conclusions

An explicit version of the Material Point Method, extended to deal with pore-fluid hydro-mechanical coupling, was developed. A computer code has also been developed and it has been applied to describe the performance and final collapse of Aznalcóllar dam.

The collapse mechanism of Aznalcóllar dam was simulated quite accurately. In the analysis performed, no prior assumptions were made about the location, shape and depth of the failure surface and these features were derived naturally from the calculation procedure. It was found that the geometry of the localization bands depends markedly on the initial stress state. For $K_0 = 1$, an acceptable hypothesis in a Miocene overconsolidated clay, the predicted collapse mechanism is similar to the observed one. The interaction between the clay brittleness, slow dissipation of pore pressures and the construction process generated a progressive failure in a horizontal area under the dam. Foundation clay failure began under the downstream foot of the dam under construction at an early stage (when the dam had a height of approximately 15 m). The points where the clay strength were reached concentrated in a narrow band at approximately 15 m below the ground surface, at the location of the failure surface identified later, after the failure. At these points peak shear strength was reached and therefore a process of stress transfer was started. As the dam reached increased heights, cracked zones eventually coalesced into a localized rupture band which was well established 11 yrs after the initiation of the dam construction, when the dam reached a height of 24 m. This band evolved towards the downstream toe of the dam and, simultaneously, in the upstream direction, towards the tailings deposit. In the final stages of the failure the rupture band bent upwards at the position of the upstream toe of the dam and crossed the tailings with a steeply inclined slope. This failure geometry is remarkably similar to the observed one, given in Figure 4.98. These results indicate that the clay stratification and the possible existence of a weaker layer or naturally sheared layer did not play a major role in the initiation of the failure. It should be stressed that the strain softening model used was calibrated against the shear response of the clay matrix. Stratification did not play a major role but it played some role. In fact, the main sliding surface seemed to follow a sedimentation plane, which dips gently (2°) in the direction of the motion. This observation suggests that once shearing started and the mechanism of progressive failure was initiated it was “easier” to follow a stratification plane. Some (small) reduction of the shear strength of sedimentation planes is therefore suspected. However, these planes were difficult to identify in most of the samples and cores recovered and they could never be isolated for laboratory shear testing.

The MPM is also well adapted to simulate large displacements and the dynamic motion after the failure. This part of the failure is not covered in this analysis. However it was interesting to present the initiation of the forward motion of the dam, once the tailings are assumed to liquefy. New shear bands seem to develop, which contribute to reproduce better the complex geometry of the passive wedge developing downstream under the dam thrust. Upstream, a wedge of tailings is isolated. It slides on the upstream slope of the dam and separates in a combined phenomenon of shearing and tensile rupture from the remaining body of tailings. Then, the tailings wedge initiates a downward motion, captured by the model.

4.2 NUMERICAL MODELLING OF SNOW-MELTING EFFECTS (ICG)

a) Snow melt theory

Rapid snowmelt caused by sudden warming spells or by rain falling on snow can add water to hillside soils and raise pore-water pressure beneath shallow soils, thus triggering landslides. (Wieczorek, 1996).

The mass balance of a snowpack is closely coupled to its energy balance, which for an open volume of snow neglecting sidewise fluxes can be expressed by (see Figure a)

$$-\frac{dH}{dt} = S_{\downarrow} + S_{\uparrow} + L_{\downarrow} + L_{\uparrow} + H_s + H_L + H_p + G \quad (1)$$

where

$\frac{dH}{dt}$	rate of change of snowpack's internal energy (W m^{-2}),
S_{\downarrow}	incoming short wave radiation (W m^{-2}),
S_{\uparrow}	outgoing short wave radiation (W m^{-2}),
L_{\downarrow}	incoming long wave radiation (W m^{-2}),
L_{\uparrow}	outgoing long wave radiation (W m^{-2}),
H_s	sensible heat flux (W m^{-2}),
H_L	latent heat flux (W m^{-2}),
H_p	flux of energy due to precipitation and blowing snow (W m^{-2}),
G	ground heat flux (W m^{-2}).

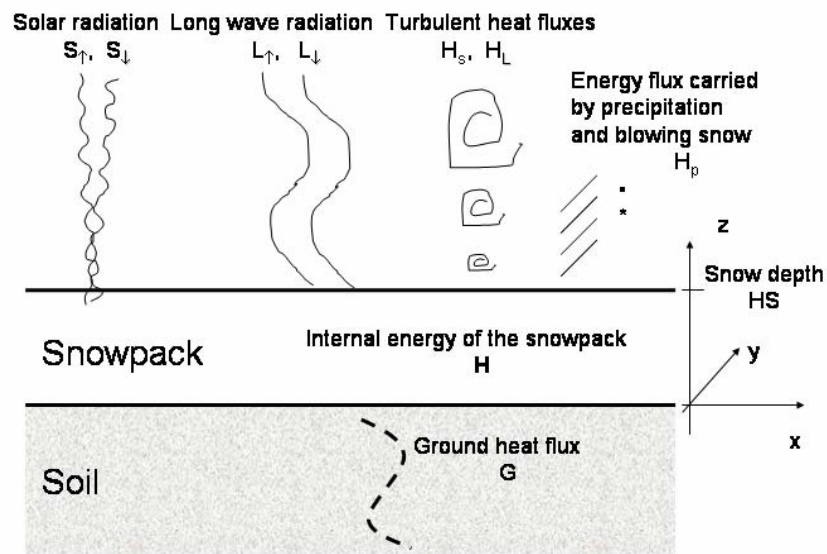
A summary of the fluxes involved in the energy balance Eq. (1) can be found in (King et al., 2008).

The change of internal energy is related to either warming and melting, or cooling and freezing (negative change, i.e. energy loss) within the snowpack. This is expressed by:

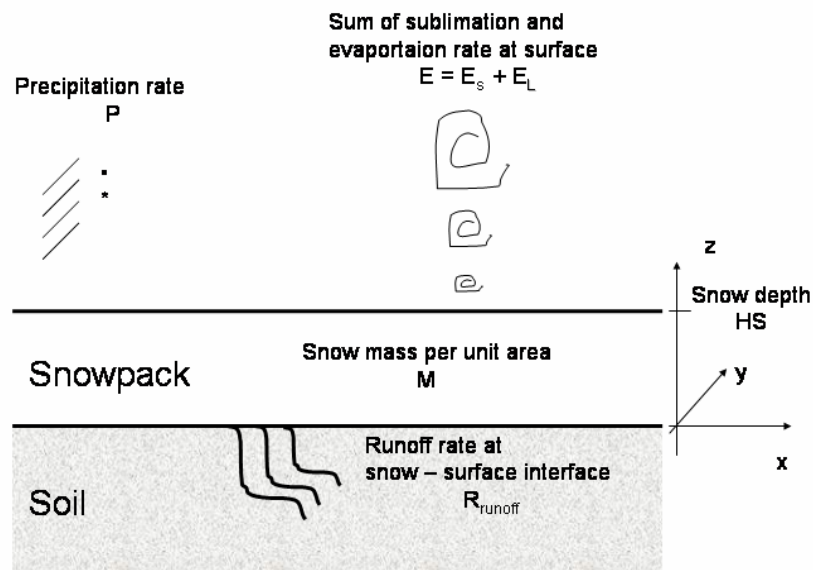
$$-\frac{dH}{dt} = L_{\ell i} (R_F - R_M) - \int_0^{HS} \left[\frac{d}{dt} (\rho_s(z) c_{p,i} T_s(z)) \right] dz \quad (2)$$

where

R_M	melting rate (kg s^{-1}),
R_F	freezing rate (kg s^{-1}),
$L_{\ell i}$	latent heat of fusion of ice ($3.34 \cdot 10^5 \text{ J kg}^{-1}$),
$c_{p,i}$	specific heat capacity of ice ($2.1 \cdot 10^3 \text{ J kg}^{-1} \text{ K}^{-1}$),
HS	Snowdepth (m),
ρ_s	density of snowpack (kg m^{-3}),
T_s	snow temperature (K).



a)



b)

Figure 4.115 - a) Energy balance for an open snow pack. b) Mass balance for an open snow pack (from King et al., 2008)

Freezing and melting rates couple the energy balance through Eq. (2) to the mass balance (see Figure 4.115b):

$$\frac{dM}{dt} = P \pm E - R_{\text{runoff}} \quad (3)$$

where

$\frac{dM}{dt}$ mass change rate of the snowpack (positive in the case of accumulation),
 P precipitation rate (accumulation),
 E = E_{sub}+E_{evap} sum of sublimation and evaporation rates at the surface,
 R_{runoff} runoff rate, which is strongly coupled to the melting rate (ablation).

A further coupling between energy and mass balance arises because the latent heat flux is related to the sublimation and evaporation rates through

$$H_L \approx L_{vi}E \quad (4)$$

where L_{vi} is the latent heat of sublimation (2.838·10⁶ J kg⁻¹ at 0°C).

During snowmelt periods the amount of melt water produced by melting may be approximated by

$$SM \approx \frac{1}{\rho_{\text{water}}L_{\ell i}} \frac{dH}{dt} \quad (5)$$

where ρ_{water} is the density of water.

b) Practical estimation of snowmelt

Empirical formulations for snowmelt estimates have been developed to solve different kinds of practical hydrological problems. These empirical methods differ in the degree of simplification but they provide reasonable estimates of snow melt rates if calibrated to local conditions.

b.1) Degree Day Method

The simplest but often used method to estimate snowmelt rates and run off is the so-called degree day method (cf. Gray & Male, 1981 Ch. 9). In this method amount of meltwater is estimated directly from air temperature data.

$$SM = M_f \max(T_i - T_b, 0) \quad (6)$$

where

SM melt produced in mm of water per unit time,
 M_f melt factor (mm/(°C unit time)),
 T_i index air temperature (°C; most commonly the maximum or mean daily temperature, and
 T_b base temperature (usually 0°C).

Values of M_f depend on the on location, time of year and meteorological conditions and typically range between 0.4 and 10 mm w.e. $^{\circ}\text{C}^{-1} \text{d}^{-1}$, using the daily mean temperature as temperature index T_i .

Figure shows an example of the melt water estimation according to Eq. (6) with varying melting factors.

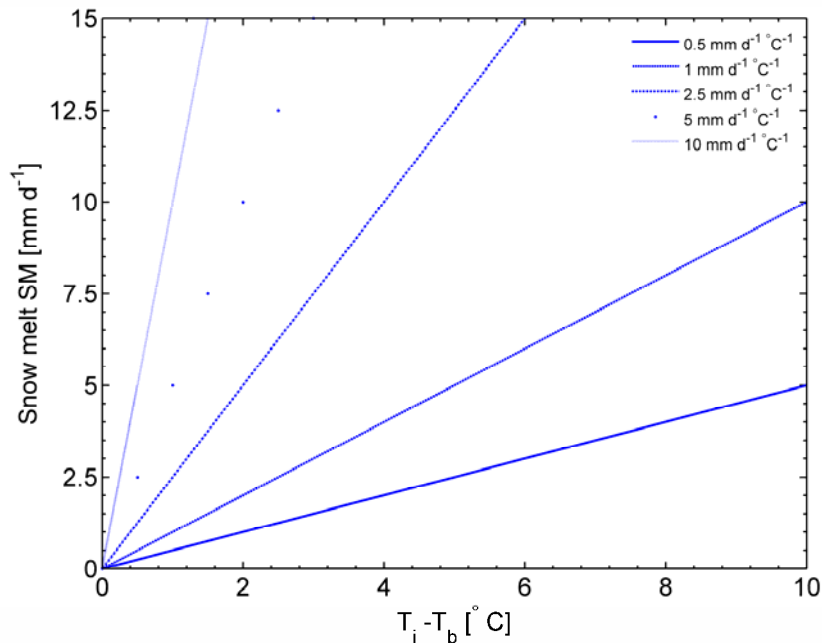


Figure 4.116 - Melt water SM per day according to a degree day method with varying melt factors.

Eggleston et al. (1971) proposed the empirical relation for the melt factor

$$M_f = k_m k_v R_I (1 - \alpha) \quad (7)$$

where

- k_m proportionally constant (for mountain regions $k_m \approx 0.4$),
- k_v vegetation transmission coefficient for radiation,
- R_I solar radiation index, and
- α snow albedo.

The change in albedo with time, t (d), is accounted for by

$$\alpha = 0.4(1 + \exp(-k_e t)) \quad (8)$$

where k_e is a time constant ($\approx 0.2 \text{ d}^{-1}$). In the case of new snow, it is assumed that $\alpha = 0.8$, while rain reduces α to 0.4. This equation holds true for deep mountain snow packs, but its accuracy is questionable for shallow prairie packs.

The vegetation transmission coefficient, k_v , is related to the decimal fraction, C_v , of vegetation canopy density

$$k_v = \exp(-4C_v) \quad (9)$$

R_I is the ratio of the radiation received by a surface, with a certain slope and aspect, normalized to that received by a horizontal surface at the same latitude and time of year. R_I is a function of the angle between the normal to the surface and the direction of the beam of radiation component. The factor can be considerable even for only slight inclined slopes (see (22)).

Using the approximation

$$H_p \approx \rho_w c_w P_{\Delta t} T, \quad (10)$$

the melt factor for periods of rain may be adjusted to

$$M_f(\text{rain}) = M_f + \frac{c_w}{L_{\ell i}} P_{\Delta t} \quad (11)$$

where

$M_f(\text{rain})$	melt factor for rain, and
$P_{\Delta t}$	rainfall intensity (mm d^{-1}).
$L_{\ell i}$	latent heat of fusion of ice ($3.34 \cdot 10^5 \text{ J kg}^{-1}$),
c_w	specific heat capacity of water ($4.185 \cdot 10^3 \text{ J kg}^{-1} \text{ K}^{-1}$),

Degree-day methods do not include the snow accumulation process, nor do they explicitly account for heat deficits, liquid-water retention and transmission, and the areal extent of the snow cover.

Figure shows an example of the melt water estimation according to Eq. (6) using Eq. (11) for $M_f = 2.5 \text{ mm d}^{-1} \text{ } ^\circ\text{C}^{-1}$.

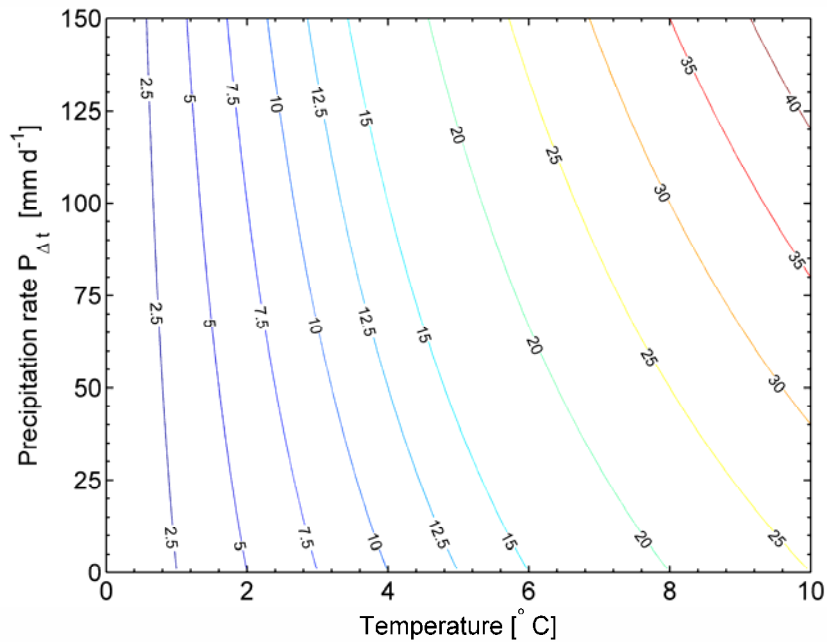


Figure 4.117 - Meltwater in mm per day as a function of temperature and precipitation rate ($M_f = 2.5 \text{ mm d}^{-1} \text{ } ^\circ\text{C}^{-1}$, $T_b = 0^\circ\text{C}$)

b.2) Harstveit’s Energy Balance model

Based on the energy balance model by Harstveit (1984), Hestnes et al. (1987) proposed a simple empirical formula for the melt water production per day using wind speed and temperature, which is easy to use. The melt water estimation is given by the empirical formula

$$SM = \frac{1}{\rho_w L_{fi}} \left[(C_1 U + C_2) \left(T + \frac{1}{\gamma} (e_{u,t} - e_0) \right) + R_N \right] \text{ (mm d}^{-1}\text{)} \tag{12}$$

where

- U wind speed,
- T air temperature ($^\circ\text{C}$),
- γ wet adiabatic lapse rate ($\approx 0.6 \text{ hPa K}^{-1}$),
- $e_{u,t}$ saturation water vapour pressure,
- e_0 saturation water vapour pressure at $T = 273 \text{ K}$ (6.11 hPa),
- R_N net radiation of snow cover,
- C_1, C_2 empirical constants ($C_1 = 3.1 \text{ J m}^{-3} \text{ K}^{-1}$ and $C_2 = 2.3 \text{ W m}^{-2} \text{ K}^{-1}$), and
- L_{fi} latent heat of fusion of ice ($3.86 \text{ W kg}^{-1} \text{ d}^{-1}$).

The saturation water vapour pressure may be approximated by

$$e_{u,t} = 6.11 \exp\left(\frac{17.966T}{247.15 + T}\right) \text{ (hPa)} \quad (13)$$

The net radiation may be approximated by

$$R_N = S_{\downarrow}(1 - \alpha) + L_{\downarrow} + L_{\uparrow} \quad (14)$$

where

- S_{\downarrow} global incoming short wave radiation,
- α snow albedo,
- L_{\downarrow} incoming long wave radiation ,
- L_{\uparrow} outgoing long wave radiation.

R_N might be approximated by the empirical formula

$$R_N = \left(-0.16(1 - C) + 0.81(1 - C)^{1/2} + 0.07\right) S_{ex} (1 + 0.13(1 - C) + 0.05 \ln D - 0.87) \\ + \left(0.265\sigma T_{KS}^4 + 18.4C - 23.9\right) - 81.8 \quad (15)$$

where

- S_{ex} extraterrestrial radiation given by the date and latitude (W m^{-2}),
- C cloud cover fraction in 1/10,
- D number of days of exposed snow surface,
- σ Stephan Boltzmann constant ($5.67 \cdot 10^{-8} \text{ W m}^{-2} \text{ K}^{-4}$),
- T_{KS} surface temperature (K) (for melting snow pack $T_{KS} \approx 273\text{K}$).

The parameterization of R_N in Eq. (15) and of H_L and H_S used in Eq. (12) is based on studies in Dyrdaalen, western Norway. In Eq. (15), varying topography is not explicitly accounted for. This can cause considerable errors for hillsides.

The extraterrestrial radiation may be approximated by

$$S_{ex} = S_0 \left(\frac{r}{r_0}\right)^2 \cos Z \quad (16)$$

where

- S_0 solar constant ($\approx 1350 \text{ W m}^{-2}$),
- Z solar zenith angle,
- $(r/r_0)^2$ squared ratio of average distance of the earth from the sun to its actual distance at any time of the year.

$$\left(\frac{r}{r_0}\right)^2 = 1.00011 + 0.034221 \cos d_0 + 0.001280 \sin d_0 + \\ + 0.000717 \cos 2d_0 + 0.000077 \sin 2d_0 \quad (17)$$

where

$$d_0 = 2\pi m/365 \quad \text{and } m \text{ is the day of the year starting with 0 on Jan. 1 and ending 364 on Dec. 31.}$$

The solar zenith with respect to an inclined surface is given by (Allen et al., 2006)

$$\begin{aligned} \cos Z = & \sin \phi \sin \delta \cos(\text{slp}) \\ & - \cos \phi \sin \delta \sin(\text{slp}) \cos(es - \pi) \\ & + \cos \phi \cos \delta \cos(\text{slp}) \cos(h_r) \\ & + \sin \phi \cos \delta \sin(\text{slp}) \cos(es - \pi) \cos(h_r) \\ & + \cos \delta \sin(\text{slp}) \sin(es - \pi) \sin(h_r) \end{aligned} \quad (18)$$

where

ϕ	latitude,
δ	solar declination,
h_r	solar hour angle
slp	slope angle ($0 \leq \text{slp} \leq \pi/2$)
es	exposition angle of the slope (north = 0, east = $-\pi/2$, south = π , and west = $\pi/2$)

The solar declination is given by

$$\delta = \frac{23.5\pi}{180} \cos[2\pi(J_d - 173)/365] \quad (19)$$

where $J_d (= m+1)$ is the Julian day.

The solar hour angle is defined by

$$h_r = \frac{15\pi}{180} (t_{GMT} - \lambda/15^\circ + E_\tau - 12) \quad (20)$$

where

t_{GMT}	Greenwich Meridian Time,
λ	west longitude in degrees, and

$$E_\tau = 0.158 \sin[\pi(J_d + 10)/91.25] + 0.125 \sin[\pi J_d / 182.5]$$

The daily mean extraterrestrial radiation on a horizontal surface is then given by

$$\overline{S_{ex}} = \frac{S_0}{\pi} \left(\frac{r}{r_0} \right)^2 (\omega_o \sin \phi \sin \delta + \cos \phi \cos \delta \sin \omega_o) \quad (21)$$

where $\omega_o = \arccos(-\tan \phi \tan \delta)$.

The daily mean ratio of the expected direct beam radiation on a slope to direct beam radiation on a horizontal may be estimated by

$$R_i \approx \frac{\overline{CZ}}{2(\omega_o \sin \phi \sin \delta + \cos \phi \cos \delta \sin \omega_o)} \quad (22)$$

where

$$\begin{aligned} \overline{CZ} = & 2\omega_o \sin \phi \sin \delta \cos(slp) \\ & - 2\omega_o \cos \phi \sin \delta \sin(slp) \cos(es - \pi) \\ & + 2 \cos \phi \cos \delta \cos(slp) \cos(h_r) \sin(\omega_o) \\ & + 2 \sin \phi \cos \delta \sin(slp) \cos(es - \pi) \cos(h_r) \sin(\omega_o) \end{aligned} \quad (23)$$

However sunrise and sunset depends heavily on the local topography and its surrounding. Therefore in most cases a radiation model is needed to obtain the correct radiation balance.

Figure shows an example of the melt water estimation according to Eq. (12) for a relative humidity of 100% ($R_N \approx 0$).

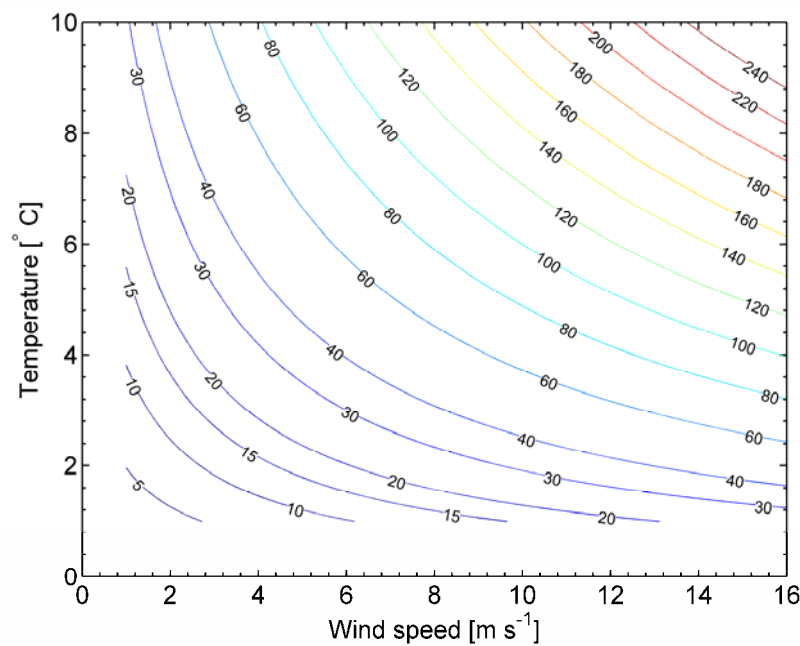


Figure 4.118 - Melt water in mm per day as a function of temperature and wind speed. Relative humidity equals 100 % ($R_N = 0$) (adapted from Hestnes, 1987)

4.3 POTENTIAL SCENARIOS RELATED TO CLIMATE CHANGES (AMRA)

The most recent data from monitoring of the mean atmosphere parameters on the Earth (temperature, rainfall, humidity, etc.) suggest that the last century has been characterised by significant climate changes. The I.P.C.C. (Intergovernmental Panel on Climate Change) reports that during the last 25 years global temperature has been subjected to an average increase of about 0.6 °C (Fig. 4.119), which is fairly high when compared to its maximum oscillation of 1°C/century estimated for the previous 4.5 billions years. In addition, during the 20th century mean sea level has risen by approximately 15 cm due largely to glacial retreat. From 1970 the world's ocean surface has experienced a 0.55 °C increase in temperature.

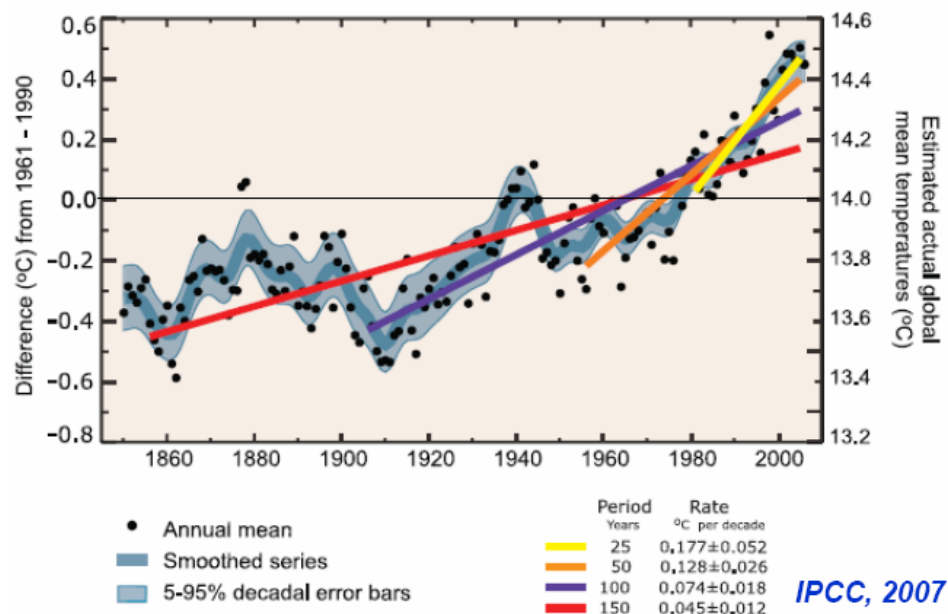


Figure 4.119 - Global temperature increase in the last 150 years (IPCC, 2007)

According to climate scenarios based on global models, in the near future weather modifications will strongly influence hydrological cycles. For example, the number of rainy days in the Mediterranean area should decrease, but the rainfall events would be more intense because precipitation will be concentrated into shorter time intervals. Such a situation should produce an impact on the stability of slopes, which are undergoing a changing rainfall regime.

Thanks to the availability of data about the piezometric regime and the displacement field of a very slow mudslide and to an extrapolation of present climate conditions in the concerned area, this section suggests a methodological approach to predict along-term scenario of the landslide behaviour related to ongoing climate changes.

4.3.1 Analysis of a test-case in fine-grained soils

a) Monitoring

The proposed case regards a mudslide in highly tectonized clay shales, whose behaviour has been investigated since 1993 (Vassallo and Di Maio, 2006, 2007, 2008). The landslide area involves an about 10° inclined slope, located in the eastern part of the urban area of Potenza, Southern Italy. The landslide body (Fig. 4.120) is about 1100 m long and extends between altitudes of 800 m and 619 m a.s.l.. The accumulation zone is located in the alluvial plain of the Basento River. Presently, the landslide displays a very low velocity (about 2 cm/year), essentially governed by cumulated rainfall over long time periods (about 3 - 4 months).

Available displacement and pore-water pressure data are provided by an inclinometer and two Casagrande piezometers (Vassallo and Di Maio, 2006, 2007, 2008). The inclinometer, reported as I3 in Figure 4.120a, is located in the main track: there is available data from February 2 2005 to July 13 2006. The slip surface has been recognized at a depth of about 10 m below the ground surface (Fig. 4.121). The two piezometers are located at depths of 15 and 34 m in the same borehole (S1) drilled in the accumulation zone: available data cover the period between January, 11, 2005, and May, 23, 2008. Figure 4.122 shows that the shallowest piezometer displays significant pore water pressure fluctuations, while the deepest one maintains a practically constant level.

Climate data regard:

- daily rainfall, from 1916 to 2007, measured by a station set at an altitude of 811 m a.s.l.;
- daily temperature (maximum, minimum and mean values), from 1924 to 2007, measured by the above mentioned station;
- rainfall, air temperature and relative humidity registered every 20 minutes, from January, 1st, 2005 until to December, 31, 2007, at an altitude of 659 m a.s.l. (ARPAB, Agenzia Regionale per la Protezione dell' Ambiente della Basilicata).

Both stations are located not so far from the site (about 7.50 Km). Figure 4.123 shows the course of the daily maximum and minimum values of air temperature and relative humidity from 2005 to 2007: during summer air temperature and relative humidity attain respectively their maximum and minimum values.

Climate data doubtless show that during the last century:

- the yearly cumulated rainfall displays a general decreasing trend of about -2.35 mm/year on average (Fig. 4.124a), which is consistent with the general trend in the Italian area (Fig. 4.124b) reported by Brunetti et al. (2006);
- maximum values of temperature are characterized by a rising trend (Figure 4.125a) in the order of 0.005 °C/year;
- minimum values of temperature are characterized by a rising trend (Figure 4.125b) of about + 0.004 °C/year.

Unfortunately, available data does not allow provision of a reliable hypothesis about the future trend of the relative humidity.

The following section reports some numerical simulations performed in order to estimate the potential impact of such climate scenario on the long-term behaviour of the landslide. In particular, it includes two different steps:

- a) calibration of a simple numerical seepage model linking weather data and piezometric regime;
 - b) setting up of a relationship relating pore pressures to landslide movements.
-

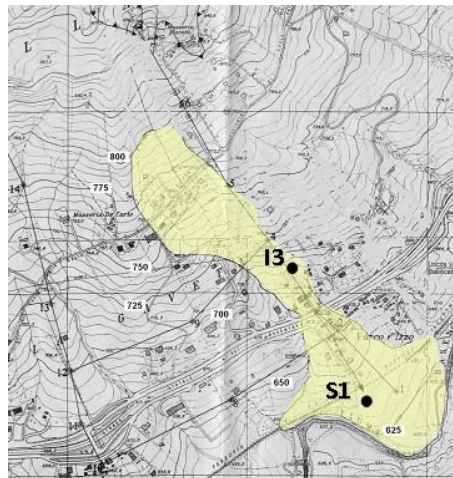


Figure 4.120 - Plan view of the analysed landslide

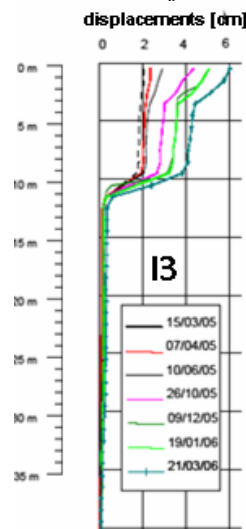


Figure 4.121 - Displacements data measured by inclinometer I3 (from Vassallo and Di Maio, 2006)

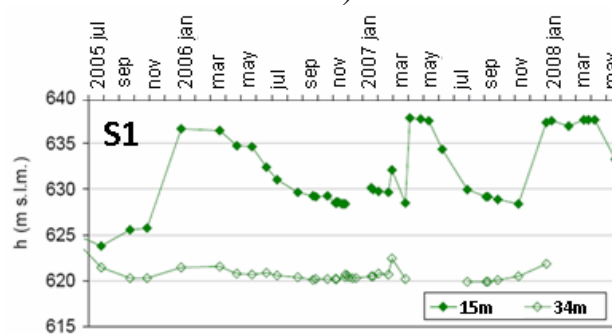


Figure 4.122 - Piezometric data measured by piezometers S1sup, installed at a depth of 15 m, and S1inf, installed at a depth of 34 m (from Vassallo and Di Maio, 2008)

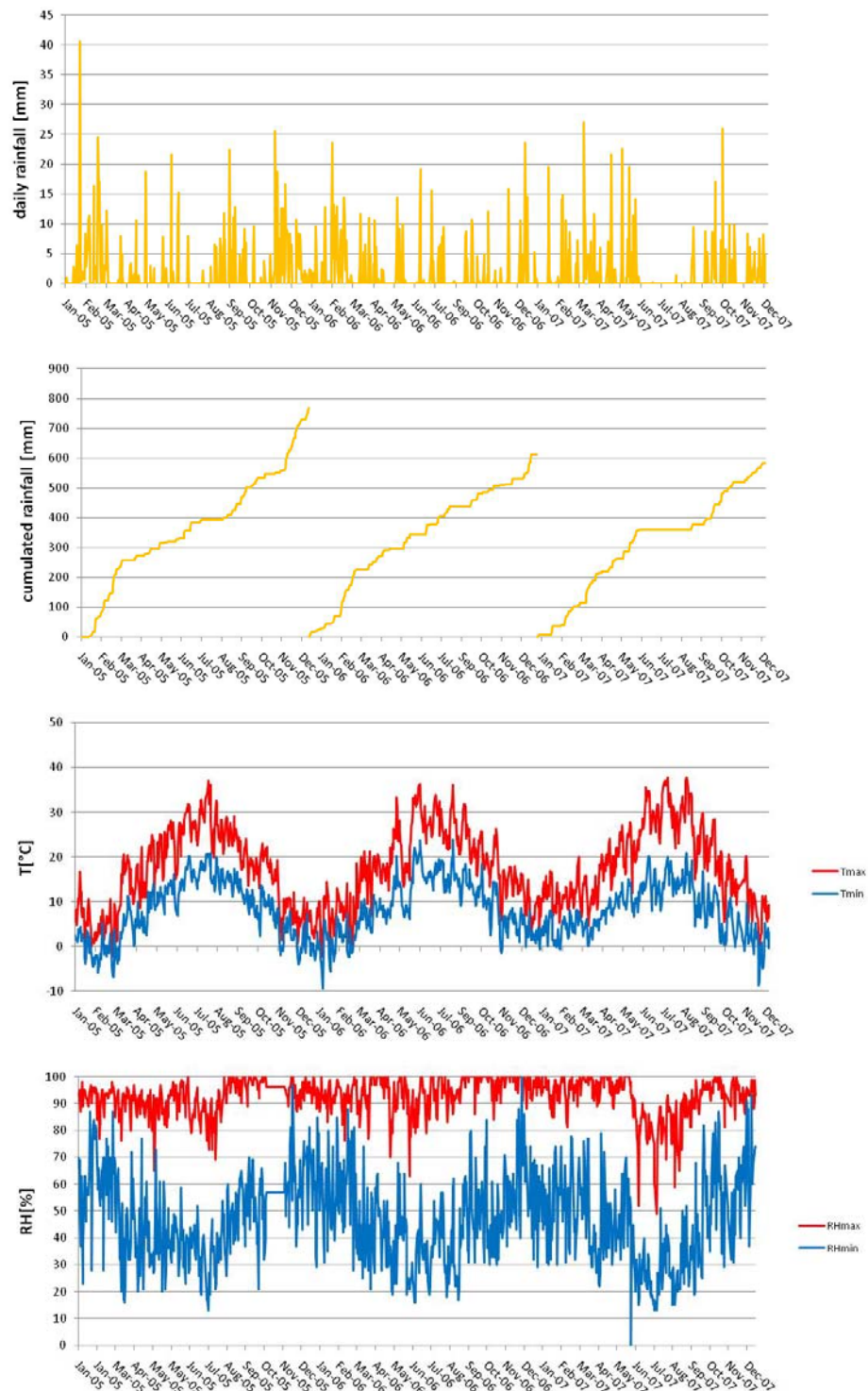
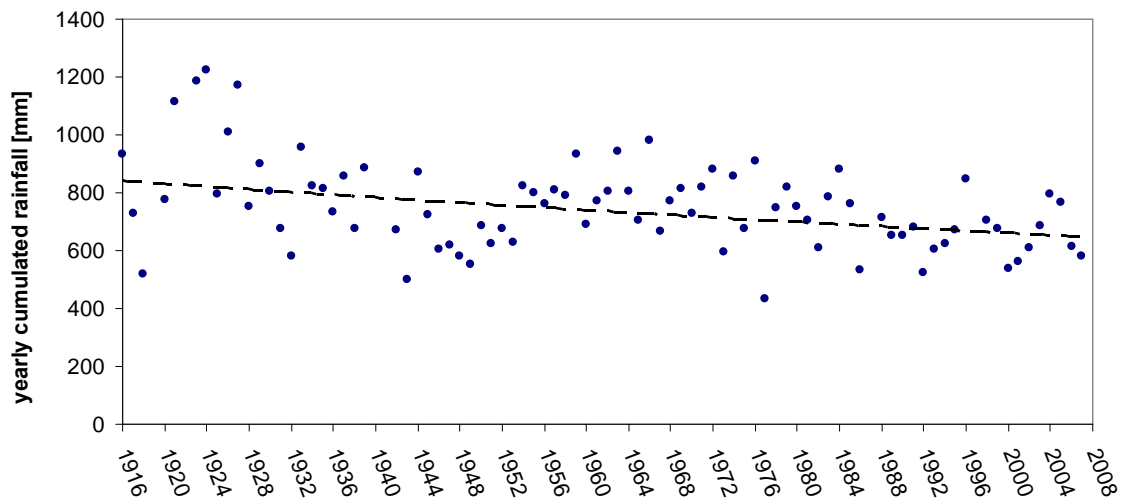
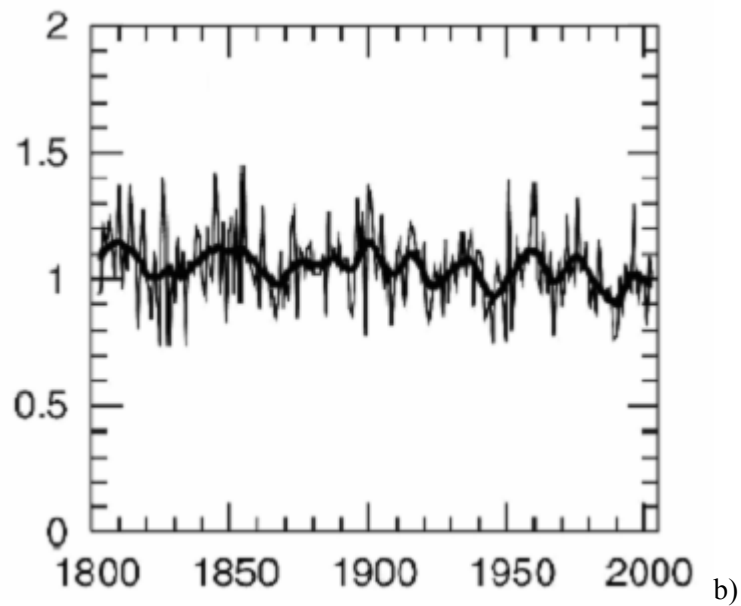


Figure 4.123 - Rainfall, maximum and minimum values of temperature T and relative humidity RH measured at the ARPAB station from 01/01/2005 to 31/12/2007

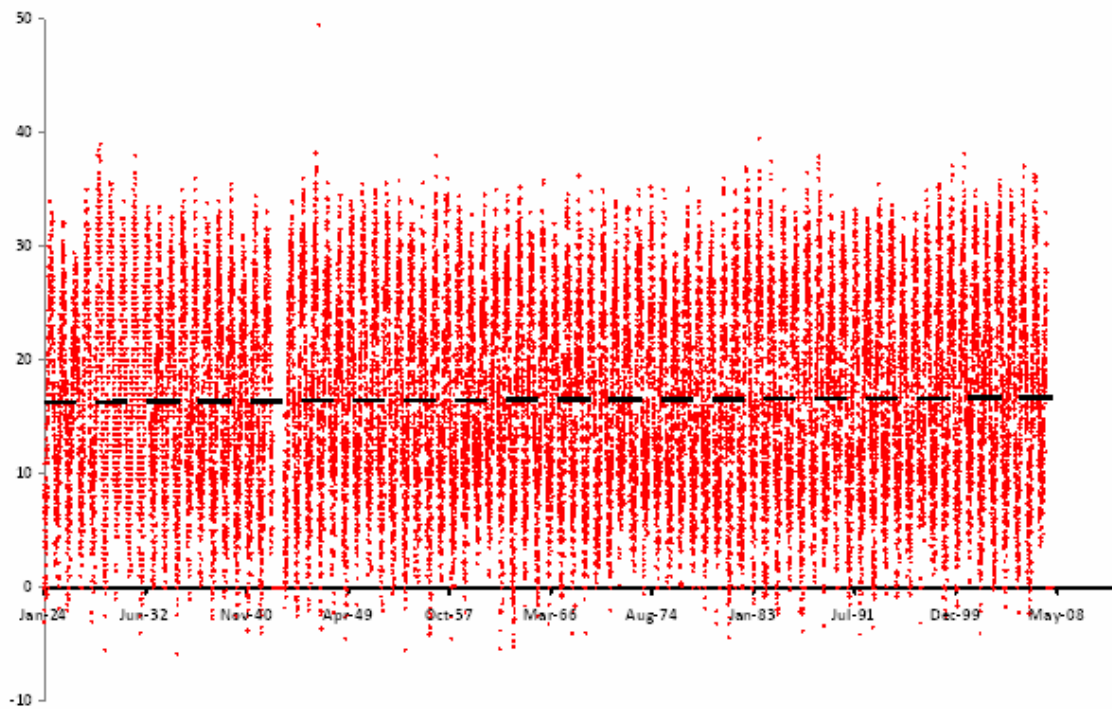


a)

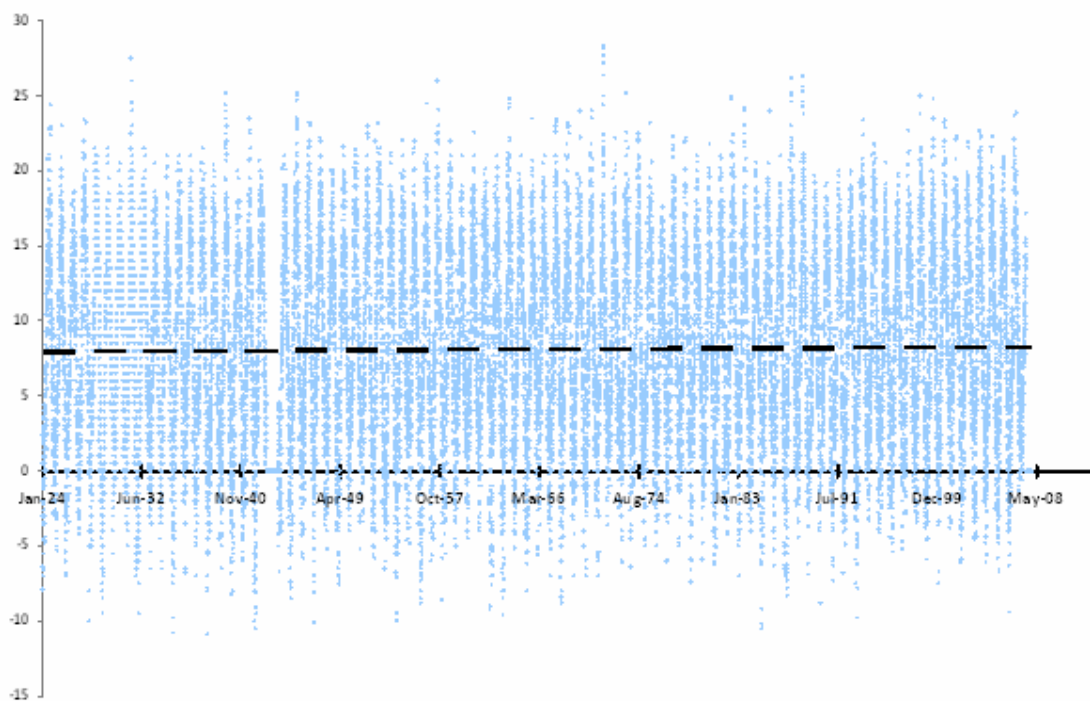


b)

Figure 4.124 - Yearly cumulated rainfalls: a) values measured in the concerned area; b) average values measured in Italy, normalized with respect to the values measured from 1961 to 1990 (from Brunetti et al., 2006)



a)



b)

Figure 4.125 - Daily maximum (a) and minimum (b) values of temperature measured at Potenza from 1924 to 2007

b) Numerical seepage analysis (climate data → piezometric regime)

The analysis has been performed by the VADOSE/W program (Krahn, 2004), described in section 4.1.2.1.4.1. It is a FEM code which, taking into account the equations solving hydraulic flow (both water and vapour phases), heat flow and gas flow, can solve seepage problems within soils subjected to non-isothermal conditions.

The following assumptions has been adopted in the analysis:

- i) one - dimensional flow;
- ii) infinite soil thickness;
- iii) gas flow neglected;
- iv). transpiration neglected.

According to these hypotheses, whose aim is to obtain reliable results without significant computational efforts, the problem is governed by three differential equations:

- 1) one-dimensional vertical hydraulic seepage;
- 2) heat transfer;
- 3) coupling of the heat and mass equations.

The soil stratigraphy is very simple, including the presence of the top soil 1 m thick (layer 2) and a semi-infinite deposit (layer 1) of tectonized clay shales. In order to solve the governing equations, the code needs information about the hydraulic and thermal properties of both soils through the following hydraulic functions

- *hydraulic conductivity curve*, $k_w - u_w$ (hydraulic conductivity – pore-water pressure);
- *volumetric water content curve* $\theta_w - u_w$ (volumetric water content – pore-water pressure),

and the following thermal functions

- *thermal conductivity curve* $k_t - \theta_w$ (thermal conductivity - volumetric water content);
- *volumetric heat capacity function* $\lambda_t - \theta_w$ (volumetric heat capacity - volumetric water content).

Based on the idea that the top soil is more pervious and more compressible than the clay shales, the assigned hydraulic and thermal properties are those which provide the best matching of the piezometric levels at a depth of 15 between January, 1st, 2005, and December, 31st, 2007. In particular, the hydraulic conductivity curve of each soil (Figure 4.126a) has been obtained as a function of matric suction $u_a - u_w$, using the formulation proposed by Mualem (1976):

$$k_w = \begin{cases} k_{ws} & \alpha \cdot (u_a - u_w) \leq 1 \\ k_{ws} \cdot [\alpha \cdot (u_a - u_w)]^{-(2+5\lambda/2)} & \alpha \cdot (u_a - u_w) > 1 \end{cases} \quad [4.3.5]$$

where k_{ws} is the saturated permeability, α is the inverse of the air-entry suction $(u_a - u_w)_e$ and λ is a dimensionless parameter representing the slope of the characteristic curve.

Regarding the volumetric water content curves (Figure 4.126b), the following formulation, modified from Brooks and Corey (1964), has been used:

$$\theta_w = \begin{cases} \theta_{ws} - m_{ws} \cdot (u_a - u_w) & \alpha \cdot (u_a - u_w) \leq 1 \\ \theta_{wr} + (\theta_{ws,aeV} - \theta_{wr}) \cdot [\alpha \cdot (u_a - u_w)]^{-\lambda} & \alpha \cdot (u_a - u_w) > 1 \end{cases} \quad [4.3.6]$$

where θ_w is the volumetric water content, θ_{ws} is the saturated volumetric water content ($u_w=0$), m_{ws} is the saturated volumetric compressibility, θ_{wr} is the residual volumetric water content, $\theta_{ws,aeV}$ is the volumetric water content at the air-entry value of the suction (u_a-u_w)_e. The hydraulic parameters used in the analysis are reported in Table 4.3.1.

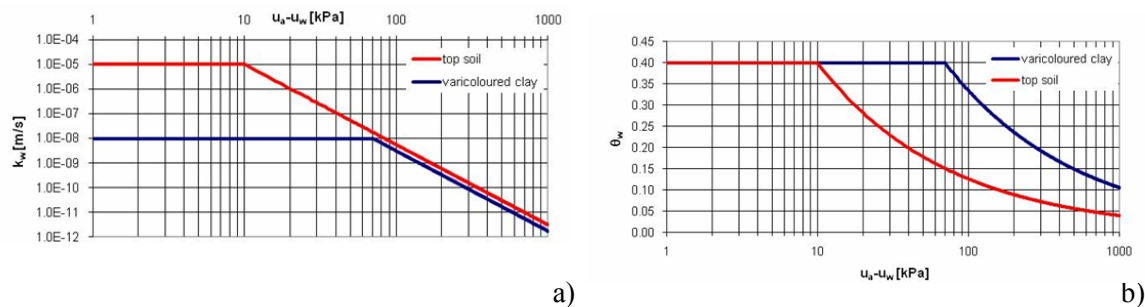


Figure 4.126 - Hydraulic conductivity–suction curves (a) and volumetric water content–suction curves (b) adopted in the analysis

Table 4.3.1 - Hydraulic parameters adopted in the analysis

	k_{ws} m/s	θ_{ws}	θ_{wr}	λ	α kPa ⁻¹	a.e.v. kPa	Vol. Compress. m_{ws} (Sr=1) kPa ⁻¹
Top soil	1.00E-05	0.40	0.00	0.50	0.100	10	1.00E-04
Varicoloured Clay	1.00E-08	0.40	0.00	0.50	0.014	70	1.00E-05

Thermal conductivity is defined as the amount of heat that flows through a unit area of a soil of unit thickness in unit time under a unit temperature gradient, so it represents the ability of a soil to transmit heat by conduction. The units used in the analyses for thermal conductivity have been [kJ / (day m °C)]. The adopted function (Fig. 4.127a) has been estimated by the code and derived from the Johansen method (1975), which is based on the volumetric water content function and the thermal conductivity of the soil mineral. In particular, the water content data is used to determine the range of possible water contents over which the thermal properties are defined. For both soils, the thermal conductivity of soil mineral has been imposed equal to 130 kJ/(day m °C), which is typical of clay shales.

The volumetric heat capacity is defined as the amount of heat required to raise the temperature of the soil by a unit degree. The units used in the analysis for heat capacity have been [kJ / (m³ °C)]. For both soils, the function (Fig. 4.127b) has been derived by the method proposed by de Vries (1963). For the mass specific heat of the soil mineral, for both soils the value 0.71 kJ/(kg °C) has been used, which is typical of soil minerals.

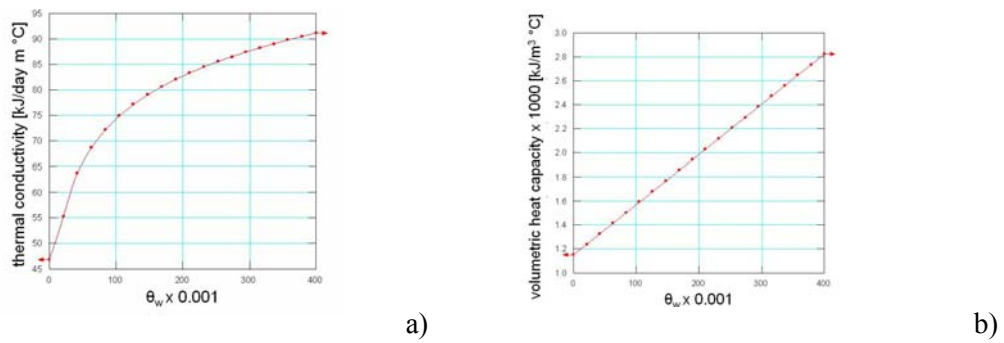


Figure 4.127 - Thermal conductivity–volumetric water content curve (a) and volumetric heat capacity–volumetric water content curve (b) adopted in the analyses

Results

Once assigned at the ground surface the measured climate data as climate boundary conditions, the analysis has been launched starting from the following initial conditions:

- in hydraulic terms: hydrostatic condition with the groundwater set at the ground surface,
- in thermal terms: an initial temperature equal to 0°C at the ground surface.

The piezometric course simulated by the analysis (Fig. 4.128) is very similar to the one measured. The agreement is rather good after the first year (2005), which depends by the initial conditions. It's worth noting that the results are the effect of simulated complex phenomena which depend on the daily net infiltration, in turn depending on the calculated net radiation and evaporation (Fig. 4.129).

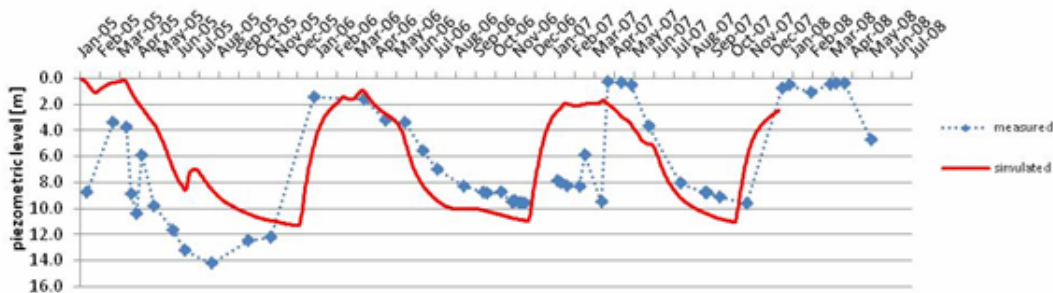


Figure 4.128 - Simulated and measured piezometric levels at a depth of 15 m

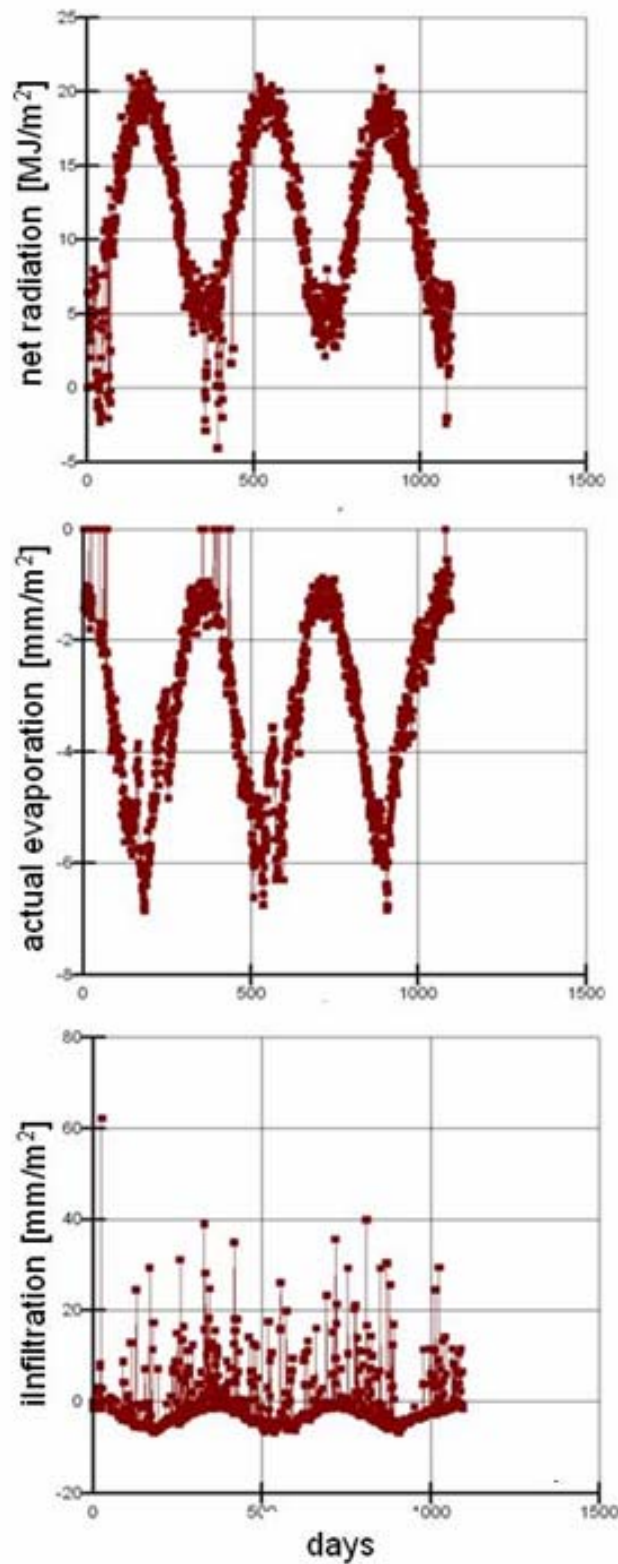


Figure 4.129 - Net radiation, actual evaporation and infiltration calculated at the ground surface

c) Analysis of the displacement

Figure 4.130 shows the displacements cumulated at the depth of the slip surface and the mean velocities versus the piezometric levels. The displacement rate is substantially governed by the piezometric level, changing as the groundwater level changes. In particular, a clear acceleration occurs from December, 2005 to March, 2006, when groundwater level approaches the ground surface: in such a period, the average rate of displacement is about 0.30 cm/month, higher than 0.10 cm/month shown before and after that time interval.

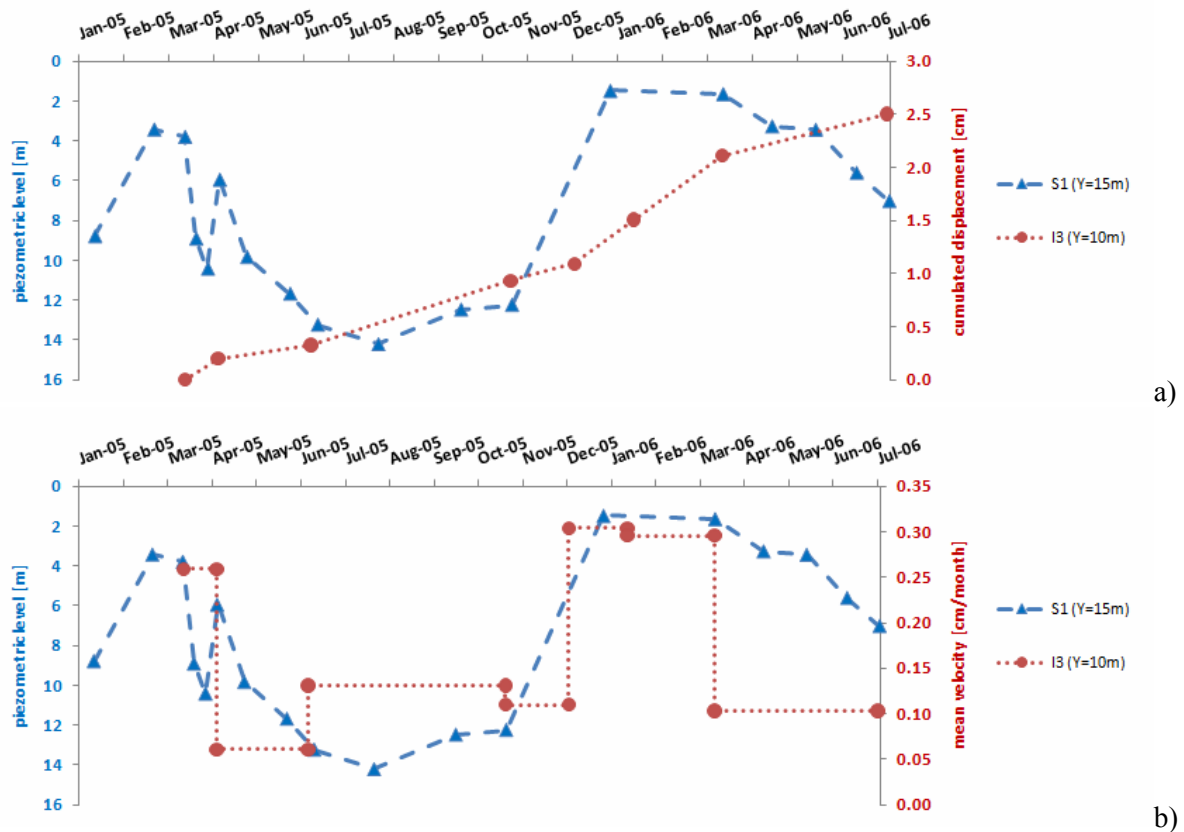


Figure 4.130 - Comparison of piezometric levels measured at piezometer S1 during the period January, 2005 - July, 2006 with: a) cumulated displacement (measured by inclinometer I3); b) mean displacement rate

In order to obtain a relationship between pore-water pressures and displacement rate, we have calibrated the empirical power law

$$v = \frac{a}{h^b} \quad [4.3.7]$$

where v [mm/day] is the velocity, h [m] is the piezometric level, a and b are back analysed empirical parameters. The empirical parameters that provide the best matching between computed and measured displacements (Fig. 4.131a) depend on the pore water trend, being different during the lowering and rising phases; they are:

- $a = 0.050$, $b = 0.90$ during groundwater rising phases

- $a = 0.013$, $b = 1.00$ during groundwater lowering phases

Therefore, for a fixed groundwater level, the rate of movement is higher during increasing piezometer levels than during decreasing phases (Fig. 4.131b). Such a hysteretic behaviour has been already observed by Bertini et al. (1986) for a landslide that involved similar soils.

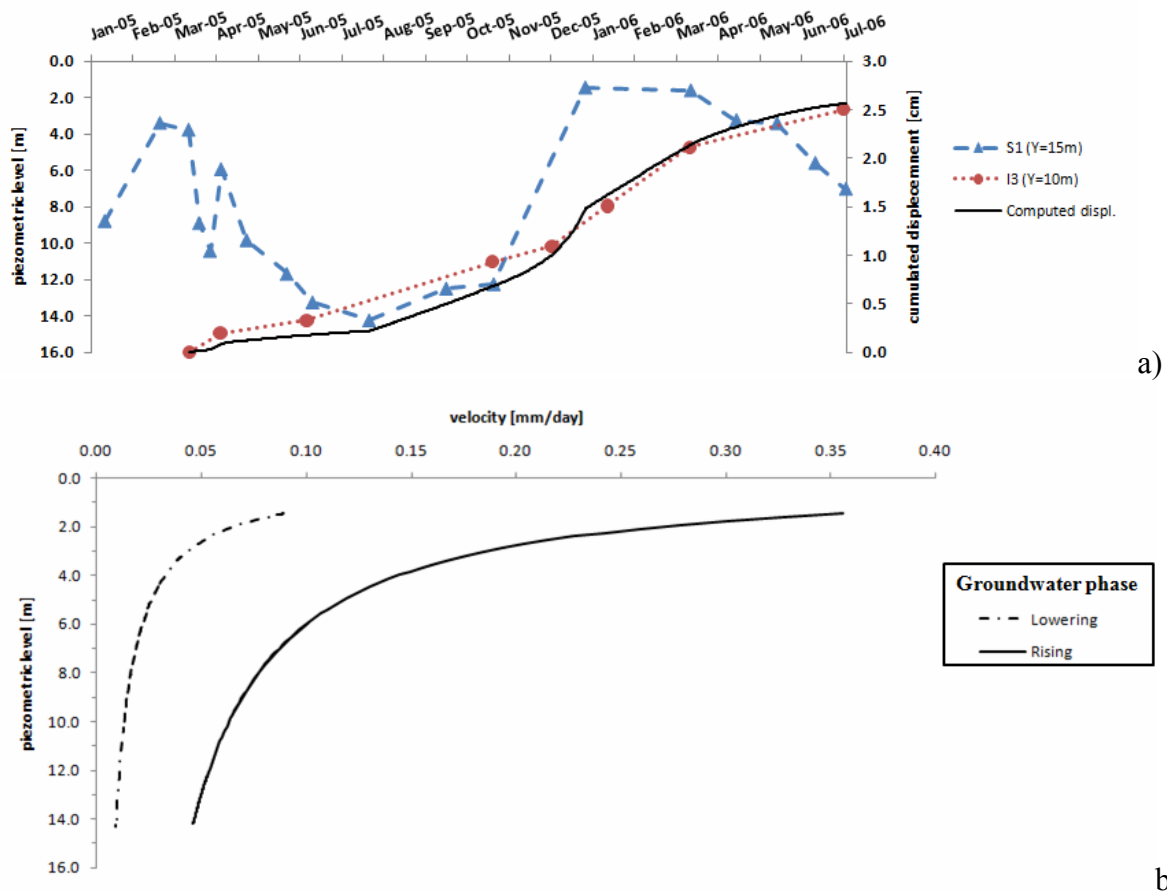


Figure 4.131 - Comparison of piezometric levels with: a) measured and computed displacements at inclinometer I3; b) computed rates of displacement

d) Potential effects of future climate scenarios on the landslide behaviour

The combination of the effects produced by the decreasing tendency of the yearly cumulated rainfall (Fig. 4.124a) and the rising tendency of the temperature (Fig. 4.125) should favour higher evaporative effects, reducing the infiltration and the hydrological slope response.

In order to evaluate the climate impact in the next 50 years, some numerical analyses have been performed, assigning at the ground surface climate boundary conditions which are consistent with the experimental evidence. The simulations that have been launched assuming climate data extrapolated from present data and bearing on the analyses carried for the period 2005-2006. The calculated piezometric levels (Fig. 4.132) display a slow reduction (about - 0.01 cm/year). The combination of these results with the empirical relationship shown above between daily pore-water pressures and velocity, provides a potential scenario about the future movements. In particular, the mean velocity could reduce of about 0.5 cm/year (Fig.

4.133). Moreover, the cumulated displacement during the next 50 years will attain a little higher than 1.00 m value (Fig. 4.134).

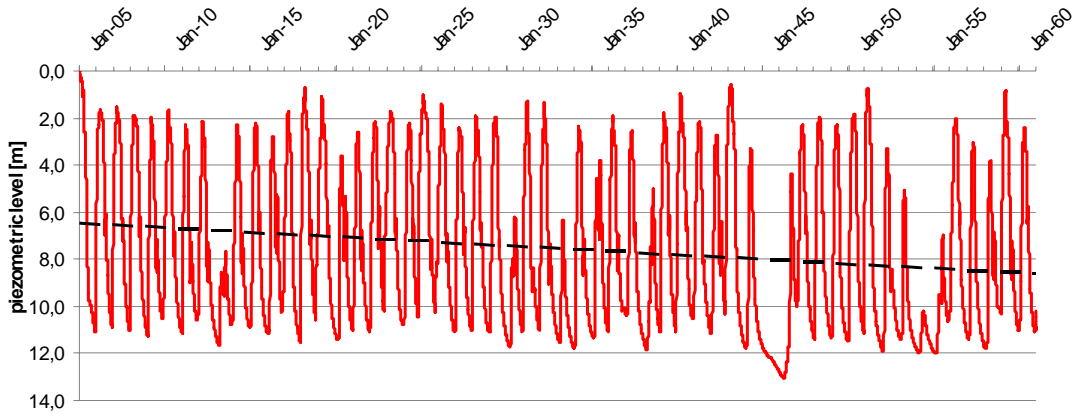


Figure 4.132 - Calculated future piezometric levels

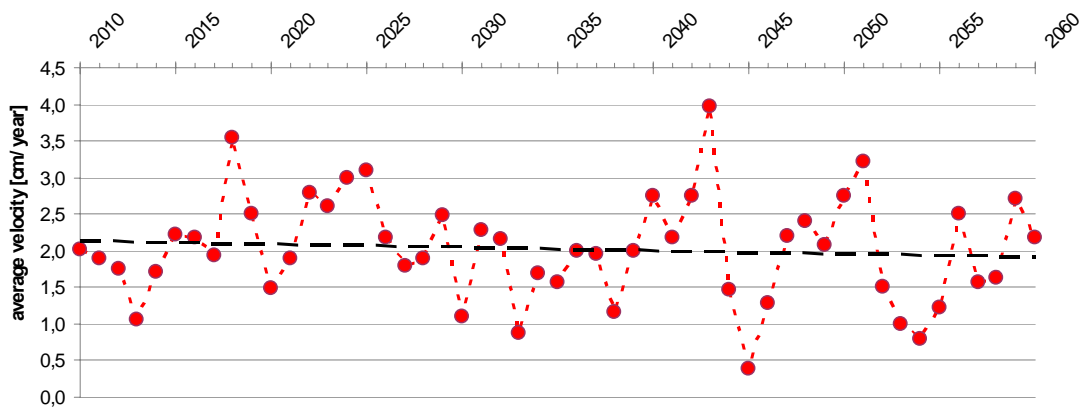


Figure 4.133 - Calculated future yearly displacement rate

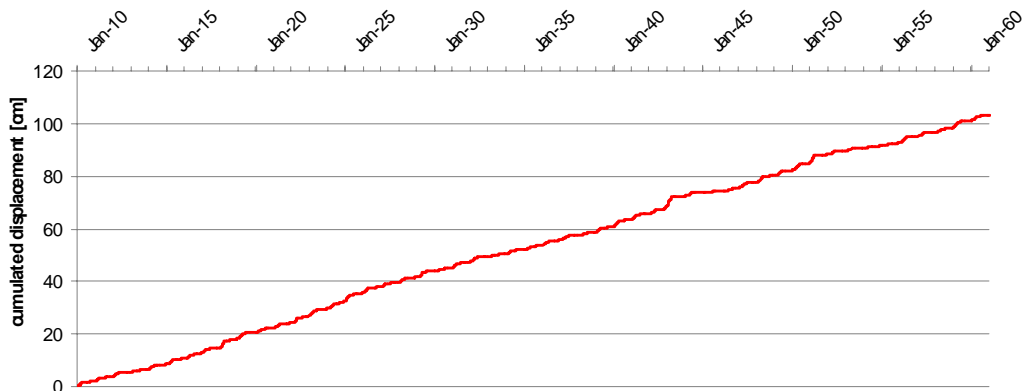


Figure 4.134 - Calculated future cumulated displacement

5. REFERENCES

- Allen, R. G.; Trezza, R. & Tasumi, M. Analytical integrated functions for daily solar radiation on slopes Agricultural and Forest Meteorology, 2006, 139, 55-73
- Alonso, E. E. & Gens, A. (2006a). Aznalcóllar dam failure. Part 1: Field observations and material properties Geotechnique, 56, No. 3, 165–183
- Alonso, E. E. & Gens, A. (2006b). Aznalcóllar dam failure. Part 3: Dynamics of the motion Geotechnique, 56, No. 3, 202–212.
- Alonso, E.E., Gens, A., Hight, D.W. (1987). Special problem soils. General Report. In: 9th European conference on soil mechanics, Dublin, vol. 3, pp 1087–1146.
- Alonso, E.E., Gens, A., Josa A. (1990). A constitutive model for partially saturated soils. Géotechnique; 40(3): 405-430.
- Anderson S.A., Sitar N. (1995). Analysis of rainfall-induced debris flows. ASCE Journal of Geotechnical Engineering, 121(7), 544-552.
- Atkinson J. (1993). The mechanics of soils and foundations. Mc Graw-Hill, 337 pp.
- AUBRY D., CHOUVET D., MODARESSI A., MODARESSI H. (1986). “Gefdyn Software – Logiciel d’Analyse du Comportement Mécanique des Sols par Eléments Finis avec Prise en Compte du Couplage Sol-Eau-Air,” Ecole Centrale Paris.
- Ayalew L., Yamagishi H., Ugawa N. (2004). Landslide susceptibility mapping using GISbased weighed linear combination, the case in Tsugawa area of Agano River, Niigata Prefecture, Japan. Landslides, 1:1 73-81.
- BAFU. 2005. Hochwasser 2005 in der Schweiz. Report by Eidgenössisches Departement für Umwelt, Verkehr, Energie und Kommunikation UVEK (in German).
- Bardenhagen, S. G. and E. M. Kober. (2004). The Generalized Interpolation Material Point Method. Computer Modeling in Engineering & Sciences. 5(6), 477-95
- Baum R.L., Coe J.A., Godt J.W., Harp E.L., Reid M.E., Savage W.Z., Schulz W.H., Brien D.L., Chleborad A.F., Mckenna J.P., Michael J.A. (2005). Regional landslide-hazard assessment for Seattle, Washington, USA. Landslides 2(4):266–279.
- Baum R.L., Savage W.Z., Godt J.W. (2002). TRIGRS - a FORTRAN program for transient rainfall infiltration and grid-based regional slope-stability analysis. U. S. Geological Survey Open-File Report 02-0424.
- Bălțeanu D. (1997) “Geomorphological hazard of Romania”, Geomorphological Hazards of Europe, C. Embelton and Christine Embelton-Hamann, Elsevier;
- Been, K. and Jefferies, M. "A state parameter for sands", Géotechnique 35, 99-112, (1985)
- Bertini T., Cugusi F., D’Elia B., Rossi Doria M. (1984). Climatic conditions and slow movements of colluvial covers in Central Italy. Proc IV Int. Symp. on Landslides, Toronto.
- Bertini, T, Cugusi, F., D’Elia, B., Rossi-Doria, M. (1986). Lenti movimenti di versante nell’Abruzzo Adriatico: caratteri e criteri di stabilizzazione. Proc. 16th Convegno Nazionale di Geotecnica, Bologna, 1, 91-100.
-

- Bhandari R.K. (1970). Mudflows in stiff fissured clays. PhD Thesis, Imperial College, University of London.
- Bjerrum L. (1967). Progressive failure in slopes of overconsolidated plastic clays. *Int. Journ. Soil Mechanics Engineering Division, ASCE, SM5*: 1-49.
- Biagioni F., Rapetti F. (2005), “Climatic features of the Muscel Valley (Buzău Subcarpathians, Romania) as from the registered data during 1961–2003”, *Geomorphology Paper*, vol. 7, pp. 107-119, Bucharest;
- Bilotta, E., Cascini, L., Foresta, V., Sorbino, G. (2005). Geotechnical characterization of pyroclastic soils involved in huge flowslides. *Geotechnical and Geological Engineering*, 23, 365 – 402.
- Bilotta, E., Pellegrino, A. & Picarelli, L. (1985). Geotechnical properties and slope stability of structurally complex clay soils. Chapter 3: Physical and mechanical properties. *Golden Jubilee Volume, AGI*: 195-214
- Biot M. A., (1941) General theory of three dimensional consolidation. *J. Appl. Phys.* 12, 155-164
- Biot, M.A. (1955). Theory of elasticity and consolidation for a porous anisotropic solid. *Journal of Applied Physics* 26 (1955) 182 – 185
- Bishop, A.W. (1959). The principle of effective stress. *Teknisk Ukeblad*; 39: 859-863.
- Bishop, A.W. (1973). The stability of tips and spoil heaps. *Quaternary Journal of Engineering Geology*, 6:335-376.
- Blight, G.E., Troncoso, J.H., Fourie, A.B. & Wolski, W. (2000). Issue in the geotechnics of mining wastes and tailings. *Int. Conf. Geotechnical and Geological Engineering GEOENG2000*: 1253-1285.
- Bolzon, G., Schrefler, B.A., Zienkiewicz, O.C. (1996). Elastoplastic soil constitutive laws generalized to partially saturated states. *Géotechnique*; 46(2): 279–289.
- Bonnard, C., L. Tacher, and M. Beniston, Prediction of landslide movements caused by climate change: Modelling the behaviour of a mean elevation large slide in the Alps and assessing its uncertainties. *Landslides and Engineered Slopes: From the Past to the Future*, Vols 1 and 2, 2008: p. 217-227.
- Brooks R.H., Corey A.T. (1964). Hydraulic properties of porous media. *Hydrology Paper No.3*, Colorado State Univ., Fort Collins, Colorado.
- Brunetti M. Maugeri M., Monti F., Nanni T. (2006). Temperature and precipitation variability in Italy in the last two centuries from homogenised instrumental time series. *International Journal of Climatology*, 26: 345-381.
- Buscarnera, G., Nova, R. (2009-a). An elastoplastic strainhardening model for soil allowing for hydraulic bonding-debonding effects. *Int. J. Numer. Anal. Meth. Geomech.*; 33:1055–1086.
- Buscarnera, G., Nova, R. (2009-b). Modelling instabilities in triaxial testing on unsaturated soil specimens. Published online on the *Int. J. Numer. Anal. Meth. Geomech.* D.O.I. 10.1002/nag.832.
-

Buscarnera, G., Nova, R. (2009-c). Modelling the onset of instability in oedometric tests on unsaturated bonded soils. Proc. 1st COMGEO, S. Pietruszczak, G.N. Pande, C. Tamagnini & R. Wan eds., 226-23.

Cai F., Ugai K. (2004). Numerical analysis of rainfall effects on slope stability. *International Journal of Geomechanics*, 4(2): 69–78.

Caine N. (1980). The rainfall intensity-duration control of shallow landslides and debris-flows. *Geografiska Annaler* 62a(1-2): 23-27

Calabresi, G., Manfredini, G. (1973). Shear strength characteristics of the jointed clay of S. Barbara. *Géotechnique*, 23, pp. 233-244

Casagrande, A. 1971. On liquefaction phenomenon. *Géotechnique* 21 (3), 197– 202.

Casagrande, A. Boston, J. 1936. Characteristics of Cohesionless Soils Affecting the Stability of Slopes and Earth Fills. *Soc. of Civ. Engrs.*, 23(1), 13-32.

Cascini E., Cascini L., Gullà G. (1992b). A back-analysis based on piezometers response. In *Proceedings of the 6th International Symposium on Landslides, Christchurch, New Zealand, 10–14 February 1992*. Edited by D.H. Bell. A.A. Balkema, Rotterdam, The Netherlands. Vol. 2, pp. 1123–1128.

Cascini L. (1986). Movimenti discontinui di una coltre di detrito della Sila Grande. In *Proceedings, 16th Convegno Nazionale di Geotecnica, Bologna, Italy, November 1986*. Vol. 1, pp. 259–262. [In Italian.]

Cascini L. (2004). The flowslides of May 1998 in the Campania region, Italy: the scientific emergency management. *Italian Geotechnical Journal*, 2: 11-44.

Cascini L. (2008). Applicability of landslide susceptibility and hazard zoning at different scales. *Engineering Geology*, 102: 164-177.

Cascini L., Critelli S., Di Nocera S., Gullà G. (1992a). A methodological approach to landslide hazard assessment: a case history. In *Proceedings of the 6th International Symposium on Landslides, Christchurch, New Zealand, 10–14 February 1992*. Edited by D.H. Bell. A.A. Balkema, Rotterdam, The Netherlands. Vol. 2, pp. 899–904.

Cascini L., Critelli S., Di Nocera S., Gullà G. (1994b). Weathering and landsliding in Sila Grande Massif gneiss (Northern Calabria, Italy). In *Proceedings of the 7th International IAEG Congress, Lisbon, Portugal, 5–9 September 1994*. Edited by R. Oliveira, L.F. Rodrigues, A.G. Coelho, and A.P. Cunha. A.A. Balkema, Rotterdam, The Netherlands. pp. 1613–1622.

Cascini L., Critelli S., Di Nocera S., Gullà G., Matano F. (1994a). Grado di alterazione e franosità negli gneiss del massiccio silano: l'area di S. Pietro in Guarano. *Geologia Applicata ed Idrogeologia*, 27: 49–76. [In Italian.]

Cascini L., Cuomo S., Ferlisi S., Sorbino G. (2009). Detection of mechanisms for destructive landslides in Campania region – southern Italy. *First Italian Workshop on landslides (IWL 2009)*, 8-10 June 2009, Napoli, Italia. L. Picarelli, P. Tommasi, G. Urciuoli, P. Versace (eds.), ISBN 978-88-89972-12-0, pp. 43 – 51.

Cascini L., Cuomo S., Guida D. (2008a). Typical source areas of May 1998 flow-like mass movements in the Campania region, Southern Italy. *Engineering Geology*, 96: 107-125.

Cascini L., Cuomo S., Pastor M. (2008b). The role played by mountain tracks on rainfall-induced shallow landslides: a case study. Proceedings of the iEMSs Fourth Biennial Meeting: International Congress on Environmental Modelling and Software (iEMSs 2008), 7-10 July 2008, Barcelona, Spain. M. Sánchez-Marrè, J. Béjar, J. Comas, A.E. Rizzoli, G. Guariso (eds.), Published by the International Environmental Modelling and Software Society (iEMSs), Manno, Switzerland. ISBN: 978-84-7653-074-0, pp. 1484-1491.

Cascini L., Cuomo S., Pastor M., Fernández-Merodo J.A. (2008c). Geomechanical modelling of triggering mechanisms for rainfall-induced triangular shallow landslides of the flow-type. Proceedings of the iEMSs Fourth Biennial Meeting: International Congress on Environmental Modelling and Software (iEMSs 2008, 7-10 July 2008, Barcelona, Spain. M. Sánchez-Marrè, J. Béjar, J. Comas, A.E. Rizzoli, G. Guariso (eds.). International Environmental Modelling and Software Society (iEMSs), Manno, Switzerland. ISBN: 978-84-7653-074-0, pp. 1516-1523

Cascini L., Cuomo S., Pastor M., Sorbino G. (2010). Modelling of rainfall-induced shallow landslides of the flow-type. ASCE's Journal of Geotechnical and Geoenvironmental Engineering, 136(1), 85-98 (doi:10.1061/(ASCE)GT.1943-5606.0000182)

Cascini L., Cuomo S., Sorbino, G. (2005). Flow-like mass movements in pyroclastic soils: remarks on the modelling of triggering mechanisms. Italian Geotechnical Journal, 4, 11-31.

Cascini L., Ferlisi S. (2003). Occurrence and consequences of flowslides: a case study. In: L. Picarelli (ed.) Proc. of the International Conference on Fast Slope Movements – Prediction and Prevention for Risk Mitigation, 11-13 May 2003 Napoli, Italy. Bologna: Pàtron Editore, Vol. I, 85-92.

Cascini, L., Guida, D., Nocera, N., Romanzi, G., Sorbino, G. 2000. A preliminary model for the landslides of May 1998 in Campania Region. In: Proc 2nd Int. Symposium on Geotechnics of Hard Soil-Soft Rock, Napoli. Balkema, 3, 1623 – 1649.

Cascini, L., Guida, D., Romanzi, G., Nocera, N., Sorbino, G. (2000): A preliminary model for the landslides of May 1998 in Campania Region. In: Evangelista, A., Picarelli, L. (eds.), Proc. 2nd Int. Symp. on The Geotechnics of Hard Soils-Soft Rocks, Napoli, 3, 1623–1649.

Cascini L., Gullà G. (1988). Sulle acque sotterranee di una coltre di detrito in frana. In Proceedings of the Symposium “Cartografia e Monitoraggio dei Movimenti Franosi”, Bologna, Italy, 10–11 November 1988. Vol. 1, pp. 85–95. [In Italian.]

Cascini L., Gullà, G. (1993). Caratterizzazione fisico-meccanica dei terreni prodotti dall’alterazione di rocce gneissiche. Rivista Italiana di Geotecnica 27: 125–147. [In Italian.]

Cascini L., Gullà G., Sorbino, G. (1995). Modellazione delle acque sotterranee di una coltre di detrito in frana: risultati preliminari. Rivista Italiana di Geotecnica, 3: 201–223. [In Italian.]

Cascini L., Gullà G., Sorbino G. (2006). Groundwater modelling of a weathered gneissic cover. Canadian Geotechnical Journal, (43): 1153-1166.

Cascini L., Versace P. (1988). Relationship between rainfall and landslides in a gneissic cover. In Proceedings of the 5th International Symposium on Landslides, Lausanne, Switzerland, 10–15 July 1988. Edited by C. Bonnard. A.A. Balkema, Rotterdam, The Netherlands. Vol. 1, pp. 565–570.

- Casini, F., Jommi, C., Springman, S.M. 2010 .A laboratory investigation on an undisturbed silty sand from a slope prone to landsliding. *Granular Matter*, 12, DOI: 10.1007/s10035-010-0182-y.
- Castro, G. (1969) Liquefaction of sands, Ph.D. Thesis, Harvard Univ., Harvard Soil Mech. Series no.81 (1969)
- Castro, G., Poulos, S.J. 1977. Factors affecting liquefaction and cyclic mobility. *Journal of the Geotechnical Engineering Division, ASCE* 103, 501–516.
- Chandler, R.J. (1984). Recent european experience of landslides in over-consolidated clays and soft rocks. *Proceed. 4th Int. Symp. on Landslides, Toronto*, 1: 61-81
- Charlier R., 1987. Approche unifiée de quelques problèmes non linéaires de mécanique des milieux continus par la méthode des éléments finis. Doctoral thesis, Université de Liège.
- Chiappone A. (1999). Gli scivolamenti planari delle Langhe: uno studio di tipo meccanico e mineralogico per la definizione del modello geotecnico, PhD Thesis, Politecnico di Torino
- Cho S.E., Lee S.R. (2001). Instability of unsaturated soil slopes due to infiltration. *Computers and Geotechnics*, 28, 185-208.
- Chu J., Leroueil S., Leong W. K. (2003). Unstable behaviour of sand and its implications for slope instability. *Canadian Geotechnical Journal*, 40, 873-885.
- Chung C.J., Fabbri A.G. (2003). Validation of Spatial Prediction Models for Landslide Hazard Mapping. *Natural Hazards*, 30:3 451-472.
- Coe J.A., Godt J.W. (2001). Debris Flows Triggered by the El Niño Rainstorm of Feb 2–3, 1998, Walpert Ridge and Vicinity, Alameda County, California. US Geological Survey Miscellaneous Field Studies Map MF-2384. Available via: <http://pubs.usgs.gov/mf/2002/mf-2384/>.
- Coe J.A., Godt J.W., Tachker P. (2004). Map showing recent (1997–98 El Nino) and historical landslides, Crow Creek and vicinity, Alameda and Contra Costa Counties, California. US Geological Survey Scientific Investigations Map 2859. Available via: <http://pubs.usgs.gov/sim/2004/2859/>.
- Coetsee, C. J., Vermeer, P. A & Basson A. H (2005). The Modelling of Anchors using the Material Point Method. *International Journal for Numerical and Analytical Methods in Geomechanics*. 29(9), 879-895.
- Coetsee, C. J., Basson A. H., & Vermeer P. A. (2007) Discrete and Continuum Modelling of Excavator Bucket Filling. *Journal of Terramechanics*. 44(2), 177-186.
- Collin F., 2003. Couplages thermo-hydro-mécaniques dans les sols et les roches tendres partiellement saturés. Doctoral thesis, Université de Liège
- Collins, B.D. and D. Znidarcic, Stability analyses of rainfall induced landslides. *Journal of Geotechnical and Geoenvironmental Engineering*, 2004. 130(4): p. 362-372.
- COMMEND S., GEISER F., TACHER L. (2004). 3D numerical modeling of a landslide in Switzerland. In *Proceedings of the International Symposium on Numerical Models in Geomechanics NUMOG IX*, Ottawa, pages 595-601.
-

- Corominas J., Copons R., Vilaplana J.M., Altimir J., Amigó J. (2003). Integrated landslide susceptibility and hazard assessment in the Principality of Andorra. *Natural Hazards* 30, pp. 421 – 435.
- Corominas J., Moya J., Ledesma A., Lloret A., Gili J.A. (2005). Prediction of ground displacements and velocities from groundwater level changes at the Vallcebre landslide (Eastern Pyrenees, Spain). *Landslides*, 2: 83-96.
- Coulomb, C.A.: *Essai sur une application des règles de maximis et minimis à quelques problèmes de statique relatifs à l'architecture*. Mémoires de Mathématique et de Physique, présentés à l'Académie Royale des Sciences par Divers Savants et lus dans ses Assemblées, 7, Paris, France, 343-382 (1773)
- Coussy, O. *Mechanics of Porous Media*. John Wiley and Sons, Chichester (1995).
- Crozier M. J. (1986) “Landslides: causes, consequences and environment”, Croom Helm, London;
- Cruden D.M., Varnes D.J. (1996). *Landslide Types and Processes*. *Landslides Investigation and Mitigation* (Turner A.K., Schuster R.L. eds). Transp. Res. Board Spec. Rep. 247, National Research Council, National Academy Press, Washington D.C., pp. 36 – 75.
- Cui, Y.J., Delage, P. (1996). Yielding, plastic behaviour and critical state of a collapsible unsaturated silty soil. *Géotechnique*; 46(2): 465-477.
- Cuomo S. (2006). *Geomechanical modelling of triggering mechanisms for flow-like mass movements in pyroclastic soils*. PhD Thesis, University of Salerno, Italy, 274 pp.
- Dai F.C., Lee C.F., Wang S.J. (1999). Analysis of slide-debris flows on Lantau Island, Hong Kong. *Engineering Geology*, 51: 279-290.
- Damiano E. and Olivares L., 2010. The role of infiltration processes in steep slope stability of pyroclastic granular soils: laboratory and numerical investigation. *Natural Hazards*, 52, pp. 329–350.
- Darve F, Laouafa F. *Instabilities in granular materials and application to landslides*. *Mechanics of Cohesive-Frictional Materials* 2000; 5(8): 627-652.
- Darve, F. Laouafa, F. *Modelling of slope failure by a material instability mechanism*, *Comput. Geotech.* 29 (2001) 301–325
- Darve, F., *Liquefaction phenomenon of granular materials and constitutive instability*, *Int. J. Eng. Comp.* 7, pp 5-28 (1995)
- Dawson, R.F., Morgenstern, N.R. & Stokes, A.W. (1998). Liquefaction flowslides in Rocky Mountain coal mine waste dumps. *Canadian Geotechnical Journal*, 35:328-343.
- de Boer, R. *Theory of porous media*. Springer-Verlag, Berlin (2000)
- de Riso, R., Budetta, P., Calcaterra, D., Santo, A. (1999): *Le colate rapide in terreni piroclastici del territorio campano*. Proc. Conf. “Previsione e Prevenzione di Movimenti Franosi Rapidi”, Trento, 133–150.
- de Riso R., Budetta P., Calcaterra D., Santo A. (2005) – *Riflessioni sul comportamento delle colate rapide non incanalate della Campania, alla luce delle conoscenze pregresse*. *Atti del*
-

Convegno Nazionale “La mitigazione del rischio da colate di fango” a Sarno e negli altri Comuni colpiti dagli eventi del maggio 1998. Napoli, 2 e 3 Maggio 2005 - Sarno 4 e 5 Maggio 2005.

de Riso R, Budetta P, Calcaterra D, Santo A (2007) Riflessioni sul comportamento delle colate rapide non incanalate della Campania, alla luce delle conoscenze pregresse. Proc National Conf on La Mitigazione del Rischio da Colate di Fango, Napoli, May, 2- 3, 2005, pp 81-92

de Vries D.A. (1963). Thermal properties of soils. p. 210–235. In W.R. Van Wijk (ed.) Physics of plant environment. North-Holland Publ. Co., Amsterdam.

D’Elia B., Picarelli L., Leroueil S., Vaunat J. (1998). Geotechnical characterization of slope movements in structurally complex clay soils and stiff jointed clays. *Rivista Italiana di Geotecnica*, 32, 3: 5-47.

D’Elia B., Tancredi G. (1979). Colate permanenti e temporanee: confronto fra due casi. *Geologia Applicata e Idrogeologia*, 1, 23-39.

di Prisco, C., Matiotti, R., Nova, R. (1995). Theoretical investigation of undrained stability of shallow submerged slopes. *Géotechnique* 45, pp. 479–496.

Di Rosario F. (2008). Comportamento di grandi frane in argilla. PhD Thesis, Università degli studi di Roma La Sapienza.

Dikau, R., Cavallin, A., Jager, S.: Databases and GIS for landslide research in Europe. *Geomorphology* 15(3-4), 227-239(1996)

Dikau R., Schrott L. (1997) “The temporal stability and activity in Europe with respect to climatic change” (Teslec). *Geograf. Fisic. e Dinam. Quatern.*, sup. III, tom. 1, Torino.

Dragotă C., Micu M., Micu D. (2008) “The relevance of pluvial regime for landslides genesis and evolution. Case study: Muscel Basin (Buzău Subcarpathians), Romania”, *Present Environment and Sustainable Development*, No. 2, Geneva

Eckersley D. (1990). Instrumented laboratory flowslides. *Géotechnique*, 40, 489-502.

Edlefsen, N.E, Anderson, A.B.C., 1943. Thermodynamics of soil moisture. *Hilgardia* 15:2, pp. 31-298.

Eggleston, K.O., Israelsen, E. K. & Riley, J. P. (1971) Hybrid Computer simulation of the accumulation and melt processes in a snowpack. Rep. PRWG65-1, Utah State Univ., Logan Utah.

Espinoza R.D., Repetto P.C., Muhunthan B. (1992). General framework for stability analysis of slopes. *Geotechnique* 42, n. 4, 603-615.

Esu F. (1977). Behaviour of slopes in structurally complex formations. Proc. Int. Symp. on The Geotechnics of Structurally Complex Formations, Capri, 2, 292-304.

Fell R., Corominas J., Bonnard C., Cascini L., Leroi E., Savage W.Z., On behalf of the JTC-1 Joint Technical Committee on Landslides, Engineered Slopes (2008a). Guidelines for landslide susceptibility, hazard and risk zoning for land use planning. *Engineering Geology* 102(3–4):85–98.

Fernandez Merodo J. A., 2001. Une approche a la modelisation des glissements et des effondrements de terrains: Initiation et propagation, Thesis, Ecole Centrale Paris.

Fernandez-Merodo J.A., Herrera G., Mira P., Mulas J., Pastor M., Noferini L., Mecatti D., Luzi G., 2008. Modelling the Portalet landslide mobility (Formigal, Spain). iEMSs 2008: International Congress on Environmental Modelling and Software Integrating Sciences and Information Technology for Environmental Assessment and Decision Making, 4th Biennial Meeting of iEMSs, 2008.

Fernandez-Merodo J.A., Pastor M., Mira P., Tonni L., Herreros M.I., Gonzalez E., Tamagnini R., 2004. Modelling of diffuse failure mechanisms of catastrophic landslides. Computer Methods in Applied Mechanics And Engineering, n° 193, p. 2911-2939.

Fernandez-Merodo J.A., Tamagnini R., Pastor M., 2005. Modelling damage with Generalized Plasticity. Italian Geotechnical Journal, n° 4, p. 32-42.

Fiorillo F., Wilson R.C. (2004). Rainfall induced debris flows in pyroclastic deposits, Campania (southern Italy). Engineering Geology, 75:263–289.

Fisher, R.A. "On the capillary forces in an ideal soil; correction of formulas by W.B. Haines", Journal of Agricultural Science, 16, 492-505, (1926)

Fourie A.B., Rowe D., Blight G.E. (1999). The effect of infiltration on the stability of the slopes of a dry ash dump. Géotechnique, 49(1): 1–13.

François B., Laloui, L., 2008. ACMEG-TS: A constitutive model for unsaturated soils under non-isothermal conditions, International Journal of Numerical and Analytical Methods in Geomechanics, vol. 32, p. 1955-1988

Frattini P., Crosta G.B., Fusi N., Dal Negro P. (2004). Shallow landslides in pyroclastic soils: a distributed modelling approach for hazard assessment. Engineering Geology, 73, 277 – 295.

Fredlund D.G. (1979). Second Canadian Geotechnical Colloquium: appropriate concepts and technology for unsaturated soils. Canadian Geotechnical Journal, 16: 121-139.

Fredlund D.G. (1984). Analytical methods for slope stability analysis. Proc. 4th Int. Symp. Landslides Toronto 1, pag. 229-250.

Fredlund, D.G. and H. Rahardjo, Soil Mechanics for Unsaturated Soils. 1993, New York: John Wiley and Sons, INC.

Gallipoli, D., Gens, A.; Sharma, R. & Vaunat, J. . "An elastoplastic model for unsaturated soil incorporating the effects of suction and degree of saturation on mechanical behaviour", Géotechnique, 53(1), 123-135 (2003)

Gardner W.R. (1958). Some steady-state solutions of the unsaturated moisture flow equation with application to evaporation from a water table. Soil Science 85:228–232.

Garnier J, Gaudin C, Springman SM, Culligan PJ, Goodings D, Konig D, Kutter B, Phillips R, Randolph R, Thorel L. 2007. Catalogue of scaling laws and similitude questions in geotechnical centrifuge modelling. Int J Phys Model Geotechn 8(3): 1–23

Gasmo J.M., Rahardjo H., Leong E.C. (2000). Infiltration effects on stability of a residual soil slope. Computers and Geotechnics, 26: 145–165

- Gens, A., Alonso, E.E. (1992). A framework for the behaviour of unsaturated expansive clays. *Can. Geotech. J.*; 29: 1013–1032.
- Gens A. & Alonso E. E. (2006). Aznalcollar Dam Failure. Part 2: Stability Conditions and Failure Mechanism. *Geotechnique*. 56 No.3, pp 185-201.
- Gens, A., Nova, R. (1993). Conceptual bases for a constitutive model for bonded soils and weak rocks, *Hard Soils-Soft Rocks*, Athens, Greece, Anagnostopoulos and others, Balkema, Rotterdam, 485-494.
- GEO-SLOPE International Ltd. (2004). Seepage modelling with SEEP/W, user's guide version 6.16. GEO-SLOPE International Ltd., Calgary, Alta.
- Geo-Slope International Ltd., 2008. Slope/W, Version 2007, Limit Equilibrium Code.
- Geotechnical Engineering Office. 1999. Slope No. 11NW-B/FR61, Beacon Hill Radar Airport Station, Final Laboratory Testing Report, Geotechnical Engineering Office, Civil Engineering Department, The Government of the HKSAR
- Glade, T. (1997) "Spatial and temporal occurrence of rainfall-triggered landslides in New Zealand", *Geogr. Fisic. e Dinami. Quatern.*, sup. III, tom. 1, Torino;
- Godt J.W., Baum R.L., Savage W.Z., Salciarini D., Schulz W.H., Harp E.L. (2008). Transient deterministic shallow landslide modeling: requirements for susceptibility and hazard assessments in a GIS framework. *Engineering Geology*, 102:214–226.
- Goodings, D.J. 1984. Relationships for modelling water effects in geotechnical models. *Proceedings. Application of Centrifuge Modelling to Geotechnical Design*. University of Manchester, 1-23
- Govi M., Mortara G., Sorzana P.F. (1985). Eventi idrologici e frane, *Geol. Appl. e Idrog.*, vol. XX, parte 2, pp. 359-375.
- Govi M., Sorzana P. F., Trepeano D. (1980) "Landslide mapping as evidence of extreme regional events", *Stud. geomorph. Carpatho-Balcanica*, vol. XV, Krakov;
- Govi M., Sorzana P.F. (1982). Frane di scivolamento nelle Langhe cuneesi febbraio-marzo 1972, febbraio 1974. *Bollettino della Associazione Mineraria Subalpina*, Anno XIX, n 1-2, marzo-giugno 1982.
- Gray, D. & Male, D. (ed.) (1981) *Handbook of Snow Principles, Processes, Management & Use*. Pergamon Press
- Guadagno F.M., Revellino P. (2005). Debris avalanches and debris flows of the Campania Region (southern Italy). In: Jakob Hungr M., Hungr O. (eds) *Debris-flow hazard and related phenomena*. Springer, Berlin, pp 489–518.
- Gullà G., Matano F. (1997). Surveys of weathering profile on gneiss cutslopes in Northern Calabria, Italy. In *Engineering Geology and the Environment: Proceedings of an International Symposium of the IAEG*, Athens, Greece, 23–27 June 1997. Edited by P.G. Marinos, G.C. Koukis, G.C. Tsiambaos, and G.C. Stournaras. A.A. Balkema, Rotterdam, The Netherlands. pp. 133–138.
-

- Gullà G., Sorbino G. (1994). Considerazioni sulla permeabilità satura dei materiali di alterazione di origine gneissica. In Proceedings of the Symposium “Il ruolo dei fluidi nei problemi di ingegneria geotecnica” Mondovì, Italy. Vol. 1, pp. 85–99. [In Italian.]
- Gullà G., Sorbino G. (1996). Soil suction measurements in a landslide involving weathered gneiss. In Proceedings of the 7th International Symposium on Landslides, Trondheim, Norway, 17–21 June 1996. Edited by K. Senneset. A.A. Balkema, Rotterdam, The Netherlands. pp. 749–754.
- Guzzetti F., Carrara A., Cardinali M., Reichenbach P. (1999). Landslide hazard evaluation: an aid to a sustainable development. *Geomorphology*, 31: 181-216.
- Guzzetti F, Peruccacci S, Rossi M, Stark CP (2007). Rainfall threshold for the initiation of landslides in central and southern Europe. *Meteorology and Atmospheric Physics* 98: 239-267.
- Guzzetti F, Peruccacci S, Rossi M, Stark CP (2008). The rainfall intensity-duration control of shallow landslides and debris flows: an update. *Landslides* 5(1): 3-17.
- Haines, W.B. (1925). "Studies in the physical properties of soils. A note on the cohesion developed by capillary forces in an ideal soil", *Journal of Agricultural Science*, 15, 529-535
- Harstveit, K. (1984) Snowmelt modelling and energy exchange between the atmosphere and a melting snow cover. University of Bergen, Geophys. Inst. Sci. Report 4.
- Hestnes, E., Bakkehøi, S., Sandersen, F., & Andresen L. (1987) Meteorological significance to slushflow release. NGI-Report 582000-5
- Hicher, P.Y., Chang C.S. (2007). A microstructural elastoplastic model for unsaturated granular materials. *Int. J. Solids and Structures*, 44, 2304-2323.
- Hird, H.H., Hassona, F.A.K. 1990. Some factors affecting the liquefaction and flow of saturated sands in laboratory tests. *Engineering Geology* 28, 149– 170.
- Hohensinn F. (1979). Bodenmechanische Analyse von Geländebrüchen bei Murenbildung in kristallinen Verwitterungsböden. *Mitt. Inst. Bodenmech. Felsmech. Grundbau*, H. 2.
- Houlsby, G.T. (1997). The work input to an unsaturated granular material. *Géotechnique*; 47(1): 193–196.
- HUJEU J.-C. (1985). “Une Loi de Comportement pour le Chargement Cyclique des Sols,” *Génie Parasismique*, Presse ENPC, pp. 287-302.
- Hung O., Evans S.G., Bovis M.J., Hutchinson J.N. (2001). A review of the classification of landslides of the flow type. *Environ. Eng. Geosci.* 7(3):221–238.
- Hutchinson J.N. (1970). A coastal mudflow on the London Clay cliffs at Beltinge, Kent. *Géotechnique*, 20, 412-438
- Hutchinson, J.N. „A sliding-consolidation model for flow slides, *Can.Geotech.J.*, 23 115-126 (1986)
- Hutchinson J.N. (1995). Keynote paper: Landslide hazard assessment. In: Bell (ed.), *Landslides*, Balkema, Rotterdam, 1805-1841.
-

- Hutchinson J.N. (2004). Review of flow-like movements in granular and fine-grained materials. In L. Picarelli (ed), Proc. Int. Work on Occurrence and Mechanisms of Flow-Like Landslides in Earthfills and Natural Slopes, 14-16 May 2003, Sorrento: 3-16. Patron, Bologna
- Hutchinson, J.N., Bhandari, R. 1971. Undrained loading: a fundamental mechanism of mudflows and other mass movements. *Géotechnique* 21: 353-358
- Hutchinson J.N., Prior D.B., Stephens N. (1974). Potential dangerous surges in an Antrim mudslide. *Quarterly Journal of Engineering Geology*, 7: 363-376.
- Iaccarino, G., Peduto, F., Pellegrino, A, Picarelli, L. 1995. Principal features of earthflows in part of Southern Apennine. Proc. 11th Europ. Conf. on Soil Mechanics and Foundation Engineering, Copenhagen, Danish Geotechnical Society, 4: 354-359.
- Imposimato, S., Nova, R. (1998). An investigation on the uniqueness of the incremental response of elastoplastic models for virgin sand. *Mech. Cohes. Frict. Mater.* **3**, pp. 65–87.
- Intergovernmental Panel on Climate Change, 2007. IPCC Fourth Assessment Report, www.ipcc.ch
- Ishihara, K. 1993. Liquefaction and flow failure during earthquakes. *Géotechnique* 43 (3), 349– 451.
- Itasca Ltd., 2008. FLAC 2D, Version 6.0, Finite Difference Code and User Manual.
- Iverson, R.M. “Differential equations governing slip-induced pore pressure fluctuations in a water-saturated granular medium”, *Mathematical Geology* 25 (8), 1027–1048 (1993)
- Iverson, R.M. 1997. The physics of debris flows. *Reviews of Geophysics* 35 (3), 245– 296.
- Iverson R.M. (2000). Landslide triggering by rain infiltration. *Water Resour. Res.* 36(7):1897–1910.
- Iverson, R.M., Denlinger, R.P. (2001). Flow of variably fluidized granular masses across three dimensional terrain. 1. Coulomb mixture theory”, *J.Geophys.Res.* 106, N0.B1, pp. 537 – 552
- Iverson, R.M. and LaHusen, R.G. “Dynamic pore-pressure fluctuations in rapidly shearing granular materials”, *Science* 246, 796–799 (1989)
- Iverson RM, Reid ME. 1992. Gravity-driven groundwater flow and slope failure potential: 1. Elastic effective-stress model. *Water Resour. Res.* 28:925–38
- Iverson, R.M., Reid, M.E., Iverson, N.R., LaHusen, R.G., Logan, M., Mann, J.E., Brien, D.L. 2000. Acute sensitivity of landslide rates to initial soil porosity. *Science* 290, 513– 516.
- Iverson, R.M., Reid, M.E., LaHusen, R.G. 1997. Debris-flow mobilization from landslides. *Annual Review of Earth and Planetary Sciences* 25, 85–138.
- Johansen O. (1975). Thermal conductivity of soils. Ph.D. diss. Norwegian Univ. of Science and Technol., Trondheim (CRREL draft transl. 637, 1977).
- Johansson, J. & K. Konagai (2007). Fault Induced Permanent Ground Deformations: Experimental Verification of Wet and Dry Soil, Numerical Findings' Relation to Field Observations of Tunnel Damage and Implications for Design. *Soil Dynamics and Earthquake Engineering.* 27(10), 938-956.
-

- Johnson K.A., Sitar N. (1990). Hydrologic conditions leading to debris-flow initiation. *Can. Geotech. J.*, **27**, 789-801.
- Jommi, C. (2000). Remarks on the constitutive modelling of unsaturated soils. *Experimental Evidence and Theoretical Approaches in Unsaturated Soils; Proceedings of the International Workshop on Unsaturated soils, Trento*; 139–153.
- Jommi, C., di Prisco, C. (1994). Un semplice approccio teorico per la modellazione del comportamento meccanico dei terreni granulari parzialmente saturi. *Conference Il Ruolo dei Fluidi nei Problemi di Ingegneria Geotecnica, Mondovì*; 167–188.
- Kenney T.C., Lau K.C. (1977). Temporal changes of groundwater pressure in a natural slope of non fissured clay. *Canadian Geotechnical Journal*, **21**, 138-146
- Kimura, T., Takemura, J., Suemasa, N., and Hiro-oka, A. 1991. “Failure of fills due to rainfall.” *Centrifuge 91*, H.-Y. Ko, ed., Balkema, Rotterdam, The Netherlands, 509–516.
- King, J. C. Pomeroy, J. W. Gray, D. M. Gray, Fierz, C. , Föhn, P. M. B. Harding R. J., Jordan, R. E. Martin, E. & Plüss, C. (2008) Snow-atmosphere energy and mass balance. In Armstrong, R. L. & Brun, E. (ed.) *Snow and Climate Physical Processes, Surface Energy Exchange and Modeling* Cambridge University Press.
- Knill JL, Lumb P, Mackey S, Mello VFB, Morgenstern NR, Richards BG. 1976. Report of the Independent Review Panel on Fill Slopes, Government of Hong Kong
- Konagai K. & Johanson J.. Two dimensional Lagrangian Particle Finite Difference Method for modeling large soil deformations. (2001). *Structural Eng./ Earthquake Eng., JSCE*, **18**, No. 2, 105s-110s.
- Konagai, K., Johansson J. & Itoh H. (2004) Pseudo-three dimensional lagrangian particle finite difference method for modeling earthquake induced soil flows, 13th World Conference on Earthquake Engineering. No 547
- Krahn J. (2004). *Vadose Zone Modeling with VADOSE /W – An Engineering Methodology*. GEO-SLOPE International Ltd., Calgary, Canada
- Kramer, K.L. 1988. Triggering of liquefaction flow slides in coastal soil deposits. *Engineering Geology* **26**, 17– 31.
- Kubota, T. 1997. An experimental study on mechanism of liquified landslides. MS thesis, Nagoya university, Japan.
- Lagioia R. and Nova R. “An experimental and theoretical study of the behaviour of a calcarenite in triaxial compression”. *Geotechnique* **45** (4): 633-648 (1995)
- Laloui L., Nuth M. (2009). On the use of the generalised effective stress in the constitutive modelling of unsaturated soils. *Computer and Geotechnics*, Vol. **36** (1-2): 20-23.
- Lam L., Fredlund D.G., Barbour S.L. (1987). Transient seepage model for saturated–unsaturated soil systems: a geotechnical engineering approach. *Canadian Geotechnical Journal*, **24**(4): 565–580.
- Lampitiello S. (2004). Resistenza non drenata e suscettività alla liquefazione di ceneri vulcaniche della Regione Campania. PhD Thesis, Seconda Università di Napoli.
-

Latelin, O., Haemmig, C., Raetzo, H. & Bonnard, C. 2005. Landslide risk management in Switzerland. *Landslides* 2:313-320.

Leach B., Herbert R. (1982). The genesis of a numerical model for the study of hydrogeology of a steep hillside in Hong Kong. *Quarterly Journal of Engineering Geology*, London, 15: 243–259.

Lee S., Chwae U., Min K. (2002). Landslide susceptibility mapping by correlation between topography and geological structure: the Janghung area, Korea. *Geomorphology*, 46: 149-162.

Leroueil S. (2001). Natural slopes and cuts: movements and failure mechanisms. *Géotechnique*, 51: 197–243.

Leroueil S., Vaunat J., Picarelli L., Locat J., Lee H., Faure R. (1996) “Geotechnical Characterization of Slope Movements”, *Proceedings of the International Symposium on Landslides, Trondheim*, , 22 pp;

Lewis, R.W. and Schrefler, B.A., *The Finite Element Method in the Deformation and Consolidation of Porous Media*, J. Wiley, Chichester, (1987)

Li, X.L. "Modelling of dilatative shear failure", *Journal of Geotechnical and Geoenvironmental Engineering*, 123, 609-616, (1977).

Li, X.L. and Dafalias, Y.F "Dilatancy for cohesionless soils", *Géotechnique* 50 449-460, (2000).

Li, X., Han X., and M. Pastor (2003). An Iterative Stabilized Fractional Step Algorithm for Finite Element Analysis in Saturated Soil Dynamics. *Computer Methods in Applied Mechanics and Engineering*. 192(35), 3845-59.

Lim T.T., Rahardjo H., Chang M.F., Fredlund D.G. (1996). Effect of rainfall on matric suctions in a residual soil slope. *Canadian Geotechnical Journal*, 33(4): 618–628

Lourenço, S. D. N., Sassa, K. and Fukuoka H. 2006, Failure process and hydrologic response of a two layer physical model: Implications for rainfall-induced landslides, *Geomorphology*, 73, 115–130.

Maâtouk, A. Leroueil, S. and LaRoche P., "Yielding and critical state of a collapsible saturated silty soil", *Geotechnique* 45, 3, pp 465-477, (1995)

Macfarlane, D.F., Observations and predictions of the behaviour of large, slow-moving landslides in schist, Clyde Dam reservoir, New Zealand. *Engineering Geology*, 2009. 109(1-2): p. 5-15.

Major, J.J., Iverson, R.M. 1999. Debris-flow deposition: effects of pore-fluid pressure and friction concentrated at flow margins. *Geological Society of America Bulletin* 111 (10), 1424– 1434.

Mandolini A., Urciuoli G. (1999) - Previsione dell'evoluzione cinematica dei pendii mediante un procedimento di simulazione statistica. *Rivista Italiana di Geotecnica*, Anno XXXIII,1, 35-42.

Manzanal, D. (2008). Constitutive model based on Generalized Plasticity incorporating state parameter for saturated and unsaturated sand (in Spanish). PhD Thesis School of Civil Engineering, Polytechnic University of Madrid.

- Melinda, F., H. Rahardjo, K.K. Han, and E.C. Leong, Shear strength of compacted soil under infiltration condition. *Journal of Geotechnical and Geoenvironmental Engineering*, 2004. 130(8): p. 807-817.
- Metzger, D. R. 2003. Adaptive Damping for Dynamic Relaxation Problems with Non-Monotonic Spectral Response. *International Journal for Numerical Methods in Engineering*. 56(1), 57-80.
- Mira P. (2002). Análisis por Elementos Finitos de Problemas de Rotura en Geomateriales. PhD Thesis, Escuela Técnica Superior de Ingenieros de Caminos, Canales y Puertos, Universidad Politécnica de Madrid
- Mira P., Pastor M., Li T., Liu X., 2003. A New Stabilized Enhanced Strain Element with Equal Order of Interpolation for Soil Consolidation Problems. *Computer Methods In Applied Mechanics And Engineering*, nº 192, p. 4257-4277.
- Mira P., Pastor M., Li T., Liu X., 2004. Failure problems in soils: an enhanced strain coupled formulation with application to localization problems. *Revue Française de Genie Civil*, vol. 8, nº 5-6, p. 735-759.
- Mira P., Tonni L., Pastor M., Fernandez-Merodo J.A., 2009. A generalized midpoint algorithm for the integration of a generalized plasticity model for sands. *International Journal For Numerical Methods In Engineering*, V77(9), pp: 1201-1223.
- Mitchell J., Eden W.J. (1972). Measured movements of clay slopes in the Ottawa area. *Canadian Journal of Earth Sciences*, 9: 1001-1013.
- Montgomery D.R., Dietrich W.E. (1994). A physically based model for the topographic control on shallow landsliding. *Water Resources Research*, 30, 1153-1171.
- Moresi L., Dufour F., Mühlhaus H.-B., 2002. A Lagrangian integration point finite element method for large deformation modeling of viscoelastic geomaterials. *Journal of computational physics*, 184, 476-497.
- Morgenstern, N. (1977). Slopes and excavations in heavily overconsolidated clays. *Proceed. 9th ICSMFE, Tokyo*, 2: 567 -581
- Moriwaki, H., Inokuchi, T., Hattanji, T., Sassa, K., Ochiai, H. and Wang, G. 2004. Failure processes in a full-scale landslide experiment using a rainfall simulator. *Landslides*, 1, 277–288.
- Moser M., Hohensinn F. (1983). Geotechnical aspects of soil slips in alpine regions. *Eng. Geol.*, 19: 185-211.
- Mualem Y. (1976). A new model for predicting the hydraulic conductivity of unsaturated porous media. *Water Resources Research*, 12, pp. 513-522.
- Mueller, R. & Loew, S. 2009. Predisposition and cause of the catastrophic landslides of August 2005 in Brienz (Switzerland). *Swiss Journal of Geosciences* 102(2): 331-344.
- Mühlhaus H.-B., Moresi L., Hoobs B. et al., 2002. Large amplitude folding in finely layered viscoelastic rock structures. *Pure and applied geophysics*, 159, 10, 2311-2333.
- Nadim F., Cepeda J., Sandersen F., Jaedicke C., Heyerdahl H. (2009). Prediction of rainfall-induced landslides through empirical and numerical models. In L. Picarelli, P. Tommasi, G.
-

Urcioli, P. Versace (eds.). First Italian Workshop on Landslides – Rainfall-induced landslides, Naples, June 8-10, 2009. 206-215.

NCG-EPFL : Association technique Norbert, De Cérenville Géotechnique & EPFL pour l'étude du glissement de La Frasse (2004). Glissement de La Frasse, modélisation et étude de faisabilité.

Ng C.W.W. (2008). Deformation and failure mechanisms of loose and dense fill slopes with and without soil nails. *Landslides and Engineered Slopes*, Chen et al. (eds), ISBN 978-0-415-41196-7, 159-177.

Ng C.W.W., Fung W.T., Cheuk C.Y., Zhang L. 2004. Influence of stress ratio and stress path on behaviour of loose decomposed granite. *ASCE Journal of Geotechnical and Geoenvironmental Engineering* 130(1):36–44

Ng C.W.W., Shi Q. (1998) A numerical investigation of the stability of unsaturated soil slopes subjected to transient seepage, *Computers and Geotechnics* 22 (1998) (1), pp. 1–28

Nicot, F. and Wan, R. (Eds) *Micromécanique de la rupture dans les milieux granulaires*, Hermes Science Lavoisier 2008

Nova, R. (1977). On the hardening of soils, *Archiwum Mechaniki Stosowanej*, 29, 445-458.

Nova R., 1988. Sinfonietta Classica: an exercise on classical soil modelling. In *Constitutive equations for granular non-cohesive materials*. A. Saada & G. Bianchini eds, Balkema 501-520.

Nova, R. (1994). Controllability of the incremental response of soil specimens subjected to arbitrary loading programmes. *J. Mech. behav. Mater.* 5 (2), pp. 193–201.

Nova, R., Castellanza, R., Tamagnini, C. (2003). A constitutive model for bonded geomaterials subject to mechanical and/or chemical degradation. *Int. J. Numer. and Anal. Meth. Geomech.*; 27: 705-732.

Noverraz, F., C. Bonnard, L. Huguenin, and H. Dupraz, Grands glissements de versants et climat. *Projet VERSINCLIM, Comportement passé, présent et futur des grands versants instables subactifs en fonction de l'évolution climatique, et évolution en continu des mouvements en profondeur*, in *Rapport final PNR 31*. 1998, FNRS: Berne. p. 314.

Nuth M., Laloui, L., 2008. Advances in modelling hysteretic water retention curve in deformable soils, *Computers and Geotechnics*, vol. 35, num. 6, p. 835-844

Olivares, L., Damiano, E. (2004): Post-failure mechanics of landslides – flowslides in pyroclastic soils. In: Lacerda, W. (ed.), *Proc. Int. Symp. on Landslides*, Rio de Janeiro, Balkema, Rotterdam, 2, 1343–1354.

Olivares L. and Damiano E., 2007. Postfailure mechanics of landslides: laboratory investigation of flowslides in pyroclastic soils. *Journal of geotechnical and geoenvironmental engineering*, ASCE, 133, 1, pp. 51-62.

Olivares L., Damiano E., Greco R., Zeni L., Picarelli L., Minardo A., Guida A., Bernini R., 2009. An instrumented flume to investigate the mechanics of rainfall-induced landslides in unsaturated granular soils. *ASTM Geotechnical Testing Journal* 32, 2, pp 1–11.

- Olivares L., Picarelli, L. (1999). Discussion on “A laboratory study of the strength of four stiff clays” by J.B. Burland, S. Rampello, V.N. Georgiannou & G. Calabresi, *Géotechnique*, 46, 3, pp. 491-514
- Olivares, L., Picarelli, L. (2001): Occurrence of flowslides in soils of pyroclastic origin and considerations for landslide hazard mapping. Proc. 14th South-East Asian Conf., Hong-Kong, 881–886.
- Olivares L. and Picarelli L., 2003. Shallow flowslides triggered by intense rainfalls on natural slopes covered by loose unsaturated pyroclastic soils. *Géotechnique*, vol. 52, 2.
- Olivares, L., Picarelli, L., Andreozzi, L., Avolio, B., Damiano, E., Lampitiello, S. (2002): Scenari di pericolosità di frana in terreni sciolti di natura piroclastica. Proc. XXI Italian Soil Mechanics Conf., L’Aquila, 173–181.
- Olivella S., Carrera J., Gens A., Alonso E.E., 1994. Non-isothermal Multiphase Flow of Brine and Gas through Saline media. *Transport in Porous Media*, 15, 271:293
- Olivella, S., A. Gens, J. Carrera, E. E. Alonso, 1996. Numerical Formulation for a Simulator (CODE_BRIGHT) for the Coupled Analysis of Saline Media. *Engineering Computations*, Vol. 13, No 7, pp: 87-112.
- Onate E. et al., 2008. Advances in the particle finite element method for the analysis of fluid-multibody interaction and bed erosion in free surface flows. *Comput. Methods Appl. Mech. Engrg.*, 197, 1777-1800.
- Pack R.T., Tarboton D.G., Goodwin C.N. (1998). The SINMAP approach to terrain stability mapping. In: *Proceedings of 8th International Congress of the International Association of Engineering Geology and the Environment*, Vancouver, vol 2. Balkema, Rotterdam, pp 1157–1165.
- Pagano L., Picarelli L., Rianna G., Urciuoli G. (2010). A simple numerical procedure for timely prediction of precipitation-induced landslides in unsaturated pyroclastic soils. *Landslides*, 7: 273-289.
- Papa R., Evangelista A., Nicotera M.V. and Urciuoli G., 2008. Mechanical properties of unsaturated pyroclastic soils affected by fast landslide phenomena. In: *Unsaturated Soils: Advances in Geo-Engineering. 1st European Conference on Unsaturated soil*. Durham, UK. 2-4 July 2008 (pp. 917-923). LONDON: Taylor & francis Group plv (UK).
- Papa R., Pirone M., Nicotera M.V., Urciuoli G. (2009). Meccanismi di innesco di colate di fango in piroclastiti parzialmente sature. In: Picarelli L, Tommasi P, Urciuoli G, Versace P (eds), Proc. 1st Italian Workshop on Landslides. Napoli 2: 91–106.
- Pareschi M.T., Favalli M., Giannini F., Sulpizio R., Zanchetta G., Santacroce R. (2000). May 5, 1998, debris flow in circum-Vesuvian areas (southern Italy): insights for hazard assessment. *Geol.* 28(7):639–642.
- Pastor M., Fernandez-Merodo J.A., Gonzalez E., Mira P., L, T., Liu X. (2004). Modelling of landslides: (I). Failure mechanisms. *Degradations and Instabilities in Geomaterials*, CISM Course and Lectures No. 461, Darve F. and Vardoulakis I. (ed.), Springer-Verlag, 287-317.
-

Pastor M., Haddad B., Sorbino G., Cuomo S., Drempetic V. (2008). A depth-integrated, coupled SPH model for flow-like landslides and related phenomena. *International Journal for Numerical and Analytical Methods in Geomechanics*, 33(2): 143-172.

Pastor M., Li T., Liu X., Zienkiewicz O.C., 1999b. Stabilized low order finite elements for failure and localization problems in undrained soils and foundations, *Computer Methods In Applied Mechanics And Engineering*, n° 174, p. 219-234.

Pastor M., Mira P., Fernandez-Merodo J. A., 2002. Practical aspects of the finite element method. In: *Numerical modelling in geomechanics*, M. Pastor & C. Tamagnini, eds., *Revue francaise de génie civil*, Hermes Science Publications, p. 1147-1168.

Pastor, M., Quecedo, M., González, E., Herreros, I., Fernández Merodo, J.A and Mira, P., *Modelling of landslides: (II) Propagation*. in F.Darve and I.Vardoulakis (Eds), *Degradations and Instabilities in Geomaterials*, Springer Wien New York, 319-367 (2004)

Pastor, M., Quecedo, M., Merodo, J.A.F., Herreros, M.I., Gonzalez, E., Mira, P.: *Modelling tailings dams and mine waste dumps failures*. *Géotechnique* 52(8), 579-591 (2002).

Pastor M., Quecedo M., Zienkiewicz O.C., 1997. A mixed displacement-pressure formulation for numerical analysis of plastic failure. *Computers and Structures*, n°62, p.13-23.

Pastor, M., Zienkiewicz, O.C.: *A Generalized Plasticity, Hierarchical Model for Sand under Monotonic and Cyclic Loading*. In 2nd International Symposium on Numerical Models in Geomechanic, Ghent, 131-149 (1986).

Pastor M., Zienkiewicz O.C., Chan A.H.C., 1990. Generalized plasticity and the modelling of soils behaviour. *International Journal for Numerical and Analytical Methods in Geomechanics*, n° 14, p. 151-190.

Pastor, M., Zienkiewicz, O.C., Leung, K.H.: *Simple Model for Transient Soil Loading in Earthquake Analysis. II: Non-Associative Models for Sands*. *International Journal for Numerical and Analytical Methods in Geomechanics* 9, 477-498 (1985b).

Pastor M., Zienkiewicz O.C., Li T., Xiaoqing L., Huang M., 1999a. Stabilized Finite Elements with Equal Order of Interpolation for Soil Dynamics Problems. *Archives of Computational Methods in Engineering*, vol 6, n° 1, p. 3-33.

Pastor, M., Quecedo, M., Merodo, J.A.F., Herreros, M.I., Gonzalez, E., Mira, P.: *Modelling tailings dams and mine waste dumps failures*. *Géotechnique* 52(8), 579-591 (2002).

Pellegrino, A., Picarelli, L., Urciuoli, G. (2004): *Experiences of mudslides in Italy*. In: Picarelli, L. (ed.), *Proc. Int. Work. on Mechanisms and Occurrence of Flow-Like Landslides in Natural Slopes and Earthfills*, Sorrento, Patron, Bologna, 191–206.

Perzyna J.K., 1966. *Fundamental problems in viscoplasticity*. *Adv. Appl. Math.* 9, 243–377.

Picarelli L. (1986). *Caratterizzazione geotecnica dei terreni strutturalmente complessi nei problemi di stabilità dei pendii*. *Proceed. 16th Conv. Italiano di Geotecnica*, Bologna, 3: 155-169.

Picarelli, L. 1988. *Modellazione e monitoraggio di una colata in formazioni strutturalmente complesse*. *Proc. Conf. Cartografia e Monitoraggio dei Movimenti Franosi*, Bologna, L. Cascini Ed., 2: 119-130.

Picarelli L. (1991). Discussion on: The general and congruent effects of structure in natural soils and weak rocks, by Leroueil S. and Vaughan P.R.. *Géotechnique*, v. 3, 281-284.

Picarelli L. (2001). Transition from slide to earthflow, and the reverse. Proc. Conference on Transition from Slide to Flow – Mechanisms and Remedial Measures, Karadeniz Technical University, Trabzon.

Picarelli, L., Deangeli, C., Olivares, L. (2003): Fenomeni di frana e di flusso nei terreni. *Conferenze di Geotecnica Monregalesi*.

Picarelli L., Evangelista A., Rolandi G., Paone A., Nicotera M.V., Olivares L., Scotto di Santolo A., Lampitiello S., Rolandi M. (2006). Mechanical properties of pyroclastic soils in Campania Region. Proc. Int. Symp. Characterisation and Engineering Properties of Natural Soils, Taylor and Francis, London (2006): 2331–2384.

Picarelli, L., Mandolini, A., Russo, C. 1999. Long-term movements of an earthflow in tectonized clay shales. Proc. Int. Symp. Slope Stability Engineering: Geotechnical and Geoenvironmental aspects, Matsuyama, 2: 1151-1158

Picarelli, L., Napoli, V. 2003. Some features of two large earthflows in intensely fissured tectonized clay shales and criteria for risk mitigation. Proc. Int. Conf. Fast Slope Movements – Prediction and Prevention for Risk Mitigation, Napoli, L. Picarelli Ed., Patron, Bologna, 1: 431-438

Picarelli L., Olivares L., Comegna L., Damiano E., 2008. Mechanical aspects of flow-like movements in granular and fine-grained soils. *Rock mechanics and rock engineering* 41, 1, pp.179-197.

Picarelli L., Olivares L., Di Maio C., Silvestri F., Di Nocera S., Urciuoli G.. 2002. Structure, properties and mechanical behaviour of the highly plastic intensely fissured Bisaccia Clay Shale. Proc.int. symp. on “Characterisation and Engineering Properties of Natural Soils”, Singapore, edited by: Tan, T. S., Phoon, K. K., Hight, D. W., and Leroueil, S., 2, 947–962, 2002.

Picarelli L, Russo C (2004) Remarks on the mechanics of slow active landslides and the interaction with man-made works. In: Lacerda W (ed) Proceedings of the 9th international symposium on landslides, Rio de Janeiro, vol 2. pp 1141–1176.

Picarelli, L., Urciuoli, G., Ramondini, M., Comegna, L. (2005): Main features of mudslides in tectonized highly fissured clay shales”. *Landslides – Journal of the International Consortium on Landslides*, 2 (1), April 2005, pp. 15-30. Springer-Verlag.

Picarelli L., Urciuoli G., Russo C. (2000). Mechanics of slope deformation and rupture in stiff clays and clay shales as a consequence of cycling pore pressures. Proc. 8th Int. Symp. on Landslides, Cardiff.

PLANAT. 2000. Ursachenanalyse der Hanginstabilitäten 1999. *Bull. Angew. Geol.* 5(1) (in German).

PLANCHAT J. (2009). La Frasse landslide (CH): analysis of the hydro-mechanical behavior of the instability and of the associated risks. Master Thesis in Civil Engineering, Ecole Polytechnique Fédérale de Lausanne, Lausanne, 124 pages.

PLANCHAT J., BONNARD Ch., PERON H., LALOUI L. (2009). After 10'000 years of movement, is the La Frasse landslide stabilized ? Numerical modeling of the crises of a large landslide and of its mitigation measures. In E. Alonso, J. Corominas, and M. Hürlimann, editors, proceedings of the VII Simposio Nacional sobre Taludes y Laderas Inestables, volume 1, pages 95-126, Barcelona, 2009. CIMNE.

Plaxis 2D, Version 8 (2006). Finite Element Code and User Manual.

Popescu M. E. (2001) "Landslide causal factors and landslide remedial options", IAEG Bulletin, pp. 1-21;

Potts D.M., Kovacevic N., Vaughan P.R., 1997. Delayed collapse of cut slopes in stiff clay. *Géotechnique* 47, n° 5, 953-982.

Quecedo, M. , Pastor, M. and Herreros, I., "Numerical modelling of impulse wave generated by fast landslides", *Int. J. Num. Meth. Eng.*, 59: 1633-1656 (2004)

Rahardjo H., Li X.W., Toll D.G., Leong E.C. (2001). The effect of antecedent rainfall on slope stability. *Geotechnical and Geological Engineering*, 19: 371–399.

Rahardjo, H., T.H. Ong, R.B. Rezaur, and E.C. Leong, Factors controlling instability of homogeneous soil slopes under rainfall. *Journal of Geotechnical and Geoenvironmental Engineering*, 2007. 133(12): p. 1532-1543.

Reid, M.E. (1997). Slope instability caused by small variations in hydraulic conductivity. *Journal of Geotechnical and Geoenvironmental Engineering*, ASCE, 123: 717–725.

Reynolds, O. 1886. Dilatancy, *Nature*, v.33 p.429-430.

Roscoe, K.H., Burland, J.B. (1968). On the generalized stress–strain behaviour of 'wet' clay. In *Engineering plasticity* (eds J. Heyman and F. A. Leckie); pp. 535–609. Cambridge: Cambridge University Press.

Roscoe K.H. and Poorooshasb, H.B. "A fundamental principle of similarity in model tests for earth pressure problems", *Conf. Asiaticque Mécanique des Sols*, Vol 1., 134-140 (1963)

Rulon J.J., Freeze R.A. (1985). Multiple seepage faces on layered slopes and their implications for slope-stability analysis. *Canadian Geotechnical Journal*, 22(3): 347–356.

Salciarini D., Godt J.W., Savage W.Z., Conversini P., Baum R.L., Michael J.A. (2006). Modeling regional initiation of rainfall-induced shallow landslides in the eastern Umbria region of central Italy. *Landslides* 3:181–194

Sanchez, M., Gens, A., Guimaraes, L., Olivella, S. (2005). A double structure generalized plasticity model for expansive materials, *Int. J. Numer. and Anal. Meth. Geomech*; 29: 751–787.

Santacana N., Baeza B., Corominas J., De Paz A., Marturiá J. (2003). A GISBased Multivariate Statistical Analysis for Shallow Landslide Susceptibility Mapping in LaPobla de Lillet Area (Eastern Pyrenees, Spain). *Natural Hazards*, 30:281–295.

Sassa, K. 1972. Analysis on slope stability: I. Mainly on the basis of the indoor experiments using the standard sand produced in Toyoura, Japan. *Journal of the Japan Society of Erosion Control Engineering* 25 (2), 5 –17 (in Japanese with English abstract).

- Sassa, K. 1974. Analysis on slope stability: II. Mainly on the basis of the indoor experiments using the standard sand produced in Toyoura, Japan. *Journal of the Japan Society of Erosion Control Engineering* 26 (3), 8–19 (in Japanese with English abstract).
- Sassa, K. 1984. The mechanism starting liquefied landslides and debris flows. *Proceedings of 4th International Symposium on Landslides, Toronto, Canada, vol. 2*, pp. 349–354.
- Sassa, K. 1996. Prediction of earthquake induced landslides. *Special Lecture of 7th International Symposium on Landslides, "Landslides"*, vol. 1, pp. 115–132.
- Sassa, K. 1998a. Recent urban landslide disasters in Japan and their mechanisms. *Proc. 2nd International Conference on Environmental Management, "Environmental Management"*, vol. 1, pp. 47–58.
- Sassa, K. 1998b. Mechanisms of landslide triggered debris flow. In: Sassa, K. (Ed.), *"Environmental Forest Science"*. *Proceedings of IUFRO Div. 8 Conference*. Kluwer Academic Publishing, Kyoto, pp. 471–490.
- Sassa, K. (2000). Mechanisms of flows in granular soils. *Int. Conf. Geotechnical and Geological Engineering GEOENG2000: 1671-1702*
- Sassa, K., Takei, A. 1977. Consider vertical subsidence in slope unstabilization: I. Stress fall phenomenon and bearing power of the sides. *Journal of Japan Landslide Society* 14 (2), 19–26 (in Japanese with English abstract).
- Savage W.Z., Godt J.W., Baum R.L. (2004). Modeling time-dependent areal slope stability. In: Lacerda, W.A., Erlich, M., Fontoura, S.A.B., Sayao, A.S.F., (eds.). *Landslides – Evaluation and Stabilization. Proceedings of the 9th International Symposium on Landslides*. Rotterdam: Balkema, 1, 23-36.
- Savage, S.B. and Hutter, K. "The dynamics of avalanches of granular materials from initiation to runout. Part I: Analysis". *Acta Mechanica* 86 201 – 223 (1991)
- Schmid, F., Fraefel, M. & Hegg, C. 2004. Unwetterschäden in der Schweiz 1972-2002: Verteilung, Ursachen, Entwicklung. *Wasser Energ. Luft* 96, 1/2: 21-28.
- Schneider, L. and Hutter, K., *Solid-Fluid Mixtures of Frictional Materials in Geophysical Context based on a concise thermodynamic analysis*, *Advances in Geophysical and Environmental Mechanics and Mathematics Series*, Springer (2009, to appear)
- Schofield, A.N., Wroth, C.P. (1968). *Critical state soil mechanics*. McGraw-Hill, New York.
- Seed, H.B. and Lee, K.H. "Undrained strength characteristics of cohesionless soils", *J. Soil Mech. and Found. Div.*, *Proc. ASCE*, 93,6, 333-360 (1967)
- Semadeni-Davies A. (1997). Monthly snowmelt modelling for large-scale climate change studies using the degree day approach. *Ecological Modelling*, 101, 303-323.
- Sheng, D.C., Sloan, S.W., Gens, A. (2004). A constitutive model for unsaturated soils: thermomechanical and algorithmic aspects. *Computational Mechanics*; 33: 453-465.
- Sica C. (2008). *Modelling the triggering of flow-type slope movements over large areas: limitations and potential of distributed physically based models*. PhD Thesis, University of Salerno, 226 pp..
-

Silvis, F., de Groot, M. B. (1995): Flow Slides in the Netherlands: experience and engineering practice. *Can. Geotech. J.* 32, 1086–1092.

Simeoni L. (1998). Fenomeni di scivolamento planare nelle Langhe, PhD Thesis, Politecnico di Torino

Simo J.C., Rifai M.S., 1990. A Class Of Mixed Assumed Strain Methods And The Method Of Incompatible Modes. *International Journal For Numerical Methods In Engineering*, V 29(8), pp. 1595-1638.

Sivakumar, V.. “A critical state framework for unsaturated soil”. PhD Thesis Department of Civil and Structural Engineering, University of Sheffield, (1993).

Skempton A. W., Hutchinson J. N. (1969) “Stability of Natural Slopes and Embankment Foundations”, 7th International Conference Soil Mechanics and Foundations Engineering, Mexico, State-of-the-Art Volume, , pp.291-340;

Skempton A.W., Petley D.J. (1967). The strength along structural discontinuities in stiff clays. *Proc. Geot. Conference, Oslo, NGI*, 2: 55-69.

Soeters R., van Westen C. J. (1996). Slope instability recognition, analysis and zonation. *Landslides, Investigation and Mitigation*, edited by A. K. Turner and R. L. Schuster, *Transp. Res. Board Spec. Rep. 247, Natl. Acad. Press, Washington, D. C.*, pp. 129–177.

Sorbino G. (1994). Il regime delle acque sotterranee nelle rocce metamorfiche alterate. Ph.D thesis, Universities of Rome “La Sapienza” and Naples “Federico II”, Rome. [In Italian.]

Sorbino G. (1995). Unsaturated hydraulic characteristics of weathered gneissic soils. In *Proceedings of the 10th Panamerican Conference on Soil Mechanics and Foundation Engineering*, 25–28 October 1995, Guadalajara, Mexico. Mexican Society of Soil Mechanics, Mexico City. pp. 25–35.

Sorbino, G., Foresta, V. (2002). Unsaturated hydraulic characteristics of pyroclastic soils. In: *Proc. 3rd International Conference on Unsaturated Soils, Recife (Brasil)*. Balkema, 1, 405 – 410.

Sorbino G., Sica C., Cascini L. (2009). Susceptibility analysis of shallow landslides source areas using physically based models. *Natural Hazards*, DOI 10.1007/s11069-009-9431-y.

Sorbino G., Sica C., Cascini L. (2010). Susceptibility analysis of shallow landslides source areas using physically based models. *Natural Hazards*, DOI 10.1007/s11069-009-9431-y.

Sorbino G., Sica C., Cascini L., Cuomo S. (2007). On the forecasting of flowslides triggering areas using physically based models. In: V.R. Schuster, R.L. Schuster, A.K. Turner (eds.). *Proc. of the 1st North American Landslide Conference (Vail, Colorado)*. AEG Publication n. 23. ISBN 978-0-975-4295-3-2.

Spence, K.J., Guymer, I. 1997. Small-scale laboratory flowslides. *Geotechnique* 47 (5), 915–932.

Srivastava R., Yeh T-C.J. (1991). Analytical solutions for one-dimensional, transient infiltration toward the water table in homogeneous and layered soils. *Water Resour. Res.* 27:753–762

Sulsky, D., Z. Chen, & H. L. Schreyer. (1994). A Particle Method for History-Dependent Materials. *Computer Methods in Applied Mechanics and Engineering*. 118(1), pp 179-96.

Sulsky D, Zhou S-J & Schreyer HL, (1995) "Application of a particle-in-cell method to solid mechanics", *Computer Physics Communications*; 87: 236-252.

Sulsky, D. & H. L. Schreyer. (1996). Axisymmetric Form of the Material Point Method with Applications to Upsetting and Taylor Impact Problems. *Computer Methods in Applied Mechanics and Engineering*. 139(1), 409-29.

Surdeanu V. (1998) "The geography of weathered terrains. I. Landslides", Clujeană Univ. Press, Cluj-Napoca (rom);

TACHER L., BONNARD Ch., LALOU L., PARRIAUX A. (2005). Modelling the behaviour of a large landslide with respect to hydrogeological and geomechanical parameter heterogeneity. *Landslides*, volume 2, pages 3-24.

Take WA, Bolton MD. 2002. An atmospheric chamber for the investigation of the effect of seasonal moisture changes on clay slopes, *Proceedings of the International Conference on Physical Modelling in Geotechnics—ICPMG_02*, pp 765–770

Take W.A., Bolton M.D., Wong P.C.P. and Yeung F.J. (2004). Evaluation of landslide triggering mechanisms in model fill slopes. *Landslides*, 1, 173-184.

Tamagnini, R. (2004). An extended Cam-clay model for unsaturated soils with hydraulic hysteresis. *Géotechnique*; 54(3): 223–228.

Tamagnini C., Castellanza R., Nova R., 2002. A generalized backward Euler algorithm for the numerical integration of an isotropic hardening elastoplastic model for mechanical and chemical degradation of bonded geomaterials. *International Journal For Numerical And Analytical Methods In Geomechanics*, V26(10), pp. 963-1004.

Tamagnini R., Pastor M., 2004. A thermodynamically based model for unsaturated soils: a new framework for generalized plasticity. *Proceedings of the Second International Workshop on Unsaturated Soils, Capri - Italie, Juin 2004*.

Tarantino A., Bosco G. (2000). Role of soil suction in understanding the triggering mechanisms of flow slides associated with rainfall. In G.F. Wieczorek & N.D. Naeser (eds.), *Debris-Flow Hazard Mitigation, Second International Conference on debris-flow hazards mitigation*, Taipei, Taiwan: 81-88. Rotterdam: A.A. Balkema.

Tarantino and Mongiovi (2003). Numerical modelling of shallow landslides triggered by rainfall. In L. Picarelli (ed.). *International Conference on Fast slope movements – prediction and prevention for risk mitigation*, Naples, May 11-13, 2003, 491-495.

Tavenas F., Leroueil S. (1981). Creep and failure of slopes in clay. *Canadian Geotechnical Journal*, 18: 106-120.

Taylor RN. 1995. Centrifuges in modelling: principles and scale effects. *Geotechnical Centrifuge Technology*

Ter-Stepanian G., Sergeev V., Avdjian A. (1968). Experience on the study of slow earthflows in Sochi. *Problems of Geomechanics*, Yerevan, 2, 76-83.

Terzaghi, K. 1950. Mechanism of landslides. In: Paige, S. (Ed.), *Application of Geology to Engineering Practice (Berkey Volume)*. Geological Society of America, New York, pp. 83–123.

Tommasi P., Pellegrini P., Boldini D., Ribacchi R. (2006). Influence of rainfall regime on hydraulic conditions and movement rates in the overconsolidated clayey slope of the Orvieto hill (central Italy). *Canadian Geotechnical Journal*, 43:70-86.

Tonni L., 2002. Modellazione numerica del comportamento di terreni granulari con la Plasticità Generalizzata. Ph.D Thesis. Politecnico di Torino (Italy).

Topor N. (1964) "Rainy and droughty years in R.P.R", IMH, Bucharest (rom);

Tsai T.L., Chen H.E., Yang J.C. (2007). Numerical modeling of rainstorm-induced shallow landslides in saturated and unsaturated soils. *Environmental Geology*. 55(6), 1269-1277.

Tsaparas, I., H. Rahardjo, D.G. Toll, and E.C. Leong, Controlling parameters for rainfall-induced landslides. *Computers And Geotechnics*, 2002. 29(1): p. 1-27.

UPC, 2009. CODE BRIGHT, A 3-D program for thermo-hydro-mechanical analysis in geological media. USER'S GUIDE, 2002.

Uriel, A.O. and Merino, M. "Harmonic response of sands in shear", Third Int. Conf. on Num. Methods Geomechanics, Aachen, 2-6, 1979

Uriel, A.O. Discussion to Spec. Session 2, Problems of non linear soil mechanics, Proc. 8th Int. Conf. Soil. Mech. Found. Eng. Moscow, Vol.4.3, 78-80, 1973

USACE U.S. Army Corps of Engineers (1998). Runoff from snowmelt, Engineer Manual 1110-2-1406, 31 March 1998.

van Genuchten, M. Th., 1980. A closed-form equation for predicting the hydraulic conductivity of unsaturated soils, *Soil Sci. Soc. Am. J.* 44:892-898

van Westen C.J. (2000). The modelling of landslide hazard using GIS. *Surveys in Geophysics* 21, pp. 241 – 255.

van Westen C.J. (2004). Geo-Information tools for landslide risk assessment: an overview of recent developments. *Landslides: Evaluation and Stabilization*, Lacerda, Ehrlich, Fontoura & Sayao (eds), 2, pp. 39 – 56.

Varnes D.J. (1978). Slope movement: types and processes. *Landslide – Analysis and Control*, Report 176, Transportation Research Board, 11-33.

Vassallo R., Di Maio C. (2006). La frana di Costa della Gaveta a Potenza: analisi preliminare. Proc. Incontro Annuale dei Ricercatori di Geotecnica 2006, Pisa, 26-28 Giugno 2006

Vassallo R., Di Maio C. (2007). La frana di Costa della Gaveta a Potenza. Proc. Incontro Annuale dei Ricercatori di Geotecnica 2006, Salerno, 4-6 Luglio 2007

Vassallo R., Di Maio C. (2008). Misure di spostamenti superficiali e profondi in un versante argilloso in frana. Proc. Incontro Annuale dei Ricercatori di Geotecnica 2008, Catania, 15-17 Settembre 2008.

Vaunat, J., Gens, A., Pontes Filho, I.D.S. (2002). Application of Localization Concepts to Discontinuous Water Content Patterns in Unsaturated Media. Eighth International

Symposium on Numerical Models in Geomechanics - NUMOG VIII, Roma. Lisse: Swets & Zeitlinger. v. 01. p. 179-184.

Vaunat J., Leroueil S., Faure R. (1994). Slope movements: a geotechnical perspective. Proc. 7th IAEG Congress, Lisboa: 397-404

Vaunat, J., Romero, E., Jommi, C. (2000). An elastoplastic hydromechanical model for unsaturated soils. Experimental Evidence and Theoretical Approaches in Unsaturated Soils; Proceedings of the International Workshop on Unsaturated soils, Trento; 121–138.

Vermeer P. A., Beuth L. & Benz T. A. (2008) Quasi-Static Method for Large Deformation Problems in Geomechanics The 12th International Conference of International Association for Computer Methods and Advances in Geomechanics (IACMAG) Goa, India

Walker, B.F., Blong, R.J. & McGregor, J.P. (1987). Landslide classification, geomorphology and site investigations. Soil Slope Instability.

Wan, R. G. & Guo P. J. "A simple Constitutive Model for Granular Soils: Modified Stress-Dilatancy Approach", Computers and Geotechnics, 22(2), 109-133 (1998).

Wang, G., Sassa, K. 2001. Factors affecting rainfall-induced flowslides in laboratory flume tests. *Geotechnique* 51 (7), 587–599.

Wang G., Sassa K. (2003) "Pore-Pressure Generation and Movement of Rainfall-Induced Landslides: Effects of Grain-Size and Fine-Particle Content", *Engineering Geology*, Volume 69, Issues 1-2, April, pp.109-125;

Wheeler, S.J., Sharma, R.S., Buisson, M.S.R. (2003). Coupling of hydraulic hysteresis and stress–strain behaviour in unsaturated soils. *Géotechnique*; 53(2): 41-54.

Wheeler, S.J., Sivakumar, V. (1995). An elasto-plastic critical state framework for unsaturated soil. *Géotechnique*; 45(1): 35-53.

White DJ, Take WA, Bolton MD. 2003. Soil deformation measurement using particle image velocimetry (PIV) and photogrammetry, *Geotechnique* 53:619–631

Więckowski Z., Youn S.K., Yeon Y.H. 1999. A particle-in-cell solution to the silo discharging problem. *Int. J. Numer. Meth. Engng.*, 45, 1203-1225.

Wieczorek G.F., (1996) Landslide Triggering Mechanisms in A. T. Turner and R.L. Schuster (editors) *Landslides Investigation and Mitigation*. Transportation Research Board, National Research Board, Special Report 247.

Wilson J.P., Gallant J.C. (2000). Primary topographic attributes, in Wilson, J.P., and Gallant, J.C., eds., *Terrain Analysis: Principles and Applications*: John Wiley and Sons, New York, pp. 51-76.

Wilson, G.W., 1990. Soil evaporative fluxes for Geotechnical Engineering Problems. PhD Thesis, University of Saskatchewan, Saskatoon, Canada.

Wroth, C.P. and Bassett, N "A stress-strain relationship for the shearing behaviour of sand", *Géotechnique* 15, 32-56, 1965

Wu W., Sidle R.C. (1995). A distributed slope stability model for steep forested basins. *Water Resour. Res.*, 602 31:2097–2110.

Yeung, F.J. 2002. Modelling of the behaviour of saprolitic slopes under severe rainfall. MPhil Dissertation: University of Cambridge.

Zace Ltd., 2003. Z_Soil.PC_3D, Finite Element Code and User Manual.

Zace Services Ltd., (2009). Z_Soil 2D, Version 9, Finite Element Code and User Manual.

Zhou, S., Stormont J. & Chen Z. (1999). Simulation of Geomembrane Response to Settlement in Landfills by using the Material Point Method. International Journal for Numerical and Analytical Methods in Geomechanics. 23(15), 1977-1994.

Zienkiewicz O.C., Chang C.T., Bettess P. (1980). Drained, undrained, consolidating dynamic behaviour assumptions in soils. Geotechnique, 30, 385-395.

Zienkiewicz O. C., Chan A. H. C., Pastor M., Schrefler B. A., Shiomi T., 1999. Computational geomechanics, with special reference to earthquake engineering. John Wiley & Sons Ltd.

Zienkiewicz OC, Humpheson C, Lewis RW (1975). Associated and non-associated viscoplasticity and plasticity in soil mechanics. Geotechnique 25(4): 671-689.

Zienkiewicz, O.C., Leung, K.H., Pastor, M.: Simple Model for Transient Soil Loading in Earthquake Analysis. I: Basic Model and its Application. International Journal for Numerical and Analytical Methods in Geomechanics 9, 453-476 (1985a).

Zienkiewicz, O.C., Mroz, Z.: Generalized plasticity formulation and applications to geomechanics. In Mechanics of Engineering Materials, Desai CS and Gallagher RH (eds). John Wiley & Sons, 655-679 (1984).

Zienkiewicz, O.C., Shiomi, T.: Dynamic behaviour of saturated porous-media – The generalized Biot formulation and its numerical solution. International journal for numerical and analytical methods in geomechanics 8(1), 71-96 (1984)